Lecture Notes in Civil Engineering

Vallam Sundar ·
S. A. Sannasiraj · V. Sriram ·
Manta Devi Nowbuth *Editors*

Proceedings of the Fifth International Conference in Ocean Engineering (ICOE2019)

Springer

Lecture Notes in Civil Engineering

Volume 106

Lecture Notes in Civil Engineering (LNCE) publishes the latest developments in Civil Engineering - quickly, informally and in top quality. Though original research reported in proceedings and post-proceedings represents the core of LNCE, edited volumes of exceptionally high quality and interest may also be considered for publication. Volumes published in LNCE embrace all aspects and subfields of, as well as new challenges in, Civil Engineering. Topics in the series include:

- Construction and Structural Mechanics
- Building Materials
- Concrete, Steel and Timber Structures
- Geotechnical Engineering
- Earthquake Engineering
- Coastal Engineering
- Ocean and Offshore Engineering; Ships and Floating Structures
- Hydraulics, Hydrology and Water Resources Engineering
- Environmental Engineering and Sustainability
- Structural Health and Monitoring
- Surveying and Geographical Information Systems
- Indoor Environments
- Transportation and Traffic
- Risk Analysis
- Safety and Security

To submit a proposal or request further information, please contact the appropriate Springer Editor:

– Mr. Pierpaolo Riva at pierpaolo.riva@springer.com (Europe and Americas);
– Ms. Swati Meherishi at swati.meherishi@springer.com (Asia - except China, and Australia, New Zealand);
– Dr. Mengchu Huang at mengchu.huang@springer.com (China).

All books in the series now indexed by Scopus and EI Compendex database!

More information about this series at http://www.springer.com/series/15087

Vallam Sundar · S. A. Sannasiraj ·
V. Sriram · Manta Devi Nowbuth
Editors

Proceedings of the Fifth International Conference in Ocean Engineering (ICOE2019)

Springer

Editors
Vallam Sundar
Department of Ocean Engineering
Indian Institute of Technology Madras
Chennai, Tamil Nadu, India

S. A. Sannasiraj
Department of Ocean Engineering
Indian Institute of Technology Madras
Chennai, Tamil Nadu, India

V. Sriram
Department of Ocean Engineering
Indian Institute of Technology Madras
Chennai, Tamil Nadu, India

Manta Devi Nowbuth
Department of Civil Engineering
University of Mauritius
Reduit, Mauritius

ISSN 2366-2557 ISSN 2366-2565 (electronic)
Lecture Notes in Civil Engineering
ISBN 978-981-15-8505-0 ISBN 978-981-15-8506-7 (eBook)
https://doi.org/10.1007/978-981-15-8506-7

This Springer imprint is published by the registered company Springer Nature Singapore Pte Ltd.
The registered company address is: 152 Beach Road, #21-01/04 Gateway East, Singapore 189721, Singapore

Advisory Committee

Professor Bhaskar Ramamurthi	India
Professor S. A. Sannasiraj	India
Professor V. N. Atri	Mauritius
Associate Professor S. Rosunee	Mauritius
Associate Professor T. Juwaheer	Mauritius
Dr. R. Badal	Mauritius
Dr. K. R. Moothien Pillay (Mrs)	Mauritius
Mr A. Donat	Mauritius
Professor V. Sundar	India

Scientific Committee

Professor R. Sundaravadivelu	India
Professor P. Ananthakrishnan	India
Professor Qingwei M. A.	UK
Professor Kyung-Duck Suh	Korea
Professor H. Schüttrumpf	Germany
Professor F. Arena	Italy
Professor D. Wan	China
Professor J. Wijetunga	Sri Lanka
Professor P. Fröhle	Germany
Professor M. Dhanak	USA
Professor Z. Huang	USA
Professor P. Lin	China
Professor A. Law	Singapore
Professor R. Manasseh	Australia
Professor Hitoshi Tanaka	Japan
Dr. P. Khedun	USA
Dr. H. Khedun	USA

Dr. K. Gopal	USA
Prof. E. Pelinovsky	Russia
Professor M. C. Deo	India
Professor D. E. Reeve	UK
Professor S. C. Yim	USA
Professor D. Greaves	UK
Mr. P. McKivergan	South Africa
Dr. M. D. Nowbuth	Mauritius
Dr. D. Surroop	Mauritius

Composition of the Joint Organising Committee (JOC)

Professor A. S. Sannasiraj	IITM
Professor V. Sundar	IITM
Dr. (Ms) Manta Devi Nowbuth	UoM

Composition of the Local Organising Committee (LOC)

Dr. M. D. Nowbuth	UoM
Dr. S. Rosunee	UoM
Mr. Nuvin Khedah	Ministry of Social Security, National Solidarity, and Environment and Sustainable Development (Environment and Sustainable Development Division)
Mr. A. Jheengut	Ministry of Social Security, National Solidarity, and Environment and Sustainable Development (Environment and Sustainable Development Division)
Mrs. Cyparsade	National Disaster Risk Reduction Management Centre (NDRRMC)
Captain M. Babooa	Mauritius Shipping Cooperation, Ltd
Mrs. Y. Basant Rai	Ministry of Ocean Economy, Marine Resources, Fisheries & Shipping (Albion Fisheries Training Centre)
Dr. M. Singh	Mauritius Oceanography Institute
Mr. H. Multra	Ministry of Energy and Public Utilities
Captain L. B. Barbeau	Mauritius Ports Authority
Mrs. K. Manna	Ministry of Industry, Commerce & Consumer Protection (Industry Division)
Dr. H. Runghen	Ministry of Defense (Continental Shelf)
Captain Rahul Batiah	Hydrography Unit, Ministry of Housing & Lands
Mr. R. Ramdhan	Ministry of Public Utilities & Land Transport
Mrs. Reshma Rughooputh	UoM

Mrs. Yashwaree Baguant Moonshiram	UoM
Mr. Asish Seeboo	UoM
Mr. D. Jogee	UoM
Mr. L. Sanassee	UoM
Dr. A. Khoodoruth	UoM
Dr. B. Rajkumarsingh	UoM

Composition of the Technical Programme Committee (TPC)

Dr. P. Krishnankutty	IITM, India
Dr. K. Murali	IITM, India
Dr. V. Sriram	IITM, India
Dr. Nilanjan Saha	IITM, India

Composition of the Financial Sub-committee (FSC)

Mrs. Yashwaree Baguant Moonshiram	UoM
Mr. Devkumar Callychurn	UoM

Composition of the Publicity and Sponsorship Sub-committee (FSC)

Mr. Asish Seeboo	UoM
Mr. Deejaysing Jogee	UoM

Preface

The Fifth International Conference in Ocean Engineering (ICOE2019) is organised by the Department of Ocean Engineering, Indian Institute of Technology Madras (IITM), jointly with the Department of Civil Engineering, University of Mauritius. This is the first time that ICOE is being held outside India for which Mauritius has been chosen as the venue given its close link to India and its upcoming development of the ocean economy.

The Department of Ocean Engineering, IITM, has achieved significant success with its dynamic profile in terms of training graduate and postgraduate professionals for careers around the globe. The department is a centre of excellence in disciplines spanning across the areas of ship design, coastal, ocean, ports and harbour engineering, deep-water technologies, marine geo-techniques, energy and areas in oil and gas. The department organised its flagship conference ICOE in 1996, 2001, 2009 and 2018. This conference is aimed at bringing experts in the field to interact with young researchers. The University of Mauritius has over the last 50 years been addressing capacity building for a purpose that of supporting developmental areas in the marine sector in particular for the country. Ocean economy is the new upcoming area of development for the country and the university is working with international partners to support the said development.

The theme of the conference is '***Ocean Engineering—Towards achieving Sustainable Development Goals***'. Ocean resources and its environment contribute significantly to the global community. As demand for resources increases and land resources getting depleted, development in the ocean sector has been increasing at a rapid rate. The ocean resources in abundance can bring along opportunities to address pertinent issues such as food, water security and social welfare, with technology being the key to sustainable development of the resources.

The technical programme of the conference has been carefully planned with eight keynote addresses by experts from Japan, Germany, France, UK, India and Mauritius. Seventy experts contributed papers and special sessions in coastal engineering and processes, ports and harbour, numerical modelling, offshore structures, climate change, numerical algorithms in ocean engineering, petroleum

engineering and floating bodies. All the papers accepted in this conference have been reviewed by experts in the procedure of blind peer review.

We would like to thank the members of the advisory committee, international steering committee, local organising committee and the reviewers, who have greatly contributed to the improvement of the quality of papers, providing constructive critical comments, corrections and suggestions to the authors. Finally, we, the editors, wish to thank all the authors who submitted papers, making this conference possible. It is the quality of their contributions and presentations that have contributed to the success of the ICOE2019 conference. We would like to thank Springer and their editorial team for publishing our ICOE conference series.

Chennai, India — Vallam Sundar
Chennai, India — S. A. Sannasiraj
Chennai, India — V. Sriram
Reduit, Mauritius — Manta Devi Nowbuth

Contents

About the Editors

Dr. Vallam Sundar is a Professor in Department of Ocean Engineering, IIT Madras. Prof. Sundar has supervised more than 20 Ph.D. theses. He has about 450 publications in conferences and journals to his credit. He is a member of the editorial board for 10 international journals and has reviewed a number technical papers submitted to peer reviewed journals. He was bestowed with the prestigious honorary doctorate award by University of Wuppertal, Germany. Recognizing his contributions to the field of Coastal Engineering, The International Association for Hydro-Environment Engineering and Research, IAHR, elected him as Chairman of its Asia Pacific division in 2006. His reports on the master plan for the two maritime states, Tamil Nadu and Kerala in connection with coastal protection including the important socio economic aspects and tsunami mitigation measures remain as the basic document for their planning and implementation by the respective state governments.

Dr. S. A. Sannasiraj is a Professor and Head of the Department of Ocean Engineering, IIT Madras. He has more than 100 publications in leading journals and conferences. He received the Indian Maritime Award, Endeavour India Executive award (from Australian Government) and Fulbright Nehru Senior Research fellowship. He works on the area of wind-wave assimilation, experimental modelling of coastal structures and has completed about 50 coastal protection design works in and around India.

Dr. V. Sriram is an Associate Professor in the Department of Ocean Engineering, IIT Madras. He received the prestigious Newton International Fellowship (from the Royal Society, UK) in 2009, Alexander von Humboldt Fellowship (from AvH foundation, Germany) in 2011, DST INSPIRE Faculty Award (from DST) and RJ Garde Research Award (from Indian Society of Hydraulics). He is a Visiting Researcher at City University of London and Visiting Professor at Leibniz Universität Hannover, Germany. He has published more than 60 papers in

international journals and conferences. His research work focuses on computational hydrodynamics. He has developed state-of-the-art numerical models applied to ocean engineering, particularly coastal and offshore engineering.

Dr. Manta Devi Nowbuth is an Associate Professor in the Department of Civil Engineering, University of Mauritius. She completed a first degree in civil engineering, University of Mauritius in 1988, Master's in Hydrology for Environmental Management at Imperial College of Science, Technology and Medicine, University of London (IC) in 1992, Ph.D. in modelling of groundwater flow through volcanic medium in 1999 at the University of Mauritius and a post doctorate research at the United States Geological Survey Institute in 2004. Her field of expertise is in water resources, covering research on a number of subjects; fluid mechanics, water resources, environmental management and geographical information systems.

Optimization of Berm Breakwater by Assessing the Toe Stability at Low Water Levels

R. Sundaravadivelu, D. P. L. Ranasinghe, Aminul Islam, G. Jayarajan, and S. Priyanka

Abstract The design of breakwater in deep water involves consideration of all the aspects of structural stability, economic viability and the construction feasibility. The main objective of this study was to assess the hydraulic stability of the breakwater against design and overload waves and assess the toe stability for possible low water levels using 2D (Flume) physical model study. The breakwater is located at −18.0 m chart datum (CD) and crest and the toe is at +7.6 m CD and −7.0 m CD respectively. The breakwater was hydraulically stable for the series of waves applied for the structure including overload waves while showing negligible damage to the 2–4 T toe for low water levels (+0.11 m CD and −1.39 m CD). The simulation of different toe elevations with low water levels is shown in Fig. 10.

Keywords Armour · Rock · Breakwater · Toe stability · Low water level

R. Sundaravadivelu (✉) · S. Priyanka (✉)
Department of Ocean Engineering, Indian Institute of Technology Madras, Chennai 600036, India
e-mail: rsun@iitm.ac.in

S. Priyanka
e-mail: nandysankaran@gmail.com

D. P. L. Ranasinghe
Lanka Hydraulic Institute Ltd., 177, John Rodrigo Mawatha, Katubedda, Moratuwa, Sri Lanka

A. Islam
ITD Cementation India Limited, National Plastic Building, A Subash Road, Paranjape B Scheme, Vile Parle (East), Mumbai 400057, India
e-mail: aminul.islam@itdcem.co.in

G. Jayarajan
Tamil Nadu Generation and Distribution Corporation Limited, 1st floor, New EB Quarters, 144, Anna Salai, Chennai 600002, India

V. Sundar et al. (eds.), *Proceedings of the Fifth International Conference in Ocean Engineering (ICOE2019)*, Lecture Notes in Civil Engineering 106,
https://doi.org/10.1007/978-981-15-8506-7_1

1 Introduction

The design of rubble mound breakwater includes various empirical and deterministic procedures. This is due to different parameters that affect the design, e.g., wave height, varying water depth, variation of stone size, slope angle, damage level and so on. The design is often based on empirical expressions developed by several experiments. Rubble mound breakwaters are used for protection of harbours and beaches against wave action.

Core—The purpose of the core is to prevent wave transmission into harbour. Hence, the core material is not too coarse. The core is usually constructed of natural gravel or quarry run.

Toe—The toe functions as the foundation for the armour layer. It also may catch armour units displaced from armour layer.

Armour layer—The purpose of armour layer is to protect the core from direct wave attacks by the dissipation of wave energy. Today the increasing size of vessels makes it necessary to construct a rubble mound breakwater in deep water. Armour layers are built of large rocks or larger concrete armour units. Figure 1 shows the components of a typical rubble mounted breakwater.

However, the paper describes about the toe stability of rubble mound breakwaters. The toe is located on the sea side of the breakwater and is basically the transition zone from primary armour layer to deeper lying layers. A toe has two main functions:

(i) The toe supports the above laying armour layer. The horizontal forces generated by the gravitational forces of the primary armour layer need to be absorbed by the supporting underlying structure. The toe gives support to the rock or concrete elements of which the primary armour layer is built.
(ii) The toe prevents erosion of underlying layers. Sublayers are stabilized by putting heavier rock on top of them according to filter rules. This way, smaller stones are not washed out. The toe is often used as part of the filter structure.

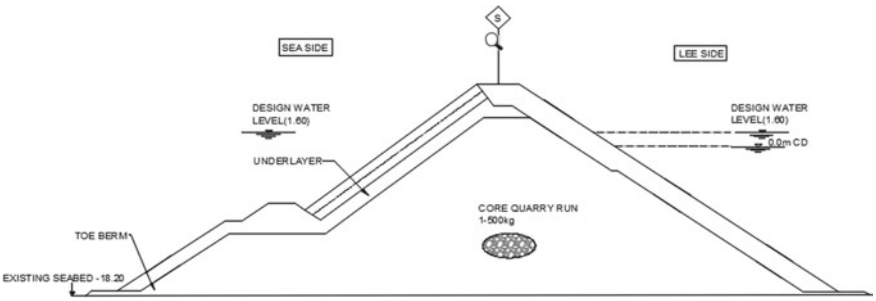

Fig. 1 Components of a typical rubble mounted breakwater

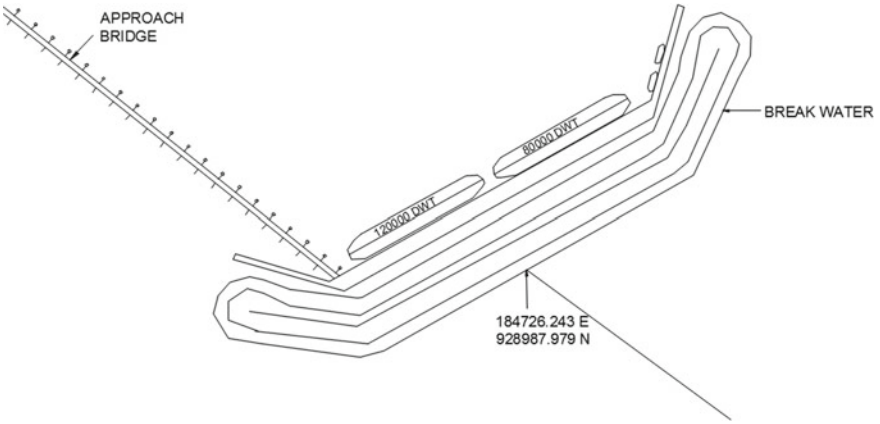

Fig. 2 Layout of the proposed offshore breakwater

2 Layout of the Breakwater

The design of the breakwater will be based on the rubble mound breakwater concept. A rubble mound structure is considered flexible and the design is based on the concept of tolerable damage or movements of the main armour layer. The breakwater is 915 m long with the main trunk portion aligned parallel to the berth. The eastern and western arms of the breakwater are at 142.66° to the main trunk section of the breakwater (Fig. 2).

3 Design Life

The design life of the offshore breakwater shall be 100 years. The breakwater shall be designed for an extreme design condition based on the wind, wave, currents and water levels associated with a storm having a return period of 100 years, as specified in BS: 6349 Part 7.

4 Design Water Levels

The design high water levels are derived based on the combined effects of tide levels, storm surge and an allowance for sea level rise (SLR) due to climate change.

$$\begin{aligned} \text{DHWL} = \text{MHWS}(+0.99\,\text{m}) + \text{SLR}_{50\text{years}}(+0.35\,\text{m}) \\ + \text{SS}(+0.25\,\text{m}) = +1.60\,\text{m CD} \end{aligned}$$

Table 1 Design wave heights as per onsite observations

State of operation	Significant wave height (m)	Mean wave period (s)
Operational conditions	1.0	6 s—sea waves 12 s—swell
Extreme conditions	3.6	6 s—sea waves 18 s—swell

Table 2 Design wave heights

	Depth (m CD)	50 year		100 year	
		H_s (m)	T_p (s)	H_s (m)	T_p (s)
P1	18.1	3.8	9.3	4.7	11.3
P2	17.9	3.8	9.3	4.7	11.3
P3	18.2	3.8	9.3	4.7	11.3

$$\text{DLWL} = \text{LLWL} = +0.11\,\text{m CD}$$

5 Design Waves

The wave heights to be considered for operational and extreme conditions at the breakwater location are given in Table 2; these wave heights are considered for the design of the breakwater (Table 1).

The extreme wave heights corresponding to various return periods have been assessed and based on a cyclone hind casting study as described, where P1, P2 and P3 describe the peak wave periods (Fig. 3).

The peak wave period associated with significant wave height based on a typicalcyclonic storm is shown in Fig. 4.

In addition to the design waves for the seaside, the extreme waves affecting the rear side armour which is based on the cyclone wave hind casting study. The results show that the significant wave height in the leeside of the breakwater will vary between 2.0 and 2.5 m during the passage of cyclonic storms of various intensities.

6 Design of Toe

The size of rock toe in front of concrete armour slope is calculated using the method proposed by Van der Meer, D'Angremond and Gerding (1995) (Table 3),

$$(H_s/\Delta \times D_{n50}) = (1.6 + 0.24(h_b/D_{n50}))\, N_{\text{od}}(0.15)$$

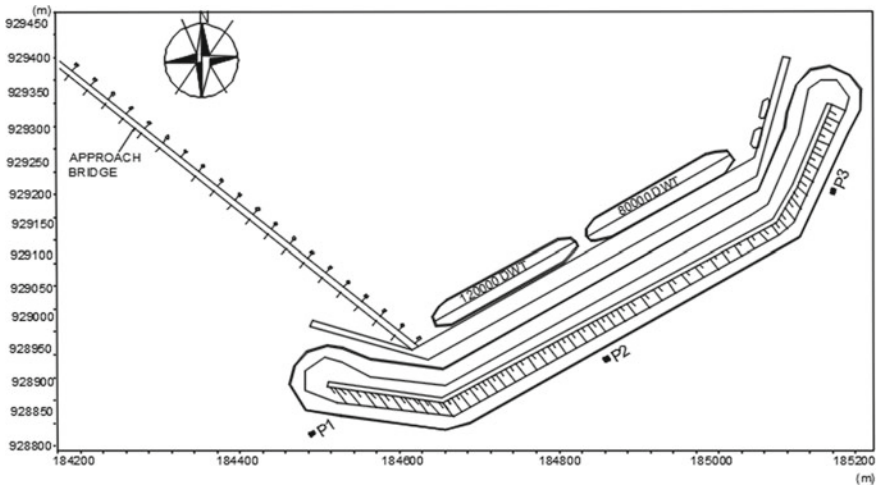

Fig. 3 Locations selected for the alignment of the breakwater

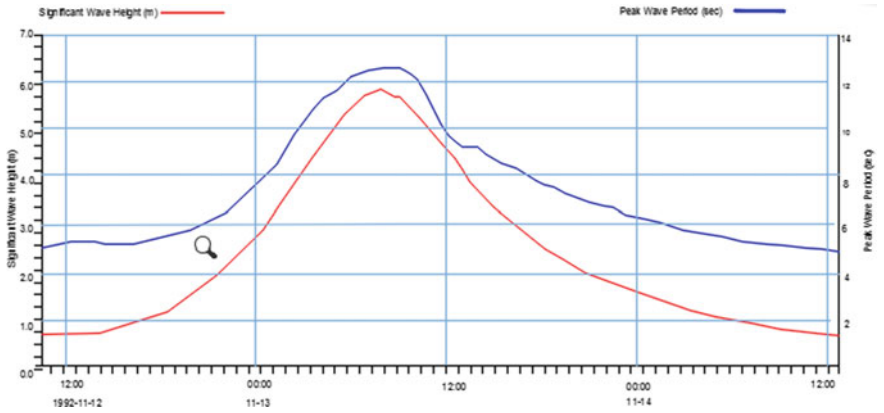

Fig. 4 Example of the peak wave period corresponding to the significant wave height for a storm event during 1992, close to the offshore breakwater

Table 3 Toe design calculations on Van der Meer

Description	Based on statistical analysis	Based on onsite observation
H_s (m)	4.7	3.6
DLWL (m CD)	0.11	0.11
N_{od} estimated	0.45	0.1
Proposed rock size (t)	2–4	2–4

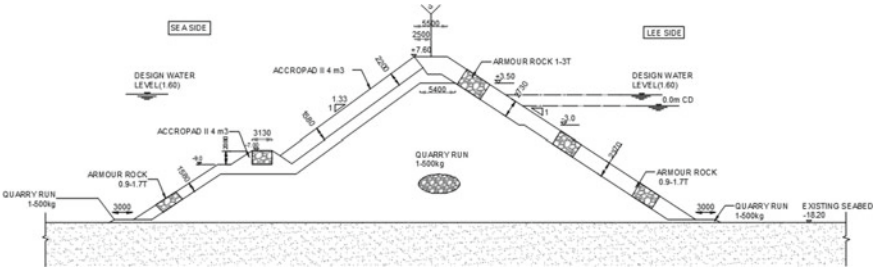

Fig. 5 Trunk cross section with modified toe level

where,

Nod 2 for no damage condition for 100-year wave condition.

h_bTotal height of water column above toe (m).

7 Physical Modelling of Breakwater

The 2D physical model testing for the trunk section at −18 m CD bed level was tested in the 2D flume. The trunk cross section of the breakwater is optimized, with the breakwater toe level on the sea side fixed at −6 m CD. All the other components of the breakwater remain the same as in the design cross section (Fig. 5).

8 Modelling Setup and Testing Procedure

The 2D model testing has been carried out in the LHI laboratory wave flume which is 30 m long, 0.8 m wide and 1.0–1.6 m deep. The wave is generated by a hydraulically operated paddle and controlled by a PC-based wave synthesizer software by Danish Hydraulic Institute (DHI). The interface between the software and active wave absorption control system (AWACS) is established through the wave generator/receiver unit. The wave generating software is capable of generating both regular and irregular waves of a pre-determined spectrum including JONSWAP spectrum. All wave gauges have been calibrated before starting the model runs (Fig. 6).

9 Model Scale Selection

The scales for the each section profile have been selected by considering wave flume or basin dimensions, seabed profile, main amour and the design wave conditions

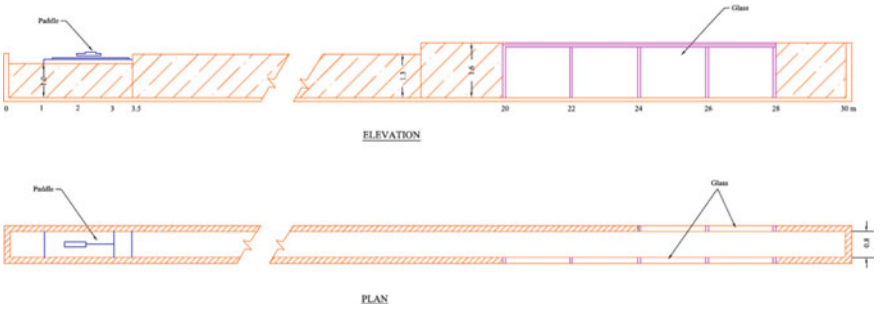

Fig. 6 LHI laboratory wave flume

Table 4 Applied model scales

Section	Scale		
	Length	Time and velocity	Forces, volume and mass
2D Section (4 m^3)	1:48:36	1:$\sqrt{}$(48.36)	1: $(48.36)^3$

to represent the actual situation. Since the primary amour is selected as ACCROPODE™ II units (by Concrete Layer Innovations—CLI) at preliminary stage availability of the model amour units were also considered as a key factor while selecting the model scales for each section. Gravity and inertia forces have to be same in both prototype and the model. Therefore, it is necessary to use Froude scaling law in order to represent the other parameters correctly in the model (Table 4).

10 Stability of Toe Structure

The toe stability was assessed by the limit for damage number (N_{od}) which is 0.5 for low water design wave condition and 2.0 for overload condition. N_{od} is the number of displaced units within a strip of width D_n (nominal diameter of rock armour).

11 Model Construction

The materials of each layer of the structures were scaled down in the model to have the correct representation of stability, permeability and porosity. The structural sections were constructed to the geometrically similar (GS) scales in a sequence from bed preparation, core, under-layer and toe.

Composition of the core and arrangement of rear armours are common for the UT-V0, UT-V1and UT-V2 sections constructed in 2D model. Few modifications were

done for the front toe, toe berm and for the crest along the front slope for the two sections of UT-V1 and UT-V2 (Table 5).

12 Construction of Test Section Ut-V0

The rock mount front toe was built at −7.0 m CD with the width of 3.13 m in prototype. However, it was found that the rock mound toe with landward mild slope is unable to provide the better support for the first row of ACCROPODE II units. Therefore, it was decided to extend the toe up to the ACCROPODE II layer. The test section is mentioned as UT-V0, UT-V1, UT-V2 and UT-V3.

13 Construction of Test Section Ut-V1

The rock mound toe (UT-V0) having a width of 3.13 m has been extended up to ACCROPODE II layer so that total toe width is 5.00 m in section (UT-V1). Further, landward slope at the toe has been steepened in the ratio of 1:1.33. In order to provide the better support for the 1st ACCROPODE II, the number of ACCROPODE II rows along with the slope has reduced to previous row with modified toe arrangement. However, in the small gap, it has been encountered at the top most ACCROPODE II row and the 1–3 T rock armours at the crest. Therefore, it is decided to add one more ACCROPODE II as next row at the edge of the crest (Fig. 7).

14 Construction of Test Section Ut-V2

Since the width of the front toe is 3.13 m in original section (UT-V0) and it was increased up to 5.0 m in section UT-V1, it was decided to use the same width of 3.13 m for the extended toe (UT-V2). Therefore, toe width, toe berm and the core below the front toe were adjusted accordingly in section UT-V2, and hence, total width has been reduced by 1.87 m from the sea side (Figs. 8 and 9).

15 Construction of Section Ut-V3

The only difference between UT-V2 and UT-V3 is the top elevation of the front toe. Originally, it was at −7.0 m CD (UT-V2), and during the testing, it was decided to assess the toe at -5.5 m CD (UT-V3). The same section of UT-V2 and dummy water level of −1.39 m CD have been used to simulate the section UT-V3 with 0.11 m CD water level. Reducing the water level up to −1.39 m CD instead of raising the toe

Table 5 Materials used in the 2D model section

Rock layer	Weight				Diameter model (mm)		Equivalent sieve (mm)				Composition (%)	Model porosity
	Prototype (kg)		Model (g)									
	Lower	Upper	Lower	Upper	Lower	Upper	Lower	Upper	Lower	Upper		
Toe	2000	4000	15.7	31.4	18.1	22.8	22	27	19	22	10	0.380
									22	25	40	
									25	27	35	
									27	31	15	

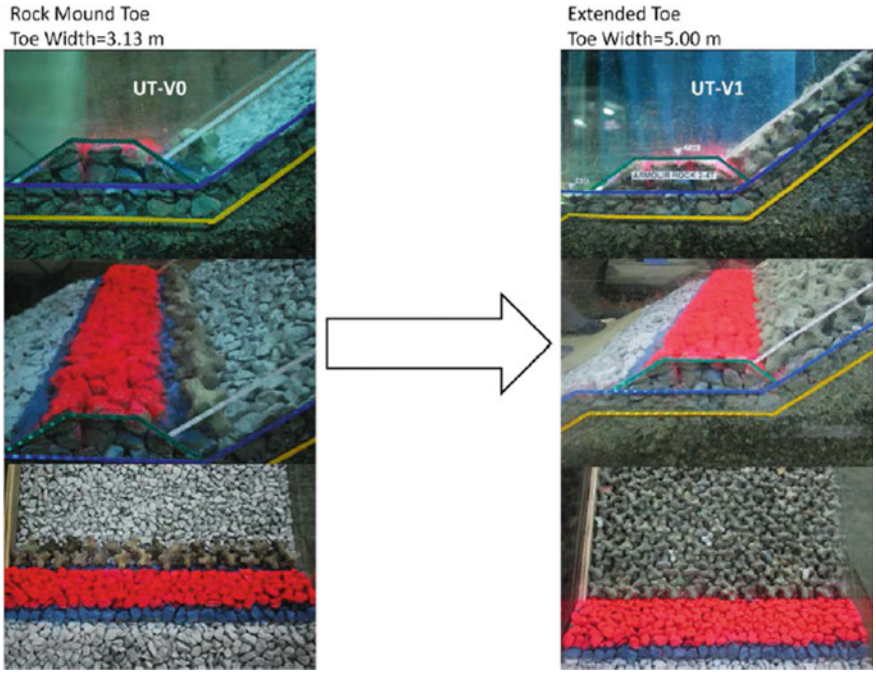

Fig. 7 Front toe details for the section UT-V0 and UT-V1

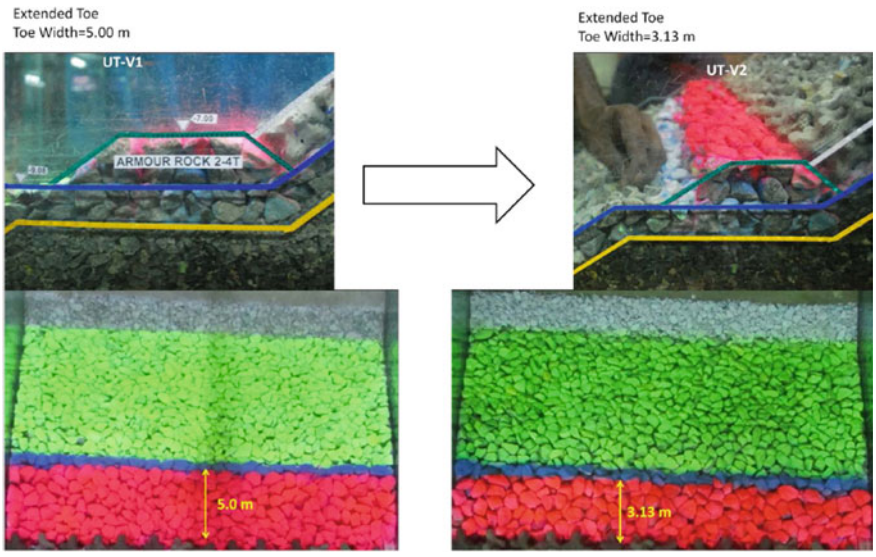

Fig. 8 Width of the front toe for the section UT-V1 and UT-V2

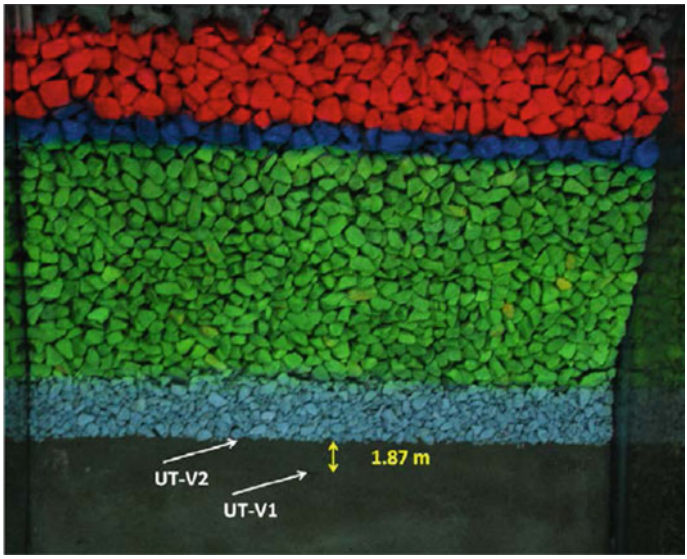

Fig. 9 Reshaping the toe berm width by 1.87 m for the section UT-V1 and UT-V2

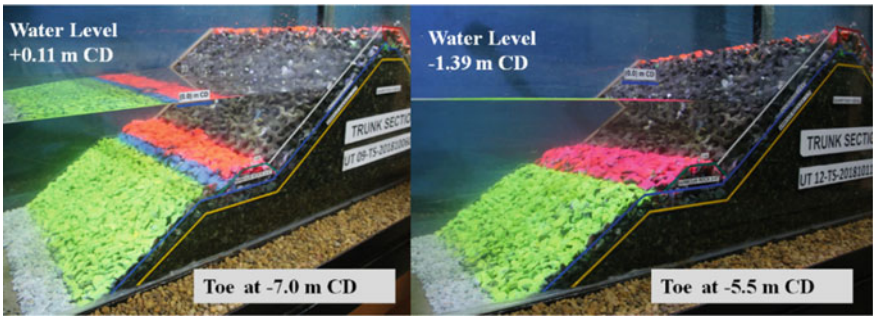

Fig. 10 Simulation of different toe elevations with low water levels

elevation by 1.5 m to get the effective water depth of 5.61 m at the toe (0.11 + 5.5 = 7 – 1.39) (Fig. 10).

16 2D Model Result and Analysis

The wave heights were measured at the locations of near the breakwater toe and near the paddle. No major damages have been observed in the sea side during all the tests carried out for MHWL, DHWL and DLWL. However, the considerable damage to the front toe was occurred during the 1.4 H_s and 1.5 H_s tests for DHWL. Similarly

rear side was also kept stable for all the tests except 1.4 H_s and 1.5 H_s DHWL tests due to the considerable overtopping. Hence, significant damage has been observed in the 1–3 T rock layers in the rear side.

17 Damage Assessment

As the waves at high water levels are hardly had any impact on the toe stability, separate tests were done under low water levels and high water level in 1.0 H_s and 1.3 Hs conditions. There was a tiny movement of rock amours at the front toe for 100YRP DLWL condition and end up with the 1 unit displacement at the end of the test, resulting N_{od} value of 0.08. The total number of displaced units was counted as 10 for 1.3 H_s DLWL tests which gives the N_{od} of 0.27 However, a minor damage to the toe has been observed for during the DHWL conditions for overload waves and estimated cumulative damage at the end of the 1.5 H_s waves was 0.46 which is far below from the acceptable limit of $N_{od} = 2.0$ (Figs. 11 and 12).

Therefore, it is decided to increase the toe level by 1.5 m considering the removal of one ACCROPODE II row at the front slope. This modification with −5.5 m CD toe level has been simulated for section UT-V2 using dummy water level of −1.39 m CD to provide the effective water depth (5.5 + 0.11 = 7 – 1.39) at the modified

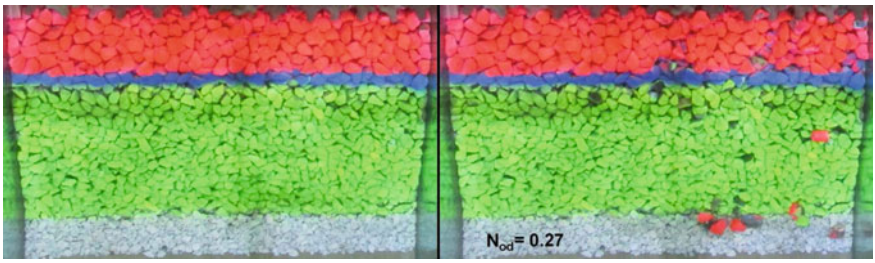

Fig. 11 Front toe UT-V2—before 1.0 H_s DLWL (left) and 1.3 H_s DLWL (right)

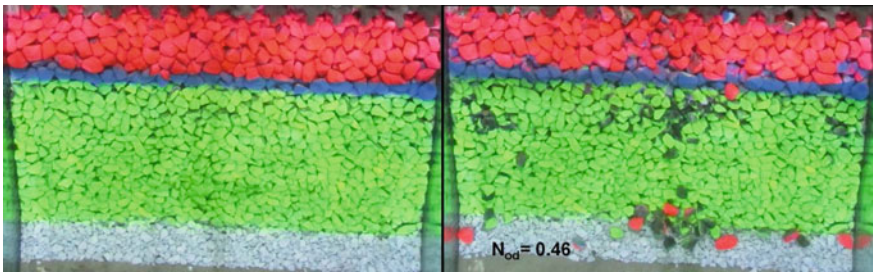

Fig. 12 Front toe UT-V2—before 1.0 H_s DHWL (left) and after 1.5 H_s DHWL (right)

toe. Three tests of 1.0Hs and 1.3 Hs were repeated with dummy water level of −1.39 m CD (LLWL) to assess the stability of the elevated toe.

18 Conclusion

The observed wave heights were within the limit of ±3% than that of required wave heights at the breakwater toe except for two tests which gave 4% difference. The recorded wave heights at the lee side were reached up to 0.37 m at 1.4 Hs overload waves at DHWL which is even lesser than the acceptable limit of 0.4 m for design waves for safe berthing. However, the wave height at the lee side was recorded as 0.5 m during the 1.5 H_s at DHWL waves which will be rarely generated.

The front toe at −7.0 m CD has shown the zero damage condition even for low water levels. Therefore, toe stability tests were carried out for the modified toe with −5.5 m CD top level to optimize the number of ACCROPODE II rows at the front slope. Based on the observation, it was found that N_{od} value for design and overload waves are 0.46 (<0.5) and 1.78 (<2.0), respectively. Therefore, it can be concluded that elevated toe is also stable enough to with stand the design (1.0 H_s) and overload (1.3 H_s) waves at low water level.

Geo-technical Stability and Sensitivity Analysis of Geo-synthetic Seawall at Pallana Beach, Kerala, India

R. Sukanya, Vallam Sundar, and S. A. Sannasiraj

Abstract The various geo-synthetic components such as geo-tubes, geo-bags, geo-mattresses, geo-containers, geo-grids, geo-cells find extensive applications in coastal engineering practice. It is more sought after due to the ease of construction, quick implementation and reduced cost as the supply of natural rocks is eluded. Innovative geo-synthetic materials of numerous units were compounded to form a sea wall cross section, to be constructed at Pallana coast (9° 17′ 55.19″ N and 76° 23′ 18.55″) of Allepey, Kerala, to prevent wave run up during high tide level. The Pallana beach is also characterized with poor soil subgrade properties and hence the proposal to construct a geo-synthetic seawall in contrast to the conventional measures. The cross section is designed to ensure stability against overturning, sliding, overtopping and scour protection. The major concerns such as UV radiation, stability against wave action, settlement of the structure and protection against scour are to be addressed prior to the implementation of the design on site. The objective of the paper is to arrive at the significant geo-technical parameters responsible for the geo-technical stability of the structure over time. The pore-water pressures beneath the structure, rapid drawdown, transient stability and sensitivity analysis are computed for the above said structure using GeoStudio software application, which employs finite element method. A visualization of the geo-technical performance can be arrived that aids to verify the design parameters adopted.

Keywords Geo-synthetic materials · Pore-water pressure · Drawdown · Maximum total stresses

R. Sukanya (✉)
National Technology Center for Ports Waterways and Coasts, Indian Institute of Technology Madras, Chennai 600036, India
e-mail: sukanyarbabu@gmail.com

V. Sundar · S. A. Sannasiraj
Department of Ocean Engineering, Indian Institute of Technology Madras, Chennai 600036, India

V. Sundar et al. (eds.), *Proceedings of the Fifth International Conference in Ocean Engineering (ICOE2019)*, Lecture Notes in Civil Engineering 106,
https://doi.org/10.1007/978-981-15-8506-7_2

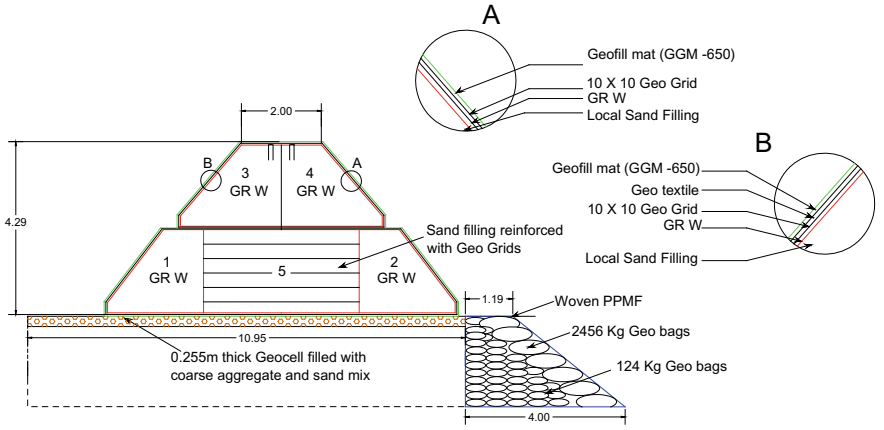

Fig. 1 Cross section of sea wall

1 Introduction

Seawalls are coastal protection structures, constructed to primarily offer shore protection, where the shoreline is highly unstable. The instability may be attributed due to fluctuations in the tidal and run up level or due to excessive movement of sediments as a result of intensive littoral drift. There are several prototypes of seawall cross sections in existence, their workability, efficiency and application are site specific. A variety of parameters, such as wave climate, soil conditions, tidal range, material availability, substantially influence the type of seawall constructed. A conventional seawall is made up of rubble stones, which, later evolved to prefabricated concrete armour units such as Accropods, Tetrapods, Corelocs, Dolos, Kolos. As opposed to the conventional hard measure of laying rubble stones and concrete units along the coast, a novel soft measure to erect a seawall using composite geo-synthetic units and locally available beach sand as shown in Fig. 1 was considered for the Pallana coast of Allepy district in Kerala, India. A model section of about 100 ft long was commissioned in the field to assess its performance in real time. Apart from the hydrodynamic stability, the geo-technical stability of the structure is also critical and dependent on the site conditions. Settlement of a gravity structure is one of the key problems in the coastal environment; hence, an analytical study was taken up through GeoStudio, to arrive at the total maximum stresses developed, displacement/settlement along the depth and transient pore-water pressures.

2 Site Conditions

The location under investigation is situated along the south-west coast of the Indian peninsula. This coastal stretch suffers moderate to excessive erosion owing to the

Table 1 Subsoil properties

Material	Depth (m)	N value	Saturated unit weight (γ_{sat}) (kN/m^2)	Submerged unit weight (γ_{unsat}) (kN/m^3)	Youngs modulus (E) (kN/m^2)	Poissons ratio (μ)	Cohesive strength (kN/m^2)	Angle of Internal Friction (φ)
Loose clay	5.7	1.142	15.2026	5.20269	2142.85	0.45	6.3045	0
Sandy clay	2.1	9.5	15.4442	5.44421	4650	0.45	7.1918	23.3
Clayey sand	2.4	9.5	15.9706	5.97068	7840	0.3	8.3359	21
Silty sand	2.4	55.5	19.9290	9.92901	160,950	0.35	7.8456	24

predominant net northerly currents. The stretch of Pallana beach is characterized by poorly graded soil; the soil subgrade properties of the site are arrived from the borehole test data and tabulated in Table 1. The water levels recorded at the said location corresponding to the varying tide levels as reported by the local authorities with respect to mean sea level were used to arrive at the three water levels corresponding to the lowest low tide, highest high tide and highest high tide + storm surge arrived as 1.19 m, 2.19 m and 3.39 m, respectively.

3 Geo-synthetic Materials

Various geo-synthetic components such as GRW units, geo-grids, geo-cells, geo-bags, geo-matt fills, woven and non-woven geo-textile were used to form the sea wall cross section.

3.1 PPMF Woven Geo-Textile

Polypropylene Woven Multifilament Geo-textiles are manufactured from polypropylene multifilament yarns with a good combination of mechanical and hydraulic characteristics. These are suitable for application involving the functions of separation, filtration and stabilization. UV stabilizers are incorporated which attributes to UV retention properties; they are also chemically inert and highly resistant to the action of alkaline, acids and oxidizing agents. A small unit of the ppmf woven geo-textile is shown in Fig. 2a.

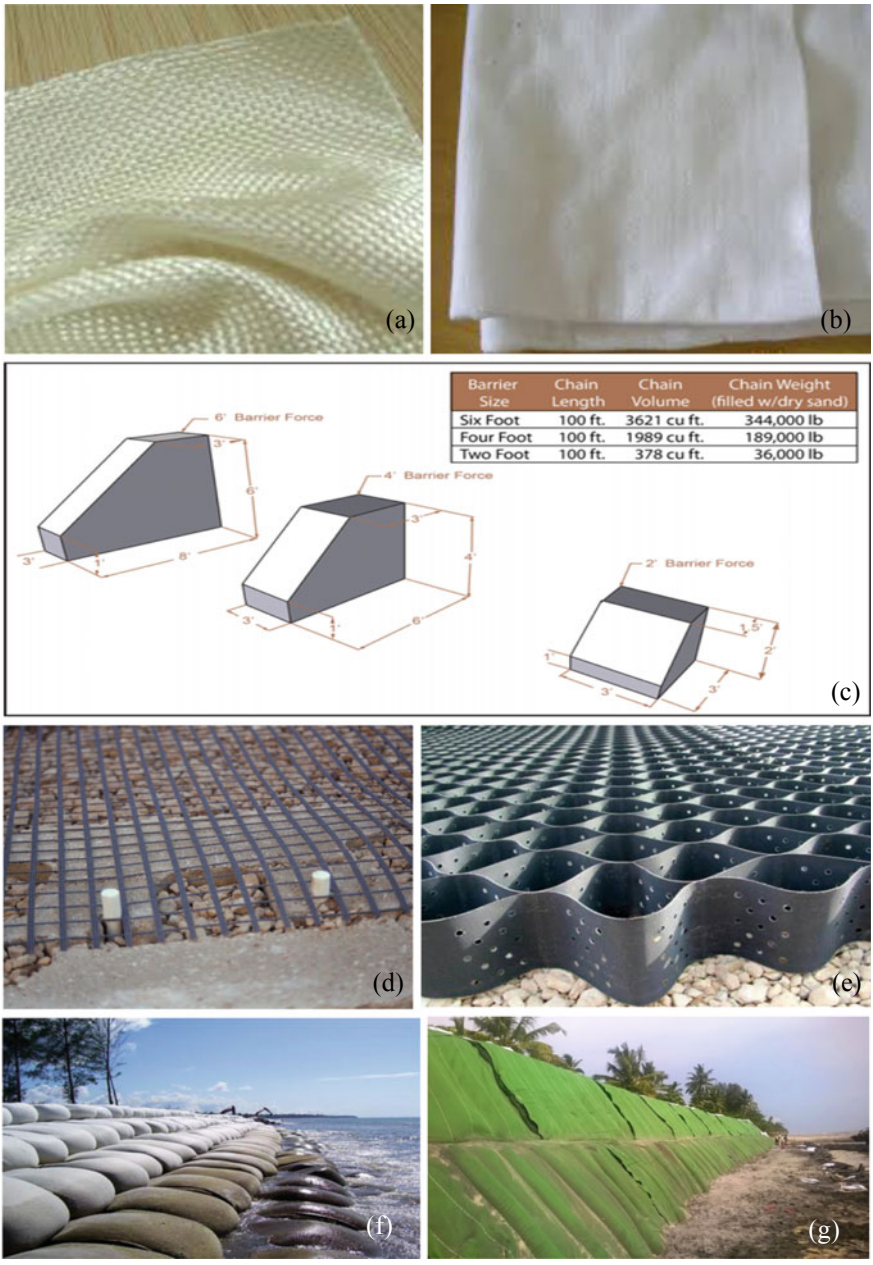

Fig. 2. Geo-synthetic components

3.2 Non-woven Geo-textile

The major application of non-woven geo-textile is prevention of soil movement in erosion control measures. It also enhances filtration of soils in drainage applications by retaining soil particles while allowing for the free flow of water. These are commonly used where retention of even fine sediments is mandated. A small unit of the non-woven geo-textile is shown in Fig. 2b.

3.3 Cell Containment System

Barrier Force™ manufactures protective cell containment systems (geo-synthetic reinforced soil retaining wall) made up of pentagon-shaped vertical bags that are connected by its side like an accordion, typically 100-foot-long segments which comes in standard dimensions as given in Fig. 2c. These segments can be used in series to run for any desirable length and could be filled with potentially a wide range of materials such as sand, silt, gravel, crushed stone, concrete.

The pentagon-shaped cells are connected to each other with a flexible wall; the fill media forms a solid barrier as the two sides conform to the common wall. This connection also forces the rising water to move the entire chain rather than allowing it to dislodge a single cell; since each cell's weight is more than twice the pressure of the water pushing against it, moving the chain is virtually impossible. The pentagonal shape is particularly advantageous for the following reasons: angled sloping section allows each cell to hold more fill media while, increasing the surface area of the base, which increases the friction through more ground contact, with an increased base-to-height ratio to eliminate tipping. The broader toe region allows for easier, more consistent filling.

3.4 Geo-cell

It is a honey comb-shaped, sturdy geo-synthetic material with pores along its wall to facilitate easy filtration in addition to serve as a foundation layer, by confining the infill material within the connected cells, the system provides structurally stable environment for infill to protect shorelines and it also reinforces the upper soil layer. It also provides resistance to erosive conditions and sliding forces. The panel acts like a large mat, distributing applied loads over an extended area. Geo-cell can reduce the amount of aggregate required to stabilize a poor load bearing soil by up to 65%. A model geo-cell unit is shown in Fig. 2d.

3.5 Geo-grids

Geo-grids resemble a very broad square mesh like structure and its ribs are often quite stiff compared to the fibers of geo-textile as shown in Fig. 2e. They primarily serve the purpose of soil reinforcement.

3.6 Geo-bags

Geo-bags are made up either woven or non-woven geo-textiles and they are filled with locally available sand or other fill materials up to over 80–85% of its volume and generally sealed using a high denure polymer threads. They can be effectively arranged in a vertical or sloping fashion to serve its purpose. For the present study, geo-bags are incorporated for toe protection alone. Figure 2f shows an image of the geo-bags positioned along the shoreline.

3.7 Geo-fill Matt

To address the problem against vandalism and protection from UV rays, the geo-fill matt layer can be incorporated in the design of exposed coastal structures as can be seen in Fig. 2g. Their surface area is spread about with a green-colored matt that offers protection from harmful UV rays which tends to affect the longevity of the geo-textile material exposed to the environment. These also have a series of slurry pockets each of 15 cm diameter that could be filled with slurry or sandy materials that can withstand puncture shear or stresses due to vandalism. In addition, they also offer a surface friction/surface roughness to the steep slopes enabling dissipation of wave energy over the highly non-porous structure.

4 Modeling in GeoStudio

Modeling with GeoStudio involves designing the mesh, defining the material properties, choosing the appropriate constitutive soil model and defining the boundary conditions. A 15 nodded triangular element is opted for mesh generation in a linear elastic constitutive model. The soil boundaries are fixed on three sides (bottom and two lateral) with a fluid pressure and atmospheric exposed boundary on the other side. The phreatic levels are defined as per the varying tide levels corresponding to the site conditions. The maximum total stresses and displacement along the depth were computed with the SIGMA/W model. The pore-water pressure was assessed with the SEEP/W model for rapid draw down under transient analysis.

4.1 Stress Deformation

The SIGMA/W model of GeoStudio is used to compute the deformations caused by earthworks in this case, an embankment with differential water heads. The geo-synthetic components are included in the model as beam elements with flexural stiffness in two-dimensional plain strain analyses. The total maximum stresses resulted are compared to that of a similar sea wall embankment without the flexural stiffness of various geo-synthetic components. The Mohr–Coulomb failure criterion enables the computation of shear stress and theoretical yield stresses.

4.1.1 Total Maximum Stresses

The total maximum stresses assessed along the depth direction for the three varying water levels are shown in the following figures (Fig. 3a–c).

The maximum total stresses developed under the toe and embankment are critical and they are compared with and without the flexural stiffness of the geo-synthetics at three points, viz end of the toe section, start of toe section and embankment side. Figure 4 shows a comparison of total stresses at the different water levels and along the depth of different points.

The maximum total stresses developed in the soil correspond to the model without geo-synthetics, since, in the latter, the self-weights are distributed through the geo-synthetic components. From the figures above, it is observed that the stresses decrease with an increase in depth. Higher magnitude of stresses is observed for greater water depths. The location start of the toe is critical for the model with geo-synthetics, and thus, it experiences higher stresses. The location, end of toe is critical for the model without geo-synthetics.

4.1.2 Displacement Along Depth

The maximum displacements along the depth for varying phreatic levels are shown in Fig. 5a–c. It can be observed that for a long-term duration set of five years the maximum displacement along the *y* direction at water levels 1.19 m, 2.29 m and 3.29 m are 0.038 m/year, 0.04 m/year and 0.05 m/year, respectively.

4.2 Transient Analysis

A transient analysis means one that is always changing; here, the water level on the sea side is undergoing rapid drawdown, i.e., water level changes from maximum to minimum. The response on how long the soil takes to respond to the user boundary conditions is analyzed with the time steps.

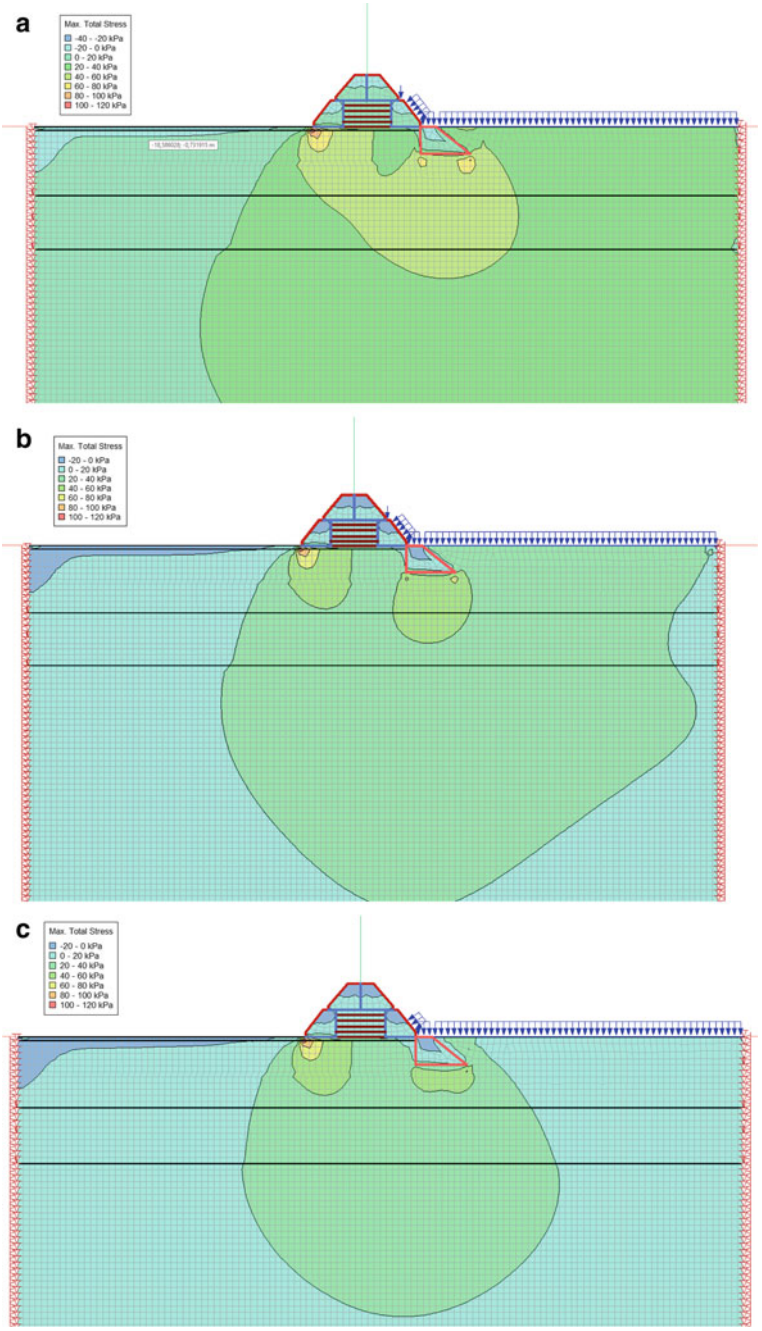

Fig. 3 **a** Maximum total stresses at 3.29 m water depth, **b** maximum total stresses at 2.29 m water depth, **c** maximum total stresses at 1.19 m water depth

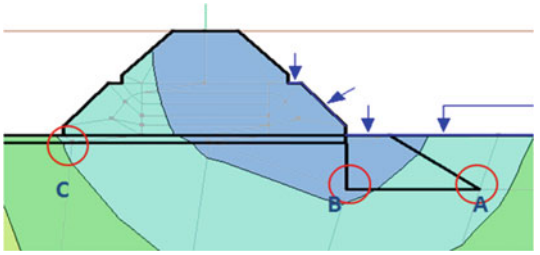

A- Start of toe; B- End of toe; C- Embankment side

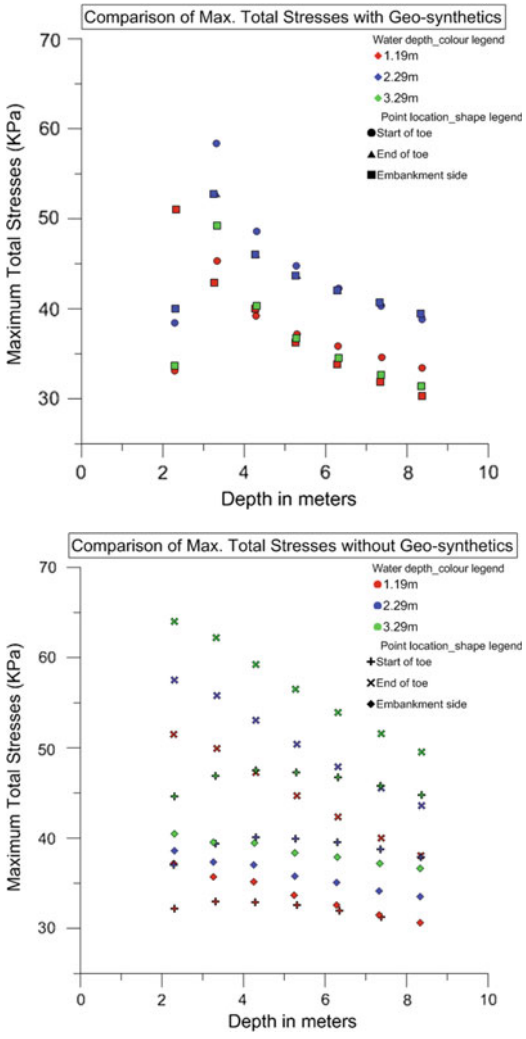

Fig. 4 Maximum total stress variation along the depth in soil subgrade

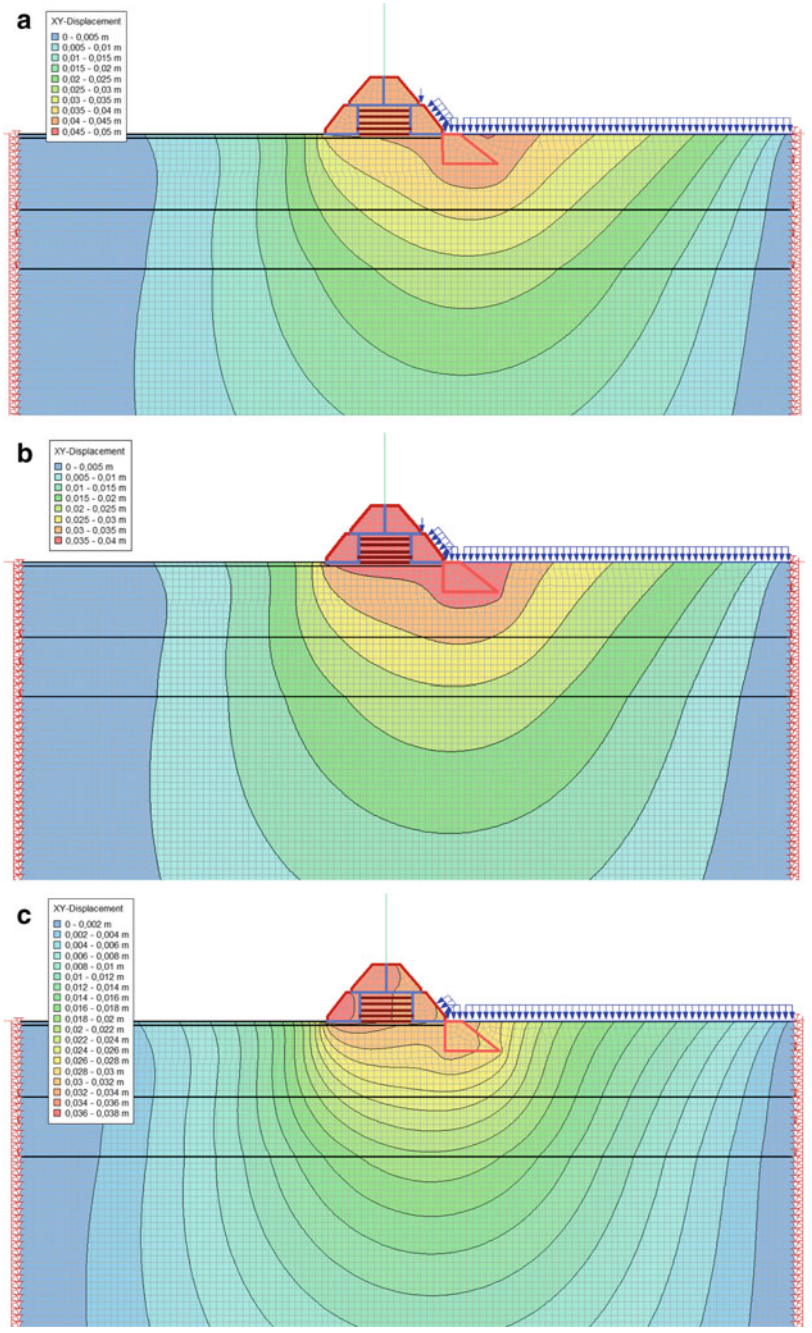

Fig. 5 **a** Total displacement at 3.29 m water depth, **b** total displacement at 2.29 m water depth, **c** total displacement at 1.19 m water depth

4.2.1 Time Stepping—Temporal Integration

An incremental time sequence is required for all transient analyses and the appropriate time sequence is problem-dependent. In the present problem, the tidal variations are rather steady and less likely to be rapid, unless in the case of extreme event. Many seepage processes related to the dissipation of excess pore-water pressures and infiltration follows an exponential form. The dissipation or infiltration is rapid at first and then decreases with time. A typical example is the consolidation of a soil.

4.2.2 Pore-Water Pressures

It refers to the pressure of groundwater held within a soil or rock, in gaps between particles. Since the pore-water pressure is dependent on the total water head and must be computed, iterative numerical techniques are required to compute the appropriate combination of pore-water pressure and the material property.

Natural soil deposits are generally highly heterogeneous and non-isotropic. In addition, boundary conditions often change with time and cannot always be defined with certainty at the beginning of an analysis. Furthermore, when a soil becomes unsaturated, the coefficient of permeability or hydraulic conductivity becomes a function of the negative pore-water pressure in the soil. The following figures show the variation of pore-water pressures in the soil layers in steady state and transient state with rapid drawdown. The water levels adopted for stress deformation are used for transient analysis as well.

From Fig. 6a, b, it can be understood that the negative pore-water pressures do not develop underneath the structure, and thus, the failure due to sinkage is not possible for the proposed structure with the given subsoil conditions. A similar trend is also observed for the water levels 2.29 and 1.19 m.

5 Conclusions

The proposed seawall cross section with geo-synthetic components was subjected to geo-technical analysis to compute the maximum total stresses, maximum displacement along the depth as well as pore-water pressures under steady and transient state. The maximum displacement did not exceed −0.05 m/year for the existing tidal levels; slope failure is avoided by the geo-synthetic layers and the structure is resistant to sinkage failure during rapid drawdown of water levels. Even with poor soil subgrade properties prevalent at the site under study, the proposed structure's performance is found to be geo-technically sound.

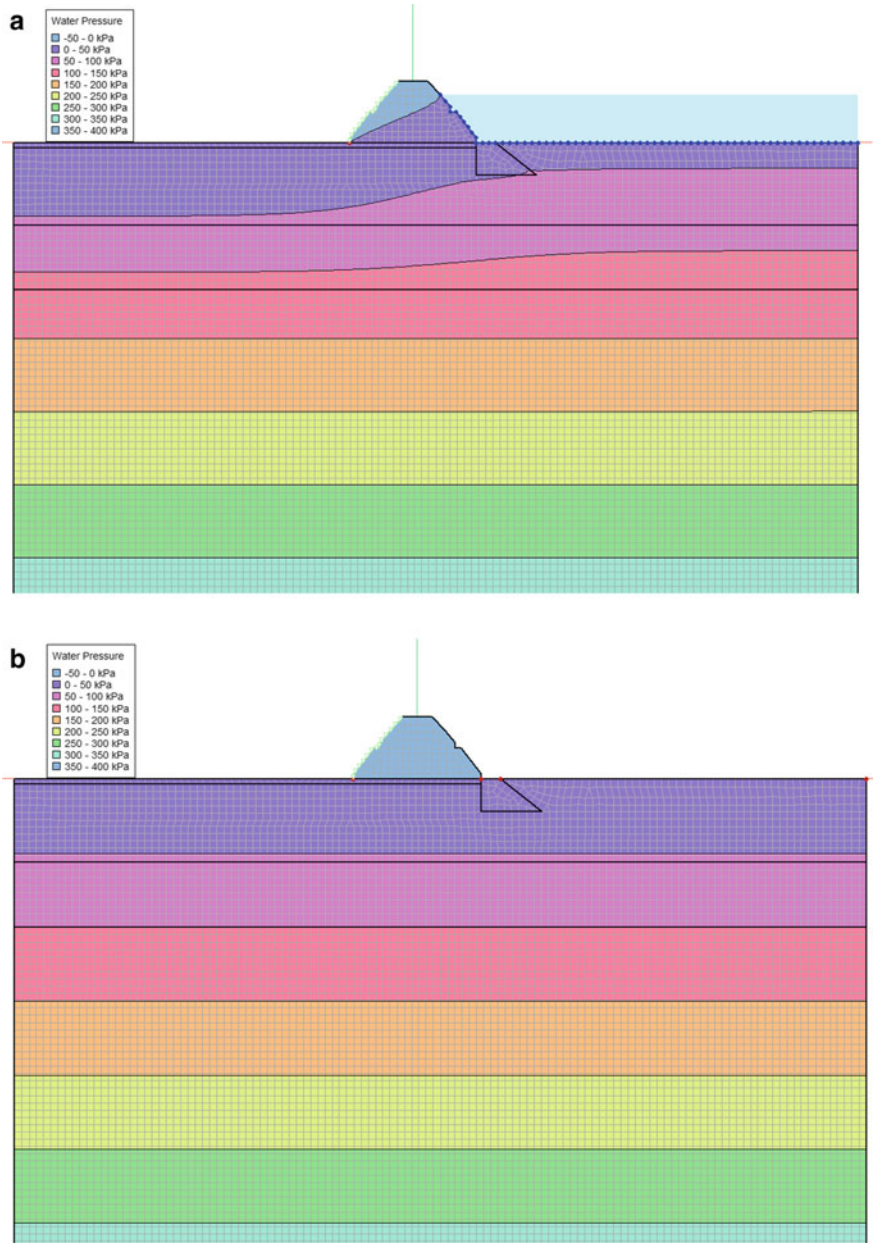

Fig. 6 **a** Steady state pore-water pressures at 3.29 m water depth, **b** Transient state pore-water pressures at 3.29 m water depth

Hydrodynamic Stability of Gabion Box Reef Breakwaters

V. K. Srineash and K. Murali

Abstract Gabion-based coastal structures are being adopted frequently in recent times due to its energy dissipation characteristics and reduction in construction time. The coastal defense has become an essential aspect for maritime facilities and for the places prone to erosion. Reef breakwaters (also called Low crested structures) are seen to cause less environmental impact which makes them popular in recent past. The present investigation involves the study of hydrodynamic stability aspects of gabion-based reef breakwaters. Though these coastal protection structures are meant for wave attenuation, a study on the stability aspects of the structure to resist wave action is essential. This knowledge on the hydrodynamic stability is essential to come out with the design basis for construction of such coastal structures in a wave environment. This investigation on gabion-based reef breakwaters is performed using physical model tests with varying wave parameters and reef geometries. The study is aimed at fetching knowledge on the determination the weight of the gabions to resist the wave action by obtaining a relation between the weight of the gabion, geometrical parameters and to that of the wave parameters. This determination of the weight of the gabions to resist wave action is essential if gabion-based structures are deployed as low crested coastal structures or reef breakwaters. This paper is based on the experimental study conducted in the shallow water wave flume facility in the Department of Ocean Engineering, IIT Madras.

Keywords Gabions · Reef breakwaters · Artificial reefs · Low crested structures · Coastal structures · Coastal defense · Coastal protection

1 Introduction

Reef breakwaters are predominantly rubble mound based structures with the crest level near or below still water level. These structures are often categorized as low crested structures as these structures are overtopped frequently [6, 13, 18, 19]. The

V. K. Srineash (✉) · K. Murali
Department of Ocean Engineering, Indian Institute of Technology Madras, Chennai 600036, India
e-mail: srineash@gmail.com

V. Sundar et al. (eds.), *Proceedings of the Fifth International Conference in Ocean Engineering (ICOE2019)*, Lecture Notes in Civil Engineering 106,
https://doi.org/10.1007/978-981-15-8506-7_3

functionality of such reef breakwaters or low crested structures extends from shore protection to other purposes such as protection of water intakes of power plants, entrance channel [1]. The most spoken advantage of these low crested reef based structures is the dissipation of energy by making the waves break prematurely [10]. The reef breakwaters are considered to preserve the aesthetics of the coast and hence, such structures are considered suitable when shore protection is required at the coast with the scope for tourism. However, these structures may become ineffective in places with appreciable tidal ranges [10] as reef based structures may offer less significant wave attenuation during high tide. Such structures are considered to be an economical option as these submerged structures consume fewer resources in comparison to the conventional structures such as breakwaters which extend well above the high tide level [1, 2, 10, 18]. These reef breakwaters are often built with no core leading to high porosity and this high porosity makes these reef based structures stable and eliminates the possibility of catastrophic failure [3]. Due to the above-mentioned advantages of reef breakwaters, the knowledge on the stability aspects of such low crested structures is essential. The studies on stability aspect of reef breakwaters are essential to come out with the design basis for construction of such structures for a given wave climate. The importance of studies on the hydrodynamic stability of reef breakwater was emphasized by past researchers [3, 18, 19]. Further, van der Meer and Daemen [18] has proposed design equations and curves for obtaining a stable configuration of submerged rubble mound structures. The work of Ahrens [3] focuses on the stability model for a reef breakwater to assess the response of the homogenous rubble mound structure for varying wave heights and crest heights.

In the present study involving model scale laboratory tests, gabion boxes were used as reef breakwaters. Gabion boxes being porous allow base flow through the voids and may help in wave attenuation. Gabions are often considered for scour protection as the porous nature of gabions reduces the secondary flow around the structure. Further ease of placement of gabions has made such modular structure preferable in wave environment. Hence in this paper, the stability tests from the experiments are compared with the equations and design curves proposed by the past researchers to obtain a stable configuration of reef breakwater for a given wave climate.

2 Laboratory Setup

The experiments for the present study was carried out in the shallow water wave flume of the Department of Ocean Engineering, Indian Institute of Technology Madras, India. The wave flume measures 72 m long 2 m wide and 2.7 m deep. A constant water depth (d) of 0.3 m was maintained at the toe of the structure through the study. More details of the testing facility may be found in Srineash and Murali [15]. The schematic sketch of the experimental setup is brought out in Fig. 1.

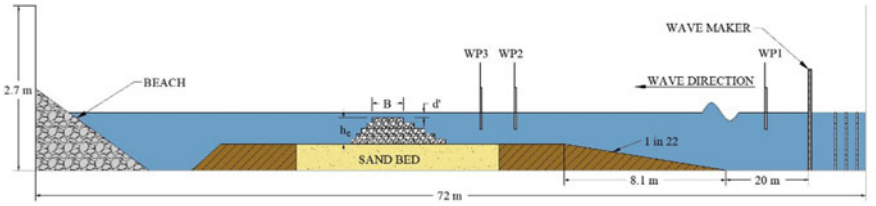

Fig. 1 Schematic sketch of the experimental setup

Resistance type wave probes were used to find the wave elevations and the location of wave measurement in the sketch is depicted as WP1, WP2, and WP3. The wave elevations were recorded at a distance of 18, 28.85 and 29.35 m respectively from the wave maker. The wave probes WP2 and WP3 were used to resolve the recorded wave elevation into the incident and reflected components based on the two probe approach proposed by Goda and Suzuki [5]. The wave probe WP1 was paced at the water depth of 0.67 m in order to find the wave elevation at that location. The sloping bed with a slope of 1 in 22 is provided on the seaward side of the model to produce severe waves. A sand bed was created below the reef breakwater model to mimic the real-time field scenario. The landward side of the model is provided with a beach to absorb the waves transmitted from the reef breakwater.

3 Methodology

The gabion box models were arranged to form the reef breakwater. A snapshot of a gabion model is portrayed in the Fig. 2. Each gabion box measures 0.05 m × 0.05 m × 0.15 m and filled with stones ranging from a size of 7.5–12.5 mm. The mass of each gabion was maintained as 0.624 kg. The overall porosity of the gabion box

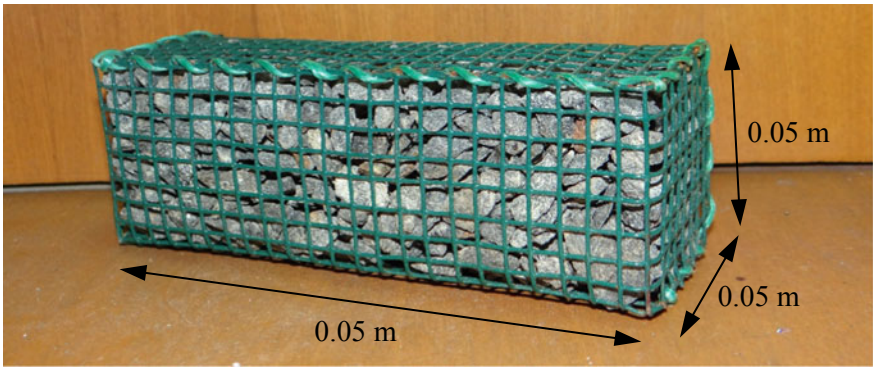

Fig. 2 Snapshot of the gabion box

is 37%. The gabions were arranged such that the longer dimension of the gabions remains parallel to the wave direction. The seaward slope of the reef breakwater is maintained with a slope of 1:2 whereas the landward side of the reef breakwater is provided with a slope of 1:1. More details regarding the gabion model may be found from Srineash and Murali [14].

The scale ratio adopted for the present study is 1:20 based on Froude's scaling law. However, it has to be understood that using Froude's scaling law, only the gravity and inertial forces are accounted. There may be influence of the other forces such as the effects due to viscosity, surface tension etc. These forces are usually neglected in hydraulic model studies [12]. There would be scale effects if the influence of these forces is greater than inertial and gravity forces. Though the scaling effects can be minimized by using models of large scale, it is seldom not possible as it is expensive and not feasible [12]. Hence, past investigators [9, 12, 17] have proposed to have Reynolds number, *Re* to be sufficiently large to make sure that the flow is turbulent. This would in turn make the viscous forces to be negligible [9, 12]. Viscous dissipation becomes dominant when the *Re* ranges from 20 to 2000. Strong turbulent dissipation is expected at $Re > 2000$ [16]. The range of *Re* considered in the present study is in a range of $1.4–2 \times 10^4$. This falls within the turbulent dissipation range [16] suggesting that the viscous effects are negligible. The effects due to surface tension may have its role in wave damping and wave velocity. However, the investigations by Le Méhauté [11] reveal that if the wave period, T is greater than 0.35 s and water depth, is greater than 0.02 m, the effects due to surface tension effects is negligible. The present experiments are well beyond this range and hence the scaling is not susceptible due to the surface tension effects. Thus the Froude's scaling law is valid in the present investigations to achieve similitude. A typical comparison of the dimensional variables between model and prototype is brought out on Table 1.

The laboratory tests covered a wide range of crest heights (h_c) ranging from 0.15 to 0.45 m. considering the fact that the water depth was maintained at $d = 0.3$ m throughout the study, the test conditions produced submerged and emerged reef breakwaters. The crest width of the structure was maintained to be $B = 0.3$ m for the investigations. During the study, the stability tests were conducted for relative

Table 1 Comparison of dimensional parameters between model and prototype

Parameter	Units	Typical prototype	Laboratory model
d	m	6	0.3
d'	m	(−)3–(+)3	(−)0.15–(+)0.15
h_c	m	3–9	0.15–0.45
Mass	kg	4992	0.624
Gabion dimension	m	3 × 1 × 1	0.15 × 0.05 × 0.05
Stone size	m	0.15–0.25	0.0075–0.0125
Porosity	–	0.37	0.37

Table 2 Nondimensional parameters considered for the study

Nondimensional parameters	Range
d'/H_s	(−)1.5–(+)1.5
d/L_p	0.1–0.14
H_s/d	0.50–0.34
H_s/L_p	0.044–0.055
d'/d	(−)0.5–(+)0.5
h_c/d	0.5–1.5
d'/H_s	(−)1.5–(+)1.5

crest height $h_c/d = 0.5$–1.5. The range of submergence ratio (d'/d) is described in Table 2. The depth of submergence (d') becomes negative for emerged conditions of reef breakwaters. Therefore the laboratory test conditions involve 4 submerged ($d'/d \geq 0$) and 3 emerged ($d'/d < 0$) configurations of reef breakwater. The range of dimensionless parameters considered in this study is presented in Table 2. During the wave flume investigations, the tests were performed with 2-dimensional random waves. JONSWAP type spectrum was used to generate waves in the deeper portion of the wave flume. For the stability investigations, the wave generation was performed to simulate a storm duration of three hours.

4 Results and Discussions

The stability of reef breakwaters or structures subjected to wave action, in general, is based on stability number (N_s) [2, 3, 18]. The past studies [8] on the stability of traditional rubble mound breakwaters documents that stability number is one of the most influential factors in deciding the stability characteristics. The traditional stability number is as given below

$$N_s = \frac{H_s}{(D_{50})\left(\frac{\rho_s}{\rho_w} - 1\right)} \tag{1}$$

where

N_s is the stability number;
ρ_s mass density of stone;
ρ_w mass density of water;
H_s significant wave height;
D_{50} nominal diameter of the stone.

In Eq. 1, the geometric parameters of the reef such as h_c and crest width (B) are not accounted. This equation relates the significant wave height incident on the structure to that of the relative weight of individual armor stones in water. However, it

is evident from Eq. 1 that the stability number (N_s) does not account for the changes due to wavelength. From the investigations based on Gravesen et al. [4], spectral stability number (N_s*) is formulated which accounts for the changes in wavelength and this spectral stability number is seen to be reliable in studies pertaining to the stability of reef breakwaters [2, 3, 18]. The expression of spectral stability number (N_s^*) is shown below in Eq. 2.

$$N_s^* = \frac{H_s}{D_{50}\left(\frac{\rho_s}{\rho_w} - 1\right)} \frac{1}{\left(\frac{H_s}{L_p}\right)^{1/3}} \tag{2}$$

where L_p is the peak wavelength defined at the toe of the structure.

Further, it has been observed by Ahrens [3] and van der Meer and Daemen [18] that for predominantly overtopped structures, the effect of wavelength has a significant effect on deciding the stability aspects of a reef breakwater. It has to be noted that the spectral stability number (N_s^*) accounts only the individual mass of stone in water to resist the given wave parameters (H_s and L_p). However, the other geometric parameters such as (h_c), crest width (B), the slope of the reef may have an effect on the stability of the reef breakwaters.

4.1 Submerged Configurations

In this section, the results pertaining to submerged configurations are presented and discussed. The d'/d and h_c/d range from 0 to 0.5 and 0.5–1 respectively. In the study of van der Meer and Daemen [18] involving submerged rubble mound low crested structures, it is observed that the author has proposed design curves and design equations for predicting the stable crest height. The equation proposed by van der Meer and Daemen [18] is as below

$$\frac{h_c}{d} = (2.1 + 0.1\mathrm{S}) \exp\left(-0.14 N_s^*\right) \tag{3}$$

This equation relates the spectral stability number with the crest height of the structure (h_c) and the water depth (d) at the toe of the structure. Here, the author has introduced damage level (S) which is described in the work of van der Meer [17]. The damage level (S) is used to categorize damage levels and the term S takes a value of 2 to represent the initiation of damage, the value of S becomes equivalent to 5 to represent moderate damage, $S = 8$–12 implies severe damage. This equation becomes handy during the design of reef breakwaters to decide upon the crest height of the structure and the nominal diameter of the stones for the given water depth and wave parameters in the field. Further, van der Meer and Daemen [18] has suggested reduction in the diameter of armor stones as a function of relative crest height and

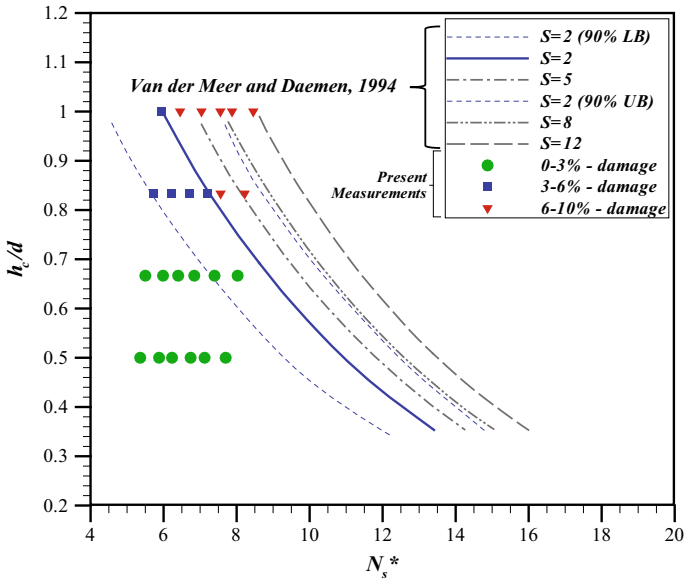

Fig. 3 Reproduced design curves from van der Meer and Daemen [18] and its correlation with the present experiments

wave steepness. This makes the submerged reef configurations stable in comparison with near surface reef configurations.

Equation 3 is used to produce the design curves as per the investigation of van der Meer and Daemen [18]. The design curves of the mentioned author are reproduced below in Fig. 3 and compared with the experimental measurements. The author has suggested that the design curves be valid for submerged structures of slopes between 1:1.5 and 1:2.5. The experiments from the present study consist of a seaward structure slope of 1:2 which falls within the range suggested by the author. In general, the slope of the submerged structure has less influence on the wave attack. The stability of such reef breakwaters are considered to be a function of relative crest height (h_c/d), spectral stability number (N_s^*) and the damage level (S) according to the investigations by van der Meer and Daemen [18]. The damage level (S) curves for $S = 2$, 5 and 8 can be observed in Fig. 3 with 90% confidence band for $S = 2$ (*LB* and *UB* in legend refers to Lower and upper bounds respectively). It is desirable to design a structure to fall within the range of $S = 2$ which damage values close to 5% and the stable reef configurations were seen to denotes the initiation of stone movement. The author has also proposed a reduction factor for the diameter of stones for low crested structures as a function of d'/H and H/L. This reduction factor is considered in the present study and the equivalent diameter of the gabion box was used (D_{50}~ 0.09 m) to calculate the spectral stability number (N_s^*) [this is done as the gabion boxes are of rectangular cross section]. It should also be noted that, in the present investigations the value of ρ_s is substituted with the mass density of gabion box ($\rho_g = 1664$ kg/m^3) instead

armor stone. It is perceived from the present study that the stability tests beyond the $S = 2$ curve is seen to suffer damage greater than 5%. The tests falling on the $S = 2$ curve is seen to take lesser spectral stability number and noticed to fall below the $S = 2$ curve. These aspects are evident from the Fig. 3.

On observing the experimental results from Fig. 3, there is a shift in the stability number with increasing relative crest height (h_c/d) which is due to the fact that the reduction factor for the diameter of stones varies with variation in d'/H_s. From Fig. 3, it is seen that the structure becomes more susceptible to damage if the crest height is close to still water level i.e., $h_c/d \sim 1$. This is in accordance with the observation made by Ahrens [3]. It is usual practice to consider removal of about 1% of the total stones in the cover layer of the structure as "no damage" condition [7]. It is seen from the present study that the tests with the higher depth of submergence yield stable configurations with no damage condition. This could be understood from Fig. 3 where the reef breakwaters with relative crest width $h_c/d < 0.7$ is seen to be stable with almost no movement of gabions. On the contrary, the tests with $h_c/d = 1$ are noticed to be susceptible to damage as the damage observed is about 6–10%; also these points are seen to take values from $S = 2$–12 depending on the wave condition. For $h_c/d = 1$, the most severe wave condition has caused damage of about 10%; the points falling outside the 90% upper limit has undergone the maximum damage. The reef breakwater with $h_c/d = 0.84$ yields a stable condition for a less severe sea state and moderate damage to severe sea state. These aspects show the applicability of the design curves (Fig. 3) and Eq. (3) for reef breakwaters made of gabion boxes.

4.2 Emerged Configurations

The investigations were also performed for emerged configurations ($d'/d < 0$) of reef breakwaters with the negative depth of submergence which leads to relative crest height as $h_c/d = 1.17, 1.34, 1.5$. A snapshot of stability tests on emerged reef breakwaters is portrayed in Fig. 4.

Since the design curves proposed by van der Meer and Daemen [18] are only applicable to submerged structures, these emerged configurations of reef breakwaters are discussed separately. Such studies of emerged reef breakwaters are seen from works of Ahrens [2, 3] where the spectral stability number (N_s^*) plays a major role in deciding the stability characteristics. The stability of emerged reef breakwaters are expressed in terms of spectral stability number and Ahrens [3] has described that approximate threshold of stone movement appear at $N_s^* = 7$. It has to be noted that the author has performed stability tests with a homogenous pile of stones and hence the author records built crest height and the final (deformed) crest height post the stability test. The author has come out with design equations relating the spectral stability number with built and final crest heights, area of cross section of reef and with the water depth at the toe of the structure. However, in the present study involving gabion boxes as reef breakwaters, only the horizontal displacement of gabions are noticed during the stability runs and hence the final and built crest height remains the

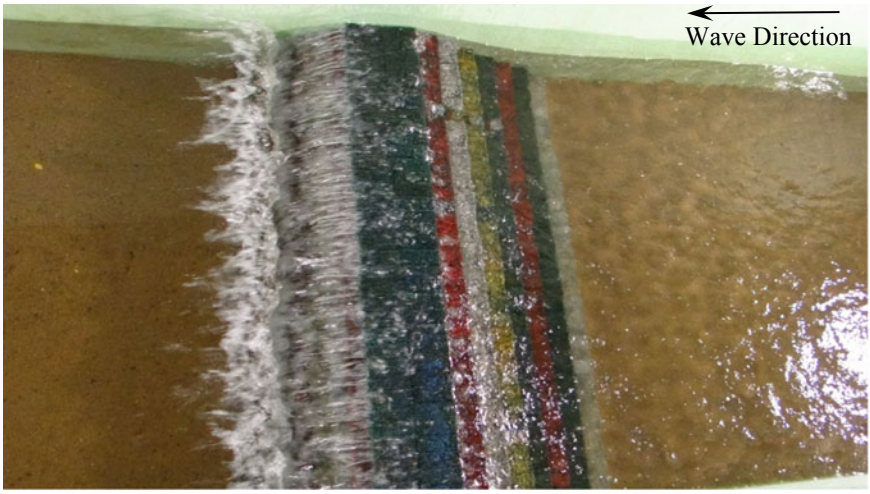

Fig. 4 Snapshot showing stability tests on emerged reef breakwaters

same. Further, the results from the present study is correlated to the damage trends produced by Ahrens [3] as shown in Fig. 5**.** The tests by Ahrens [3] corresponds to configurations with different bulk numbers ($B_n = A_t/D_{50}^2$). The tests with $h_c/d = 1.09$ and 1.19 correspond to lower bulk number ($B_n = 222$) while other tests are with $B_n > 350$ and hence the damage trends of $h_c/d = 1.09$ and 1.19 seem to be less

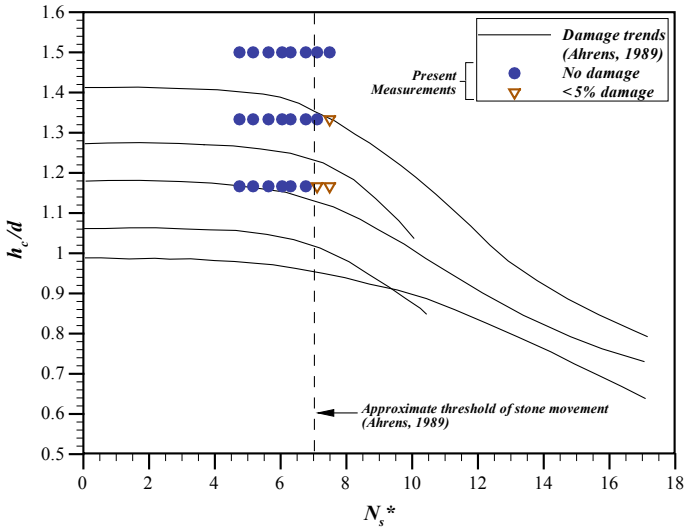

Fig. 5 Reproduced damage trends from Ahrens [3] and its correlation with the present experiments

stable. This also indicates the role of crest width in stability. It is evident from this observation that the increase in crest width increases the stability.

During the present investigations $H_s/L_p = 0.044 – 0.055$, there was no damage observed as the spectral stability number was $N_s^* < 7$. The observation made by Ahrens [3] is recalled here where the author points out that initiation of stone movement occurs for emerged reef breakwaters for $N_s^* > 7$. This observation is corroborated in the present study. In order to study further, two more wave steepness's were considered for emerged configurations which are $H_s/L_p = 0.038$ and 0.076. These two wave combinations produce a spectral stability number as $N_s^* = 7.1$ and 7.5 respectively. These additional tests were considered to examine if the displacement of gabions takes place past $N_s^* > 7$. It is noticed the additional tests with $N_s^* > 7$ tests with h_c close to still water has initiated damage as perceived from Fig. 5. The tests with $h_c/d = 1.17$ is seen to suffer damage as high as 4.5% for $N_s^* = 7.5$ on the contrary the tests with $h_c/d = 1.5$ is seen to suffer no damage for $N_s^* = 7.5$. The test condition with $h_c/d = 1.34$ is seen to undergo about 3% damage for $N_s^* = 7.5$. It may be inferred based on the observation that the configurations with crest height closer to still water is less stable in comparison with the configurations with relatively high crest height (h_c).

There is a scope for research to come up with design guidelines for stability aspects of emerged reef breakwaters with gabions. Such an investigation is not possible in the present study due to the limited number of data sets available. Further, it should be mentioned that the present studies are carried out with a constant crest width ($B = d$; $B = 2G$) and effects of stability on the variation of crest width are not investigated presently. It is seen [3] that the increase in crest width will increase the stability of reef breakwaters. During the examination, few tests were conducted with $B/d = 0.5$ (i.e., one gabion box on crest $B = 1G$) which is not analyzed and discussed in the manuscript. These tests with $B/d = 0.5$ were seen to be weekly stable and seen to undergo catastrophic failure and hence these tests were not considered. A snapshot of less stable configuration ($B = 1G$) undergoing catastrophic failure is illustrated in Fig. 6.

5 Conclusions

The stability aspects of reef breakwaters made of gabion boxes are investigated and discussed in the study. The tests cover a wide range of reef configurations ranging from $h_c/d = 0.5 – 1.5$ which consists of submerged and emerged conditions. Means of adopting the spectral stability number with relevance to gabion boxes has been discussed in the present study.

The stability characteristics of submerged reef configurations with $h_c/d = 0.5 – 1$ is seen to correlate with the design curves and equation proposed by van der Meer and Daemen [18]. The study also describes the ways of adopting the design aids proposed by van der Meer for the design of gabion-based reef breakwaters. For

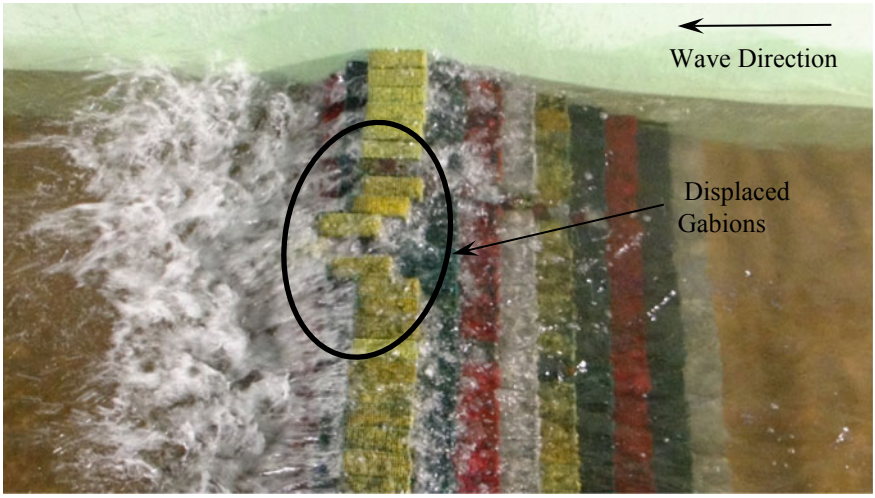

Fig. 6 Snapshot showing damaged reef breakwater

the given wave parameters, the structure close to the still water ($h_c/d = 1$) is more vulnerable to damage in comparison with a structure having greater submergence.

The Reef breakwaters with emerged configurations ($1 > h_c/d \geq 1.5$) were also examined and the test conditions with Spectral stability number $N_s^* < 7$ is found to be stable. For tests with highest crest height considered ($h_c/d = 1.5$), there was no notable displacement of gabions observed. This signifies that the structure is more susceptible to damage for tests with crest height close to still water ($h_c/d = 1$).

6 Appendix: Notation

The following symbols are used in this paper:

A_t Area of cross section the reef (m^2).
B Crest width of the reef (m).
D Water depth (m).
D_{50} Nominal Diameter of the Stone (M)
G Length of one gabion [=0.15 (m)].
H_s Incident significant wave height (m).
L_p Peak Wavelength (m).
d'' Freeboard (depth of submergence of the crest) (m).
h_c Crest height (m).
ρ_s Mass density of stone (kg/m^3).
ρ_w Mass density of water (kg/m^3).
ρ_g Mass density of gabion box (kg/m^3).

B_n Bulk number.
S Damage level.
N_s Stability number.
N_s* Spectral stability number.

Acknowledgements The authors are thankful to the Department of Ocean Engineering for providing the experimental facilities.

References

1. Ahrens JP (1984) Reef type breakwaters. In: Proceedings of the 19th Coastal Eng. Conference, Houston, Tex, pp 2648–2662 (1984)
2. Ahrens JP (1987) Characteristics of reef breakwaters, technical report CERC-87-17. U.S. Army Corps of Engineers, Waterways Experiment Station, Vicksburg
3. Ahrens JP (1989) Stability of Reef type breakwaters. J Waterw Port Coast Ocean Eng 115(2):221–234
4. Gravesen H, Jensen J, Sorensen T (1980) Stability of rubble mound breakwaters II. Danish Hydraulic Institute, Copenhagen, Denmark
5. Goda Y, Suzuki Y (1976) Estimation of incident and reflected waves in random wave experiments. In: Proceedings of 15th coastal engineering conference, vol 1, pp 828–845
6. Hall KR, Seabrook SR (1998) Design equation for transmission at submerged rubble mound breakwaters. J Coastal Res 26:102–106
7. Hudson RY (1959) Laboratory investigations on rubble-mound breakwaters. J Waterw Harbour Coast Eng Div ASCE 88:93–105
8. Hudson RY, Davidson DD (1975) Reliability of rubble-mound breakwater stability models. In: Proceedings of the ASCE symposium on modeling techniques. San Francisco, Calif, pp 1603–1622
9. Hughes SA (1993) Physical models and laboratory techniques in coastal engineering, vol 7. World Scientific
10. Johnson JW, Fuchs RA, Morison JR (1951) The damping action of submerged breakwaters. Trans Am Geophys Union 32(5):704–718
11. Le Méhauté B (1976) Similitude in coastal engineering. J Waterw Harbours Coast Eng 102(3):317–335
12. Oumeraci H (1984) Scale effects in coastal hydraulic models. In: Kobus H (ed) Proceedings in the symposium on scale effects in modeling hydraulic structures. International Association for Hydraulic Research, pp 7.10.1–7.10.7
13. Pilarczyk KW (2003) Design of low-crested submerged structures—an overview. In: 6th international conference on coastal and port engineering in developing countries. Pianc-Copedec, Colombo, Sri-Lanka, pp 1–16
14. Srineash VK, Murali K (2015) Pressures on gabion boxes as artificial reef units. In: Procedia Engineering: 8th international conference on Asian and Pacific Coasts (APAC 2015), vol 116(1), pp 552–559
15. Srineash VK, Murali K (2018) Wave shoaling over a submerged ramp: an experimental and numerical study. J Waterw Port Coast Ocean Eng 144(2):04017048–1–12
16. Teh HM (2012) Hydrodynamic performance of free surface semicircular breakwaters. Ph.D Thesis. The University of Edinburgh, United Kingdom
17. Van der Meer JW (1988) Rock slopes and gravel beaches under wave attack. Ph.D. thesis, Delft University of Technology, Delft, The Netherlands

18. Van der Meer, J.W., Daemen, I.F.R., Stability and wave transmission at low crested rubble mound structures, J. Waterw. Port, Coast. Ocean Eng., 1, 1–19 (1994).
19. Vidal A (1992) universal analysis for the stability of both low-crested and submerged breakwaters. In: Proceedings of 23rd international conference on coastal engineering, vol 128, pp 1679–1692

Development of Port Infrastructure at VOC Port, Tuticorin

R. Sundaravadivelu, S. Sakthivel, K. Jayachandran, C. Balakrishnan, and K. S. Roja

Abstract This paper reviews the salient features about development of port infrastructure at VOC Port, either modernising inner harbour or development of outer harbour. In order to increase the current cargo handling capacity from 64 Million Tonnes to 125 Million Tonnes, two alternatives are considered: Alternative I—Deepening of inner harbour basin up to (−)16.50 m CD and strengthening of existing berths for handling 6th generation Container vessels of 8000–12,500 TEU capacity and Post Panamax 95,000 DWT carriers and tankers having maximum draft of 15.20 m. Alternative II—Deepening and development of outer harbour with extension of Northern Break water and Southern Break Water, and Construction of new berths inside Break waters. The implementation of Alternative I and Alternative II will take 5 years and 10 years respectively. For prompt development, Alternative I is found to be most feasible. The total capital cost arrived for implementation of Alternative I is found to be 20% cheaper than Alternative II. The dredging quantity is more for Alternative I, but the dredge materials are utilised for reclamation. The schemes for upgradation/retrofitting of existing berths for deeper draft without affecting the cargo handling are also discussed.

Keyword Cargoes · Alternatives · Deepening · Strengthening · Implementation · Capital cost

R. Sundaravadivelu (✉) · S. Sakthivel · K. Jayachandran · K. S. Roja
Department of Ocean Engineering, Indian Institute of Technology Madras, Chennai 600036, India
e-mail: rsun@iitm.ac.in

S. Sakthivel
e-mail: enggoecrd@gmail.com

K. Jayachandran
e-mail: k_jaya_chandran@yahoo.co.in

K. S. Roja
e-mail: roja31396@gmail.com

C. Balakrishnan
V. O. Chidambaranar Port, Tuticorin 628004, India
e-mail: baluvocport@gmail.com

V. Sundar et al. (eds.), *Proceedings of the Fifth International Conference in Ocean Engineering (ICOE2019)*, Lecture Notes in Civil Engineering 106,
https://doi.org/10.1007/978-981-15-8506-7_4

1 Introduction

V. O. Chidambaranar Port (VOCPT) is one of the 12 major ports of India and the second largest port in Tamil Nadu. The port is strategically located near the international sea routes. The port is an artificial all weather port, it has a protected harbour basin with two rubble mound breakwaters of length 4085 and 3876 m on northern and southern side respectively. The total land area of the port is 2597.70 acres with a water spread area of 960 acres and is located south Old Tuticorin Harbour. Presently, the port has fourteen berth including ten alongside berths, three North Cargo Berth and two coal jetties. The current handling capacity for all berths of VOCPT is 65.90 million tonnes (MT). It predominantly handles dry bulk cargoes and containers followed by liquid bulk cargoes. The total cargo handled in the year 2017–2018 is 36.58 MT.

2 Site Location

VOCPT (8° 45′ N and 78° 13′ E) is an artificial deep water port located inside Gulf of Mannar in Tuticorin district, Tamil Nadu. The latitude and longitude of VOCPT is 8° 45′ N and 78° 13′ E.

VOCPT is well connected with roadways, railways and airways.

3 Geotechnical Data

The soil profile of the design borehole considered layer wise is detailed below, as shown in Fig. 1.

Dense gravels are found from (−)11.0 to (−)11.30 m. Calcareous sand stones are found from (−)11.30 to (−)12.50 m. Weak to moderately strong, weathered hard calcareous with voids are from (−)12.50 to (−)21.50 m. Weak to moderate weak, weathered lime stone are found from (−)21.50 to (−)27.50 m. Very weak residual formation of lime stone are found from (−)27.50 to (−)30.0 m.

4 Bathymetry

The bathymetry chart shown in the Fig. 2 gives the location of the berths inside VOC Port harbour basin and existing bed levels of the port in detail.

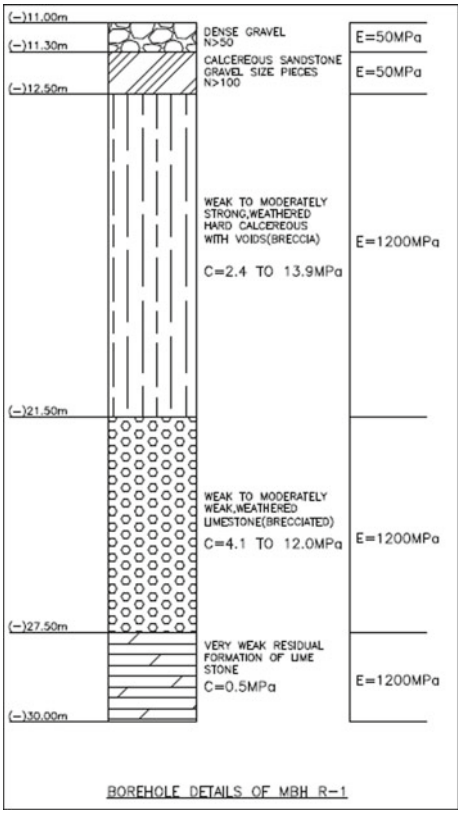

Fig. 1 Soil profile of design borehole considered

5 Oceanographic Data

5.1 Wave Data

Peak wave heights are observed during the mid of May and August of the order of 2.20 m and during December of the order of 1.50 m. The peak wave period is 9 s with the wave approaching from South of South East. The peak wave heights are 1.75 and 2.25 m with the wave approaching from East and South respectively. The port also experienced the shadow of a cyclone, which crossed near Tuticorin in December, 2000, during which the maximum wave height recorded by NIOT, was 3.00 m.

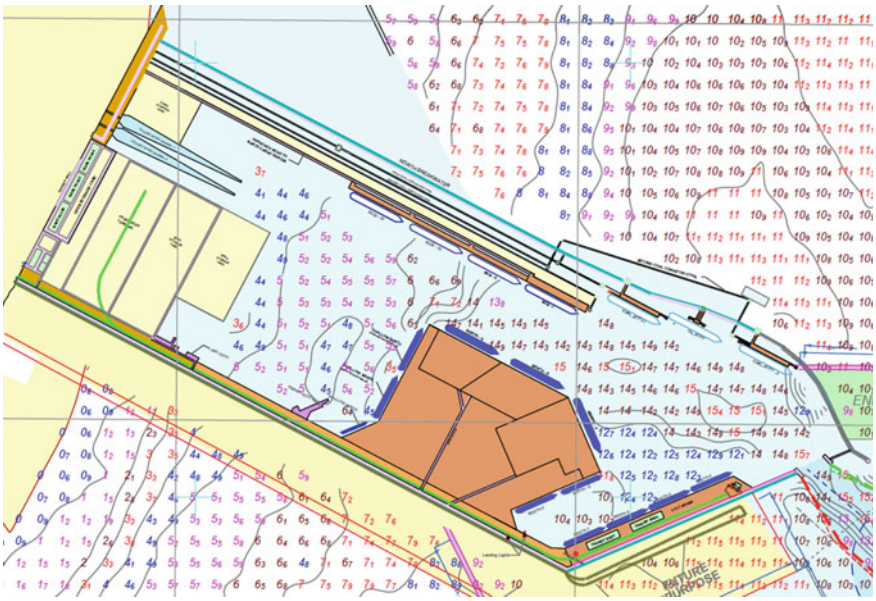

Fig. 2 Bathymetry chart

5.2 Tidal Data

The tidal levels with respect to Chart Datum at VOCPT are given below:

- Lowest Low Water Level: (+)0.11 m.
- Mean Lower Low Water Springs: (+)0.25 m.
- Mean Low Water Springs: (+)0.29 m.
- Mean Low Water Neaps: (+)0.55 m.
- Mean Sea Level: (+)0.64 m.
- Mean High Water Neaps: (+)0.71 m.
- Mean High Water Springs: (+)0.99 m.
- Highest High Water Level: (+)1.26 m.

6 Existing Berthing Facilities

The present berthing infrastructure at VOCPT consists of coal and oil berths/jetties along the north breakwater and container, multipurpose and shallow draft berths along the south breakwater. The details of existing berths is shown in Table 1.

With the existing facilities, the total handling capacity of the port is assessed at 65.90 million tonnes. The port handled around 36.58 million tonnes of cargo traffic during the year 2017–2018.

Table 1 Existing berth details

Existing name	Type of berth	Present bed level/dredge level (m) w.r.t. CD	Quay length (m)	DWT of vessel handled
Berth No-I	Alongside	(−)10.30	168	25,000
Berth No-II	Alongside	(−)10.30	168	40,000
Berth No-III	Alongside	(−)11.90	192	50,000
Berth No-IV	Alongside	(−)11.90	192	50,000
Berth No-V	Alongside	(−)10.30	168	40,000
Berth No-VI	Alongside	(−)10.30	168	40,000
Berth No-VII	Alongside	(−)14.10	370	50,000
Berth No-VIII	Alongside	(−)14.10	345.5	65,000
Berth No-IX	Alongside	14.10	334.50	75,000
Coal Jetty-I	Jetty	(−)14.10	225	50,000
Coal Jetty-II	Jetty	(−)14.10	225	60,000
NCB-I	Alongside	(−)14.10	306	75,000
NCB-II	Alongside	(−)14.10	306	95,000
NCB-III	Alongside	(−)6.20	306	95,000
Oil Jetty	Jetty	(−)14.10	200	65,000

7 Need for the Study

VOCPT is one of the fastest growing among Indian ports. As per statistics, the demand for coal is expected to increase by 43% by 2017–19 and container volumes are expected to reach 1.18 million TEU by 2025 in Tamilnadu.

VOCPT is not able to handle fully loading Panamax vessels due to current limitations of drafts and navigation. The depth of channel and the existing berths having maximum depth of 15.2 m which means 11.5 m draft Post Panamax only can be handled. In order to handle fully loaded Post Panamax vessel the port have to do partial transshipment until the vessel is lightened to the permissible draft. But anchorage handling is not effective as compared to handling at the berths. Apart from multiple handling, the lack of tranquil conditions at anchorage leads to significantly low productivity.

In this scenario, in order to improve the cargo handling capacity, the following two alternatives are proposed.

Alternative I: Deepening of inner harbour basin up to (−)16.50 m CD and strengthening of existing berths for handling 6th generation Container vessels of 8000 to 12,500 TEU capacity and Post Panamax 95,000 DWT carriers and tankers having maximum draft of 15.20 m.

Alternative II: Deepening and development of outer harbour with extension of Northern Break water and Southern Break Water, and Construction of new berths inside Break waters.

8 Alternative I

Proposed Alternative I have following components:

- Deepening of Inner harbour for berth 1–9, NCB-I to III, Coal jetties and oil jetty up to (−)16.50 m CD to handle 6th generation container vessels and Post Panamax vessels having maximum draft of 15.2 m.
- Strengthening/upgradation of existing berths if required.

The proposed layout of alternative I is shown in Fig. 3.

8.1 Berth I–VII

Berth I–VII are blocked wharf structure constructed in the 1960s. In order to handle 6th generation container vessels of 8000–12,500 TEU, the following development are needed.

- Deepening of harbour basin up to (−)16.50 m CD.
- Upgradation of Berth I–VII into Container terminals.

Fig. 3 Proposed layout of alternative I

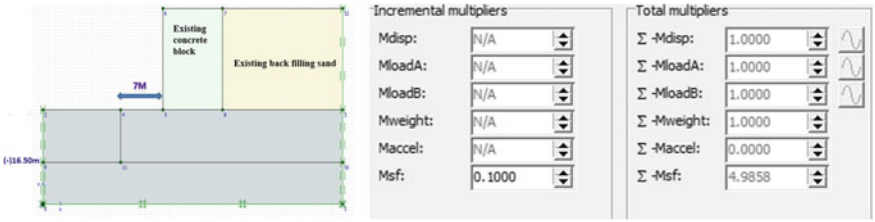

Fig. 4 Plaxis model and results of slope stability analysis of existing block wharf structures

The modification of existing block work into container terminal is not feasible with 10 m with wharf. The existing berths are not capable to handle the increased berthing and mooring force along with dynamic loading from cranes. Therefore upgradation of existing berth I–VII by constructing pile structure with suitable deck system is proposed.

A minimum clearance of 7 m from the berthing face of existing block wharf structure for upgradation is proposed as per active wedge calculation.

The slope stability analysis using plaxis is carried out to confirm the minimum clearance of 7 m for deepening of basin up to (−)16.50 m CD. The plaxis model and results of slope stability analysis is shown in the Fig. 4.

The factor of safety obtained from plaxis is about 4.9 against the minimum factor of safety of 1.4. This is clearly indicates that the proposed dredge slope is stable.

It is observed that strengthening/upgradation of berths is not required for dredging but it is required for handling higher draft container vessels.

The proposed plan of upgradation for existing block wharf structure is shown in Table 2.

8.2 Berth-VIII and X, NCB-I, II III, CJ-I and II

Berth no. VIII and IX, NCB-I, II and III and CJ-I and II are piled structures. The draft in front of these berths is (−)14.10 m. These berthing structures didn't cross its design life. STAAD Pro analysis for these berths is carried out to check adequacy for handling increased berthing and mooring force along with dynamic loadings from the cranes.

It is found that there is potential for existing berths Berth no. VIII and IX, NCB-I, II and III and CJ-I and II to handle higher draft vessels without any upgradation.

The proposed plan for existing berths Berth no. VIII and IX, NCB-I, II and III and CJ-I and II considering its adequacy is shown in Table 3.

Table 2 Proposed plan of upgradation for existing block wharf structure

Berth No.	Proposed scheme for upgradation	Dimension of proposed berth (m)	Proposed dredge level (m CD)	Proposed vessel draft (m)	Proposed vessel size	Crane proposed
Berth No-I Berth No-II	Addition of 4 rows of pile; 1 row in front and 3 rows at rear side of block work—to be converted to Container Terminal II(a)	420 × 36	(−)16.50	15.2	8000–12,500 TEU	1. RMQC 30 m c/c 2. LHM 550
Berth No-III Berth No-IV	Addition of 4 rows of pile; 1 row in front and 3 rows at rear side of block work—to be converted to Container Terminal II(b)	420 × 36	(−)16.50	15.2	8000–12,500 TEU	1. RMQC 30 m c/c 2. LHM 550
Berth No-V Berth No-VI	Addition of 4 rows of pile; 1 row in front and 3 rows at rear side of block work—to be converted to Container Terminal I	397 × 36	(−)16.50	15.2	8000–12,500 TEU	1. RMQC 30 m c/c 2. LHM 550
Berth No-VII	Addition of 4 rows of pile; 1 row in front and 3 rows at rear side of block work	370 × 36	(−)16.50	15.2	8000 TEU	1. RMQC 30 m c/c 2. LHM 550

8.3 Berth Capacity

The berth capacity for the proposed plan of Alternative I is shown in Tables 4 and 5 for container berths and coal berths respectively.

Table 3 Proposed plan for existing berths Berth no. VIII and IX, NCB-I, II and III and CJ-I and II

Berth No.	Existing dredge level	Proposed dredge level (m CD)	Proposed vessel draft (m)	Proposed vessel size
Berth No-VIII	(−)14.10	(−)16.50	15.20	8000 TEU
Berth No-IX	(−)14.10	(−)16.50	15.20	8000 TEU
NCB-I	(−)14.10	(−)16.50	14.60	96000 DWT
NCB-II	(−)14.10	(−)16.50	14.60	96000 DWT
NCB-III	(−)14.10	(−)16.50	14.60	96000 DWT
CJ-I	(−)16.00	(−)16.50	14.50	80000 DWT
CJ-II	(−)16.00	(−)16.50	14.50	80000 DWT

Table 4 Berth capacity for the proposed plan of container terminals

S. No.	Berth	Capacity	
		MTEU	MMPTA
1	Container Terminal I	0.88	12.58
2	Container Terminal II (A&B)	1.76	25.16
3	Berth—VII	0.74	10.58
4	Berth—VIII	0.69	9.86
5	Berth—IX	0.67	9.58
	Total	4.95	67.76

Table 5 Berth capacity for the proposed plan of coal berths

S. No.	Name of berths	Capacity (MMTPA)
1	Coal jetty—I	12.10
2	Coal jetty—II	9.00
3	NCB—I	12.10
4	NCB—II	12.10
5	NCB—III	12.10
	Total	57.40

9 Alternative II

Proposed Alternative II has following components:

- Extension of north breakwater of length 830 m
- Extension of south breakwater of length 2570 m
- Construction of new container terminals I and II of dimension of 420 × 36 m and container terminals III and IV 450 × 36 m
- Dredging up to (−)16.50 m CD in front of Coal jetties.

The proposed layout of Alternative II is shown in Fig. 5.

Fig. 5 Proposed layout of Alternative II

Table 6 Berth capacity for the proposed plan of container terminals

S. No.	Berth	Capacity	
		MTEU	MMPTA
1	Container Terminal I	0.87	12.62
2	Container Terminal—II	0.87	12.62
3	Container Terminal—III	0.93	13.48
4	Container Terminal—IV	0.93	13.48
	Total	4.95	77.44

Table 7 Berth capacity for the proposed plan of coal berths

S. No.	Name of berths	Capacity (MMTPA)
1	Coal jetty—I	12.10
2	Coal jetty—II	9.00
	Total	21.1

9.1 Berth Capacity

The berth capacity for the proposed plan of Alternative II is shown in Tables 6 and 7 for container berths and coal berths respectively.

10 Block Cost Comparison

Table 8 shows the block comparison of alternative I and II.

Table 8 Block cost comparison of Alternative I and II

S. No.	Description	Inner harbour Alternative I optimisation (INR. in crores)	Outer harbour development (INR. in crores)
1	Capital dredging	2532 (11.45 M. Cum)	1900 (8.95 M. Cum)
2	Bund construction	139 (2961 m length)	115 (2125 m length)
3	Widening of port entrance	10	–
4	Breakwater construction	49	455
5	Strengthening/construction of berths/terminal	320 (quay length of 420 m)	960 (quay length of 1775 m)
6	Total	3050 ($ 508 Million)	3430 ($ 572 Million)

11 Conclusion

The salient features about development of port infrastructure at VOC Port, either modernising inner harbour or development of outer harbour are discussed in this study.

It is observed that the Alternative I is cost effective compared to alternative II.

On the other hand, the dredging quantity is more for Alternative I, but the dredge materials are utilised for reclamation.

Berth capacity for Alternative I is 125 Million tonnes which is more compared to Alternative II of 98.54.

For prompt development, Alternative I is found to be most feasible.

Effect of Uncertainty on Slow Drift Motion of TLP

Vini Anna Varghese and Nilanjan Saha

Abstract Offshore structures are subjected to nonlinear and irregular wave forces. These structures try to attain their stability in the neighbourhood of their designed equilibrium point through their responses. The excitation forces consist of harmonic inertial wave components and drag dominated forces which changes according to water plane area. Being a multi-degree of freedom system, coupling among these degrees of freedom poses difficulties in obtaining the response. Therefore, these nonlinear structures require investigation in a stochastic framework for understanding their behaviour (sub-harmonic motions, chaotic responses). This paper models the slow drift motion of tension leg platform using a nonlinear stochastic differential equation. These stochastic differential equations are attempted using stochastic methods such as higher order Milstein scheme in an Ito framework. The impact of varying uncertainty on the nonlinear dynamics of system is studied

Keywords Stochastic · Ito calculus · Milstein scheme

1 Introduction

One of the complexities that researchers need to navigate while understanding the dynamics of offshore structures is the inherent non linearity involved. The fact that these structures are also subjected to stochastic loads in the form of wind, waves, and currents adds a further degree of complexity. Nonlinear dynamic behaviour of ocean structures is observed frequently. This includes coexisting periodic (harmonic, subharmonic, ultra-harmonic, ultra-subharmonic) and aperiodic (quasiperiodic, chaotic) motions and have been researched by scientists [1, 2]. System stability becomes further complex under near resonant phenomenon and it is sensitive

V. A. Varghese (✉) · N. Saha
Department of Ocean Engineering, Indian Institute of Technology Madras, Chennai 600036, India
e-mail: viniann08@gmail.com

N. Saha
e-mail: nilanjan@iitm.ac.in

V. Sundar et al. (eds.), *Proceedings of the Fifth International Conference in Ocean Engineering (ICOE2019)*, Lecture Notes in Civil Engineering 106,
https://doi.org/10.1007/978-981-15-8506-7_5

to initial conditions. Some of the ocean nonlinear problems studied by researchers are Slow drift motion of a tension leg platform, Mathieu instability of a tension leg platform, Impact forces on fender, etc. Thompson [1], Papoulias and Bernitsas [3], Bishop and Virgin [4], Sharma et al. [5], Bernitsas and Chung [6] and Gottlieb and Yim [7–9] observed the complex nonlinear and chaotic responses of compliant offshore structures [1, 3–9]. Such structures characterize nonlinearity in restoring, damping and coupled hydrodynamic exciting forces.

Usually, ocean mathematical models are handled in a deterministic manner under external loads due to which nonlinear ordinary differential equations govern physical systems. While considering the deterministic model, the assumption was that initial data can be obtained and measurement errors are avoidable. With the advancement of modelling uncertainty through Brownian motion model, scientific community can finally understand the importance of stochastic differential equation in an Ito based calculus framework. Researchers have also reported that considering randomness with nonlinearity can dramatically increase the amplitudes of subharmonic and chaotic responses [10]. Hence to simulate a realistic model it is essential to address the nonlinearity and uncertainty in a proper framework.

Now, the response of a nonlinear dynamic system subjected to stochastic loads can be solved using frequency domain, probability domain and time domain techniques. The choosing of the domain depends on the problem at hand. Since most frequency domain techniques uses some sort of linearization techniques it does not work well for nonlinear systems and may not give accurate results near resonating condition. The disadvantage of probability domain technique is that the solution is not available till date for various types of random noise, nonlinearities and for systems with multi degrees of freedom.

Based on these insights, one can infer that numerical time domain techniques are the most sought out for the study of stochastic nonlinear dynamics. Unlike the frequency and probability domain techniques, numerical time domain technique works for nearly all types of random noise, nonlinearities as well as for systems with multi degrees of freedom. The main drawback of numerical time domain technique is that it takes too much computational time. However, with the advent of modern computers, the computational time has reduced drastically.

The study of stochastic nonlinear dynamics in the field of ocean structures is age-old, given the loading conditions they are subjected to. Brief literature survey in the area of offshore field revealed that methods used by various researchers till date for studying the stochastic dynamics of offshore structures are, linearization techniques [11–16], stochastic averaging method [17–19], Fokker–Planck equation and path integral method [20–23].

Research based on time domain approach is relatively new in the field of ocean engineering. One may take recourse to time domain analysis such as numerical integration techniques which are still unexplored in the case of ocean structural dynamics. Some examples are Euler–Maruyama Method, Stochastic Heun Scheme, Milstein's Higher Order Method and Higher Order Stochastic Runge–Kutta (SRK) Schemes. In these schemes, the sample paths of the numerical approximations are obtained and they provide considerable insights into qualitative behaviour and nonlinear dynamics

of ocean structures. Since these methods are obtained in an ensemble manner, variance reduction techniques become important as it allows a considerable decrease in the required sample sizes, thereby reducing computational costs [24]. It is also seen that computational costs such as time and memory required increases with the dimension of the problem.

In this paper, the mathematical models of ocean structures are considered taking into account nonlinearity and uncertainty associated with the system/loads to predict nonlinear dynamic behaviour. The ocean structure will be represented as a nonlinear stochastic differential equation (NSDE). The numerical integration technique used to solve this equation will be Higher order Milstein scheme.

2 Mathematical Formulation

Ocean waves are 'highly' irregular and generally the sea state can be represented as a sum of a set of stationary processes with predominant wave frequencies. During design, only the predominant frequency is considered, and the uncertainty associated with the process may be modelled as stationary Gaussian white noise process (meaning that one is interested in predicting the short-term sea state). Here the additive and/or multiplicative white noise vector process is defined as formal derivatives of Weiner vector process.

Thus, a stochastically driven offshore structural system can be generally represented as a nonlinear oscillator with n degrees of freedom, in the form of a standard nonlinear stochastic differential equation (NSDE).

$$M\ddot{X} + C\dot{X} + KX + A_{nl}\left(X, \dot{X}, t\right) = F(t) + \sum_{r=1}^{n} B_r\left(X, \dot{X}, t\right)\dot{W}(t) \tag{1}$$

Here $X, \dot{X} \in R^n$ are the n dimensional state vectors, M, C, K are $n \times n$ mass, stiffness and damping matrices, and $A_{nl}\left(X, \dot{X}, t\right)$ denotes the nonlinear part of the velocity drift vector. $F(t)$ denotes the externally applied deterministic force vector. The diffusion vectors $B_r\left(X, \dot{X}, t\right)$ are coefficients of r independently evolving Weiner processes where $B_r(0) = 0$ and $E[B_r(t)B_r(s)] = \min(t, s)$. As Weiner process is continuous and differentiable nowhere in time, it exists only as a measure and is not a valid mathematical function. Now, we can appropriately recast the governing equation (Eq. 1) as the following system of $2n$-dimensional and incremental state space equations:

$$\begin{aligned} \mathrm{d}X_1 &= X_2\mathrm{d}t \\ \mathrm{d}X_2 &= A(X_1, X_2, t)\mathrm{d}t + \sum_{r=1}^{n} \sigma_r(X_1, X_2, t)\mathrm{d}W_r(t) \end{aligned} \tag{2}$$

where $A(X_1, X_2, t) = -KX_1 - CX_2 + F(t) - A_{nl}(X_1, X_2, t)$ is the velocity drift vector field written as a function of the displacement ($X_1 := X \in R^n$) and velocity ($X_2 := X \in R^n$) components of the $2n$-dimensional response vector $X = \left\{X_1^T, X_2^T\right\} \in R^{2n}$.

In order to check the boundedness of the solution vector X, we require the drift $a^T = \left\{x_2^{(p)}, A^{(p)}\right\} \in R^{2n}$ and diffusion vectors $b_r^T = \left\{0, \sigma_r^{(p)}\right\} \in R^{2n}$ to satisfy the Lipchitz and linear growth condition:

$$|a(x,t) - a(y,t)| + |b_r(x,t) - b_r(y,t)| \leq K_1|x - y| \tag{3}$$

$$|a(x,t)|^2 + |b_r(x,t)|^2 \leq K_2^2\left(1 - |x|^2\right) \tag{4}$$

for some positive (real) constant K_1 and K_2 and $x, y \in R^{2n}$. Under these conditions there will be a unique non-anticipating solution $X(t)$ in the range $[t_0, T]$. For weak solutions, only the Lipschitz conditions are sufficient for boundedness of solutions.

3 Numerical Integration Solution

The review article by Kloeden and Platen [24] contains an up-to-date bibliography on numerical methods as Runge–Kutta, Euler and Milstein schemes [24]. Higham [25] has provided an algorithmic introduction to strong Euler–Maruyama and Milstein methods and discussed rates of convergence of these methods [25]. The solution (Markov process) of the NSDEs driven by Gaussian white noise (Weiner process) cannot be generally expressed in terms of Reimann integrals because of the rapid fluctuations of the integrator Weiner process. Hence, the formulated NSDE based on Weiner process is solved using Stochastic (Ito) calculus. A major difference from the deterministic differential equations is the chain rule for the differentials called Ito Lemma. The state space NSDE equation is discretized in time by using the Stochastic Ito–Taylor expansion [24]. Thus, we consider discretization times $t_0 = 0 \leq t_1 \leq t_2 \leq \cdots \leq t_j \leq \cdots$ with $\Delta_j = t_{j+1} - t_j$; $j = 0, 1, 2, \ldots$. We presently adopt a uniform step size to stay focused on the basic elements of the method. A 1.5 local-order strong Ito–Taylor expansion of the SDE leads to the numerical solution and has its ith component given by

$$x_{k+1}^i = x_k^i + a^i\Delta + \frac{1}{2}L^0a^i\Delta^2 + \sum_{j=1}^{s}\left(b^{i,j}I_j + L^0b^{i,j}I_{(0,j)} + L^ja^iI_{(j,0)}\right)$$

$$+\sum_{j_1,j_2=1}^{s} L^{j_1} b^{k,j_2} I_{(j_1,j_2)} + \sum_{j_1,j_2,j_3=1}^{s} L^{j_1} L^{j_2} b^{k,j_3} I_{(j_1,j_2,j_3)} \quad k = 0, 1, 2, \ldots, \tag{5}$$

where, the operators are given by

$$L^r = \sum_{j=1}^{n} b^{j,r} \frac{\partial}{\partial x^j} \text{ and}$$
$$L^0 = \frac{\partial}{\partial t} + \sum_{j=1}^{n} a^j \frac{\partial}{\partial x^j} + \frac{1}{2} \sum_{r=1}^{s} \sum_{i,j=1}^{n} b^{r,i} b^{r,j} \frac{\partial^2}{\partial x^i \partial x^j} \tag{6}$$

The quantities I_j, $I_{(j,0)}$, $I_{(0,j)}$, $I_{(j_1,j_2)}$ and $I_{(j_1,j_2,j_3)}$ appearing in equation are known as Multi stochastic integrals (MSIs). They are given by

$$I_{(j)} = \int_{t_k}^{t_{k+1}} \mathrm{d}W_\tau^j,\ I_{(0,j)} = \int_{t_k}^{t_{k+1}} \int_{t_k}^{\tau_1} \mathrm{d}s \mathrm{d}W_{\tau_1}^j \text{ and}$$
$$I_{(j,0)} = \int_{t_k}^{t_{k+1}} \int_{t_k}^{s_1} \mathrm{d}W_s^j \mathrm{d}s_1,$$
$$I_{(j_1,j_2)} = \int_{t_k}^{t_{k+1}} \int_{t_k}^{\tau_1} \mathrm{d}W_{\tau_2}^{j_1} \mathrm{d}W_{\tau_1}^{j_2} \text{ and}$$
$$I_{(j_1,j_2,j_3)} = \int_{t_k}^{t_{k+1}} \int_{t_k}^{\tau_1} \int_{t_k}^{\tau_2} \mathrm{d}W_{\tau_3}^{j_1} \mathrm{d}W_{\tau_2}^{j_2} \mathrm{d}W_{\tau_1}^{j_3} \tag{7}$$

Now for studying the response of a tension leg platform we are interested in the moments of the response only. Hence weak approximation of the Milstein scheme is considered where in the multiple stochastic integrals are modelled using correlated random variables and solved in the Monte Carlo framework.

4 Discretization of Differential Equations

For illustration, the governing equation of an oscillator subjected to Gaussian white noise is given below:

$$M\ddot{x} + C\dot{x} + Kx = c\dot{W}(t) \tag{8}$$

The corresponding SDEs (Eq. 8) may be expressed in the following incremental form (Eq. 9) as

$$\begin{aligned} \mathrm{d}x_1 &= x_2 \mathrm{d}t \\ \mathrm{d}x_2 &= \frac{1}{M}\{-Kx_1 - Cx_2\}\mathrm{d}t + \sigma \mathrm{d}W \end{aligned} \tag{9}$$

Now the higher order Milstein scheme solution for the above SDE considering uniform step size is given by Eq. (10). In this equation the displacement and velocity components of the dynamical system are mapped stochastically.

$$\begin{aligned} x_1(t) &= x_1(t_0) + x_2\Delta + (-K_1x_1 - Cx_2)\frac{\Delta^2}{2} + \sigma\Delta Z \\ x_2(t) &= x_2(t_0) + (-Kx_1 - Cx_2)\Delta \\ &\quad + \{-x_2K - C(-Kx_1 - Cx_2)\}\frac{\Delta^2}{2} \\ &\quad + \sigma\Delta W - \sigma C\Delta Z \end{aligned} \tag{10}$$

4.1 Numerical Illustrations

4.1.1 Slow Drift Motion of TLP

The nonlinear model for the surge motion of floating offshore structures such as tension leg platform is taken from Naess et al. [26] and is subjected to uncertainty (Eq. 11). Here the nonlinearity is due to the set down effect of TLP due to which a vertical tension component is added. Hence the physical model becomes a nonlinear stochastic differential equation. When we consider nonlinearity, we can detect the sub-harmonic, super-harmonics and chaotic motions. A floating offshore structure can be briefly characterized by two distinct timescales, i.e. the fast and the slow timescales. The fast timescale falls in the dominant sea state period of interest. The slow timescale (also named as slowly varying drift) is defined by the natural period of the mooring system. This slowly varying drift motion response occurs in lateral motion modes (surge, sway and yaw) and often leads to resonance periods in these motion modes of the order of minutes. They are caused due to three factors; second order hydrodynamic pressure due to the first order wave, interaction between the first-order motion and the first order wave, and finally, second order potential due to slowly varying forcing on body surface and free-surface. They are also caused due to variation in free surface elevation near TLP columns and nonlinear feedback of the structural response to the wave loads. Lot of research work has been conducted on the effect of different mechanism on the slow drift motion but less work has been done by incorporating the uncertainties present.

Table 1 Structural properties of TLP under consideration [26]

Properties	Value
Mass (including added mass), kg	1.5×10^7
Damping, Ns/m	7.32×10^4
Stiffness, N/m	3.57×10^4
Density, kg/m^3	1030
C_m	2.0
C_d	1.0
Submerged volume, m^3	13420
Submerged area, m^2	700

In the present work, the nonlinear dynamics is studied in presence of uncertainties considering only surge motion governed by [26]:

$$x + C\dot{x} + K_1 x + K_2 x^3 = \sigma \dot{W}(t) \tag{11}$$

The structural properties of the TLP under consideration for the present work are given in Table 1. We consider a sea state of $H_s = 10$ m and $T_p = 11$ s and calculate the Morison wave force for TLP under consideration.

The robustness of the numerical Milstein scheme algorithm is found out by comparing with analytical solution given by the Fokker–Plank equation. The exact joint density function of the model subjected to Gaussian white noise can be obtained through a reduced Fokker–Planck equation. Using this function, we can further derive the statistical moments for comparison.

$$p(x, \dot{x}) = \mathrm{Re}\left[xp\left(\frac{-C\dot{x}^2}{\sigma^2} - \int_0^x C \frac{K_1 q + K_2 q^3}{0.5\sigma^2} \mathrm{d}q \right) \right] \tag{12}$$

The normalization constant R must be found to satisfy the probabilistic constraint $\int \int_{-\infty}^{\infty} p(x, \dot{x}) \mathrm{d}x \mathrm{d}\dot{x} = 1$. The statistical moments of any deterministic function $\Phi(x, \dot{x})$ can then be found out as $\mathbf{E}[\Phi(x, \dot{x})] = \int \int_{-\infty}^{\infty} \Phi(x, \dot{x}) p(x, \dot{x}) \mathrm{d}x \mathrm{d}\dot{x}$. Hence, these moments can be used for comparison to confirm the robustness of the numerical scheme. For convergence study, we can conclude that an accurate result can be obtained with a step size of 0.01, total time 5000 s and 500 Monte Carlo simulations (Figs. 1 and 2). By comparing variance with the Fokker–Planck equation, the accuracy and robustness of the numerical higher order Milstein scheme is validated (Fig. 1).

For the analysis, the system is subjected to harmonic loads with the presence of uncertainty. The intensity of uncertainty is varied to capture the change in nonlinear dynamics. We chose 3 cases with uncertainty intensity $\sigma = 0.10, 0.15, 0.25$. It is observed that as the uncertainty is increased, higher peaks in the displacement and velocity response of the system are obtained (Fig. 3).

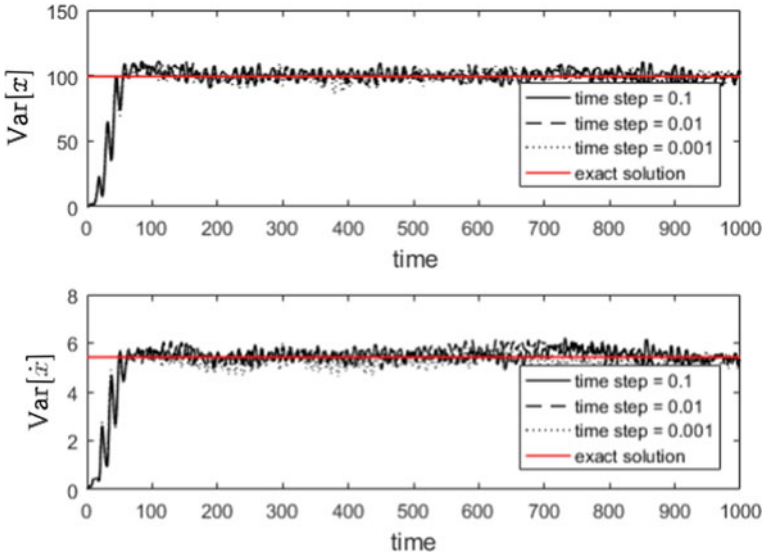

Fig. 1 Variance of displacement and velocity for step sizes compared with FPK solution (exact one)

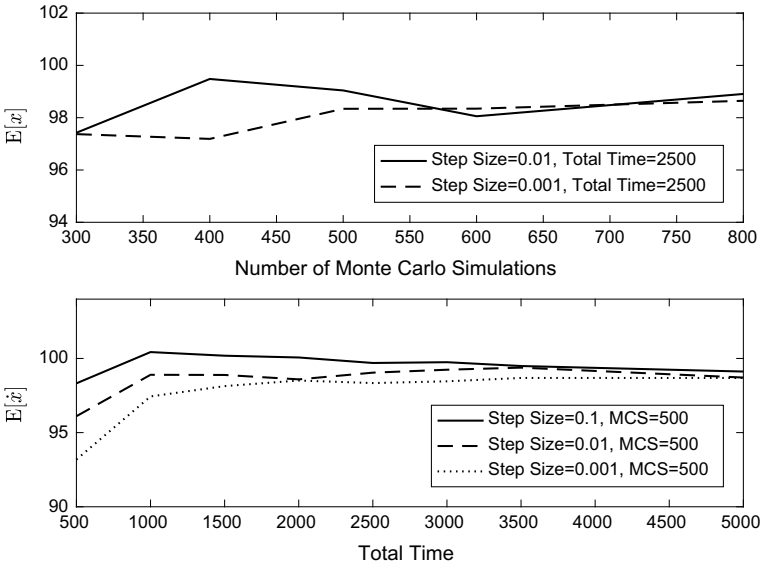

Fig. 2 Convergence diagrams with respect to simulations and step sizes

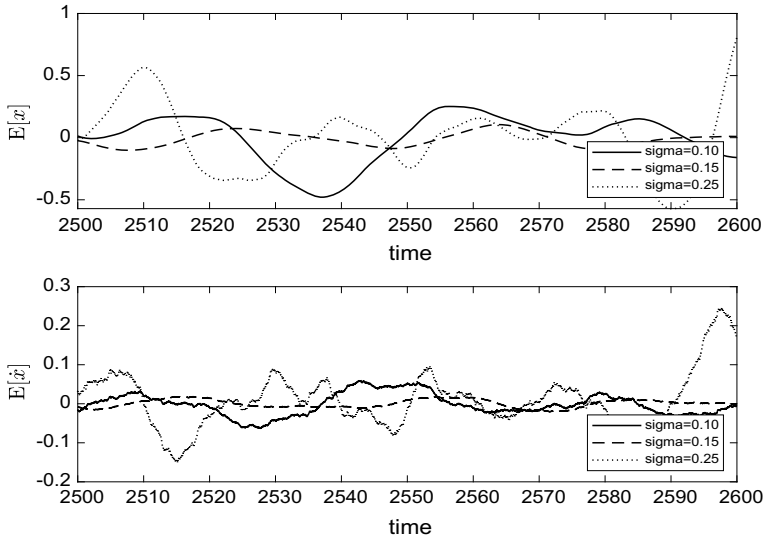

Fig. 3 Mean stochastic flow of displacement (x) and velocity ($\dot{x}$) for varying uncertainties

Figure 4 displays the transient solution in the marginal PDF format at different time instants and we observe that the maximum of the transient solutions goes down with the increase in time. As expected transient solution tends to be stationary once it reaches a particular time. It is also observed from the marginal PDF plots that the altitude of peaks decreases as the uncertainty increases.

5 Conclusions

In the present work, the focus is on the study of impact of uncertainties on a nonlinear offshore system. Numerical time domain technique using the Ito based stochastic differential equations is used for this study. Milstein scheme is used to bring out the features associated with the system. The accuracy and robustness of the scheme is compared with the Fokker–Planck equation solution. It is observed that nonlinear dynamic behaviour of the system is substantially altered by the presence of uncertainties along with which one may capture the transient dynamics usually determined through evolution of the probability density function. Also, while doing experiments on ocean structures, one may encounter chaotic motions which can be understood in a better way using these numerical schemes by accounting for uncertainties. As a study, an illustration on slow drift motion of Tension Leg Platform is considered. It is seen that Milstein scheme can be used to solve nonlinear offshore problems with ease giving accurate results. However, further studies are underway to understand more complex offshore structures.

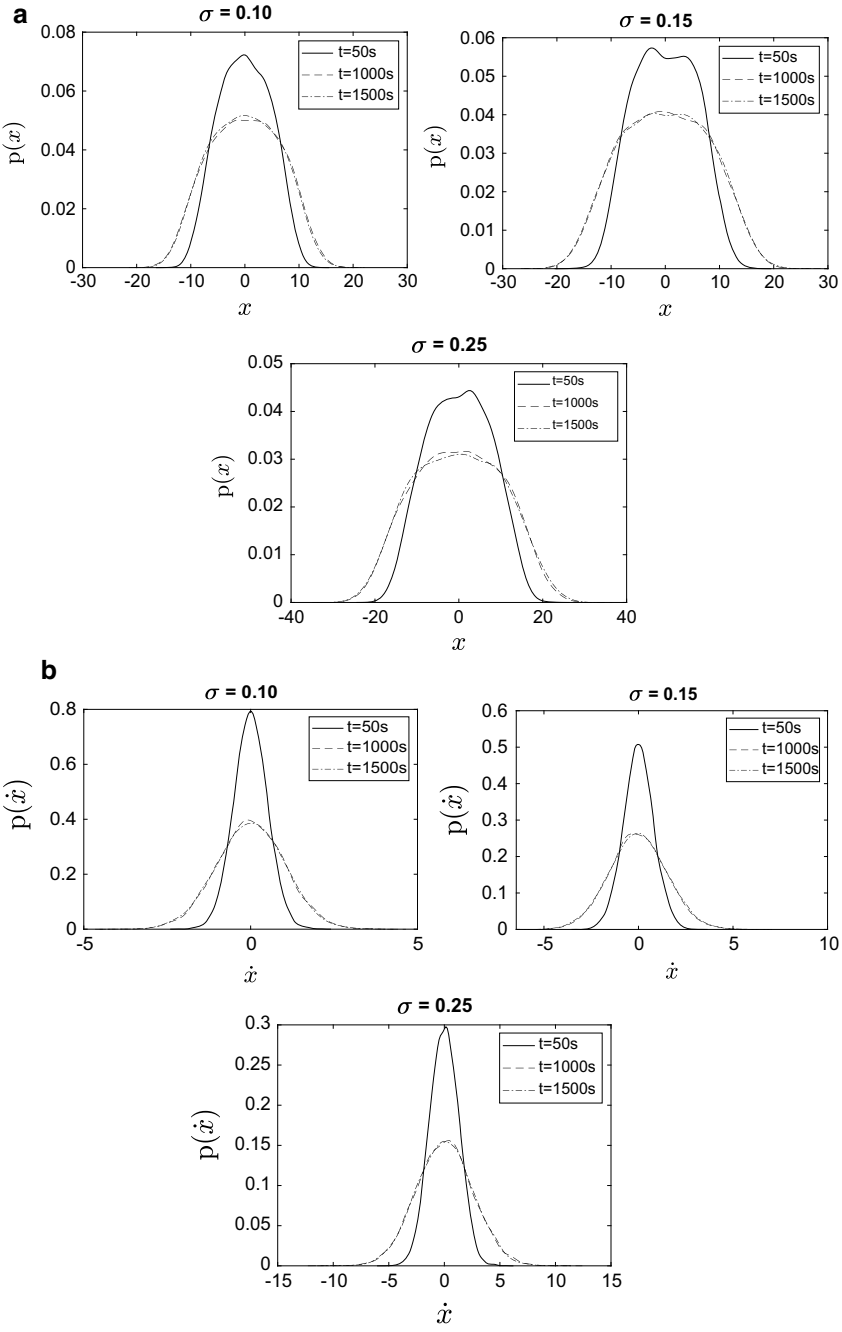

Fig. 4 **a** Evolutionary marginal probability density function for **a** displacement (x), **b** velocity ($\dot{x}$) for varying uncertainty σ and at different time instants

References

1. Thompson JMT (1983) Complex dynamics of compliant off-shore structures. Proc Royal Soc London A Math Phys Sci 387(1793):407–427
2. Adrezin R, Bar-Avi P, Benaroya H (1996) Dynamic response of compliant offshore structures. J Aerosp Eng 9(4):114–131
3. Papoulias FA, Bernitsas MM (1988) Autonomous oscillations, bifurcations, and chaotic response of moored vessels. J Ship Res 32(03):220–228
4. Bishop SR, Virgin LN (1988) The onset of chaotic motions of a moored semi-submersible. J Offshore Mech Arct Eng 110(3):205–209
5. Sharma SD, Jiang T, Schellin TE (1988) Dynamic instability and chaotic motions of a single-point-moored tanker. In: 17th Symposium on naval hydrodynamics
6. Bernitsas MM, Chung JS (1990) Nonlinear stability and simulation of two-line ship towing and mooring. Appl Ocean Res 12(2):77–92
7. Gottlieb O, Yim SCS (1993) Drag-induced instabilities and chaos in mooring systems. Ocean Eng 20(6):569–599
8. Gottlieb O, Yim SC (1997) Nonlinear dynamics of a coupled surge-heave small-body ocean mooring system. Ocean Eng 24(5):479–495
9. Gottlieb O, Yim SC (1992) Nonlinear oscillations, bifurcations and chaos in a multi-point mooring system with a geometric nonlinearity. Appl Ocean Res 14(4):241–257
10. Jefferys ER (1988) Nonlinear marine structures with random excitation. J Offshore Mech Arct Eng 110(3):246–253
11. Atalik TS, Utku S (1976) Stochastic linearization of multi-degree-of-freedom non- linear systems. Earthquake Eng Struct Dynam 4(4):411–420
12. Sigbjörnsson R, Smith EK (1980) Wave induced vibrations of gravity platforms: a stochastic theory. Appl Math Model 4(3):155–165
13. Brynjolfsson S, Leonard JW (1988) Response of guyed offshore towers to stochastic loads: time domain vs frequency domain. Eng Struct 10(2):106–116
14. Spanos PD, Ghosh R, Finn LD, Halkyard J (2005) Coupled analysis of a spar structure: Monte Carlo and statistical linearization solutions. J Offshore Mech Arct Eng 127(1):11–16
15. Ellermann K (2007) Techniques for the analysis of the stochastic dynamics of offshore systems. In: ASME 2007 26th International Conference on Offshore Mechanics and Arctic Engineering. American Society of Mechanical Engineers Digital Collection, pp 487–496
16. Spanos PD, Nava V, Arena F (2011) Coupled surge-heave-pitch dynamic modeling of spar-moonpool-riser interaction. J Offshore Mech Arctic Eng 133(2):021301
17. Rajagopalan A, Taylor RE (1982) Dynamics of offshore structures, part II: stochastic averaging analysis. J Sound Vib 83(3):417–431
18. Banik AK, Datta TK (2003) Stochastic response and stability analysis of single leg articulated tower. In: ASME 2003 22nd international conference on offshore mechanics and arctic engineering. American Society of Mechanical Engineers Digital Collection, pp 21–28
19. Kougioumtzoglou IA, Zhang Y, Beer M (2015) Softening duffing oscillator reliability assessment subject to evolutionary stochastic excitation. ASCE-ASME J Risk Uncertainty Eng Syst Part A Civil Eng 2(2):C4015001
20. Naess A, Johnsen JM (1993) Response statistics of nonlinear, compliant offshore structures by the path integral solution. Probab Eng Mech 8:91–106
21. Kougioumtzoglou IA, Spanos PD (2014) Stochastic response analysis of the softening Duffing oscillator and ship capsizing probability determination via a numerical path integral approach. Probab Eng Mech 35:67–74
22. Chai W, Naess A, Leira BJ (2015) Stochastic dynamic analysis and reliability of a vessel rolling in random beam seas. J Ship Res 59(2):113–131
23. Zhu HT, Duan LL (2016) Probabilistic solution of non-linear random ship roll motion by path integration. Int J Non-Linear Mech 83:1–8
24. Kloeden PE, Platen E (1992) Numerical solution of stochastic differential equations, 1st edn. Springer, Berlin

25. Higham DJ (2001) An algorithmic introduction to numerical simulation of stochastic differential equations. SIAM Rev 43(3):525–546
26. Naess A, Gaidai O, Teigen PS (2007) Extreme response prediction for nonlinear floating offshore structures by Monte Carlo simulation. Appl Ocean Res 29(4):221–230

Design of a Minor Fishing Harbor in India with Special Reference to Training of the Mouth of River Chapora

D. K. Maiti, Vallam Sundar, and S. A. Sannasiraj

Abstract Most of the fishing harbors along the Indian coast are located within the tidal inlets, barring a few on the open coast. Fishing harbor on an open coast needs protection in the form of breakwaters or training walls for providing tranquility conditions and safe vessel maneuvering and landing facilities. Practically, all inland fishing harbors suffer siltation problems. The studies on the development of a new inland fishing harbor on River Chapora (15° 36′4 6.22″ N and 73° 44′ 51.34″ E) in the state of Goa in India with such problem were carried out, the results of which are reported in this paper.

Keywords Training wall · Fishing harbor · Numerical modeling

1 Introduction

The west coast of India is flourishing with fisheries-related activities owing to the fauna of variety of fish catchment regions. Goa is a predominant union territory thriving on tourism and fisheries-related activities. River Chapora in Goa (Fig. 1), drains into the Arabian Sea. An L-shaped jetty has been constructed in the river mouth region at a distance of about 800 m from the coast for providing fishing boat landing facilities as shown in Fig. 2. The existing jetty is inadequate, and thus, expansion and establishment of a fishing harbor of the aforesaid location have been proposed. The existing infrastructure at the present jetty is very much inadequate to take care of post-harvest fishing activities. Moreover, mouth of River Chapora has siltation problem due to various coastal processes. This inadequate navigational draft hinders the entry and exit of fishing vessels across the varying seasons over a year, resulting

D. K. Maiti (✉)
West Bengal Fisheries Corporation Limited, Kolkata 700091, India
e-mail: dkm6675@gmail.com

V. Sundar · S. A. Sannasiraj
Department of Ocean Engineering, Indian Institute of Technology Madras, Chennai 600036, India

V. Sundar et al. (eds.), *Proceedings of the Fifth International Conference in Ocean Engineering (ICOE2019)*, Lecture Notes in Civil Engineering 106,
https://doi.org/10.1007/978-981-15-8506-7_6

Fig. 1 Location map

Fig. 2 Chapora jetty

Table 1 Wave climate of Chapora mouth

Month	Significant wave height (m)	Mean wave period	Wave direction from north
January	1	5	350
February	1	5	330
March	1	5	320
April	1	5	320
May	1	5	270
June	2	6	260
July	2.5	6	250
August	2.5	6	250
September	1.5	5	260
October	1	5	300
November	1	5	350
December	1	5	350

in a loss of a number of fishing operation days as well as deterioration of harvested marine fish quality.

2 Site Conditions

The wave climate and the tidal data are to be analyzed to arrive at the sedimentation pattern that could facilitate an optimal design. Wave climate data is obtained from NIO wave atlas and the tidal data from Indian Tide Table.

2.1 Wave Climate

It collectively includes the mean values of significant wave height, wave period and wave direction averaged over 19-years ship observed data in the deep waters. Table 1 represents the wave climate of the Chapora fishing harbor location.

2.2 Wave Heights

The monthly distributions of deep-water wave heights in terms of percentage of occurrence were derived from available wave data. It is observed that the wave

heights vary in between 1.0 and 2.50 m with a percentage of maximum height of 2.50 m occurrence varying from 10 to 20%.

2.3 Wave Period

The monthly distribution of wave periods as obtained from the wave atlas shows that the maximum percentage of occurrence is with waves associated with periods ranging between 5 and 6 s.

2.4 Wave Direction

The monthly distribution of wave directions with respect to geographic north as obtained from the wave atlas shows variation from 250 to 350°.

2.5 Tide Levels

The standard tide levels furnished in Indian Tide Table published by the Surveyor General of India for Marmagao are equally applicable for Chapora fishery harbor. The tide levels are presented in Table 2.

3 Proposed Layout of the Chapora Fishing Harbor

Layout of the proposed fishing harbor is shown in Fig. 3. The design of the various components of the fishing harbor complies with the Indian code of practice and

Table 2 Tide information of Chapora mouth

Stage of tide	Level (m)
HHW	+2.30
MHHW	+2.06
MLHW	+1.78
MSL	+1.30
MHLW	+1.05
MLLW	+0.37
LLW	+0.00

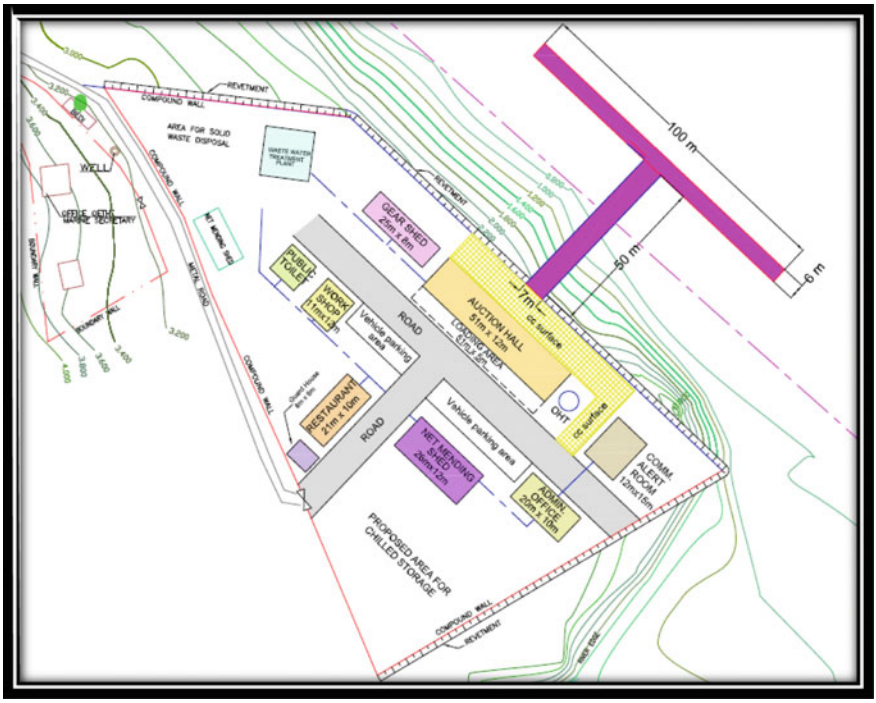

Fig. 3 Layout of Chapora fishing harbor

CEM (CERC) [1]. The following surveys and investigations were carried out prior to commissioning of the final layout.

- Topographic survey of landside harbor area
- Bathymetry survey from new harbor location to the outfall of River Chapora along the river
- Geotechnical investigations for landside facilities and waterfront jetties
- Tidal observation for continuous 15 days
- Data on MFVs and landing of harvested marine fish

4 Mathematical Model

A detailed study was carried out to investigate on training the river mouth for safe maneuverability of the fishing vessels against to waves, tides and currents. This study encompasses the river training works and subsequent wave disturbances near the river mouth. The impact of the proposed construction of shore-connected structures on the neighborhood shoreline is predicted.

4.1 Littoral Drift

The wave data has been analyzed to obtain the monthly average wave height, wave period and wave direction. The average breaking wave characteristics were derived from the deep-water wave climate as discussed in the earlier section. The results indicate that the maximum breaker height varies from about 1.0 to 2.1 m. The month-wise distribution of sediment transport was also computed based on the methodology proposed by Komar [2–3]. Further, the monthly sediment transport has been estimated using the method of energy flux [1] and by integrating the distribution of sediments within the surf zone as suggested by Komar [2–3]. The results obtained from the above three methods have yielded similar results. The net drift is towards the south to an extent of about 4.65 lakh m^3/year. Hence, a suitable training wall is required to avoid river mouth closure as well as to maintain sufficient water depth throughout the year.

The results indicate the surf width is found to range between 439 and 914 m in the months of January to December and the maximum occurring during June to September. This is the season for active longshore drift in the surf zone. The month-wise distribution of sediment transport was also computed based on the methodology proposed by Komar [2–3]. Further, the monthly sediment transport has been estimated using the method of energy flux [1] and by integrating the distribution of sediments within the surf zone as suggested by [2–3]. The results obtained from the above three methods have yielded similar results. The net drift is towards the south to an extent of about 4.65 lakh m^3/year. Hence, a suitable training wall is required to avoid river mouth closure as well as to maintain sufficient water depth throughout the year. The results Fig. 4a–d show the monthly variation of maximum breaker height, breaker angle, surf zone width and longshore sediment transport rate, respectively.

5 Proposed Training Wall

The proposed layout consists of a single training wall on the northern bank of the river mouth since the rocky protrusion would act as a southern training wall for the smooth navigation of fishing vessel in between the proposed training wall and the rocky outcrops. The length of the proposed northern training wall is about 790 m, and it extends up to a water depth of 2 m. In the presence of the training wall, the navigability of the vessel to maneuver through the training wall has to be checked through wave tranquility studies, and the impact on the neighborhood shorelines should be checked to avoid erosion. Figure 5 presents the proposed layout of the training wall at the river mouth. The aforesaid proposal encompasses a training that is cited on the north end of the mouth of River Chapora. This ensures the trapping of the net southerly littoral drift thereby leading to advancement of shoreline on the north and preventing the trapping of sediments in the mouth. However, periodical

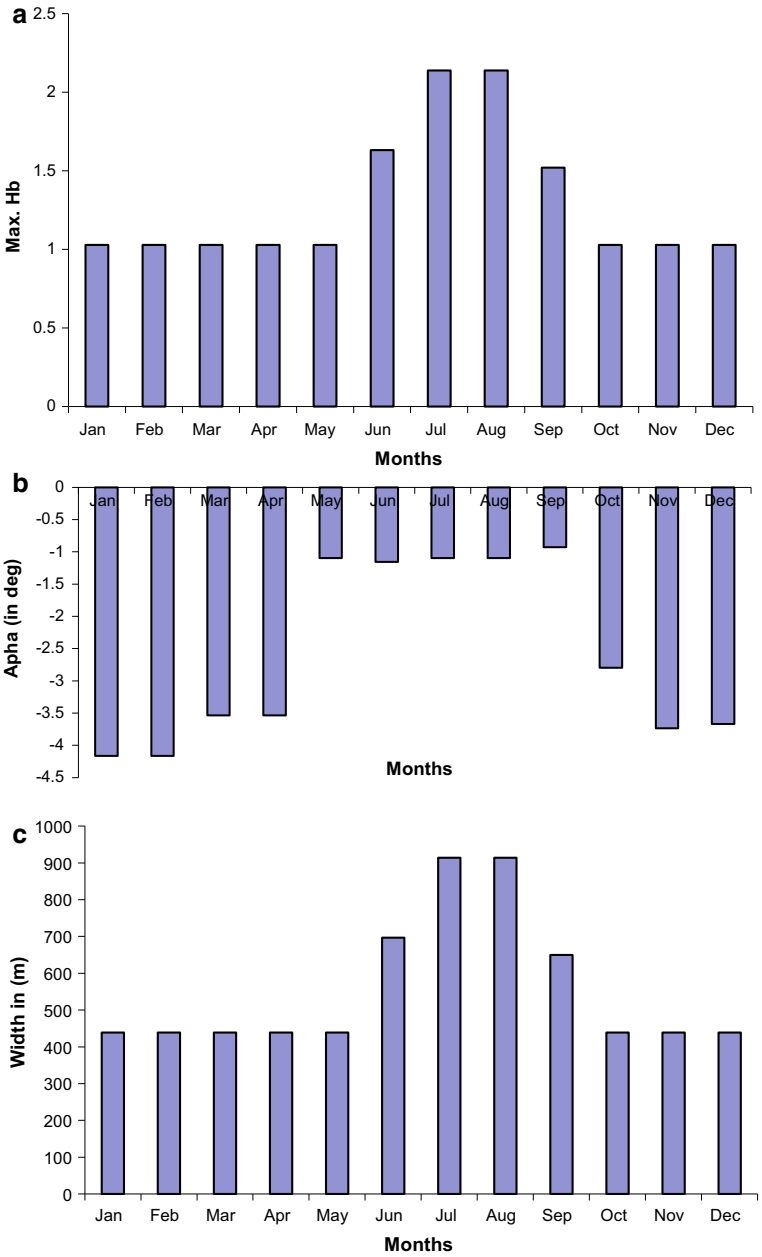

Fig. 4 **a** Maximum breaker height, **b** breaker angle with respect to shore normal, **c** surf zone width, **d** longshore sediment transport

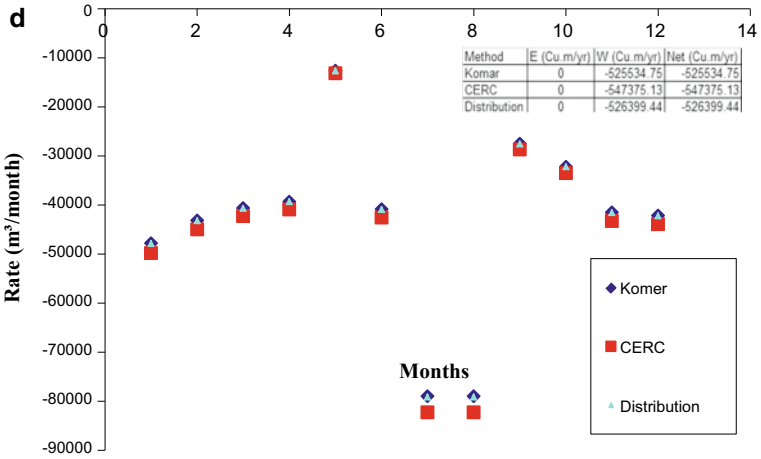

Fig. 4 (continued)

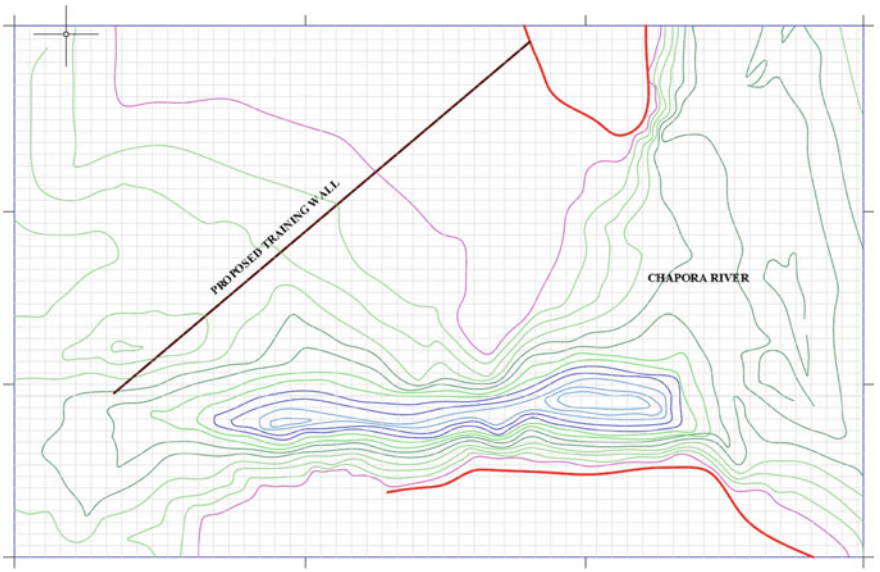

Fig. 5 Longshore sediment transport

monitoring of the mouth is recommended, and if deemed necessary, dredging has to be carried out.

6 Combined Refraction-Diffraction Model

The effect on combined diffraction–refraction of waves due to the presence of nearshore structures developed in-house at Dept. of Ocean Engineering, IIT Madras. The model is developed using the mild slope equation because of its generality in dealing with complex wave fields. The mild slope equation is solved by generalized conjugate gradient method as it has a fast convergence rate.

The combined refraction–diffraction equation that describes the propagation of periodic, small-amplitude surface gravity waves over an arbitrarily varying mild sloped sea bed according to Berkhoff [4] is,

$$\nabla \cdot CC_g \nabla \varphi + \frac{C_g}{C}\sigma^2 \varphi = 0 \tag{1}$$

where φ-complex velocity potential; σ-angular wave frequency; C-phase celerity; and C_g-group celerity.

The above equation is transformed into a Helmholtz equation of the form,

$$\nabla^2 \varphi + K^2(x, y)\varphi = 0 \tag{2}$$

Using the following relations

$$\begin{aligned} \phi &= \varphi\left(CC_g\right)^{0.5} \\ K^2 &= k^2 - \frac{\nabla^2\left(CC_g\right)^{0.5}}{\left(CC_g\right)^{0.5}} \end{aligned} \tag{3}$$

where k-wave number; K and ϕ are modified wave number and wave potential function.

Finite difference scheme is employed for the numerical discretization of Helmholtz equation. The derivatives are approximated using centered difference scheme. Writing the discretized form of Eq. for each grid in the domain and applying suitable boundary conditions, the system of resulting algebraic equations can be written in matrix form as,

$$A\phi = f \tag{4}$$

where A is the coefficient matrix, ϕ is the nodal values of velocity potential, and f is a vector obtained from the boundary conditions.

The numerical solution of the above system of equations is arrived using generalized conjugate gradient method. The method successively estimates new approximations to the solution, considering the direction of residual error vector, till the prescribed accuracy is achieved. The offshore boundary is modeled as an open

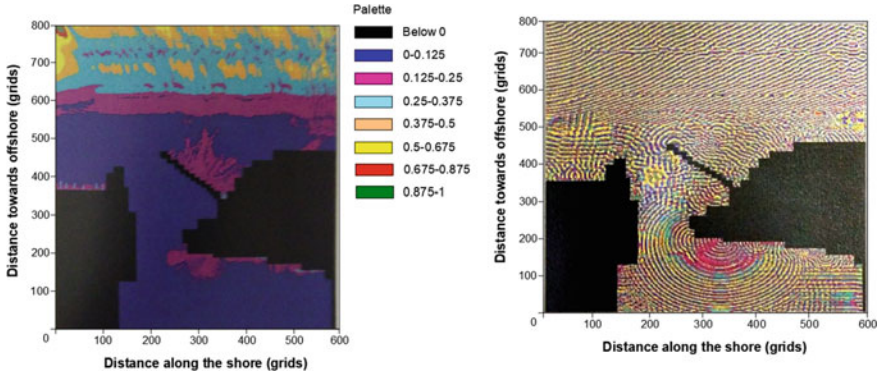

Fig. 6 Amplitude and phase variations response to offshore wave angle corresponding to 270°

boundary in which case only incident waves and reflected waves are allowed to propagate. The lateral boundary as well as the shore is considered to absorb the wave energy. The groins or any other obstruction are treated as partially reflecting boundaries by prescribing the reflecting coefficients. The model requires the wave characteristics (viz. wave height, wave period and its direction) and the water depths at all the grid points. It also requires the location of the groins. The model gives the wave characteristics inside the domain. Figure 6 shows the amplitude and phase response of the proposed structure to an offshore wave angle corresponding to 270°.

7 Shoreline Evolution Model

The construction of a shore-connected structure often leads to changes in the shoreline. This warrants a study on the shoreline due to presence of the shore-connected structures. Such a study is very much essential in planning stage so as to assess the impact of shore-connected structures on the adjacent shoreline. Numerical models offer the capability to study the effect of the wave characteristics, structure dimensions and other associated parameters in providing reasonable estimates of the shoreline response [7]. As the ocean waves approach the nearshore, it undergoes transformations like shoaling, refraction, diffraction and breaking. The phenomena of wave breaking throw sediments to the surface due to the turbulence generated. The sediments in suspension are then driven by the wave-induced currents. Since the direction of waves in the nearshore is oblique, the currents induced by them have two components. One along the shore called longshore current mainly responsible for the longshore sediment transport, which plays an important role in the shoreline changes especially due to the shore-connected structures. The other component is in the direction normal to the shore in which case the mode of sediment transport is called onshore–offshore sediment transport. When a structure normal to the shoreline is constructed, it will intercept the free passage of longshore sediment transport,

which results an imbalance in the quantity of sediment in the nearshore especially near the structure. This leads to accretion on the up drift side and erosion on the down drift side of the structure.

Kraus and Harikai [5] proposed a numerical scheme to solve the one-line model using Crank–Nicolson implicit finite difference method. The non-dimensional equation of shoreline is

$$y^*_{n,t^*+1} = B\left\{Q^*_{n,t^*+1} - Q^*_{n+1,t^*+1}\right\} + C_n \tag{5}$$

where

$$B = \frac{\delta t^*}{2 \times \delta x^*}$$
$$C_n = B\left\{Q^*_{n,t^*+1} - Q^*_{n+1,t^*+1} + 2\delta x^* q^*_{n,t^*}\right\} + y^*_{n,t^*} \tag{6}$$

The non-dimensional shoreline is divided into 'n' grid points at equal non-dimensional interval, δx^*. Then shoreline changes over a non-dimensional time, and δt^* is calculated using Crank–Nicolson finite difference scheme. This method was adopted by Senthil Kumar et al. [6] to assess the shoreline dynamics in the vicinity of the micro-tidal inlet.

In this method, Q^* at the time interval ($t^* + 1$) is expressed in terms of the shoreline co-ordinate of y^*, first isolating the term involving α_{sp} (angle of shoreline normal to x-axis) using trigonometric identities. One of the terms involving α_{sp} is then expressed as first-order quantities in y^* at time step ($t^* + 1$).

$$Q^* = K_D^2 \cos(\alpha_o) \sin(\alpha_b) \tag{7}$$

where $\alpha o = \alpha$ - α_{sp} and α is wave direction with respect to x-axis.

The elliptical form of mild slope equation, which deals with combined refraction–diffraction, is

$$Q^* = K_D^2 \cos\left(\alpha - \alpha_{sp}\right) \sin(\alpha_b) \tag{8}$$

$$Q^* = K_D^2 \sin(\alpha_b)\left\{\cos(\alpha) \sin\left(\alpha_{sp}\right) \cot\left(\alpha_{sp}\right) + \sin(\alpha) \sin\left(\alpha_{sp}\right)\right\} \tag{9}$$

$$Q^* = E_n\left\{y_{n-1,t^*+1} - Q^*_{n,t^*+1}\right\} + F_n \tag{10}$$

where

$$E_n = K_D^2\left\{\cos(\alpha) \sin\left(\alpha_{sp,t^*}\right) \sin\left(\alpha_{b,t^*}\right)\right\}/\delta x^* \tag{11}$$

$$F_n = K_D^2\left\{\sin\left(\alpha_{sp,t^*}\right) \sin\left(\alpha_{b,t^*}\right)\right\} \tag{12}$$

By substituting above equations, give the final equation as given below

$$\begin{aligned} &\mathrm{BE}_n Q^*_{n-1,t^*+1} - (1 + 2\mathrm{BE}) Q^*_{n,t^*+1} + \mathrm{BE}_n Q^*_{n+1,t^*+1} \\ &= E_n\left[C_n - C_{n-1}\right] - F_n \end{aligned} \tag{13}$$

The above equations represent a set of $(N - 1)$ linear equation for $(N - 1)$ unknowns. The end values are specified as boundary conditions, that is, $Q * 1 = 0$ and $Q * N + 1 = Q * N$. The above equation results into a tridiagonal form which is solved for Q^*. This process is repeated for the entire duration, and non-dimensional quantity is converted into real quantities using the corresponding scale factors [8].

The numerical model to predict the shoreline evolution due to the shore-connected structures has been used to predict the shoreline changes due to the proposed groynes. The wave characteristics given as the input to the numerical model are as per given Table 1. The length of the groynes, water depth at the end of the groynes and the present status of the shore are to be given as the input to the numerical model.

The numerical model was executed for the most frequently occurring wave characteristics for the different months as stated earlier. The result of the predicted shoreline variations over years is given in Fig. 7. The shoreline prediction has been made at the end of 1, 5, 10, 15, 20 and 25 years after the construction of the groynes and has been presented by superimposing the shoreline patterns.

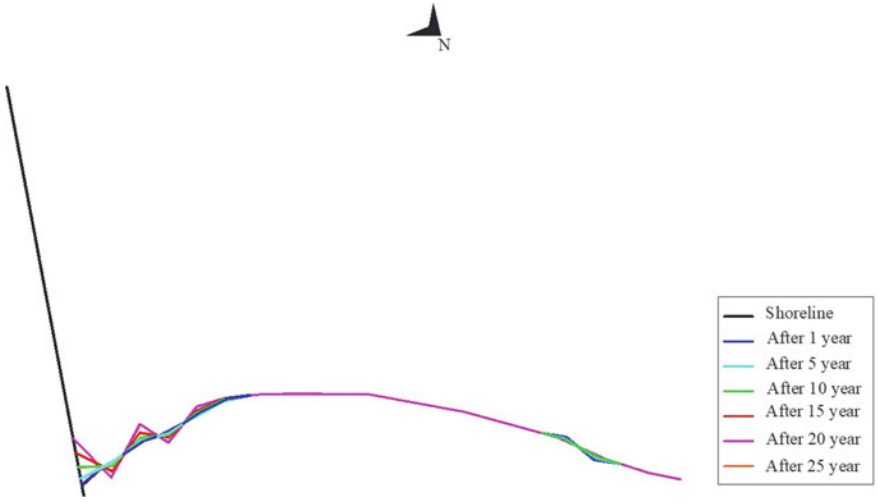

Fig. 7 Shoreline evolution model

8 Conclusion

The coast along the Chapora river mouth is dominated by strong longshore littoral currents that drives sediments at the rate of about 4.65 lakh m^3/year towards south. This phenomenon apart from the inland river currents circulation leads to excessive siltation that hinders effective operation of fisheries-related activities along the existing *L*-shaped jetty; thus, it is mandatory to establish sufficient infrastructure to develop an efficient fishing harbor. In lieu of which the proposed training wall, north of the river mouth was subjected to wave and shoreline transformation studies. Based on the model results, the construction of the 790 m long training wall extending up to a water depth of −2 m is recommended for construction.

Acknowledgements The project report was prepared by West Bengal Fisheries Corporation Limited (WBFCL) for Government of Goa, Fisheries Department, India. The hydraulic model studies were carried out at the Indian Institute of Technology Madras (IIT-M) Chennai, India. The authors are grateful to the respective authorities.

References

1. CERC (1984) Shore protection manual. Coastal Engineering Research Centre, US
2. Komar PD (1976a) Beach process and sedimentation. Prentice–Hall Englewood Cliffs, NJ, 429p
3. Komar PD (1976b) Longshore currents and sand transport on ocean Eng. III, ASCE, pp 333–354
4. Berkhoff JCW (1972) Computation of combined refraction-diffraction. In: Proceedings of 13th conference on coastal engineering, Vancouver, Canada.
5. Kraus NC, Harikai S (1983) Numerical model of the shoreline change at Oarai Beach. Coastal Eng. 7:1–28
6. Senthilkumar R, Murali K, Sundar V (2017) Stability of micro-tidal inlets along coastlines dominated by littoral drift. J Coast Conserv 21:789–801
7. Sundar V, Sannasiraj SA (2016) Shore protection for the coast of Mousuni Island in West Bengal, India. Int J Ocean Clim Syst 7(2): 35–46
8. Suresh PK, Sundar V (2011) Comparison between measured and simulated shoreline changes near the tip of Indian peninsula. J Hydro-environ Res 5(3), 157–167

Numerical Investigation of Wave Run-Up on Curved Dikes

Suba Periyal Subramaniam, Babette Scheres, and Holger Schüttrumpf

Abstract There is an increasing risk of dike failures along the coasts worldwide due to increase in relative MSL (Mean Sea Level) rise and increase in storm intensity. Wave run-up plays a key role in planning and design of coastal structures. Numerous research works were carried out on wave run-up and wave overtopping in the last few decades. However, limited information is available on the effect of the curvature in coastal dikes on wave run-up and overtopping. This research focuses on influence of curved dikes on wave run-up using numerical models. The numerical models used for this research are DualSPHysics and OpenFOAM. Analysis covers both wave run-up estimation and the underlying wave transformation processes at the curvature. The numerical analysis results show a complex behavior in wave transformation processes for curved dikes. Hence, this research aims to contribute a more precise analysis and understanding the influence of the curvature in the dike line and thus ensuring a higher level of protection in the future development of coastal structures.

Keywords Wave run-up · Curved dike · DualSPHysics · OpenFOAM

1 Introduction

Coastal Dikes are widely used as flood defense structures around the world. Wave run-up and overtopping are the most important factors in the design of coastal structures exposed to wave attack as they determine the crest height. Since exact description of wave run-up and overtopping is not possible due to its stochastic nature, predictions based on empirical equations are available in EurOtop manual [5]. Wave run-up and overtopping have been extensively researched in the past decades by means of physical and numerical modeling approaches. Nevertheless, the researchers are continuing to explore the influence of many aspects of the hydrodynamics on coastal structures. This study is a fundamental investigation on the interaction between waves

S. P. Subramaniam (✉) · B. Scheres · H. Schüttrumpf
Institute of Hydraulic Engineering and Water Resources Management, RWTH Aachen University, Mies-van-der-Rohe-Straße 17, 52056 Aachen, Germany
e-mail: subramaniam@iww.rwth-aachen.de

V. Sundar et al. (eds.), *Proceedings of the Fifth International Conference in Ocean Engineering (ICOE2019)*, Lecture Notes in Civil Engineering 106,
https://doi.org/10.1007/978-981-15-8506-7_7

and coastal dikes that are bent due to geographical characteristics or influence of anthropogenic activities. The overall objective is to improve our understanding of the hydraulic phenomena on dikes with various opening angles of concave or convex dike under different angles of wave attack.

2 Methodology

The advancement in computer technology over recent years helps us to estimate the wave run-up using numerical modeling. Though a variety of computational models is available to simulate hydrodynamic processes, not all software is suitable for the present study. The wave-structure interaction involves complex hydrodynamic processes and hence the software used for modeling wave run-up on curved dikes has to be chosen carefully. Relevant numerical software tools were identified within a comprehensive literature study. The selected numerical tools to accomplish this research are DualSPHysics, a mesh-less model based on Smoothed Particle Hydrodynamics (SPH) [2] and OpenFOAM, a mesh-based model using Volume Of Fluid (VOF) method for two-phase simulations (e.g., air and water) [10]. The numerical results will then be compared to experimental results in future.

3 Influence of Curvatures in the Dike Line

There are no detailed experimental or numerical studies available on the influence of curvatures in the dike line. However, some assumptions are available based on EurOtop [6], which indicates that a concave curvature (bent to the countryside) in a dike line could lead to an accumulation of the wave energy, thus wave run-up and overtopping will increase. For a convex curvature (bent to the sea), EurOtop [6] assumes the opposite as for the concave shape: the wave run-up and overtopping will decrease at the convex curvature due to the distribution of wave energy. These are only theoretical assumptions and not based on experimental investigations. There are some contributions from Napp et al. [10], Goda [8] and Bornschein et al. [1] for convex or concave profiles on beaches or seawalls and the primary focus of their study did not include the influence of curvature. Goda [8] presented a numerical solution for the wave reflection effect on a concave seawall corner whereas Napp et al. [10] assessed overtopping on vertical seawalls with an opening angle of 90° and 120° bathymetry in the foreshore. Bornschein et al. [1] within the HydralabIV project CornerDike assessed the influence of oblique wave attack on wave overtopping for a 90° corner in the dike line. Hence, in this research, in-depth numerical investigations on the influence of curvature in the dike line and its hydrodynamic processes depending on the various opening angle with different set of wave parameters and angles of wave attack is aimed to provide solid knowledge.

4 Numerical Model Setup

In both the numerical model DualSPHysics and OpenFOAM, the reference dike model adopted for the convergence and calibration study is a straight aligned dike of 1:6 slope. The dike height is taken as 0.7 m and the width as 4.2 m. The chosen wave parameters for the numerical simulation are described in Table 1.

The OpenFOAM convergence study is done concerning cell size and Courant number and DualSPHysics convergence study is done for the size of the inter-particle distance.

The OpenFOAM convergence results for cell size (see Fig. 1) shows a cell size of 0.01 m has a good agreement with Hunt's formula (1959). However, a cell size of 0.025 m is chosen for further analysis to reduce the computation time. Figure 2 shows the results of the simulation for Courant number and compared to Hunt's formula

Table 1 Wave parameters for the numerical simulation in OpenFOAM and DualSPHysics

Wave height H (m)	Wave period, T (s)	Water depth, d (m)
0.07	1.22	0.55
0.10	1.46	0.55
0.10	1.79	0.55

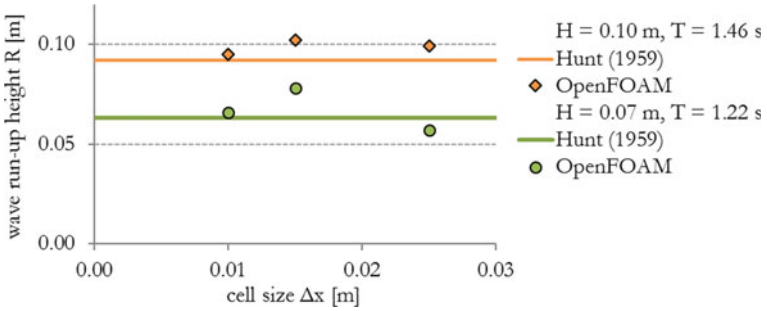

Fig. 1 Convergence results of the OpenFOAM concerning cell size

Fig. 2 Convergence results of the OpenFOAM concerning the courant number

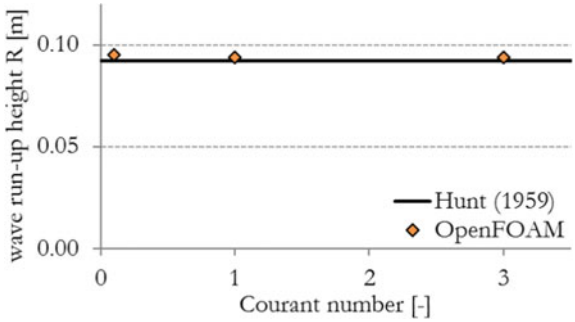

(1959). The results show no obvious influence of the Courant number is observed. Though there is no obvious influence of the Courant number, the selected Courant number is 1.0 to assure that the fluid particles move maximally one cell within one-time step. In case of DualSPHysics, the inter-particle distance size is studied and the results show the smaller the inter-particle distance, the better the accuracy. Nevertheless, smaller inter-particle distance size will lead to higher computational time and higher data storage volume. Hence, the chosen inter-particle distance size is 0.03 m for further investigations in DualSPHysics model (Fig. 3).

Calibration was performed on a 3D straight aligned dike to validate wave generation and wave absorption and the numerical results obtained from DualSPHysics and OpenFOAM are compared with Hunt's formula (1959) are shown in Fig. 4.

Both numerical models reproduce the expected values fairly well. The described numerical results for wave run-up on straight dikes are taken as reference values for comparisons with wave run-up on curved dikes in subsequent analysis.

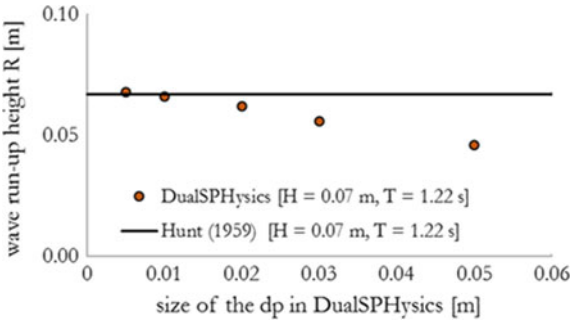

Fig. 3 Convergence results of the DualSPHysics concerning size of the inter-particle distance

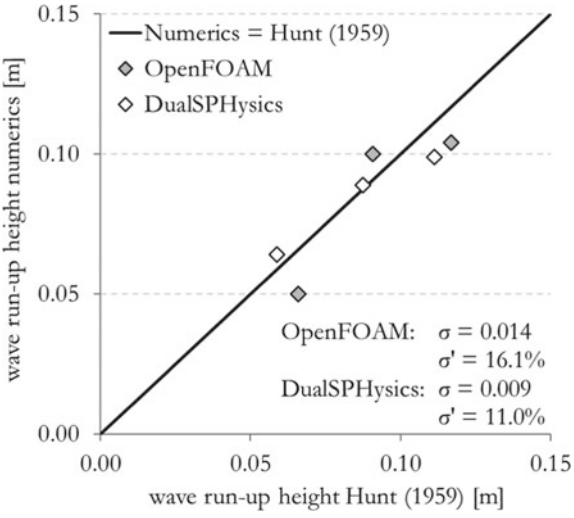

Fig. 4 Calibration results of wave run-up on a 3D straight dike compared to Hunt [9, 11]

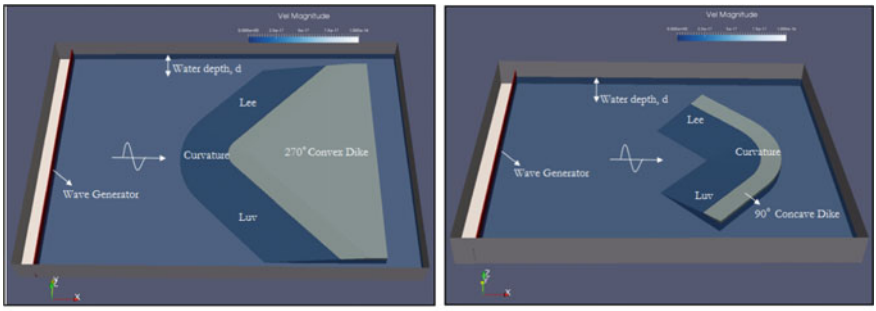

Fig. 5 3D Numerical model for curved dikes in DualSPHysics **a** 270° convex dike, **b** 90° concave dike [11]

5 Numerical Simulation on Curved Dikes

To find the effects of wave run-up on a curved dike, numerical model tests were done for a selected range of both concavely and convexly curved dikes with different opening angles and angles of wave attack for various wave parameters (see Table 1). For the simulation of wave run-up on curved dikes, a 3D numerical model is used. Figure 5 illustrates the 3D models of a concavely and convexly curved dike with its boundaries. Numerical simulations were carried out for different opening angles of curvature with various set of wave parameters for both perpendicular and oblique wave attack.

Active wave absorption method is used in the numerical wave basin, i.e., the velocity profiles are corrected at the boundaries so that no reflection occurs. For wave generation, static wave generation method is applied in OpenFOAM and dynamic boundary wave generation method is used in DualSPHysics. The simulation time is set between 20 and 40 s.

6 Wave Transformation Processes

The transformation processes for a curved dike is different from straight dike. In the following, a general pattern for convex and concave shaped dikes are discussed although the various processes are strongly dependent on the wave parameters, angle of wave attack and opening angle.

a. Convexly curved dikes
   When the incoming waves meet the convexly curved dike, concentration of the wave energy is seen at the center of the curvature and then shoaling and wave-breaking effects on the curvature are noticed. At the dike flanks, diffraction and refraction effects occur and the interaction between the redirected waves from

the curvature to the dike flanks and incoming waves leads to a very irregular wave run-up on the dike flanks.

b. Concavely curved dikes
The wave run-up at the concave curvature is influenced by refraction, converging of waves at the center of the curvature and downward currents resulting in a turbulent, transient and irregular run-up.

7 Numerical Results and Analysis

Numerical simulation program with different opening angles and angles of wave attack for various wave parameters are performed to analyze the wave run-up and wave transformation processes on a curved dike. Figures 6, 7, 8 and 9 show exemplary results of wave run-up on concave and convex dike profiles with a wave parameter input of $H = 0.10$ m, $T = 1.46$ s and $\beta = 0°$ and 45°. The wave run-up heights along the dike line R_x in relation to the wave run-up heights at the center of the curvature $R_{x=0}$ are plotted against their position x. A definition of the variable x is given within the figures.

Figure 6 shows the numerical results of wave run-up obtained from OpenFOAM and DualSPHysics for a 270° convex shaped dike under perpendicular wave attack. The wave run-up height is relatively constant along the dike line except with small oscillations are observed along the dike flanks in both numerical models.

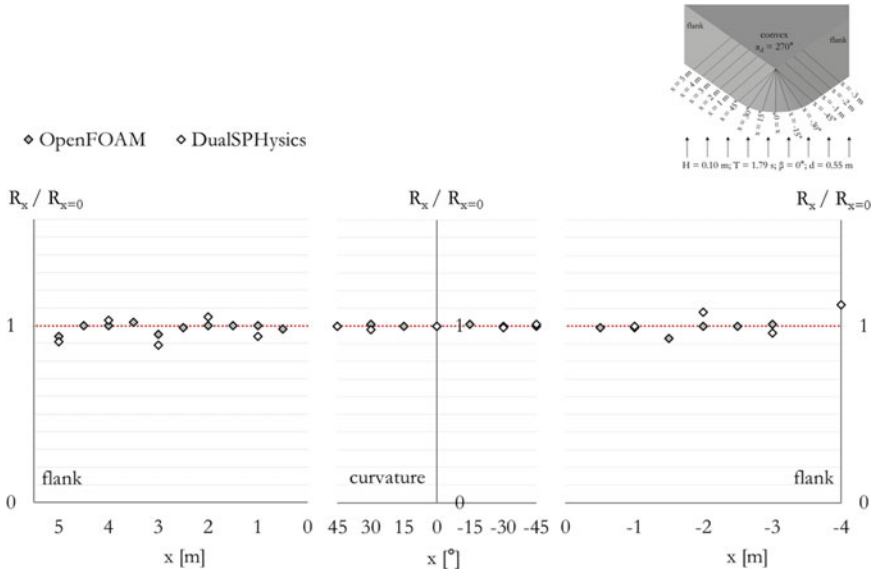

Fig. 6 Wave run-up results for a 270° convexly curved dike under perpendicular wave attack with $H = 0.10$ m and $T = 1.46$ s

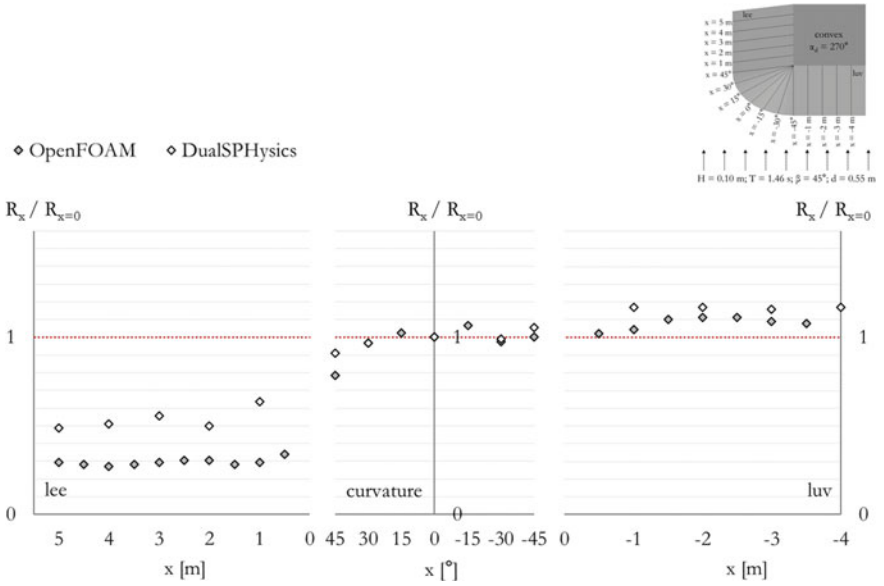

Fig. 7 Wave run-up results for a 270° convexly curved dike under 45° oblique wave attack with $H = 0.10$ m and $T = 1.46$ s

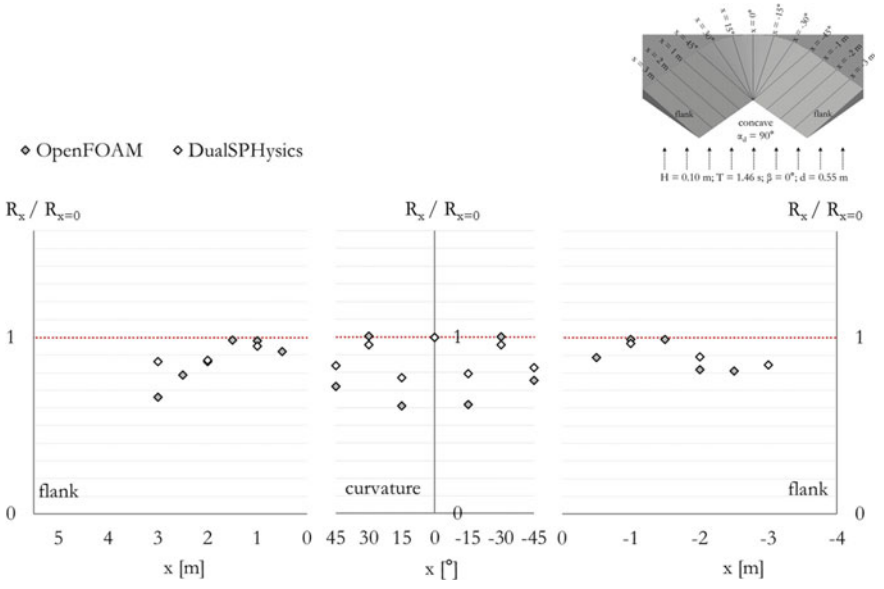

Fig. 8 Wave run-up results for a 90° concavely curved dike under perpendicular wave attack with $H = 0.10$ m and $T = 1.46$ s

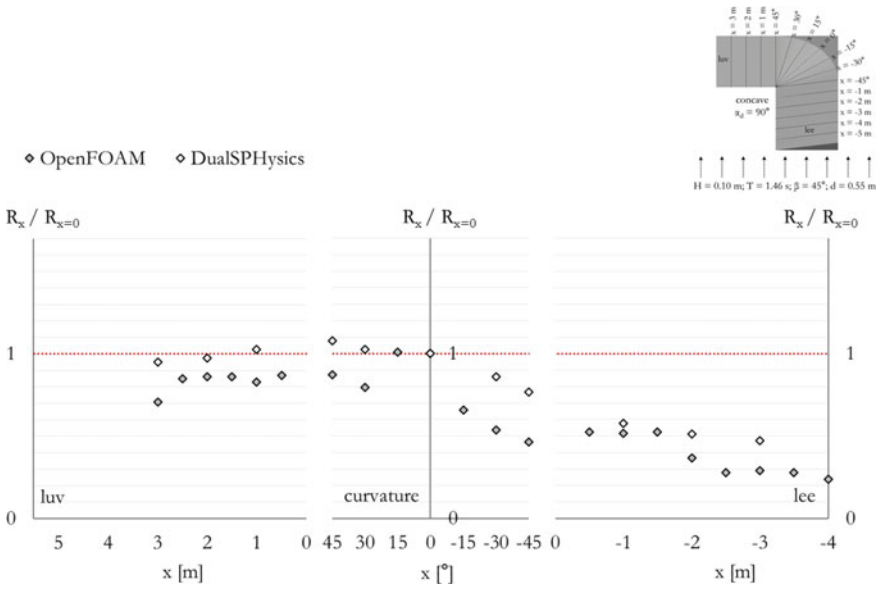

Fig. 9 Wave run-up results for a 90° concavely curved dike under 45° oblique wave attack with $H = 0.10$ m and $T = 1.46$ s

Figure 7 shows the wave run-up for a 270° convexly curved dike under 45° oblique wave attack. Here, the angle of wave attack, β approaches the lee side of the convex dike parallel and the luv side of the convex dike perpendicular. As a result, the wave run-up is seen decreased at the lee side. At the luv dike flank, the wave run-up heights of the numerical simulations slightly increase compared to the wave run-up height at the center of the curvature.

The results of wave run-up on a 90° concave shaped dike with $H = 0.10$ m, $T = 1.46$ s and $\beta = 0°$ and 45° are shown in Fig. 8 and 9. For perpendicular wave attack (Fig. 8), the behavior of wave run-up was unpredictable as it shows very unsteady run-up results at the dike curvature. This behavior was observed in both the numerical model. At the dike flanks, run-up first increases to a maximum value that corresponds to the wave run-up height at the curvature and then decreases.

For $\beta = 45°$ (Fig. 9), wave run-up height results follow the same trend as convex shaped dike under 45° oblique wave attack. As waves approach the lee flank parallel and the luv flank perpendicularly in case of $\beta = 45°$, wave run-up decreases at the lee flank while the run-up heights at the luv flank correspond more or less to the run-up height at the center of the curvature.

7.1 Analysis Approach

To determine the influence of curvature along a coastal dike line, a correction factor is introduced. This correction factor γ_c based on the influence of curvature is derived similar to the correction factor due to obliquity, γ_β derived by the [7].

$$\gamma_\beta = \frac{R_{\text{influence}}}{R_{\text{no influence}}} = \frac{R_{\beta i}}{R_{\beta=0^\circ}} \tag{1}$$

Similar to Eq. 1, the run-up measurements from the curved dike that have influence due to the curvature are compared to measurements from the straight dike that have no influence due to the curvature by using a correction factor γ_c. The correction factor describing the influence of curvature γ_c, which is defined as follows, is implemented for the analysis. Based on this new influence factor γ_c, the further analyses for convex and concave dikes are carried out.

$$\gamma_c = \frac{R_{\text{influence}}}{R_{\text{no influence}}} = \frac{[R/(H \cdot \xi_0)]_{\beta,\alpha_d}}{[R/(H \cdot \xi_0)]_{\beta,\alpha_d=180^\circ}} \tag{2}$$

8 Wave Run-Up on Convex and Concave Profile in a Dike Line

The wave run-up on convexly and concavely curved dikes for regular waves under perpendicular wave attack is analyzed and the results are summarized in the following. The wave run-up heights from the curved dikes are compared to the straight dike by using Eq. 2. Figures 10 and 11 show the influence factor γ_c at the center of the curvature on convexly and concavely curved dike lines for perpendicular wave attack plotted against the opening angle α_d. For convex shaped dikes under perpendicular wave attack, a higher run-up is observed for the larger opening angles. For concavely curved dikes under perpendicular wave attack, an increase in wave run-up height is noticed as the opening angle decreases.

9 Conclusions and Future Research Work

The main aim of this research is to investigate wave run-up due to the influence of curvature in a dike line. To achieve this, two numerical software OpenFOAM and DualSPHysics were chosen based on thorough research. 3D numerical models have been set up for the analysis of wave run-up on concave and convex shaped dikes in both the numerical software. The numerical simulation includes various simulation

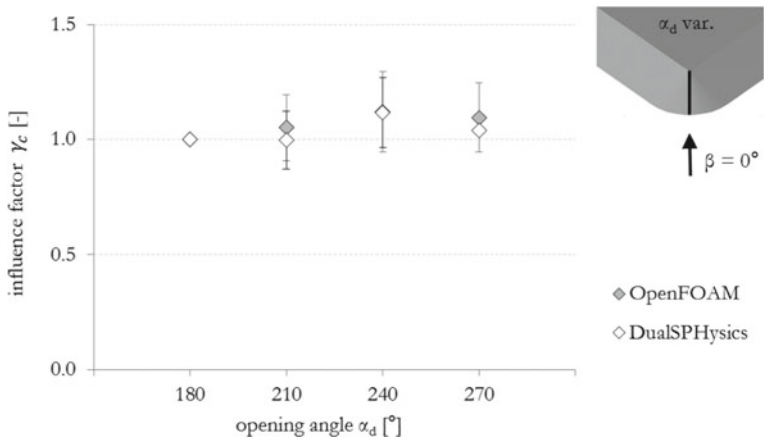

Fig. 10 Wave run-up on convexly curved dike lines for different opening angles under perpendicular wave attack

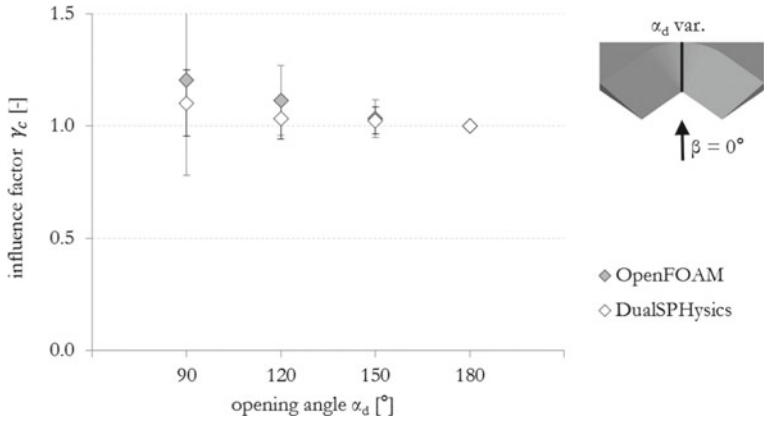

Fig. 11 Wave run-up on concavely curved dike lines for different opening angles under perpendicular wave attack

programs for different opening angles, angles of wave attack and sea state parameters. In addition, wave transformation processes on both convex and concave dikes are discussed. Exemplary results are discussed in this paper and the research will continue to analyze for other opening angles with different wave attack for different set of wave parameters in the future. Based on the present study, following conclusions can be made. Wave transformation process at the curved dikes shows complex behavior. There is a slight dependency on wave run-up on both convex and concave shaped dikes are observed in both the numerical model.

Acknowledgements This research work was financed by the Federal Ministry of Education and Research, Germany under ConDyke Project BMBF_03KIS108.

References

1. Bornschein A, Pohl R, Scheres B, Wolf V, Spano M (2014) Cornerdike final report: effect of very oblique waves on wave run-up and wave overtopping. Dresden, p 180
2. Crespo AJC, Dominguez JM, Rogers BD, Gomez-Gesteira M, Longshaw SM, Canelas R, Vacondio R, Barreiro A, Garcia-Feal O (2015) DualSPHysics: open-source parallel CFD solver based on smoothed particle hydrodynamics (SPH). Comput Phys Commun 187:204–216
3. Crespo AJC, Dominguez JM, Rogers BD, Gomez-Gesteira M, Longshaw SM, Canelas R, Vacondio R, Altomare C (2007) DualSPHysics User Guide (2016) User Guide for DualSPHysics Code. DualSPHysics_v4.0
4. EurOtop. Wave overtopping of sea defences and related structures: assessment manual. Die Küste. Bd. Heft 73. Kuratorium für Forschung im Küsteningenieurwesen, Pullen T, Allsop NWH, Bruce T, Kortenhaus A, Schüttrumpf H, Van der Meer JW (eds)
5. EurOtop (2016) Manual on wave overtopping of sea defences and related structures. An overtopping manual largely based on european research, but for worldwide application. Allsop W, Van der Meer JW (eds)
6. Goda Y (2000) Random seas and design of maritime structures, 2nd edn. World Scientific, Singapore
7. Hunt IA (1959) Design of seawalls and breakwaters. J Waterways Harbors Div 85:123–152
8. Napp N, Bruce T, Pearson J, Allsop NHW (2004) Violent overtopping of vertical seawalls under oblique wave conditions. In: Proceedings of the 29th international conference of coastal engineering, pp 4482–2293
9. OlaFoam Reference Manual (2016). https://github.com/phicau/OLAFOAM
10. OpenFOAM User Guide (2015) OpenFOAM—The Open Source CFD Toolbox—User Guide. Version 3.0.1
11. Subramaniam SP, Scheres B, Schilling M, Liebisch S, Kerpen N, Schlurmann T, Altomare C, Schüttrumpf H (2019) Influence of convex and concave curvatures in a coastal dike line on wave run-up. Water 11(7):1333

Numerical Studies on Dune Breaching Due to the Hydrodynamic Impact of Storm Surges Based on a Large-Scale Research Dune

Constantin Schweiger, Nils Koldrack, Christian Kaehler, and Holger Schüttrumpf

Abstract The aim of the collaborative project PADO ("Processes and implication of dune breaching at the German Baltic Sea Coast") is the investigation of dune breaching and the resulting flooding of the hinterland based on a large-scale research dune. During the physical model test, which was located at the beach of Rostock-Warnemuende, the dune was destroyed by a storm surge in November 2018. The measured data served as basis for the set-up of a numerical coastal erosion model with XBeach. The application of the latest XBeach-X release with the default settings results in an underestimation of the mean wave height at the model entrance. Moving closer to the shore, the underestimation decreases leading to a good agreement with observed wave heights in the nearshore zone, especially after the first third of the simulation. Furthermore, the model computes dune erosion due to collision and overwash which is in line with the observation. The predicted final dune erosion is in good agreement with the post-storm measurements of the dune topography and, hence, only minor calibration is needed.

Keywords Xbeach · Coastal erosion model · Dune breaching · Large-scale research dune

1 Introduction

As dunes are an important element of coastal protection, a detailed understanding of their resistance to the hydrodynamic load of storm surges is of high interest. Although

C. Schweiger (✉) · H. Schüttrumpf
Institute of Hydraulic Engineering and Water Resources Management, RWTH Aachen University, Aachen, Germany
e-mail: schweiger@iww.rwth-aachen.de

N. Koldrack
Geodesy and Geoinformatics, University of Rostock, Rostock, Germany

C. Kaehler
Geotechnics and Coastal Engineering, University of Rostock, Rostock, Germany

V. Sundar et al. (eds.), *Proceedings of the Fifth International Conference in Ocean Engineering (ICOE2019)*, Lecture Notes in Civil Engineering 106,
https://doi.org/10.1007/978-981-15-8506-7_8

many physical and numerical studies have already focused on the investigation of dune breaching, 2D-high-resolution measurement data of before, during and after a breaching event is still rare. Therefore, the aim of the collaborative project PADO ("Processes and implications of dune breaching at the German Baltic Sea Coast") is the investigation of dune breaching and the resulting flooding of the hinterland. The project consists of five different tasks:

- Physical modeling (Chair of Geotechnics and Coastal Engineering, University of Rostock),
- 3D surveying (Chair of Geodesy and Geoinformatics, University of Rostock),
- Numerical modeling of dune breaching (Institute of Hydraulic Engineering and Water Resources Management, RWTH Aachen University),
- Numerical modeling of groundwater infiltration (Chair of Hydrology and Applied Meteorology, University of Rostock),
- Ecological and social impact (Institute of Ecological Economy Research (IöW Berlin).

Within the framework of the project, a physical model test was conducted at the German Baltic Sea coastline between the period of 10/2018 and 12/2018. It included a large-scale research dune located at the beach of Rostock-Warnemuende (see Fig. 1), that was destroyed by a storm surge between 18 and 20 November 2018. The data that has been collected during the experiment was used to set-up a dune erosion model with XBeach [1]. This chapter presents first results of the numerical modeling.

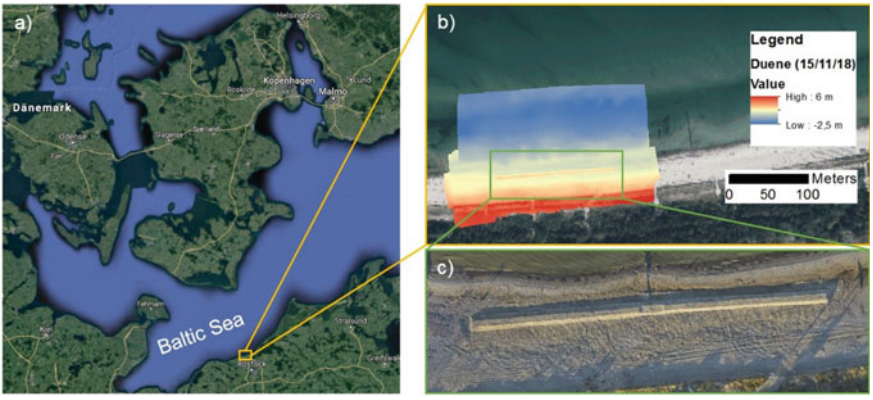

Fig. 1 **a** Location of the study site (Google Maps, 2019), **b** measured initial bathymetry, c initial research dune (Nils Koldrack, University of Rostock, 2019)

2 Methods

2.1 Numerical Model

XBeach is an open-source, nearshore numerical model which solves coupled two-dimensional horizontal (2DH) equations for wave propagation, sediment transport and the resulting update of the bottom [1]. In this chapter the surf beat mode is applied using the single-dir option [2]. It solves short wave motion on the wave group time scale using a time dependent (reduced) version of the wave-action balance equation (see 1) including the directional distribution of the wave-action density. First, the mean wave directions are calculated by an alternating stationary run and afterwards the short-wave propagation along these directions is solved

$$\frac{\partial A}{\partial t} + \frac{\partial c_c \cdot \cos\bar{\theta} A}{\partial x} + \frac{\partial c_c \cdot \sin\bar{\theta} A}{\partial y} = -\frac{D_w + D_f + D_v}{\sigma} \tag{1}$$

where A is the wave-action, c_g is the wave group velocity, $\bar{\theta}$ the mean wave direction, σ the intrinsic wave frequency and short-wave dissipation due to breaking (D_w), friction (D_f) and vegetation (D_v).

The dissipation of wave energy serves as a source term for a coupled roller energy balance, which takes the directional distribution into account, but reduces the frequency spectrum to a single mean frequency. Both the wave-action and the roller energy contribute to wave-induced radiation stresses that, in turn, serve as an input for the shallow water equations (see 2–4). The shallow water momentum and continuity equations are used for low-frequency waves and mean flows. To include wave-induced mass-flux and subsequent return flow, XBeach uses the Generalized Lagrangian Mean formulation [3]:

$$\frac{\partial u^L}{\partial t} + u^L \frac{\partial u^L}{\partial x} + v^L \frac{\partial u^L}{\partial y} - f \cdot v^L - \upsilon_h \left(\frac{\partial^2 u^L}{\partial x^2} + \frac{\partial^2 u^L}{\partial y^2} \right) = \frac{\tau_{sx}}{\rho h} - \frac{\tau_{bx}^E}{\rho h} - g \frac{\partial \eta}{\partial x} + \frac{F_x}{\rho h} + \frac{F_{v,x}}{\rho h} \tag{2}$$

$$\frac{\partial v^L}{\partial t} + u^L \frac{\partial v^L}{\partial x} + v^L \frac{\partial v^L}{\partial y} - f \cdot u^L - \upsilon_h \left(\frac{\partial^2 v^L}{\partial x^2} + \frac{\partial^2 v^L}{\partial y^2} \right) = \frac{\tau_{sy}}{\rho h} - \frac{\tau_{by}^E}{\rho h} - g \frac{\partial \eta}{\partial y} + \frac{F_y}{\rho h} + \frac{F_{v,y}}{\rho h} \tag{3}$$

$$\frac{\partial \eta}{\partial t} + \frac{\partial h u^L}{\partial x} + \frac{\partial h v^L}{\partial y} = 0 \tag{4}$$

where u^L and v^L are the Lagrangian Velocities, F_x and F_y are the wave-induced stresses, ν_h is the horizontal viscosity, f is the Coriolis coefficient, η is the water level, τ_{sx} and τ_{sy} are the wind shear stresses and ${\tau_{bx}}^E$ and ${\tau_{by}}^E$ are the bed shear stresses (based on Eulerian Velocities).

Sediment transport is modeled with a depth-averaged advection–diffusion equation (see 5) based on equilibrium concentrations [4]:

$$\frac{\partial hC}{\partial t} + \frac{\partial hCu^E}{\partial x} + \frac{\partial hCv^E}{\partial y} + \frac{\partial}{\partial x}\left[D_h h \frac{\partial C}{\partial x}\right] + \frac{\partial}{\partial y}\left[D_h h \frac{\partial C}{\partial y}\right] = \frac{hC_{eq} - hC}{T_s} \quad (5)$$

where C is the depth-averaged sediment concentration, D_h is the sediment diffusion coefficient, h is the water depth, C_{eq} is the equilibrium concentration and T_s is an adaption time to represent the entrainment of sediment. If the effect of wave skewness and asymmetry is considered, u^E and v^E are replaced by $(u^E - u_a\, sin\theta_m)$ and $(v^E - u_a\, cos\theta_m)$. In this case, u_a is calculated as a function of the root-mean square velocity u_{rms}, wave skewness S_k, wave asymmetry A_s and the model free parameter γ_{ua} (6):

$$u_a = \gamma_{ua} \cdot u_{\text{rms}} \cdot (S_k - A_s) \quad (6)$$

A higher value for u_a (and thus γ_{ua}) will result in a stronger onshore sediment transport component. Based on sediment transport gradients the update of the bed is calculated as (7):

$$\frac{\partial z_b}{\partial t} + \frac{f_{\text{mor}}}{(1 - por)} \cdot \left(\frac{\partial q_x}{\partial x} + \frac{\partial q_y}{\partial y}\right) = 0 \quad (7)$$

where zb is the bed level, f_{mor} is morphological acceleration factor and q_x and q_y are the sediment transport gradients.

In order to account for storm induced slumping of sandy material, sediment is exchanged between two adjacent cells when a critical slope is exceeded. This avalanching mechanism distinguishes between dry and wet cells and, hence, considers that inundated areas are more prone to slumping (default values are 1.0 and 0.3). It continues until the slope falls below the critical slope again.

2.2 Input Data

The dimensions of the research dune were approximately 150 m × 8 m × 1 m (length, width, height) with a crest width of 4 m. An initial breach of approx. 0.2 m depth and 8 m length was implemented in order to force the breach initiation to the center of the dune. The initial (November 15th) and the final (November 19th) topography were measured with an unmanned aircraft system (UAS) and transformed to digital elevation models (DEM) with a resolution of 0.032 m using photogrammetry.

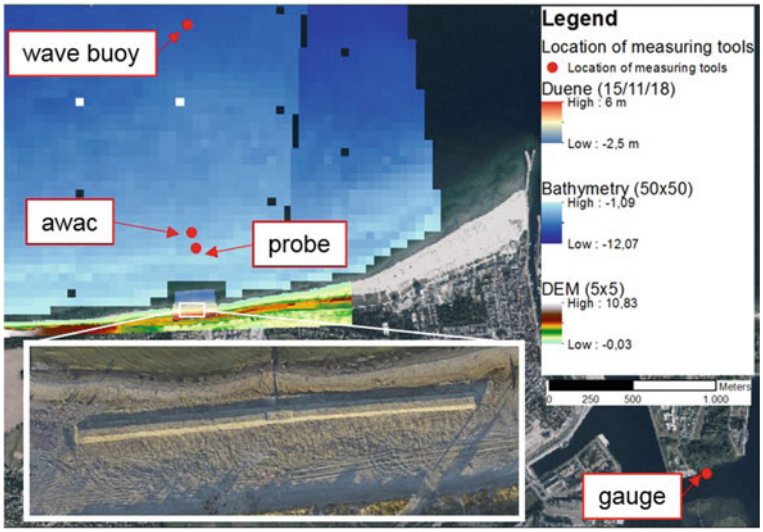

Fig. 2 Research dune and location of measuring tools

Tachymetry (Leica TS06plus) and Real Time Kinematic (Leica Viva Net-Rover) was used for the pre- and post-storm nearshore bathymetry measurements on November 7th and November 19th, respectively, both on an area of approx. 250 m alongshore (as) by 100 m cross-shore (cs). The offshore bathymetry data was obtained from the freely accessible *GeoSeaPortal* of the Federal Maritime and Hydrographic Agency of Germany with a resolution of 50 m × 50 m. The DEM of the surrounding coast and hinterland with a resolution of 5 m × 5 m was provided by the University of Rostock. It is pointed out that the nine existing groins (every 90 m longshore) in the model area with a length of approx. 50 m in cross-shore direction were neglected. All bathymetric data was merged using standard MATLAB routines.

The water level time series was obtained from a gauge located in Rostock-Warnemuende, the input wave parameters (H_{m0} wave height, peak wave period T_p and mean wave direction θ) were measured by a wave buoy at 10 m water depths. Furthermore, sea state times series of two additional measurement instruments (AWAC and wave probe) were used for the hydrodynamic calibration. All locations of the measurement instruments are shown in Fig. 2.

2.3 Model Setup

The grid was created with a varying grid size: while the area of interest (research dune) is discretized with an equal cell size of $dy_{\min} = dx_{\min} = 1$ m, the cell size increases both in longshore and in cross-shore direction to $dy_{\max} = 10$ m and $dx_{\max} = 14$ m, respectively. At a water depth of approx. 10 m, the grid was artificially extended with

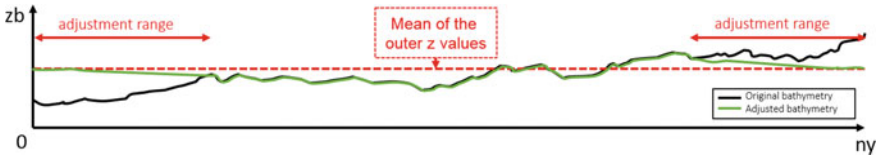

Fig. 3 Height adjustment of lateral boundaries (for cyclic = 1)

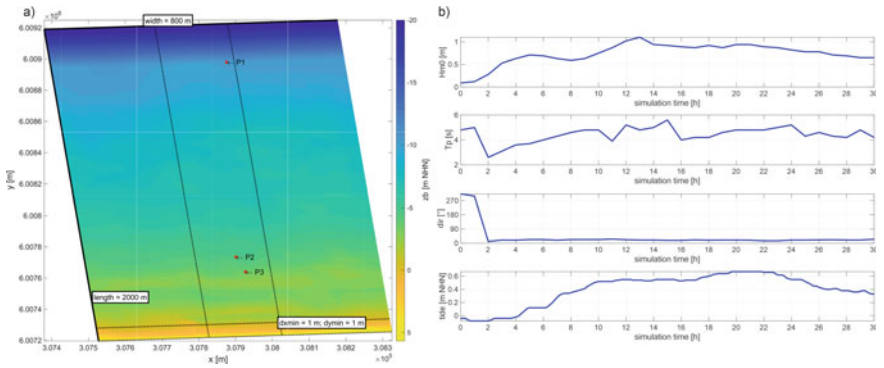

Fig. 4 Final XBeach grid, dashed black lines delimit the area with the minimum dx and/or dy, the red dots are the locations for sea state observations (**a**); input boundary conditions (**b**)

a constant slope of 0.04 to a water depth of 20 m. As cyclic boundaries (*cyclic* = 1) were used for the simulations, the two outer cross-shore profiles were first replaced by their mean and then the height difference was linearly adjusted along five grid cells to the actual height (see Fig. 3).

The final grid consists of $ny = 324$ and $nx = 279$ cells, covering an area of 800 m longshore and 2000 m cross-shore (see Fig. 4, left). A constant manning friction value of $n = 0.02$ is applied, values for $D50 = 0.3$ mm and $D90 = 0.5$ mm are based on grading analysis conducted by the University of Rostock in 2016. The imposed time-varying hydrodynamic boundary conditions are given in Fig. 4 (right): H_{m0} wave height is varying between 0.1 and 1.1 m, peak wave period T_p between 2.6 s and 5.5 s, mean wave direction between 300° and 35° and the water level between − 0.1 m NHN (standard elevation zero in Germany) and 0.67 m NHN. A total duration of 30 h is split into a spin-up time of 6 h ($t_{\text{start}} = 21{,}600$ s) followed by a global output every hour and a mean output (*H_mean*) every half an hour. In this chapter, the MPI version 1.23.5526 of the XBeach-X release is used running on three cores.

2.4 Data Analysis

To evaluate the performance of the morphodynamic module of XBeach, the statistical parameters Brier-Skill-Score (BSS) and Bias (see 8) are applied [5]:

$$\mathrm{BSS} = 1 - \frac{\sum_{i=1}^{N}(|\mathrm{zb_c} - \mathrm{zb_m}| - \Delta zb_m)^2}{\sum_{i=1}^{N}(\mathrm{zb_0} - \mathrm{zb_m})^2}, \mathrm{BIAS} = \frac{1}{\mathrm{N}}\sum_{\mathrm{i=1}}^{\mathrm{N}}(\mathrm{zb_c} - \mathrm{zb_m}) \quad (8)$$

where zb_c is the computed, zb_m is the measured, Δzb_m is the error of measured bed level and zb_0 is the initial bed level at N nodes. Based on the BSS, the model skill can be defined as bad (<0), poor (0 – 0.3), fair (0.3 – 0.6), good (0.6 – 0.8) and excellent/best (0.8 – 1) [6].

3 Results

3.1 Hydrodynamic

The hydrodynamics are evaluated on the basis of the observed (H_{m0}) and the simulated wave heights (*H_mean*, corresponds to H_{rms}). In order to enable a reliable comparison, the time-averaged spatial output is multiplied by $\sqrt{2}$ [7]. Figure 5 shows the observed (black crosses) and simulated (red line) H_{m0} wave heights at the aforementioned three locations. While there is a tendency of underestimation at locations P1 and P2 ($\mathrm{Bias_{P1}} = -0.12$ m and $\mathrm{Bias_{P2}} = -0.11$ m), the observed and simulated wave heights at location P3 are generally in good agreement ($\mathrm{Bias_{P3}} = -0.04$ m). However, during the first third of the simulation, a time lag and an underestimation can be observed at all three locations. This might be due to a too short spin-up time which requires further investigations. Nevertheless, the storm surge regimes collision and overwash (see [8]) as observed during the measurement also occur during the simulation. Therefore, the hydrodynamics are considered as satisfactorily.

3.2 Morphodynamics

In Fig. 6, a first comparison between the measurement (left) and simulation results (right) is shown: the post-storm bed levels at the top, an overview and a detailed view of the difference between the final and initial bed levels at the center and the difference between the final bed levels (simulation–measurement) at the bottom. The black crosses delimit the base of the research dune. Generally, the simulated final topography of the research dune is in good agreement with the post-storm measurements. Especially the area where the entire dune was eroded between 400 and 480 m longshore is calculated satisfactorily. The same applies to the area of accretion in front of the dune and the adjacent area of erosion (in offshore direction). The largest differences occur in the nearshore between 1900 m $< x <$ 1920 m, where more sediment deposition is predicted by the model.

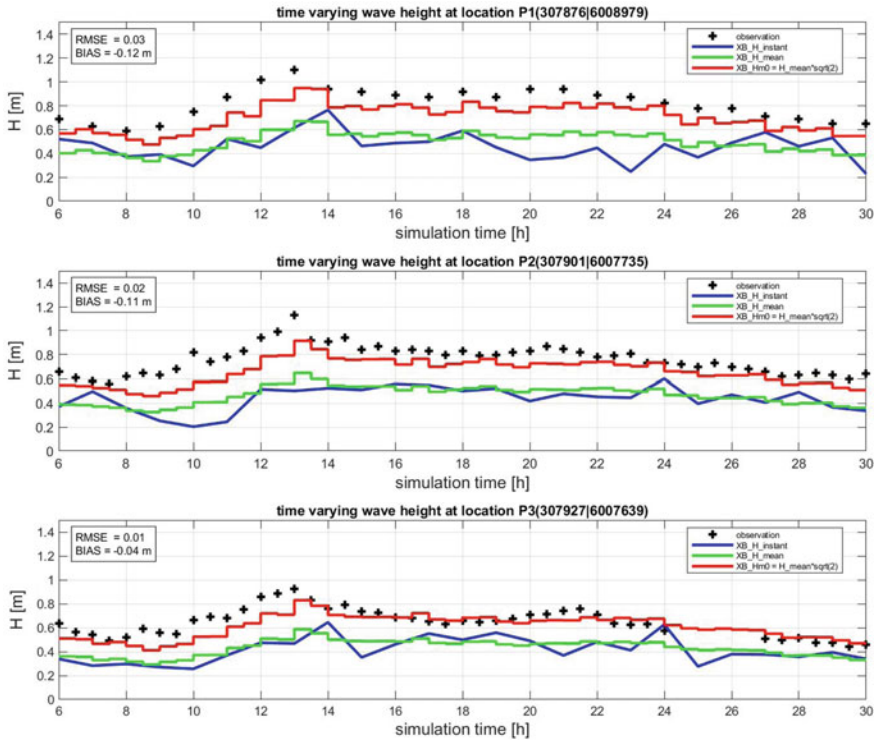

Fig. 5 Comparison of observed and simulated wave heights

A closer look at six cross-shore profiles (334, 344, 357, 404, 434, 464 m) and four longshore profiles (1949, 1950, 1951, 1952 m) reveals this first impression. As shown in Fig. 7, the simulated erosion of the research dune is in line with the post-storm measurements. Only at longshore profiles 1951 and 1952 m differences occur at the remaining part of the dune (see also cross-shore profiles 334 and 387). On the contrary, XBeach predicts too much deposition in the nearshore below $z = 0$ m leading to the evolution of a scarp berm at the end of the active zone (-1.5 m $< z < -1$ m).

The calculation of the BSS with a measuring error of $\Delta zb_m = 0.05$ m both in cross-shore and longshore direction is given in Fig. 8. In cross-shore direction, two BSS were calculated based on a separation at $z = 0$ m NHN in order to evaluate the model skill below and above the waterline. In cross-shore direction, the prediction of the model in the area of the research dune varies between poor and excellent with a tendency of increasing skill from right to left. Only at the right part of the dune the performance is bad due to the simulated erosion. The computed overestimation of accretion in the nearshore zone results in a lower performance (BSS < 0). In longshore direction, the overall skill in the area of the dune is very well in line with the measurements with a BSS varying between 0.59 ($x = 1952$ m) and 0.94

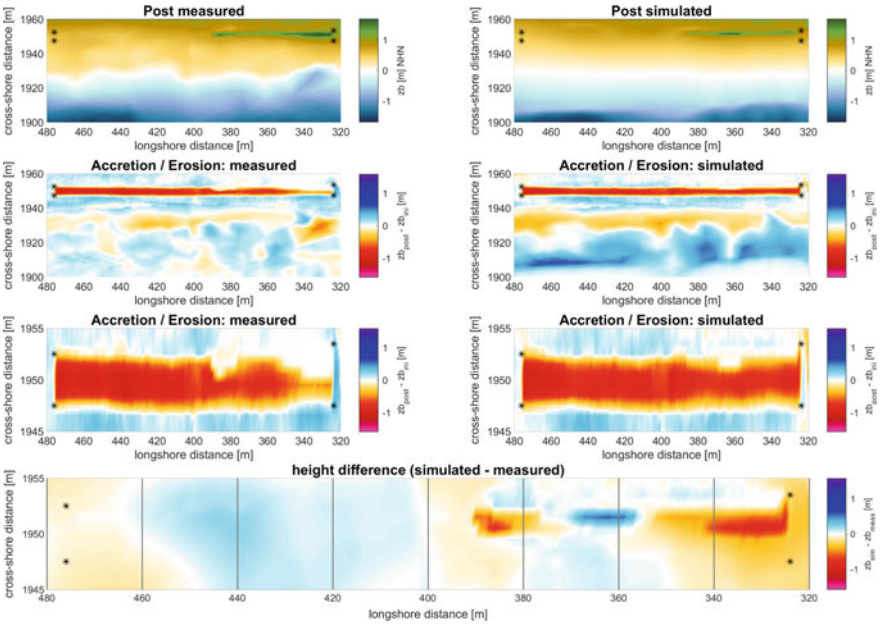

Fig. 6 Post-storm bed levels (top); difference (final–initial) for the measurement (left) and the simulation (right) (center and bottom) for area where post-storm measurement data is available. Black crosses delimit the base of the research dune

($x = 1950$ m). Again, the nearshore zone between 1900 m $< x <$ 1925 m is in bad agreement with the post-storm measurement. One way of improving the performance of the model could be the consideration of the existing groins which cover the entire longshore area between 1900 m $< x <$ 1950 m.

4 Conclusions

Applying the latest XBeach-X release with the default settings to a storm surge hitting a research dune at the German Baltic Sea coastline results in a good prediction of the morphodynamics and the final dune erosion. Major differences occur in the nearshore zone, where the implementation of the existing groins could improve the accuracy of the model.

On the contrary, the comparison of the hydrodynamics shows an offset between the observed and computed wave heights at all three measuring locations at least during the first third of the simulation; a longer spin-up time could be beneficial. After a simulation time of 12 h the offset and the differences to the measured data decrease in shallower water which leads to a good agreement with the observations

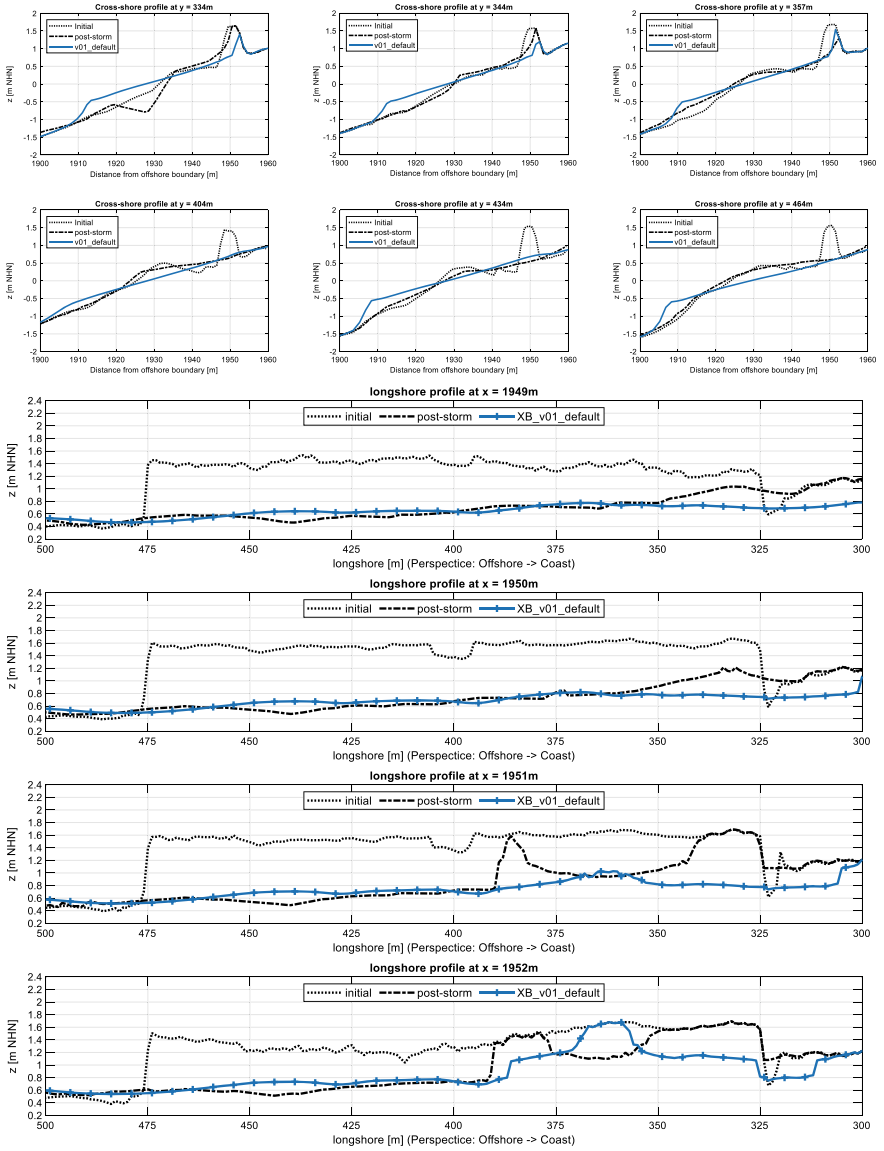

Fig. 7 Initial, post-storm and simulated dune erosion at six cross-shore profiles (top) and four longshore profiles (bottom)

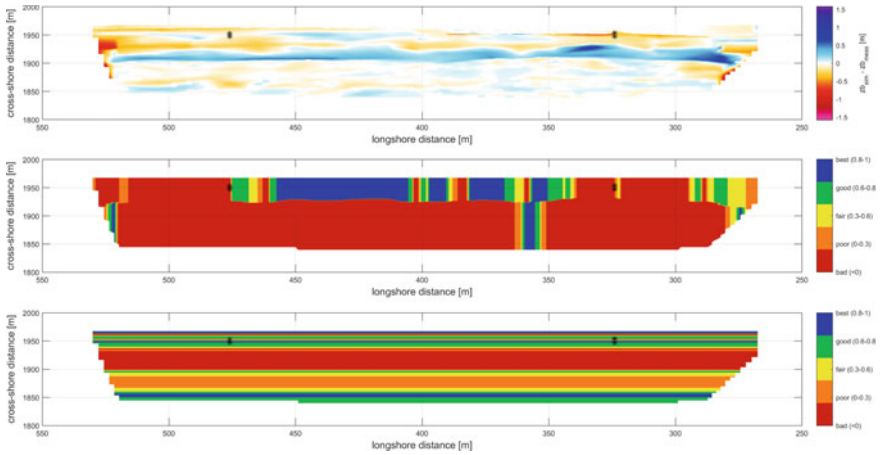

Fig. 8 Difference between computed and measured bed levels (top), cross-shore-calculated BSS (split at $z = 0$ m NHN) (center) and longshore-calculated BSS (bottom)

especially in the nearshore zone. Furthermore, the simulated storm regimes collision and overwash are in line with the observations.

Next, a calibration of XBeach will be conducted. As the seaside slope of the research dune was measured continuously during the storm surge, a large high-resolution 2D dataset is available which allows a detailed analysis of the computed evolution of the dune erosion.

Acknowledgements This research is funded by the Federal Ministry of Education and Research (BMBF) within the project "territorial sea research" of the FONA 3 (Research of sustainable development) program (funding code: 03F0760 A–C).

References

1. Roelvink D, Reniers A, van Dongeren A, van Thiel de Vries J, McCall R, Lescinski J (2009) Modelling storm impacts on beaches, dunes and barrier islands. Coast Eng 56(11–12):1133–1152. https://doi.org/10.1016/j.coastaleng.2009.08.006
2. Roelvink D, McCall R, Mehvar S, Nederhoff K, Dastgheib A (2017) Improving predictions of swash dynamics in XBeach. The role of groupiness and incident-band runup. Coast Eng. https://doi.org/10.1016/j.coastaleng.2017.07.004
3. Andrews DG, Mcintyre ME (1978) An exact theory of nonlinear waves on a Lagrangian-mean flow. J. Fluid Mech. 89(4):609–646. https://doi.org/10.1017/S0022112078002773
4. Galappatti G, Vreugdenhil CB (1985) A depth-integrated model for suspended sediment transport. J Hydraul Res 23(4):359–377. https://doi.org/10.1080/00221688509499345
5. Sutherland J, Peet AH, Soulsby RL (2004) Evaluating the performance of morphological models. Coast Eng 51(8–9):917–939. https://doi.org/10.1016/j.coastaleng.2004.07.015
6. van Rijn LC, Walstra DJR, Grasmeijer B, Sutherland J, Pan S, Sierra JP (2003) The predictability of cross-shore bed evolution of sandy beaches at the time scale of storms and seasons using

process-based Profile models. Coast Eng 47(3):295–327. https://doi.org/10.1016/S0378-3839(02)00120-5
7. Holthuijsen LH (2007) Waves in oceanic and coastal waters. Cambridge University Press, Cambridge
8. Sallenger AH (2000) Storm impact scale for Barrier Islands. J Coast Res 16(3):S890–895

Design and Modeling of Coastal Protective Structures: Case Study of La Prairie

A. Bundhoo and A. Seeboo

Abstract Climate change is becoming a prevailing issue for the many countries around the world. The Republic of Mauritius being part of the Small Island Developing states has a higher probability of encountering larger damages from gradual sea level rise and more intense storms. The purpose of this study was to provide a solution to enhance the protection of the coast line of a specific region on the island, namely, "La Prairie" from wave attacks during severe climatic events. It has been observed that the existing structure is not working as it should be and during the wave attacks that part of the island is not accessible. A design assessment of the existing hard structure was carried out followed by the design of an emergent breakwater as an alternate structure. This structure was then modeled using MATLAB software and a comparison of armor porosity and structure height was done to get a more cost-efficient structure for construction. This paper also contains a cost estimate and a detailed section of the proposed structure. With the application of the proposed solution this specific part of the island would then be protected from wave attacks and hence accessible to the public.

Keywords Design · Modeling · Protective structure · Break waters

1 Introduction

According to the United Nations [19], climate change is already impacting directly on almost every country in the world, disturbing the economy and affecting lives. From intensifying natural hazards to shoreline regression, these phenomena are predicted to spread 170 times faster only due to human activities (Davey 2017) and has left countries listed in the Small Island Developing States (SIDS) the most vulnerable to

A. Bundhoo (✉) · A. Seeboo
Department of Civil Engineering, University of Mauritius, Reduit, Mauritius
e-mail: adityaraj.bundhoo@umail.uom.ac.mu

A. Seeboo
e-mail: a.seeboo@uom.ac.mu

V. Sundar et al. (eds.), *Proceedings of the Fifth International Conference in Ocean Engineering (ICOE2019)*, Lecture Notes in Civil Engineering 106,
https://doi.org/10.1007/978-981-15-8506-7_9

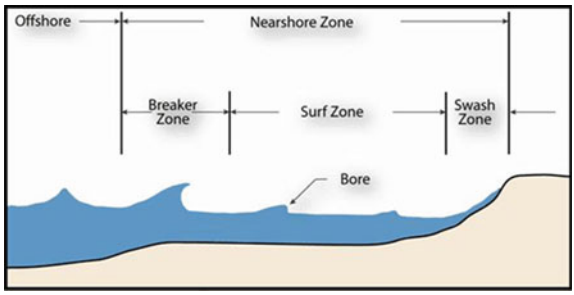

Fig. 1 Wave transformation

this impact [18]. As far as Mauritius is concerned, it ranked as the 7th most exposed country to natural hazards [12] and experiences shoreline regression up to 2.7 m/year [4].

In order to gain a better understanding of the potential damages related to coastal erosion, it is essential to have a description of the environmental conditions surrounding it. Coastal/Beach erosion is caused by waves dissipating the energy that they carry on the surface they hit, displacing sediments along the shoreline. However, the environment in which the wave travel can have a significant impact on its behavior. Usually, when a wave approaches the shore, it transitions from deep to shallow waters (refer Fig. 1). In the shallow water region, the wave's velocity is reduced as it experiences friction with the seabed with decreasing water depth. This causes the wave to gradually deform and break at some point in time. Moreover, Inch [6] points out that the wave breaking point is the most significant parameter into wave-dominated coastal environments and is responsible for driving several interrelated, hydrodynamic processes in the surf zone and on the coast such as the wave run-up.

The solutions to protect the wave propagation is vast. Most of the conventional hard structures available have proved to be expensive short-lived structures which are not eco-friendly [4]. On the other hand, soft methods provide inexpensive measures that uses the natural features of the environment to reduce the effect of erosion.

The present chapter describes the research aiming to evaluate the implementation of an offshore emergent breakwater through design, modeling with the provision of a cost estimate, on a coastal region of Mauritius, which is at risk to severe climatic conditions.

The area of study that was selected is La Prairie beach. It is located near the village of Baie du cap, along the route B9 in the south western portion of Mauritius. The coastline of La Prairie extends over 2.5 km in which nearly 500 m is occupied by the public beach Fig. 2.

The public beach is in western part of La Prairie which is protected by coral reefs that surrounds Le Morne. In addition, the site is located along the road B9 Fig. 3 which is the only route found at the bottom extremity of the island which connects Baie du cap, Maconde, La Prairie and Le Morne.

The problem related to this site is towards the vulnerability of this road B9 to wave attacks. Due to the break in coral reefs Fig. 4, strong undisturbed currents from

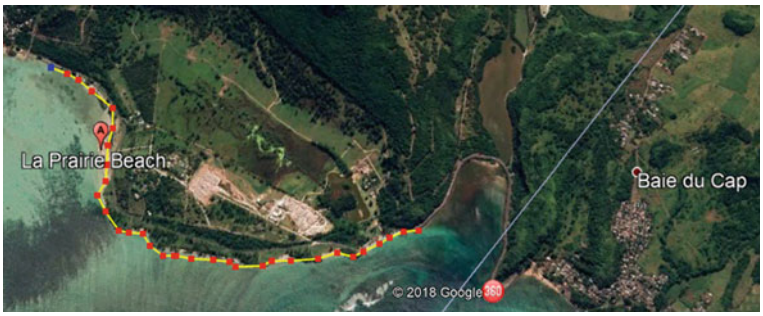

Fig. 2 La Prairie coastline (Google Earth, 2018)

Fig. 3 Road B9 (Google Earth, 2018)

deep sea water are reaching the shore, making nearby infrastructures on the road B9 a target to wave attack.

As a result, on September 24, 2018, waves ranging from 4–5 m in height overtopped the road B9 and flooded nearby infrastructure, bringing large deposit of sediments on the road [9]. This situation created a potential risk for road users of encounter accidents and slide off the road track.

Fig. 4 Site location (Google Earth, 2018)

Fig. 5 Deposit of sediments on road B9 [9]

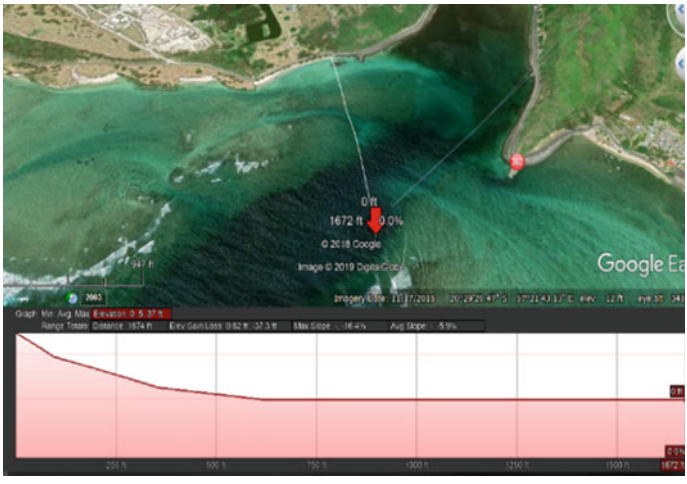

Fig. 6 Seabed profile (Google Earth, 2018)

2 Methodology

The location chosen along La Prairie consisted of nearly 250 m of Gabion baskets acting as protective structure for the road B9. Site visits were conducted, and relevant measurements were taken for the design assessment stage, which was based on the Gabion design manual provided by Environmesh [3]. During the design stage, the surface surcharge was taken to be 10 kN/m^2.

Several possibilities of structure were reviewed in order to get the most suitable structure that would provide adequate protection from which the option of selecting a breakwater was chosen.

- Rock Revetments,
- Sea wall combined with Rock revetments,
- Offshore Detached Emergent Breakwater,
- Offshore Submerged Breakwater or Artificial Reefs.

Breakwaters are offshore structures that are made of several layers of materials with a selected permeability to restrict access to waves to the shoreface. The design is dependent on parameters associated with deep sea waves namely; Wave height and Wave period. The following design procedure was followed according to Abelhamid [1].

Primary Layer.

(i) Weight of Armor
The weight of a unit armor layer is calculated by the formula provided by the Hudson formula:

$$W_{50} = \frac{\gamma_a H^3}{K_D (SG-1)^3 cot\alpha} \tag{1}$$

where,
γ_a: unit weight of armor unit material (2.65 t/m^3); H: Incident wave height; K_D: armor unit stability coefficient [7], $\gamma_w = 1.025$ t/m^3; SG: specific gravity of armor material, (γ_a/γ_w); α: angle between seaward structure slope and horizontal.

(ii) Thickness of armor
The thickness of the unit armor layer is calculated as follows:

$$r = nK_0 D_{n50} \tag{2}$$

where,
n: Number of layers; K_0: Layer coefficient; D_{n50}: Medium diameter of armor unit $= \left(\frac{W_{50}}{\gamma_a}\right)^{1/3}$

Secondary layer.

This layer is the under layer of the armor layer which binds the primary layer to the core layer. In the design stage, the filter criteria between the two upper layers must be satisfied.

(i) Weight of armor

$$W_s = \frac{W_{\text{armor}}}{10} - \frac{W_{\text{armor}}}{15} \tag{3}$$

(ii) Filter criteria

$$\frac{D_{15\_\text{armor}}}{D_{85\text{secondlayer}}} < 5 \tag{4}$$

where,

$$D_{15\_\text{armor}} = 0.4\left(\frac{W_{50}}{\gamma_a}\right)^{1/3};\ D_{85\text{secondlayer}} = 1.96\left(\frac{W_s}{\gamma_a}\right)^{1/3}$$

Thickness of rock layer

$$ts = nK_0\left(\frac{W_s}{\gamma_a}\right)^{1/3} \tag{5}$$

where,

n: Number of layers; K_0: Layer coefficient [7].

Core layer.

(i) Weight of rocks
This layer consists of rocks with smaller diameter stacked together to provide stability to the overall structure.

$$W_c = \frac{W_{\text{armor}}}{200} - \frac{W_{\text{armor}}}{6000} \tag{6}$$

(ii) Filter criteria

$$\frac{D_{15\_\text{secondlayer}}}{D_{85\text{core}}} < 5 \tag{7}$$

where,

$$D_{15\_\text{secondlayer}} = 0.4\left(\frac{W_s}{\gamma_a}\right)^{1/3};\ D_{85\text{core}} = 1.96\left(\frac{W_c}{\gamma_a}\right)^{1/3}$$

Toe design.

A toe is usually constructed on the seaward side of the structure. This is necessary to:

- Prevent scouring of sediments under the front face of the breakwater forming a scour hole that can destabilize the whole structure,
- Support the primary armor layer of the breakwater from sliding.

The design consists of calculating the weight and dimension of rocks that will be used. The equations are as follows:

(i) Toe width

$$B_t = 0.4h \tag{8}$$

where,
h is the height of the structure.

(ii) Weight of the rock unit

$$W = \frac{\gamma_a \times H^3}{N_S \times (SG - 1)^3} \tag{9}$$

where,
γ_a: unit weight of armor unit material (2.65 t/m^3); H: Incident wave height; N_s: stability number = 2.77; γ_w = 1.025 t/m^3; SG: specific gravity of armor material, (γ_a/γ_w).

(iii) Diameter of rock unit

$$D = \left(\frac{W}{\gamma_a}\right)^{1/3} \tag{10}$$

(iv) Base length

$$BL = B_\mathrm{t} + 2[SWL - h_\mathrm{b}]\cot\alpha \tag{11}$$

where,
B_t: Toe upper width; SWL: Still water level; h_b: Water depth above toe = (Water depth – Assumed toe height).

Dimension of Structure

(i) Top Crest width

$$B_c = 3K_\Delta\left(\frac{W}{\gamma_a}\right)^{1/3} \tag{12}$$

(ii) Base Width

$$B_b = B_c + 2(SWL + R)\cot\alpha \tag{13}$$

where,

SWL: Still water level; R: Wave run-up $= \left(H \times {}^{a\xi_m}/_{1 + b\xi_m}\right)$; ξ_m: Wave similarity $= \xi_m = \tan\alpha / \sqrt{{}^{H}/_{L_o}}$.

3 Conceptual Model

The model was built by using linear equations and compiling them into a numerical based model. The software used was MATLAB from MathWorks. In order to generate the suitable outcome from a model, a section profile of La Prairie was used combined water wave equations.

The seabed profile of La Prairie was obtained from the Google Earth Pro software. The process consists of plotting multiple point coordinates and to change the altitude to clamped to sea floor to obtain the seabed profile. Furthermore, the maximum vertical distance that the sea profile extends as we move in the deep sea is about 9 m, the design water level was assumed to be 9.0 m.

For this project, the wave parameters (Wave height and Wave period) was obtained from the Mauritius Wave Energy Resources Assessment report published by the University of Western Australia [15]. This report comprises measurements obtained from buoys setup at 3 sites around the island which includes one at Souillac, which is the nearest site to our point of interest. The latest data from the Souillac buoy (set off 2 km offshore in 40 m water depth), dated from past January 2017 was used in this model.

When the wave travels in deep sea conditions, it is assumed that the sea bed is flat with constant water depth. Equation (14) illustrates the wave height above still water level with respect to time and distance traveled.

$$\eta = \frac{H}{2}\cos\left\{2\pi\left(\frac{x}{L} - \frac{t}{T}\right)\right\} \tag{14}$$

Since the water depth remains unchanged as the wave progresses in deep water conditions, the value of L remains constant, thus η is also constant. As the wave reaches the shallow water zone, due to the change in slope of the sea bed, the wavelength is affected.

According to Stoke's wave theory, the change in wavelength with changing water depth is given by the equation below:

$$L = \frac{gT^2}{2\pi}\tanh\left(\frac{2\pi d}{L}\right) \tag{15}$$

Equation (15) is an iteration process which provides the value of wavelength at each point along the axis on which the wave travels. It is then replaced in Eq. (14) to obtain the value of wave height above the SWL.

Wave refraction and Wave shoaling are the two main transformation that causes a wave to change and is as follows:

(i) *Wave refraction*
The wave refraction, denoted by K_r is given by:

$$K_r = \left(\frac{\cos\alpha_0}{\cos\alpha}\right)^{0.5} \tag{16}$$

where,
α_0 is assumed to be 40°; $\alpha = \sin^{-1}\frac{C\sin\alpha_0}{C_0}$, and $C = \sqrt{gL/2\pi}$.

(ii) *Wave shoaling*
This process causes the wave to increase in height. The resulting wave height is given by a combination of the wave velocity, wave height and the refraction coefficient.

$$H = H_0 \times \sqrt{\frac{C_0}{2nC}} \times K_r \tag{17}$$

where,

$n = 0.5\left(1 + \frac{2kd}{\sinh 2kd}\right)$; $k = 2\pi/L$

(iii) *Wave breaking*
According to SPM Vol. 1 [11], pp. 2–37), as the wave moves in the shallow zone, it is slightly deformed by shoaling until it breaks at one point. When the consecutive ratio of wave height and respective wavelength (H/L) becomes less than 1/7, breaking occurs. In the model, the point on the wave profile at $H/L = 1/7$ was found through interpolation which is indicated by a red line on the model. For each different values of wave height inserted, the depth at which the wave breaks will be given.

(iv) *Wave setup*
The wave setup is the maximum vertical distance traveled by the wave when it hits the shoreface. According to CEM (2003), the maximum setup is given by:

$$\eta_{\max} = \eta_s + \frac{\mathrm{d}\eta}{\mathrm{d}x}\Delta x \tag{18}$$

where,

$\eta_s = \left(-\frac{H^2 \times (2\pi/L)}{8\sinh\left(\frac{4\pi d}{L}\right)}\right) + \left[\frac{1}{1+{}^{8}/_{3\gamma_b^2}}\right] \times d$; $\Delta x = \frac{\eta_s}{\tan\beta - \left(\frac{1}{1+{}^{8}/_{3\gamma_b^2}}\right)\tan\beta}$; d is the breaking depth; β is the slope at which breaking occurs; γ_b is the breaker index; H is the wave height.

(v) *Porosity and armor layer*
Applying porosity as a dependent variable of Armor layer.
The porosity of a rock layer is defined from Stuart et al. [14], p. 5 by:

$$n = 1 - {}^{\rho_b}/_{\rho_a} \tag{19}$$

where,
ρ_b is the bulk density (assumed to be 2.45 t/m^3 for concrete units); ρ_a is the armor unit density = 2.65 t/m^3;
By making ρ_a subject of formula and replacing Eq. (15) into D_{n50},

$$D_{n50} = \left(\frac{[1-n]W_{50}}{2.45}\right)^{1/3} \tag{20}$$

Varying the porosity will yield in different diameter of armor layer which is an important parameter used in the equations to follow. Van der Meer et al. (2009) listed the different porosity that will be used in the model is as follows:

(vi) *Wave Transmission coefficient*
When a wave hits an emergent offshore structure, a fraction of the wave energy will be transmitted on the leeside of it. The fraction that is transmitted is represented by the Transmission coefficient, K_t.

According to Zhang (2014), K_t for rubble mound emergent breakwater is denoted by the following equation:

$$K_t = \frac{aR_c}{D_{n50}} + b \tag{21}$$

where,
R_c: crest freeboard; $a = \frac{0.031 H_s}{D_{n50}} - 0.024$; $b = -5.42 S_{op} + 0.0323 \frac{Hs}{D_{n50}} - 0.017\left(\frac{B}{D_{n50}}\right)^{1.84} + 0.51$; $S_{\text{op}} = 2\pi H_s/(gT^2)$; H_s: incident wave height; D_{n50}: diameter of armor layer; B: crest width; S_{op}: wave steepness.

4 Analysis and Discussions

The 2-D Numerical model was used accordingly to the previously mentioned procedure to examine the effect of a breakwater on the different wave parameters along the sea bed profile of La Prairie beach. The deep-water wave parameters namely; Wave height and Wave period, were obtained from Fig. 9 which were input in the model. Thus, the relationship between the porosity of different armor layer used in breakwater construction was varied accordingly and its effects on the following parameters, the wave breaking distance, wave setup, transmission coefficient and rate of energy dissipation of breakwater were analyzed and tabulated. The model results are displayed and discussed in the following sections.

The graphical results obtained from the model is displayed in the Fig. 11.

In Fig. 11, the wave profile is constant until it reaches 150 m from the shore. At this point, it starts to deform and eventually breaks.

When the breakwater was inserted, the porosity of its armor layer and its freeboard crest height was varied (1–5 m) and the behavior of the wave profile is illustrated in the Figs. 7, 8, 9, 10 and 11. From the above comparison, it can be observed that the wave is less disturbed when confronted with a lower structure with high porosity. The porosity and height of the structure were varied, and the relationship of the results are discussed in the following sections.

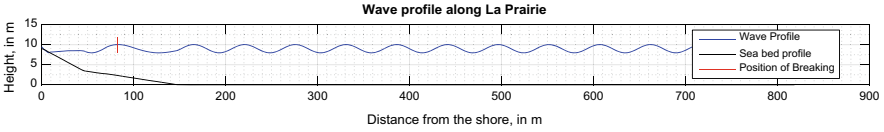

Fig. 7 Wave profile without breakwater

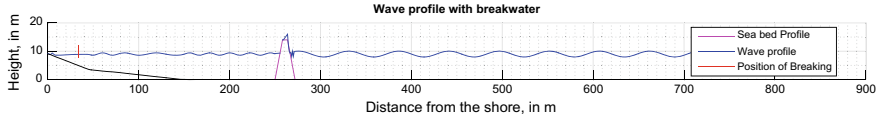

Fig. 8 Wave profile with breakwater ($n = 0.6$, $H = 14$ m)

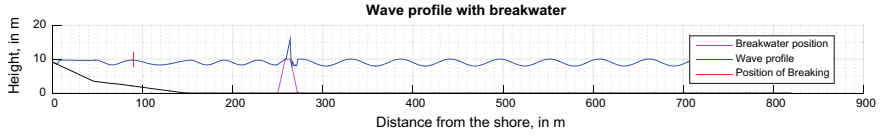

Fig. 9 Wave profile with breakwater ($n = 0.6$, $H = 10$ m)

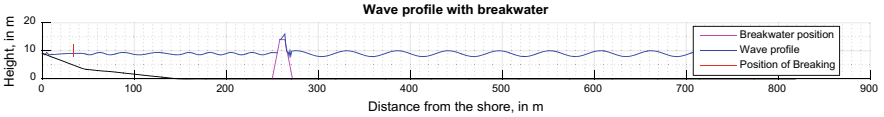

Fig. 10 Wave profile with breakwater ($n = 0.38$, $H = 14$ m)

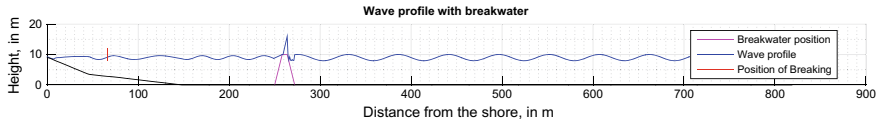

Fig. 11 Wave profile with breakwater ($n = 0.38$, $H = 10$ m)

5 Porosity and Breaker Distance

Figure 12 shows the relationship between porosity and breaker distance. The main observations are as follows:

- As the porosity of the armor layer is increased, the wave breaks farther to the shore.
- With increasing freeboard crest of the breakwater, the breaking distance is closer to the shore.

A wave is subject to breaking when its driving parameters (H and L) have sufficiently diminished until it satisfies the ratio of 1/7 as described in SPM [11]. When we increase the porosity of the armor, more wave energy is allowed to flow through

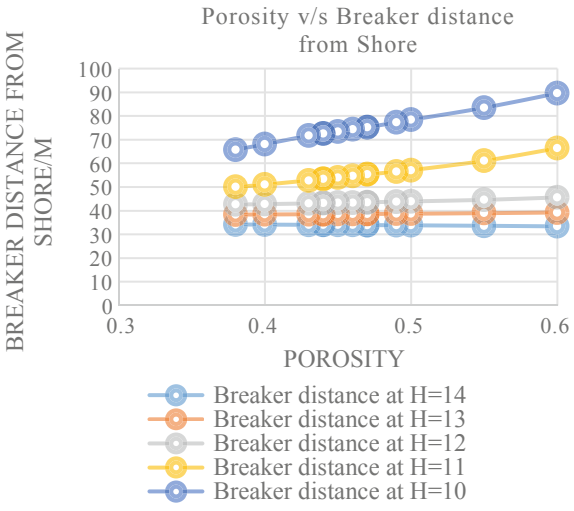

Fig. 12 Porosity versus breaker distance

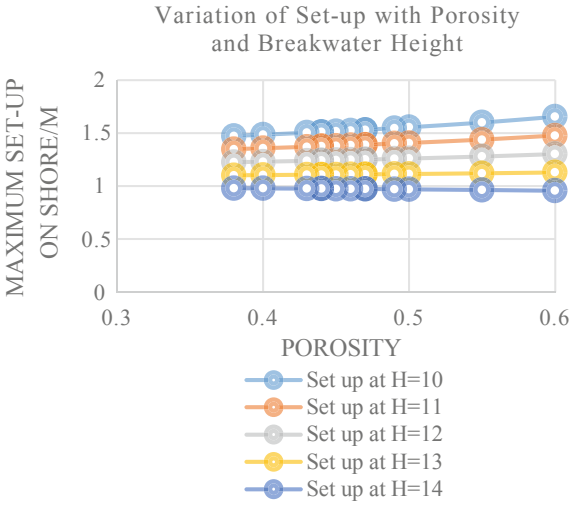

Fig. 13 Porosity versus setup

the structure. But it can be seen that the height of the structure has significant effect on the wave behavior. When the height is from 10 to 11 m, the graphs are linear and increasing, showing that the wave starts to break farther to the shore. This may be due to the large portion of the wave overtopping the breakwater and part of the energy passing through the structure.

However, when the height is at 12, 13 and 14 m, the breaking distance remains nearly constant as the structure become more porous. But the breaking distance is closer to the shore. This is maybe due to the obstruction created by the additional height, decreasing the portion of the wave that overtops. Then the transmitted wave reaches will have a greater decrease in energy and when it will reach an adequate water depth as it adapts to the seabed profile, breaking occurs.

6 Porosity and Setup

The setup is the maximum distance covered by the wave as it propagates on the shoreface after breaking in the surf-zone. Normally, the more energy a wave carries upon breaking, the longer the setup will be.

In general, increasing the porosity of the structure leads to increasing setup as a portion of the wave will pass through the structure. Thus, the transmitted wave loses little energy, hence the resulting wave energy will propagate on a larger extent.

When the breakwater height is increased, it is observed that the setup decreases with increasing height with maximum porosity. This indicates that the higher the structure gets; the more protection is providing against the propagation of wave energy to the shoreface.

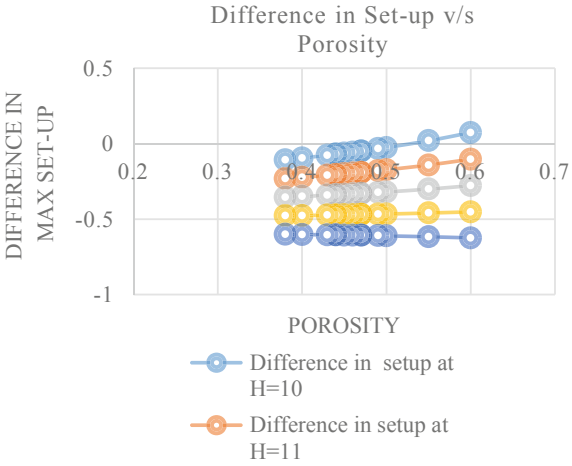

Fig. 14 Porosity versus difference in setup

Figure 14 shows the relation with the difference in setup before and after the placing of the breakwater. It could be observed that with increasing porosity, the difference in setup follows an increasing positive curve trend. This implies that the setup is reduced in the presence of the structure. On this attempt, each height from 10 to 14 m showed a positive output in controlling the setup for $H_s = 3.5$ m. Therefore, this result satisfies the use of breakwater in reducing the wave setup on the shoreface.

7 Porosity and Transmission Coefficient K_t

The transmission coefficient indicates the percentage of the incident wave that was transmitted on the leeside of the structure and reflected on the seaside of the structure. From the Fig. 15, it can be seen that the transmission coefficient is dependent on the porosity and on the breakwater height. As the porosity increases, K_t increases since the structure provide less obstruction to the wave impact. However, with increasing breakwater height, wave overtopping is reduced, resulting in a less wave passing over the top of the structure, therefore a lower value of K_t with increasing height.

8 Selection of Breakwater Dimension

The construction of emergent breakwaters can be very costly. However, as Ibrahim et al. [5] mentioned that the efficacy of emergent breakwater in wave dissipation and preventing erosion compared to submerged structures, the cost of emergent breakwater still remains a factor as the higher is the freeboard, the more protection it covers.

Fig. 15 Porosity versus K_t

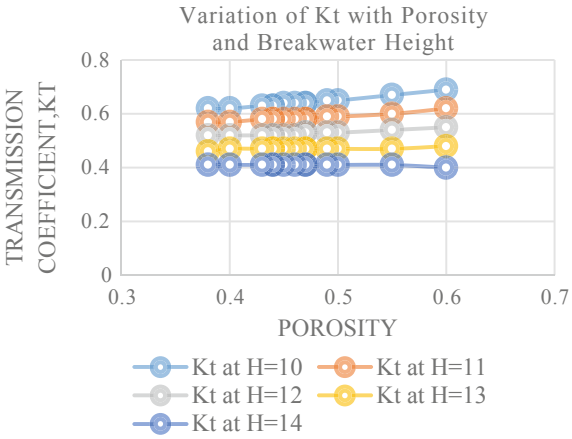

For the purpose of the modeling, a breakwater of regular dimensions (base width 60 m and Breakwater height 14 m) was designed with maximum crest height of 14 m. The performance of the breakwater was then analyzed with varying freeboard values and varying porosity. From the set of data, when the breakwater height is at 12 m, it demonstrated nearly a linear relation with varying porosity and other parameters listed above. With increasing porosity, the output parameters such as the transmission coefficient K_t and the maximum setup are changed by a little amount.

Moreover, D'Angremond and Tutuarima [17] compared the cost of construction of breakwaters using different armor layer. The tables below show the compilation of the range of prices of constructions and prices of materials by D'Angremond and Tutuarima [10] and [17], p. 68.

In order to reduce construction cost, D'Angremond and Tutuarima ([17], p. 1943) suggested to replace heavy rock armor by concrete units. Remarkable savings were observed when replacing one heavy stone unit with an Accropodes unit. The use of concrete units provides a more attractive finish to the structure and provides a smoother slope due to less rock volume.

For the cost estimate, the different armor layer was computed in Table 4. The normal concrete armor is seen to be cheaper than all the other alternatives. However, due to the geometric shape that the Tetrapod and Accropode armor units possess, they provide better interlocking abilities which provide enhanced resistance against wave actions. For "La Prairie" site, concrete cube is foreseen as the armor layer.

9 Conclusion

As an alternative measure, the model that was generated from MATLAB provided plausible results when it comes to the use of breakwater in dissipating wave energy. The different freeboard crest and porosity that were varied throughout the study

Table 1 Porosity for different armor layer (Van der Meer et al. 2009)

Type of armor unit	Porosity, n
Rock (one layer; impermeable core)	0.6
Rock (two layers; impermeable core)	0.55
Antifer	0.5
Cube (single layer	0.49
Cube	0.47
Haro	0.47
Accropode	0.46
Rock (one layer; permeable core)	0.45
Xbloc	0.44
Core-Loc	0.44
Dolosse	0.43
Rock (two layers; permeable core)	0.4
Tetrapod	0.38

Table 2 Compilation of cost of materials

Activities	Unit costs/USD
Armor unit production (quarry stone)	15/ton
Transport of rocks	
<300 Kg	0.25/ton Km
>300 Kg	0.4/ton Km
Construction costs	
Core (quarry run stones)	60/m^3
Rock armors	45/m^3
Normal concrete (Density = 2700 kg/m^3)	150/m^3
Concrete armor units	
Cubes	300/m^3
Tetrapods	325/m^3
Accropodes	400/m^3
Mobilization and demobilization (approx.)	2 million

Table 3 Dimensions of breakwater

Components	Dimensions
Crest width/m	4
Base width/m	60
Height/m	12
Slope	2:1
Number of layer, n	3

Table 4 Total cost

Items	Construction cost		Area/m^2/m	Total cost/USD
Core material	Core (quarry run stones)	60/m^3	176	10,560
Secondary armor	Quarry stones	75/m^3	47	3,525
Armor layer + toe	Normal concrete	150/m^3	178.5	24,150
	Concrete armor units			
	Cubes	300/m^3		53,550
	Tetrapods	325/m^3		58,000
	Accropodes	400/m^3		71,400

enabled to better understand the hydrological changes in the wave behavior on breaking and setup. It also showed that the use of an offshore structure can provide sufficient results in diminishing the energy carry capacity of a wave.

This also helped to devise a rough cost estimate from the selected dimension and armor layer and this assisted in providing cost effective structure that would provide sufficient protection.

However, the material cost for construction of offshore breakwaters can require large resources and also skilled labor, but with its capacity to provide satisfactory protection and possibly restore the shoreline over time might provide the solution to protect the road B9 and the coast line of La Prairie.

Acknowledgements First and foremost, I would like to express my deepest appreciation to my project coordinator and supervisor Mr. Asish Seeboo for his valuable guidance and advice with regards to this degree project. My deepest appreciation is expressed to my family and friends for their love, motivation, help and support during my four years of study.

References

1. Abdelhamid N (2013) Design of breakwaters: rubble mound breakwater, Cairo, University of Cairo. Available from https://www.unimasr.net/cgi-sys/suspendedpage.cgi. Accessed on 14 Jan 2019
2. Davey M (2019) Humans causing climate to change 170 times faster than natural forces. The guardian. Available at https://www.theguardian.com/environment/2017/feb/12/humans-causing-climate-to-change-170-times-faster-than-natural-forces. Accessed on 31 Sept 2018
3. Enviromesh (2007) Designing with gabions, Bristol. Available from https://www.enviromeshgabions.co.uk/specsheets/gabion%20design%20manual%2015-1-10.pdf. Accessed on 21 Jan 2019
4. Hedge A (2010) Coastal erosion and mitigation methods—global state of art. Indian J Geo-Marine Sci 39(4), India. Available from https://nopr.niscair.res.in/bitstream/123456789/10799/1/ijms%2039%284%29%20521-530.pdf. Accessed on 14 Sept 2018
5. Ibrahim I, Razak MS, Safari MD (2018) A short review on submerged breakwater. Matec web of conferences. Available from https://www.matec-conferences.org/articles/matecconf/pdf/2018/62/matecconf_iccoee2018_01005.pdf. Accessed on 14 Sept 2018

6. Inch K (2014) Surf zone hydrodynamics: measuring waves and currents. Research gate, Kris inch. Available from https://www.researchgate.net/publication/311536127_surf_zone_hydrodynamics_measuring_waves_and_currents. Accessed on 14 Sept 2018
7. Kamphuis J (2012) Introduction to coastal engineering and management, New Jersey. Available from https://www.scribd.com/document/334459788/kamphuis-introduction-to-coastal-engineering-and-mangaement. Accessed on 17 Feb 2019
8. le défi quotidie (2018) Erosion: plusieurs plages du pays défigurées. Available from: https://www.defimedia.info/erosion-plusieurs-plages-du-pays-defigurees. Accessed on 15 Nov 2018
9. Le Mauricien (2018) Fortes houles: les pompiers mobilisés à la prairie. Available from https://www.lemauricien.com/article/fortes-houles-les-pompiers-mobilises-a-la-prairie/. Accessed on 18 Nov 2018
10. Massie PE (1976) *Breakwater design*. The Netherlands. Delft University of Technology. Available from https://repository.tudelft.nl/islandora/object/uuid%3a010a725c-c507-4107-b5ee-0ec64aab2f42. Accessed 14 Sept 2018
11. Shore protection manual volume 1 (1984) Coastal engineering research centre [online] Washington, DC, U.S. army corps of engineers. Available from https://ft-sipil.unila.ac.id/dbooks/s%20p%20m%201984%20volume%201-1.pdf. Accessed on 11 Jan 2019
12. Soomaroo G, Koodoruth I (2016) Global environment facility small grants programme. Available from https://sgp.undp.org/all-documents/country-documents/600-op6-sgp-mauritius-country-programme-strategy/file.html. Accessed on 03 Oct 2018
13. Statistics Mauritius ministry of finance & economic development (2017) International travel & tourism year 2017. Ministry of finance & economic development
14. Stuart T, Newberry S, Latham J, Simm J (2003) Packing and voids for rock armour in breakwaters. Available from https://eprints.hrwallingford.co.uk/690/1/sr621.pdf. Accessed 4 Mar 2019
15. The University of Western Australia (2017) Chart for sea wave height and period for year 2016. Available at https://www.mrc.org.mu/english/documents/mauritius%20wave%20energy%20resource%20assessment%20report2018.pdf. Accessed on 3 Nov 2018
16. The World Bank (2016) International tourism, number of arrivals. Available from https://data.worldbank.org/indicator/st.int.arvl?end=2016&locations=mu&start=2000&view=chart. Accessed on 24 Sept 2018
17. Tutuarima W, Dangremond K (1999) Cost comparison of breakwater types. Available from https://journals.tdl.org/icce/index.php/icce/article/view/5735/5405
18. UNFCCC (2005) Small island developing states and climate change. Bonn, Germany
19. United Nations (2018) Planet at risk for irreversible damage if world does not act fast to implement Paris commitments, secretary-general warns during climate change event | meetings coverage and press releases. Available at https://www.un.org/press/en/2018/sgsm19245.doc.htm. Accessed on 27 Oct 2018
20. US army corps of engineers (2003) Us army coastal engineering manual chapter 4: surf zone hydrodynamics. Available from: https://www.a-jacks.com/coastal/generalinfo/cem/partii_coastalhydrodynamics/ii-4_surf_zone_hydrodynamics.pdf. Accessed on 18 Nov 2018

Stochastic Control of Single Legged ALP Using Stochastic Averaging

Kushal Solomon and Deepak Kumar

Abstract Articulated Leg Platform (ALP) is a compliant offshore structure. The static and dynamic stability of ALP depends on buoyancy force, mainly generated by buoyancy chamber. It is highly flexible in surge and sway direction. Due to high flexibility in these degrees of freedom, sometime response exceeds working comfort. Depending on nature of excitation, it can create unfavorable working condition on the platform too. Response control device can help to reduce the response of platform and can create favorable working conditions. ALP is mathematically modeled as an inverted pendulum. Excitation force on ALP is generated due to fluid structure interaction due to random waves. Generally, structure dimensions are such that Morisons equation is valid for obtaining the excitation forces. Probabilistic approach, which can handle non linearity, is suited to obtain response of such a problem. Stochastic averaging technique along with Fokker Planck equation is one such technique which can handle ALP problem easily, subjected to normalized forces which are small enough to minimize the error. An optimal feedback control along with stochastic averaging technique for ALP is developed, in order to control the response of ALP under wave loads.

Keywords Stochastic averaging · Fokker Planck equation · Optimal feedback control

1 Introduction

Structural control becomes very important under some situations to enhance its life span. Thus, several response control techniques and devices are developed and implemented all over the world. There are different techniques for control of dynamic

K. Solomon (✉) · D. Kumar
Department of Ocean Engineering, Indian Institute of Technology Madras, Chennai 600036, India
e-mail: kushal.sdmcet@gmail.com

D. Kumar
e-mail: deepakkumar@iitm.ac.in

V. Sundar et al. (eds.), *Proceedings of the Fifth International Conference in Ocean Engineering (ICOE2019)*, Lecture Notes in Civil Engineering 106,
https://doi.org/10.1007/978-981-15-8506-7_10

response of structures. They include passive, active, and semi-active control strategies. These methods of reducing the response of structures, results in limiting the damage of structures and can even prevent the total failure. Semi-active control devices works intelligently based on excitation and response of systems and also consumes less energy in comparison to active control systems. This is the reason several researches [2, 8, 12] worked on semi-active devices for control of structures. Few researchers have studied and showed the effectiveness of semi-active devices in control of offshore structures [11]. Response control of ALP has not been widely reported in literature. Few researchers made an attempt to control the response of ALP by developing an active controller without bringing in the actuator dynamics [5, 9]. Study on control of offshore structures is very important because the cost of construction involved is very high and they are also subjected to severe dynamic loads under service, as a result its structural life span gets affected. It is uneconomical to make offshore structures highly rigid as the cost of construction is high. So, it is better to use a control device to reduce the dynamic response and enhance the service life of offshore structures. In nature all the loads are random and therefore the response analysis and control techniques should be based on probabilistic approach. One such technique is the use of stochastic averaging along with Fokker-Planck-Kolmogorov equation to obtain probability density function of response of systems. An optimal feedback control can be developed over stochastic averaging technique along with FPK equation for control of highly nonlinear systems [7]. Stochastic optimal feedback control of offshore structure using stochastic averaging method over FPK equation is less explored area. Here we are going to analyze a single hinged Articulated leg platform, which consist of highly nonlinear damping terms generated due to fluid structure interaction. The PDF response of ALP is obtained using stochastic averaging technique over FPK equation. Feedback optimal control is developed to control the PDF response of ALP.

2 Response of the System Using Stochastic Averaging Procedure

A nonlinear SDOF system subjected to both additive and multiplicative excitations is considered. The system includes both stiffness and damping nonlinearities. The equation of motion can be written in the following form [3]

$$\ddot{x} + f(x) = \epsilon g(x, \dot{x}) + \epsilon^{1/2} \sum_{k=1}^{m} g_k(x, \dot{x}) \eta k(t) \tag{1}$$

where $f(x)$ denotes nonlinear restoring force. ηk is the excitation force which is stationary and ergodic process with zero mean. For small values of ϵ the motion of the system will be nearly periodic. Assuming a, ϕ, θ, ψ to be random processes. The response of the system is given by

$$x(t) = a(t)cos\phi(t) + b \tag{2}$$

$$\dot{x}(t) = -a(t)\beta(a,\phi)sin\phi(t) \tag{3}$$

where, $\beta(a,\phi)$ is instantaneous frequency of oscillation.
The total Energy E of the system is given by

$$E = \frac{1}{2}\dot{x} + V(x) \tag{4}$$

$$V(x) = \int_0^x f(u)du \tag{5}$$

$V(x)$ is the potential energy. Substitute Eqs. 2 and 3 in Eq. 4 to obtain the expression for $\beta(a,\phi)$ as given below

$$\beta(a,\phi) = \sqrt{\frac{2[V(a+b) - v(acos(\phi)+b)]}{(asin(\phi)^2}} \tag{6}$$

The solution of Eq. 1 can be regarded as set of random van der pol transformation from x, $\dot{x}$ to a and ϕ. Taking partial derivative of Eq. 2, results in the following equation

$$\dot{x} = cos(\phi)\dot{a} - \dot{\phi}asin(\phi) \tag{7}$$

Equating Eqs. 3 and 7 and performing algebraic simplifications the following expressions are obtained

$$\dot{a} = \epsilon q_1(a,\phi) + \epsilon^{1/2}\sum_{k=1}^{m}\sigma_{1k}(a,\phi)\eta_k \tag{8}$$

$$\dot{\phi} = \epsilon q_2(a,\phi) + \epsilon^{1/2}\sum_{k=1}^{m}\sigma_{2k}(a,\phi)\eta_k \tag{9}$$

where,

$$q_1(a,\phi) = -af_k g(a,\phi)\beta(a,\phi)sin(\phi) \tag{10}$$

$$q_2(a,\phi) = q_1(cos\phi)/asin(\phi) \tag{11}$$

$$\sigma_{1k}(a,\phi) = -af_k g_k(a,\phi)\beta(a,\phi)sin(\phi) \tag{12}$$

$$\sigma_{2k}(a,\phi) = \sigma_{1k}(cos\phi)/asin(\phi) \tag{13}$$

$$g(a,\phi) = g[(acos\phi + b, -a\beta(a,\phi)sin(\phi)] \tag{14}$$

$$g_k(a,\phi) = g_k[(acos\phi + b, -a\beta(a,\phi)sin(\phi)] \tag{15}$$

$$f_k = 1/f(a) \tag{16}$$

The Ito's equation of the limiting diffusion process represented by Eqs. 8 and 9 is of the form [3]

$$da = u(a) + \sigma(a)dB(t) \tag{17}$$

where $u(a)$ and $\sigma(a)$ are the drift and diffusion coefficients which are time independent, thus representing the average property of the process over the time interval t. The average drift and diffusion coefficients for a particular value of a are given by

$$\begin{aligned} u(a) = q_{1o} + \sum_{k=1}^{m}\sum_{l=1}^{m}\pi(\sigma_{1ko})\sigma_{1lo}s_{kl}(o) + \sum_{k=1}^{m}\sum_{l=1}^{m}[(\pi/2)\sum_{n=1}^{\infty}\{(\sigma_{1kn}^{r})\sigma_{1ln}^{r} \\ + (\sigma_{1kn}^{i})\sigma_{1ln}^{i} + n(\sigma_{1kn}^{i}\sigma_{2ln}^{r} - \sigma_{1kn}^{r}\sigma_{2ln}^{i})\}s_{kl}(nw(a))] \end{aligned} \tag{18}$$

$$\begin{aligned} \sigma^2(a) = \sum_{k=1}^{m}\sum_{l=1}^{m}2\pi\sigma_{1ko}\sigma_{1lo}s_{kl}(o) \\ + \sum_{k=1}^{m}\sum_{l=1}^{m}[\pi\sum_{n=1}^{\infty}(\sigma_{1kn}^{r}\sigma_{1ln}^{r} + \sigma_{1kn}^{i}\sigma_{1ln}^{i})s_k l(nw(a))] \end{aligned} \tag{19}$$

since the functions $q_1(q, \phi)$,$\sigma_{1k}(a, \phi)$, etc. are periodic,FFT of the functions are obtained for different values of 'a'. σ_{1kn}^{i},σ_{1kn}^{r} etc. are the real and imaginary parts of the FFT of $q_1(q, \phi)$,$\sigma_{1k}(a, \phi)$. s_{kl} is the cross power spectral density function between η_k and η_l.

The averaged FPK equation associated with ito's Eq. 17 is of the form

$$p(a) = \frac{c}{\sigma^2(a)}exp\left[\int_0^a \frac{2u(s)}{\sigma^2(s)}ds\right] \tag{20}$$

The probability density function of total energy E, can be obtained as given below

$$p(E) = \frac{p(a)}{f(a)} \tag{21}$$

The joint pdf of displacement and velocity responses can be obtained from $p(E)$ as follows

$$p(x, \dot{x}) = \frac{p(E)}{T(E)} \tag{22}$$

From joint pdf, $p(x)$ can be obtained by integrating out the velocity term.

$$p(x) = \int_{-\infty}^{\infty} p(x, \dot{x})d\dot{x} \tag{23}$$

3 Equation of Motion

Equation of motion of Articulated tower is given below [3]

$$\ddot{\theta} + 2\eta\omega_s\dot{\theta} + \omega_s^2(1+\theta^2)\theta = a_1F_1(t)|\dot{\theta}| - \frac{k_{do}}{I_o}|\dot{\theta}|\dot{\theta} - b_1F_2(t) + c_1F_3(t) \quad (24)$$

The right hand side of Eq. 24 represents the wave force obtained from Morison's equation for flexible structure.

Comparing Eqs. 1 and 24

$$f(x) = w_s^2(\theta + \theta^3) \quad (25)$$

$$g(\theta, \dot{\theta}) = -2\eta w_s\dot{\theta} - \frac{k_{do}}{I_o}\dot{\theta}|\dot{\theta}| \quad (26)$$

$$g_1(\theta, \dot{\theta})\eta_1 = \frac{\rho_w c_d}{I_o}|\dot{\theta}|F_1(t) \quad (27)$$

$$g_2(\theta, \dot{\theta})\eta_2 = -\frac{\rho_w c_d}{2I_o}F_2(t) \quad (28)$$

$$g_3(\theta, \dot{\theta})\eta_3 = \frac{\rho_w c_m}{I_o}F_3(t) \quad (29)$$

$$v(\theta) = \int_0^\theta f(u)du = w_s^2\frac{\theta^2}{2} + w_s^2\frac{\theta^4}{4} \quad (30)$$

$$\beta(a, \phi) = \sqrt{\left[\frac{2w_s^2}{(asin\phi)^2}\left[\frac{a^2}{2} + \frac{a^4}{4} - \frac{a^2cos^2\phi}{2} - \frac{a^4cos^4\phi}{4}\right]\right.} \quad (31)$$

The above mentioned parameters are used to obtain the drift and diffusion coefficients, which are further used in FPK equation to obtain the displacement and velocity response in terms of probability density function.

4 Controller

Linear Quadratic regulator is a state feedback control scheme, which drives the system from initial state x_o to the final state $x(t_f) = 0$, by minimizing the following quadratic cost function [10]

$$J = \int_0^\infty (x^TQx + u^TRu)dt \quad (32)$$

where Q_{2*2} is positive definite or positive semi-definite weighting matrix associated with state variables and R_{2*2} is a positive definite weight matrix associated with control input. The matrices are tuned by a trial and error method until you get the

desired results. The starting point of the trial and error method is given by Bryson's rule [1]

$$Q_{ii} = \frac{1}{max(x_i^2)} \qquad i \in (1, 2) \tag{33}$$

$$R_{jj} = \frac{1}{max(u_j^2)} \qquad j \in (1) \tag{34}$$

The second term on the right hand side of the Eq. 32 accounts for expenditure of energy of the control signal. The feedback control law is given by (Ogata and Yang 2002)

$$u = -kx = -R^{-1}B^*Px \tag{35}$$

The matriX P is obtained by solving the following reduced-matrix ricatti equation.

$$A * P + PA - PBR^{-1}B^*P + Q = 0 \tag{36}$$

A is a state matrix, B is a input matrix, x represents the state variables and $\dot{x}$. Matrix P is a positive definite matrix. Subsequently the feedback gains k are obtained by solving the equation

$$k = R^{-1}B^*P \tag{37}$$

Using the feedback control law given in Eq. 35 the equation of motion of articulated tower can be rewritten as

$$\ddot{\theta} + 2\eta\omega_s\dot{\theta} - k_2(\dot{\theta}) + \omega_s^2(1 + \theta^2)\theta - k_1\theta = a_1F_1(t)|\dot{\theta}| - \frac{k_{do}}{I_o}|\dot{\theta}|\dot{\theta} - b_1F_2(t) + c_1F_3(t) \tag{38}$$

Comparing Eqs. 1 and 38

$$f(x) = w_s^2(\theta + \theta^3) + k_1(\theta) \tag{39}$$

$$g(\theta, \dot{\theta}) = -2\eta w_s\dot{\theta} - k_2(\dot{\theta}) - \frac{k_{do}}{I_o}\dot{\theta}|\dot{\theta}| \tag{40}$$

$$g_1(\theta, \dot{\theta})\eta_1 = \frac{\rho_w c_d}{I_o}|\dot{\theta}|F_1(t) \tag{41}$$

$$g_2(\theta, \dot{\theta})\eta_2 = -\frac{\rho_w c_d}{2I_o}F_2(t) \tag{42}$$

$$g_3(\theta, \dot{\theta})\eta_3 = \frac{\rho_w c_m}{I_o} F_3(t) \tag{43}$$

$$v(\theta) = \int_0^{\theta} f(u)du = w_s^2 \frac{\theta^2}{2} + w_s^2 \frac{\theta^4}{4} + k_1 \frac{\theta^2}{2} \tag{44}$$

$$\beta(a, \phi) = \sqrt{\left[\frac{2w_s^2}{(asin\phi)^2}\left[\frac{a^2}{2} + \frac{a^4}{4} + \frac{k_1 a^2}{2w_s^2} - \frac{a^2 cos^2\phi}{2} - \frac{a^4 cos^4\phi}{4} - \frac{k_1 a^2 cos^2\phi}{2w_s^2}\right]\right]} \tag{45}$$

The aforementioned parameters are used to obtain the drift and diffusion coefficients, which are further used in FPK equation to obtain the controlled probability density function response of angular displacement.

5 Numerical Example

For the present study a single Hinged articulated tower installed in a water depth 141 m is considered. The physical and dynamical properties of ALP are listed in Tables 1 and 2 respectively (Fig. 1).

The response of the tower is analyzed in a sea state represented by P-M spectrum [6] with a significant wave height of 16 m.

$$s(\omega) = \frac{8.10}{10^3} \frac{g^2}{\omega^5} exp^{-(\frac{5}{4})(\omega_m/\omega)^4} \tag{46}$$

Table 1 Physical properties Of ALP

Components of ALP	Weight (kN)	Diameter (m)	Height (m)	Buoyancy (kN)
Upper shaft (above MSL)	2810	6	29.3	0
Upper shaft (below MSL)	1740	6.3	18.1	5220
Buoyancy chamber	7210	6.3	15	27170
Lower shaft	22,580	6.3	75.1	23390
Ballast chamber	40,140	10.5	25.6	24700
Lowest chamber	840.40	6.3	7.7	320.06

Table 2 Dynamical properties

Mass moment of inertia (I_o)	Restoring moment (R_0)	Natural frequency (ω_s)	Time period(T_n)	Damping ratio (ζ)
1.04×10^{11}	1.25×10^9	0.11	57	0.05

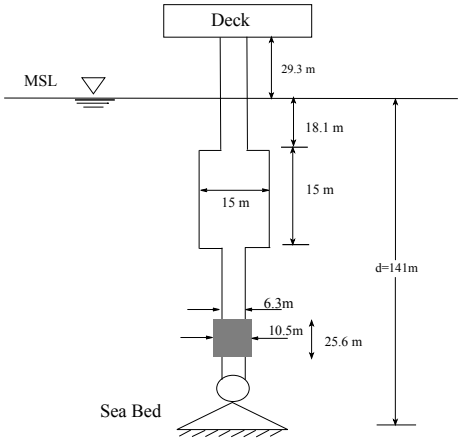

Fig. 1 Idealised articulated tower

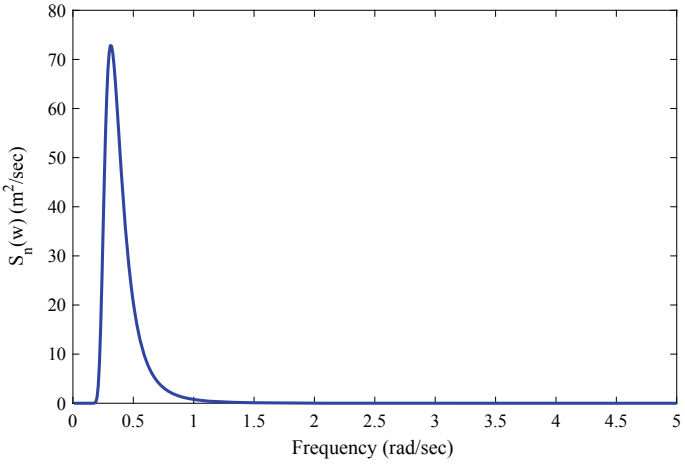

Fig. 2 Sea spectrum

where ω_m denotes the peak frequency. The wave spectral energy is concentrated in the neighbourhood of the peak frequency.

$$\omega_m = 0.4\sqrt{\frac{g}{H_s}} \tag{47}$$

where, H_s denotes the significant wave height. pm spectrum 16 m wave height is represented in Fig. 2, which is utilized to obtain the wave forces mentioned in right hand side of Eq. 24.

The values of drag coefficient C_d and inertial coefficient C_m are assumed to be same throughout the depth and are taken as $C_d = 0.6$ and $C_m = 2.0$ ([4]).
From LQR control technique we found that the optimal gain values $k1 = 0.0099$ and $k2 = 0.0173$ are required to achieve around 25% control in pdf response of angular displacement (θ).

6 Conclusion

The Response of an articulated leg platform under random sea states governed by pm-spectrum is obtained in terms of probability density function. Herein stochastic averaging procedure is used to obtain the averaged drift and diffusion coefficients

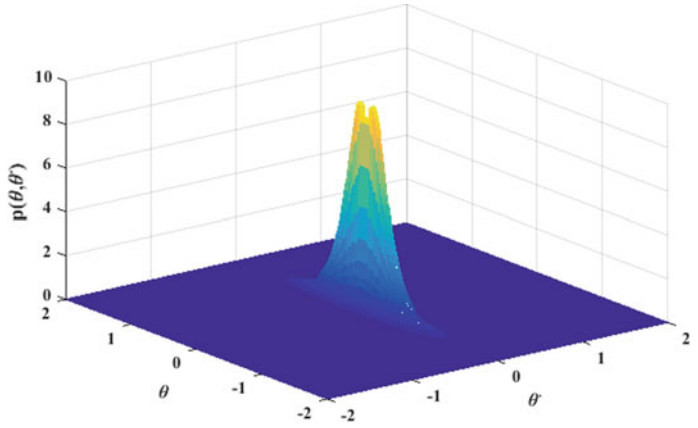

Fig. 3 Joint probability density function of angular displacement and angular velocity

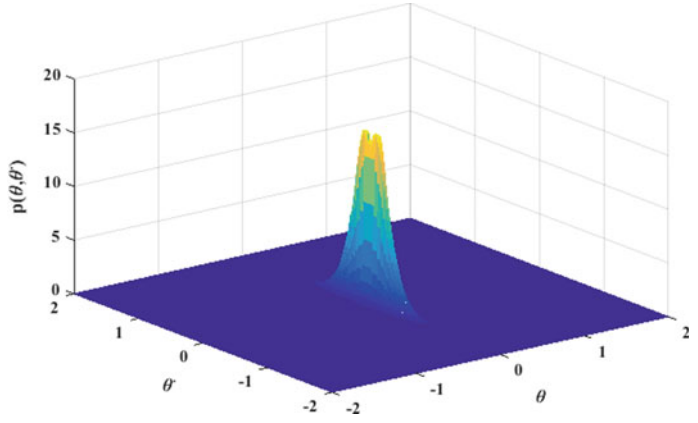

Fig. 4 Controlled joint probability density function of angular displacement and angular velocity

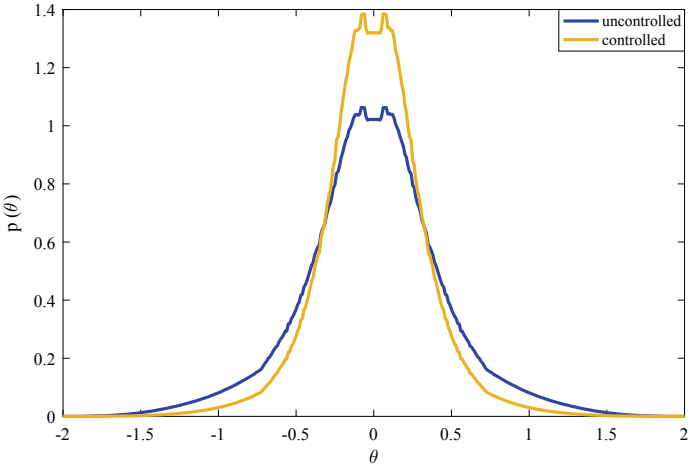

Fig. 5 Comparison for pdf response of angular displacement

of Ito's equation. Finally, FPK equation is solved numerically to obtain the pdf response. For the present study an articulated tower installed in a water depth 141 m is considered. The pdf response of alp under the influence of sea state represented by PM spectrum is obtained using stochastic averaging technique along with fpk equation.significant wave height 16 m is considered.The governing equation of motion of controlled system is redefined in Eq. 38. This equation is solved to obtain the reduced pdf response. The joint pdf of θ and $\dot{\theta}$ of ALP is represented in Fig.3 joint pdf is obtained by solving Eq. 22. From Fig. 3 it is visible that the maximum angular displacement is approximately θ_{max}=1.6 rad and maximum angular velocity is $\dot{\theta}_{max}$=0.176 rad/sec. Figure 4 represents joint pdf of θ and $\dot{\theta}$ of ALP for controlled system. It is clear that the base of the pdf is reduced .pdf of angular displacement is obtained by solving Eq. 23. Figure 5 shows a comparison between controlled and uncontrolled pdf of angular displacement. The rms value of uncontrolled and controlled pdf response of angular displacement is found to be 4.50 and 3.33 respectively. Percentage control in rms value of pdf response is 26%. The base of the pdf is reduced after using the controller, which implies that the amplitude of response is reduced. There is lot of scope for improving the control technique to reshape the pdf response and one can also incorporate the actuator dynamics for future study.

References

1. Datta TK, Jain AK (1990) Response of articulated tower platforms to random wind and wave forces. Comput Struct 34(1):134–137. https://doi.org/10.1016/0045-7949(90)90307-N
2. Dyke SJ, Spencer BF Jr, Sain MK, Carlson JD (1996) Modeling and control of magnetorheological dampers for seismic response reduction. Smart Mater Struct 5(5):565
3. Hespanha JP (2018) Linear systems theory. Princeton University Press, Princeton
4. Kumar D, Datta TK (2008) Stochastic response of articulated leg platform in probability domain. Probab Eng Mech 23(2–3):227–236. https://doi.org/10.1016/j.probengmech.2007.12.015
5. Ochi MK (2005) Ocean waves: the stochastic approach. Cambridge University Press, Cambridge
6. Ogata K, Yang Y (2002) Modern control engineering, vol 4. Prentice hall India
7. Paul S, Datta TK, Kapuria S (2009) Control of fixed offshore jacket platform using semi-active hydraulic damper. J Offshore Mech Arct Eng 131(4)
8. Soong TT, Spencer Jr BF (2002) Supplemental energy dissipation: state-of-the-art and state-of-the-practice. Eng Struct 24(3):243–259
9. Suneja B, Datta TK, et al. (1999) Nonlinear open-close loop active control of articulated leg platform. Int J Offshore Polar Eng 9(02)
10. Suneja BP, Datta TK (1998) Active control of ALP with improved performance function. Ocean Eng 25(10):817–835. https://doi.org/10.1016/S0029-8018(97)10007-5
11. Symans MD, Constantinou MC (1999) Semi-active control systems for seismic protection of structures: a state-of-the-art review. Eng Struct 21(6):469–487. https://doi.org/10.1016/S0141-0296(97)00225-3
12. Zhu WQ, Huang ZL, Ko JM, Ni YQ (2008) Optimal feedback control of strongly non-linear systems excited by bounded noise. J Sound Vib 274(3–5):701–724. https://doi.org/10.1016/S0022-460X(03)00746-6

Surge Response Control of FPSO Using Nonlinear MTLDs

Saravanan Gurusamy and Deepak Kumar

Abstract Floating Production Storage and Off-loading (FPSO) systems are being utilized world widely by offshore industries. The surge response of FPSO subjected to severe sea states needs to be suppressed in order to keep a particular station for operational purposes. The oil cargo tanks of FPSO can be used as passive dampers for minimizing the surge displacement response of FPSO. These cargo tanks can act as Tuned Liquid Dampers (TLDs) if the natural frequency of the liquid oscillation in containers is tuned to the surge natural frequency of FPSO or tuned to the excitation frequency. The containers can be partitioned into several tanks (as Multiple Tuned Liquid Dampers, MTLDs) with different lengths and liquid depths. The natural frequencies of MTLDs can also be distributed over a range around the natural frequency of FPSO. The present study attempts to comprehend the response control of FPSO under surge motion and so the FPSO is modeled as a single degree of freedom under random sea state. The containers can be modeled as either linear TLDs or nonlinear TLDs. Each linear TLD can be modeled by an equivalent Tuned Mass Damper (TMD) analogy based on linear wave theory. In order to account the nonlinear liquid motion in TLD, an impact damper analogy is used along with the TMD analogy. The study includes the efficiency and robustness of MTLD and it compares the response control obtained by using linear MTLDs and nonlinear MTLDs.

Keywords Floating production storage and off-loading (FPSO) · Surge · Tuned liquid damper (TLD) · Tuned mass damper (TMD) · Multiple tuned liquid damper (MTLD) · Impact damper

S. Gurusamy (✉)
Indian Institute of Technology, Madras, Chennai 600036, India
e-mail: saravanandoe@gmail.com

D. Kumar
Department of Ocean Engineering, Indian Institute of Technology Madras, Chennai 600036, India
e-mail: deepakkumar@iitm.ac.in

V. Sundar et al. (eds.), *Proceedings of the Fifth International Conference in Ocean Engineering (ICOE2019)*, Lecture Notes in Civil Engineering 106,
https://doi.org/10.1007/978-981-15-8506-7_11

1 Introduction

Moored floating structures for drilling, extracting and processing of crude oil, are being used by off-shore industries since many years. In general, tension leg platforms, semi-submersible systems and FPSOs are common facilities available in worldwide. In ever-increasing water depths, the sub-sea pipelines may not be possible; the FPSOs can be used for storing and processing the cargo. Hence, it is practical interest to address the issues related to dynamic motion of FPSO vessel under severe sea state. Ocean wave forces on the vessel leads to strong-interaction between FPSO and the oil containers; the liquid motion in the containers may affect the dynamics of FPSO significantly. Consequently, the wave forces tend to shift the vessel from its desired position. Excessive surge motion can cause damage for mooring and riser systems and so the whole production unit may get affected. Therefore, the motion control of FPSO is important to study in detail.

For achieving robustness and effectiveness, Multiple Tuned Liquid Dampers (MTLDs) may be preferred rather than single TLD. Using linear wave theory, TLDs can be modeled as equivalent mechanical models namely Tuned Mass Dampers (TMDs); and so MTLDs can also be modeled as equivalent Multiple Tuned Mass Dampers (MTMDs). Several researchers have explored efficiency and robustness of Multiple Tuned Mass Dampers (MTMD). Clark [1] has proposed a Multiple Tuned Mass Dampers (MTMD) for minimizing earthquake induced structural motion, by extending the work of Den Hartog [9] who has used single TMD for motion control. Igusa and Xu [11] have studied the effectiveness and robustness of MTMDs. They have also considered MTLDs with natural frequencies uniformly distributed over a range and cantered at the natural frequency of primary structure which is subjected to wide-band excitation. Kareem and Kline [14] have extended the study of Igusa and Xu [11] by investigating the MTMDs with frequencies uniformly and non-uniformly distributed within a particular range. They have indentified that MTMDs with non-uniform frequency distribution do not benefit any advantages over MTMDs with uniform frequency distribution. Fujino and Sun [5] have attempted the implementation of MTLDs for SDOF systems.

TLDs have also been proposed for motion control of ocean structures by many researchers. Lee and Reddy [18] have used cylindrical LTD to reduce the motion of fixed offshore-platforms. Jin et al. [13] have done both experimental and numerical studies on TLDs for suppressing earthquake response motion of jacket offshore platform. Sorkhabi et al. [24] have investigated the use of multiple shallow water tanks in motion control of MDOF systems. Ha and Cheong [8] have studied the pitch motion of a spar-type floating structure using a multilayer TLD. Further, they have found that the multilayer TLD can effectively suppress the motion than the single layer TLD. Zhang et al. [29] have studied the performance of a full-scale TLD in mitigating lateral tower vibrations of multi-megawatt wind turbines. Saravanan et al. [21] have studied the surge response control of FPSO using linear MTLDs. Further, Saravanan and Kumar [22] have extended their earlier study for MTLDs with the effect of multiple response frequencies of TLD on surge motion control.

The recent studies of TLDs emphasize that there are very few studies pertaining to flexible structures such as FPSO, wind turbines and spar-type structures. Hence, this paper extends the earlier work of Saravanan and Kumar [21], where a TLD is modeled, using linear wave theory, as an equivalent single degree of freedom (SDOF) system. The present study attempts to model a TLD using two SDOF systems to account the nonlinear effects. In order to account the nonlinear liquid motion, an impact damper is used along with the TMD. The study also addresses the effects of the proposed nonlinear model on the response control of FPSO and compares the effects with that of the linear model.

1.1 Linear Sloshing Model

A simple way to understand the sloshing in a rectangular tank is based on the equivalent mechanical models. A typical equivalent mechanical model consists of mass-spring-damper system. The equivalent mass, stiffness and damping correspond to the first modal sloshing, using linear wave theory, are given as follows [27] (Fig. 1).

$$m_1 = \frac{8\rho b L^2}{\pi^3} \tanh\left(\frac{\pi h}{L}\right) \tag{1}$$

$$k_1 = \frac{8\rho b L g}{\pi^2} \tanh^2\left(\frac{\pi h}{L}\right) \tag{2}$$

$$\omega_1 = \sqrt{\frac{\pi g}{L} \tanh\left(\frac{\pi h}{L}\right)} \tag{3}$$

$$c_1 = 2\left(\sqrt{\frac{3\mu}{8(1+\mu)}}\right) m_1 \omega_1, \mu = \frac{m_s}{m_1} \tag{4}$$

In case of shallow water TLDs, as the amplitude of excitation increases, a part of the liquid mass starts traveling and impacts on the side walls of tank. This impact mass undergoes to and fro motion between the tank walls. There is an evident mechanical analogy between the slamming (impacts of liquid mass on the tank walls) of liquid

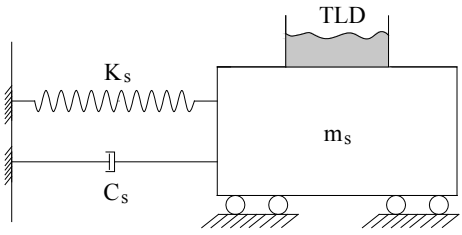

Fig. 1 SDOF system with a TLD

and an impact damper [15], therefore the slamming can be modeled as an impact mass damper ("also known as acceleration damper") which suppresses the response amplitude of mechanical system through momentum transfer [6]. The impact damper is a mass placed in a container, which is attached to a primary mass. A clearance is kept between the container wall and the impact damper by choosing the dimensions of the dampers to be sufficiently smaller than those of the container. Therefore, collisions take place between the damper and container walls successively whenever the relative displacement of the primary structure and the impact damper exceeds the clearance [23]. Slamming mass in TLD dissipates the energy in terms of wave run-up on the walls, wave breaking. In the present study, half a length of the TLD-tank is the required clearance for impact mass. The issue of determining the clearance or the length of the tank needs to be clearly addressed so that the vibration of the primary structure suppresses effectively.

2 Sloshing–Sloshing Analogy for TLD

The nonlinear motion in a TLD can be idealized by the combination of linear sloshing and slamming modes. The sloshing–slamming analogy for TLD, which is illustrated in Fig. 2, describes the behavior of the TLD as a linear sloshing model (mass-spring-dashpot system) augmented with an impact damper (slamming mode). The impact damper idealizes the nonlinear motion of TLD. So the nonlinear behavior of TLD can be modeled as a secondary system consists of an equivalent mechanical model having sloshing and slamming modes. The central idea of this concept is the mass transfer between linear sloshing mass and slamming mass [15].

If the amplitude (X) of motion of primary mass increases sufficiently, a part of the linear sloshing mass m_1 is exchanged into slamming mass m_2 and causes the dominant slamming motion.

Note that m_o is the liquid mass undergoes rigid body motion as the primary mass. On the other hand, if the amplitude (X) decreases substantially, the slamming mass transfers to the linear sloshing mass. This results in a predominant linear sloshing in TLD.

2.1 Jump Phenomenon of Shallow Water TLD

As the amplitude of excitation increases, the sloshing resonance frequency also increases. This phenomenon, as shown in Fig. 3, is reported in many literatures [2, 3, 4, 7, 12, 10, 16, 17, 19, 20, 25, 26, 28] have obtained an empirical relation for nonlinear resonance frequency of shallow water sloshing.

$$\beta = 1.038\Lambda^{0.0034} \text{ for } \Lambda \leq 0.03 \text{ weak wave breaking} \tag{5}$$

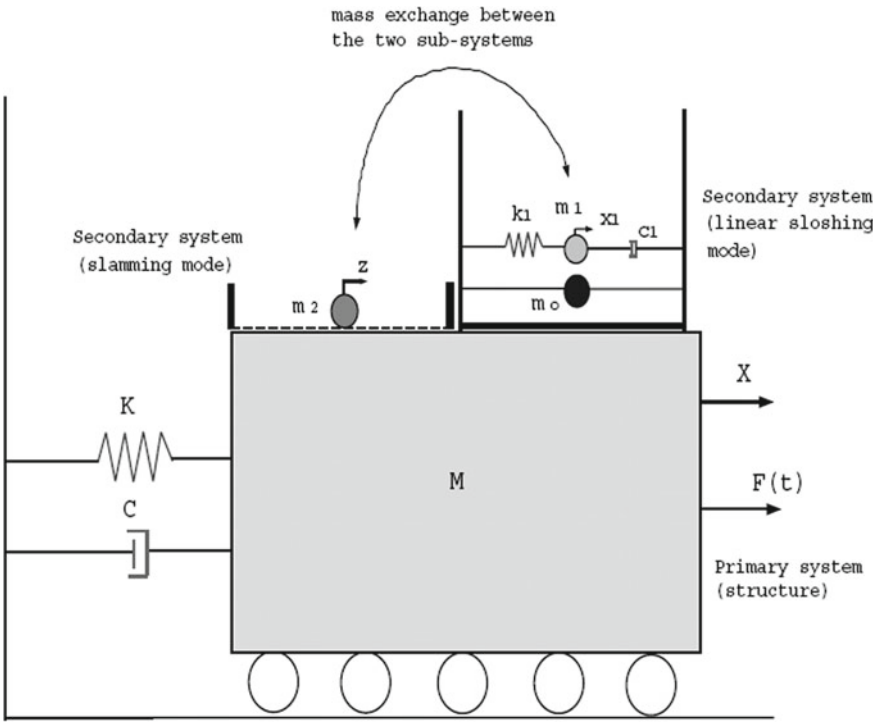

Fig. 2 Sloshing and slamming analogy for TLD

$$\beta = 1.59\Lambda^{0.125} \text{ for } \Lambda > 0.03 \text{ strong wave breaking} \tag{6}$$

Here, the ratio of nonlinear resonance frequency to linear sloshing frequency, (β) is a function of the non-dimensional amplitude of excitation (Λ), the amplitude of excitation is normalized with the tank length.

2.2 Mass Transfer Between Sloshing and Slamming

In the present analysis, since the resonance frequency changes due to mass transfer between sloshing and slamming, it is assumed that the stiffness of TLD is constant. Then, from the above relations (5) and (6), the change in resonance frequency ratio can related to the mass exchange between the linear damper and nonlinear dampers. In order to comprehend this concept, a mass exchange parameter (γ) is introduced. This parameter indicates that the portion of the liquid mass acting in the linear sloshing mode when the mass transfer takes place.

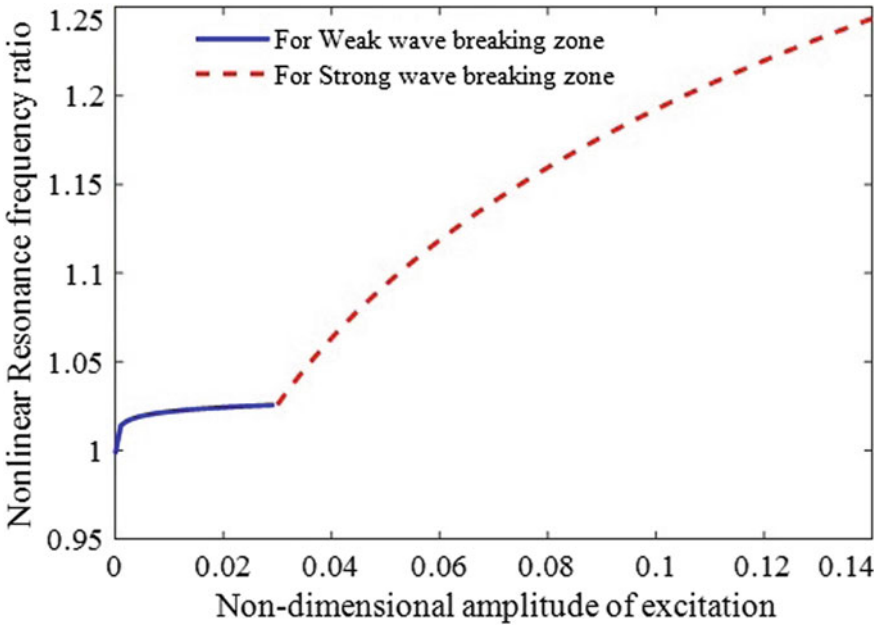

Fig. 3 Jump phenomenon of shallow water TLD

$$\tilde{m}_2(\gamma) = m_2 + (1-\gamma)m_1 \text{ and } \tilde{m}_1(\gamma) = \gamma m_1 \tag{7}$$

$$\beta = \frac{\tilde{\omega}_1}{\omega_1} \text{and } \tilde{\omega}_1^2 = \frac{k_1}{\tilde{m}_1} = \frac{\omega_1^2 m_1}{\tilde{m}_1} = \frac{\omega_1^2}{\gamma} \tag{8}$$

$$\frac{\tilde{\omega}_1^2}{\omega_1^2} = \frac{1}{\gamma} \text{and } \beta = \sqrt{\frac{1}{\gamma}} \tag{9}$$

3 Mathematical Formulation

The basic model for investigation is a moored FPSO vessel in deep water as shown in Fig. 4. In this study, different configurations (schematic views are shown in Fig. 5) of FPSO as in Table 1 are taken to study the surge response control of FPSO using nonlinear TLD model illustrated in Fig. 2. Moreover, the parameters of the FPSO-MTLD system are given in Table 2. In the present analysis, Pierson-Moskowitz spectrum is used to represent the fully developed sea state with significant wave height, $H_s = 16$ m, for consideration survival condition of the vessel.

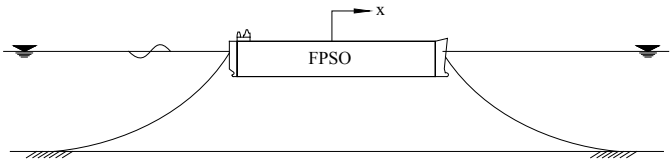

Fig. 4 Side view of a moored FPSO

$$(m+a)\ddot{x} + (2\xi\omega m)\dot{x} + kx = f(t) \tag{10}$$

$$\text{where, } f(t) = \frac{1}{2}\rho C_D BD|\dot{u}-\dot{x}|(\dot{u}-\dot{x}) + \rho C_M BDL\ddot{u} - (C_M-1)\rho C_M BDL\ddot{x} \tag{11}$$

The equation of motion of linear TLD_i:
For $i = 1, 2, 3, \ldots$

$$m_i\ddot{x}_i + c_i(\dot{x}_i - \dot{x}) + k_i(x_i - x) = 0 \tag{12}$$

The equation of motion of slamming mass, for $i = 1, 2, 3, \ldots$

$$m_i^s\ddot{x}_i^s = 0 \tag{13}$$

Here, $\{m,\xi,\omega\}$ are the mass, damping ratio and surge natural frequency of the FPSO vessel respectively; 'a' is the added mass due to surge motion of FPSO; the set $\{x_i,\dot{x}_i, \ddot{x}_i\}$ denotes displacement, velocity and acceleration of linear TLD_i. Let $\{m_i,k_i,c_i,\omega_i\}$ indicate the mass, stiffness, damping constant and natural frequency of the linear $\text{TLD}_{i,}$ respectively. Let $\{m_i^s,\ \ddot{x}_i^s\}$ denote the mass and acceleration of slamming damper in each TLD_i. In Eq. (11), 'k' refers to the linear spring constant of the moored FPSO.

The collisions of impact damper are idealized as discontinuous processes governed by conservation of linear momentum and the horizontal coefficient of restitution. The velocities of M and m_2 just before and immediately after a collision are related by the following equations.

$$\frac{\mathrm{d}x_+}{\mathrm{d}t} = \frac{(1-\mu e)}{(1+\mu)}\frac{\mathrm{d}x_-}{\mathrm{d}t} + \frac{\mu(1+e)}{(1+\mu)}\frac{\mathrm{d}x_{i-}^s}{\mathrm{d}t} \tag{14}$$

$$\frac{\mathrm{d}x_{i+}^s}{\mathrm{d}t} = \frac{(1+e)}{(1+\mu)}\frac{\mathrm{d}x_-}{\mathrm{d}t} + \frac{(\mu-e)}{(1+\mu)}\frac{\mathrm{d}x_{i-}^s}{\mathrm{d}t} \tag{15}$$

where, $\mu = m_i^s/m$ the mass ratio, and e is the horizontal coefficient of restitution,

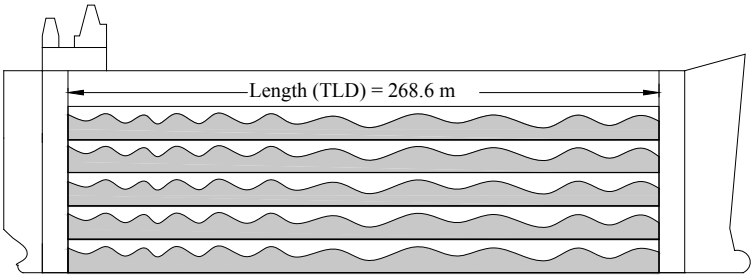

(a). FPSO configuration- 1

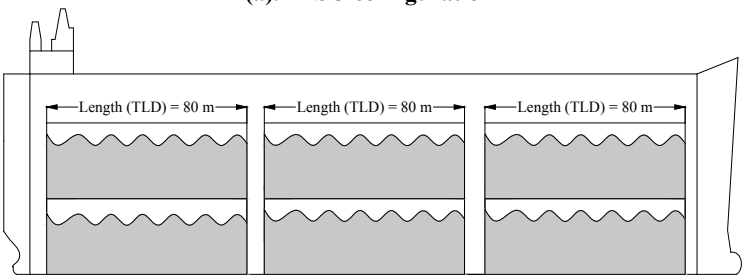

(b). FPSO configuration- 2

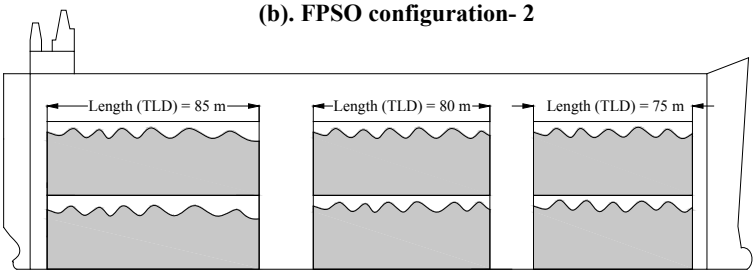

(c). FPSO configuration- 3

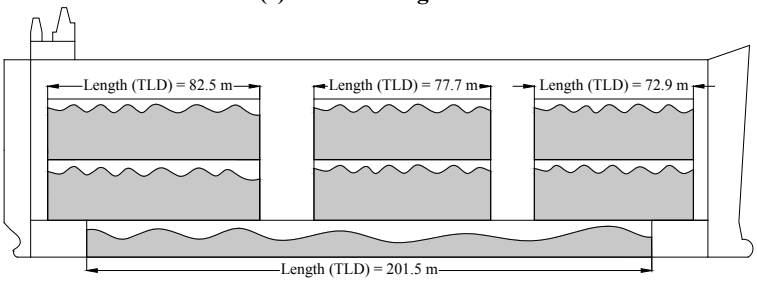

(d). FPSO configuration- 4

Fig. 5 a FPSO configuration-1. b FPSO configuration-2. c FPSO configuration-3. d FPSO configuration-4

Table 1 Details of different configurations of FPSO with MTLDs

Cases	No. of TLDs	Particulars of TLDs		
		Tank length (m), L_n	Liquid depth (m) h_n	Slosh frequency (rad/s)
Config. 0	0	–	–	–
Config. 1	5	268.6 m	2.93	0.06269
Config. 2	6	80 m	8.5	0.35216
Config. 3	6	85 m (2-identical TLDs)	8.5	0.33212
		80 m (2-identical TLDs)	8.5	0.35216
		75 m (2-identical TLDs)	8.5	0.37473
Config. 4	7	201.5 m	1.65	0.06272
		82.5 m (2-identicals)	8	0.33227
		77.7 m (2-identicals)	8	0.35214
		72.9 m(2-identical TLDs)	8	0.37448

Table 2 Parameters of FPSO-MTLD system

Mass,$m = 136{,}004{,}663$ (Kg)	Damping ratio, $\xi = 0.05$
Length, $L = 312$ (m)	$k = 675{,}490$ (N/m)
Maximum beam, $B = 45$ (m)	Surge period = 100.05 s
Draft, $D = 10$ (m)	Density of liquid in TLD, $\rho = 850$ kg/m^3
Height, $H = 30$ (m)	$C_M = 1.25$, $C_D = 0.7$

$$e = -\left(\frac{\mathrm{d}x_{i+}^{s}}{\mathrm{d}t} - \frac{\mathrm{d}x_{+}}{\mathrm{d}t}\right) \Big/ \left(\frac{\mathrm{d}x_{i-}^{x}}{\mathrm{d}t} - \frac{\mathrm{d}x_{-}}{\mathrm{d}t}\right) \tag{16}$$

The subscripts $-$ and $+$ are indicating the velocities just before and immediately after a collision, respectively. The nonlinear system is solved using Newmark's Beta method. At each time step, irrespective of mass transfer, the TLD is assumed to be a Tuned Mass Damper (TMD); the initial displacement and velocities of the all masses are assumed to be very small. The initial mass ratio, between linear sloshing mass and slamming mass, prior to the mass transfer, has been taken to be small; which means that initially almost all the liquid mass is in the linear sloshing mode. With these initial assumptions, the pseudo responses of the system are calculated for the first time step; using pseudo response of the primary structure and (Eq. 7), the sloshing and slamming masses are updated. Now, the revised masses are being used to re-simulate the responses for the first time step itself. The differences between pseudo responses and updated responses are calculated. If the difference is within the prescribed tolerance limit, then the updated responses will be kept for the first

time step. If not, using the updated structural response, the sloshing and slamming masses will be updated again in order to simulate for the first time step. This updating procedure, for the simulation at the first time step, will continue until the prescribed tolerance limit meets.

Then the numerical impact condition is being checked. If an impact happened, the structural and slamming damper velocities are being updated using (Eqs. 14 and 15), otherwise they are being kept unchanged. The same procedure is followed for successive time steps.

4 Results and Discussions

Surge response control of an FPSO using linear MTLDs and nonlinear MTLDs is investigated. Results are obtained based on time domain simulation. In order to comprehend the effects of linear and the nonlinear models on motion control, the Power Spectral Density (PSD) functions of displacement of FPSO are obtained. Being moored structure, it is identified that the energy of the FPSO's motion is dominant in the range of wave excitation frequencies rather than in its surge natural frequency as seen in Fig. 6a through d. Further Fig. 6a compares the PSDs of displacements of configuration-0 and configuration-1. The PSDs have predominant energy at FPSO's surge natural frequency ($f_s = 0.0629$ (rad/s)) and at wave excitation frequencies. Energy content in the range of wave excitation frequencies is not suppressed substantially. On the other hand, the energy at f_s is suppressed in configuration- 1of both linear and nonlinear models. However, the peak at f_s due to the linear model is little higher than that of the nonlinear model, because, in the linear model, the total mass of TLDs acting at f_s is higher than that of the nonlinear model where the total liquid mass transfers between linear sloshing and slamming modes. The mass transfer affects the damping properties of linear sloshing mode.

After seeing the response of configuration-1 in comparison to configuration-0, an attempt is made to minimize the energy over the wave excitation frequencies by tuning the TLDs to wave excitation frequencies. This tuning can be possible for implementation, as one can expect a particular range of wave frequencies, at a certain ocean site. Based on this argument, in configuration-2, the TLDs are tuned to a dominant wave frequency, 0.3519 (rad/s). It is noted that, as seen in Fig. 6b, a substantial energy is reduced around the excitation frequencies. Since, there are no TLDs tuned to FPSO' frequency, f_s, the energy reduction around f_s is not significant. Further, it is noted that the response control using linear model and the nonlinear model does not differ significantly. Figure 6c compares the PDS functions of displacements of configuration-0 and configuration-3 where TLDs are tuned to a range of dominant wave excitation frequencies. The response control using both linear and the nonlinear models is almost the same. With the same effectiveness, the configuration-3 will be more robust, because TLDs are tuned to a range of frequencies and is preferable to implement, than the configuration-2.

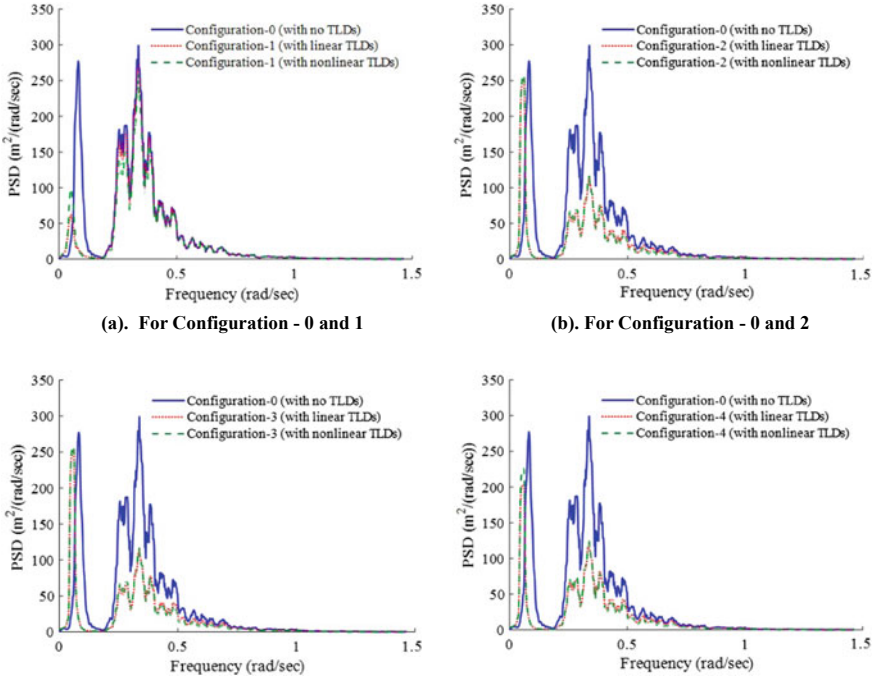

(a). For Configuration - 0 and 1

(b). For Configuration - 0 and 2

(c). For Configuration- 0 and 3

(d). For Configuration - 0 and 4

Fig. 6 PSDF of displacement of FPSO

In addition, the combined (TLDs tuned to wave excitation and FPSO frequencies) effect on response control is investigated. So, in configuration-4, seven TLDs, of which six are tuned to wave excitation frequencies and one TLD is tuned to f_s. It is seen that the energy around f_s is reduced. In comparison to linear model, the nonlinear model gives slightly less control. In case of nonlinear model, the mass exchange between the linear sloshing and slamming takes place continuously and so damping of TLDs changes at every time instant. The change in damping properties of linear TLDs reduces the response control of FPSO.

The ratio between the total mass of TLDs to mass of FPSO, for the configurations 1–4 is kept as constant for both the linear model and nonlinear model. Since the total mass of MTLDs on FPSO plays a key role in response control, one may vary the mass ratio depending on the mass of FPSO (Table 3).

5 Conclusions

The present study has attempted to examine the response control of FPSO with linear and nonlinear MTLDs. The available cargo tanks in FPSO are modeled as

Table 3 Response control using both linear and nonlinear models

Cases	Linear model	Nonlinear model	Mass ratio	Control from linear model (%)	Control from non-linear model (%)
	RMS of displacement (m)	RMS of Displacement (m)			
Config. 0	7.1034	7.1034	–	–	–
Config. 1	6.4266	6.7536	0.475	9.52	4.92
Config. 2	5.007	5.4916	0.475	29.51	22.69
Config. 3	5.0111	5.4555	0.475	29.45	23.19
Config. 4	4.9964	5.5155	0.475	29.66	22.35

liquid dampers. Being a flexible structure, the classical approach, in which MTLDs are tuned to FPSO's surge frequency, provides very minimal control. In order to enhance the response control, MTLDs are also tuned to excitation frequencies. Based on the present analysis, the following remarks can be given:

1. The response control based on linear MTLDs is higher than that of nonlinear MTLDS. In case of nonlinear model, the mass exchange between sloshing and slamming affects the response control in all FPSO-configurations with MTLDs.
2. The performance of MTLDs tuned to a single wave excitation frequency, MTLDs tuned to a range of wave excitation frequencies, MTLDs tuned to FPSO's frequency as well as to a range of wave excitation frequencies does not differ significantly but robustness of control can increase when MTLDs are tuned to a band of frequencies.
3. The present study reflects that for flexible structures, MTLDs are effective if they are tuned to excitation frequencies.

References

1. Clark AJ (1988) Multiple passive tuned mass dampers for reducing earthquake induced building motion. In: Proceedings of Ninth World Conference on Earthquake Engineering
2. Frandsen JB (2004) Sloshing motions in excited tanks. J Comput Phys 196(1):53–87
3. Frandsen JB (2005) Numerical predictions of tuned liquid tank structural systems. J Fluids Struct 20:309–329
4. Forbes LK (2010) Sloshing of an ideal fluid in a horizontally forced rectangular tank. J Eng Math 66:395–412
5. Fujino Y, Sun LM (1993) Vibration control by multiple tuned liquid dampers. J Struct Eng 119(12):3482–3502
6. Grubin C (1973) Comments on several papers on impact dampers. J Acoust Soc Am 53(6):1746
7. Gardarsson SM, Yeh H (2007) Hysteresis in shallow water sloshing. J Eng Mech 133(10):1093–1100
8. Ha M, Cheong C (2016) Pitch motion mitigation of spar-type floating substructure for offshore wind turbine using multilayer tuned liquid damper. J Ocean En 116:157–164

9. Hartog, Den JP (1956) Mechanical vibrations, 4th edn. McGraw Hill, Inc. NY
10. Hill DF (2003) Transient and steady-state amplitudes of forced waves in rectangular basins. Phys Fluids 15(6):1576–2158
11. Igusa T, Xu K (1994) Vibration control using multiple tuned mass dampers. J Sound Vib 175(4):491–503
12. Ikeda T, Nakagawa N (1997) Non-Linear vibrations of a structure caused by water sloshing in a rectangular tank. J Sound Vib 201(1):23–41
13. Jin Q, Li X, Sun N, Zhou J, Guan J (2007) Experimental and numerical study on tuned liquid dampers for controlling earthquake response of jacket offshore platform. Marine Struct 20:238–254
14. Kareem A, Kline S (1995) Performance of multiple mass dampers under random loading. J Struct Eng 121(2):348–361
15. Kareem A, Yalla S, McCullough M (2009) Sloshing-slamming dynamics-S2—analogy for tuned liquid dampers, vibro-impact dynamics of ocean systems and related problems, Springer. In: Lecture notes in applied and computational mechanics, vol 44, 123–133
16. Khosropour R, Cole SL, Strayer TD (1995) Resonant free surface waves in a rectangular basin. Wave Motion 22:187–199
17. Lepelletier TG, Raichlen F (1988) Nonlinear oscillations in rectangular tanks. J Eng Mech ASCE 114(1):1–23
18. Lee SC, Reddy DV (1982) Frequency tuning of offshore platforms by liquid sloshing. Appl Ocean Res 4(4):226–230
19. Ockendon JR, Ockendon H (1973) Resonant surface waves. J Fluid Mech 59:397–413
20. Gurusamy S, Kumar D (2017) Experimental study on shallow water sloshing. In: Proceedings of 13th international conference proceedings of on vibration problems (ICOVP). IIT Guwahati
21. Gurusamy S, Kumar D, Saraswat R (2018) Response control of FPSO using multiple tuned liquid dampers. In: Proceedings of fourth international conference in ocean engineering (ICOE). IIT Madras
22. Gurusamy S, Kumar D (2019) Surge response control of FPSO using multiple tuned liquid dampers—a study on effect of multiple frequencies in TLD. In: Proceedings of 38th international conference on ocean, offshore and arctic engineering (OMAE). Glasgow, Scotland
23. Semercigil SE, Lammers D, Ying Z (1992) A new tuned vibration absorber for wide-band excitations. J Sound Vib 156(3):445–459
24. Sorkhabi AA, Kristie J, Mercan O (2014) Investigations of the use of multiple tuned liquid dampers in vibration control. In: Proceedings of ASCE-structure congress
25. Sun LM, Fujino Y, Chaiseri P, Pacheco BM (1992) The properties of TLDs using a TMD analogy. Earthquake Eng Struct Dyn 24:967–976
26. Sun LM, Fujino Y, Koga K (1995) A model of TLD for suppressing pitching motions of structures. Earthquake Eng Struct Dyn 24:625–636
27. Tait MJ (2008) Modeling and preliminary design of a structure-TLD system. Eng Struct 30:2644–2655
28. Yu J, Wakahara T, Reed DA (1999) A non-linear numerical model of the tuned liquid damper. Earthquake Eng Struct Dyn 28:671–686
29. Zhang Z, Stain A, Basu B, Nielsen S Performance evaluation of full-scale tuned liquid dampers (TLDs) for vibration control of large wind turbines using real-time hybrid testing. Eng Struct 126:417–431 (2016)

Experimental Investigation of Concrete Jacket Structures Upending Process Under Regular Waves

P. Vineesh, V. Sriram, and A. Hildebrandt

Abstract Offshore water depths varying from 30 to 50 m have a tremendous potential to harvest wind energy ≥6 MW. The roughness of the sea makes it very difficult for the installation of substructures from small tripod or jacket structures to floating substructures. More generic, we have to wait for calm sea period in the offshore for the installation of any such structures. It has created a need for research in investigating installation of structures in all-weather condition. Hence in order to increase the potential of installation of offshore structure, understanding the structural behavior during installation is vital. For understanding aforementioned structural behavior in installation, jacket structure which is very common fixed substructure is chosen and studied for all type of waves. In order to study such substructure, heaviest jacket for the given aspect ratio (HyConCast) is chosen. The concept of HyConCast jacket has advantages of combined ductile iron casting knots and precast concrete pipes which is the reason for the heavy mass of the structure. Because of its high mass compared to other offshore structures, its dynamic and excitation responses in regular waves during installation are unknown. In this chapter, the results from experimental study on response of the jacket model for different upending stages under regular waves are discussed.

Keywords Concrete jacket · Installation · Upending process · Motion response · Wind energy

1 Introduction

Need for tackling energy requirement is one of the major concerns for countries all around the globe. At the same time, they have to make sure that environmental

P. Vineesh (✉) · V. Sriram
Indian Institute of Technology Madras, Chennai 600036, India
e-mail: vineesh12323@gmail.com

A. Hildebrandt
Leibniz Universität Hannover, Nienburger Str. 4, Hanover, Germany

V. Sundar et al. (eds.), *Proceedings of the Fifth International Conference in Ocean Engineering (ICOE2019)*, Lecture Notes in Civil Engineering 106,
https://doi.org/10.1007/978-981-15-8506-7_12

concerns must be addressed. Non-conventional energy sources like wind energy have importance in this regard since they are more environmental friendly than conventional energy sources. Even though large numbers of wind farms exist in land, further development of wind farms will be restricted by availability of land. Thus, engineers are finding an alternative to install wind turbines in ocean. Even though both floating and fixed structures can be used as platform for wind turbines, fixed structures like jacket platform will be more economical for low water depth.

Several researches are undergoing to reduce the cost and to improve the durability of jacket platform. The concept of hybrid jacket platform, where precast concrete members are used instead of steel members, is one of such research area.

The usage of concrete members reduces the construction and maintenance cost considerably. The performance of concrete members under fatigue loading is found to be superior to steel members. Other advantages of concrete members include good impact resistance, good resistance to crack propagation, slower thermal response, resistance against corrosion and high durability. However, the usage of concrete increases the total weight of the structure considerably. Generally, installation of jacket structures will be conducted in calm sea state. But in the case of installation of wind turbine platform, waves will be always present and its effects should be considered in the analysis of installation process. The installation process of heavy jacket structure in the presence of waves is a relatively new area of research.

The conventional method, such as float over method, is used for the installation of jacket structures. In this method, jacket is transported to the required location on barge, and then it is launched from barge to sea. The jacket will be floating in horizontal position after launching. By ballasting the buoyancy tanks and lifting using crane, jacket is then upended. Since the installation process of jacket platform costs about 40% of the total platform costs, extensive studies had been conducted in this area in past years. Bhattacharya and Idichandy [1] investigated the load out launching and upending process of offshore steel jackets in calm water condition using experimental methods. A more recent study by Hu et al. [3] concentrates on the pitch motion characteristics of jacket and the force coming on rocker arm during launching operations. The authors carried out experimental as well as numerical investigations and compared with field measurements. Since literatures addressing appending process of jackets in wave conditions are less, experimental studies regarding the response of other floating offshore platforms in waves are also considered for literature review. Downie et al. [2] studied the response characteristics of a truss spar platform and the measured vertical force acting on the horizontal porous plates attached on it. They employed both regular wave tests and irregular wave tests for the experiment. A numerical and experimental study on buoy form spar platform by Nallayarasu and Senthil [4] also analyzes the motion characteristics of a floating structure in detail. An experimental investigation on the motion response of hybrid jacket platform in regular waves was done by Welzel et al. [5] where four large buoyancy tanks were used to make the heavy jacket float. The response of the structure was measured for vertical position of the jacket in both 0° and 45° wave direction. Based on the structure response, authors assessed the feasibility of installation concept in the common waves for the suggested area of installation. These studies indicate the

necessity of detailed analysis of response of the jacket structure during upending in wave loading. In the present study, motion characteristics of a jacket in regular waves are analyzed for three different stages of upending (horizontal position, 45° inclinations, and vertical position). Further, eight cylindrical buoyancy tanks with less diameter are used for jacket launching, making the structure entirely different from the model used by Welzel et al. [5]. Based on the modified configurations, with the different buoyancy tank, the experimental investigation on the motion response of a heavy jacket platform during various stages of upending under wave loading has been carried out. Both beam sea and head sea conditions for horizontal, vertical and 45° position are tested and reported in this chapter.

2 Experimental Investigations

The experiments were conducted in wave basin at department of ocean engineering, IIT Madras. The wave basin has a dimension of 30 m × 30 m × 3 m, and it is fitted with a paddle type wave maker at one end and wave absorbers at other three sides. The wave maker can generate a maximum wave height of 0.3 m. The model was placed at a distance 8 m from wave maker and 15 m from either side of the basin as represented in Fig. 1.

The duration of wave generation is selected such that reflected waves will not be affecting the measurements. The model is free to oscillate in all the six degrees of freedom. Among these, heave, pitch and roll are measured using instruments placed on the jacket. Accelerometer is used to measure heave acceleration, and a biaxial inclinometer is used to measure pitch and roll angles. The heave acceleration time series obtained from accelerometer is then converted to heave displacement. The

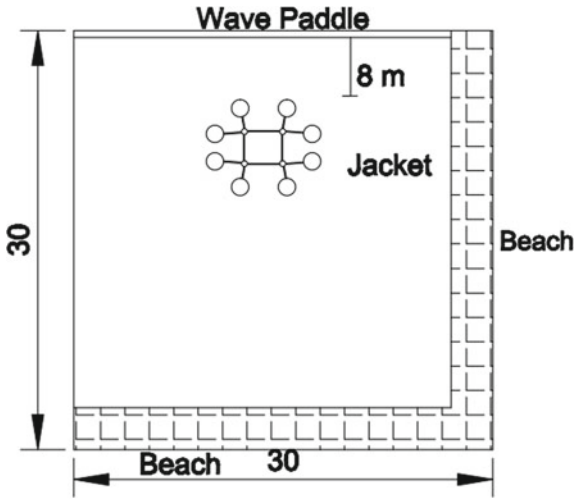

Fig. 1 Experimental setup

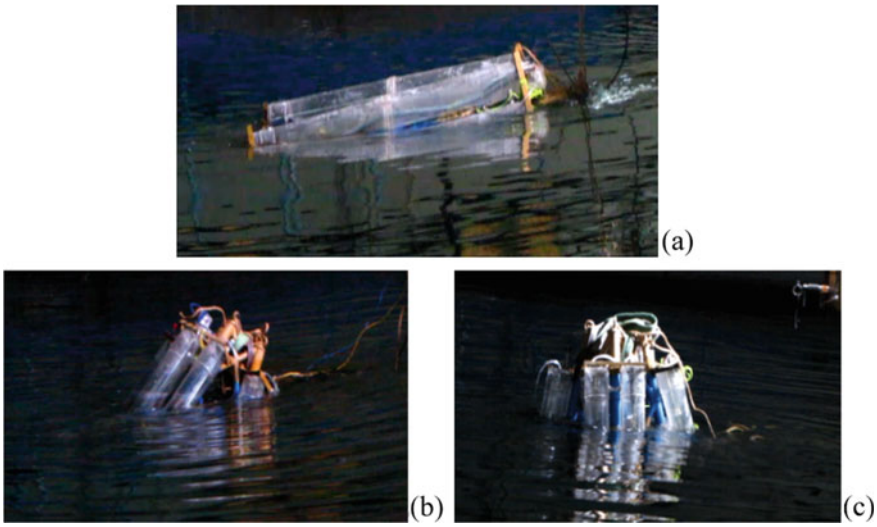

Fig. 2 Different jacket positions: **a** horizontal, **b** 45° position, **c** vertical position

incident wave height is measured using a wave probe fixed at 1 m in front of the model. Figure 2 represents different positions of jacket during the experiment.

2.1 Physical Model

The physical model of jacket platform is constructed using steel tubes. The model is scaled according to Froude model law, and a scale ratio of 1:37 is used. A total number of eight buoyancy tanks are constructed such that one buoyancy tank will be attached at either side of jacket main leg (refer Fig. 3). The position of jacket leg is adjusted such that while launching the jacket from barge, it should float in horizontal position. Before model testing, preliminary design and analysis of jacket structure are carried out for floatation analysis. The amount of water required for ballasting of buoyancy tanks is calculated by floatation analysis. The details of jacket model and buoyancy tanks prepared are given in Tables 1 and 2, respectively.

Fig. 3 Jacket model without buoyancy tanks (left side) and after attaching buoyancy tanks (right side)

Table 1 Jacket model parameters according to Froude scaling

	Full scale	Model scale
Height	61.42 m	1.66 m
Mass	3089 tons	61 kg
Density of water	1025 kg/m^3	1000 kg/m^3

Table 2 Buoyancy tank parameters according to Froude scaling

	Full scale	Model scale
Mass	130.7 tons	2.58 m
Volume	577.44 m^3	0.0114 m^3
Diameter	4 m	0.11 m
Length	44.4 m	1.2 m

3 Results and Discussions

3.1 Decay Test

Free decay tests are conducted to find out the natural frequency of structure in heave, pitch and roll modes of vibration. An initial displacement will be given in each degree of freedom, and the resulting time series is then recorded. Free decay tests are done

Table 3 Natural period

Jacket position	Natural period (s)		
	Heave	Pitch	Roll
Horizontal position	1.6	2.2	2.8
45° position	2.1	10.8	5.1
Vertical position	2.2	6.7	6.7

for all the different stages of upending positions (horizontal position, 45° and vertical position). Natural periods of the jacket model in different position for heave, pitch and roll degree of freedom are determined from respective time series. The results from the free decay tests are presented in Table 3.

For a floating body, stiffness in heave direction is directly proportional to water-plane area of the body. From Fig. 2, it is clear that water-plane area for horizontal position will be the largest among the three positions. Moreover, the mass of the jacket will be increasing in upending process since ballast water will be added to buoyancy tanks. Thus, both the higher water-plane area and lower mass of the jacket in horizontal position are the reason for the lowest value of heave natural period corresponding to that position. In the case of roll and pitch motions, stiffness is directly proportional to transverse and longitudinal metacentre, respectively. For horizontal position of jacket, longitudinal metacentre is more than that of transverse metacentre. Hence, the pitch natural period is found to be less compared to roll natural period at this jacket position. Compared to other jacket positions, horizontal position has the lowest values for natural period in heave, pitch and roll, leading to stability in this position. But, the natural periods in this position are within the range of normal wave periods in ocean (model scale); hence, motions are more susceptible to resonance. Further, among heave, pitch and roll motions, heave in all the positions is more prone to resonance effect.

3.2 Regular Wave Tests

In order to find out the response amplitude operator for different degree of motion of the structure, regular wave tests are conducted. The wave periods are defined according to the field data obtained from one of the German Research Platform, FINO1, in Northern Sea. Major part of wave energy in this location is distributed in waves having period from 6 to 14 s [5]. Thus, the periods of waves used for the experiment are ranging from 1 to 2.9 s. The lower value of period corresponds to the lower value of wave period which exists in the field conditions. The upper value of time period is selected to capture the RAO of different motions near to resonance, but limited by the capability of the wave maker facility. The regular wave tests are conducted for both head sea and beam sea orientations of the jacket for each of the three upending positions.

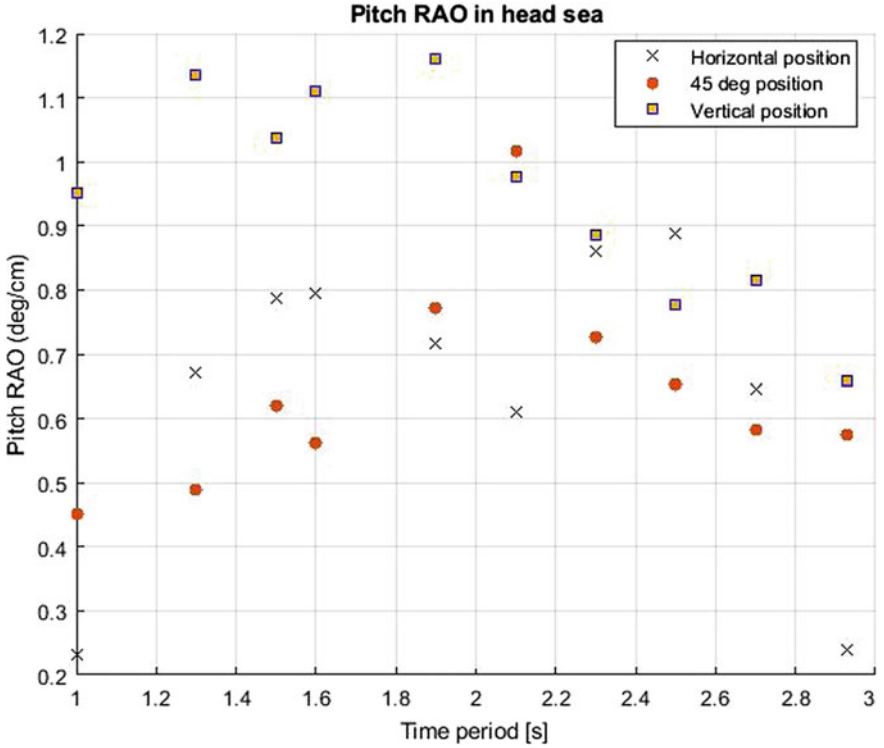

Fig. 4 Pitch RAO in head sea for different jacket positions

Heave, pitch and roll RAO for all the three positions of jacket model are found out using regular wave tests. Since pitch is predominant in head sea and roll is predominant in beam sea, only corresponding results are discussed. Figure 4 represents the pitch RAO in head sea for all the jacket positions.

For horizontal position of jacket, peaks in RAO plot are observed near to pitch as well as heave natural period. In the case of 45° and vertical position of jacket, only heave natural period is coming within the time period of regular waves generated. A peak in pitch RAO plot is present in both 45^0 and vertical position, corresponding to heave natural period of that particular position. Pitch RAO at heave resonance corresponding vertical jacket position is observed to be more than other jacket positions. Since peaks in pitch RAO plots are present corresponding to heave natural period also, we can say that both pitch and heave motions are coupled.

The roll RAO in beam sea for different jacket positions is shown in Fig. 5. In the case of roll RAO, for horizontal position of jacket two peaks are present corresponding to heave and roll natural period. Thus, it is evident that for horizontal jacket position, roll motion is coupled with heave. The absence of peak corresponding to heave natural period in roll RAO plots for both 45° and vertical position of jacket suggests that coupling between roll and heave motions is not that much visible in

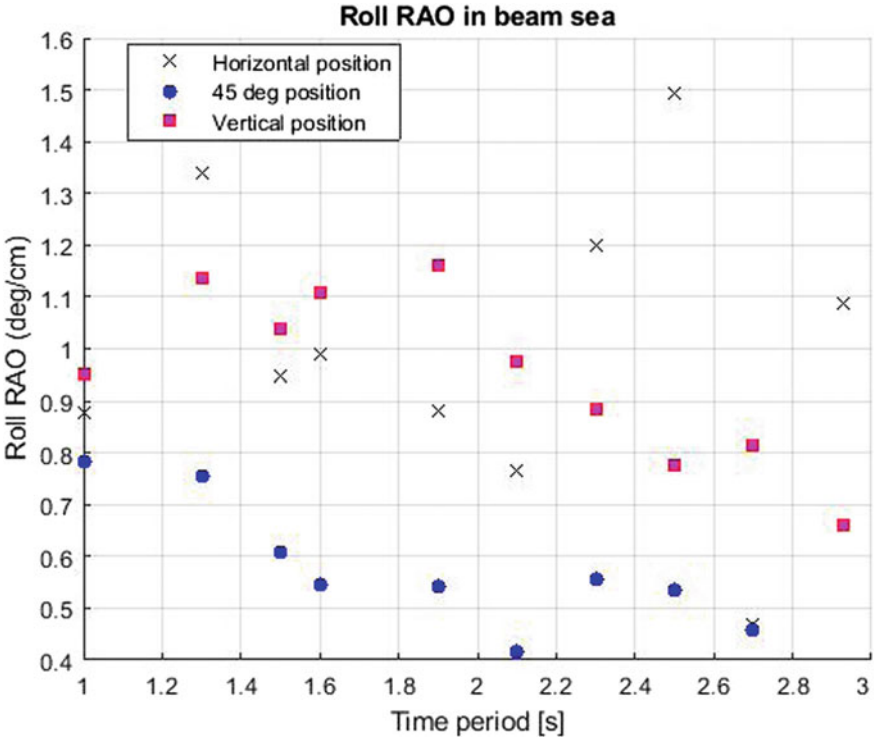

Fig. 5 Roll RAO in beam sea for different jacket positions

motion of jacket at corresponding positions. Roll motions in horizontal position are large compared to roll at other jacket position particularly because of the resonance effect from heave as well as roll motions.

Heave RAO for the three jacket positions in head sea and beam sea is given in Fig. 6 and Fig. 7, respectively. For horizontal position of jacket, two peaks are observed in heave RAO plots also. In heave RAO plot for head sea, one of this peaks corresponds to heave natural period and other corresponds to pitch natural period, whereas in heave RAO for beam sea, the first peak corresponds to heave natural period and the second peak corresponds to roll natural period. Since pitch motion is dominant in head sea and roll is dominant in beam sea, and they are coupled with heave motion, and this type of characteristic is expected. But in heave RAO plots for other positions of jacket, only one peak which corresponding to heave natural period is present. This is because the natural period of pitch and roll motions for these positions is well beyond the wave periods used in the experiment. The heave motions in vertical position of jacket are more compared to other two positions which underly the importance of employing response control arrangements for this position of jacket.

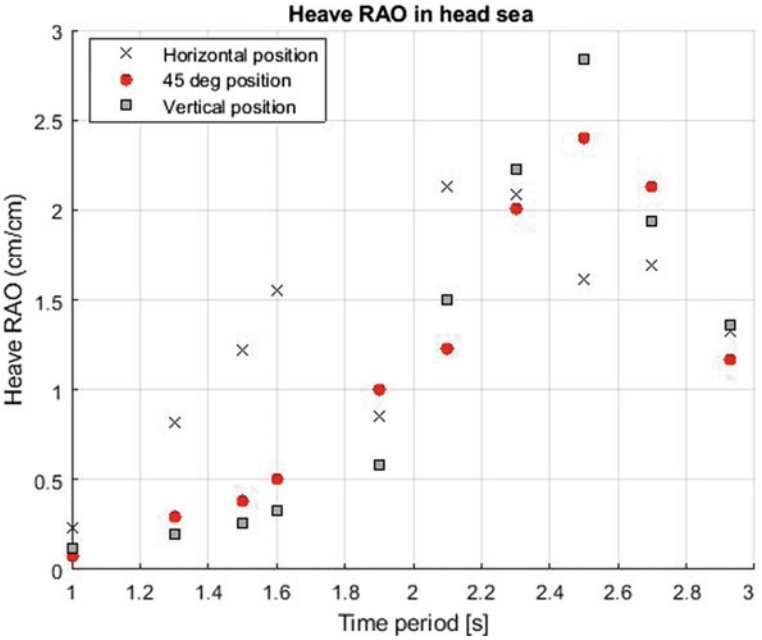

Fig. 6 Heave RAO in head sea for different jacket positions

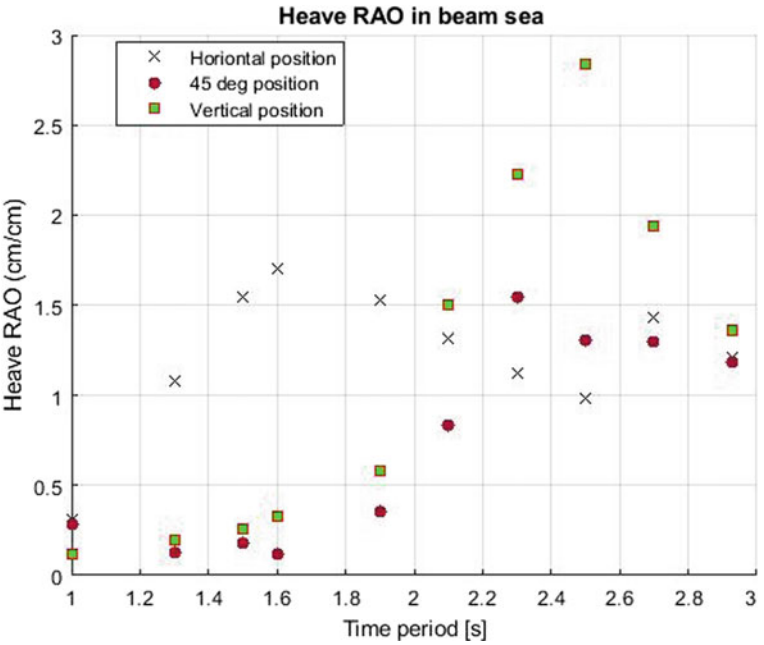

Fig. 7 Heave RAO in beam sea for different jacket positions

4 Conclusions

The heave, pitch and roll response of heavy jacket model in various stages of upending during regular waves are analyzed experimentally. From the experimental results, it is clear that both pitch and roll motions are coupled with heave motion. This leads to high pitch and roll motion amplitudes for wave periods corresponding to heave natural periods for the jacket positions. The horizontal position of jacket is expected to be more stable than other jacket position due to high restoring force available at this configuration. However, the natural periods of its degrees of freedom lie within the wave periods, and this position is more susceptible for resonance effects. Hence, suitable measures need to be adopted during this stage. The vertical position of jacket exhibits more displacement in roll, pitch and heave compared to other jacket positions, and this needs to be studied in detail.

Acknowledgements The authors would like to acknowledge the support of Department of Science and Technology (DST), Government of India and German Academic Exchange Service (DAAD).

References

1. Bhattacharyya SK, Idichandy VG (1985) On experimental investigation of load-out, launching and upending of offshore steel jackets. Appl Ocean Res 7:24–34
2. Downie MJ, Graham JMR, Hall C, Incecik A, Nygaard I (2000) An experimental investigation of motion control devices for truss spars. Marine Struct (13):75–90
3. Hu Z, Li X, Li J, Yang JM (2016) Comparative study on a jacket launching operation in South China Sea. Ocean Eng (111):335–347
4. Nallayarasu S, Kumar NS (2017) Experimental and numerical investigation on hydrodynamic response of buoy form spar under regular waves. Ships Offshore Struct 12:19–31
5. Welzel M, Kreklow T, Schlurmann T, Hildebrandt A (2017) Excitation and dynamic responses of jacket structures in regular waves for offshore installation. Coast Eng Proc 1(35)

Performance of the Single Round Nozzle of the Marine Outfall System for Buoyant Fluid at Stable Water in the Unstratified Water Depth

D. R. Danish and K. Murali

Abstract The marine outfall system is used for disposal of effluent into the ocean. There is a strong belief that the ocean is an ultimate sink for the disposal of wastewater making sure that the disposed of effluent is within the standard disposal limits. For the large-quantity effluent discharge, multiport diffuser type marine outfall system is effective. The multiport diffuser is a series of main outfall pipe connected to the diffuser system with multiple nozzle ports connected in parallel to each other with an optimum spacing. In this study, the performance of the single round nozzle for buoyant fluids at a stable water condition in the unstratified water depth is carried out. The same is carried out for the multiple port round nozzle by varying the spacing distance between the consecutive ports. The numerical simulation for the single round nozzle for varying port outlet velocities is carried out achieving acceptable densimetric Froude number enhancing the performance of the round nozzle's diffusion rate for the positively buoyant, neutrally buoyant and negatively buoyant effluent, and its respective plume characteristics are studied.

Keywords Marine outfall system · Effluent · Multiport diffuser · Round nozzle · Buoyant fluid · Densimetric Froude number · Diffusion rate

1 Introduction

The one commodity which is important for life and all its processes is water, where 71% of our earth is filled with it, out of which 97% is the ocean. More than half the world population and most of the manufacturing, production, operation and logistics are concentrated in and around the coast. There is always been a strong belief among top experts, engineers and scientists that the ocean is the ultimate sink for all

D. R. Danish (✉) · K. Murali
Department of Ocean Engineering, Indian Institute of Technology Madras, Chennai 600036, India
e-mail: civildanish@gmail.com

K. Murali
e-mail: murali@iitm.ac.in

V. Sundar et al. (eds.), *Proceedings of the Fifth International Conference in Ocean Engineering (ICOE2019)*, Lecture Notes in Civil Engineering 106,
https://doi.org/10.1007/978-981-15-8506-7_13

disposal of wastewater which require maximum protection, in agreement with that the disposed of wastewater (i.e., effluent) is under the standard disposal limits in terms of concentration, temperature, density, etc. [11]. The production, manufacturing and operation involve millions and millions of liters of water which are drawn directly from the ocean through the infiltration well or pipes through pumps. The collected seawater is converted to potable water by removing salt through different desalination process for drinking and other industrial processes as per the requirement. The used water during those processes will become effluent either due to increase in concentration of salt or temperature. These wastewaters are flushed back into the ocean either after treatment and sometimes untreated. The marine outfall system with diffusers is used to flush the wastewater back to the ocean which can either be a point source outfall system or the multiport diffuser type outfall system. For the very large-quantity wastewater disposal, it is better to have multiport diffuser type outfall system for quick diffusion rate (i.e., the rate of diffusion through a solution).

The multiport diffuser type outfall system is a collective of wastewater (i.e., domestic wastewater and industrial wastewater) collected in a collecting tank connected to the wastewater pre-treatment plant with a series of pipelines to the outfall point which will be away from the shore about few hundred meters to few kilometers into the ocean at a water depth of 10–100 m [5].

The design of the marine outfall diffuser type system to enhance the mixing phenomenon of the disposed of wastewater in the ambient water environment such as the distance of the outfall point from the shore, wind, wave, tide and underwater current characteristics for different seasons at the outfall point location, bathymetry of the location, diameter of the main outfall pipe, type of diffuser nozzle port (i.e., round, duckbill, etc.), nozzle port diameter, orientation of the nozzle port (i.e., vertical, horizontal, inclined 60°, inclined 45° and inclined 30°), velocity of the main outfall pipe, diffuser port outlet velocity, spacing between each port, wastewater jet and plume characteristics [8].

The jet and plume characteristics vary for the different buoyant wastewater (i.e., positively buoyant and negatively buoyant) depending on the concentration, temperature and density of the disposed of wastewater with the respective ambient environment water condition. The turbulent jet and plumes are produced by momentum and buoyant fluxes [7]. The spacing between each consecutive port is also a very important factor to determine the point of convergence of the wastewater plume; the convergence plume varies for the different buoyant wastewater. By placing the ports too closely will increase the concentration of the wastewater in that one particular region making it difficult to mix with the ambient, and placing it too far will not help in the quick mixing of the wastewater. So placing the consecutive ports at an optimum distance according to the different buoyant wastewater plays a very important role in enhancing the mixing phenomenon [5].

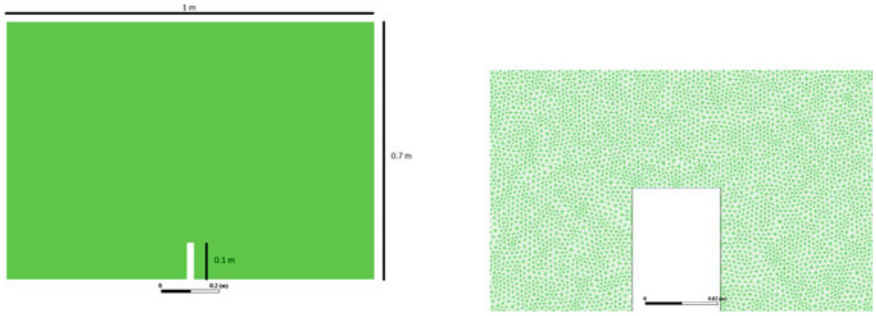

Fig. 1 **i** Domain dimensions. **ii** Mesh structure

2 Domain and Model

In this chapter, we are simulating round buoyant jet and plume for different density effluent 1010, 1005, 990, 995 and 1000 kg/m^3 with ambient temperature of 293 K (K) and the effluent temperature of 303 K and variation of port exit velocity at 0.5, 1, 1.5 and 2 m/s using Ansys Fluent k-ε realizable model with scalable wall function for multiphase energy model.

The pressure-based solver was used with transient time with absolute velocity formulation in 2D planar space. In the multiphase, volume of fluid models both volume fraction parameter and body for formulation is solved implicitly. The governing equations are solved using the pressure-implicit with splitting of operators (PISOs) method. The domain is geometrically scaled down at 1:10 ratio, and the corresponding velocities are scaled using Froude scaling. The domain is 1 m long and 0.7 m height with nozzle diameter of 0.02 m, and height of the nozzle is 0.1 m as shown in Fig. 1i. The mesh is unstructured and fine with 670,000 node points as shown in Fig. 1ii.

3 Governing Equations and Boundary Conditions

The mass conservation or continuity equation from the Ansys Fluent

$$\frac{\partial \rho}{\partial t} + \nabla \cdot (\rho \vec{v}) = S_m \tag{1}$$

$$\frac{\partial \rho}{\partial t} + \frac{\partial}{\partial x}(\rho v_x) + \frac{\partial}{\partial r}(\rho v_r) + \frac{\rho v_r}{r} = S_m \tag{2}$$

where,

ρ is the density.

x is the axial coordinate.
r is the radial coordinate.
V_x is the axial velocity.
V_r is the radial velocity.

The momentum conservation equation is given

$$\frac{\partial}{\partial t}(\rho v) + \nabla \cdot (\rho \vec{v}\vec{v}) = -\nabla p + \nabla \cdot (\bar{\bar{\mathrm{T}}}) + \rho \vec{g} + \vec{F} \tag{3}$$

$$\bar{\bar{\mathrm{T}}} = \mu[(\nabla \vec{v} + \nabla \vec{v}^T) - \frac{2}{3}\nabla \cdot \vec{v} I] \tag{4}$$

where,

P is the static pressure.
T is the stress tensor.
F is the external body force.
ρg is the gravitational force.
μ is the molecular viscosity.
I is the unit tensor.

The multiphase flow transport equation is given as

$$\frac{\partial \rho_m \varphi^k}{\partial t} + \nabla \cdot (\rho_m \vec{v}_m \varphi^k - \Gamma_m^k \nabla \varphi^k) = S^{km}, \quad k = 1, \ldots, N \tag{5}$$

where

ρ_{m} mixture density.
V_{m} is the mixture velocity.
K is the mixture diffusivity.
Γ_m^k is the dilution coefficients.
S^{km} is the source term.
φ^k is the mixture of phases.

The energy equation is given as

$$\frac{\partial}{\partial t}(\rho E) + \nabla \cdot (\vec{v}(\rho E + p)) = \nabla \cdot (k_{eff} \nabla T - \sum_j h_j \vec{J}_j + (\bar{\bar{\mathrm{T}}}_{eff} \cdot \vec{v})) + S_h \tag{6}$$

$$E = h - \frac{p}{\rho} + \frac{v^2}{2} \tag{7}$$

$$h = \sum_j Y_j h_j + \frac{p}{\rho} \tag{8}$$

$$h_j = \int_{T_{ref}}^{T} c_p \cdot j \mathrm{d}T \tag{9}$$

where,

k_{eff} is the effective conductivity.
J_j is the diffusion flux of species j.
h is the enthalphy.
E is the volumetric heat source.
Y_j is the mass fraction of species j.

4 Results and Discussion

The nearfield mixing is predicted by understanding the dynamics of jets, plume and buoyant jets. Discharge from outfall will have both momentum and buoyancy [3]. The Richardson number [$R_o = (QB^{1/2})/M^{5/4}$] is between 0.02 and 0.08, where Q is the discharge, B is the buoyancy flux, M is the momentum flux, and it is given by $Q = (\pi/4)Di^2V$, momentum flux, $M = VQ$, buoyancy flux, $B = g'Q$ where V is the port exit velocity, D_i is the internal diameter of pipe, and g' is the altered acceleration due to gravity. The Reynolds number is within 9900–40,400 and the Froude number from 1 to 64. According to Wright [12], the length scale lq and lm are the characteristic length for the volume flux and the characteristic length for the momentum flux respectively, in this study lq is about 0.177 m and lm is between 0.2 and 0.9 m as shown in Figs. 2 and 3.

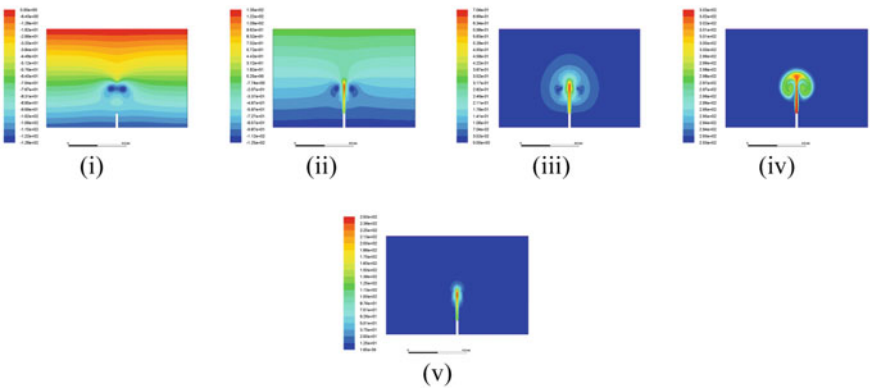

Fig. 2 Contour plot **i** static pressure, **ii** dynamic pressure, **iii** velocity magnitude, **iv** total temperature distribution, **v** total pressure distribution for density, $\rho = 1010$ kg/m^3, velocity, $V = 0.5$ m/s at $T = 2$ s

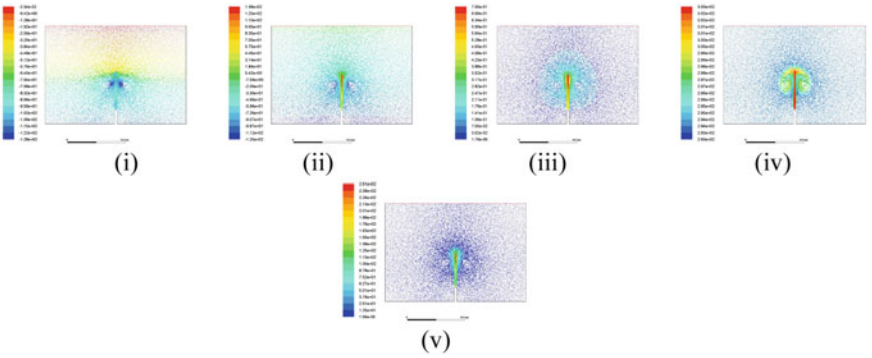

Fig. 3 Vector plot **i** static pressure, **ii** dynamic pressure, **iii** velocity magnitude, **iv** total temperature distribution, **v** total pressure distribution for density, $\rho = 1010$ kg/m^3, velocity, $V = 0.5$ m/s at $T = 2$ s

The velocity magnitude and the total temperature decrease from its initial exit velocity and initial temperature. As the effluent mix with the ambient fluid the dynamic pressure rises because of the side boundary (Table 1) and the flow velocity proportionately increases which enhance the mixing of the temperature as eddies are formed as noticed in the vector velocity (Fig. 3iii) and vector temperature plot (Fig. 3iv).

From Figs. 4 and 5, it shows at v = 1 m/s, and the height of the jet at $Y = 2$ s is different compared to Figs. 2 and 3 as it reaches $Y/D = 27.5$ (where D—port internal diameter), and the eddies formed are big as the velocity increased with the effect of the side walls which enhances the mixing of the effluent.

The depth varying velocity is normalized with the initial velocity (V_y/V_i) as the depth Y is normalized by the port internal diameter D (i.e., 0.02 m). As shown in Fig. 6, the velocity varies across depth as its concentration and temperature diffuse. For the higher density (i.e., 1010 and 1005 kg/m^3), the velocity travels across the depth as jet and plunges into plumes at a distance of 10D–12D, while at the lower densities (i.e., 990 and 995 kg/m^3), the jet diffuses sooner at a distance of about 5D–6D.

Likewise at lower velocity (i.e., $v = 0.5$ m/s), the plume plunges sooner as there is not enough momentum flux where it is influenced by buoyancy flux as the distance is about 3D–5D Fig. 7a. The overall comparison of the normalized velocity to the non-dimensional depth parameter is shown in Fig. 8.

Table 1 Boundary condition

Top	Pressure outlet with zero gauge pressure
Bottom	Stationary wall with no slip shear condition
Side	Stationary wall with no slip shear condition
Pipe side	Stationary wall with no slip shear condition
Nozzle	Pressure inlet velocity

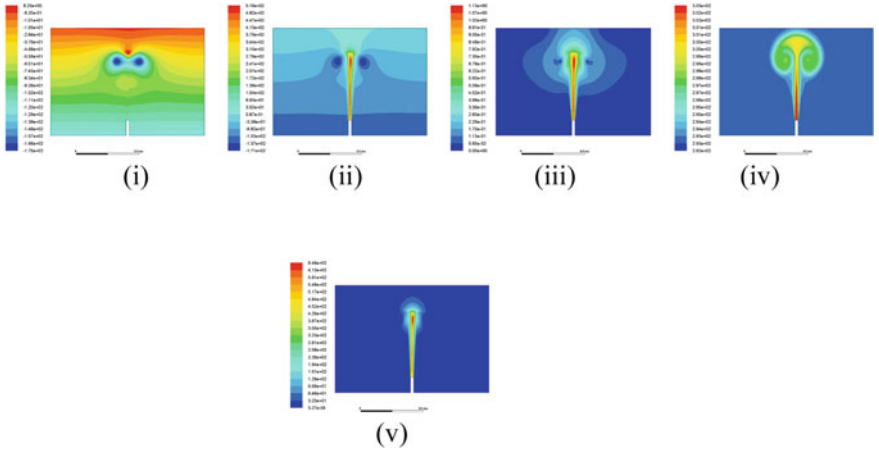

Fig. 4 Contour plot **i** static pressure, **ii** dynamic pressure, **iii** velocity magnitude, **iv** total temperature distribution, **e** total pressure distribution for density, $\rho = 1010$ kg/m^3, velocity, $V = 1$ m/s at $T = 2$ s

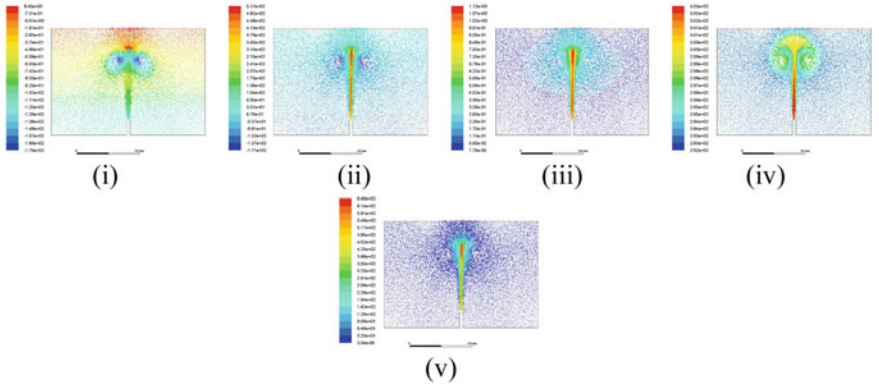

Fig. 5 Vector plot **i** static pressure, **ii** dynamic pressure, **iii** velocity magnitude, **iv** total temperature distribution, **v** total pressure distribution for density, $\rho = 1010$ kg/m^3, velocity, $V = 1$ m/s at $T = 2$ s

Figures 9, 10 and 11 show that the temperature mixes at a distance more than 10D for varying density and varying velocities, and for higher velocities, it goes till 15D because of the side wall effect, and the diffusion of temperature enhances as the velocity increases because of the formation of eddies (Fig. 12).

The velocity, total temperature and total temperature distribution along the depth Y and along X at different depth are shown in the figure for density, $\rho = 1010$ kg/m^3, velocity, $V = 0.5$ m/s at $T = 2$ s. The width of the plume is noticed from figure (iiic) which is about 0.3 m (15D) for the temperature, while from figure (ia), the velocity width is noticed which is about 0.2 m (10D).

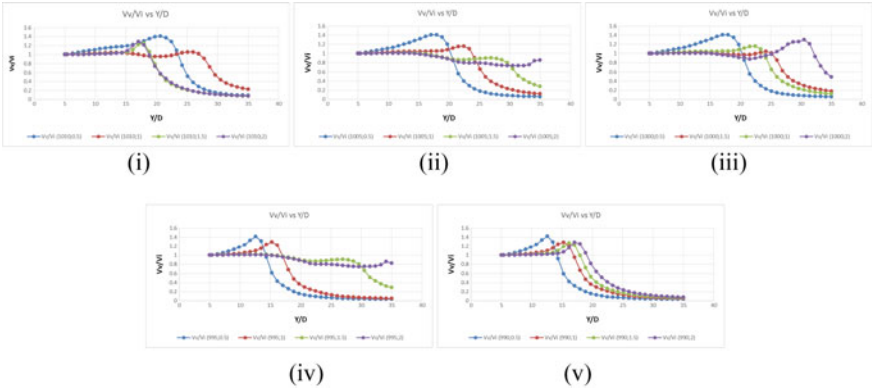

Fig. 6 Comparison of normalized velocity to the nondimensionless depth parameter (Y/D) at $T = 2$ s **i** $\rho = 1010$ kg/m^3 for various velocity, **ii** $\rho = 1005$ kg/m^3 for various velocity, **iii** $\rho = 1000$ kg/m^3 for various velocity, **iv** $\rho = 995$ kg/m^3 for various velocity, **v** $\rho = 990$ kg/m^3 for various velocity

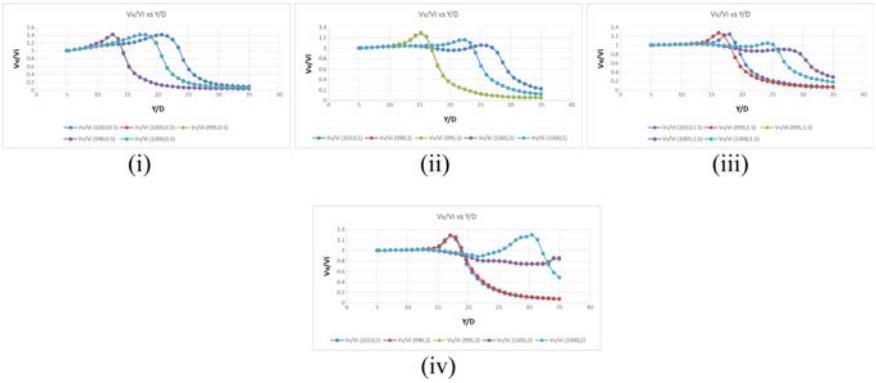

Fig. 7 Comparison of normalized velocity to the nondimensionless depth parameter (Y/D) at $T = 2$ s **i** $V = 0.5$ m/s for varying densities, **ii** $V = 1$ m/s for varying densities, **iii** $V = 1.5$ m/s for varying densities and **iv** $V = 2$ m/s for varying densities

Fig. 13iiic shows the maximum temperature width distribution is noticed to be 0.4 m (20D), and the maximum velocity width is about 0.4 m (20D) from Fig. 13iiic. The center line semiempirical equation for minimum dilution [3] for Y/DFr $\gg 1$ is given as $S_m/Fr = 0.107\ (Y/DFr)^{5/3}$ and for Y/DFr > 0.5 is given by [1] as $S_m/Fr = 0.54(0.66 + 0.38(Y/DFr))^{5/3}$. This numerical study which very well matches with Fischer et al. [3] and Cederwall [1] is as shown in Fig. 14, and the nearfield dilution for the round plume source is three times the surface centerline value according to Tian et al. [9, 10] which is given by $S_n/Fr = 0.32(Y/DFr)^{5/3}$ which also matches the trend as shown in Fig. 15.

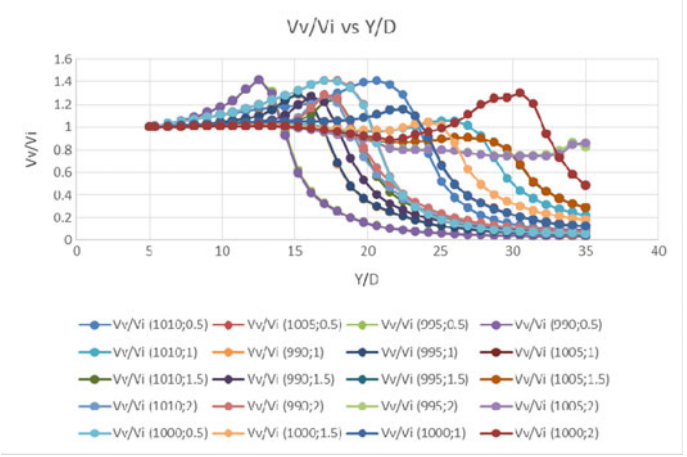

Fig. 8 Overall comparison of the normalized velocity to the non-dimensionless depth parameter (*Y*/*D*)

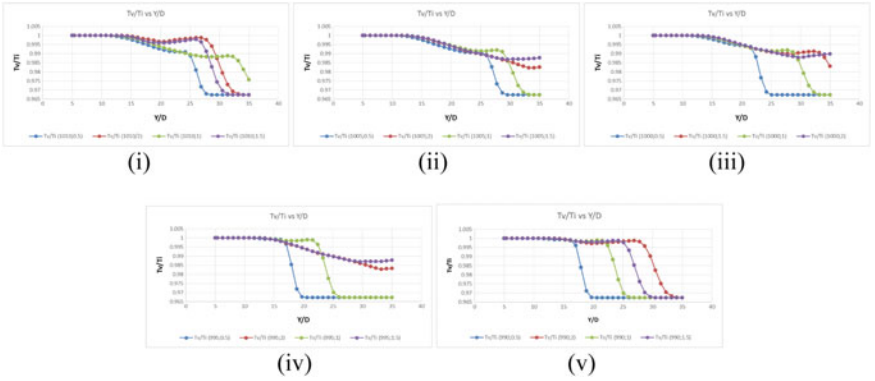

Fig. 9 Comparison of normalized temperature to the nondimensionless depth parameter at $T = 2$ s **i** $\rho = 1010$ kg/m^3 for various velocity, **ii** $\rho = 1005$ kg/m^3 for various velocity, **iii** $\rho = 1000$ kg/m^3 for various velocity, **iv** $\rho = 995$ kg/m^3 for various velocity, **v** $\rho = 990$ kg/m^3 for various velocity

5 Conclusion

The depth varying velocity (Vv) distribution for the denser effluents (1010 and 1005 kg/m^3) is about 10D–12D and for the lighter effluents (990 and 995 kg/m^3) is about 5D–6D, and for the same with at velocity 0.5 m/s, it was about 0.3D. The depth varying temperature (Tv) at higher and lower densities and varying velocity is about 10D–15D, and for velocity 2 m/s, it reaches till 18D–20D. The maximum velocity width distribution along X axis for 0.5 m/s and 1 m/s is about 10D and 20D, respectively, and the maximum temperature width distribution at 0.5 m/s and 1 m/s

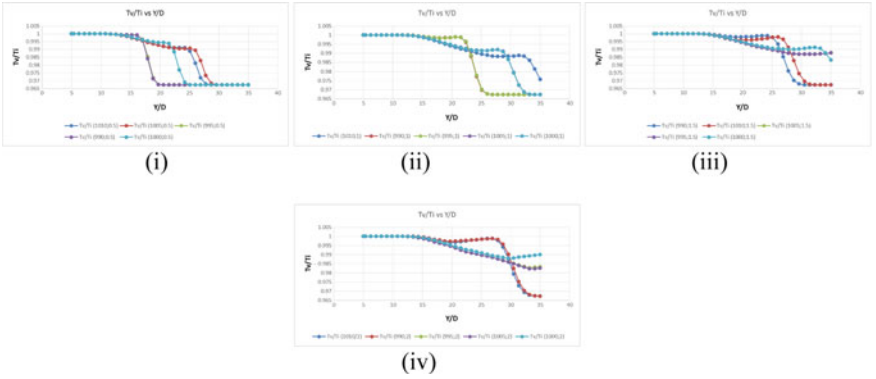

Fig. 10 Comparison of normalized temperature to the nondimensionless depth parameter (Y/D) at $T = 2$ s **i** $V = 0.5$ m/s for varying densities, **ii** $V = 1$ m/s for varying densities, **iii** $V = 1.5$ m/s for varying densities and **v** $V = 2$ m/s for varying densities

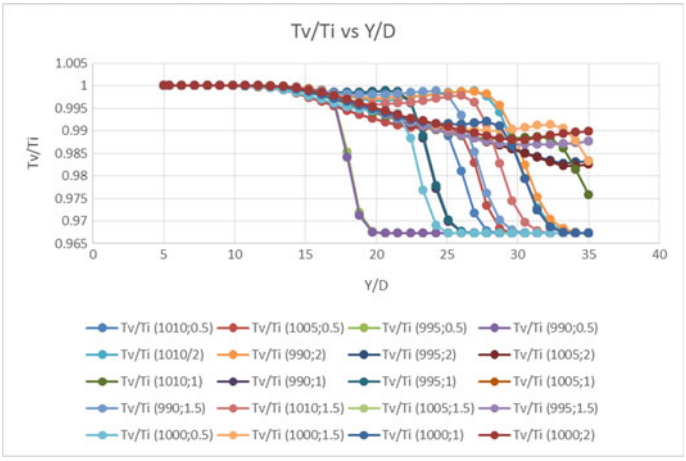

Fig. 11 Overall comparison of the normalized temperature to the non-dimensionless depth parameter (Y/D)

is about 15D and 20D, respectively. The jets formed initially diffuse into plumes for Y/DFr $\gg 1$ having required depth for it to transform from jet to plume where the ocean outfall discharges usually operate.

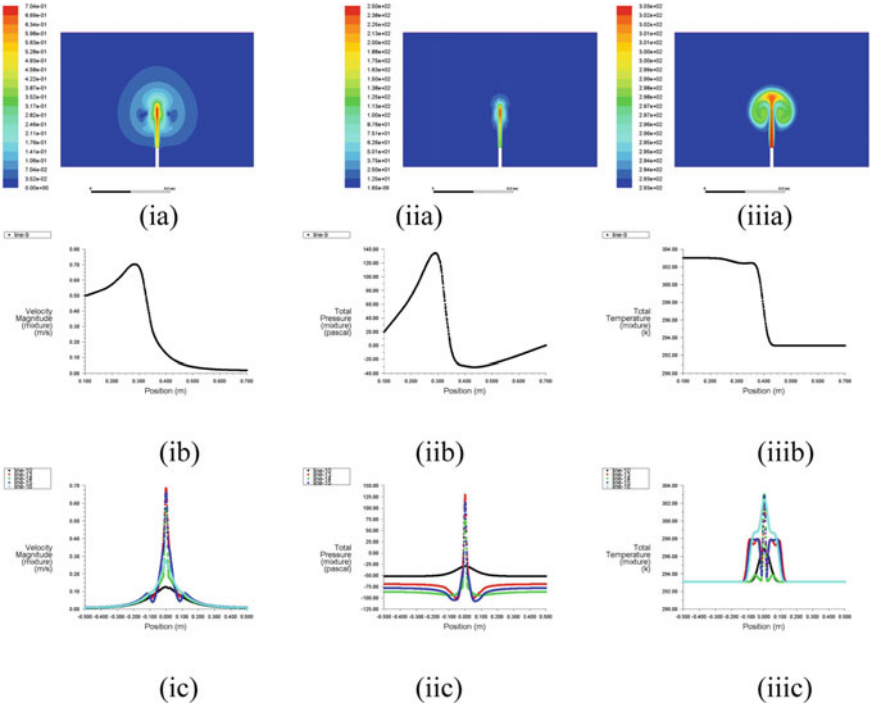

Fig. 12 **ia** Contour plot of velocity magnitude, **ib** contour plot of total pressure, **ic** contour plot of total temperature, **iia** velocity magnitude distribution along depth Y, **iib** total pressure along depth Y, **iic** total temperature along depth Y, **iiia** velocity magnitude distribution along X axis varying depth, **iiib** total pressure along X axis varying depth, **iiic** total temperature along depth X axis varying depth for density, $\rho = 1010$ kg/m^3, velocity, $V = 0.5$ m/s at $T = 2$ s

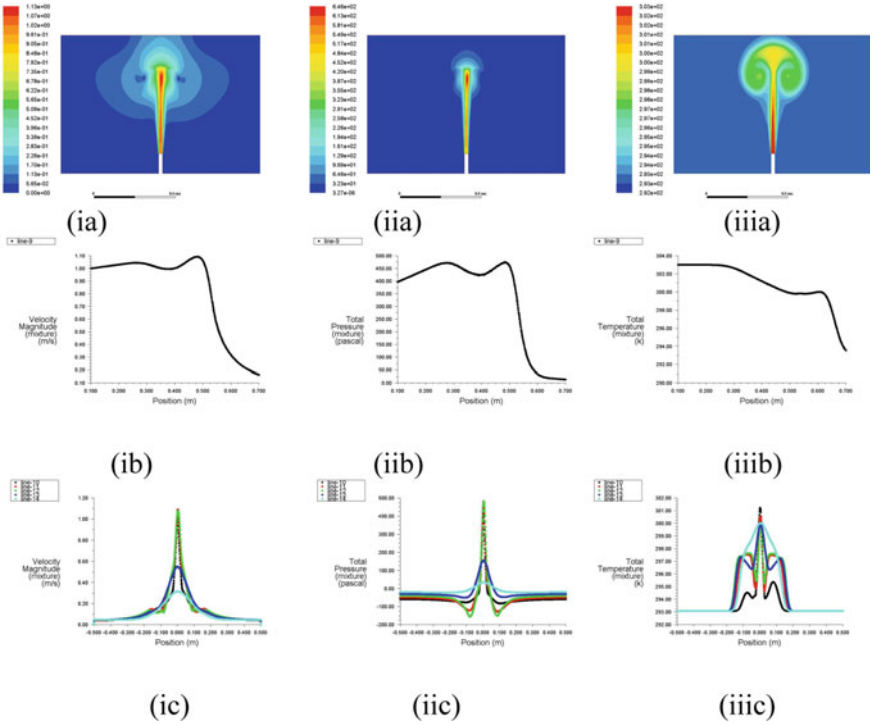

Fig. 13 **ia** Contour plot of velocity magnitude, **ib** contour plot of total pressure, **ic** contour plot of total temperature, **iia** velocity magnitude distribution along depth Y, **iib** total pressure along depth Y, **iic** total temperature along depth Y, **iiia** velocity magnitude distribution along X axis varying depth, **iiib** total pressure along X axis varying depth, **iiic** total temperature along depth X axis varying depth for density, $\rho = 1010$ kg/m^3, velocity, $V = 1$ m/s at $T = 2$ s

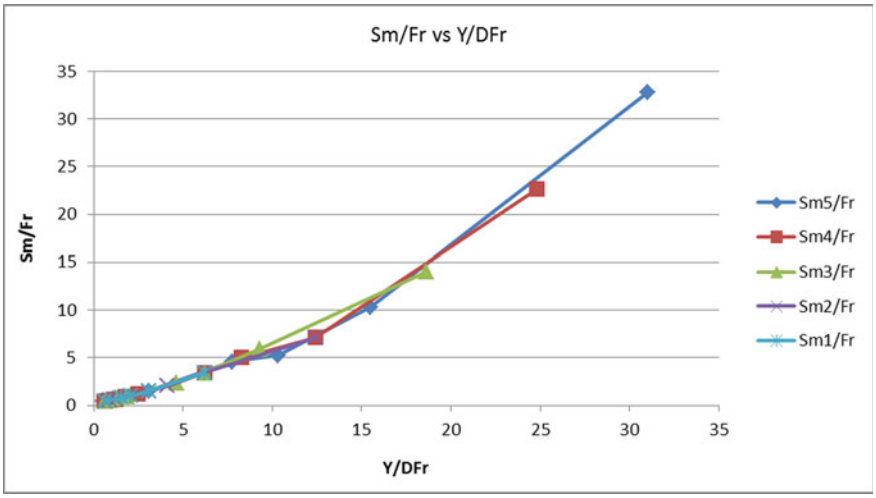

Fig. 14 Centerline dilution of the vertical buoyant jet into unstratified steady water

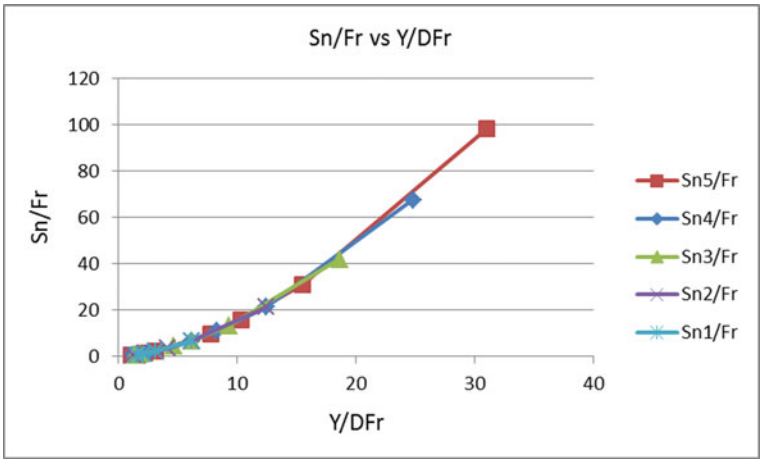

Fig. 15 Nearfield dilution of the round vertical buoyant jet into unstratified steady water

References

1. Cederwall K (1968) Hydraulics of marine waste water disposal, vol 74. Chalmers tekniska högskola
2. Cederwall K (1971) Buoyant slot jets into stagnant or flowing environments
3. Fischer HB, List JE, Koh CR, Imberger J, Brooks NH (1979) Mixing in inland and coastal waters. Academic Press
4. Fragkou A, Papanicolaou P (2018) Positively and negatively round turbulent buoyant jets into homogeneous calm ambient. In: Multidisciplinary digital publishing institute proceedings, vol

2, No 11, p 572
5. Grace RA (1978) Marine outfall systems: planning, design, and construction. Prentice-Hall
6. Koh RC, Brooks NH (1975) Fluid mechanics of waste-water disposal in the ocean. Annu Rev Fluid Mech 7(1):187–211
7. Lee JHW, Chu V (2012) Turbulent jets and plumes: a Lagrangian approach. Springer Science & Business Media
8. Roberts PJ, Salas HJ, Reiff FM, Libhaber M, Labbe A, Thomson JC (2010) Marine wastewater outfalls and treatment systems. IWA publishing
9. Tian X, Roberts PJ, Daviero GJ (2004) Marine wastewater discharges from multiport diffusers. II: unstratified flowing water. J Hydraul Eng 130(12):1147–1155
10. Tian X, Roberts PJ, Daviero GJ (2004) Marine wastewater discharges from multiport diffusers. II: unstratified flowing water. J Hydraul Eng 130(12):1137–1146
11. Wood IR, Bell RG, Wilkinson DL (1993) Ocean disposal of wastewater
12. Wright SJ (1984) Buoyant jets in density-stratified crossflow. J Hydraul Eng 110(5):643–656

Embedment Length of Steel Liner in Different Types of Soil

R. Sundaravadivelu, S. Sakthivel, S. Maheswari, S. M. Madhumathy, and S. Sherlin Prem Nishold

Abstract Steel liners are used in the construction of bored cast in situ RCC piles especially in water borne transport infrastructure. Embedment length of the liner is the length between dredge level/bed levels to the termination level of the liner. Sufficient embedment length for steel liner ensures the quality of the pile. The minimum embedment depth of liner is calculated as per IS 2911 using the same procedure as given for piles. A parametric study is carried out to develop design charts for embedment length of liner for different water depths in sand, clay and rock and the details are given in this paper. The comparison between twice the fixity depth and embedment depth is also given.

Keywords Steel liner · Embedment length · Soil type · Pile · Water depth

1 Introduction

Steel liners play an important role in construction of cast in situ piles especially in marine conditions. Temporary steel liners are used to stabilize the sides of the borehole during construction. In port and harbour structures liners become permanent part of foundation, which requires minimum load carrying capacity to withstand the construction loads. Liner is used to maintain the clear cover between the main reinforcement and concrete surface during the stages of construction. It is used for

R. Sundaravadivelu (✉) · S. Sakthivel · S. Maheswari · S. M. Madhumathy · S. Sherlin Prem Nishold
Department of Ocean Engineering, Indian Institute of Technology Madras, Chennai 600036, India
e-mail: rsun@iitm.ac.in

S. Maheswari
e-mail: maheswari.srinivasagan@gmail.com

S. M. Madhumathy
e-mail: madhumathysm13@gmail.com

S. Sherlin Prem Nishold
e-mail: sherlinprem@gmail.com

V. Sundar et al. (eds.), *Proceedings of the Fifth International Conference in Ocean Engineering (ICOE2019)*, Lecture Notes in Civil Engineering 106,
https://doi.org/10.1007/978-981-15-8506-7_14

bored cast in situ pile that extends through very soft soils, such as marsh deposits, to reach an underlying stratum which is more stable. In such cases, the liner is used to prevent the outward bulging of the fluid concrete into the surrounding soft soils. If a bulge forms at an elevation corresponding to an extremely soft stratum, there can be a risk of defects in the concrete due to a neck in the pile above the bulge, or deformation of the reinforcement cage.

In construction practice there is no standardized method to fix the minimum embedment length of liner. The objective of the study is to determine the minimum embedment length of liner by using the same procedure given for bored cast in situ piles as per IS2911 part 1/sec2 2010. The embedment length of liner depends on the stiffness of the steel liner and soil properties.

2 Literature Survey

IS2911 part 1/sec2 2010 [1], Tomlinson and Woodward [3] describes about the method to determine the embedment depth of RCC bore caste in situ pile. The properties of different soil types are referred from IS2911 part 1/sec2 2010 [1]. The relationship between the shear strength and unconfined compressive of soil, influence of soil properties in embedment of pile is enlightened in Baker [2], Terzaghi et al. [4]. US Department of Transportation, Federal Highway Administration 2008 illustrates about the selection liner property and importance of liner in pile driving technique.

3 Embedment Depth

The minimum length of the liner that is to be embedded in the soil strata from the Dredge/Bed level is embedment length. The embedment length of liner and pile need not necessarily be the same. The schematic representation of embedment depth is shown in Fig. 1.

In cohesion less soil, penetration resistance or$N$ values are used to determine the modulus of subgrade reaction of soil sample, which is helpful to determine the embedment depth of steel liner in sandy soil.

In clayey soil and rocky strata the embedment depth of liners is based on the undrained shear strength of the soil, moment of inertia of the liner and Young's modulus of the liner material. The unconfined compressive strength is assumed as two times the undrained shear strength.

Fig. 1 Embedment depth

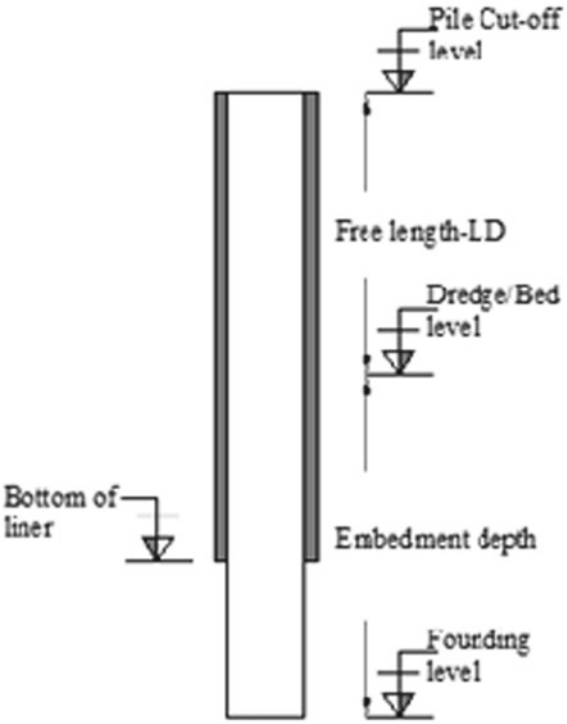

4 Method to Calculate Embedment Depth

The lateral load resistance of vertical pile mainly depends on the interaction between the structural element and soil stiffness. To determine the embedment depth, the behaviour of pile is determined by the stiffness factor for the respective soil type. The stiffness factor T and R depends on the material property, soil type and soil property. T and R are used to ascertain the embedment length of the liners. The procedure to calculate the stiffness factor is presented in IS: 2911 part1/Sec2:2010.

Stiffness factor in Sand and normally loaded clay (Eq. 1),

$$T = \sqrt[5]{\frac{EI}{\eta_h}} \mathrm{T} = \sqrt[5]{\frac{\mathrm{EI}}{\eta_\mathrm{h}}} \tag{1}$$

where E is the Young's modulus of liner material is MN/m^2. I is the moment of inertia of liner cross section in m^4. η_h is modulus of subgrade reaction for granular soil in MN/m^3.

Stiffness factor in preloaded clay and Rock (Eq. 2),

Table 1 Embedment depth

S. No.	Type of pile	Relation of embedded length with stiffness factor	
		Linearly increasing	Constant
1	Short (rigid) pile	$L \leq 2T$	$L \leq 2R$
2	Long (Elastic) pile	$L \geq 4T$	$L \geq 3.5R$

$$R = \sqrt[4]{\frac{EI}{KB}} \tag{2}$$

where E is the Young's modulus of liner material is MN/m^2. I is the moment of inertia of liner cross section in m^4. B is diameter of liner shaft. K shall be calculated by using Eq. 3

$$K = \frac{k_1}{1.5} \times \frac{0.3}{B} \tag{3}$$

K_1 is modulus of subgrade reaction for cohesive soil in MN/m^3. The soil modulus K_1 has been related to Terzaghi's concept of a modulus of horizontal subgrade reaction.

Based on the above stiffness factor R and T, the criteria for behaviour as a short rigid pile or long elastic pile are related with embedment depth. Similarly, the embedment depth of steel liner is defined as given in Table 1.

5 Determination of Depth of Fixity

Depth of fixity is helpful to determine the deflection and moment due to relatively small lateral loads acting on the pile top. The boundary conditions are assumed as the pile is fixed at an arbitrary depth below ground level and at the top it is free head or fixed head pile which is free to translate. At the point of fixity deflection is assumed as zero and moment is maximum. As per IS: 2911:part1/sec2:2010 the fixity depth of pile is determined by using the graph plot between the ration of unsupported length to stiffness factor and depth of fixity to stiffness factor (Fig. 2).

Selection of Liner and Soil Parameters

Steel liner is mostly preferred for construction of bore cast in situ piles in the port and harbour structures. The following liner properties are considered to develop the design charts (Table 2).

Selection of suitable soil parameter is important phenomena in embedment depth determination. The critical variables are unconfined compressive strength, shear strength and modulus of subgrade reaction for clay, sand and rock. The average$N$ values and other parameters for different type of soils are chosen from IS

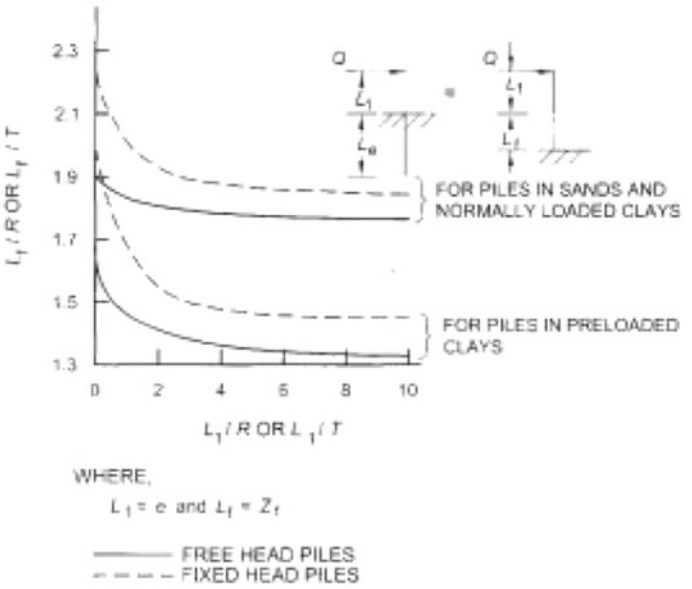

Fig. 2 Fixity depth

Table 2 Property of liner

S. No.	Unsupported/Free length (L_1) (m)	Liner property		
		Diameter (m)	Thickness (mm)	Young's modulus (MN/m^2)
1	6	0.8	6	210,000
2	8			
3	10			
4	8	1	6	
5	10			
6	12			
7	12	1.2	6	
8	14			
9	16			
10	14	1.4	6	
11	16			
12	18			

Table 3 Property of sandy soil (for submerged condition)

Description	Soil type sand				
	Very Loose sand	Loose sand	Medium dense sand	Dense sand	Very dense
SPT (N Value)	4	10	30	50	70
Modulus of subgrade reaction k_1 (MN/m^2)	0.2	1.4	4.25	7.14	10

Table 4 Property of clay soil

Description	Soil type clay				
	Very soft clay	Soft clay	Firm clay	Stiff clay	Very stiff clay
SPT (N Value)	2	7	12	25	40
Shear strength (kN/m^2)	10	35	60	125	200
Unconfined compressive strength (kN/m^2)	20	70	120	250	400
Modulus of subgrade reaction k_1 (MN/m^2)	3.6	12.6	21.6	45	72

Table 5 Property of rocky strata

Description	Soil type clay				
	Grade F	Grade E	Grade D	Grade C	Grade B
SPT (N Value)	80	120	200	300	600
Shear strength (kN/m^2)	600	900	2000	4000	10,000
Unconfined compressive strength (kN/m^2)	1200	1800	4000	8000	20,000
Modulus of subgrade Reaction k_1 (MN/m^2)	216	324	720	1440	3600

2911:Part1/Sec2:2010. The following soil parameters are considered to determine the Embedment length of steel liner (Tables 3, 4 and 5).Query

6 Results and Discussion

The embedment depth of steel liner for different soil type and fixity depth of liner are is determined as per IS2911 part 1/sec2 2010. The fixity depth is a function of unsupported length of steel liner. The comparison is made between the ration of embedment depth to diameter and twice the fixity depth to the diameter as a function

of normalized unsupported length with diameter for different steel liner property, unsupported length and soil type.

Twice the fixity depth can be considered as minimum required embedment depth, since the long elastic pile criteria given in Table 1 is conservative. The twice the fixity depth is a function of not only stiffness factor but also the unsupported length ($L1$). The design charts are developed between the ratio of embedment depth to diameter and soil penetration (N) values.

Figures 3, 4, 5, 6, 7, 8, 9, 10, 11, 12, 13 and 14 clearly shows that twice the fixity depth is less than the embedment depth of liner considering the long elastic behaviour. The embedment depth versus$N$ values represents that the depth of embedment decreases with increase in$N$ values. On increase in the diameter and liner thickness, the embedment depth increases for a specific$N$ value. The change of L_1/D ratio does not influence the fixity depth significantly.

The embedment depth of steel liner is calculated similar to embedment depth of RCC piles, considering only the property of liner and soil as per IS2911. The results indicate that the embedment depth increases from 10 to 20D with reduction in$N$ values from 40 to 2 for clay soil, 11D–23D for the$N$ values of 70–4 in sandy soil and in rock strata 3.6D–7D for the$N$ values of 600–80. The above procedure does not consider the unsupported length of steel liner.

The unsupported length of steel liner has an influence of fixity depth. The comparison is made between embedment depth and twice the fixity depth. The results indicate that twice the fixity depth for clay and sand decreases as$N$ value increases. The change of soil properties from soft clay to stiff clay or loose sand to dense sand or weak rock to hard rock influence the fixity depth significantly.

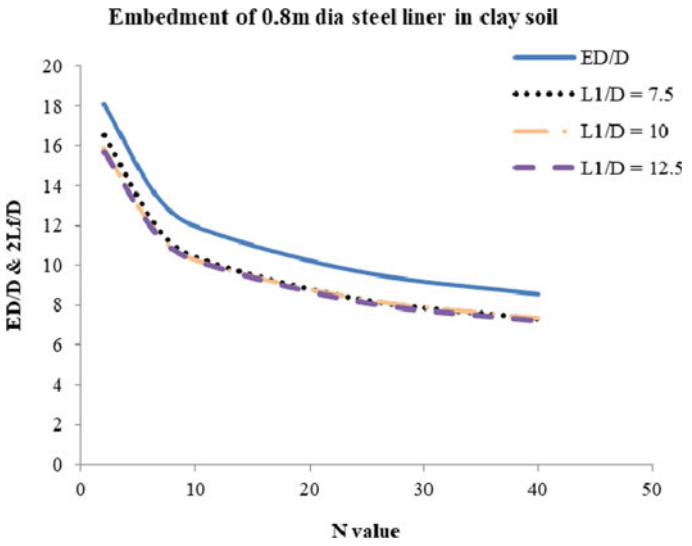

Fig. 3 Embedment depth of 0.8 m diameter steel liner in clay soil

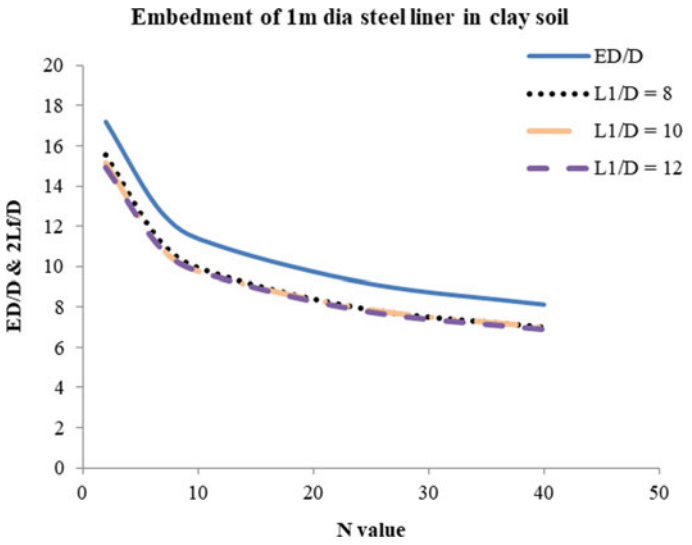

Fig. 4 Embedment depth of 1.0 m diameter steel liner in clay soil

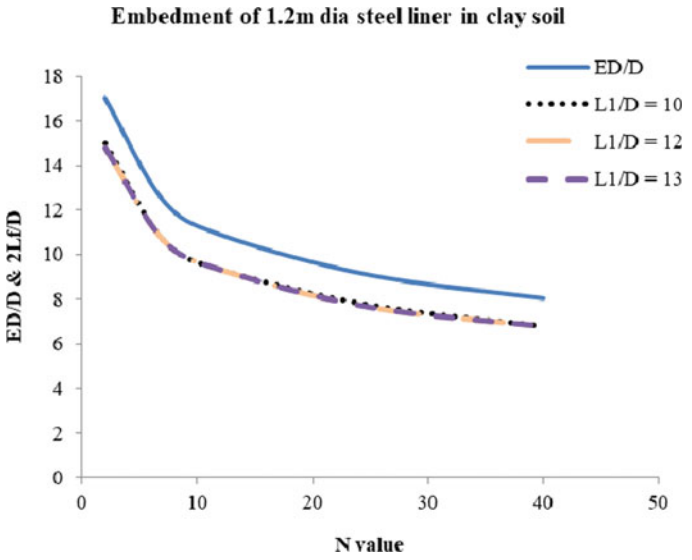

Fig. 5 Embedment depth of 1.2 m diameter steel liner in clay soil

7 Conclusion

The embedment depth of steel liner is calculated similar to embedment depth of RCC piles, considering only the property of liner and soil as per IS2911. The results

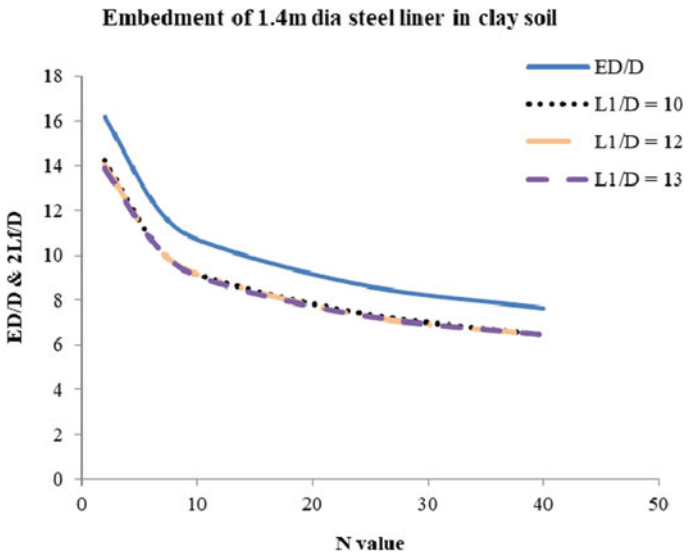

Fig. 6 Embedment depth of 1.4 m diameter steel liner in clay soil

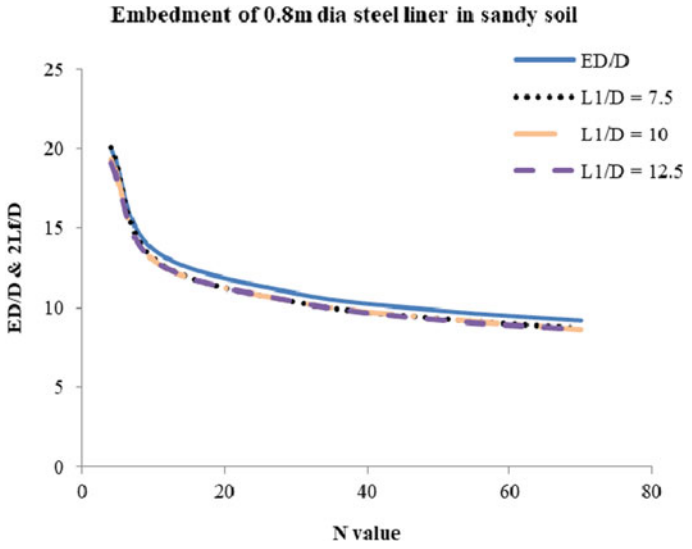

Fig. 7 Embedment depth of 0.8 m diameter steel liner in sandy soil

indicate that the embedment depth increases from 10 to 20D with reduction in*N* values from 40 to 2 for clay soil, 11D to 23D for the*N* values of 70 to 4 in sandy soil and in rock strata 3.6D–7D for the*N* values of 600–80. The above procedure does not consider the unsupported length of steel liner.

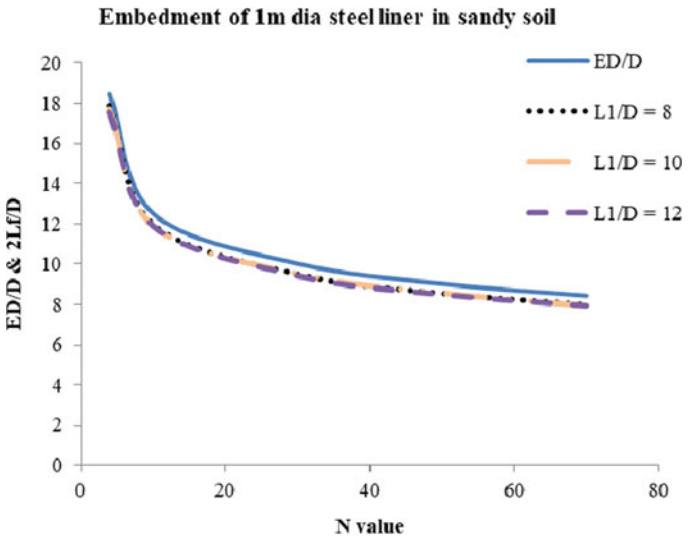

Fig. 8 Embedment depth of 1.0 m diameter steel liner in sandy soil

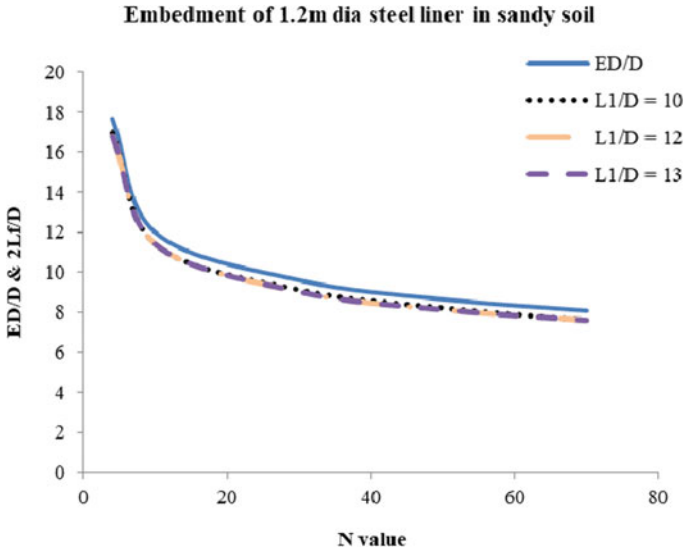

Fig. 9 Embedment depth of 1.2 m diameter steel liner in sandy soil

The unsupported length of steel liner has an influence of fixity depth. The comparison is made between embedment depth and twice the fixity depth. The results indicate that twice the fixity depth for clay and sand decreases as*N* value increases. The

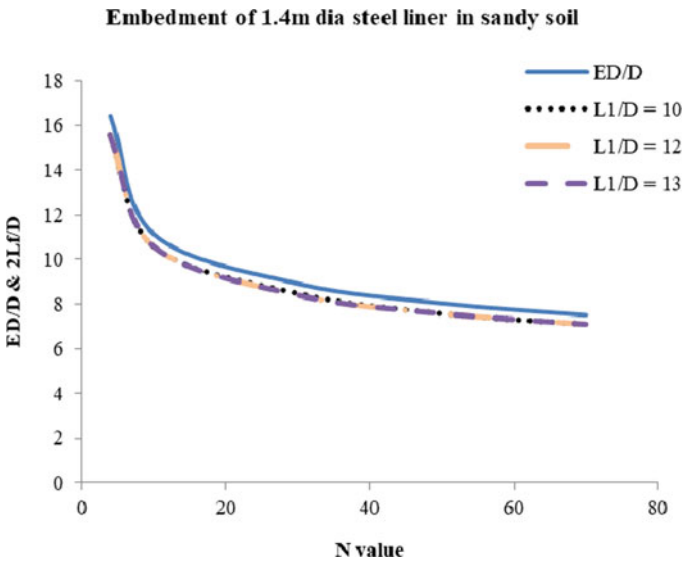

Fig. 10 Embedment depth of 1.4 m diameter steel liner in sandy soil

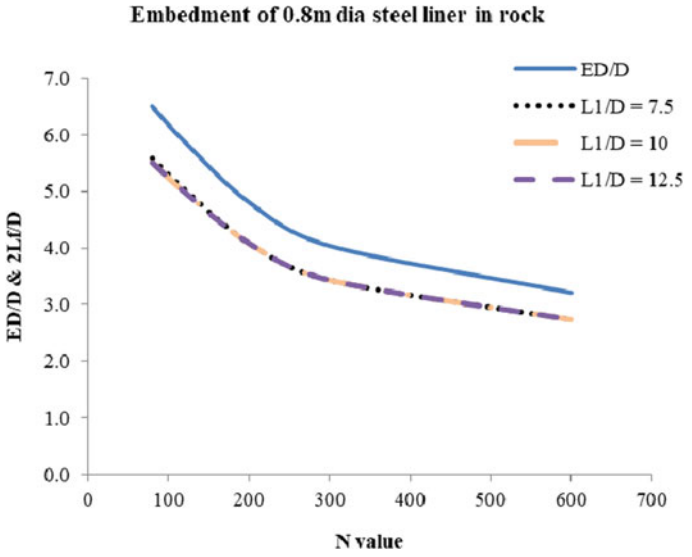

Fig. 11 Embedment depth of 0.8 m diameter steel liner in rock

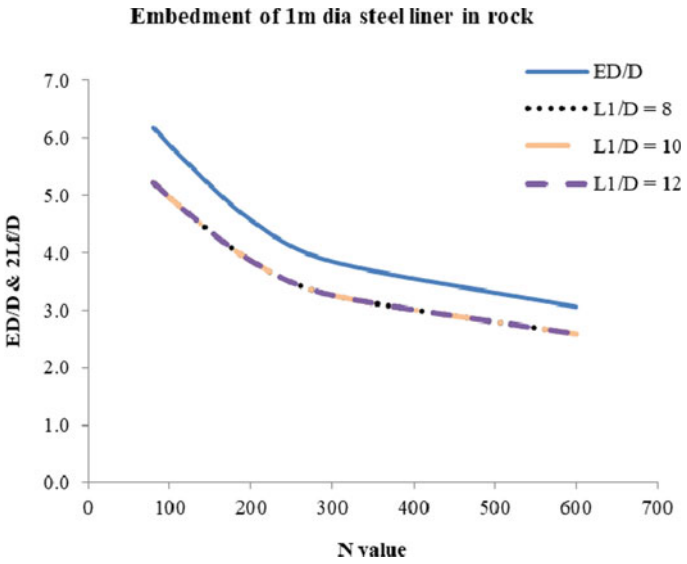

Fig. 12 Embedment depth of 1.0 m diameter steel liner in rock

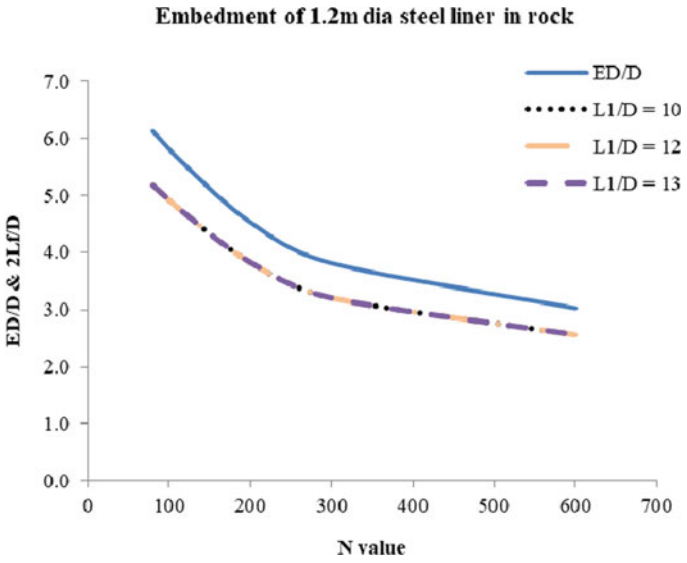

Fig. 13 Embedment depth of 1.2 m diameter steel liner in rock

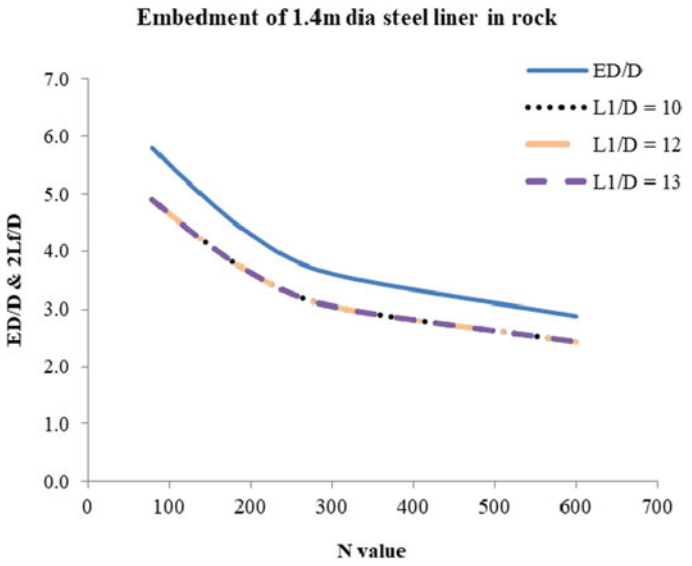

Fig. 14 Embedment depth of 1.4 m diameter steel liner in rock

change of soil properties from soft clay to stiff clay or loose sand to dense sand or weak rock to hard rock influence the fixity depth significantly.

References

1. Baker CN Jr Pile foundation: know—how to determine pile depth of embedment.IS 2911 Design and construction of pile foundation—code of practice
2. Terzaghi K, Peck RB, Mesri G (1996) Soil mechanics in engineering practice, 3 edn
3. Tomlinson M, Woodward J (2008) Pile design and construction practice, 5 edn
4. U.S Department of Transportation, Federal Highway Administration (2008) Drilled shafts: construction procedures and LRFD design methods

Studies on Locating Sediment Trap for Reducing Dredging in Jellingham Navigational Fairway, Kolkata

N. Saichenthur, K. Murali, and V. Sundar

Abstract Formation of shoals in an estuarine environment creates significant problems such as reduction in depth in navigational channels, decreased discharges and degradation of water quality. One of the widely used solutions to reduce sedimentation is the implementation of a sediment trap by creating a trench or a pit in the submerged bottom at specific locations. A sediment trap is defined as a section of the estuarine bed deepened to a depth greater than its surroundings. The lower velocity allows sediments to deposit in the trap rather than move past over it. Implementation of a silt trap at specific locations in a highly dynamic domain like Hooghly estuary helps to optimize the dredge quantity or the maintenance dredging can be localized to a specific location (the trap) rather over a wide submerged area. This study involves optimization of the location and shape of a silt trap near the Haldi-Hooghly confluence point, West Bengal, India. The trap was designed to reduce the dredging quantity in the downstream Jellingham channel which is a part of the navigational channel en route to Haldia Dock Complex in the Hooghly estuary. Based on a comprehensive numerical study, an option of irregular polygon shaped silt trap of a surface area of 250,000 m^2 positioned in such a way to trap the sediments from both the Hooghly and the Haldi rivers near the Haldia anchorage was finalized which was found to perform efficiently in reducing the dredge quantity in the Jellingham channel. The details of the study are reported in this paper.

Keywords Silt trap · Dredging · Hooghly estuary · Sedimentation · Siltation and navigational channel

N. Saichenthur (✉) · K. Murali · V. Sundar
Department of Ocean Engineering, Indian Institute of Technology Madras, Chennai 600036, India
e-mail: saichenthur@gmail.com

K. Murali
e-mail: murali@iitm.ac.in

V. Sundar
e-mail: vsundar@iitm.ac.in

V. Sundar et al. (eds.), *Proceedings of the Fifth International Conference in Ocean Engineering (ICOE2019)*, Lecture Notes in Civil Engineering 106,
https://doi.org/10.1007/978-981-15-8506-7_15

1 Background

The Hooghly river estuary is a distributary of the river Ganges, located in the eastern part of Indian subcontinent in West Bengal. The Hooghly estuary is an area, wherein, high tidal flux is experienced, from the Bay of Bengal in the south and with a huge magnitude of discharge, from Farakka feeder canal, from the north. The Hooghly River is known as Bhagirathi River in its upstream. River Rupnarayan is the other river draining into the Hooghly river estuary. Situated in this highly dynamic estuarine basin are the two major ports Kolkata Dock System (KDS) and Haldia Dock Complex (HDC) governed by Kolkata Port Trust (KoPT) as shown in Fig. 1. Both the ports have their navigational routes situated in this estuarine system. The navigation to Haldia Dock Complex (HDC) is through the Middleton-Auckland-Jellingham channels of Hooghly River and this channel to Haldia Port is maintained with 25 Mm^3 per annum, Dubey et al. [4]. The estimated loads vary in the order between 2.6×10^5 and 1.09×10^5 m^3 s^{-1} during peak flood and ebb cycles at the estuarine mouth, Nandy et al.

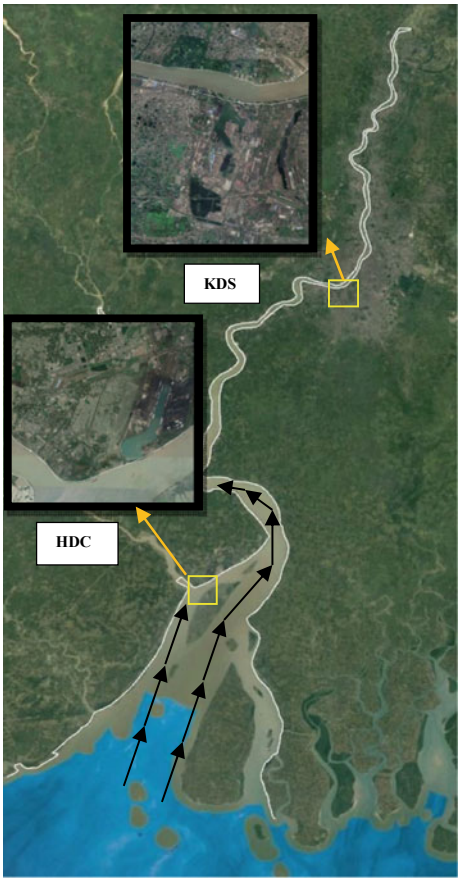

Fig. 1 Navigational route to HDC and KDS

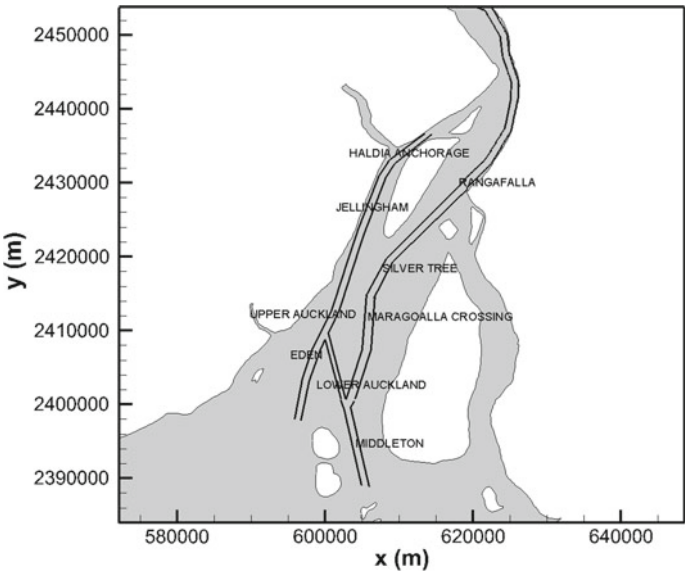

Fig. 2 Schematic locations of estuarine channels en route to KDS and HDC

[6]. Hence, one of the perennial problems for these major ports is to manage this sediment influx from the upstream river efficiently by developing dredging plans. The maximum flooding and ebbing velocities in the navigational channels could reach up to 1.7–2.0 m/s during spring tide and the velocity range during neap tide is 1.2–1.5 m/s, Saichenthur et al. [8]. The wave activity in this region is less with significant wave heights, H_s less than 0.35 m. In the navigation channel, the H_s are less than 0.25 m during the winter months, and relatively higher during the southwest monsoon period Bhaskaran et al. [2].

The present navigation to Haldia Dock Complex (HDC) is through Eden-Upper Auckland-Jellingham channels Fig. 2. The Kolkata Port Trust, in particular Haldia Dock Complex (HDC) has been facing siltation issues over the past several years. The Jellingham shoal, which is like a doorstep of HDC, continuously has been facing reduction in the depth at a few locations along the navigational channel, thus hampering smooth passage of vessels. Jellingham shoal is in a dynamic equilibrium, with navigable depths constantly under threat near the vicinity of the shoal. However, there are frequent encroachments from the east due to the slowing of currents adjacent to the western banks of Nayachara and from the west due to the influx of sediments from the Haldi River. In order to maintain the minimum required draft, the authorities of KoPT have been continuously exploring new techniques by improving the dredging methods and in disposing the dredged spoil. Through, a detailed hydrodynamic analysis by Saichenthur et al. [8], a suitable technique to reduce the silting in

Jellingham navigational fairway, i.e., implementation of silt trap in a suitable location near the Hooghly confluence was proposed. This paper discusses the options considered for optimizing the location and shape of silt.

2 Concept of Silt Trap

Sediment traps or basins are used primarily to accomplish two functions, namely the reduction in flow and the trapping of sediments. Trap efficiency is defined as the percent by which the effluent suspended sediment load is reduced with respect to the influent suspended sediment load (removal ratio). In a tidal situation, the seaward edge of the trap will be the influent side during flood tide and the effluent side during ebb tide, and vice versa for the upstream river edge. To create a silt trap, the depth at the chosen location is increased by dredging. By holding the trap depth and location constant and varying the discharge of the river system, the efficiency of a trap can be assessed for different flow discharges. Selection of a silt trap needs a continuous investigation on the variation in the bathymetry of the proposed area and the nearby water bodies, soil types or nature of sediments. To improve the effectiveness of the trap basin, it should be located at low lying areas, so as to intercept the largest possible amount of sediments capturing into the trap and secondly it will retain the large amount of silt laden water to settle by gravitational force. The sizing of the silt trap mainly depends on the quantity of sediments in motion at the proposed section. Based on all these aspects the methodology of this study has been set up.

3 Methodology

Four different options of silt trap have been considered in this study. These options are varied based on the shape and location of the traps. The locations of the silt trap that are to be analysed are described in Table 1. Options-1, 3 and 4 are on the downstream side of Haldi River and option-2 is across the Haldi River near the confluence region as shown in Fig. 3. Options-1 and 4 are suggested mainly because it is along the ebbing flow from the Haldi River. The flow vectors are distributed within these silt traps. It was expected that these silt traps can trap the influent sediment from the river, thus justifying its ability to function effectively in reducing the amount of silt in its effluent side i.e., Jellingham channel and it was the reason behind using these silt traps for the study. Option-2 is across the Haldi River, hence this trap acts as a pit and reduces the ebb flow velocity and thereby, it is expected to trap considerable quantity of sediments from the river. Option-3 is along the banks of Nandigram, south of Haldi river entrance.

The hydrodynamic and morphological modelling are carried out using Ocirc (Ocean circulation model), an in-house model of IIT Madras. In this model developed by Chitra et al. [3], the hydrodynamic equations governing the ocean flow field are the

Table 1 Details of the silt trap options considered for the study

Options for silt trap	Location	Auckland channel depth	Eden channel depths	Upper Auckland channel depths	Jellingham channel
Option 1 (250,000 m^2 × 4 m)	Along the flow path of the river near Nandigram banks, west of Jellingham channel	2 tracks Dredged to—3.8 m	As it is	As it is	As it is for all the options, with more fine mesh around silt trap area
Option 2 (500 m × 500 m × 4 m)	Across the Haldi river	2 tracks Dredged to—3.8 m	As it is	As it is	
Option 3 (500 m × 500 m × 4 m)	South of confluence near the Nandigram banks	2 tracks Dredged to—3.8 m	As it is	As it is	
Option 4 (250,000 m^2 × 4 m)	Near the entrance of the confluence along the flow path of the river	2 tracks Dredged to—3.8 m	As it is	As it is	

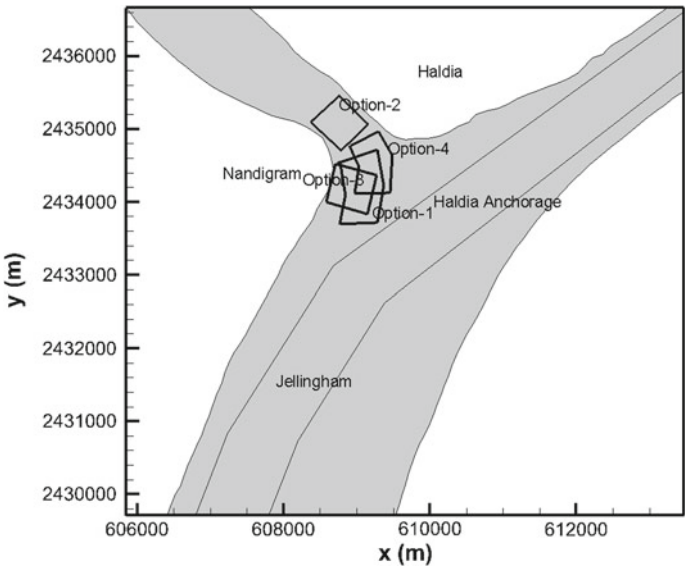

Fig. 3 Location and shape of different silt trap options

vertically integrated form of Shallow Water Equations (SWE) which is discretized by Finite Volume Method (FVM). Rigorous validation of the model Ocirc 1.0 has been performed in the past Murali et al. [5]. The hydrodynamic and morphodynamic model was set up based on Saichenthur et al. [8], and the details are discussed below. The bathymetry configuration of the Hooghly estuary, which is the most basic data for hydrodynamic modelling, is provided by the Hydraulics Study Department (HSD) of KoPT. This data corresponds to [2] survey in most parts of the estuary and extends up to south of Sagar roads. For the purpose of model setup, the extent of estuary is from Diamond Harbour in the north along with the sea portion of Sagar roads in the south and the elevation boundary conditions are provided at these locations. The model domain is discretized with triangular elements or cells for the purpose of obtaining numerical solutions to the hydrodynamic equations. The average mesh size is about 75–200 m over the entire upper reaches of the computational domain. Therefore, the model is able to capture the details of the bathymetry as realistically accurate as possible. The simulations are executed for one full neap-spring-neap cycle to ensure stability of hydrodynamic and morphodynamic model over time. 15 days tidal elevations at 15 min frequency are used as boundary conditions along the open boundaries. Free radiation of velocities along the open boundaries is enabled. Natural boundary conditions are imposed along the coastal boundaries. For the case of monsoon condition, the suspended sediment concentration (SSC) is considered for about 2 g/l based on previous studies. The high values of SSC, in the Hooghly estuary, range between 160–2686 mg/l both at surface and bottom throughout the year Sadhuram et al. [7]. This numerical model set up is calibrated to match the field results by Saichenthur et al. [8].

For the present conceptual design of the sand trap, the location is proposed at the confluence with a water depth ranging between −3 m to −3.5 m over an area of 500 m × 500 m or net area is 250,000 m^2. The depth of the trap below the natural riverbed will have to be maintained as 4 m, i.e., the water level to be maintained in the silt trap region is −7.5 m. This design caters for holding of about one million m^3. The mesh is refined near the trap location to capture the siltation rate in the trap accurately. The sediment transport model used for the study is based on Ackers and White, [1], sediment transport equation. The different silt trap options are analysed based on the quantity of sediment they trap and the subsequent change in bed level these traps induce on their effluent side.

4 Hydrodynamic and Morphodynamic Modelling of Hooghly Estuary

4.1 General

Generally, Hooghly estuary is a tide dominated region and tidal elevation is the open boundary forcing considered for this study. The tide propagates more than 120 km

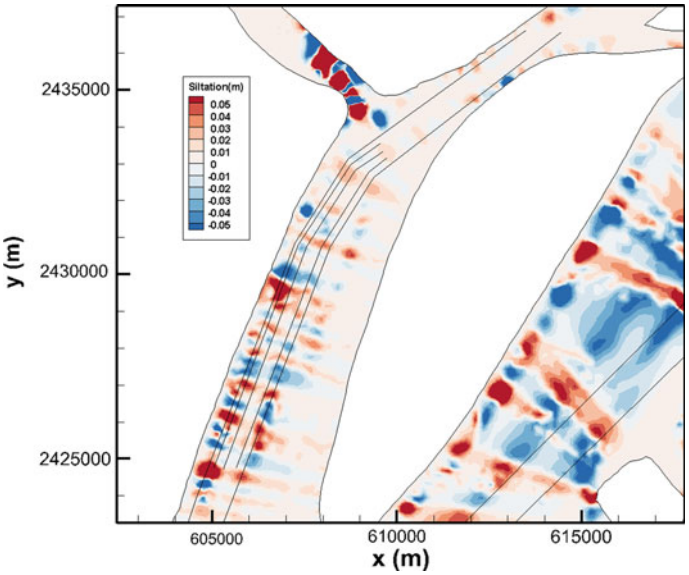

Fig. 4 Bed level changes in Jellingham Fairway without silt trap

inside the estuary from south of Sagar roads, wherein tidal oscillation is induced in the southern part of numerical domain. In the Jellingham channel, the flow directions are north-easterly and south-westerly with a magnitude of 0.7–1 m/s in neap time and 1.2–1.5 m/s in spring time. At the Haldia confluence, region where, the Haldi River drains into Hooghly estuary, severe eddies are observed during high and low tide. The ebb flux at the confluence is also contributed by the discharge from Haldi River.

The sediment is transported through the Haldi river confluence and discharged to the Jellingham area leading to wide spread siltation. Due to rapid reduction of velocity during high and low tide time, the prominent shoaling is observed in this region. Presence of oscillating shoals in this region contributes to reduction in depth and silting rate is also higher. Reduction in bed level in the Jellingham channel, at the Haldia confluence, at a rate of 0.1–0.12 m/14 days is observed. A typical siltation pattern without any silt trap, observed in the morphodynamic model results is given in Fig. 4.

4.2 Hydrodynamics and Siltation Analysis for the Silt Trap Options

The option-1 silt trap is a shape of irregular polygon with the approximate area of 250,000 m^2, positioned in such a way that the flow vectors from ebb tide from Haldi

River are concentrated within this trap. It is also positioned in such a way that it can trap silt from ebb flow in the estuary. The peak flood flow velocity in the trap is about 1.2 m/s during spring and around 0.7 m/s during neap and during ebbing there is reduction velocity by 10–20%. During the high tide and low tide eddies are formed inside the traps. The velocity of eddies is around 0.1–0.15 m/s. The velocity around the silt trap is comparatively higher in magnitude to the velocity inside the trap during high and low tides. It is during this time period, the sediments tend to settle in the trap. The option-2 silt trap is a rectangular shape with an approximate area of 500 × 500 m^2 which is positioned right across the flow of Haldi River. The flood and ebb flow velocity is about 1.2 m/s and 1.4 m/s respectively during spring and around 0.6 m/s and 0.8 m/s respectively during neap in the option-2 silt trap, along Haldi River. During the high tide and low tide prominent eddies are observed inside the traps. The velocity of eddies is around 0.08–0.14 m/s. The option-3 silt trap is a rectangular shape with an approximate area of 500 × 500 m^2, which is positioned in such a way it traps silt from the tidal flow along the estuary. The velocity in the trap reduces by 10–20% compared to the velocity in the influent side. In the effluent side of the trap, there is a sudden rise in velocity due to the sudden reduction in depth. The peak flood flow velocity is north-easterly in direction with 1.5 m/s during spring and around 0.8 m/s during neap. During ebb, the velocity magnitude is 1.2 m/s and 0.7 m/s during spring and neap respectively with reversal in direction. During the high tide and low tide eddies are formed inside the traps. The velocity of eddies is around 0.1–0.15 m/s. The option-4 silt trap is similar to option-1 but slightly on the northern side. The silt trap is positioned in such a way that it traps silt from the tidal flow along the estuary and the discharge from the Haldi River. The velocity in the trap reduces by 20–30% compared to the velocity in the influent side. The peak flood flow velocity is about 1.5 m/s during spring and around 0.8 m/s during neap. During the ebb, the velocity magnitude is 1.2 m/s and 0.7 m/s during spring and neap respectively with reversal in direction. During the high tide and low tide eddies are formed inside the traps. The velocity of eddies is found to be in the range of 0.09–0.14 m/s.

The silting rate in the silt trap option-1 is around 1 mm/h. on an average with the maximum rate of 2 mm/h. during spring time. The rate of siltation is increasing during spring time means, this trap is effective only when the water level is relatively high. Nearly 30–40% trap area gets silted up at a rate of 0.05 m/14 days as observed in Fig. 5. This trap does not cause any hindrance to the navigation in Jellingham tracks and in Haldi River if any. This trap causes adverse effects of siltation in the Jellingham channel at the Haldia anchorage. The option-2 trap gets silted up around the edges first corresponding to the weak eddies and the siltation slowly progress to the centre of the trap. Nearly 70–80% trap area gets silted up at a rate of 0.25 m/14 days as observed in Fig. 6. This trap does not cause any hindrance to the navigation in Jellingham tracks but may affect navigation in Haldi River if any. This trap does not cause any adverse effects of siltation in the Jellingham channel. The silting rate in the silt trap is around 3–4 mm/h. on an average with the maximum rate of 5 mm/h. during neap time when hydrodynamics is relatively weak. The silting rate in the silt trap option-3 is around 2–3 mm/h. on an average with the maximum rate of 4 mm/h.

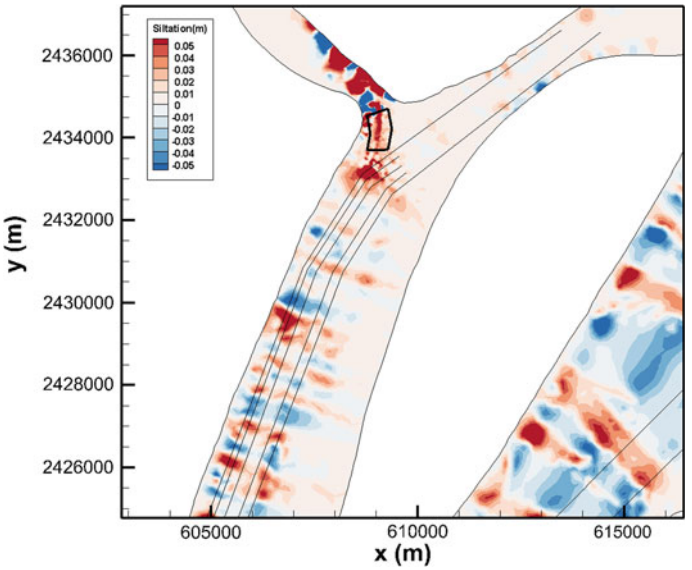

Fig. 5 Bed level changes with the presence of option-1 silt trap

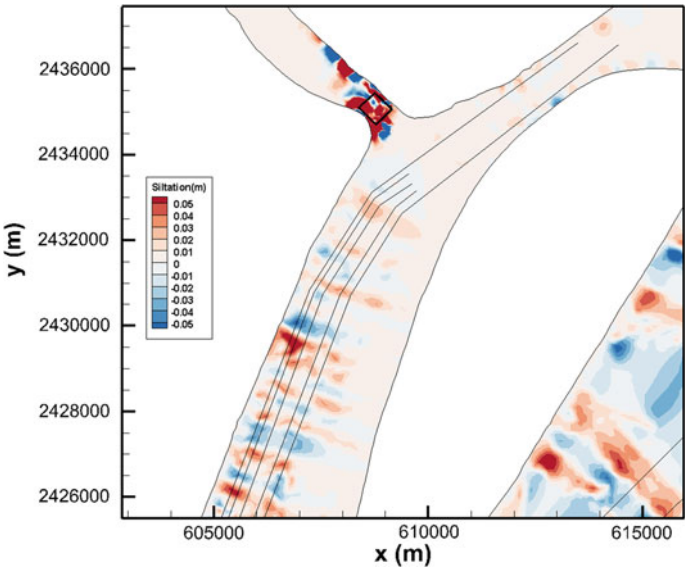

Fig. 6 Bed level changes with the presence of option-2 silt trap

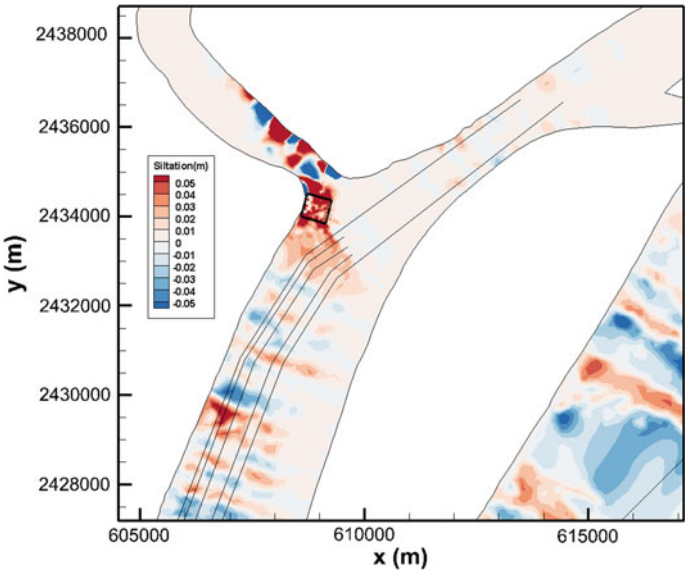

Fig. 7 Bed level changes with the presence of option-3 silt trap

during neap time. In this trap the deposited volume of silt gets eroded during spring time. Nearly 60–70% trap area gets silted up at a rate of 0.05 m/14 days as observed in Fig. 7. This trap does not cause any hindrance to the navigation in Jellingham tracks and in Haldi River if any. This trap causes adverse effects of siltation in the Jellingham channel at the Haldia anchorage. The silting rate in the option-4 silt trap is around 5–6 mm/h on an average with the maximum rate of 7 mm/h during neap time when hydrodynamics are relatively calm. Nearly 75% of trap area gets silted up at a rate of 0.35 m/14 days as observed in Fig. 8. This trap does not cause any hindrance to the navigation in Jellingham tracks and navigation in Haldi River. This trap does not cause any adverse effects of siltation in the Jellingham channel. The filling up rate of each silt trap over the 14 days simulation time period is given in Fig. 9. The rate of siltation per hour over the tidal variation of neap to neap cycle is given in Fig. 10.

5 Comparative Analysis of Impacts of Different Silt Trap Options on the Jellingham Channel Bed Level Changes

The silt trap option-1 seems to have the lowest impact in reducing the dredge quantity in the Jellingham channel. It has the lowest rate of siltation and also has the most adverse effect on the navigational fairway. Option-2 silt trap has a sizeable impact on reducing the siltation quantity in Jellingham fairway. Option-2 traps about 1.2 Mm^3

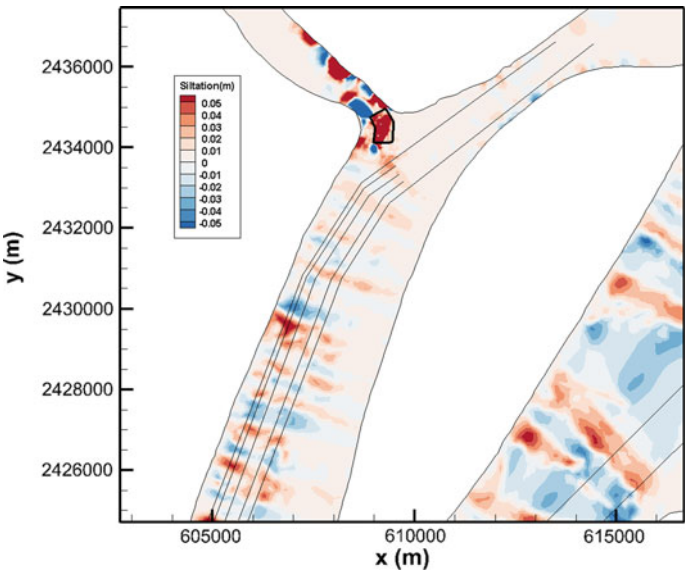

Fig. 8 Bed level changes with the presence of option-4 silt trap

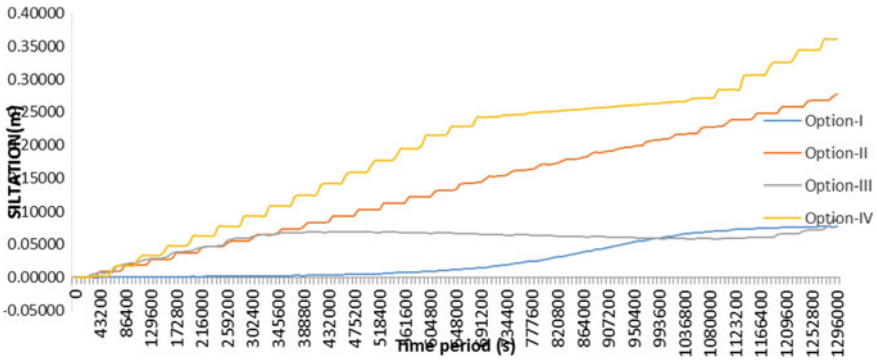

Fig. 9 Filling up rate of silt traps over 14 days simulations

of silt that gets deposited on the Jellingham channel. The silt trap option-3 has a very less effect on reducing the dredge quantity in Jellingham channel. It also causes an adverse effect by increasing siltation in Jellingham fairway near its vicinity. Option-4 has a clear advantage over all other traps in trapping the silt. It traps nearly 1.7 Mm^3 of silt and reduces the dredging quantity in Jellingham fairway by 60%. The comparison of these silt trap effects on Jellingham fairway is carried out based on the bed level changes all along the channel from Haldia anchorage to south and the details are depicted in Figs. 11, 12 and 13, with the presence of each trap separately. The details of the factors considered for silt trap study is given in Table 2 and the

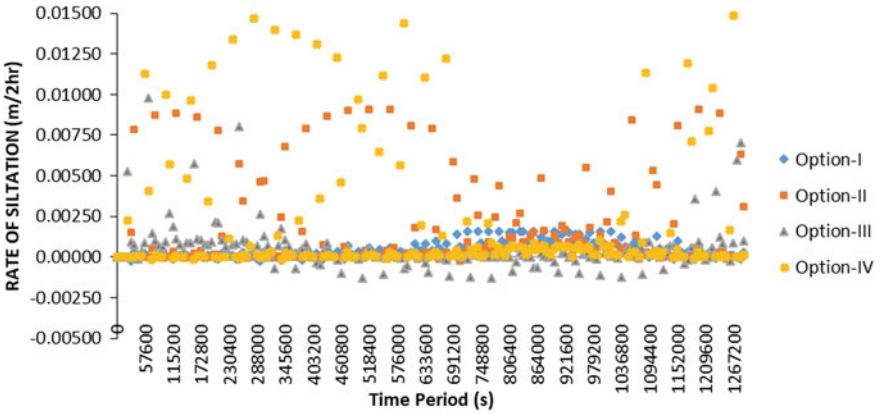

Fig. 10 Comparison of rate of siltation in each silt trap over 14 days simulations

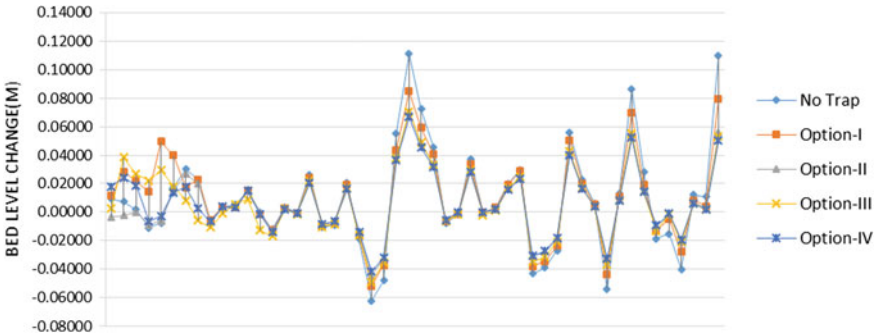

Fig. 11 Comparison of bed level change along western part of Jellingham channel from north to south for different silt trap options

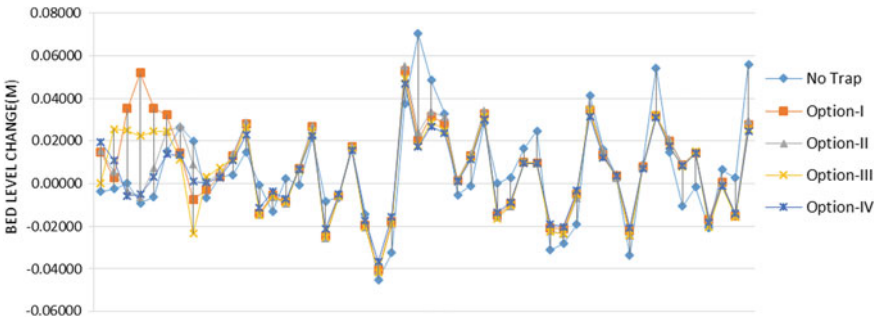

Fig. 12 Comparison of bed level change along middle part of Jellingham channel from north to south for different silt trap options

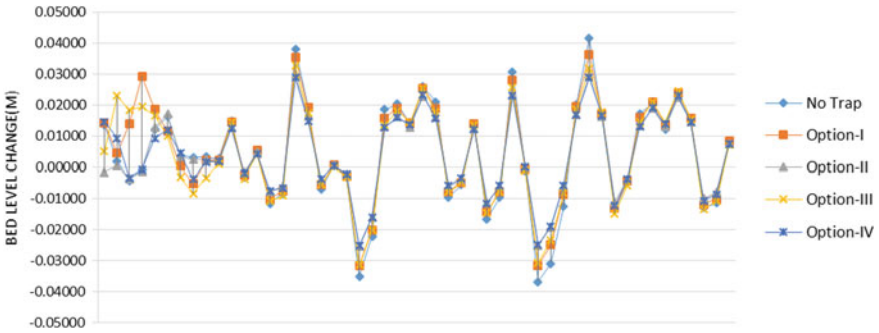

Fig. 13 Comparison of bed level change along eastern part of Jellingham channel from north to south for different silt trap options

estimated silt volume trapped within the silt trap is discussed in Table 3. It is also observed that in all the silt traps the rate of siltation reduces as the traps get filled up.

6 Summary

The analysis depicts that the net cost of dredging for the part of sediments (50–60%) trapped which will not be dredged in the Jellingham channel, is clear advantage in implementing a silt trap. Option-4 of the silt trap considered for the study is recommendable based on various essential factors analysed. This option can trap around 1.7 million cubic metre of silt every year. No adverse effect in siltation is identified in Jellingham channel for this option.

Table 2 Detailed analysis of silt trap options based on essential factors

Factors	Option-1	Option-2	Option-3	Option-4
Impression	Nearer to dredge spoil dumping site. Positioned such way that it could trap sediment flowing along the river and also the sediment flowing along the estuary	Farthest distance among all other options, from dredge spoil dumping site. Act as a pit across Haldi river and expected to reduce velocity and thereby trapping the silt	Nearest to dredge spoil dumping site. Expected to trap sediment moving along the western part of Nayachara island	Away from dredge spoil dumping site. Along the flow path of river at the entrance of confluence and is expected to trap sediment from the river
Trapping efficiency	Based on the simulation study this option traps silt for about 30–40% of its area at a maximum silting rate of 0.1 m/month	Based on the simulation study this option traps silt for about 75–80% of its area at a maximum silting rate of 0.5 m/month	Based on the simulation study this option traps silt for about 40% of its area at a maximum silting rate of 0.12 m/month	Based on the simulation study this option traps silt for about 75% of its area at a maximum silting rate of 0.7 m/month
Navigation in Jellingham	Not affected	Not affected	Not affected	Not affected
Navigation in Haldi River	Not affected	May be affected	Not affected	Not affected
Adverse siltation effect on Jellingham channel	Considerable amount of adverse effect is caused in Jellingham channel	No adverse effect	Considerable amount of adverse effect is caused in Jellingham channel	No adverse effect
Shape	Irregular polygon	Square	Square	Irregular polygon
Distance to dump site	1450 m appx. to Nandigram site and 3750 m appx to Nayachara site	1700 m appx. to Nandigram site and 4300 m appx to Nayachara site	1250 m appx. to Nandigram site and 3550 m appx to Nayachara site	1500 m appx. to Nandigram site and 4100 m appx to Nayachara site

Table 3 Dredge quantity estimation within the silt trap

Silt trap options	AREA (m^2)	Trapping Efficiency (%)	Siltation rate (m/month)	Siltation rate (m/year)	Volume of silt to be dredged per year (m^3)
OPTION-1	250,000	40	0.1	1.2	120,000
OPTION-2	250,000	80	0.5	6.0	1,200,000
OPTION-3	250,000	40	0.12	1.4	140,000
OPTION-4	250,000	75	0.75	9.0	1,687,500

References

1. Ackers P, White WR (1973) Sediment transport: new approach and analysis. J Hydraul Div 99(hy11):2041–2060
2. Bhaskaran PK, Mangalagiri S, Subba Reddy B (2014) Dredging maintenance plan for the Kolkata port, India. Current Sci 107
3. Chitra K, Murali K, Mahadevan R (1996) Simulation of storm surges along east coast of India using an explicit FEM. In: International conference in ocean engineering '96. Ocean Engineering Centre, IIT, Madras, pp 17–22
4. Dubey RP, Samarawickrama S, Gunaratna PP, Halgahawatta L, Pathirana KPP, Raveenthiran K, Subasingha K, Das B, Sugandika TAN (2014) Mathematical model studies for river regulatory measures for the improvement of draft in hoogly estuary, India. Evol Trends Eng Technol 2:1–12. ISSN: 2349-915X
5. Murali K, Lou J, Kumar K (2002) An unstructured model simulations for Singapore strait. Maritime Port J Singapore
6. Nandy S, Bandyopadhyay S (2011) Trend of sea level change in Hugli Estuary, India. Indian J Geomarine Sci 40(6):802–812
7. Sadhuram Y, Sarma VV, Ramana Murthy TV, Prabhakara Rao B (2005) Seasonal variability of physico-chemical characteristics of the Haldia channel of Hooghly estuary, India. J Earth Syst Sci
8. Saichenthur N, Murali K, Sundar V (2019) Study on stability of eden navigational channel in Hooghly river estuary. In: Proceedings of the fourth international conference in ocean engineering (ICOE2018). Lecture notes in civil engineering, vol 23. Springer, Singapore, pp 337–352

Semi-arid River Basin Flood: Causes, Damages, and Measures

Sanjay M. Yadav and Nikunj K. Mangukiya

Abstract Due to climate change, the semi-arid region received rainfall of 1 in 100 year return period which causes a flood in the region. In the present study, analysis of July 2017 flood of the semi-arid region of Banas River basin caused due to heavy rainfall has been carried out. The Dantiwada and Sipu dams on Banas River and tributary of Banas River received heavy inflows during this period. This resulted in short duration huge releases from the dams. These releases were more than carrying capacity of the river which resulted in flooding of adjoining areas. 226 numbers of villages including two major districts were inundated. 224 people lost their lives, and around 34,000 people have been evacuated. Total damages worth of Rs. 1653 crore (16.53 billion Rs.) has been reported. In the present study, reasons for flooding, damage assessment, and measures to check flooding using 1D hydrodynamic modeling have been presented. MIKE Hydro River has been used for the computation of water surface elevation along 123 km river reach. The 1D hydrodynamic model developed from cross-sections extracted from the DEM. The outcome of the present study recommends careful operation of Dantiwada and Sipu dams as well as the relocation of people living in the floodplain areas of Banas River.

Keywords Semi-arid · Flood · 1D · MIKE · DEM · Dam

1 Introduction

India has witnessed a rapid growth in its population in the past 50 years, which cause changes in land-use pattern, cropping pattern, water storage, irrigation, and drainage [1]. Due to this, hydrological cycle of semi-arid regions has been modified [2]. The impact of climate change which includes increased precipitation and storm intensity,

S. M. Yadav (✉) · N. K. Mangukiya
Department of Civil Engineering, Sardar Vallabhbhai National Institute of Technology, Surat, Gujarat 395007, India
e-mail: shvinam27@gmail.com

N. K. Mangukiya
e-mail: nikk.mangukiya@gmail.com

V. Sundar et al. (eds.), *Proceedings of the Fifth International Conference in Ocean Engineering (ICOE2019)*, Lecture Notes in Civil Engineering 106,
https://doi.org/10.1007/978-981-15-8506-7_16

particularly in semi-arid region resulted into the increased chances of flooding in the cities located on the banks of the river and in the floodplain [3, 4]. Floods are most frequently occurred natural disaster in India [5, 6]. It affects the emotional, social, as well as economic life of the peoples who are affected by it [6, 7]. Floods are mainly caused by excess rainfall [8] which generates more surface runoff [9]. But anthropogenic activities has increased the risks of flooding [10, 11], for example, by the construction of roads and bridges on the land which were previously occupied by vegetation can reduce the infiltration capacity of the land, and thus, it generates runoff more quickly [12]. Planning decisions such as the construction of houses in floodplains can also increase the risk of floods [13]. Thus, reliable hydraulic models are required to accurately predict the water level and flow at various locations along the river [14]. Generally, levels are predicted along the river, and inflows are predicted for reservoirs [15]. Apart from that, for effective management of future flooding, insurance studies, and for development of risk maps, prediction of water levels are essential. Thus, the estimation of water levels in floodplains is of prime importance. Stages in the river and its corresponding discharges and various other parameters are dependent on the channel roughness. Hence, prediction of channel roughness also plays a major role in the study of open channel flow, especially in hydraulic modeling [16]. The end-to-end flood forecasting system plays a very significant role in floodplain management. With the advancement in the computer technology, computation of river hydraulics and modeling became easier now by use of various one-dimensional, two-dimensional, and three-dimensional models, though one-dimensional (1D) models are more popular due to their simplicity for setup and calibration [17]. The prediction of stage and discharge in the river with time is considered as the flood warning parameters in any river which can be computed using St. Venant equation [18, 19]. It is very difficult to generate exact solutions of the St. Venant equation. However, approximate solutions of this equation can be obtained by using numerical methods with appropriate assumption. Methods like finite difference method (FDM), finite volume method (FVM), and finite element method (FEM) can be used to convert St. Venant equation in the form of equivalent finite difference equations, and then the solution can be generated by the different scheme [20]. Many studies have been conducted to develop various hydraulic model based on the above-mentioned method for computational river hydraulic in the past decades [21]. The different available hydraulic models like MIKE 11, HEC-RAS, etc. are using these methods for computation of flow and level of water at different grid point along the river [22, 23]. The comparative performances of these models with advantages and limitations have been investigated by many researchers [24, 25].

Studies on one-dimensional modeling for river hydraulics have certain limitations in India due to the absence of decent quality of surveyed data. The scarcity of the observed stage and flow hydrograph and limitation of surveyed cross-sections are the main reason for the restriction of studies on the river hydraulic in India [21]. The present study was carried out for the semi-arid region of Banas River basin located in the northern part of the Indian state of Gujarat which is flooded in 2017 because of change in climatic conditions. Due to less number of available surveyed river cross-section in the region, hydraulic studies have not been carried out in that zone.

In the present study, river cross-sections have been extracted from Shuttle Radar Topography Mission (SRTM) Digital Elevation Model (DEM) of 1-arc second using MIKE Hydro River software to overcome the problem of less available surveyed river cross-sections. These cross-sections were used for development of a 1D hydrodynamic model for the Banas River using MIKE Hydro River and were calibrated for 2017 flood. The calibrated model was used to compute the water level to identify critical river reach and the highest overflowing points along the 123-km reach of the river for peak discharges corresponding to 2017 flood event for flood-control measures.

2 Study Area and Data Collection

The Banas River rises near Pindwara village in Sirohi district of Rajasthan at an elevation of 372.5 m above mean sea level. The river flows in a southwesterly direction from the origin, travels a total length of 266 km, and ends into little Rann of Kutch. The basin lies between the geographical coordinates of 71° 15′ to 73° 15′ east longitudes and 23° 30′ to 24° 55′ north latitudes. It is bounded by Luni basin in the north, Saraswati basin in the south, Aravalli hill ranges in the east, and finally the Arabian Sea in the west. The Banas River is trans-boundary river which drains an area of 8,674 km^2 out of which nearly 38% lies in Rajasthan state and the remaining 62% falls in Gujarat state. In Fig. 1, the index map of the Banas basin has been shown along with latitudes and longitudes, i.e., where the basin is located in India. It also shows the digital elevation of Banas basin and locations of the tributary, dam site, Narmada main canal, and various gauging stations. The elevation of basin changes from 1.81 to 1691.77 m with a mean elevation of 245.41 m and standard deviation of 200.02. There are two major hydraulic structures in the Banas River basin, namely Dantiwada and Sipu dams. Dantiwada dam is on Banas River at chainage of 105 km from its origin with a catchment area of 2,862 km^2. Sipu dam is on Sipu River (a tributary of Banas River) at a chainage of 60 km from its origin with a catchment of 1222 km^2. Releases from these dams are used for irrigation purpose.

The study area for the present study starts from the downstream of Dantiwada and Sipu dams. Both Banas and Sipu River meets at Bhadath village near Deesa district, i.e., around 13 km from Dantiwada and Sipu dams. From the digital elevation of the basin, it can be clearly identified that the region after the confluence of the river is almost flat with low elevation which makes this area more vulnerable to flooding. The end boundary of the study area is taken as Kamalpur gauging station which is located in Banas River near Kamalpur village, i.e., 123 km from Dantiwada dam. The 1D hydrodynamic model was calibrated for July 2017 floodwater level at Umbari gauging station which is located in Banas River near Umbari village, i.e., 53 km from Dantiwada dam.

The data for the present study was procured from dam authorities, Central Water Commission (CWC-Gandhinagar), and river gauging section offices. The present study area starts from Dantiwada and Sipu dams, and the structural details and

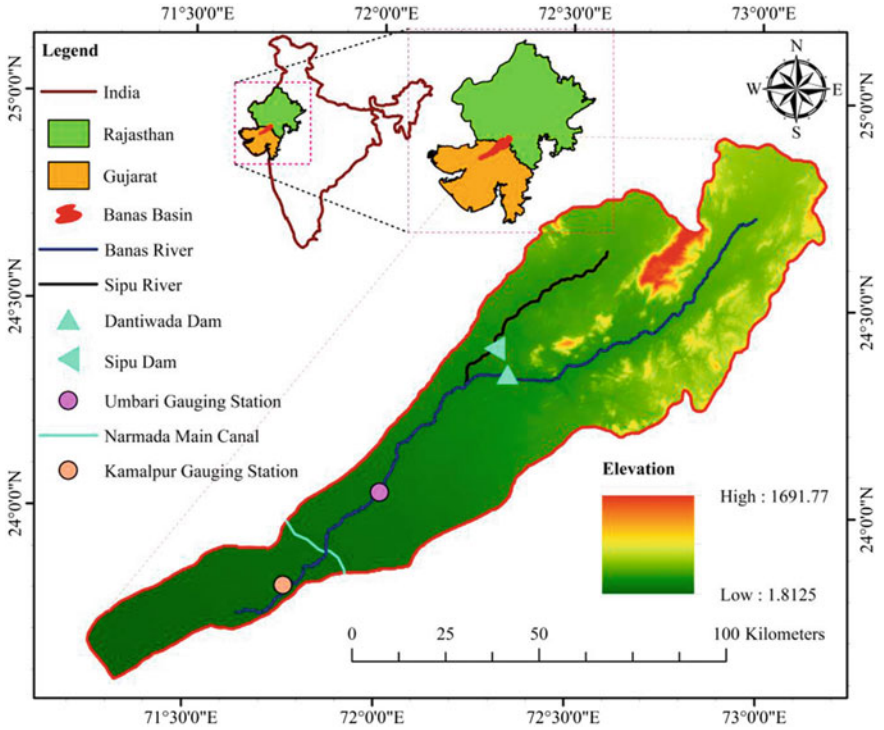

Fig. 1 Index map of Banas basin with DEM and location of structures

releases from these two dams were obtained from the respective dam authorities. The cross-sectional details and flow hydrograph for the Kamalpur gauging station were obtained from CWC while cross-sectional details and flow hydrograph for Umbari gauging station were obtained from river gauging section office, Palanpur. The SRTM DEM of the 1-arc second resolution was downloaded from the United States Geological Survey (USGS) for extraction of cross-sections. The flood damage data was obtained from different government reports and newspaper articles.

3 Methodology

The methodology includes the identification of causes of floods, development of 1D hydrodynamic model, flood damage assessment, and preventive measures. Figure 2 shows the flowchart depicting methodology. The causes of the flood have been identified firstly by means of rainfall data, topography of the region, newspaper articles, and government reports. The second step was to collect the required data for the present study which was procured from the competent authorities and public survey.

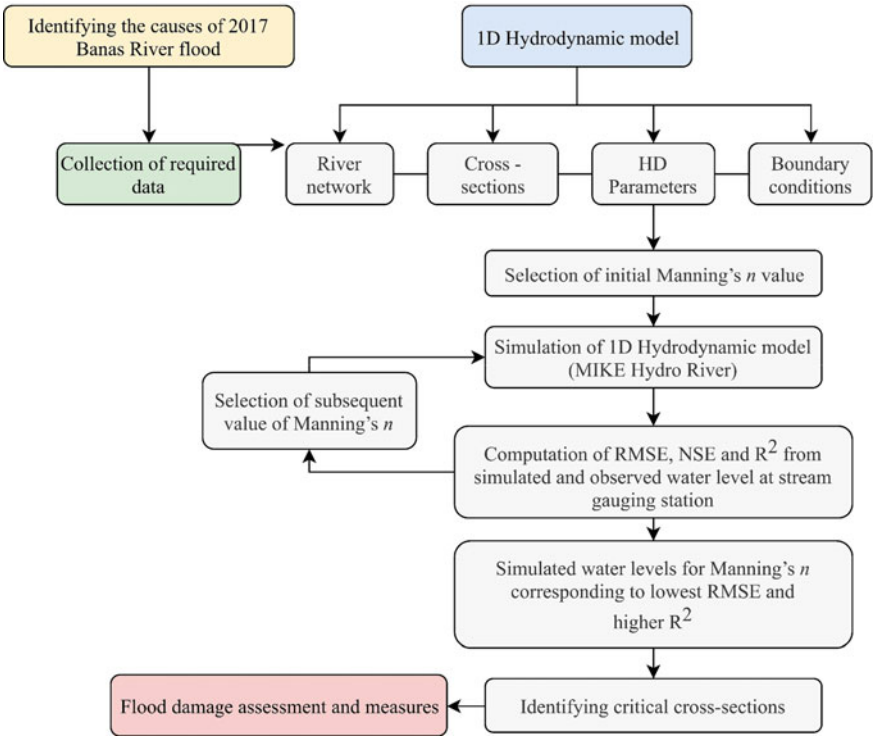

Fig. 2 Flowchart depicting methodology

The 1D hydrodynamic model has been developed for 123 km of river reach using MIKE Hydro River tool. The SRTM DEM downloaded from the United State Geological Survey was pre-processed using Spatial Analyst Tools featured in ArcGIS Desktop v10.5. This pre-processed DEM then imported in MIKE Hydro River for tracing of river reach and generation of the cross-section. Cross-sections for the model have been extracted from DEM by using "auto-generate cross-sections" tool of MIKE Hydro River. The generated cross-sections were then modified according to available surveyed cross-sectional data at some locations. The time step is taken as 10 s, and grid spacing is taken as 250 m for stability assurance. There are three open boundary conditions, and time series of releases of the Dantiwada and Sipu dams were given as upstream boundary conditions while the observed stage hydrograph at Kamalpur gauging station was given as downstream boundary condition. The initial value of Manning's n is taken as 0.03 for the simulation of the 1D hydrodynamic model. The model is calibrated for July 2017 flood period for observed stage and flow hydrograph at Umbari gauging station by changing global roughness coefficient. The range of Manning's n was taken from literature [26] for calibration of the model. The assessment of performance of the model has been carried out by calculation of performance indices, i.e., root mean square error (RMSE), Nash–Sutcliffe efficiency

(NSE), and R^2 (coefficient of determination). Finally, the critical cross-sections have been identified from the calibrated model for 2017 flood.

The flood damage assessment is comprehensively collected from government reports, newspaper articles, government authorities, and questionnaire survey to local people. The preventive measures have been identified from the 1D hydrodynamic model and field investigations.

4 Results and Result Analysis

4.1 Causes of 2017 Banas Flood

The Banas River was flooded in July 2017 due to unprecedented inflow in the river. The Mount Abu, Deesa, Banaskantha, and Dantiwada regions of the catchment received a rainfall of 1473 mm, 269 mm, 150 mm, and 490 mm respectively within 48 h, i.e., on 24/7/2017 and 25/7/2017, while the annual rainfall of the basin is 921 mm. The historical data shows that the rainfall occurred on the 23rd and 24th of July 2017 was the maximum of the past 112 years. This high rainfall was due to activation of low-pressure system in Bay of Bengal and Arabian Sea simultaneously, which is a rare phenomenon. In addition to it, Mount Abu being hilly region produced high runoff received at dam site within shorter time interval. The dam was filled up to rule level due to local rainfall. These circumstances forced the dam authorities to make a decision of sudden releases from the dams. The flow hydrograph and dam water level for Dantiwada and Sipu dams are shown in Figs. 3 and 4. Being a semi-arid region, the basin area and depth of the river are almost flat after the confluence

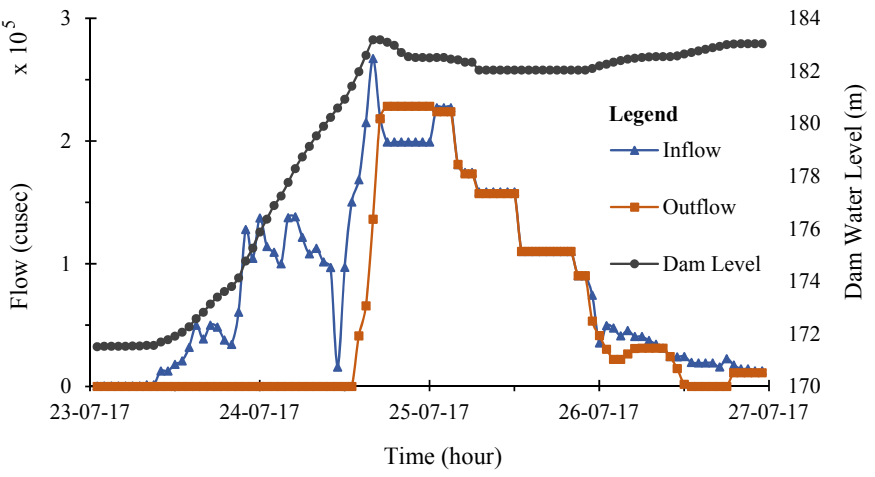

Fig. 3 Flow hydrograph and dam water level at Dantiwada dam

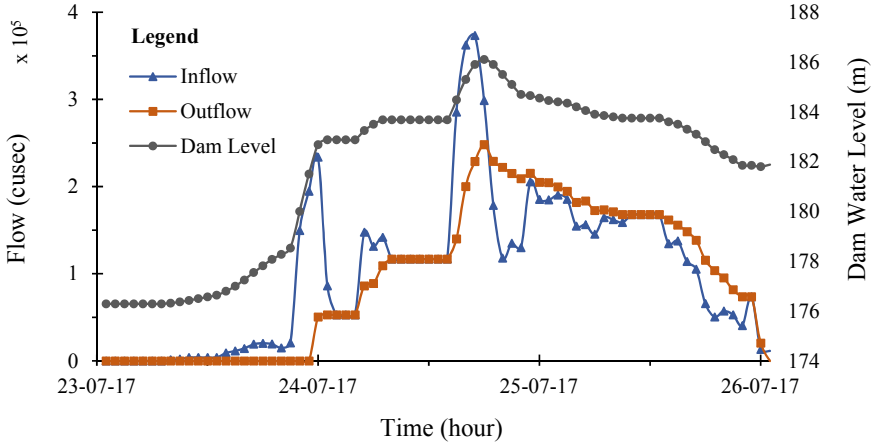

Fig. 4 Flow hydrograph and dam water level at Sipu dam

of Banas and Sipu River (can be identified from Fig. 1 also). Because of these, the carrying capacity decreases from downstream of the confluence of the river. The depth of the river near Mota Jampur and Khariya village (i.e., 78 km downstream of Dantiwada dam) is around 2–3 m, i.e., nearby villages and the bed of the river are at almost same elevation. The water in this region has a tendency to spread in the lateral direction which resulted in severe flooding. In addition to it, Narmada main canal which is having total depth of 8 m and constructed partly above and partly below the ground was also breached at various locations near Thara village. The cross-drainage works of Narmada main canal were not sufficient to pass the floodwater, which resulted in an increase of inundation of flood depth.

4.2 Results of 1D Hydrodynamic Model

The 1D hydrodynamic model has been calibrated and validated with reference to observed data for the flood period of July 2017. The maximum release from Dantiwada dam was 6465.9 m^3s^{-1}, and from Sipu dam, it was 7025.04 m^3s^{-1}. These maximum releases were at the same time, i.e., 24th July 2017 at 18:00:00 h which makes highest flow of 13,490.94 m^3s^{-1} in the river. During the calibration process, the global value of Manning's n has been changed to match the observed and simulated stage hydrograph at Umbari gauging station. Table 1 represents the results of observed and simulated stage value of Umbari gauging station with different roughness coefficient. Finally, the calibrated value of Manning's n was obtained as 0.02 with RMSE (m), NSE and R^2 value as 1.618, 0.695 and 0.891 respectively for observed and simulated stage hydrograph.

Table 1 Comparison of stage hydrograph for different Manning's *n*

Manning's *n*	0.020	0.022	0.024	0.026	0.028	0.030
RMSE (m)	1.618	1.661	1.676	1.727	1.773	1.868
NSE	0.695	0.673	0.665	0.639	0.613	0.559
R^2	0.891	0.897	0.907	0.910	0.911	0.889

Figure 5 shows the graphical representation and scattered plot of observed and simulated stage value with Manning's roughness coefficient, $n = 0.02$ at Umbari gauging station for 2017 flood. It can be observed from Fig. 5 that the simulated stage values are higher than the observed ones which may be due to the presence of Narmada main canal which is not considered in the present study. Also the bed of river is made up of fine sand which is having tendency to infiltrate the water in low discharges, and as the developed 1D hydrodynamic model does not consider the amount of infiltration, the simulated water level results are on higher side then the observed one.

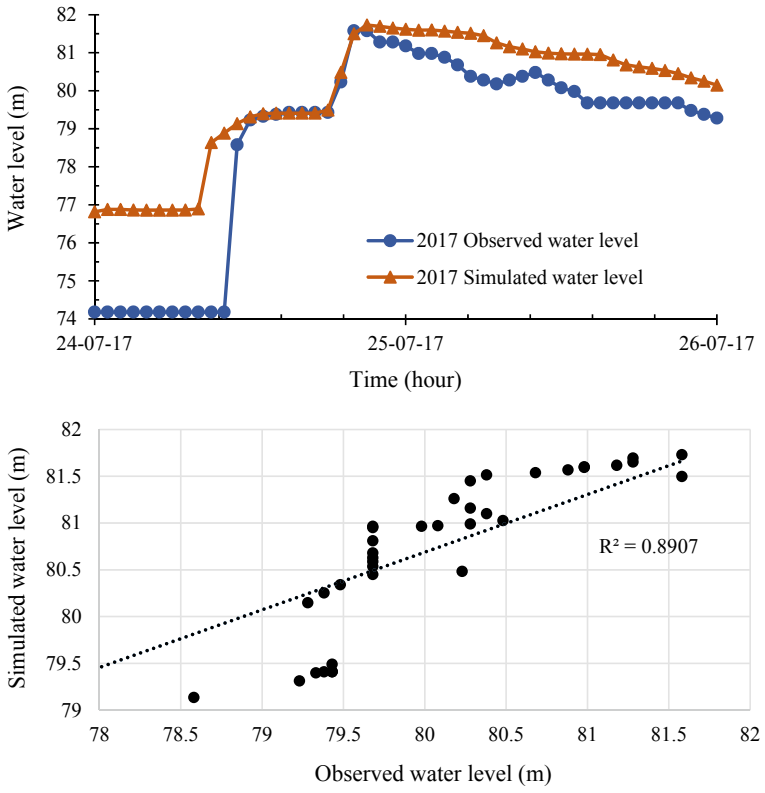

Fig. 5 Comparison and scatter plot of observed and simulated stage hydrograph

Table 2 Height of water level above river bank at all cross-sections

Cross-sectional chainage (m)	Right bank R.L. (m)	Left bank R.L. (m)	Water level (m)	Height of water level above	
				Right bank (m)	Left bank (m)
82,619	118.786	117.131	123.148	4.362	6.017
44,491	77.444	76.663	81.742	4.298	5.079
23,433	52.131	53.1	56.753	4.622	3.653
19,760	49.475	48.006	54.376	4.901	6.37
17,895	48.35	48.006	52.128	3.778	4.122
13,921	44.236	43.349	48.476	4.24	5.127
12,169	43.038	41.441	47.803	4.765	6.362

From the calibrated and validated 1D hydrodynamic model, the critical (most overflowing) cross-sections have been identified. Table 2 shows the reduced level (R.L.) of left and right bank with chainage and water level for critical cross-sections. The most critical cross-sections identified from the water surface elevation profile of model are located at (i) chainage 82,619 which is Deesa Taluka located at downstream of the confluence of Banas and Sipu River, (ii) chainage 44,491 which is near Umbari village, and (iii) chainage 19,760 which is near Khariya and Mota Jampur village. The width of the river near confluence is around 3 km while it becomes around 1 km near the Deesa Bridge located at chainage 82,619, which makes this area more vulnerable to flood. The Deesa Taluka was fully submerged due to 2017 flood in Banas River which has been reported by local media as well as government offices. The width of the river near Umbari village located at chainage 44,491 also decreases, and the surrounding regions are almost at a same elevation which causes a flood in this region. The highest overflowing cross-section which is located at chainage 19,760, near Mota Jampur and Khariya village where the depth of the river is around 2–3 m. The Khariya and Mota Jampur village located at just upstream of the Narmada main canal. The canal is partly above the ground level which causes the obstruction to floodwater. Due to this, the upstream area of Narmada main canal is inundated.

4.3 Flood Damages

Due to the floods, the livelihoods and lives have been affected in the region. The damages to roads, national- and state-level highways, railways, and airports because of flood have impacted education and public transportation as well. 550 panchayats roads, 156 state highways, and 5 national highways were affected due to Banas flood in 2017. For the rescue of villagers, National Disaster Response Force (NDRF), Army, and Air Force were also deployed with the State Disaster Response Force and fire brigade personnel. As per the officials of state administration, 54,517 people were

shifted to safe areas due to flooding of low-lying areas. According to government official reports, about 4333 villages having an agricultural area of 10.98 lakh hectares and 2431 villages having horticulture area of 16,808 hectares were affected due to 2017 floods in northern Gujarat. Devastating floods in parts of Gujarat damaged agricultural crops worth Rs. 867 crore, while horticulture damage stands at Rs. 9.71 crores. As many as 6.44 lakh farmers have faced agricultural crop losses and about 4989 farmers have faced loss in horticulture crop. Almost 25 percent of kharif crops like groundnut, cotton, pulses, castor, cereals, and guar have been lost because of torrential rain and flooding in the semi-arid region of Gujarat. The electricity supply of 492 villages has been affected, out of which 418 villages are in Banaskantha district. As per the results of extensive survey for damage assessment by the state government, total payable relief for land damage, agriculture, and horticulture lost stands at Rs. 1653 crore. Cattle loss stood at 14,300 while more than 200 human lives were lost during the 2017 monsoon season. 18 members of the same family found dead in Khariya village in Banaskantha because of Banas flood in 2017.

5 Conclusions

Following outcomes can be summarized from the present study:

Due to activation of low-pressure system in Bay of Bengal and Arabian Sea simultaneously, the Mount Abu, Deesa, Banaskantha, and Dantiwada regions of the catchment received a maximum of the past 112 years rainfall of 1473 mm, 269 mm, 150 mm, and 490 mm respectively within 48 h, i.e., on 24/7/2017 and 25/7/2017, while the annual rainfall of the Basin is 921 mm. The Dantiwada dam received an inflow of 267,216 cusecs, and at the time, dam was already filled up to rule level, i.e., 182.5 m due to local rainfall on 24/7/2017. Due to this, the authorities were forced to release inflowing water as a direct outflow in the river for the safety of the dam. The Sipu dam received an inflow of 373,329 cusecs on 24/7/2017 which cause the dam water level 186 m (i.e., 4 m above rule level). So for the safety of the dam, all the gates were kept open releasing nearly 2 lakh cusecs of water. The one-dimensional hydrodynamic model has been developed for Banas River reach from downstream of Dantiwada and Sipu dams up to Kamalpur gauging station. The maximum releases from Dantiwada dam were 6465.9 m^3s^{-1}, and from Sipu dam, it was 7025.04 m^3s^{-1}. These releases were at same time which makes highest flow of 13,490.9 m^3s^{-1}. The developed model has been calibrated for 2017 flood event and identified best performance for Manning's n value of 0.02. The performance of the 1D hydrodynamic model has been assessed by different performance indices like RMSE, NSE, and R^2. The obtained value of RMSE, NSE, and R^2 for July 2017 flood is 1.618, 0.695, and 0.891, respectively. The critical cross-sections have been identified from 1D hydrodynamic model which shows that the cross-sections of the river at chainage 82,619 (i.e., near Deesa Taluka), 44,491 (i.e., near Umbari village), and 19,760 (i.e., near Narmada main canal) are most critical sections.

Following measures are proposed to mitigate the flood conditions:

The operational policies of both the dam should be revised to have a flood-control reservation for the accommodation of floodwater. The planning policy should be formed to stop the habitat settlement and construction of roads in flood plains. The capacities of available cross-drainages in Narmada main canal should be increased to safely pass the floodwater to the downstream of the river.

References

1. Bhagat RB (2011) Emerging pattern of urbanisation in India. Econ Polit Wkly 46:10–12
2. Mall RK, Gupta A, Ranjeet Singh RS, Singh LSR (2006) Water resources and climate change: an indian perspective. Curr Sci 90:1610–1626
3. Guhathakurta P, Sreejith OP, Menon PA (2011) Impact of climate change on extreme rainfall events and flood risk in India. J Earth Syst Sci 120:359–373. https://doi.org/10.1007/s12040-011-0082-5
4. Ranger N, Hallegatte S, Bhattacharya S et al (2011) An assessment of the potential impact of climate change on flood risk in Mumbai. Clim Change 104:139–167. https://doi.org/10.1007/s10584-010-9979-2
5. Mohapatra PK, Singh RD (2003) Flood Management in India. Nat Hazards 28:131–143. https://doi.org/10.1023/A:1021178000374
6. Patel DP, Ramirez JA, Srivastava PK et al (2017) Assessment of flood inundation mapping of Surat city by coupled 1D/2D hydrodynamic modeling: a case application of the new HEC-RAS 5. Nat Hazards 89:93–130. https://doi.org/10.1007/s11069-017-2956-6
7. Wright NG, Villanueva I, Bates PD et al (2008) Case study of the use of remotely sensed data for modeling flood inundation on the river severn, U.K. J Hydraul Eng 134:533–540. https://doi.org/10.1061/(ASCE)0733-9429(2008)134:5(533)
8. Mishra V, Aaadhar S, Shah H et al (2018) The Kerala flood of 2018: combined impact of extreme rainfall and reservoir storage. Hydrol Earth Syst Sci Discuss: 1–13.https://doi.org/10.5194/hess-2018-480
9. Tingsanchali T (2012) Urban flood disaster management. Procedia Eng 32:25–37. https://doi.org/10.1016/j.proeng.2012.01.1233
10. Zhu H-F, Kang M-Y, Zhao W-W, Guo W-W (2008) Effect of human activities on flood season runoff in water and soil conservation region. Shuikexue Jinzhan/Adv Water Sci:19
11. Papaioannou G, Loukas A, Vasiliades L, Aronica GT (2016) Flood inundation mapping sensitivity to riverine spatial resolution and modelling approach. Nat Hazards 83:117–132. https://doi.org/10.1007/s11069-016-2382-1
12. Sahoo SN, Sreeja P (2015) Development of flood inundation maps and quantification of flood risk in an urban catchment of Brahmaputra River. ASCE-ASME J Risk Uncertain Eng Syst Part A Civ Eng 3:A4015001. https://doi.org/10.1061/ajrua6.0000822
13. Tarlock D, Albrecht J (2018) Potential constitutional constraints on the regulation of flood plain development: three case studies. J Flood Risk Manag 11:48–55. https://doi.org/10.1111/jfr3.12274
14. Mehta DJ, Yadav SM (2020) Hydrodynamic simulation of river ambica for riverbed assessment: a case study of Navsari Region. In: Lecture Notes in Civil Engineering. pp 127–140. https://doi.org/https://doi.org/10.1007/978-981-13-8181-2_10
15. Mani P, Chatterjee C, Kumar R (2014) Flood hazard assessment with multiparameter approach derived from coupled 1D and 2D hydrodynamic flow model. Nat Hazards 70:1553–1574. https://doi.org/10.1007/s11069-013-0891-8
16. Parhi PK, Sankhua RN, Roy GP (2012) Calibration of channel roughness for Mahanadi River, (India) Using HEC-RAS model. J Water Resour Prot 04:847–850. https://doi.org/10.4236/jwarp.2012.410098

17. Seyoum SD, Vojinovic Z, Price RK, Weesakul S (2012) Coupled 1D and Noninertia 2D flood inundation model for simulation of urban flooding. J Hydraul Eng 138:23–34. https://doi.org/10.1061/(asce)hy.1943-7900.0000485
18. Wang JS, Ni HG, He YS (2000) Finite-Difference TVD Scheme for computation of dam-break problems. J Hydraul Eng 126:253–262. https://doi.org/10.1061/(ASCE)0733-9429(2000)126:4(253)
19. Patra JP, Kumar R, Mani P (2016) Combined Fluvial and pluvial flood inundation modelling for a project site. Procedia Technol 24:93–100. https://doi.org/10.1016/j.protcy.2016.05.014
20. Abbott MB (1979) Elements of the theory of free surface flows. Monogr Surv Water Resour Eng Pitman, London
21. Pramanik N, Panda RK, Sen D (2010) One dimensional hydrodynamic modeling of river flow using DEM extracted river cross-sections. Water Resour Manage 24:835–852. https://doi.org/10.1007/s11269-009-9474-6
22. Patro S, Chatterjee C, Mohanty S et al (2009) Flood inundation modeling using MIKE FLOOD and remote sensing data. J Indian Soc Remote Sens 37:107–118. https://doi.org/10.1007/s12524-009-0002-1
23. Price RK (2018) Toward flood routing in natural rivers. J Hydraul Eng 144:04017070. https://doi.org/10.1061/(ASCE)HY.1943-7900.0001414
24. Vanderkimpen P, Melger E, Peeters P (2009) Flood modeling for risk evaluation—a MIKE FLOOD vs SOBEK 1D2D benchmark study. Flood Risk Manag Res Pract: 77–84
25. Teng J, Jakeman AJ, Vaze J et al (2017) Flood inundation modelling: a review of methods, recent advances and uncertainty analysis. Environ Model Softw 90:201–216. https://doi.org/10.1016/j.envsoft.2017.01.006
26. Chow VT (1959) Open-channel Hydraulics. McGraw-Hill, New York

Numerical Modeling of Flooding and Salinity Intrusion Along River Ambica, Gujarat

R. Balaji and J. Satheeshkumar

Abstract Ambica is one of the major rivers in the Indian state of Gujarat. The river originates from Saputara Hill ranges in the Nasik district of Maharashtra. Ambica has a drainage area of about 2715 km^2, and it travels 136 km before joining with the Arabian Sea. The objective of the study is to understand the hydrodynamics of the tidally influenced river Ambica and to assess the effect of the proposed tidal barrage on the salinity intrusion characteristics. A two-dimensional depth-averaged hydrodynamic model has been developed, using Delft3D modeling scheme, to fulfill the objectives. The open ocean boundary of the numerical model is forced with tidal constituents and the upstream boundary of the river forced with discharge. The numerical model has been simulated for two different cases: (i) with and (ii) without the proposed tidal barrage. Results of the numerical model show the inundation and saline water ingression characteristics along river stretch for various discharge conditions.

Keywords Ambica River · Salinity intrusion · Tidal hydrodynamics · Delft3D-Flow · Numerical modeling

1 Introduction

The river is considered to be one of the essential factors in human society, as they are an important source for freshwater supply, inland waterway, and other natural resources. However, few risk factors are associated with this because of the sudden change in the environment, which leads to flooding or drought. Floods are usually called natural disasters because they can create sudden damage and huge long-term loss to the environment, human activities, and economic development of a society. Major cities in India are located nearer to coastal floodplains and low-lying river-banks, and they are vulnerable to flooding because of changes in climatic conditions and sea-level rise around the globe [1]. It was even worse during monsoon seasons

R. Balaji (✉) · J. Satheeshkumar
Indian Institute of Technology, Bombay, India
e-mail: rbalaji@iitb.ac.in; rbalaji@civil.iitb.ac.in

V. Sundar et al. (eds.), *Proceedings of the Fifth International Conference in Ocean Engineering (ICOE2019)*, Lecture Notes in Civil Engineering 106,
https://doi.org/10.1007/978-981-15-8506-7_17

with a combined effect of monsoonal freshwater discharge and high tides (spring) in the coastal urban floodplain. The two-dimensional (2D) hydrodynamic models have enough potential to estimate or understand the spatial and temporal variations of hydrodynamics, morphology, and sedimentological processes of rivers and floodplains. In the past, various studies have been carried out using two-dimensional numerical models to simulate or map the inundation area during flooding [3, 5, 6, 10]. Lindner and Miller [9] carried out a modeling study and developed a discharge relationship curve for stream gauges in Baltimore, Maryland, with an uncertainty range of between 0.021 and 0.085 m^3s^{-1}. Wilson et al. [12] used a TELEMAC [7] modeling scheme and developed a 2D hydrodynamic model to derive the rating curve of discharge for laboratory flume experiments, and the simulated results indicated that the developed model achieved an accuracy percentage of 10–34. Smith et al. [11] developed a model to simulate a peak river discharge of 120 m^3s^{-1}, and model results reveal good agreement with field-surveyed datasets. The objective of this study is to estimate flooding and salinity intrusion in a macro-tidally dominated river like Ambica. To achieve this, two-dimensional tidal hydrodynamic model was developed using Delft3D modeling software. The details of modeling and results were discussed in further sections.

2 Study Area

Ambica River is a west-flowing river; it begins from Saputara Hill ranges in the Nasik district of Maharashtra, as shown in Fig. 1. The basin covers the Gujarat and Maharashtra, in which it covers the district of Navsari in South Gujarat coastline. The river outfall is ended in the Arabian Sea with an overall length from origin to the outfall of about 164 km. The river basin lies in between the coordinates of 20°34′–20°57′ N latitudes and 72°48′–73°52′ E longitudes. The overall catchment area is

Fig. 1 View of the extent of the study area (*Source* Google Earth)

about 2830 km^2, in which Maharashtra covers only 102 km^2, and the remaining 2728 Km^2 lies in Gujarat. The area of 145 km^2 near river mouth is low lying, marshy, and cannot be beneficially utilized. The Western Ghats and ridges surround the basin of Ambica basin, and they are dividing Ambica and Tapi rivers in east, Auranga and Par rivers in south, and Ambica and Purna rivers on north. The critical main tributaries of Ambica basin are Khapri, Olan, Kaveri, and Kharera.

3 Materials and Methods

3.1 Model Description

The numerical modeling will be carried out using Delft3D model. For modeling of hydrodynamics, the Delft3D-Flow model will be utilized. Delft3D-Flow [8] is a multi-dimensional (2D or 3D) hydrodynamic (and transport) simulation program which calculates non-steady flow and transport phenomena that result from tidal and meteorological forcing on a rectilinear or a curvilinear, boundary-fitted grid using finite difference technique, with appropriate initial and boundary conditions. It solves the continuity, Eq. (1) moreover, Navier–Stokes Eqs. (2 and 3) also, advection–diffusion Eq. (7) for an incompressible fluid following the hydrostatic pressure and Boussinesq approximations.

$$\frac{\partial \eta}{\partial t} + \frac{\partial}{\partial x}(d+\eta)u + \frac{\partial}{\partial y}(d+\eta)v = 0 \tag{1}$$

$$\frac{\partial u}{\partial t} + u\frac{\partial u}{\partial x} + v\frac{\partial u}{\partial y} + g\frac{\partial \eta}{\partial x} - fv + \frac{\tau_x}{\rho_w(d+\eta)} - \frac{F_x}{\rho_w(d+\eta)} - \nu\left(\frac{\partial^2 u}{\partial x^2} + \frac{\partial^2 u}{\partial y^2}\right) = 0 \tag{2}$$

$$\frac{\partial v}{\partial t} + u\frac{\partial v}{\partial x} + v\frac{\partial v}{\partial y} + g\frac{\partial \eta}{\partial y} - fv + \frac{\tau_y}{\rho_w(d+\eta)} - \frac{F_y}{\rho_w(d+\eta)} - \nu\left(\frac{\partial^2 v}{\partial x^2} + \frac{\partial^2 v}{\partial y^2}\right) = 0 \tag{3}$$

where u, v are the flow velocities in x, y directions, respectively; f is the Coriolis parameter; ρw is the reference density of water; τ_x and τ_y are bottom stress parameters; F_x and F_y are the external forces in x and y direction, respectively; ν is the vertical eddy viscosity.

For two-dimensional depth-averaged flow, the bottom stresses induced by the flow in Eqs. (2) and (3) are governed by a quadratic friction law, given by

$$\tau_x = \frac{\rho g u|u|}{C^2} \tag{4}$$

$$\tau_y = \frac{\rho g v|v|}{C^2} \tag{5}$$

where u and v are the depth-averaged velocity in x and y directions, respectively, and C is Chezy's coefficient.

Under the shallow water assumption, which is valid for large horizontal scales, the vertical momentum equation is reduced to the hydrostatic pressure equation. Vertical accelerations due to buoyancy effects or sudden changes in bottom topography are neglected, and only gravitational acceleration is taken into account. The hydrostatic pressure equation depicts pressure forces being balanced by the weight of the water column and is given by:

$$\frac{\partial P}{\partial z} \cong -\rho g \tag{6}$$

The advection-diffusion equation is solved to calculate the transport of matter (sediment), and is written as:

$$\frac{\partial c}{\partial t} + \frac{\partial uc}{\partial x} + \frac{\partial vc}{\partial y} + \frac{(\partial(w - w_s)c)}{\partial z} = \frac{\partial}{\partial x}\left(D_H \frac{\partial c}{\partial x}\right) + \frac{\partial}{\partial y}\left(D_H \frac{\partial c}{\partial y}\right) + \frac{\partial}{\partial z}\left(D_v \frac{\partial c}{\partial z}\right) + S \tag{7}$$

where c is the mass concentration; w_s is the particle settling velocity in a mixture; D_H and D_v are the eddy diffusivities in horizontal and vertical direction, respectively; S gives the source and sink terms per unit area.

3.2 Model Setup

The computational model grid covers the Ambica river basin, as shown in Fig. 2. The bathymetry of the river and nearshore coastal features such as inlets and estuaries were extracted from Admiralty charts (no. 1486 and 3460), and the height of the barrage is given as 5 m above the ground level as shown in Fig. 3. The rectilinear grid was used for the model simulation with a spatial resolution of 100 m [2]. The open boundary of the model was specified at the 10 m water depth, and it was forced with tidal astronomical constituents extracted from a TPXO7.1 global tidal model [4]. On the upstream side of the river has been forced with various river discharge values to simulate different flooding scenarios.

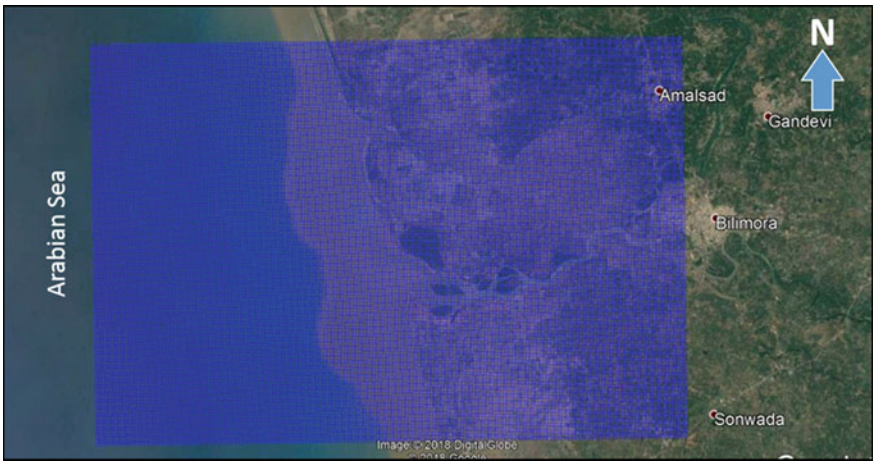

Fig. 2 View of a model rectilinear grid overlaid that cover the entire study area

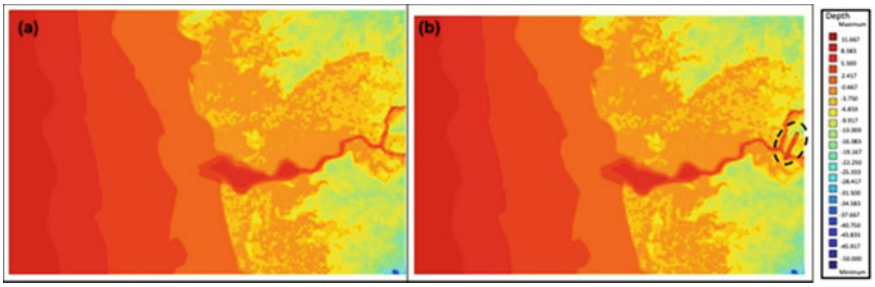

Fig. 3 Interpolated view of seabed contours and topography **a** without barrage, **b** with a barrage

3.3 Discharge

In the present study, discharge data at various locations in the Ambica basin were taken from water yearbook published by Central Water Commission, Surat, under Hydrological Observation Circle, Gandhinagar. As indicated in the book, the discharge observations in all sites were conducted once in a day by area velocity method. The width of the river is measured by an old conventional method using steel or wire rope/tape spread across the river and marking attached in it when river width is quite small. The data observed as above at the site are entered in the prescribed standard format to compute the total river discharge, and it is further scrutinized at various levels before finalization. The average runoff of Ambica River, in general, appears to be a random variable. The time series of discharge from 1979 to 2014 is as shown in Fig. 4.

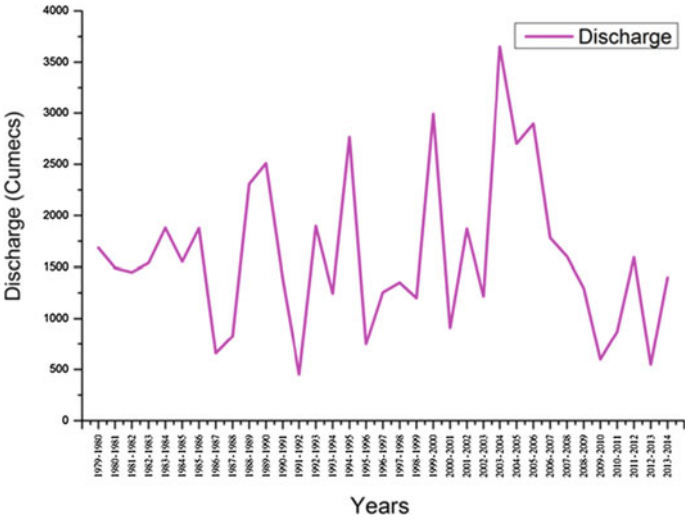

Fig. 4 Time series of discharge data from 1979 to 2014

4 Results

4.1 Water Level and Velocity

The developed model has been simulated for ten days that covers filed measurement period. The in situ measurement has been conducted on 07/10/2016 to estimate the water level and flow velocity using a total station and surface drifters. The measured values were used for comparison of simulated water level and velocity. The time series of simulated water level and velocity is as shown in Fig. 5. It can be seen from the results maximum water level, and velocity reaches 2.5 m and 1.65 m/s, respectively. The contour plots of water level variations for different discharge cases are as shown in Figs. 6, 7 and 8. The view of the inundation area can be seen in Fig. 9.

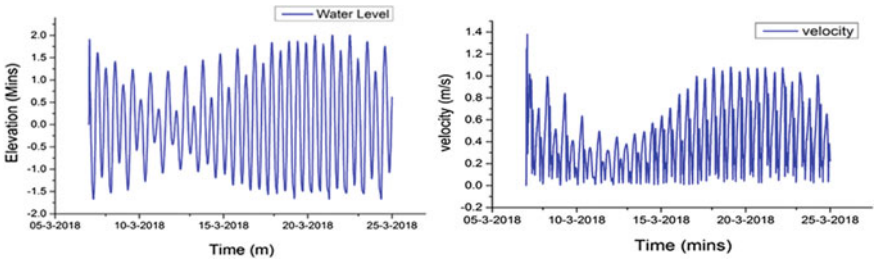

Fig. 5 Typical view of water level variation and velocity

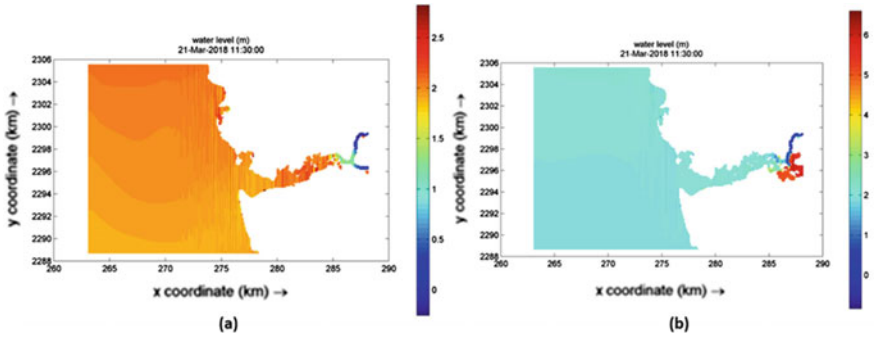

Fig. 6 Typical view of simulated water level variation with a discharge of 100 m^3/s. **a** without barrage, **b** with a barrage

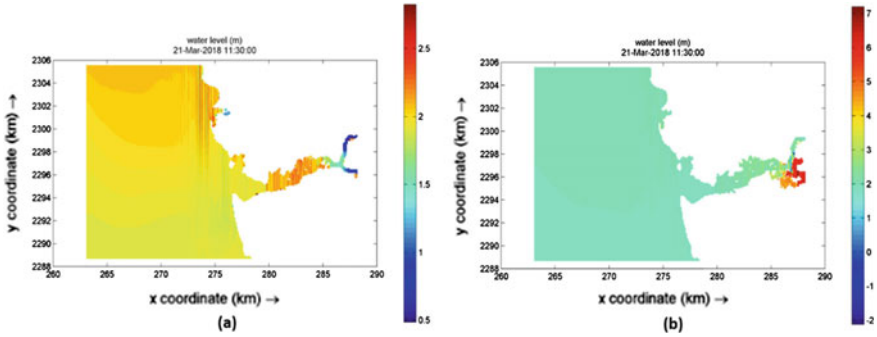

Fig. 7 Typical view of simulated water level variation with a discharge of 1500 m^3/s **a** without barrage, **b** with a barrage

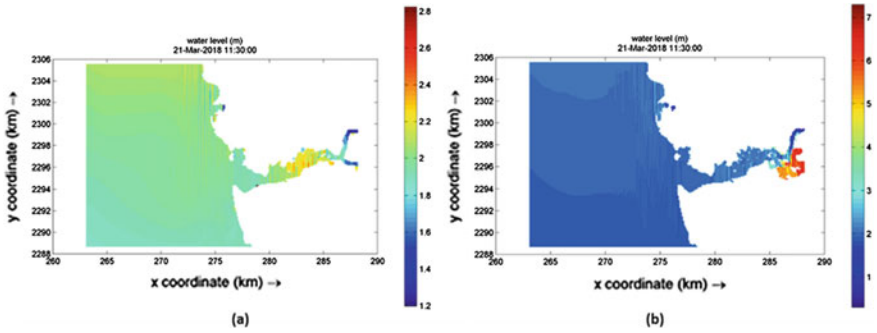

Fig. 8 Typical view of simulated water level variation with a discharge of 3000 m^3/s **a** without barrage, **b** with a barrage.

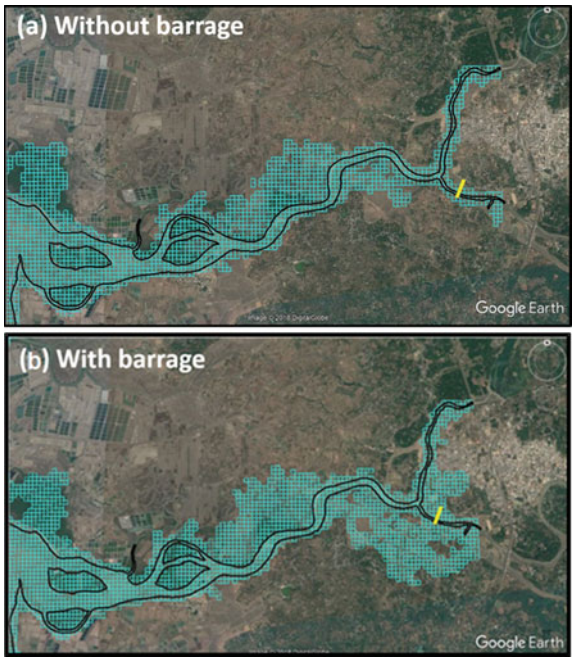

Fig. 9 Typical view of inundation area with extreme discharge condition (3000 m^3/s)

4.2 Intrusion of Salt Water

The model was simulated with a salinity value of 35 ppt at the open ocean boundary and 0.5 ppt at the upstream freshwater river boundary. Along with salinity, the discharge value of 500 m^3/s was applied on the upstream river boundary. The results obtained from the model were shown in Fig. 10. It can be seen from the figure that intrusion of salt water is less in case of with barrage simulation then without barrage. Hence, the construction of barrage will help to reduce the intrusion of salt water in this region. The view of saltwater intrusion without barrage condition is shown in Fig. 11.

5 Conclusion

This paper highlights the numerical modeling of flooding and salinity intrusion of Ambica river basin with the proposed tidal barrage. The hydrodynamic model has been developed, and the simulated results were analyzed to estimate the inundation area. The results show that the maximum surface velocity reaches 0.9 m/s inside the river, and the increase in flood level is about 4 m from the ground level. The inundation area was calculated for different discharge cases with and without tidal

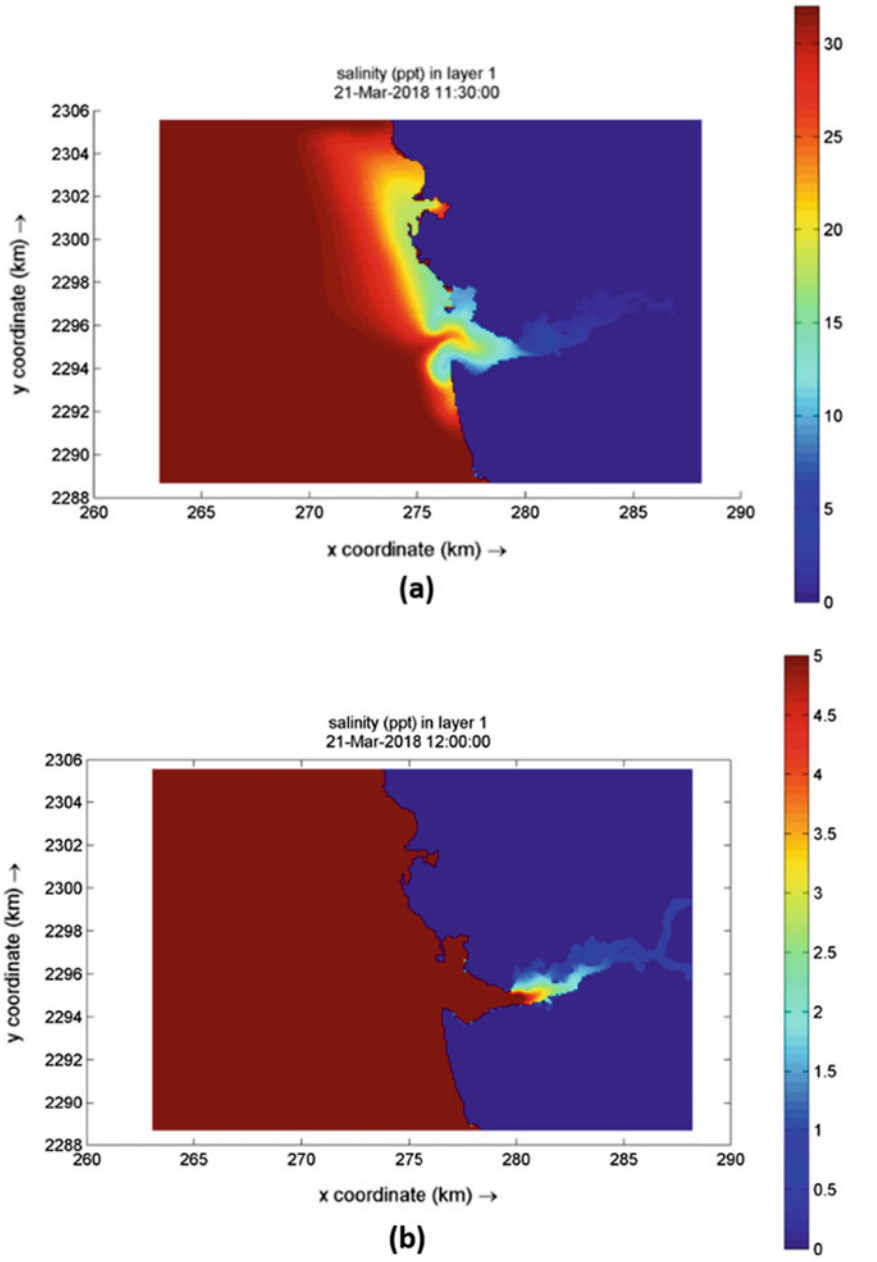

Fig. 10 Typical views of saltwater intrusion with maximum discharge condition **a** without barrage, **b** with a barrage

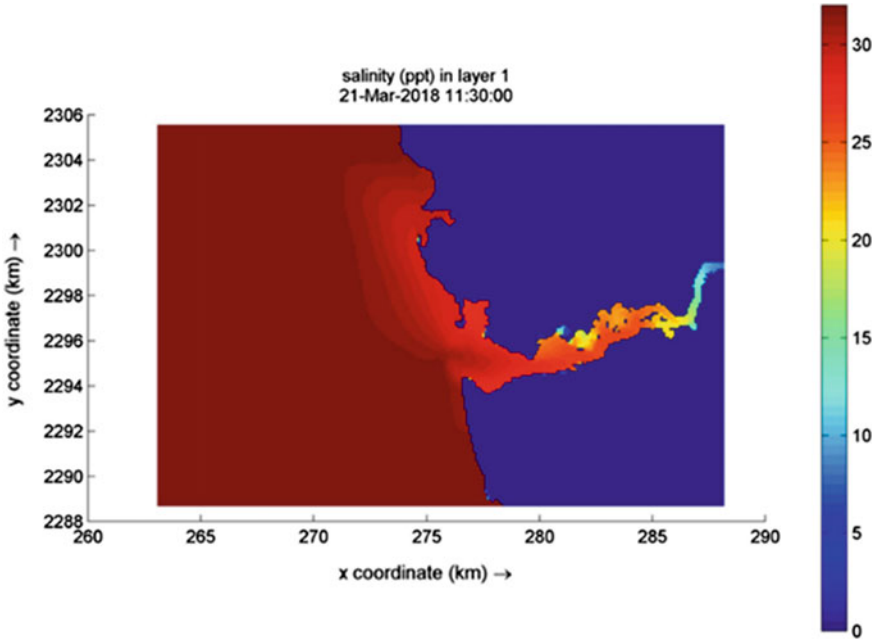

Fig. 11 View of saltwater intrusion without discharge and barrage condition

barrage. It is concluded from the results that the construction of barrage will increase the flooding and reduce saltwater intrusion nearby low-lying areas.

References

1. Adhikari Y, Osti R, Noro T (2010) Flood-related disaster vulnerability: an impending crisis of megacities in Asia. J Flood Risk Manage 3(3):185–191
2. Arakawa A, Suarez MJ (1983) Vertical differencing of the primitive equations in Sigma coordinates. Mon Weather Rev 111:34–45
3. Cook A, Merwade V (2009) Effect of topographic data, geometric configuration and modelling approach on flood inundation mapping. J Hydrol 377(1–2):131–142
4. Egbert GD, Bennett AF, Foreman MGG (1994) Topex/Poseidon tides estimated using global inverse model. J Geophys 99:24821–24852
5. Gallegos HA, Schubert JE, Sanders BF (2009) Two dimensional, high-resolution modelling of urban dam-break flooding: a case study of Baldwin Hills, California. Adv Water Res 32(8):1323–1335
6. Haider S, Paquier A, Morel R, Champagne J-Y (2003) Urban flood modelling using computational fluid dynamics. Proc ICE Water Marit Eng 156(2):129–135
7. Hervouet J-M (2000) TELEMAC modelling system: an overview. Hydrologic Processes 14(13):2209–2210
8. Lesser GR, Roelvink JA, van Kester JATM, Stelling GS (2004) Development and validation of a three-dimensional morphological model. Coast Eng 51:883–915

9. Lindner GA, Miller AJ (2012) Numerical modelling of stage-discharge relationship in urban streams. J Hydraulic Eng 59:590–596
10. Mignot E, Paquier A, Haider S (2006) Modelling floods in a dense urban area using 2D shallow water equations. J Hydrol 327(1–2):186–199
11. Smith JA, Miller AJ, Baeck ML, Nelson PA, Fisher GT, Meierdiercks KL (2005) Extraordinary flood response of a small urban watershed to short-duration convective rainfall. J Hydrometeorol 6(5):599–617
12. Wilson CAME, Bates PD, Hervouet J-M (2002) Comparison of turbulence models for stage-discharge rating curve prediction in reach-scale compound channel flows using two-dimensional finite element methods. J Hydrol 257(1–4):42–58

A New Semi-analytical Shoreline Model for the Assessment of Complicated Coastal Systems

D. E. Reeve, A. Valsamidis, M. Ranjan Behera, P. Chowdhury, and H. Karunarathna

Abstract A new semi-analytical solution to the one-line model is presented in this work which can be used for the description of complicated coastal systems. An application of the semi-analytical model to Borth case study in Wales, UK, is presented. Additionally, Calangute beach in Goa, India, will be discussed as a future case study where the model will be applied.

Keywords One-line model · Shoreline evolution · Beach modelling · Coastal erosion

1 Introduction

As coastal erosion threatens most beaches worldwide [2], including the properties near the beaches, coastal engineers develop process-based models to simulate the coastal morphological evolution and investigate the performance of proposed or installed coastal defence schemes. The one-line model, based on the concept of continuity of sediment material and a longshore sediment transport equation (e.g. [5 6]), has been proved to be a robust tool for this purpose (e.g. [9]). Specifically, numerical solutions to the one-line model can incorporate very effectively many coastal elements into the modelling process (see, e.g., [3]).

D. E. Reeve (✉) · A. Valsamidis · H. Karunarathna
College of Engineering, Swansea University, Fabian Way, Skewen, Swansea S1 8EN, UK
e-mail: d.e.reeve@swansea.ac.uk

A. Valsamidis
e-mail: antonios.valsamidis@swansea.ac.uk

H. Karunarathna
e-mail: h.u.karunarathna@swansea.ac.uk

M. R. Behera · P. Chowdhury
Indian Institute of Technology Bombay, Powai, Mumbai 400076, India
e-mail: manasa.rb@iitb.ac.in

V. Sundar et al. (eds.), *Proceedings of the Fifth International Conference in Ocean Engineering (ICOE2019)*, Lecture Notes in Civil Engineering 106,
https://doi.org/10.1007/978-981-15-8506-7_18

In contrast, analytical solutions to the one-line model are imposed to many restrictions; however, they can be useful when independent studies of specific coastal processes are executed [4].

2 Case Study

2.1 General Information About Borth Beach

Borth beach near the fishing village of Borth is located in Cardigan Bay in Mid Wales, facing the Irish coasts (Fig. 1a). It extends northwards from the cliffs of Craig y Delyn up to the Dyfi estuary 5 km away (Fig. 1b). The hard rock headland of Pen Y. Graig which from now on will be briefly mentioned as the headland constitutes the southern boundary of Borth beach. The sand in Borth beach is fine with an approximate grain size $D_{50} = 0.3$ mm (e.g. [1]). Borth is a touristic attraction, offering a variety of marine activities, for instance: water skiing, sailing, surfing, motor boating, canoeing and fishing. However, it is exposed to waves with predominant direction: SW-NE. They can be either wind-generated offshore wards of Borth or swell waves which may travel great distances in the Atlantic Ocean before reaching the Welsh coasts. Borth beach is not naturally protected by such waves and consequently is subjected to a serious erosion threat. To this end, various structures have been applied for the coastal defence of Borth, for instance breastworks and timber groynes. However, all the previous coastal protection structures have exceeded their life span, and a new coastal defence scheme was constructed in 2011.

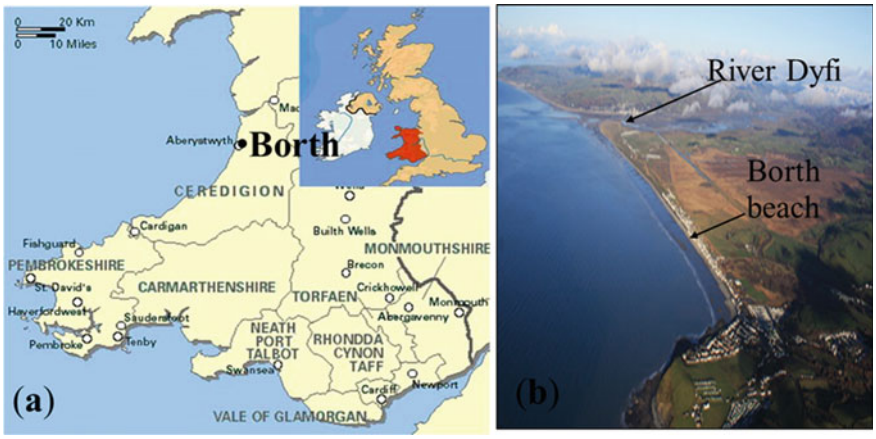

Fig. 1 **a** Location of Borth in Wales; **b** Borth beach extends from the headland in the south up to the Dyfi estuary in the north (adopted from Valsamidis et al. [10])

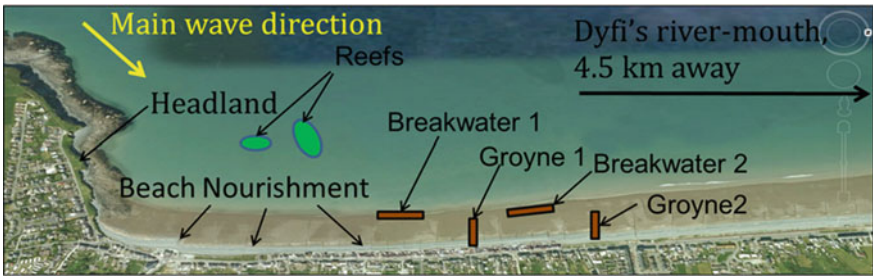

Fig. 2 Schematic representation of the Borth coastal defence scheme

It comprises of two rocky groynes, two rocky detached breakwaters, initial beach nourishment and two multi-purpose reefs (Fig. 2).

The local wave climate in conjunction with the new coastal defence scheme is the dominant factor of morphodynamic evolution at Borth beach. However, the Dyfi estuary in the vicinity of Borth is a counterpart factor which had to be taken into the account as well. Consequently, the following subsection provides more specific information about Dyfi estuary.

2.2 Dyfi Estuary

Dyfi estuary (Fig. 3) is located about 5 km away from the southern boundary (the headland) of Borth beach. Two rivers flow into this estuary: the Dyfi and the Leri, having an annual flow of 25 m^3/s and 5 m^3/s, respectively [8]. The estuary was named though after Dyfi River since it is the primary river discharging into it. The length of the estuary is 9 km, and its mouth (which from now on will be called: river mouth) has an active width of 800 m since part of it is blocked by Ynyslas spit which has been developed at the southern bank of the river mouth [1].

The distance from the headland to the middle of the active river mouth is $x_R =$ 6900 m. The short of sediment material in Dyfi estuary consists mostly of sand with grain size between $d_{50} = 0.24$ mm and $d_{50} = 0.35$ mm.

3 Methodology

Aiming at an analytical model with the capability to describe complicated coastal systems, a combination of semi-analytical solutions was used. Specifically, the semi-analytical solution introduced by Reeve [7] for the assessment of shoreline evolution in the vicinity of a groyne and the semi-analytical solution developed by Zacharioudaki and Reeve [11] for the assessment of shoreline evolution in a groyne compartment were combined via the appropriate internal boundary condition. The result was

Fig. 3 Mouth of Dyfi estuary; on the right-hand side part of the photo is Ynyslas spit and further away on the same direction of the Borth beach

a more sophisticated semi-analytical model, capable of describing the complexity of Borth case study in a more accurate way.

The key idea was to divide the case study into three discrete areas and assess separately the shoreline evolution in each one of them. Then with the proper internal boundary condition, exchange of sediment material would be allowed among these areas, and eventually, the beach at Borth might be modelled as a whole.

Borth beach was analysed in the following three discrete areas (Fig. 4).

Area 1, lying between the headland and Groyne 1, with a total length of 800 m is a groyne compartment. Area 2, extending from Groyne 1 to Groyne 2, is also a groyne compartment. Its total length is 300 m. Finally, Area 3 is considered to be

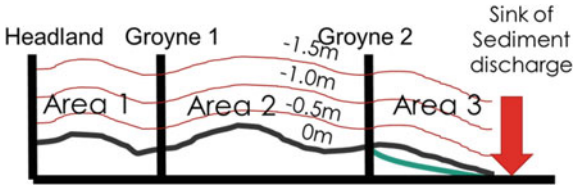

Fig. 4 The case study of Borth has been divided into three discrete areas (Area 1, 2 and 3) The coastal defence system has been represented with groynes: 1 and 2. The Dyfi river mouth which acts as a sink of sediment material has also been taken into account

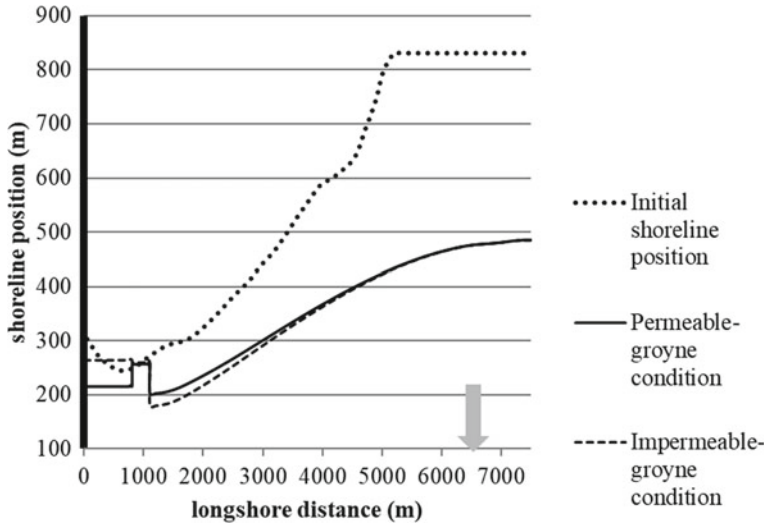

Fig. 5 The vertical arrows at 800 and 1100 m away from the headland indicate groynes 1 and 2, respectively. The grey arrow on the right-hand side of the case study marks the position of the sink of sediment material (Dyfi river mouth)

the part of the beach from Groyne 2 up to 6400 m away including the river mouth which is located 5800 m away from Groyne 2.

Next the new semi-analytical scheme was evaluated, and results are presented in Fig. 5 where the shoreline position at the end of the simulation period has been plotted versus the initial shoreline position (29/07/2007) and the corresponding shoreline position for the case that groynes 1 and 2 were considered impermeable and of infinite length. Thus, in the latter case, no exchange of sediment material between Areas 1, 2 and 3 was considered.

In addition to Fig. 5 where results are presented for the entire case study, the assessed shoreline position corresponding to each one of Areas 1, 2 and 3 is presented separately in Figs. 6, 7 and 8.

4 Conclusions

The semi-analytical model presented in this study will further be improved and will be applied to more case studies. The first targeted cases-study is the Calangute beach in Goa, India (Fig. 9). This is an open sandy beach located between two rocky headlands (Baga in the north and Aguda in the south). Calangute beach is situated on the west coast of India (15° 32′ 30″ N 73° 45′ 43″ E) and is about 7 km in length. The sediment size of this region is reported to be 600 μm.

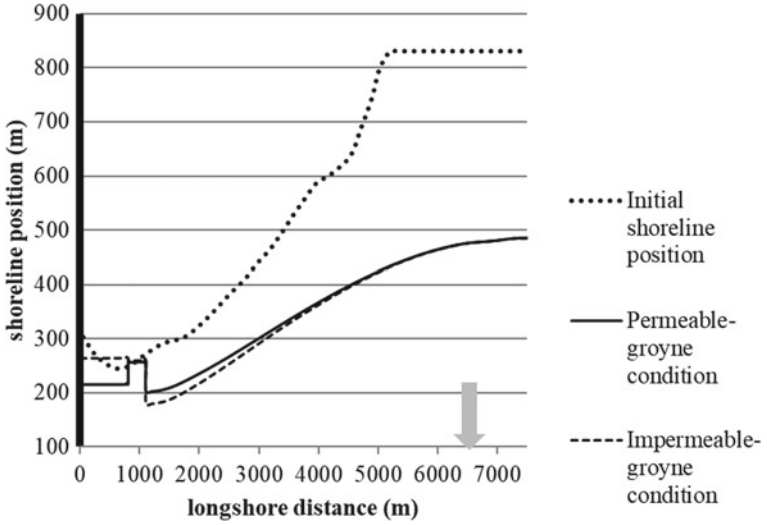

Fig. 6 The dotted line corresponds to the initial shoreline position, the dashed line illustrates the shoreline position for the case that Groyne 1 is considered impermeable, and the solid line shows the shoreline position for permeable groyne conditions at Groyne 1

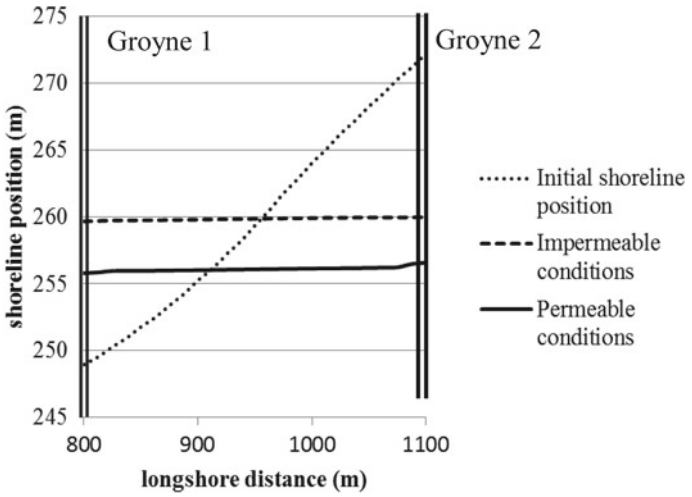

Fig. 7 The dotted line corresponds to the initial shoreline position, the dashed line illustrates the shoreline position for the case that groynes 1 and 2 are considered impermeable, and the solid line shows the shoreline position for permeable groyne conditions at groynes 1 and 2

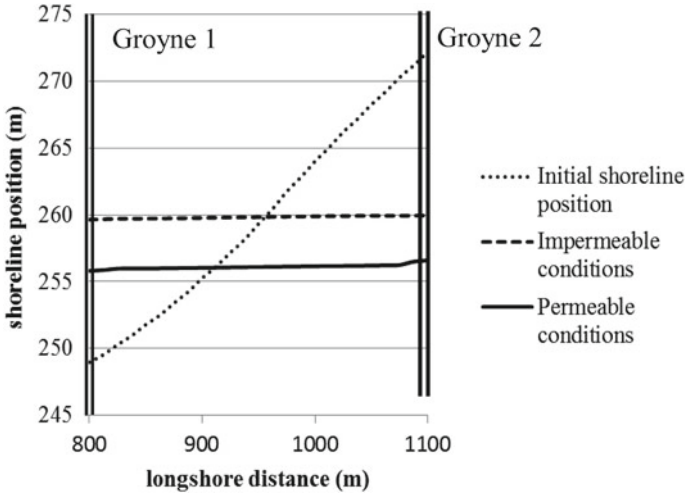

Fig. 8 The dotted line corresponds to the initial shoreline position, the dashed line illustrates the shoreline position for the case that Groyne 2 is considered impermeable, and the solid line shows the shoreline position for permeable groyne conditions at Groyne 2 impermeable, and the solid line shows the shoreline position for permeable groyne conditions at groynes 1 and 2

Fig. 9 Shoreline position in 1990 (black) and 2015 (magenta)

Regarding the sediment dynamics of Calangute beach, the overall littoral movement is towards north. Satellite images with minimal cloud coverage over the area of interest were extracted for 1990 and 2015. All images were then referenced to the latest 2015 image with clearly visible reference points which are identifiable in the entire period since 1990. This approach is expected not to affect the final result because our ultimate aim is to track relative shoreline position change. Shoreline evolution was computed using DSAS tool of Arc-GIS.

The south side of the beach was heavily eroded during this period and showed the maximum shoreline shift of about 60 m with maximum erosion of 2.8–3 m/year between 1990 and 2015.

References

1. Brown JM, Davies AG (2009) Methods for medium-term prediction of the net sediment transport by waves and currents in complex coastal regions. Cont Shelf Res 29:1502–1514
2. Dean RG, Dalrymple RA (2002) Coastal processes with engineering applications. Cambridge University Press, Cambridge, p 488
3. Gravens MB, Kraus NC, Hanson H (1991) GENESIS: generalized model for simulating shoreline change, Report 2, Workbook and System User's Manual. U. S, Army Corps of Engineers, Vicksburg
4. Hanson H (1987) GENESIS-a generalized shoreline change numerical model for engineering use. Lund Institute of Technology University of Lund, Lund
5. Larson M, Hanson H, Kraus NC (1997) Analytical solutions of one-line model for shoreline change near coastal structures. J Waterw Port Coast Ocean Eng 23:180–191
6. Larson M, Hanson H, Kraus NC (1987) Analytical solutions of the one-line model of shoreline change. In: Technical Report CERC-87-15, USAE-WES, Coastal Engineering Research Center, Vicksburg
7. Reeve DE (2006) Explicit expression for beach response to non-stationary forcing near a Groyne. J Waterw Port Coast Ocean Eng 132:125–132
8. Robins PE (2009) Development of a morphodynamic model of the Dyfi Estuary to inform future management decisions CAMS. Bangor University, Bangor, Volume 898a p. 86.
9. USACE (2002) Coastal engineering manual (CEM), 20314–1000. U.S Army Corps of Engineers, Washington, DC, p 86
10. Valsamidis A, Cai Y, Reeve DE (2013) Modelling beach-structure interaction using a Heaviside technique: application and validation. J Coast Res (65):410–415, ISSN: 0749-0208
11. Zacharioudaki A, Reeve DE (2008) Semianalytical solutions of shoreline response to time-varying wave conditions. J Waterw Port Coast Ocean Eng 134:265–274

Remedial Measures to Combat Sea Erosion Along West Coast of India

R. Sundaravadivelu, S. Sakthivel, and P. K. Suresh

Abstract The west coast of India from Kanyakumari (Cape Comorin) to Trivandrum bordering Arabian sea is a thickly populated one. Fishing is the main occupation of the hamlets. The coast is prone to southwest (June–September) and northeast monsoon (October–December) waves in every year. The southwest monsoon is severe along the coast creating heavy erosion resulting loss of valuable lands, roads, worship places and houses. Mandaikadu is one such affected coast located on the west coast of Indian Ocean. Studies in the form of field observations, bathymetry and numerical model studies were carried out. Based on the findings, groin field with six numbers were proposed, and field observations indicate littoral drift is directed towards west direction. The details of studies and effect of groins were highlighted in the paper.

Keywords Groin · Littoral drift · Numerical model

1 Introduction

The coastal regions of India are densely populated and nearly 20% of the total population of India living in these regions. Further, there is an increase in the developmental activities in the coastal regions in the recent years for shipping, setting up of industries, developing recreation centers, land reclamation and utilizing marine resources of various kinds. Further, the exploration of natural living and non-living resources in the ocean has necessitated construction of a variety of structures like jetties, dykes, seawalls, groins, platforms, pipelines, etc. which are linked to the economy of the coastal states and ultimately to our national economy. In order to combat erosion,

R. Sundaravadivelu (✉) · S. Sakthivel · P. K. Suresh
Department of Ocean Engineering, Indian Institute of Technology Madras, Chennai 600036, India
e-mail: rsun@iitm.ac.in

S. Sakthivel
e-mail: enggoecrd@gmail.com

P. K. Suresh
e-mail: sureshpk2000@gmail.com

V. Sundar et al. (eds.), *Proceedings of the Fifth International Conference in Ocean Engineering (ICOE2019)*, Lecture Notes in Civil Engineering 106,
https://doi.org/10.1007/978-981-15-8506-7_19

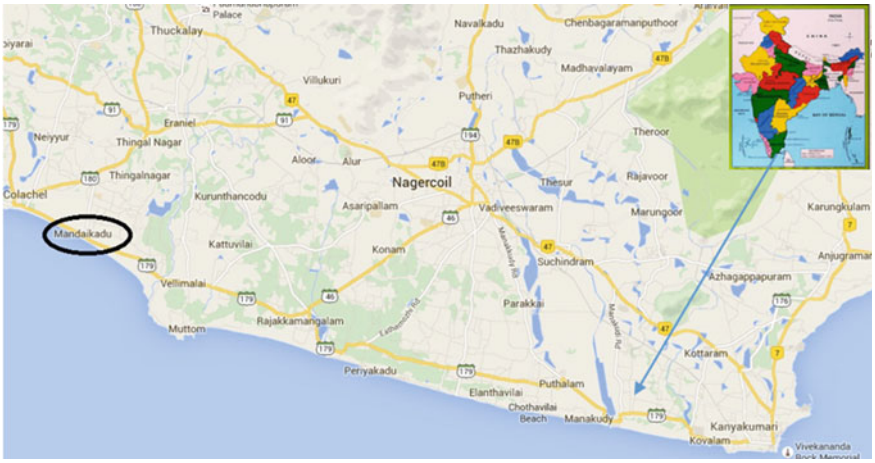

Fig. 1 Study area

construction of seawall had been the most widely adopted structural measure. Over the last few years, coastal protection measures like sea wall and groins were adopted. The results of the projects have been found fruitful as claimed by Sundar [1]. The western coast of Tamil Nadu in India is steep and characterized by several rocky outcrops. The coast experiences high swell waves during the southwest monsoon that break near the coast leading to heavy erosion of beaches, whereas during the post-monsoon season, the coast experiences accretion resulting in recovery of lost beaches. Mandaikadu is one such affected coast which has a latitude of 8° 23′ N and longitude 77° 32′ E on the west coast of Indian (Fig. 1). As a part of designing remedial measure, the studies were carried out.

2 Scope of the Work

As a part of protection measures, a groin field was designed based on the bathymetric details furnished by the client.

3 Methodology

The components include the following as detailed below.

- Bathymetric survey
- Field visit
- Desk studies

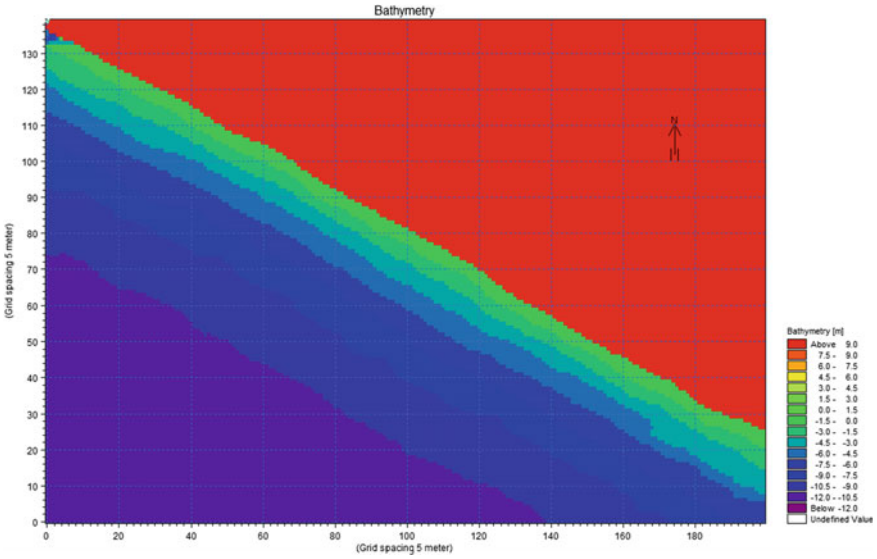

Fig. 2 Digitized bathymetry

- Numerical model studies
- Formulation of proposal

3.1 Bathymetric Survey

A detailed survey of the area covering a distance of 1100 m alongshore and 600 m towards water was carried out. A total of 1706 numbers of water depth points were collected. The shore is existing with an elevation of (+) 6.00 m at a distance of 50 m behind shoreline. The bed slope in water depth of (−) 10 m is 0.0455. The foreshore slope was seen up to a water depth of about (−) 10.00 m which is about 0.0455. The bed slope up to (−) 3.00 m is 0.060 indicating that profile has steeper slope in the shallow depth compared to deep water. This can result in run-up of wave height ranging from 1 to 3 m and break close to the shore. The digitized form of bathymetry and original one is shown vide Fig. 2.

3.2 Field Visit

In order to ascertain the details of coastal process activity along Mandaikadu coast, field visit was undertaken. The coast is found to be oriented in east–west direction from Kanyakumari to Trivandrum and takes a south–north orientation. The site has

a big church located very near the coast and a famous temple inside along east and west boundaries. Beach of width about 20 m is seen along the length. The coast undergoes severe erosion in southwest monsoon, and hence, temporary protections at selected location by dumping stones and retaining walls are noticed.

3.3 Desk Studies

Along the west coast, there is heavy erosion during southwest monsoon months and then deposition during the other months. Along this coast, the onshore–offshore transport is high during SW monsoon. The magnitude of erosion during SW monsoon increases from Manakudy to Erayumanthurai. This is due to an increase in the foreshore slope. This also indicates that the cross-shore sediment transport plays a major role along the west coast. The analyses of existing data on beach migration indicate that beaches along the coast are visible from January to May and disappear during southwest monsoon. This is because of wave actions almost normal to the shore and creating erosion profile. During the months of January to April, the occurrences of swell waves bring back the beach successfully. Beaches are seen on the east side of protruding structures indicating net longshore transport is on towards west.

3.4 Wave Climate

The data on wave climate is an important parameter while estimating the shoreline changes. Unfortunately, measured or visually observed wave data is available only for locations of port. Hence, numerical models were resorted to for the simulation of wave climate. In the present study, the wave data is adopted from the wave climate generated [4] by numerical models. The two wave models that were adopted are offshore spectral wave (OSW) or WAM model and near spectral wave (NSW) models of MIKE21 developed by Hydraulic Institute, Denmark [2]. The coast is influenced waves from south. Waves are predominantly from southeast, south and southwest. The monthly average wave climate is as described in Suresh [4] presented rose sketch of wave climate is prepared for three seasons, namely non-monsoon (NM) (January–May), southwest monsoon (SW) (June–September) and northeast monsoon (NE) (October–December). The diagrams are furnished vide Fig. 3.

3.5 Analyses of Critical Wave Climate

The west coast is oriented in E–W direction receiving waves from SE, SW direction. The bathymetry was digitized using Mike21 software. Parabolic mild slope model was used for analyzing a value of 3 m wave height. The results of the analyses were

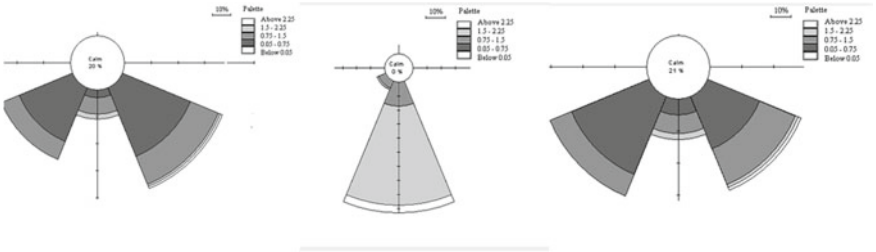

Fig. 3 Wave rose (NM, SW and NE)

plotted in the form of contours showing wave height for all the above-mentioned conditions. The results indicate high wave heights prevailing in the vicinity of shore (Fig. 4). This high energy waves finally dissipate on the coast leading to erosion of the coast.

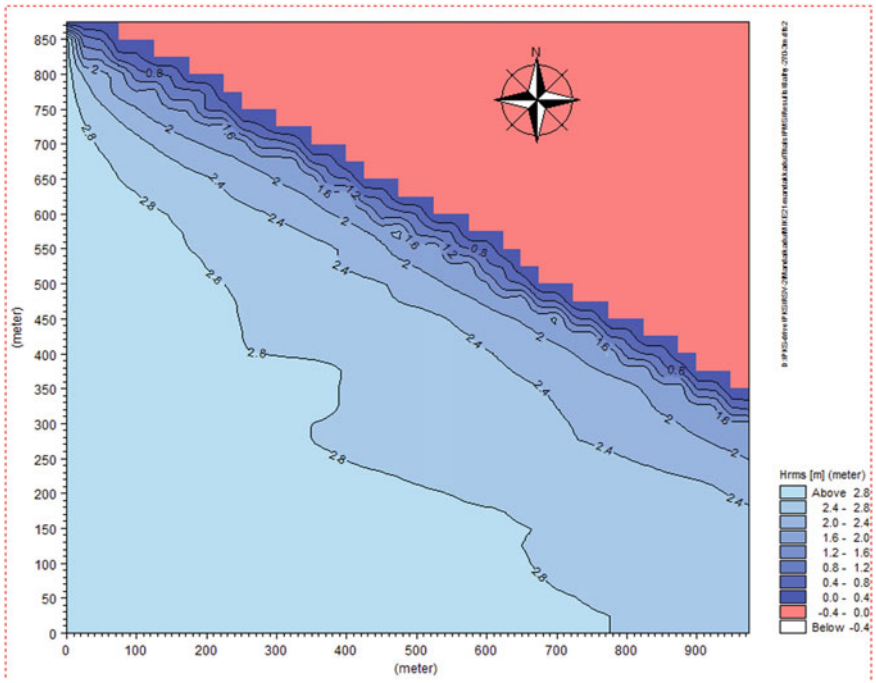

Fig. 4 Wave propagation from west

3.6 Tides

Mean high water spring (+) 1.20 m CD.
Mean sea level (+) 1.00 m CD.
Mean low water neap (+) 0.90 m CD.
Mean low water spring (+) 0.70 m CD.
A storm surge of up to 1.0 m is expected at site during design cyclone, based on the storm surge analysis.

3.7 Protection Measures

The protection measures consist of a groin field with five groins. The commencement of the groin field is from the coast adjacent to church. It consists of six groins G1, G2, G3, G4, G5 and G6 of length 65 m, 81 m, 90 m, 60 m, 63 m and 60 m, respectively. The corresponding depth at which the above groins terminate is (−) 2.0 m, (−) 3.0 m, (−) 3.0 m, (−) 2.0 m, (−) 2.0 m and (−) 2.0 m. The spacing between the groins G1 to G6 is 100 m, 150 m, 150 m, 150 m and 100 m, respectively (Fig. 5).

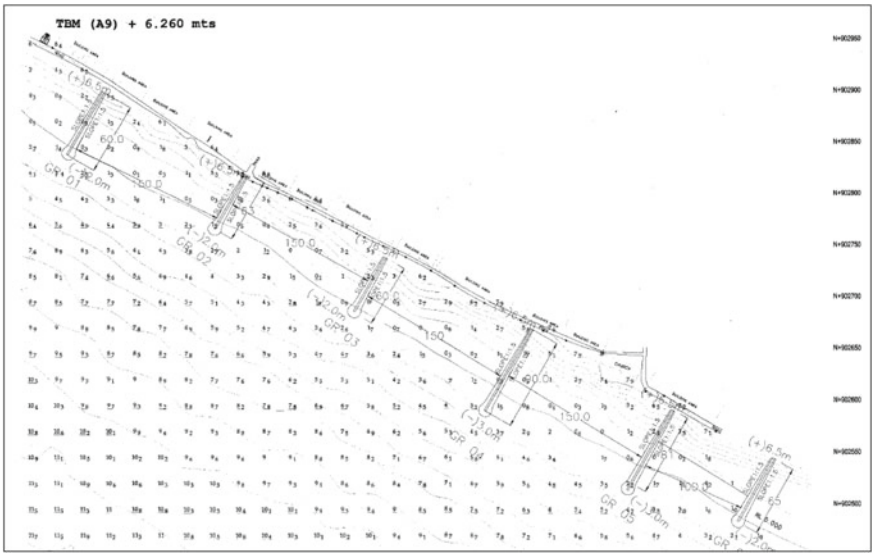

Fig. 5 Proposed groyne field

4 Breaker Angle Variation

The direction of sediment transport mainly depends on breaker angle values. The monthly breaker angle values are estimated based on Snell's law, and furnished (Fig. 6) alongshore current is responsible for accretion near protruding structures. Many empirical relationships are available. The important parameters are breaker angle, breaker height, slope, orientation of shoreline and particle size. As per the studies and findings of Suresh [4], the expression by Van Rijn [3] is suitable. The alongshore sediment transport was calculated using the approach of Van Rijn [3] for the coast.

The longshore sediment transport is dominant during the months of January–April and October–December. Based on the estimated values of breaker angle, the sediment transport in the alongshore direction is assessed as 0.05 million cubic meter. The direction as assessed from calculations and satellite imageries is directed towards west. During the other months, the formation of rip currents results in erosion profile formulations along the coastal reach discussed, and this type of formation is discussed.

4.1 Shoreline Evolution

The artificial interventions in the form of hard structures like groins will have impact on the existing shoreline and should be done carefully after doing prediction of shoreline changes. In the present study, six groins are recommended and the shoreline prediction adjacent to them is predicted for one year [5]. These predictions are based on the approach of Kraus and Harikai [6]. The procedures adopted by Suresh et al. [7] are adopted for assessing the changes along the shore in the presence groin field. The predictions indicate that groins will be bypassed. After the initial construction, it is to be provided with a "T" head in later stage. The construction commenced in December 2017. The four groins namely G3, G4, G5 and G6 has commenced. G3

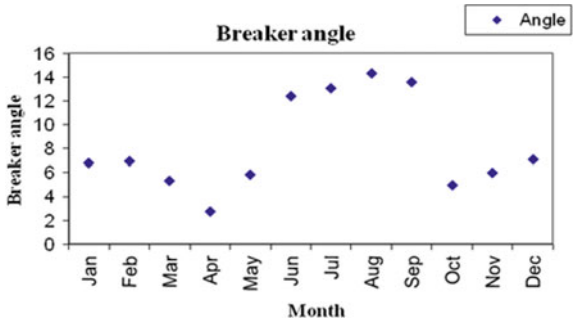

Fig. 6 Breaker angle

Fig. 7 Pre- and post-project scenario

is almost completed. The beach formation up to 80 m was noticed by January 2019, and it is offering very good protection against the waves (Fig. 7).

5 Conclusion

The coast under study is under heavy threat of erosion. The groin field was proposed after detailed bathymetry, desk studies and numerical modeling. The post-performance of the project indicates that model predictions were reasonably well, and once completed in full fledge, the erosion will be minimized. The net littoral drift predicted towards west was well validated by beach observation on east side of groins.

References

1. Sundar V (2005) Behaviour of shoreline between groin field and its effect on the tsunami propagation. In: Proceedings of solutions to coastal disasters conference of ASCE, 8–11, Charleston, South Carolina, USA
2. Danish Hydraulic Institute DHI (2001) User manual and reference guide for LITPACK and MIKE21
3. Van Rijn LC (2001) Longshore sediment transport. Delft Hydraulics
4. Suresh PK (2010) Ph. D thesis. Studies on the nearshore sediment dynamics along Tamil Nadu Coast. IIT Madras, Chennai, India
5. Sundaravadivelu R (2016) Design report for construction of groyne at mandaikkadu, kannyakumari. IIT Madras
6. Kraus NC, Harikai S (1983) Numerical model for shoreline changes of Oarai Beach. Coastal Eng l7: 1–28
7. Suresh PK, Sundar V, Sannasiraj S (2010) Longshore sediment transport and shoreline evolution along the coast south of Chennai, India. In: 17th IAHR-APD congress at New Zealand

Numerical Study on Flow Around Circular Conduits in Tandem Arrangement at Higher Re of O (10^6)

S. R. Jaya Chandran, K. Murali, Purnima Jalihal, and Abhijeet Sajjan

Abstract Risers are vertical offshore circular conduits that connects the reservoir beneath the water surface to a fixed or floating platform at the water surface, when the riser are subjected to sea currents the flow started to separate from its outer surface and vortices are formed in the downstream leads to vortex shedding. So there is need to spoil vortex shedding and suppress Vortex-induced vibration (VIV) to prevent damage on structures and on the other hand there is equal chance for utilization of energy as sustainable source from the ocean currents. The present numerical study is the done on larger diameter circular conduits which is used to draw cold water from deeper water depths for floating barge desalination plant deployed by National Institute of Ocean Technology (NIOT) would be susceptible to vortex-induced vibrations. Two such conduits held together in tandem arrangement using spacer is studied extensively for higher Re of O (10^6) in this work. The aspect ratio (L/D) of the cylinder is an important parameter to be considered. In this study modeling of cylinder for aspect ratio of 9 is chosen to capture the 3D effect along the length of the cylinder. The present work is focused on studying flow behavior around the conduits and its vortex shedding using commercial CFD software STAR-CCM+. The numerical simulation was carried out at Re of O (10^6) for tandem arrangement of 2D center to center spacing of Re ranging from 0.8×10^6 to 3.2×10^6. In this orientation the effect of lift, drag and pressure variation along the length and also on circumference of conduits was analyzed and it is correlated with the various flow velocities of circular conduits.

Keywords Vortex-induced vibrations (VIV) · Computational fluid dynamics (CFD) · STAR-CCM+

S. R. Jaya Chandran (✉) · K. Murali
Indian Institute of Technology Madras, Chennai 600036, India
e-mail: jayachan.iitm@gmail.com

P. Jalihal · A. Sajjan
National Institute of Ocean Technology, Chennai 600036, India

V. Sundar et al. (eds.), *Proceedings of the Fifth International Conference in Ocean Engineering (ICOE2019)*, Lecture Notes in Civil Engineering 106,
https://doi.org/10.1007/978-981-15-8506-7_20

1 Introduction

Vortex-induced vibration is a well-known challenge for circular structure deployed in the field of offshore engineering because of its practical application such as riser, vertical and slender structures. Due to the effect of VIV, these kinds of structure are subjected to high amplitude oscillation which leads to structure failure and tremendous economic loss. Since vortex-induced vibration is a nonlinear phenomenon in which structure oscillation is highly influenced by the vicinity wake disturbance and this leads to changes in induced forces on the structure. The flow across the structure causes alternate shedding of vortices result in hydrodynamic forces in cross and inline directions. The frequency of cross flow force follows the Strouhal relation (St = Fv D/U). In general, St varies from 0.19 to 0.21 [1] for the Re ranging from 10^2 to 10^5. Beyond this, it increases with Re. When the shedding frequency amount of energy from the flow thereby sustaining its amplitude of vibration at a relatively high level. This phenomenon is known as vortex-induced vibration (VIV). In order to equal to its natural frequency it is called lock-in, the cylinder extracts the maximal possible understand the effect of vortex shedding on stricture, the structure is customized ad rigid and steady flow is passed over it.

2 Work Methodology

2.1 Computational Domain

The Computational domain forms the environment where the solution is calculated. Geometry parts are used only to define the faces, edges, and vertices that make up the surfaces of the model. The simulation domain on which mesh is generated, and for which physics is solved, is defined using regions, boundaries, and interfaces. An essential part of the process in setting up your simulation is therefore to define the relationship between geometry parts and regions, boundaries, and interfaces. In this study computation domain is 28D long 21D wide, where D is the diameter of the conduit. The distances of the upstream and downstream boundaries are 5D and 20D. In the fluid domain the direction of flow is specified from left to right. In the numerical simulation cylinder is stationary and rigid. Computational domain is given in Fig. 1.

2.2 Boundary Conditions

There are several boundary conditions needed to solve the numerical equation of the flow field. Velocity inlet, pressure outlet, symmetry plane, free slip wall, no slip wall are used in this study.

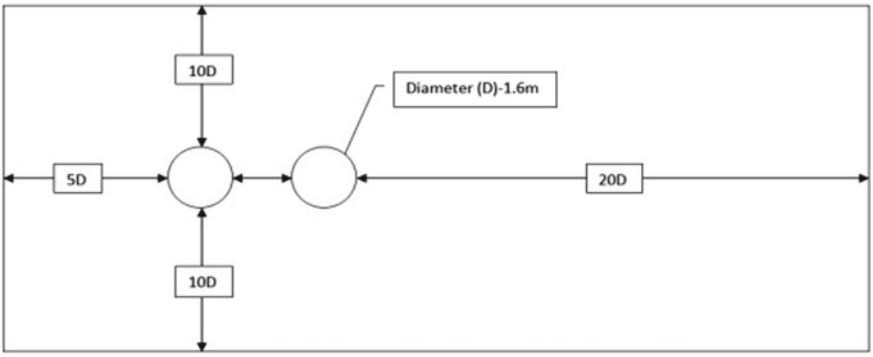

Fig. 1 Schematic diagram

Inlet—velocity inlet.
Outlet—pressure outlet.
Two sides—symmetry plane.
Top and bottom—wall (free slip).
Cylinder—wall (no slip).

2.3 Mesh Configuration

The mesh of computational domain is the discrete locations at which the variables are to be calculated and to be solved. The mesh divides the solution domain into a finite number of sub domains, for instance elements, control volumes etc., in which the physics solvers use to provide a numerical solution. Presently in this work two blocks are provided in the background region for applying volumetric control to make refinement in vicinity of conduits as shown in Figure. And it has the dimension 0–44.8 m in x direction, 0–33.6 m in y direction and 0–14.4 m in z direction Figure. The meshing models selected for generation of mesh are surface remesher and trimmed mesher (Fig. 2; Table 1).

2.4 Physics Modeling

Physics model in STAR-CCM+ defines how a physical phenomenon takes place in a continuum and what mathematical formulation is used to generate the solution (Table 2).

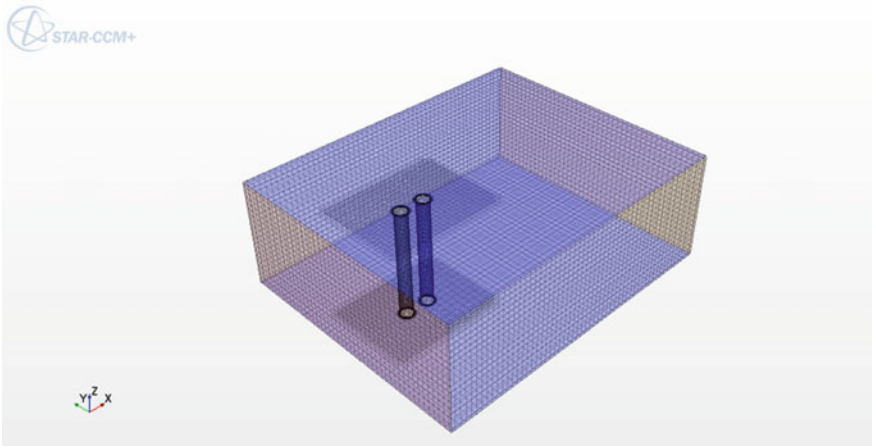

Fig. 2 Computational mesh

Table 1 Meshing details of mesh

Node	Value
Base size	0.1 m
Maximum cell size	160 mm (160% of base)
Minimum cell size	5 mm (5% of base)
No. of cells	9,845,214

Table 2 Physics models

Material	Liquid water
Time	Implicit unsteady
Flow	Segregated flow
Viscous regime	Turbulent
Turbulence model	RANS

2.5 Material Modeling

The material model is responsible for managing the material that is substance being simulated in the continuum. In this study circular conduit is fully submerged in the water. Hence single phase model is selected. So the computational domain contains water. The properties of water used are as shown in Table 3.

Table 3 Material model

Material	Density	Dynamic viscosity
Water	1025 kg/m^3	8.887 E−4 Pa s

2.6 Modeling Flow

The Segregated Flow model is an alternative for incompressible or mildly compressible flows, particularly when computational resources are an issue, so the segregated flow model is selected which is suitable for incompressible flow. The Segregated Flow model solves the flow equations (one for each component of velocity, and one for pressure) in a segregated or uncoupled manner. The linkage between the momentum and continuity equations is achieved with a predictor–corrector approach. The Implicit Unsteady model is the only unsteady model available with the Segregated Flow and it uses the Implicit Unsteady solver. Since segregated flow model is selected, implicit unsteady model is selected.

2.7 Solvers

Solvers control the solution and are activated once per iteration. Typically, a model elects the solvers that are required. Different models can use the same solver and sometimes models need more than one solver. Some models control other models and some only perform tasks when the solution is initialized. For this reason, not all models elect solvers. Models can also elect solvers that perform subsidiary tasks in addition to the solver that the model elected to control it. Following solvers have been used in this study.

2.8 Solver Parameters

In order to solve present problem certain parameters are needed to be fix so that computational grid can be solved effectively to achieve approximate solution of real problem. The solver parameters used in present investigation are listed in Table 4.

Table 4 Solver parameters

Parameters	Adopted solver settings
Solver	Implicit unsteady
Velocity formulation	Absolute
Viscous model	k-SST model
Operating pressure	101,325 Pa
Gravitational constant	9.81 m/s^2
Water density	1000 kg/m^3
Water viscosity	0.0010 kg/m s

Table 5 Stopping criteria

Time step (implicit unsteady)	0.08 s
No. of iterations per time step	5
Maximum physical time	200 s

2.9 Stopping Criteria

Stopping criteria allows specifying the solution runs time and the conditions in which simulation need to stops iteration. Each specified stopping criterion is evaluated at the completion of every simulation step and a logical rule is used to determine if the interaction of all of the criteria stops the solver. Condition given in this study is shown in Table 5.

3 Results and Discussion

3.1 Validation of CFD Approach for Single Cylinder

The computational domain, grid generation, solver properties are same as that used in Sect. 3.4. Mean drag coefficient and Strouhal number for riser has been validated.

Flow Velocity—1 m/s
Flow Reynolds no—1.6×10^6
L/D Ratio—9
Length—14.4 m
Shedding Frequency (f_s) = 0.18/s
Strouhal number = f_s x D/V = 0.288
Strouhal number from the above vortex shedding frequency is 0.288 (Figs. 3 and 4).

3.2 Comparison on Flow Over an Isolated Conduit for Various Velocities

In this part, results from numerical simulations for the flow over a single conduit for various velocities have been summarized. This numerical study is performed to establish drag and lift coefficients of a conduit and the result are also investigated comparatively (Figs. 5, 6, 7 and 8).

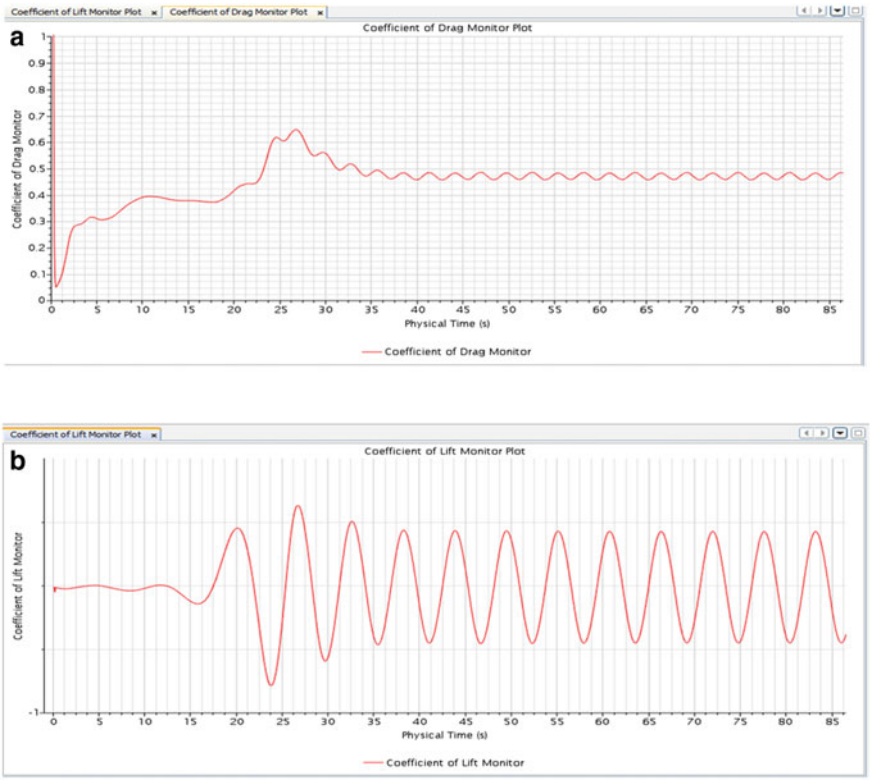

Fig. 3 **a** C_d plot of flow over a single conduit, **b** C_l plot of flow over a single conduit

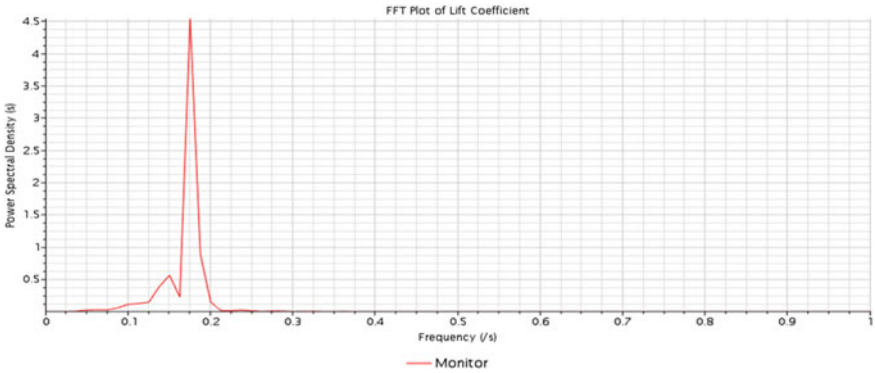

Fig. 4 FFT of C_l plot for flow over a single conduit

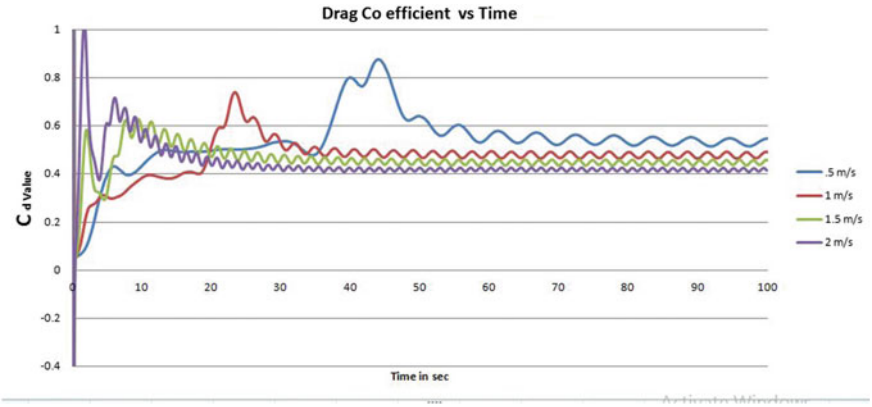

Fig. 5 C_d plot of flow over a single conduit for various flow velocities

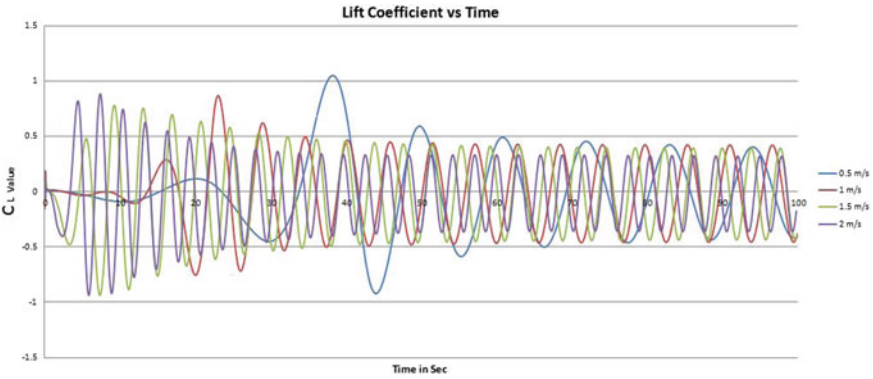

Fig. 6 C_l plot of flow over a single conduit for various flow velocities

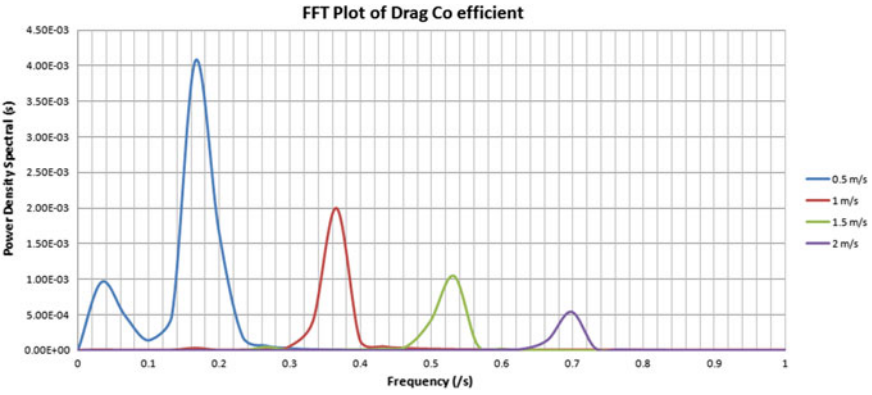

Fig. 7 FFT of C_d plot for flow over a single conduit for various flow velocities

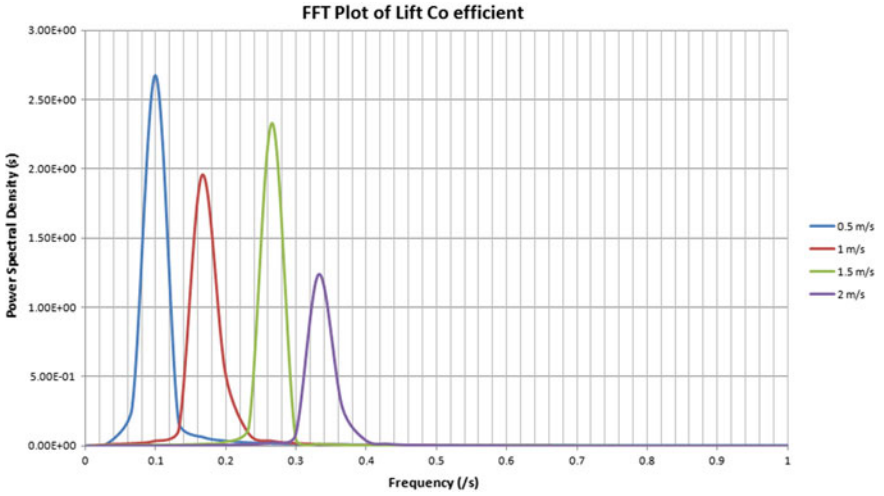

Fig. 8 FFT of C_l plot for flow over a single conduit for various flow velocities

3.3 Tandem Arrangement

In this case, conduits are in tandem arrangement is behind, shown in Fig. 9, vortex scalar scene of conduit in tandem arrangement. The separated flow slightly reattaches onto the downstream cylinder it would have been distinct if both cylinders were of same size. The mean drag forces of both cylinders, in particular the downstream cylinder, decrease rapidly due to the change of pressure distributions. The reattachment of the separated flow not only suppresses the vortex shedding from the

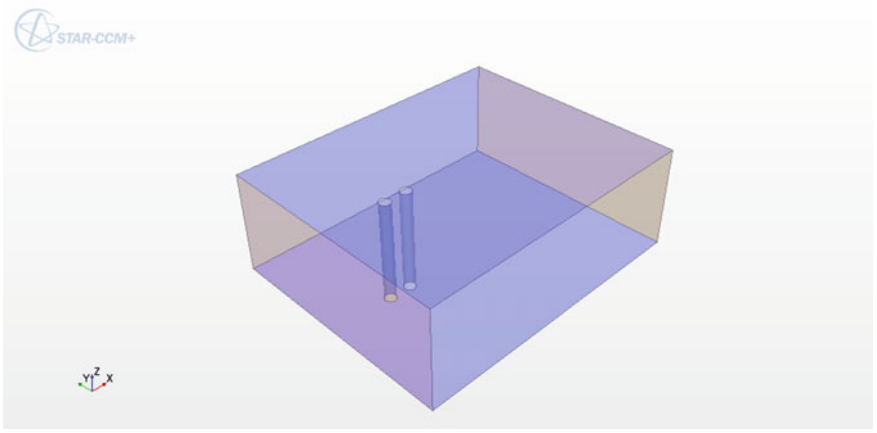

Fig. 9 Geometry of flow domain

upstream cylinder but also affects the shedding frequency of the downstream cylinder (Figs. 10, 11, 12).

A peculiar observation which we can see only in this tandem arrangement is that the drag coefficient of the conduit in downstream has negative values. Figure 13

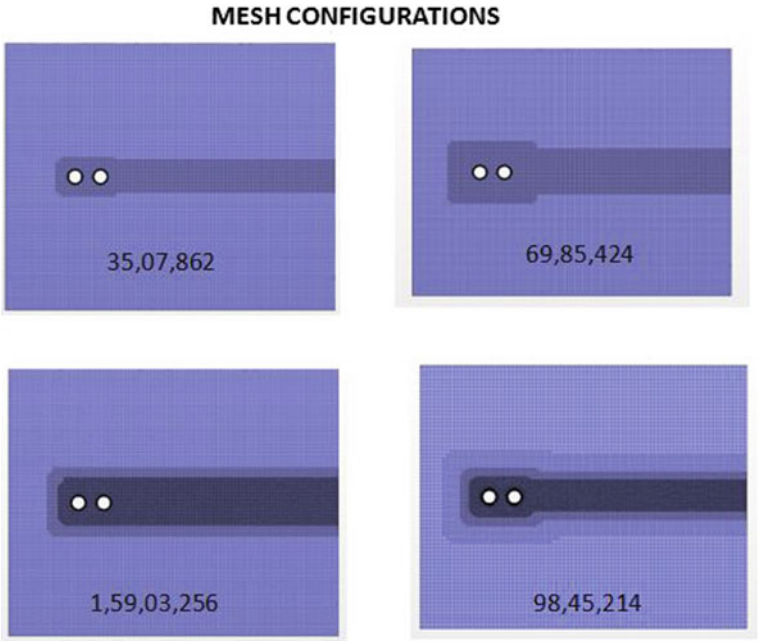

Fig. 10 Mesh configurations

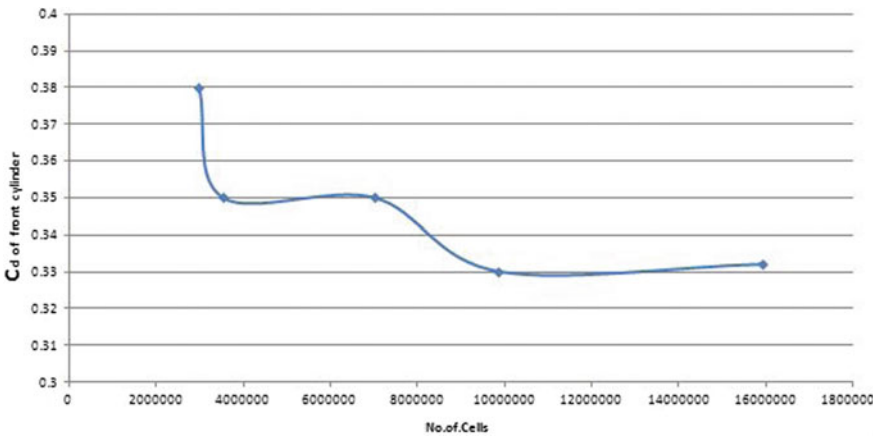

Fig. 11 Plot for C_d of front cylinder versus No. of. cells

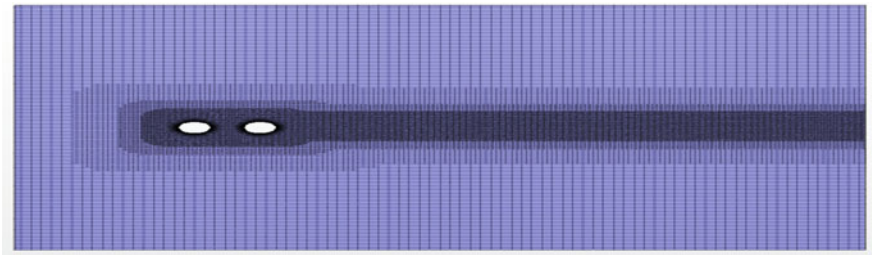

Fig. 12 Modified mesh configuration

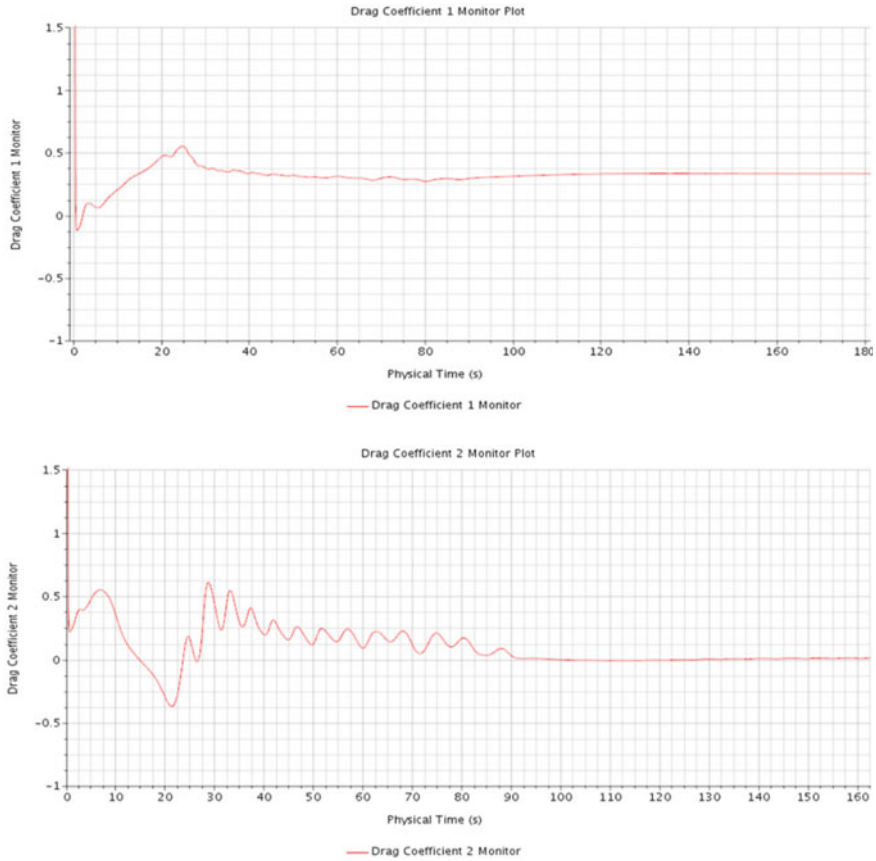

Fig. 13 C_d plot of flow over a conduit in tandem arrangement for Re 1.6×10^6

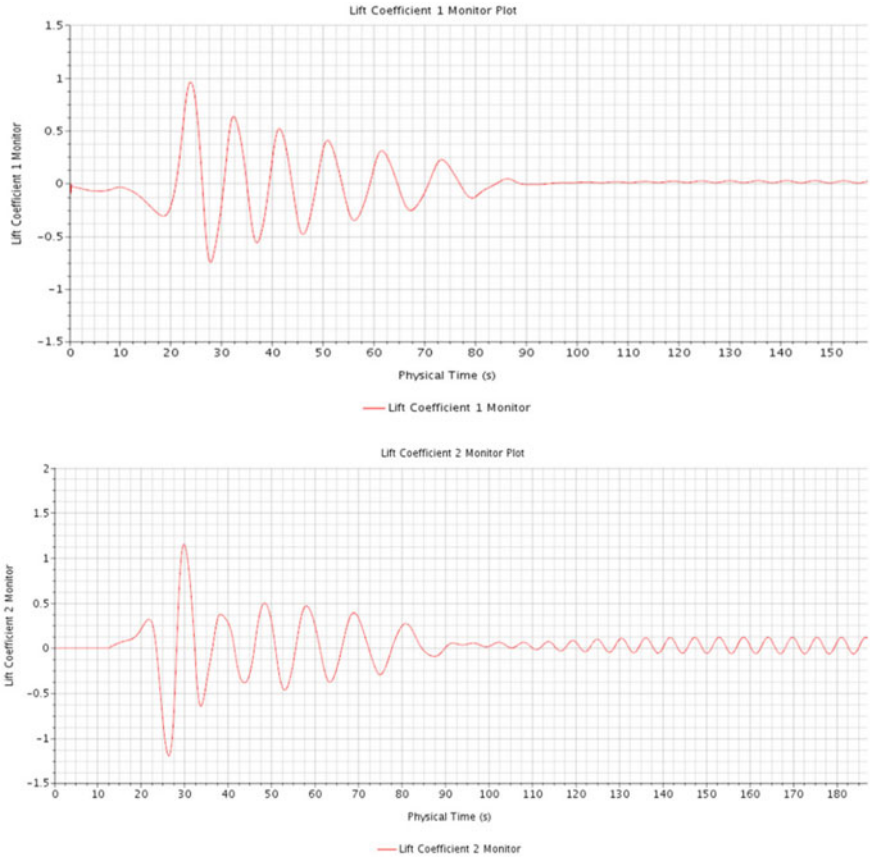

Fig. 14 C_l plot of flow over a conduit in tandem arrangement for Re 1.6×10^6

exemplifies this phenomenon. Lift force as well was found to be elevated when compared to an isolated conduit, paradigm of this occurrence can be seen in Fig. 14.

3.4 Mesh Convergence Study

Numerical simulations are approximations for real problems. Numerical solution of any problem included errors due to discretization of computational domain into control volume, machine and truncation error. Machine and truncation can be minimized by using appropriate techniques. However discretization error should minimize, so that approximate solution have no dependency on computational grid. Grid independence analysis is very important to achieve previous conditions. A grid independence analysis was performed. Three different grids have been selected on the

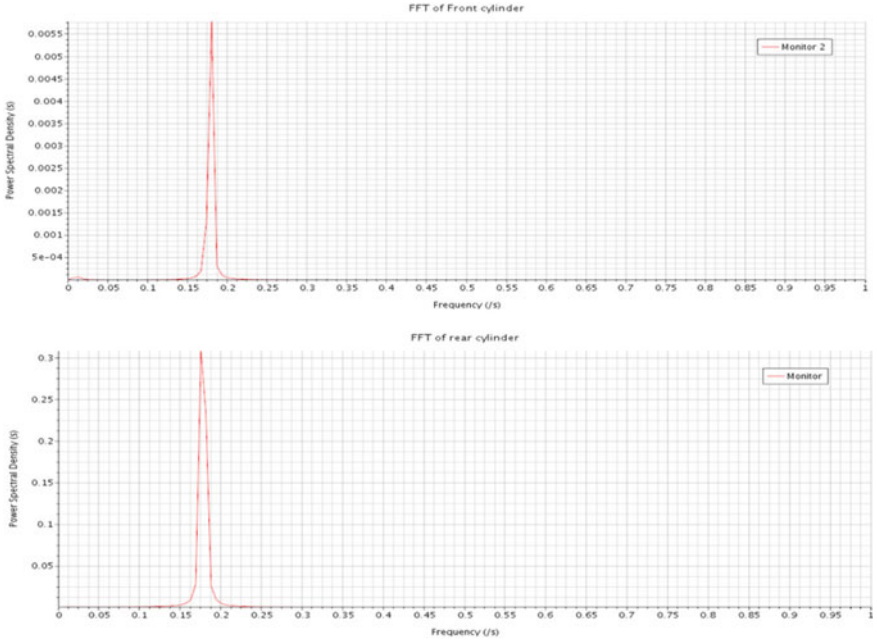

Fig. 15 Comparison of FFT of C_l plot of cylinder in tandem arrangement

Table 6 Mesh convergence study

Parameter	Actual grid	Grid 1	Grid 2	Grid 3	Grid 4
No of cells	296,587	3,507,862	6,985,424	9,845,214	15,903,256
C_d	0.38	0.35	0.34	0.33	0.332

basis of total number of cells on grid to simulate the C_d on stationary conduits in tandem arrangement. The solution domain was tested for all the three grids and Grid 3 is found to be converged (Fig. 15; Table 6).

3.5 Comparison on Flow Over Conduits in Tandem for Various Velocities

In this part of the chapter, a result from numerical simulations for the flow over conduits in tandem arrangement for various velocities has been summarized. This numerical study is performed to establish drag and lift coefficients of a conduit and the result are also investigated comparatively (Figs. 16, 17, 18 and 19).

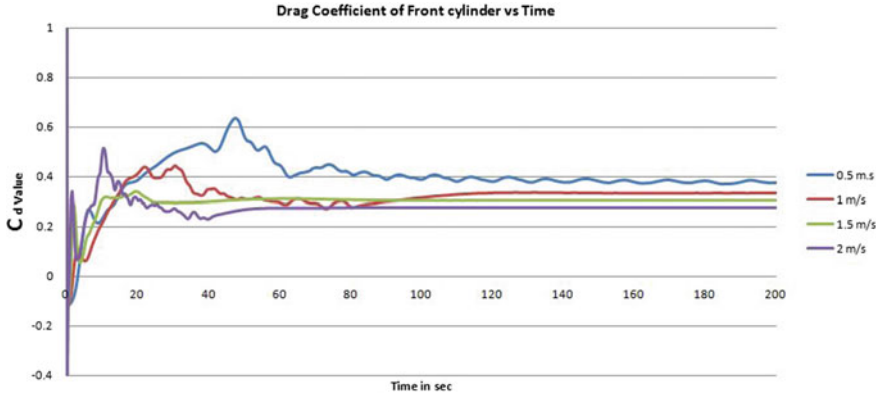

Fig. 16 C_d comparison of front circular conduits for various velocities in tandem

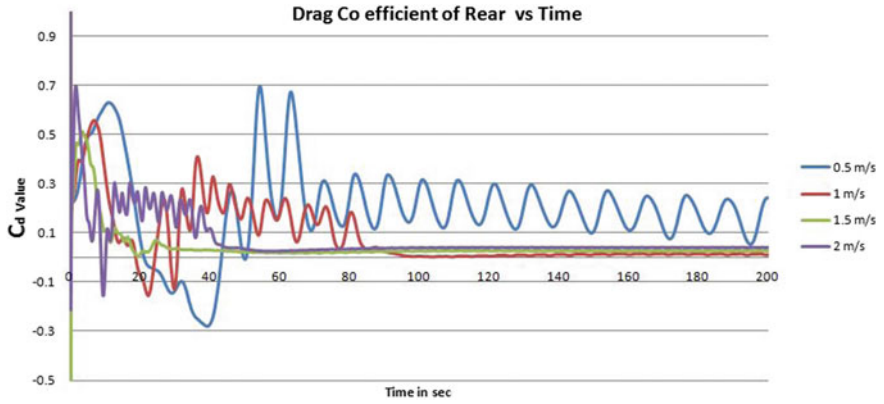

Fig. 17 C_d comparison of rear circular conduits for various velocities in tandem

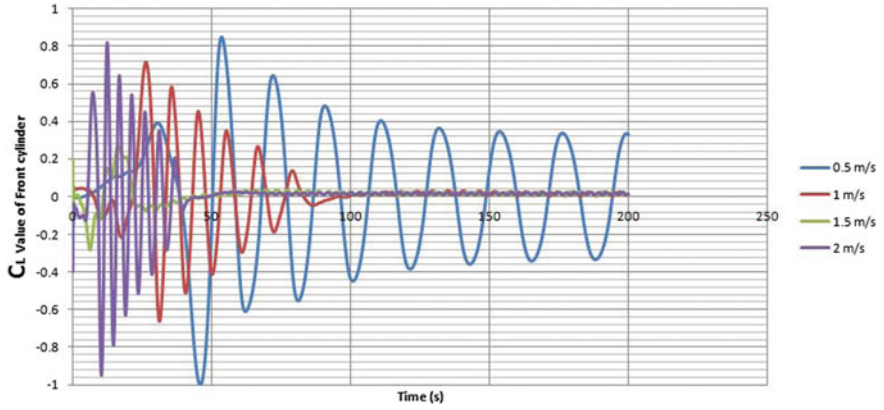

Fig. 18 C_l comparison of front circular conduits for various velocities in tandem

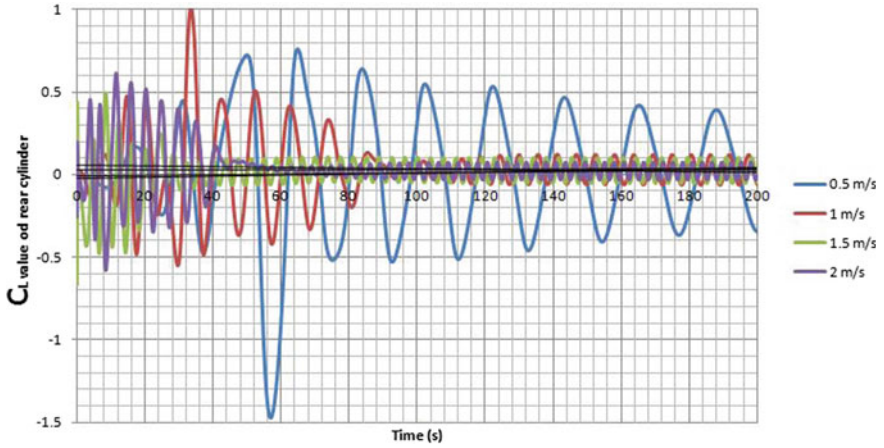

Fig. 19 C_l comparison of rear circular conduits for various velocities in tandem

4 Summary

The summary of this work comprises the numerical simulations of flow past circular conduits was carried out at Re of 1.6×10^6 for tandem arrangement of circular conduits. STAR-CCM+ software is used for solver of the numerical simulation and it was carried out for four different velocities. The effect of the presence of cylinder one another were analyzed, the parameter such as lifts and drags effects and also pressure variation along the length and it is correlated with the various flow velocities for the tandem arrangement of circular conduits of 2D center to center spacing.

5 Conclusion

The salient conclusions from the study of flow past a cylinder at Re of 1.6×10^6 for tandem arrangement, there is presence of large wake even beyond cylinder interference and the drag coefficient for isolated conduits decrease with increase in the velocity ranging from 0.5 to 2 m/s. The shedding frequency tends to increase with the increase of flow velocity. For the tandem arrangement, drag force coefficient on the front is positive and for the rear cylinder is fluctuates near zero this leads the increment of lift force coefficient on the rear cylinder than on the front one. The frequency of shedding of the front cylinder is greater than the rear cylinder. The maximum resultant force acting on the cylinder over its total length is lesser than the force acting along the length of single cell due to out of phase shedding of vortex cells is concluded in this 3D numerical simulation study.

Reference

1. Lienhard JL (1967) Synopsis of lift, drag and vortex frequency data for rigid circular cylinders, vol 300. Washington State University College of Engineering Research Department

Modelling of Breaking Focused Wave Interaction with an Offshore Wind Turbine Support Structure in Intermediate Water

Vijaya Kumar Govindasamy, Mayilvahanan Alagan Chella, S. A. Sannasiraj, and R. Panneer Selvam

Abstract Offshore wind turbine (OWT) substructures are exposed to extreme waves under severe environmental conditions especially in intermediate and shallow waters. These extreme waves are highly nonlinear, which cause high intensity short duration impact forces on OWTs. The main objective of the study is to investigate numerically and experimentally wave impact forces on a vertical slender cylinder which resembles a monopile substructure for offshore wind turbines subjected to focused breaking waves in intermediate water depth. Both laboratory measurements and numerical simulations are performed in order to obtain more insights into the breaking wave impact problem. The total response forces on a monopile substructure were measured at higher resolution in a well-controlled programmable wave flume. In addition, acceleration of the monopile, the wave surface elevations around the breaking region were measured for different intensities of breaking wave impacts. Further, the evolution of focused breaking waves along the tank and their characteristics were examined. Numerical experiments are carried out in a computational fluid dynamics based three-dimensional numerical wave tank, REEF3D. The model is based on the incompressible Reynolds-averaged Navier–Stokes equations together with the $k - \omega$ for turbulence and the level set method for free surface. The experimentally measured main wave crest of the breaking focused wave group is fairly well captured in the numerical simulation.

Keywords Breaking focusing wave · Wave structure interaction · Monopile · REEF3D

V. K. Govindasamy (✉) · S. A. Sannasiraj · R. Panneer Selvam
Department of Ocean Engineering, Indian Institute of Technology Madras, Chennai 600036, India
e-mail: gvijayakumaraero@gmail.com

M. Alagan Chella
Department of Civil and Environmental Engineering and Earth Sciences, University of Notre Dame, Notre Dame, IN 46556, USA

V. Sundar et al. (eds.), *Proceedings of the Fifth International Conference in Ocean Engineering (ICOE2019)*, Lecture Notes in Civil Engineering 106,
https://doi.org/10.1007/978-981-15-8506-7_21

1 Introduction

Monopile is vertical slender cylinder and is the one of the most suitable bottom fixed support structures for offshore wind turbines (OWT) in shallow and intermediate waters. These substructures have to be designed to withstand a severe sea environment, i.e. extreme waves events. The extreme waves exert high intensity short duration impact forces on OWT. The extreme wave events can occur due to one of or combination of four physical processes such as wave-current interaction, wave-sea bottom interaction, wave-wave interaction and wind-wave interaction. The concept of linear superposition of different wave components based on the wave-wave interaction can be used to generate a phase focused wave group which nearly resembles an extreme wave group in intermediate waters. Longuet-Higgins [12] first introduced the method based on the wave-wave interaction to generate a focused wave group. Later, Chan et al. [8] elucidated wave impacts on vertical cylinders through an experimental investigation. Wienke and Oumeraci [14] conducted a series of large-scale experiments to investigate wave impact loads on vertical and inclined slender cylinders and they showed that the impact force strongly depends on the distance between the breaking location and the cylinder. Hildebrandt et al. [10] carried out experimental and numerical investigations on the breaking wave interaction with a tripod structure in intermediate water depth. The dynamic excitation of a monopile was investigated due to regular breaking waves by de Ridder et al. [9] and steep and irregular breaking waves by Bredmose et al. [5]. Ghadirian et al. [6] investigated breaking focused wave loads on offshore wind turbine monopiles with OpenFOAM. Manjula et al. [13] discussed the hydrodynamic response of a slender vertical cylinder fixed at top due to breaking wave impacts. The open-source computational fluid dynamics (CFD) model REEF3D [3] has been exclusively utilized to model breaking waves and their interaction with slender cylinders [1, 4]. By using REEF3D, Bihs et al. [4] analysed the interaction of focused waves with a vertical cylinder and Alagan Chella et al. [2] investigated wave impact pressures and kinematics during the interaction of breaking waves with a vertical cylinder. Understanding breaking wave forces and the response of substructures under the influence of breaking waves is essential for both design and operation purposes. Several experimental investigations have been performed on modelling breaking wave impact forces on a vertical cylinder, however, the complete physical processes and the relationship between the dynamic responses and the impacts are not fully understood yet. The main objective of the present study is to investigate breaking wave forces on a monopile and the associated responses for different intensities of breaking wave impacts in intermediate waters. The characteristics and the evolution of breaking focused waves and the envelope of maximum wave surface elevations along the tank are examined. Further, numerical simulations of the focused wave group of a plunging case are carried out in a numerical wave tank, REEF3D. A comparison between numerical and experimental results is presented and discussed.

2 Physical Wave Tank

The experiments are conducted in a well-controlled wave cum current flume at Department of Ocean Engineering, IIT Madras. The wave flume is 30 m long, 2.0 m wide and 1.8 m deep as shown in Fig. 1. Waves are generated in the flume by a piston type wave maker having rubble mound wave absorber at the far end. The wave absorber is used to dissipate the incoming waves in order to avoid the wave reflection from the rear end of the flume. The experimental setup consists of a horizontal bed portion with a constant water depth of 0.8 m. A cylinder model is made of acrylic material of 0.20 m diameter, 0.005 m thickness and length of 1.3 m. The cylinder model with instrumentation used in the present study is shown in Fig. 2. It is placed in the middle of 2 m wide flume and it was fixed on a rigid steel plate and firmly bolted to the flume bottom, while the top side of the model was kept free. The cylinder joints were completely sealed to make it a water tight unit. A force

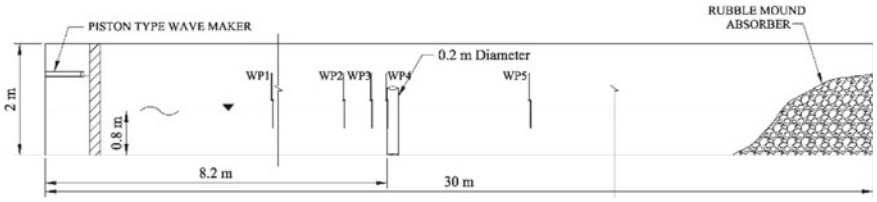

Fig. 1 Sectional view of the wave flume

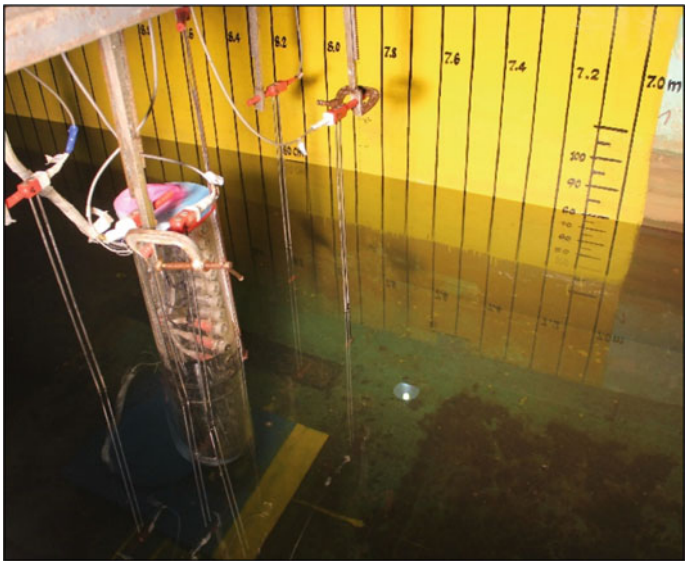

Fig. 2 Photograph of the test cylinder (monopile) with instrumentation

transducer was placed at the bottom of the cylinder model to measure the horizontal wave force from breaking waves. A total 15 wave gauges were installed at different locations along the wave flume to capture the evolution of the focused wave group.

3 Numerical Wave Tank

The numerical model REEF3D is based on the incompressible Reynolds-Averaged Navier–Stokes (RANS) equations. The governing equations are the mass and momentum equations as follows:

$$\frac{\partial U_i}{\partial x_i} = 0 \tag{1}$$

$$\frac{\partial U_i}{\partial t} + U_j \frac{\partial U_i}{\partial x_j} = -\frac{1}{\rho}\frac{\partial P}{\partial x_i} + \frac{\partial}{\partial x_j}\left[(\nu + \nu_t)\left(\frac{\partial U_i}{\partial x_j} + \frac{\partial U_j}{\partial x_i}\right)\right] + g_i \tag{2}$$

U is the velocity averaged over the time t, x is the spatial geometrical scale, ρ is the water density, ν is the kinematic viscosity, ν_t is the eddy viscosity, P is the pressure, and g is the gravitational constant. Discretization of the convective terms in the RANS equations is performed with the 5th order Weighted Essentially Non-Oscillatory (WENO) scheme. Time discretization is carried out with a Total Variance Diminishing (TVD) 3rd order Runge–Kutta scheme. An adaptive time-stepping method is employed for the dynamic determination of the time step size for the numerical simulation. Solid boundaries are represented using the ghost cell immersed boundary method (GCIBM). The interface deformation is captured with the level set method. Turbulence evolved under the breaking waves and the interaction with structure is described using the two-equation $k - \omega$ model. A staggered grid arrangement is employed in the numerical model to ensure the strong velocity–pressure coupling at the interface. At the inlet, the numerical wave generation is based on a piston wave maker, while at the outlet the active beach is incorporated. Further details about the numerical model are presented in Bihs et al. [3].

4 Results and Discussion

4.1 Breaking Focused Wave Characteristics in the Physical Wave Tank

In this present study, a focused wave group was generated by focusing wave energy to a particular point at a pre-defined time and space in the laboratory. The wave energy focusing was achieved by the constructive interference of several wave components

Table 1 Wave parameter for the laboratory breaking focused waves

F_I	F_N	F_C	N	T_C	L_C	K_C	C
0.42	1.1	0.76	28	1.32	2.701	2.327	2.053

of different frequencies and amplitudes based on linear wave theory [7]. For the wave focusing process, the wave amplitudes are actually arbitrary, it can be kept constant or it can be assumed inversely proportional to the corresponding wave number. i.e. constant steepness. In this paper, the generation of a wave packet is based on the constant steepness approach and this method works better than a constant amplitude wave packet. In order to minimize the influence of reflected waves, high frequency waves were generated first such that the wave breaking event is completed before the reflected waves reach the focusing point. The wave packet parameters used for the wave generation are listed in Table 1. The focused wave groups were simulated in a constant water depth of 0.8 m (influence of shoaling effect is avoided) based on the constant steepness wave packet (CS) [11] approach. Five different breaking intensities of focused waves were generated by adjusting the gain factor (G_a) (tuning factor).

F_I = Initial frequency (Hz), F_N = Final frequency (Hz), F_C = Centre frequency (Hz), N = No of frequency components, T_C = Characteristic wave period (s), L_C = Characteristic wave length (m), K_C = Characteristic wave number (m^{-1}), C = Characteristic wave speed (m/s).

These G_a was found by a trial and error method until the expected wave breaking was achieved. As the gain factor (G_a) increases, the focusing point shifts shoreward as listed in Table 2. Five different wave impact cases are identified with both the visual observations and wave gauge measurements. The four plunging cases exert large forces when a focused wave group breaks on or just before the cylinder. The fifth loading case is non-breaking wave case. The above terminologies (Plunging cases 1, 2, 3, 4 and non-breaking wave case) are given just to differentiate between complex breaking events qualitatively and did not quantify the wave breaking. The tuning factor influences the overall energy level in the generated wave packet and thus, it controls the intensities of wave breaking. The breaking wave characteristics

Table 2 Measured focusing location and maximum free surface elevation for all cases

Types of focused waves	Gain parameter (G_a)	Focusing location from the wave maker (m)	Measured maximum free surface elevation (m)
Plunging case 1	0.74	7.8	0.2843
Plunging case 2	0.72	8.0	0.2627
Plunging case 3	0.70	8.0	0.2624
Plunging case 4	0.68	8.2	0.2604
Non-breaking wave	0.60	8.2	0.2267

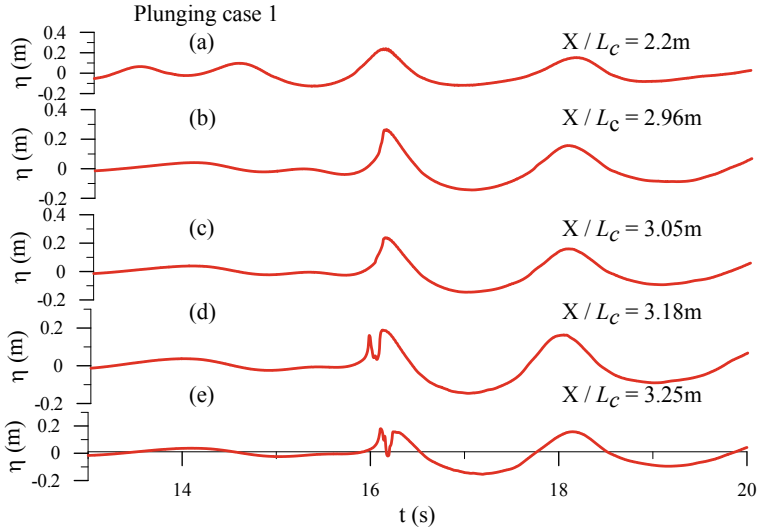

Fig. 3 Time series of free surface elevations for plunging case 1

such as the maximum wave height at breaking (H_b) and the breaking location (x_b) for five different intensities of focused wave groups are given in Table 2.

Figure 3 shows the measured free surface elevation at five selected locations along the wave flume in the breaking region for plunging case 1. From the visual observation and measurement from the wave gauges, the waves attain the maximum wave height just before breaking nearly at 8.0 m ($X/L_c = 2.96$ m) from the wave paddle. Since the wave group of different frequencies and amplitudes begins to propagate, wave energy starts to focus around the intended focus point as seen in Fig. 3a, b. As a result, the wave height of the main wave crest (focused) increases continuously and attains the maximum wave height before breaking (Fig. 3b). After breaking, the height of main wave crest decreases as the wave group approaches the beach (Fig. 3d, e).

Figure 4 presents the envelope of the maximum normalized wave height (H/L_c) over the normalized flume length (X/L_c). The measured wave heights at different locations along the wave flume are normalized with the characteristic wave length for four plunging cases and a non-breaking wave case.

4.2 Total Horizontal Forces on the Monopile Substructure

In this section, the total horizontal force on the monopile is presented for four plunging and non-breaking waves as given in Table 2. The measurements were performed by using the PMX Data acquisition with a sampling rate of 9600 Hz to capture the impact force. The total horizontal wave forces on the cylinder model were measured at five various location along the wave flume ($X/L_c = 2.88, 2.92, 2.9618,$

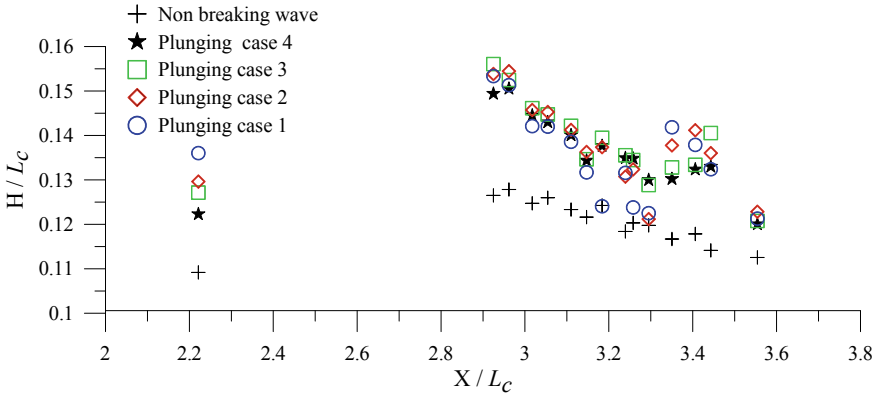

Fig. 4 Measured normalized free surface elevation versus normalized distances along the tank at 15 different locations for five breaking wave impacts

3.03 and 3.10 m) for five different loading cases. Figure 5 shows the measured maximum breaking wave force over time for five different wave impacts as listed in Table 2. For plunging case 1, the maximum breaking wave force at $x/L_c = 2.88$ which is 350 N, while for plunging case 2 the maximum force occurs at $x/L_c = 2.96$ and is 322 N. Similarly, for plunging 3 the maximum force of 260 N at $x/L_c = 2.96$. Even though the focusing location is the same for plunging case 2 and 3, the largest force occurs for Plunging case 1. The total force rise time (time between the last zero-up crossing to peak) for plunging case 1 is 0.37 s which is far away from the natural period (0.06 s) of cylinder model in 0.8 m water depth. The measured maximum horizontal force corresponding with rise time and acceleration of cylinder for all

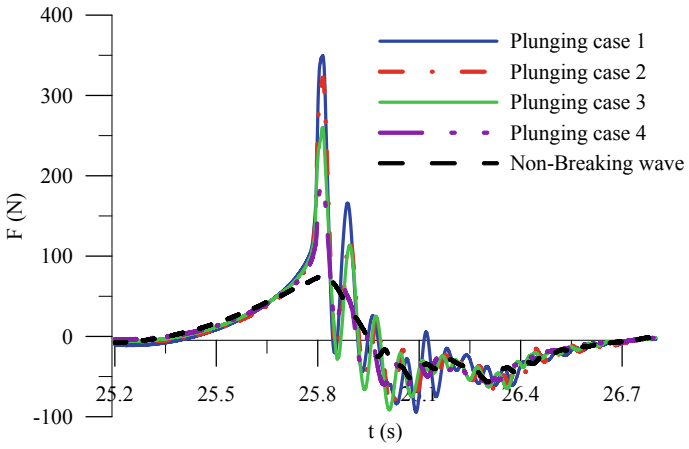

Fig. 5 Measured maximum horizontal wave force for five different wave impacts

Table 3 Measured maximum force, acceleration, total force rise time

Types of focused waves	Maximum horizontal force (N)	Maximum acceleration (m/s^2)	Total force rise time (s)
Plunging case 1	350	72.26	0.37
Plunging case 2	322	93.94	0.39
Plunging case 3	260	66.35	0.42
Plunging case 4	189	22.12	0.45
Non-breaking wave	74	4.19	0.46

wave cases are listed in Table 3. The largest maximum force occurs for Plunging case 1 is nearly five times the non-breaking wave force.

4.3 Accelerations of the Monopile Substructure

The wave induced accelerations of the cylinder model were measured at top of the cylinder simultaneously with the force measurements. A shear accelerometer (model: 393B04 PCB PIEZOTRONICS) was used to measure acceleration of the structure in the laboratory experiments. An accelerometer was fixed in the horizontal position on the top of the cylinder. The sensitivity of the accelerometer was given as 104.3 mV per m/s^2. Figure 6 shows the measured maximum acceleration of the monopile with the corresponding free surface elevation (measured parallel to cylinder model) over time for five different wave impacts as given in Table 2. Although the largest breaking wave force occurs for plunging case 1, the maximum acceleration response of the cylinder occurs for plunging case 2 which is 93.94 m/s^2. For other cases, it varies between 4 and 70 m/s^2. The maximum acceleration of the cylinder for plunging case 2 is 22 times the acceleration for the nonbreaking wave.

4.4 Numerical Simulation of Breaking Focused Waves Using REEF3D

A grid refinement study is carried out for the plunging case 1 with three different grid sizes of $dx = 0.01, 0.02, 0.03$ m. The numerical free surface elevation is compared with experimental free surface elevation to validate the numerical model. Figure 7 shows the computed free surface elevation with different grid sizes for plunging case 1 with experimental free surface elevation. We have noticed good agreement near to focusing point with the experimental free surface elevation. It has to be noted that wave paddle displacement from the laboratory measurements is given as input to the numerical wave tank to generate a focused group and it is very similar to the

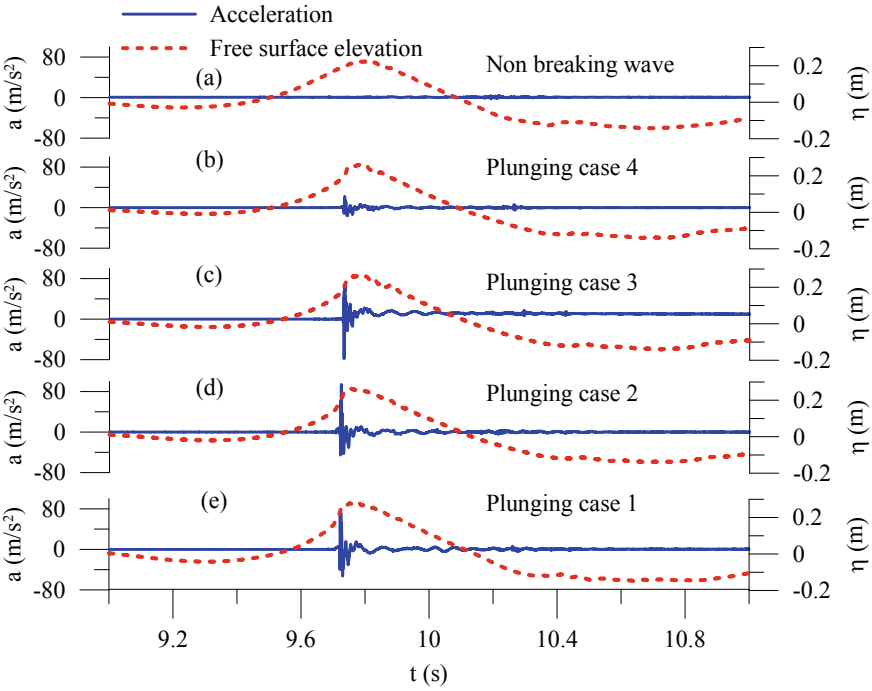

Fig. 6 Measured accelerations and wave surface elevations versus time for five different impacts

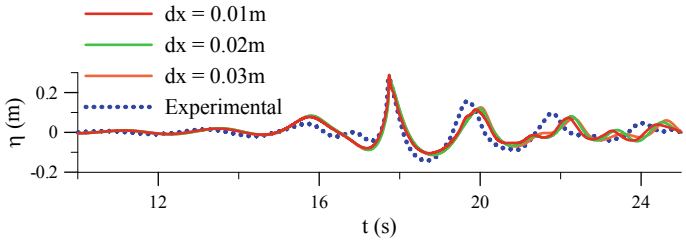

Fig. 7 Comparison of simulated and measured wave surface elevation versus time for plunging case 1

laboratory wave generation. Figure 8 shows the simulated free surface profiles with horizontal velocity (u) at two distinct time instances $t = 5.5$ s and 6.25 s for plunging case 1. As can be seen, the height of the main wave crest increases as the wave group advances forward in the numerical wave tank. As can be seen from Fig. 8b, the main wave crest becomes unstable after attaining the maximum wave height during the focusing the process. Moreover, the numerically simulated figures resemble the free surface flow features observed in the laboratory and the simulated free surface

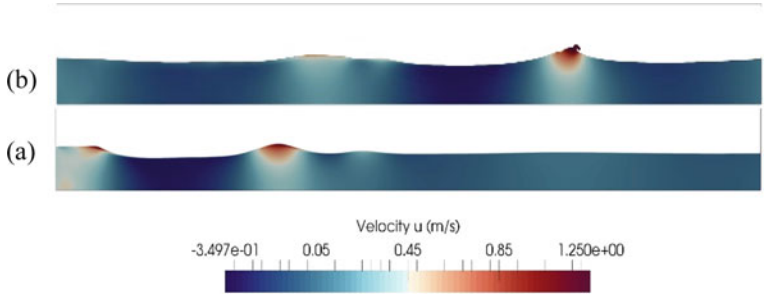

Fig. 8 Simulated free surface profiles at $t = 5.5$ and 6.25 s for plunging case 1

profiles shows that the propagation of a focused wave group is well reproduced in the numerical wave tank.

5 Summary and Conclusions

In this study, an experimental investigation of breaking wave impact on a monopile substructure has been carried out for five different intensities of focusing waves using the constant steepness spectrum method. This main focus of the investigation is to study breaking wave force and the dynamic response of monopile substructure due to breaking focused waves. The focus wave group generation is based on the principle of energy focusing by the linear superposition of wave components in laboratory. The free surface elevation, total horizontal wave force and accelerations of cylinder model were measured for four different types of plunging cases and compared with corresponding nonbreaking wave. The largest maximum total horizontal force is occurred for plunging case 1. But the maximum acceleration is appeared for plunging case 2. In the numerical investigation, the open-source CFD model REEF3D is used to model the propagation of breaking focused wave group in the numerical wave tank. The numerical model is able to reproduce the laboratory measured data in the numerical wave tank. Further, in future studies the interaction of a breaking wave with a monopile will be simulated numerically for a wide range of cases and the breaking wave kinematics and the free surface flow scenarios will be investigated in detail.

Acknowledgements The research work has been funded by DST (India) through the project "Hydrodynamic Loads on Offshore Wind Turbine Substructures due to Nonlinear Irregular Breaking, High Steep and Extreme Waves" (project number: 246810). The first author would like to thank Dr. Hans Bihs for the discussion regarding the numerical wave tank.

References

1. Alagan Chella M, Bihs H, Myrhaug D, Muskulus M (2017) Breaking solitary waves and breaking wave forces on a vertically mounted slender cylinder over an impermeable sloping seabed. J Ocean Eng Mar Energy 3(1):1–19
2. Alagan Chella M, Bihs H, Myrhaug D (2019) Wave impact pressure and kinematics due to breaking wave impingement on a monopile. J Fluids Struct 86:94–123
3. Bihs H, Kamath A, Alagan Chella M, Aggarwal A, Arntsen ØA (2016) A new level set numerical wave tank with improved density interpolation for complex wave hydrodynamics. J Comput Fluids 140:191–208
4. Bihs H, Alagan Chella M, Kamath A, Arntsen ØA (2017) Numerical investigation of focused waves and their interaction with a vertical cylinder using REEF3D. J Offshore Mech Arctic Eng 139(4):041101
5. Bredmose H, Slabiak P, Nielsen LS, Schlütter (2013) Dynamic excitation of monopiles by steep and breaking waves. Experimental and Numerical study. In: 32nd international conference on ocean, offshore and arctic engineering. American Society of Mechanical Engineers
6. Ghadirian A, Bredmose H, Dixen M (2016) Breaking phase focused wave group loads on offshore wind turbine monopiles. J Phys Conf Ser 753
7. Chan ES, Melville WK (1989) Plunging wave forces on surface-piercing structures. J Offshore Mech Arctic Eng 111:92–100
8. Chan ES, Cheong HF, Tan BC (1995) Laboratory study of plunging wave impacts on vertical cylinders. Coast Eng 25:87–107
9. de Ridder EJ, Aalberts P, van den Berg J, Buchner B, Peeringa J (2011) The dynamic response of an offshore wind turbine with realistic flexibility to breaking wave impact. In: ASME 2011 30th international conference on ocean, offshore and arctic engineering. American Society of Mechanical Engineers, pp 543–552
10. Hildebrandt A, Sriram V, Schlurmann T (2013) Simulation of focusing waves and local line forces due to wave impacts on a tripod structure. In: the twenty-third international offshore and polar engineering conference. International Society of Offshore and Polar Engineers
11. Lekshmi GR, Sannasiraj SA (2007) Correlation of breaking wave characteristics with energy dissipation. J Coast Res:307–311
12. Longuet-Higgins MS, Cokelet ED (1976) The deformation of steep surface waves on water-I. A numerical method of computation. Proc Roy Soc London A Math Phys Sci 350(1660):1–26
13. Manjula R, Sannasiraj SA, Palanichamy K (2014) Experimental investigations of acceleration on slender cylindrical member under breaking waves. Int J Ocean Clim Syst 5(3): 117–125
14. Wienke J, Oumeraci H (2005) Breaking wave impact force on a vertical and inclined slender pile—theoretical and large-scale model investigations. Coast Eng 52(5):435–462

Spatial and Seasonal Variations of Harmful Benthic Dinoflagellates in the Coastal Waters of Mauritius

P. Neermul, G. Dhunnoo, V. Emrith, M. Fakoo, N. Jeenally, R. Bhantooa, and K. Elaheebocus

Abstract Harmful algal bloom (HAB) events can have severe consequences such as mass fish kills and problems to public health. The Albion Fisheries Research Centre has an ongoing HAB monitoring programme at established coastal sites in Mauritius including Grand Baie, Albion, Le Morne and Blue Bay. The commonly observed benthic dinoflagellates are from the genera *Amphidinium* sp., *Coolia* sp., *Gambierdiscus* sp., *Ostreopsis* sp., *Prorocentrum* sp. and *Synophysis* sp. These are the causative agents of fish toxicity such as ciguatera. The monitoring data at the four monitoring sites for the period 2013–2017 were analysed to evaluate the temporal, spatial and seasonal variations in the densities of harmful marine microalgae species. Recurrent high densities were recorded at all the sites during the years. The genera *Prorocentrum* and *Ostreopsis* were observed at relatively higher densities throughout the years at the four study sites whilst the other genera occurred only occasionally. An increase in the mean cell densities of *Ostreopsis* sp. and *Prorocentrum* sp. were observed from 2013 to 2016 followed by a decline in the abundance in 2017 at most of the study sites. The cell densities of these two genera were found to be higher during summer seasons, and their occurrences were more significant at two sites, namely Blue Bay and Le Morne which are located in the South Coast of the Island. This warrants further studies to determine the influence of oceanographic parameters, seawater quality and environmental conditions on the cell densities of harmful marine microalgae in Mauritius.

Keywords Harmful algal bloom · Dinoflagellates monitoring · *Prorocentrum* sp. · *Ostreopsis* sp

P. Neermul · G. Dhunnoo · V. Emrith · M. Fakoo · N. Jeenally · R. Bhantooa (✉) · K. Elaheebocus
Albion Fisheries Research Centre, Albion, Petite Riviere, Mauritius
e-mail: rbhantooa@govmu.org

V. Emrith
e-mail: vemrith@govmu.org

M. Fakoo
e-mail: mfakoo@govvmu.org

V. Sundar et al. (eds.), *Proceedings of the Fifth International Conference in Ocean Engineering (ICOE2019)*, Lecture Notes in Civil Engineering 106,
https://doi.org/10.1007/978-981-15-8506-7_22

1 Introduction

Accumulations of phytoplankton in coastal waters are frequent phenomena around the world.

Large biomass blooms have been observed along the coasts of the United States, Inland Sea of Japan, the Black Sea and China [3]. It is estimated that 3400–4100 phytoplankton species occur in marine waters; out of which, about 300 is responsible for blooms also known as 'red tides'. These species comprise mostly diatoms, dinoflagellates, silicoflagellates, prymnesiophytes and raphidophytes [16]. However, only 60–80 species are known to cause harmful algal blooms (HABs) due to their biotoxins, irradiance reduction, physical damage and anoxia amongst others [15].

HABs in marine environments can be attributed to two primary causes: natural such as upwelling, ocean currents and increasing temperature; and anthropogenic such as nutrient inputs and coastal developments [14]. HAB events can have devastating effects in the immediate marine environment, thereby affecting the marine life. Substantial algal blooms may lead to anoxic conditions resulting in kills of fish and invertebrates. In other instances, algal species such as raphidophytes (*Chatonella* and *Heterosigma*) and dinoflagellates (*Karenia*, *Cochlidinium* and *Karlodinium*) can produce exudates and reactive oxygen species which affect the gills of fish eventually leading to their death, thereby affecting fisheries stocks [4].

In addition, a great concern to human health is algal species which have the abilities to produce potent toxins which can find their way along the food web to man [2]. The HAB toxins can be grouped according to their syndromes as paralytic shellfish poisoning, neurotoxic shellfish poisoning, amnesic shellfish poisoning, diarrhetic shellfish poisoning, azaspiracid shellfish poisoning, ciguatera fish poisoning (CFP) and cyanobacteria toxin poisoning [14].

The dinoflagellate *Gambierdiscus toxicus* is considered to be one of the causative agents for ciguatoxin in fish. It occurs commonly in the tropical regions including Mauritius and Reunion Islands. These are found attached to macroalgae, dead coral rubbles or other substrates and are consumed by herbivorous fish. Ciguatoxin is bio-accumulated such that organism higher in the food chain has higher concentrations [12]. In 2001, Hamilton et al. [5] demonstrated that various ciguatoxins were involved in ciguatera in the Indian Ocean, and the dinoflagellate *Gambierdiscus* sp. was identified as the most probable causative agent for producing the toxin.

This study zeniths the temporal, spatial and seasonal variations in the density of the most commonly occurring benthic harmful dinoflagellates, namely *Amphidinium* sp., *Coolia* sp., *Gambierdiscus* sp., *Ostreopsis* sp., *Prorocentrum* sp. and *Synophysis* sp. in the coastal waters of Mauritius at the four monitoring sites, namely Grand Baie, Albion, Le Morne and Blue Bay, for the period 2013–2017.

2 HAB Monitoring in Mauritius

The Inter-Governmental Oceanic Commission of the UNESCO conducted a baseline study of species involved in HAB for the Indian Ocean region including Mauritius from 1998 to 1999. During the study, macroalgae samples were collected on a monthly basis at two sampling sites for isolation of epiphytic microalgae. Several potentially toxic species belonging to the genera *Prorocentrum, Ostreopsis, Gambierdiscus, Coolia, Amphidinium* and *Synophysis* were observed during the study [6].

Consequently, the Albion Fisheries Research Centre (AFRC) had put up in place a HAB monitoring programme at four coastal sites, namely Albion, Blue Bay, Le Morne and Trou aux Biches; whereby, macroalgae samples were collected once every two months. Grand Baie was added as an additional monitoring site as from 2014.

3 Materials and Methods

3.1 Site Description

Mauritius, Rodrigues and Reunion Islands form the Mascarene Archipelago located in the Western Indian Ocean. The republic of Mauritius has an exclusive economic zone of 1.9 million km^2 and an extended continental shelf of 396 000 km^2 in the Mascarene plateau jointly managed with the republic of Seychelles. It has Mauritius as mainland and several outlying Islands, namely Rodrigues, St. Brandon or Cargados Carajos Archipelago, Agalega, Tromelin and the Chagos Archipelagos, including Diego Garcia. The EEZ includes coral reefs, seagrass beds, rough and sandy areas, submerged oceanic banks and oceanic waters. The mainland Mauritius has a coastline of 322 km and is surrounded by 150 km of protective coral reefs, covering a lagoon area of around 243 km^2. The coastal zone consists of sandy beaches, coastal dunes, rocky shores, wetlands and mangroves, lagoon corals, fringing coral reefs and all their associated marine life [9].

Mauritius, being a Tropical Island, witnesses a maritime climate all over the year. The Island has two seasons, namely: summer from November to April and winter which extends from June to September. May and October are known as the transition months. Mean summer temperature is 24.7 ºC, and mean winter temperature is 20.4 ºC. The temperature difference between the seasons is only 4.3 ºC. January and February are known to be the warmest months with a mean day maximum temperature of 29.2 ºC whilst July and August are the coolest months with average night minimum temperatures of 16.4 ºC [8].

This study comprises HAB monitoring data for Grand Baie for the period 2014–2017; and Albion, Le Morne and Blue Bay for the period 2013–2017. Figure 1 illustrates the locations of the monitoring sites.

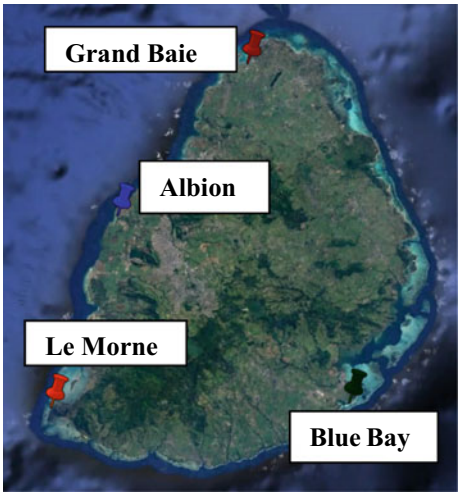

Fig. 1 Location of HAB monitoring sites [*Source* Google Earth, 2019]

Grand Baie. Grand Baie remains the most popular beach of all the northern tourist spots. The bay is heavily occupied by boats, catamarans and pleasure crafts belonging to hotels, private owners and fishermen. Rock revetments have been implemented to protect the receding shoreline on a length of 100 m. Grand Baie lies in the centre of many hotels, commercial spaces and residences. There is no natural river and canals in the vicinity of the beach, but small storm water drains are present [7].

Albion. Albion is located in the west of Mauritius and has a coastline of 1.5 km. It is enclosed by basaltic cliffs at both the northern and southern ends. The beach can be divided into three areas; (a) northern area for private residences and villas (b) central area for public beach approximately 300 m long and (c) southern area for AFRC and hotel. The lagoon is approximately 400 m wide and is used for the anchorage of pleasure crafts and fishing boats. It also receives inputs of freshwater from a river that runs through agricultural fields, animal farming areas and a wetland at the southern end of the beach [7].

Le Morne. Le Morne is located on the South-West coast of Mauritius and surrounded by reefs. The beach is used for recreational purposes. The lagoon is 500 m wide at the west and wider at the north and south. Hotels and a public beach is located along the coast. In the lagoon, kite and wind surfing are popular because of the good wind conditions at the south part. The coast is inscribed as the Le Morne Cultural Landscape of World Heritage Sites in 2008 by UNESCO [7].

Blue Bay. Blue Bay is situated in the South-East of Mauritius and is enclosed by coral reefs. It is a popular tourist spot and is extensively used for recreational purposes. There is no river mouth or estuaries at Blue Bay. The coastline has witnessed many developments projects in the coastal region including hotels, restaurants and private apartments. In addition, the seawater quality is influenced by surface runoff during heavy rainfall increasing turbidity and siltation [7].

3.2 Sampling and Analysis

The HAB monitoring programme involves collection of about 500 g of macroalgae samples at about 5 m from the shoreline. Each site comprised three sampling stations, and samples were collected once every two months. The samples were stored and transported to the laboratory in a thermos-insulated box at ambient temperature and were analysed within 24–48 h.

The macroalgae were shaken vigorously for 1 min with seawater in a 2L plastic bottle to dislodge epiphytic dinoflagellates. The resulting seawater was sieved through mesh size 150, 75 and 38 μm. The residues from the 38 μm sieves were collected in a beaker, diluted to 25 ml with filtered seawater and fixed with 0.2 ml of Lugol solution. 1 ml of this solution was transferred to a Sedgwick Rafter cell for counting under a light microscope. The number of the epiphytic dinoflagellates, namely *Prorocentrum* sp*, Ostreopsis* sp.*, Gambierdiscus* sp.*, Coolia* sp.*, Amphidinium* sp. and *Synophysis* sp was expressed as number per 100 g of macroalgae.

4 Results

4.1 Temporal Dynamics of Harmful Marine Microalgae

The temporal variability of the studied harmful marine microalgae at Grand Baie, Albion, Le Morne and Blue Bay is summarised in Fig. 2. The genera *Prorocentrum* and *Ostreopsis* were most abundant through the monitoring period whilst other genera occurred less frequently.

The maximum cell densities recorded at the four monitoring sites from 2013 to 2017 are listed in Table 1. The highest cell densities for *Amphidinium* sp. (746), *Coolia* sp. (1312) and *Prorocentrum* sp. (28,336) occurred at Blue Bay in December 2016, January 2014 and February 2015, respectively. High densities of *Ostreopsis* (45,617) and *Synophysis* (283) were also observed at Blue Bay in June and February 2014, respectively. The maximum cell density for *Gambierdiscus* sp. (461), *Ostreopsis* sp. (55,495) and *Synophysis* sp. (341) occurred at Le Morne in March 2015, November 2016 and November 2015, respectively.

Recurrent peak densities of the dinoflagellates were recorded during the years, however, these were of short duration, and a decline in the densities was noted during subsequent monitoring. The highest cell density events for all the dinoflagellates occurred at Blue Bay and Le Morne. In addition, the high cell density events at the four monitoring sites were most prominent during 2015 and 2016. However, no high cell densities were recorded during subsequent samplings following these events.

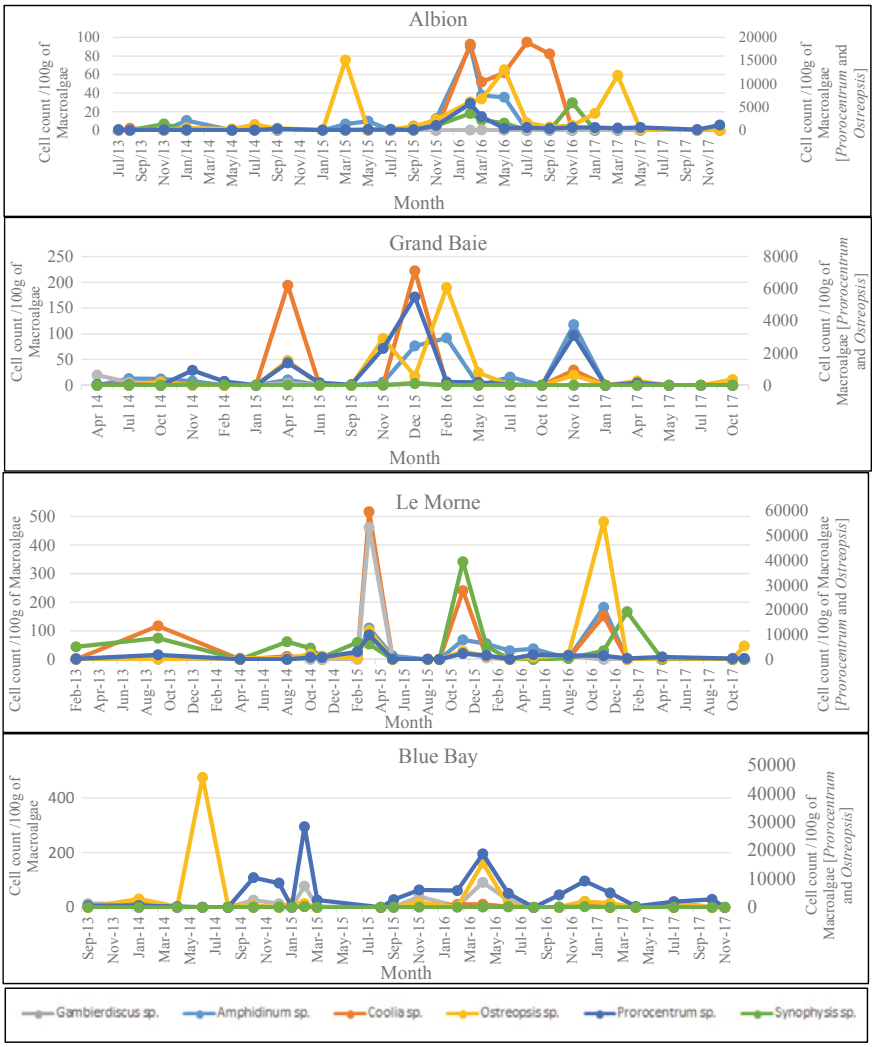

Fig. 2 Temporal variability of the genera *Prorocentrum, Ostreopsis, Gambierdiscus, Coolia, Amphidinium* and *Synophysis* at Grand Baie, Albion, Le Morne and Blue Bay

4.2 Dynamics of Prorocentrum *Sp. and* Ostreopsis *Sp.*

The SPSS software was used to determine the correlation between the cell occurrences, and the data are presented in Table 2. Given that the genera *Prorocentrum* and *Ostreopsis* were most abundant through the monitoring period; their correlation with the occurrences of other genera were evaluated. A moderate positive correlation [0.5 $< r <$ 0.66] was observed between the cell densities of *Prorocentrum* sp. with those of

Table1 Maximum cell densities recorded at the four monitoring sites from 2013 to 2017

Cell	Maximum cell counts/100 g of macroalgae							
	Grand Baie		Albion		Le Morne		Blue Bay	
Amphidinium sp.	118	Nov 16	91	Feb 16	182	Nov 16	**746**	**Dec 16**
Coolia sp.	222	Dec 15	95	Jul 16	516	Mar 15	**1312**	**Jan 14**
Gambierdiscus sp.	20	Apr 14	134	Jan 17	**461**	**Mar 15**	91	Apr 16
Ostreopsis sp.	6072	Feb 16	15,111	Mar 15	**55,495**	**Nov 16**	**45,617**	**Jun 14**
Prorocentrum sp.	5784	Dec 15	5754	Feb 16	9861	Mar 15	**28,336**	**Feb 15**
Synophysis sp.	107	Dec 15	30	Nov 16	**341**	**Nov 15**	**283**	**Feb 14**

Table 2 Correlation between the occurrences of the cell densities of the genera *Amphidinium*, *Coolia*, *Gambierdiscus*, *Ostreopsis*, *Prorocentrum* and *Synophysis* at the four study sites

	AM	CO	GD	OS	PR	SY	AM	CO	GD	OS	PR	SY
	Le Morne						Blue Bay					
AM	1.0						1.0					
CO	0.7	1.0					0.4	1.0				
GD	0.4	*0.9*	1.0				0.5	0.5	1.0			
OS	0.9	0.4	0.1	1.0			0.0	0.1	0.1	1.0		
PR	*0.5*	*0.9*	*0.9*	0.2	1.0		0.5	0.3	*0.9*	0.0	1.0	
SY	0.2	0.4	0.1	0.0	0.2	1.0	0.7	0.3	0.7	0.0	*0.8*	1.0
	Albion						Grand Baie					
AM	1.0						1.0					
CO	0.6	1.0					0.4	1.0				
GD	0.3	0.2	1.0				0.0	0.2	1.0			
OS	0.4	0.3	0.2	1.0			0.5	0.1	−0.1	1.0		
PR	0.9	*0.6*	0.4	0.2	1.0		*0.6*	*0.7*	0.1	0.2	1.0	
SY	0.5	0.3	0.1	0.1	*0.5*	1.0	0.3	0.7	0.1	0.0	*0.7*	1.0

Amphidinium sp., *Coolia* sp., *Gambierdiscus* sp. and *Synophysis* sp. No significant correlation ($p > 0.001$) was noted between the cell density of *Ostreopsis* sp. and the remaining dinoflagellates.

The annual trend in the mean cell densities of *Ostreopsis* sp. and *Prorocentrum* sp. indicated an increase in densities from 2013 to 2016 followed by a decline in the abundance in 2017 at most of the study sites. A significant drop in the cell density

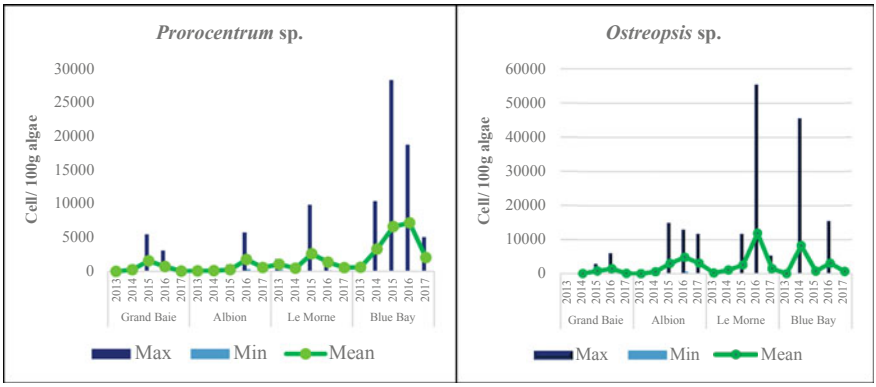

Fig. 3 The annual trends in the mean cell densities of *Prorocentrum* sp. and *Ostreopsis* sp. at Grand Baie, Albion, Le Morne and Blue Bay

of *Ostreopsis* sp. was observed at Blue Bay in 2015 as compared to 2014 as shown in Fig. 3.

Am: *Amphidinium* sp., CO: *Coolia* sp., GD: *Gambierdiscus* sp., OS: *Ostreopsis* sp., PR: *Prorocentrum* sp. and SY: *Synophysis* sp.

4.3 Seasonal Variations in the Cell Densities of Ostreopsis *Sp. and* Prorocentrum *Sp.*

The seasonal variations in the cell densities of *Prorocentrum* sp. and *Ostreopsis* sp. are shown in Figs. 4 and 5, respectively. The cell densities during summer seasons were much higher as compared to winter seasons at the four study sites. In addition,

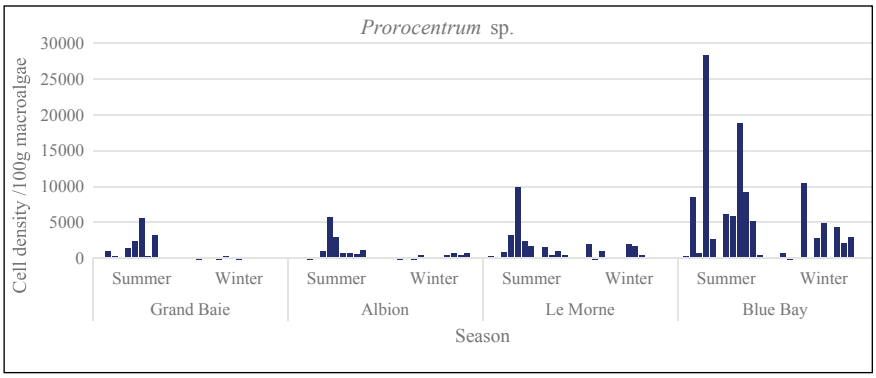

Fig. 4 Seasonal variations of *Prorocentrum* sp. at Grand Baie, Albion, Le Morne and Blue Bay

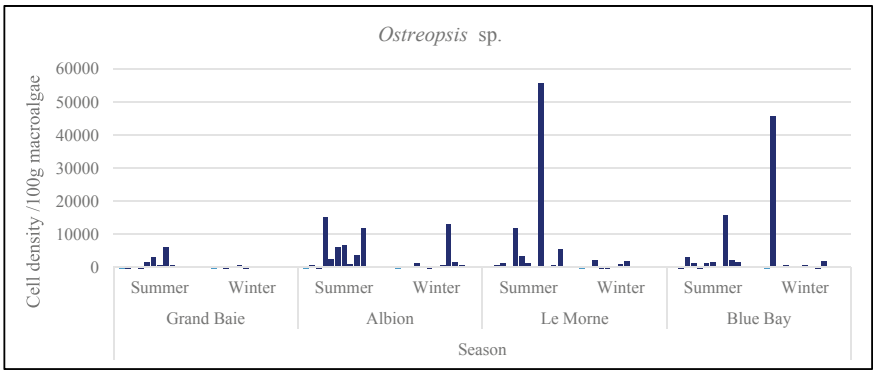

Fig. 5 Seasonal variations of *Ostreopsis* sp. at Grand Baie, Albion, Le Morne and Blue Bay

it was observed that the cell density of *Prorocentrum* sp. during summer seasons was relatively higher at Blue Bay followed by Le Morne indicating that the southern region of Mauritius is more prone to algal blooms.

5 Discussion

The ocean conditions and the environment interact to generate favourable conditions for HABs and subsequent HAB related diseases in humans and other animals [10]. Blue Bay and Le Morne are situated in the southern region of Mauritius, and the environmental conditions are directly affected by the South-East Trade Winds. In addition, summer season in Mauritius is characterised by warmer temperature and higher precipitation rate compared to winter season [8]. These may have influenced the proliferation of microalgae cells witnessed at the two sites.

Similar observations were reported along the coast of Oman; whereby, temporal and spatial distributions of microalgae cells were perceived to be affected by meteorological conditions such that monsoon winds caused an increase in HAB events [1]. Although temperature is believed to play a key role in HAB events, wind directions or flow of ocean currents and precipitation also affect variability of cell densities. Heavy rainfall may induce.

HABs due to a decline in salinity to brackish level and inflow of nutrients [11].

Furthermore, Sastre et al. [13] observed that the composition and density of certain harmful marine microalgae along the coast of Argentina showed large spatial and temporal variabilities. High densities were observed during summer in the southern, and it produced toxic accumulations. However, the high densities witnessed in winter in the northern region were below the threshold values to produce toxic accumulations.

6 Conclusion

There were variable trends in the cell densities at the four sites during the study period. However, there are some indications that the cell densities were influenced by seasons and locations with high densities being more prominent in summer and in the southern region. Further, studies are warranted to determine the influence of oceanographic parameters, seawater quality and environmental conditions on the cell densities of harmful marine microalgae in Mauritius.

In addition, peak densities of harmful marine microalgae observed during several occasions suggest that there is a real risk of HAB in the future. Accordingly, national HAB monitoring programme need to be re-designed to mitigate the environmental, socio-economic and health impacts of potential HABs events. The HAB monitoring programme shall encompass the following:

(a) Increase the number of monitoring sites and the frequency of monitoring;
(b) Establish species-specific HAB threshold values to trigger HAB alerts;
(c) Increase subsequent monitoring frequency following high density events;
(d) Isolate and enumerate benthic dinoflagellates in dead coral rubbles and sediments;
(e) Analyse seawater quality in terms of physico–chemical parameters including nutrient levels when collecting macroalgae samples;
(f) Establish a contingency plan for HAB events;
(g) Implement a surveillance programme for fish intoxication and HAB-related diseases to support management activities;
(h) Conduct detailed studies on the socio-economic losses related to HAB events.

Acknowledgements We are grateful to the staff of the Ministry of Ocean Economy, Marine Resources, Fisheries and Shipping for their constant encouragement and for full support throughout this study. The authors appreciate the invaluable contribution of Mrs. S. D. Thacoor and Miss B. Komul. We acknowledge the support of the International Atomic Energy Agency through the project RAF7014—Applying Nuclear Analytical Techniques to Support Harmful Algal Bloom Management in the context of climate and environmental change, phase II.

References

1. Al-Azri RA, Piontkovski AS, Al-Hashmi AK, Goes IJ, Gomes HDR (2010) Recent outbreaks of harmful algal blooms along the coast of Oman: Possible Response to climate change? Indian Ocean Tropical Cyclones and Climate Change, vol 34958. Springer, Berlin
2. Anderson DM, Cembella AD, Hallegraeff GM (2012) Progress in understanding harmful algal blooms: paradigm shifts and new technologies for research, monitoring and management. Annu Rev Mar Sci 4:143–176
3. Anderson M (2002) Harmful algal blooms and eutrophication: Nutrient sources, composition, and consequences. Estuaries Coasts 25(4):704–726
4. Hallegraeff GM (2010) Ocean climate change, phytoplankton communıty responses, and harmful algal blooms: a formidable predictive challenge. J Phycol 46:220–235

5. Hamilton B, Hurbungs M, Vernoux JP, Jones A, Lewis JL (2001) Isolation and characterisation of Indian Ocean Ciguatera. Toxicon 40:685–693
6. Intergovernmental Oceanographic Commission of UNESCO (2001) Potentially harmful microalgae of the eastern Indian Ocean—a guide based on a preliminary survey IOC Manuals and Guide No 41
7. Japan International Cooperation Agency (JICA) (2015) Final report: the project for capacity development on coastal protection and rehabilitation in the Republic of Mauritius. Coastal Conserv Plan 2
8. Mauritius Meteorological Services (2019) Climate of Mauritius. Available at https://metservice.intnet.mu/climate-services/climate-of-mauritius.php. Accessed on 04 Jan 2019
9. Ministry of Agro-Industry and Food Security (2015) Fifth national report on the convention on biological diversity, pp 86
10. Moore KS, Trainer LV, Mantua JN, Parker SM, Laws AE, Backer CL, Fleming EL (2008) Impacts of climate variability and future climate change on harmful algal blooms and human health. Environ Health 7(Suppl. 2):S4
12. Rey JR (2014) Ciguatera. Entomology and Nematology Department. University of Florida. Available at https://nifa.usda.gov/sites/default/files/resource/Ciguatera.pdf. Accessed on 04 Jan 2019
13. Sastre VA, Santinelli HN, Solis EM, Pérez BL, Ovejero DS, Villalobos GL, Cadaillón A, D'Agostino CV (2018) Harmful Marine Microalgae in coastal waters of Chubut (Patagonia, Argentina). Plankton Ecology of the Southwestern Atlantic
14. Sellner KG, Doucette GJ, Kirkpatrick GJ (2003) Harmful algal blooms: causes, impacts and detection. J Ind Microbiol Biotechnol 30:383–406
15. Smayda TJ (1997) Harmful algal blooms: their ecophysiology and general relevance to phytoplankton blooms in the sea. Limnolo Oceanogr 42 (5, part2):1, 1137–1153
16. Sournia A (1995) Red tide and toxic marine phytoplankton of the world ocean: an inquiry into biodiversity in Harmful Marine Algal Blooms. In: Proceedings of the 6th international conference on toxic Marine Phytoplankton, Oct 1993, Nantes, France, pp 103–112
11. Qi Y, Chen Y, Wang Z, Xu N, Wang Y, Shen P, Lu S, Hoggkiss IJ (2004) Some observations on harmful algal bloom (HAB) events along the coast of Guangdong, southern China in 1998. Hydrobiologia 512:209–214

Dredging and Siltation Study in the Gulf of Khambhat

R. Sundaravadivelu, M. V. Ramana Murthy, S. Sakthivel, P. K. Suresh, Saranya, S. Kreesa Kumaran, and A. Satya Kiran Raju

Abstract The Gulf of Khambhat is an inverted funnel-shaped indentation on the Arabian Sea of India. The maximum water depth of Gulf of Khambhat region is 35 m. Tidal range is high with semi-diurnal type. The current is very strong with magnitude of 2.5 m/s which occurs during mid-tide. Gulf of Khambhat (21° 03′ 41.49″ N, 72° 25′ 18.26″ E) receives enormous sediment from the discharge of three major rivers: Narmada, Tapti, and Sabarmati. The shoal movement as well as shoal enhancement has been observed in this region. At certain locations, the depth of water is reduced from 20 to 2 m in ten years. The dredging at an area of about 300 by 300 m from −2 to −20 m and disposal in deep contour is proposed, and the siltation rate in the dredge area and disposal area is studied. MIKE 21 HD flow module is used for tidal propagation, and for the siltation analysis, MIKE 21/3 integrated module is used. Desk studies are done analyzing satellite imageries. The results of analyses indicate that the sediment flow at dredge location is dominated by tidal current and the river flow is having no significance at the site which is located 24 km from confluence point. It can be observed that the bed level accretion works out to 180 cm

R. Sundaravadivelu (✉) · S. Sakthivel · P. K. Suresh · Saranya · S. Kreesa Kumaran
Department of Ocean Engineering, IIT Madras, Chennai 600036, India
e-mail: rsun@iitm.ac.in

S. Sakthivel
e-mail: enggoecrd@gmail.com

P. K. Suresh
e-mail: sureshpk2000@gmail.com

Saranya
e-mail: oe16m036@smail.iitm.ac.in

S. Kreesa Kumaran
e-mail: kreesa89@gmail.com

M. V. Ramana Murthy · A. Satya Kiran Raju
National Institute of Ocean Technology, Pallikaranai, Chennai 600100, India
e-mail: mvr@niot.res.in

A. Satya Kiran Raju
e-mail: mvr@niot.res.in

V. Sundar et al. (eds.), *Proceedings of the Fifth International Conference in Ocean Engineering (ICOE2019)*, Lecture Notes in Civil Engineering 106,
https://doi.org/10.1007/978-981-15-8506-7_23

per year. The disposal location was also identified where the siltation rate is assessed as 7 cm per year. The details of studies are furnished in the paper.

Keyword Dredging · Off shore · Dredge · Disposal

1 Introduction

A Public Sector Undertaking (PSU) of Government of India (GoI) has a well-head oil platform, located in at Gulf of Khambhat. IT has three oil exploration wells for a depth of 2500–4000 m in the Gulf of Khambhat, off northwest Gujarat Coast. The proposed project activity is maintenance dredging of the pathway to one of its well, which is currently defunct as it lost its contour of 27 m in 2009 to a meager 2–3 m presently. Unless, it is dredged to maintain a minimum of −12 m depth, rig movement is not possible to deploy the rig at the platform, Hence, organization is proposing a maintenance dredging project along with offshore disposal of dredged spoil.

The location was in 27 m contour when it was installed and commissioned during 2009. The draft has gone down to 16–17 m during 2011–12, by severe siltation. The present draft in the area around the platform and also in the pathway is 2–3 m contour, and so the rig operations were temporarily suspended since 2014.

2 Need for the Project

It is proposed to make the platform operational for the rig deployment. Hence, there is a need and requirement for a feasible draft of −12 m to facilitate the movement of rig. The proposed project is principally twofold viz maintenance dredging to gain back a minimum of −12 m contour for the location and offshore disposal of dredged spoil in an environmentally compatible way without harming the marine life and physical systems.

The proposed maintenance dredging is to regain and maintain a minimum of -12.00 m thought out the year for the smooth deployment of drilling rigs to the platform. The platform lies to true north, and the drilling rig approaches from the northwest direction of the platform.

From the naval hydrographic chart, it is observed that lots of sediment disposal are from two major rivers Narmada and Tapti. The well platform is around 12.8 nautical miles from the mouth bar of river Tapti, and the sediment transportation deposition is very high in this region.

An area of about 160,000 m^2 (375 m × 420 m) needs to be dredged for the smooth deployment of the rig. It is necessary to know about the siltation after dredging around the platform. Hence, the technical studies related to siltation after dredging has to be carried out.

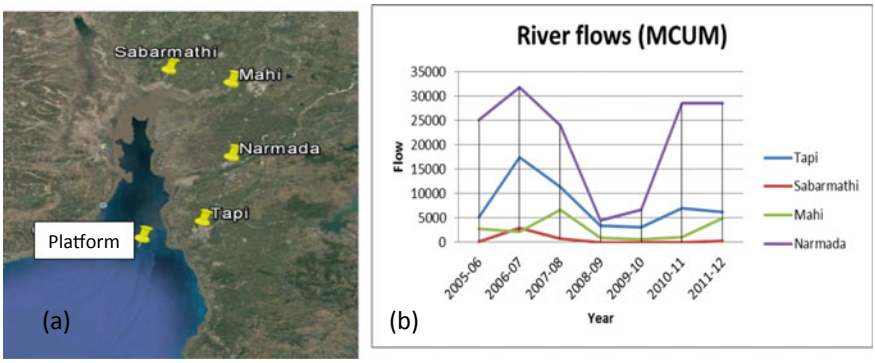

Fig. 1 **a** Satellite image of rivers near ONGC platform **b** discharge of rivers. *Source* CWC data

3 Site Location and Siltation Characteristics

The well-head platform is located in the Gulf of Khambhat which is like inverted funnel shape. It has a width varying from 5 to 15 km with an area of about 3120 km^2. It is dominated by four rivers such as Sabarmathi, Mahi, Narmada, and Tapti; they brings sediments during southwest monsoon. The bed slope is 19/10,000 from north to the platform (Fig. 1).

Sediment transportation is a process of sediment movement. Fluid motion leads to the sediment transport in ocean, rivers, lakes, seas, and other water bodies due to currents and tides. Knowledge of sediment movement is necessary to understand the causes of deposition or erosion at the sea bed and the rate at which the erosion or deposition is occurring.

The Gulf of Khambhat is having a geometry of an inverted funnel-shaped indentation on the Arabian Sea of India, covering the state of Gujarat. The maximum water depth of Gulf of Khambhat region is (−) 50.00 m. Gulf of Khambhat receives enormous sediment from the discharge of three major rivers: Narmada, Tapti, and Sabarmati. Considerable amount of shoal movement as well as shoal enhancement has been observed along the rivers. The sea bed and sediments are mainly fine to coarse grained sand.

4 Methodology

The objective is the study of sediment transport pattern due to currents in the gulf region. The numerical model MIKE 21/3 integrated module is adopted. The methodology flowchart is shown below.

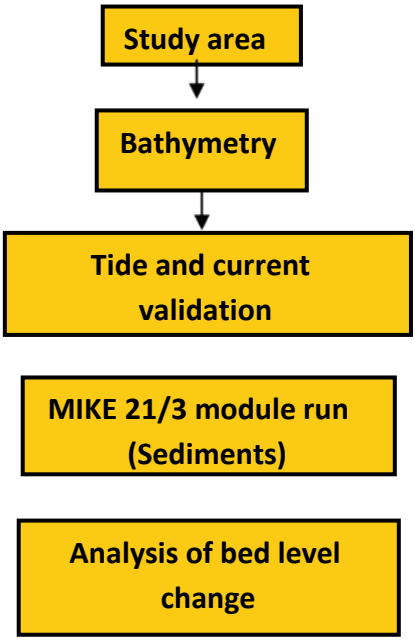

5 Bathymetry

This involves plotting of sea bed contours. The overall area considered for the siltation analysis is 45 × 45 km, and relatively less area is considered to get accurate answer. The bathymetry of this overall area is generated using Delft dashboard taking the data from GEBCO (General Bathymetric Chart of the Oceans). Once this bathymetry is generated the bathymetry of dredging area was superimposed on it and the model was made ready. Flexible mesh type of model was generated (Fig. 2).

Using flexible mesh, the model complexity can be reduced by giving different resolution of mesh based on the area of interest. The area away from location can be provided with coarser mesh, and the area near to the well-head platform is designed with finer mesh. This flexible meshing helps to reduce the simulation time.

5.1 Validation of Model

- Validation of the surface elevation is done using the global tidal data.
- Validation of current is done using the already existing data obtained from the HD model.

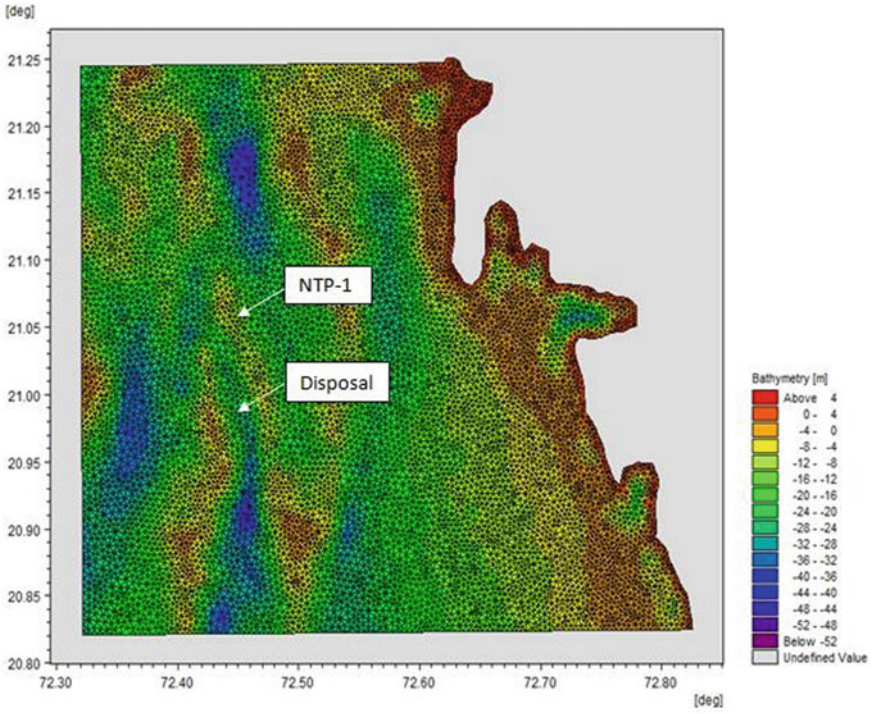

Fig. 2 Generated bathymetry by incorporating field data

5.2 Validation of Tidal Parameter

The model was created by incorporating the bathymetry. Before performing the trial runs, the model calibration is to be carried out. The tidal data for Gulf of Khambhat was generated with the tide generation tool box available with Mike 21. The generation was done based on bathymetry and the spatial position of study area. The tide data was generated for a period of one month. The generated data is to be calibrated before using for further analysis. Hence, the tide data for the project area was extracted from the domain of global tide elevation for the generated period of one month. The generated data and extracted data were in fairly good agreement (Fig. 1). The comparison of the two datasets is furnished in Table 1 (Fig. 3).

The above graph shows the comparison of global tide elevation and model-simulated tidal elevation. This comparison is made for the validation purpose.

Table 1 Tidal condition

Tidal condition	Simulated data	Global tide data
Spring tide (m)	6	6
Neap tide (m)	3	3

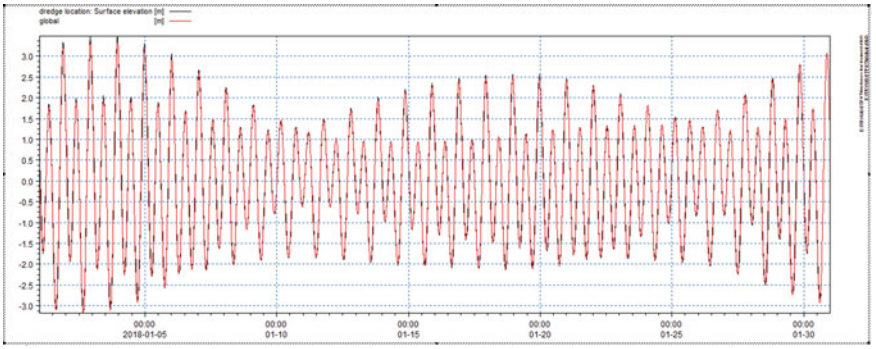

Fig. 3 Time series of water-level variation obtained by simulation and global data

5.3 Validation of Current at the Location of Dredge Locationplatform Before and After Dredging

The tidal model run was performed with the calibrated data for the location of the well-head platform. Initially, the first trial was carried out for the present existing condition where the bed level is (−) 4.00 m. Then, the second trial was performed after simulating the dredging condition with the bed level dredged to (−) 20.00 m. The current values are extracted for well-head platform (Table 2) (Fig. 4).

Table 2 Current speed

	Before dredging	After dredging
Maximum current speed (m/s)	2.6	1.3
Minimum current speed (m/s)	0.7	0.4

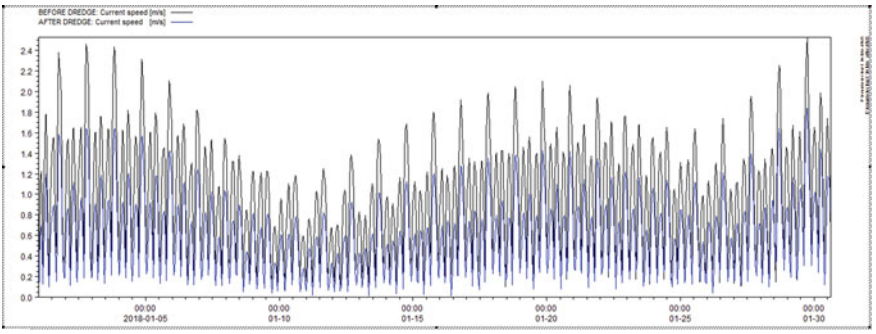

Fig. 4 Time series plot of current speed at NTP location, before and after dredge location

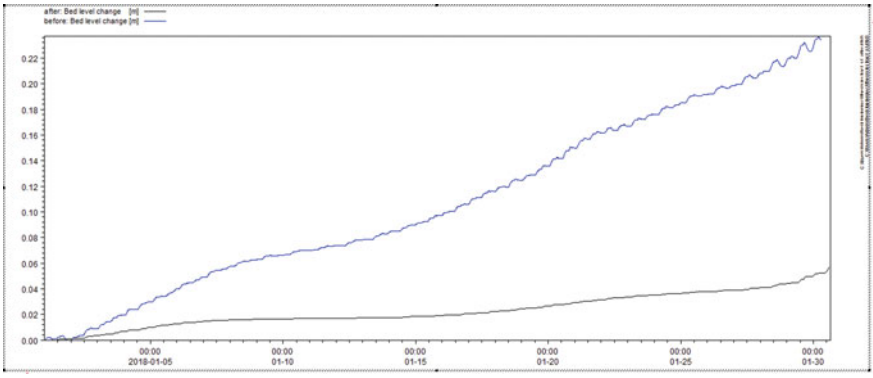

Fig. 5 Plot showing bed level change before and after dredging at NTP location

It can be observed that the current value matches with the previous data obtained in HD module. After calibrating the model with the observed or existing parameters, the model is made ready for further trials.

6 Rate of Bed Level Change at Dredge Location

The well-head platform is located approximately 24 km from the Tapti river outflow. During the monsoon period, the river discharges ample amount of sediment into Gulf of Khambhat through runoff which increases the suspended load and the bed loads of the region. But this sediment content does not contribute to the sediment deposit near well-head platform since the source.

The average rate of bed level change in a spring tide (7 days) is 2.3 m/year, and the average rate of bed level change in a neap tide (7 days) is 0.3 m/year.

From the above graph (Fig. 5), it can be observed that bed level before dredging is 0.22 m for a month; therefore, the bed level change for a year will be 2.64 m. Similarly, after dredging, its 0.04 m per month and for a year 0.48 m (Fig. 6).

7 Bed Level Change Due to Current at the Disposal Location

It can be observed that the bed level change for one month at disposal location is approximately 0.007 m.

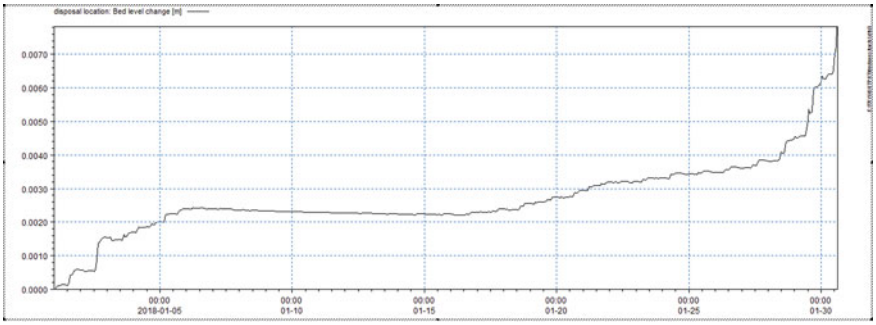

Fig. 6 Plot showing bed level change at disposal location

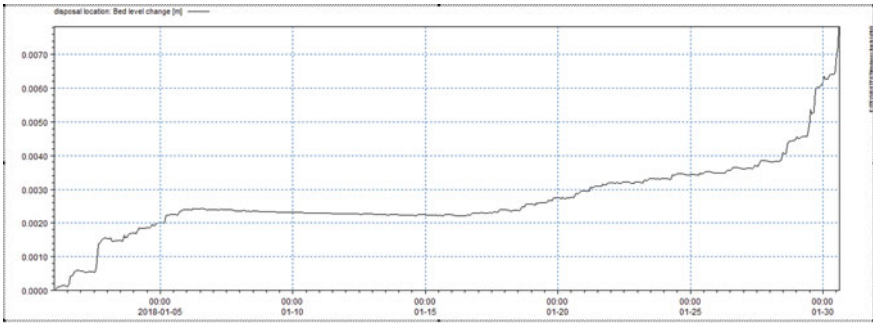

Fig. 7 Rate of bed level change at disposal location

7.1 Rate of Bed Level Change at Disposal Location

The details of sediment deposition in the reach is extracted from the model result and shown vide Fig. 7. The average rate of bed level change in a spring tide (7 days) is 0.21 m/year, and the average rate of bed level change in a neap tide (7 days) is − 0.0005 m/year (erosion) (Fig. 7).

8 Findings of the Study

Siltation analysis after dredging for dredging location was simulated with MIKE21/3 integrated module which couples the hydrodynamic with the sediment transport. The domain area is of size approximately 45 km by 45 km. The tidal data was generated, calibrated, and propagated in the model. Then, the calibrated model is coupled with the sediment model. The model run was performed for the following site conditions;

1. Well-head platform at existing condition with bed level (−) 4.00 m

2. Well-head platform with dredged bed level of (−) 18.00 m
3. Disposal area where the bed level is (−) 33.00 m

The observations of the siltation analysis were extracted and analyzed. The findings of the siltation analysis are as below;

1. It can be observed that the water level in spring tide is nearly about 6.00 m and neap is 3.00 m.
2. It can be observed that the current speed before dredging is 2.6 m/s and after dredging is 1.3 m/s.
3. It can be observed that sediment transport rate at the location of well-head platform is 2.64 m/year before dredging and 0.48 m/year after dredging.
4. The average rate of bed level change during the spring tide is 2.3 m/year, and the average rate of bed level change during neap tide is 0.3 m/year at the location of well-head platform.
5. The average rate of bed level change during the spring tide is 0.21 m/year, and the average rate of bed level change during neap tide is -0.0005 m/year (erosion) at disposal location.

9 Dredging Methordlogy Adopted Based on the Study

The dredging works were commenced on 10th November 2018. The dredging works were executed by a trailler suction hopper dredger and supported by sea-bed leveling device, i.e., (water injection dredger WID) (Figs. 8, 9, 10and 11.

Area of Dredging and Disposal Working principle of dredging at offshore platform:

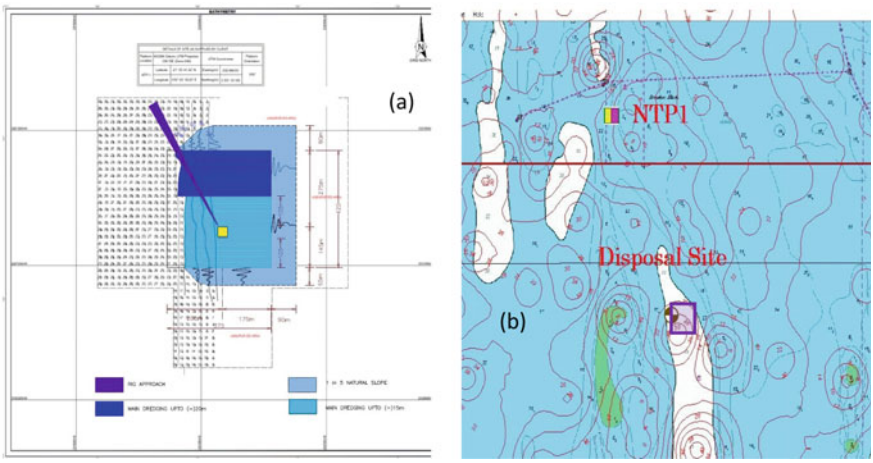

Fig. 8 **a** Area of dredging at ongc platform **b** disposal location at deeper contour

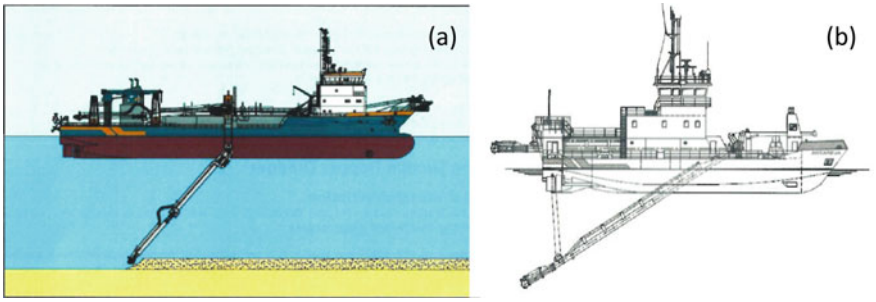

Fig. 9 **a** Working principle of TSHD dredger at dredging location **b** WID

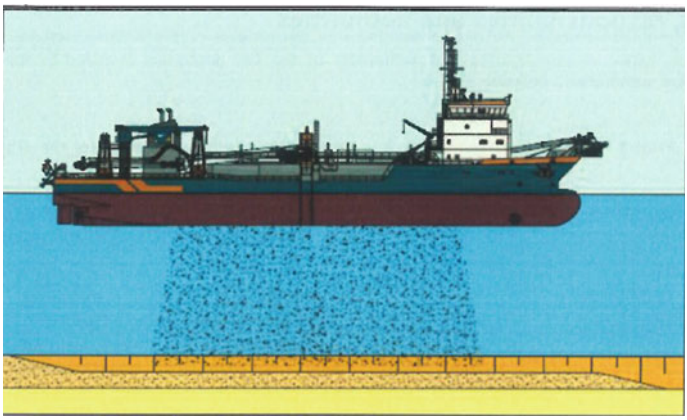

Fig. 10 Working principle of TSHD dredger at disposal location

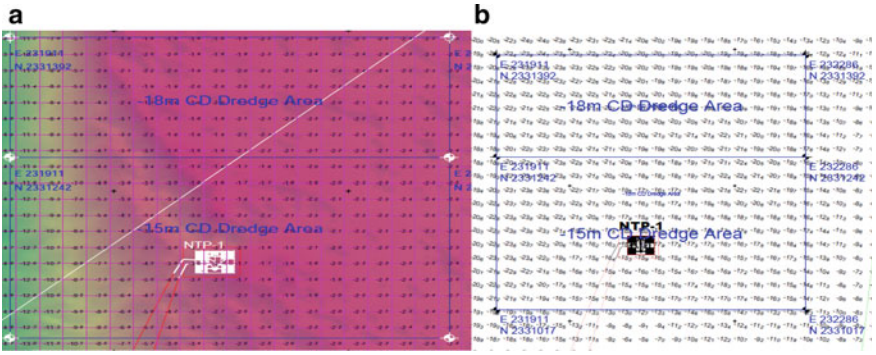

Fig. 11 **a** pre-dredge survey at dredging location **b** post-dredge survey at dredging location

The dredging and disposal cycle of a **TSHD** consists of the following	The dredging cycle of a **WID** consists of the following
• Lowering suction pipe at the dredging location. • Dredging at the proposed location. • Raising Suction Pipe. • Sail to the disposal location 11 km from dredging • Location. • Open bottom doors • Discharge hopper loads • Close bottom doors • Sail to dredging area Repeat the process.	• WID level the bed level were TSHD cannot reach. • WID shall slide the dredging material from the area closer to the platform towards the deeper contour. • This will enable toTSHD to dredge closer to the platform. • Finally after dredged up to desired depth WID shall level the slopes and sea bed.

10 Maintenance Dredging

From the siltation studies, it is evident that there is an active sand movement in and around the well-head areas which is moving from northeast to southwest direction. The drilling rig maneuvering required a depth of (−) 12 m with reference to CD. The existing dredge levels are (−) 15.00 m & (−) 18.00 m. Based on the sediment transport report, the rate of sediment movement rate after dredging is 0.48 m/year, say 0.5 m/year. Considering the shoal moment and sediment transport pattern in Gulf of Khambhat, a factor of 1.5 times is added which results in 0.75 m/year. The area where dredging is carried for (−) 18.00 m is considered as sand trap, and hence, the sand trap shall be dredged once in every three years.. The maintenance dredging shall be carried out only in this region. The sand trap is 3.00 m deeper, and once the sand trap is filled up to (-) 15.00 m, maintenances dredging operation should be commence.

11 Conclusion and Recommendations

Based on the study, it is observed that sediment transport rate at the location of dredge location platform is 2.64 m/year before dredging and 0.48 m/year after dredging. The average rate of bed level change during the spring tide is 2.3 m/year, and the average rate of bed level change during neap tide is 0.3 m/year at the location of well-head platform. The average rate of bed level change during the spring tide is 0.21 m/year, and the average rate of bed level change during neap tide is −0.0005 m/year (erosion) at disposal location recommended to conduct bathymetry survey in and around the platform before deploying the rig and after deploying the rig. By this exercise, the real-time sediment transportation can be observed and monitor for the upcoming years.

The dredging was completed on 24th Dec, 2018, and drilling rig was successfully deployed at the platform on 25th Jan, 2019, and the drilling operational will be in progress till April 19 for the financial year 2018 and 2019.

Health Monitoring of Berthing Structures

R. Sundaravadivelu, V. Rajendran, K. Balasubramanian, and S. Kreesa Kumaran

Abstract It is increasingly recognized in the recent past that reinforced concrete (RC) berthing structures are not permanently durable and free from maintenance. A large number of cases of damage and failure in RC berthing structures have been reported worldwide, and rehabilitation of such structures involves phenomenal cost, besides challenging technical problems in identifying appropriate rehabilitation techniques and materials. In order to arrive at a suitable rehabilitation strategy, non-destructive tests (NDT) are carried out to assess the condition of concrete in the distressed RC structural elements. Health monitoring of berthing structures through in situ testing is a specialized job requiring reliable test methods and instruments. The paper discusses in detail the rehabilitation of berthing structures at Cochin, Tuticorin and Chennai Port Trusts. In the case of the Cochin Port Trust, distressed RC structural elements of the North Tanker Berth (NTB) jetties and South Tanker Berth (NTB) jetties exhibited half-cell potentials more than −350 mV indicating that there is a greater than 90% probability that reinforcing steel corrosion is occurring in that area at the time of measurement as per the reference guidelines of ASTM C-876. Based on the analysis of the various NDT tests, viz. ultrasonic pulse velocity (UPV) test, core drilling and carbonation tests and the evaluation of chlorides and pH, a detailed rehabilitation methodology including under water micro-concrete jacketing has been suggested for the distressed RC structural elements of the central platform, Breasting dolphin and the approach trestle of both the jetties. coal jetties 1 and 2 and the oil jetties at Tuticorin Port Trust were rehabilitated after conducting detailed NDT investigation in the RC structural elements of the berthing dolphin, main jetties, approach jetties, mooring dolphin and catwalk of the three jetties. The severe distress in the RC structural elements of the three jetties could be attributed to the failure of the earlier repair carried out using shotcreting. Based on the extensive

R. Sundaravadivelu (✉)
Department of Ocean Engineering, Indian Institute of Technology Madras, Chennai 600036, India
e-mail: rsun@iitm.ac.in

V. Rajendran · K. Balasubramanian · S. Kreesa Kumaran
Hitech Concrete Solutions Chennai Private Limted, Chennai 600095, India
e-mail: kbs@hitechconcre.net

V. Sundar et al. (eds.), *Proceedings of the Fifth International Conference in Ocean Engineering (ICOE2019)*, Lecture Notes in Civil Engineering 106,
https://doi.org/10.1007/978-981-15-8506-7_24

NDT tests conducted, the condition of the concrete was assessed and a rehabilitation methodology consisting of micro-concrete jacketing and installation of self-regulating anodes was suggested for the various distressed RC structural elements of the three jetties. Modification/rehabilitation of finger jetties was carried out at the Chokhani floating dry dock in Chennai Port Trust. NDT tests were conducted to arrive at the rehabilitation methodology. The heavily corroded pile liners were cut and removed from −0.20 m level by using under water cutting gear. The cracked and spalled concrete was fully removed to expose the full circumference of the steel. The rust in steel was completely removed and cleaned by chemical means. Additional steel was provided for modification of pile for fender arrangement. Sacrificial zinc anodes were installed, and leads were provided for connecting to a monitoring box. Under water micro-concrete was used after coating the rebars with a zinc primer. The UPV tests conducted after repair for a period of nearly 6 years at every 6 month interval indicated that the integrity of the concrete were still good. The half-cell potentials measured at every 6 month interval for a period of 6 years showed values more positive than −200 mV indicating that there is a greater than 90% probability that no reinforcing steel corrosion is occurring in that area at the time of measurement. The half-cell potential values more positive than −200 mV even after six years clearly indicate that the self- regulating anodes were effective in preventing further distress to the RC structural elements.

Keywords Rehabilitation · Non-destructive tests · Cochin Port Trust · Micro-concrete jacketing · Tuticorin Port Trust · Shotcreting · Chennai Port Trust · Rebars · Half-cell potentials

1 Introduction

It is well known that reinforced concrete is a versatile, economical and successful material. It is durable and strong, performing well throughout its service life. However, the corrosion of reinforcing steel in concrete, particularly in Marine structures, is increasingly becoming a major durability issue leading to the failure of reinforced concrete structures [1]. In the case of Marine structures affected by chlorides, the protective passive film in the reinforcing rods is destroyed. Corrosion in the form of rust formation and/or loss in cross section of the reinforcing steel occur in the presence of oxygen and water [2].

The corrosion of steel in concrete essentially is an electrochemical process [3], where at the anode, iron is oxidized to iron ions that pass into pore solution and at the cathode, oxygen is reduced to hydroxyl ions. In other words, it is chemical reaction involving the transfer of charge (electrons) from one species to another [4]. Anode and cathode form a short-circuited corrosion cell, with the flow of electrons in the steel and of ions in the pore solution of the concrete. The corrosion between actively corroding areas of the reinforcing steel and passive areas is of great concern because

it results in very high local anodic current densities with corrosion rates of 0.5–1 mm/year [5]. The resulting local loss in cross section has dangerous implications for the structural safety, if the corroded steels are located in a zone of high tensile or shear stresses.

The experience of the marine engineers is that normally after the repair of the corrosion affected marine structures using standard surface coating on the rebars, the corrosion reoccurs after a year, necessitating in further rehabilitation measures after a period of time.

It is increasingly recognized in the recent past that reinforced concrete (RC) berthing structures are not permanently durable and free from maintenance. A large number of cases of damage and failure in RC berthing structures have been reported worldwide, and rehabilitation of such structures involves phenomenal cost, besides challenging technical problems in identifying appropriate rehabilitation techniques and materials. In order to arrive at a suitable rehabilitation strategy, non-destructive tests (NDT) are carried out to assess the condition of concrete in the distressed RC structural elements. Health monitoring of berthing structures through in situ testing is a specialized job requiring reliable test methods and instruments. The paper discusses in detail the rehabilitation of berthing structures at Cochin, Tuticorin and Chennai Port Trusts.

2 Cochin Port Trust

2.1 North Tanker Berth

Non-destructive tests (NDT) were conducted to assess the condition assessment of concrete in the reinforced concrete (RC) structural elements of the central platform of the North Tanker Berth (NTB) jetties at M/s Cochin Port Trust, Kochi. Figure 1 shows a general view of the NTB jetties at M/s Cochin Port Trust, Kochi.

Non-destructive tests (NDT) were conducted on the central platform of the NTB jetties. A visual survey was also carried out in the central platform of the NTB jetties.

The visual inspection of the central platform revealed that spalling of concrete and exposure of rebars were noticed in all the edge beams as well as most of the RC beams. Most of the locations of the RC deck slab in the central platform showed spalling of concrete and exposure of rebars with loss in diameter due to corrosion (Fig. 2). A few of the pile heads in the central platform showed minor spalling of concrete and exposure of rebars with loss in diameter due to corrosion.

The ultrasonic pulse velocity tests conducted on a majority of the structural elements of the central platform of the NTB jetties revealed that the integrity of the concrete falls under the category of "good" as per the guidelines of IS: 13311 (Part I)—992 [6]. It should be noted that the UPV tests were not conducted at the spalled and distressed locations of the structural elements. The tests were conducted at the unspalled locations to check if the visually good locations are also good in terms of

Fig. 1 General view of the NTB jetties at M/s Cochin Port Trust, Kochi

Fig. 2 View of the spalling of concrete with exposure and loss in diameter of rebars in the RC deck slab in the central platform

the integrity of the core of the concrete. The Rebound hammer tests conducted in the various RC structural elements of the central platform of the NTB jetties indicated that the quality of concrete in the near surface range from "satisfactory" to "good."

The results of the half-cell potential readings in the various RC structural elements of the central platform of the NTB jetties are more than -350 mV indicating that there is a greater than 90% probability that reinforcing steel corrosion is occurring in that area at the time of measurement as per the reference guidelines of ASTM C-876 [7]. The tentative reinforcement details provided in the RC structural elements of the central platform of the NTB jetties, viz. RC deck beams and RC deck slab of the NTB jetties were evaluated through a Profoscope survey.

It was recommended to rehabilitate the distressed RC structural elements in the splash zone of the central platform using under water micro-concrete jacketing, wherever the elements are under water during the low tide. The distressed structural elements that are above water are to be rehabilitated using the normal micro-concrete jacketing. The bill of quantity and the detailed estimate to carry out the rehabilitation of the structural elements in the central platform of the NTB jetties were also furnished to the M/s Cochin Port Trust, Kochi.

2.2 South Tanker Berth (STB)

Non-destructive tests (NDT) were conducted on the central platform, berthing dolphin 1, 2 and 3 of the STB jetties (Fig. 3). A visual survey was also carried out in the various structures of the STB jetties including the approach trestle.

The visual inspection of the central platform revealed that most of the RC beams and the RC deck slab showed spalling of concrete and exposure of rebars with loss in diameter due to corrosion. Spalling of concrete and exposure of rebars were noticed in all the edge beams of the central platform.

Spalling of concrete and exposure of rebars with loss in diameter due to corrosion were noticed in most of the RC columns and top deck RC beams of the berthing dolphin 1 (Fig. 4). Extensive distress and cracking were noticed at the junction of the pile haunch and the bottom beams of the berthing dolphin 1. Mis-alignment was noticed at the junction of the pile haunch and the bottom beams in some of the locations of the berthing dolphin 1 causing a significant eccentricity (Fig. 5).

Spalling of concrete and exposure of rebars with loss in diameter due to corrosion were noticed in most of the top deck beams and a few of the RC columns of the berthing dolphin 2 and 3. Cracking and minor spalling of concrete were noticed in

Fig. 3 A view of the STB jetties of M/s BPCL at M/s Cochin Port Trust, Kochi

Fig. 4 View of the spalling of concrete noticed in the RC top deck beam of the berthing dolphin 1

Fig. 5 Mis-alignment was noticed at the junction of the pile haunch and the bottom beams in some of the locations causing a significant eccentricity in the berthing dolphin 1

all the bottom deck beams as well as few edge beams of the berthing dolphin 3. The fender beams showed spalling of concrete and exposure of rebars with loss in diameter due to corrosion in all the three berthing dolphin.

Spalling of concrete and exposure of rebars with loss in diameter due to corrosion were noticed in all the deck beams of the jetties of the approach trestle. Most of the pile heads in the approach trestle showed spalling of concrete and exposure of rebars with loss in diameter due to corrosion. The RC columns in the front of the Trestle at the higher elevation alone showed cracking and spalling were noticed in a few of the columns.

The ultrasonic pulse velocity tests (Fig. 6) conducted on a majority of the structural elements of the STB jetties revealed that the integrity of the concrete falls under the category of “good" and "medium" as per the guidelines of IS: 13311 (Part I)—1992. It should be noted that the UPV tests were not conducted at the spalled and distressed locations of the structural elements. The tests were conducted at the unspalled locations to check if the visually good locations are also good in terms of the integrity of the core of the concrete. The Rebound hammer tests conducted in the various RC structural elements of the STB jetties indicated that the quality of concrete in the near surface range from “satisfactory” to “good.”

The concrete core samples (Fig. 7) extracted from selected locations of the berthing dolphin 1, 2 and 3 showed carbonation depths varying between 10 and 15 mm. The permeability of concrete of the core samples in the RC columns and RC deck beams of the berthing dolphin 1, 2 and 3 varied from 28 to 42 mm. The equivalent cube compressive strengths of the core samples in the three berthing dolphin varied from a low of 18.2 N/mm^2 to a high of 37.5 N/mm^2.

The results of the half-cell potential readings in the various RC structural elements (Fig. 8) of the central platform, berthing dolphin 1, 2 and 3 indicated that there is a greater than 90% probability that reinforcing steel corrosion is occurring in that area at the time of measurement as per the reference guidelines of ASTM C-876. The chloride contents in the RC columns and RC deck beams of the berthing dolphin 1, 2 and 3 are more than the threshold limit of 0.6 kg/m^3 at the time of placing as specified in IS: 456-2000. The pH of the concrete samples in the RC columns and RC deck beams of the berthing dolphin 1, 2 and 3 are between 10.00 and 12.49, and this indicates a reduction in alkalinity. The tentative reinforcement details provided in the RC structural elements, viz. RC columns, RC deck beams and RC deck slab of the STB jetties, were evaluated through a Profoscope survey.

Fig. 6 Half-cell potential test in progress in a RC column of the berthing dolphin of the STB jetties

Fig. 7 View of the coal jetties at VOC Port

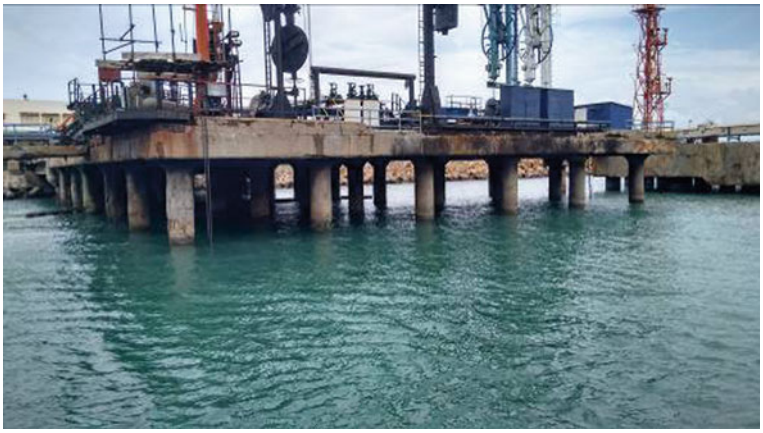

Fig. 8 View of the oil jetties at VOC Port

Based on the results of the NDT tests, it was recommended to rehabilitate the distressed RC structural elements in the splash zone of the various structures, viz. central platform, berthing dolphin 1, 2 and 3 and approach trestle using under water micro-concrete jacketing, wherever the elements are under water during the low tide. The distressed structural elements that are above water were recommended to be rehabilitated using the normal micro-concrete jacketing. A methodology was also suggested for the mis-aligned piles in the berthing dolphin 1.

3 Tuticorin Port Trust

The coal jetties and the oil jetties were constructed with reinforced concrete structural element and the following are the various components:

A coal jetties 1 and 2 (Fig. 9).

- Mooring dolphin 1
- Catwalk 1
- Approach jetties
- Main jetties
- Catwalk 2
- Mooring dolphin 2

B oil jetties (Fig. 10).

- Approach jetties
- Berthing dolphin 1
- Catwalk 1
- Jetties Head
- Catwalk 2
- Berthing dolphin 2

The visual inspection of all the three jetties revealed extensive distress in the various RC structural elements. Figures 11, 12 and 13 give some of the distresses noticed in the jetties.

Detailed NDT investigations, viz. Rebound Hammer Test, half-cell potential measurement and determination of chlorides and pH, were carried out in the three jetties.

Fig. 9 View of the damaged steel liner of the piles of dolphin 1 of the coal jetties 1

Fig. 10 View of distressed front portion in the jetties head of coal jetties 1

Fig. 11 View of distressed sides in the jetties head of the oil jetties

Fig. 12 View of the corrosion affected finger jetties before rehabilitation

Fig. 13 View of positioning of Galvanic anode, form work and jointing compound

Coal jetties 1 and 2 and the oil jetties at Tuticorin Port Trust were rehabilitated after conducting detailed NDT investigation in the RC structural elements of the berthing dolphin, main jetties, approach jetties, mooring dolphin and catwalk of the 3 jetties. The severe distress in the RC structural elements of the three jetties could be attributed to the failure of the earlier repair carried out using shotcreting. Based on the extensive NDT tests conducted, the condition of the concrete was assessed and a rehabilitation methodology consisting of micro-concrete jacketing and installation of self-regulating anodes was suggested for the various distressed RC structural elements of the three jetties. The bill of quantity and the detailed estimate to carry out the rehabilitation of the structural elements in the three jetties was also furnished to the M/s Tuticorin Port Trust, Kochi.

4 Chennai Port Trust

The marine structure taken up for the case study in the Chennai Port Trust is an existing finger jetties at Chennai with a berthing face of 218 m on east and west sides. It is 12 m wide throughout its 218 m length (Fig. 14). It is an open type piled finger jetties supported on piles. It was constructed about 25 years ago and had undergone severe damage due to corrosion. The finger jetties had suffered extensive cracking in all the members, viz. piles, pile caps and beams. Hence, the authorities wanted to rehabilitate the corrosion affected finger jetties and to modify it for berthing higher capacity vessels. Modification/rehabilitation of finger jetties was carried out at the Chokhani floating dry dock in Chennai Port Trust.

Fig. 14 View of the corrosion monitoring box

NDT tests were conducted to arrive at the rehabilitation methodology. The heavily corroded pile liners were cut and removed from −0.20 m level by using under water cutting gear. The cracked and spalled concrete was fully removed to expose the full circumference of the steel. The rust in steel was completely removed and cleaned by chemical means. Additional steel was provided for modification of pile for fender arrangement. Sacrificial zinc anodes were installed, and leads were provided for connecting to a monitoring box. Under water micro-concrete was used after coating the rebars with a zinc primer.

The galvanic anode used in the rehabilitation of the structure was an amphoteric zinc block embedded within a specially formulated cementitious mortar having a pore solution pH, which is sufficiently high for corrosion of the anode to occur and for passive film formation on the anode to be avoided as described in patent number PCT/GB94/01224. Galvanic anode was positioned in such a way to ensure all round contact with the jacketed micro-concrete and was attached to the existing/additional reinforcement using the wire ties. Galvanic anode fixing tool was used to tighten the wire ties, so that no free movement was possible, thus ensuring electrical continuity. Figure 15 shows a view of the fixing of galvanic anode to the pile. To check the electrical continuity between wire ties and reinforcement bar, a voltmeter was used.

The number of galvanic anodes to be provided in the micro-concrete jacketed portion was determined based on the quantity of the steel provided in the micro-concrete jacketed portion. The connectivity was checked before and after installation of the galvanic anodes. Leads were taken from the steel and also from the sacrificial anodes to the junction boxes which were fixed on the surface of the micro-concrete, so

Fig. 15 Complete view of the jetties after jacketing with under water micro-concrete

that readings could be taken as and when required to monitor the corrosion potentials over a period of time to evaluate the efficiency of the galvanic anode. Figure 16 shows a closer view of the corrosion monitoring box to be fixed on the surface of the jacketed portion for monitoring half-cell potential readings over a period of time. Figure 17 shows a view of the rehabilitated finger jetties.

The half-cell potentials measured at every 6 month interval for a period of 2 years showed values more positive than −200 mV indicating that there is a greater than 90% probability that no reinforcing steel corrosion is occurring in that area at the time of measurement. The half-cell potential values (Table 1) more positive than −200 mV even after 2 years clearly indicate that the self-regulating anodes were effective in preventing further distress to the RC structural elements. The UPV tests conducted after repair for a period of nearly one and a half years at every 6 month interval indicated that the integrity of the concrete was still good (Table 2).

5 Conclusions

The UPV measurements conducted in the finger jetties at the Chennai Port Trust clearly reveal that the integrity of the concrete in the rehabilitated structural elements of the finger jetties is good, indicating the efficiency of the micro-concrete jacketing technique designed and executed. The finger jetties has not shown any distress on account of corrosion even after a period of nearly 2 years as evident from the half-cell potential readings taken at every 6 month interval. The provision of galvanic anodes, i.e., the galvanic protection system, is performing well in the finger jetties and from the pattern of the half-cell potential readings observed over a period of

Table 1 Summary of the half-cell and potential difference readings in - mV

Id	Before repair	Immediately after repair	After 6 months	After 12 months	After 18 months	After 24 months
A8	-457-422-412	-004-007-008	-052-047 -038	-098-065-092	-085-085-095	-110-115-125
A12	-399-401-395	-006-006-007	-030-027-032	-075-072-075	-080-095-099	-130-125-132
A16	-419-398-412	-009-007-008	-024-032-040	-076-083-073	-095-098-099	-128-136-137
A18	-452-465-430	-005-006-008	-040-042-034	-070-085-082	-078-088-085	-125-145-138
B8	-365-372-385	-001-007-008	-046-052-043	-093-090-095	-085-085-100	-125-120-130
B13	-386-395-402	-004-007-006	-030-027-034	-085-080-082	-085-082-089	-145-140-141
B15	-395-401-389	-005-006-009	-021-029-035	-076-080-082	-085-089-092	-136-147-152
B18	-412-408-399	-006-008-008	-042-037-046	-093-085-087	-085-085-103	-135-146-148
C10	-425-436 -418	-004-008-009	-029-027-022	-060-065-068	-075-075-072	-110-125-134
C12	-412-389-395	-004-006-006	-034-042-049	-072-072-082	-075-082-093	-135-132-140
C16	-375-385-399	-008-011-009	-034-044-050	-074-065-073	-080-080-087	-128-132-143
C18	-391-401-391	-004-007-006	-021-027-051	-078-070-075	-082-088-090	-135-152-148
D6	-385-400-408	-006-009-008	-042-037-034	-077-085-090	-090-090-105	-125-133-141
D14	-365-385-401	-011-009-012	-024-033-034	-078-080-082	-090-090-098	-122-130-131
D16	-398-401-420	-008-006-006	-034-042-055	-065-060-072	-096-098-098	-135-126-122
D18	-399-385-398	-005-006-009	-042-052-056	-070-067-065	-085-092-090	-118-126-128

2 years, and it may be concluded that this may continue to perform well for a few more years without causing any problem. In addition to that, even if the corrosion was to reoccur after probably 5 years, it is required only to cut open the particular place to install another piece of galvanic anode, instead of resorting to an expensive large-scale rehabilitation measure resulting in closing down of the operation of the finger jetties during the period of rehabilitation.

The rehabilitation methodology suggested to the Cochin Port Trust and the Tuticorin Port Trust is also expected to increase the service life of the structures as in the case of the Chennai Port Trust.

It can be concluded that the galvanic protection system using the galvanic anodes are techno commercially viable system to be adopted for the rehabilitation of the corrosion damaged marine structures and they can be a useful tool to be installed even during the construction of the marine structures resulting in considerable savings to the government agencies.

Table 2 Summary of the UPV readings

Sl. No.	Location	No. of points	Average UPV values (km/s)
Before retrofitting			
1	A–Row pile and pile muff	21	2.46
2	B–Row pile cap	12	2.97
3	C–Row pile cap	12	2.53
4	D–Row pile and pile muff	14	2.89
5	A–Row beam	2	1.65
6	B–Row beam	2	1.99
After retrofitting			
7	A–Row pile and pile muff	21	3.97
8	B–Row pile cap	15	3.98
9	C–Row pile cap	14	4.03
10	D–Row pile and pile muff	20	3.97
11	A–Row beam	2	3.94
12	B–Row beam	2	3.93
After 12 months			
13	A–Row pile and pile muff	7	3.87
14	B–Row pile cap	6	3.85
15	C–Row pile cap	6	3.82
16	D–Row pile and pile muff	7	3.95
After 18 months			
17	A–Row pile and pile muff	14	3.91
18	B–Row pile cap	9	3.95
19	C–Row pile cap	11	3.88
20	D–Row pile and pile muff	11	3.75

References

1. Montemor MF, Simoes AMP, Ferreira MGS (2003) Chloride –induced corrosion on reinforcing steel. In: Fundamentals to the monitoring techniques, Cement & Concrete Composites, 25, pp 491–500
2. Tullmin MAA, Hansson CM, Roberge PR (2008) Electrochemical Technique for measuring reinforcing steel Corrosion. www.corrosionsource.com/events/intercorr/techsess/session1/abstract/tullmin. 8/6/2008

3. Hansson MC (1984) Comments on Electrochemical measurements of the rate of corrosion of steel. Conc-Ceme Conc Res 14:574–584
4. Yoo J-H, Park Z-T, Kim J-G, Chung L (2003) Development of a galvanic sensor system for detecting the corrosion damage of the steel embedded in concrete structures: part 1. Lab Tests Correlate Galvanic Curr Actual Damage-Ceme Con Res 33:2057–2962
5. Bautisa A, Gonzalez JA (1996) Analysis of the protective efficiency of Galvanizing against corrosion of reinforcements embedded in chloride contaminated concrete. Cem C Con Res 26(2):215–224
6. IS13311 (Part 1) 1992 - Methods of non-destructive testing of concrete Reaffirmed Oct 2008 Part 1. Ultrasonic Pulse Velocity
7. ASTM C 876 – 09 Standard test method for Half-Cell potentials of uncoated reinforcing steel in concrete

Modelling of Oil-Sediment Aggregates Trajectories Along Gulf of Khambhat, West Coast of India

S. Sathish Kumar, R. Balaji, V. Suneel, and P. Vethamony

Abstract Oil spill accidents on the marine waters impose great threat to the marine organism, humans and economic. Continuous efforts have been made to achieve effective mitigation measures to avoid the damage to the marine environment. Countermeasures, to combat the spilled oil, are to be taken, by the response action team, with thorough knowledge on the spilled oil conditions, characteristics and projected trajectory of oil sleek movements on the water surface. In the present study, experimental investigations are carried out to understand the interaction between the oil droplets and suspended sediments to form aggregates. Further, the laboratory results on the formed aggregates (OSAs) sizes are used as an input to the numerical model investigation. To demonstrate the use of numerical model to estimate the trajectories of a hypothetical oil spill incident, a 2D oil spill trajectory model is developed for Gulf of Khambhat, West Coast of India. A finite element method-based numerical scheme, TELEMAC-2D, is used for this study, which also capable of estimating the ambient hydrodynamics that drive the spilled oil to spread spatially. In addition to the estimate of spilled oil trajectory, oil-sediment aggregates trajectories are also investigated using the numerical model. From the numerical model results, it is evident that the area influenced by the OSAs is significantly small compared the ambient oil spill conditions, which may be thought of an alternate option for combating any future oil spill incidents.

Keywords Oil spill accident · Oil-sediment aggregates · Trajectory model · Mitigation measures · TELEMAC-2D

S. S. Kumar · R. Balaji (✉)
Department of Civil Engineering, Indian Institute of Technology Bombay, Mumbai 400076, India
e-mail: rbalaji@civil.iitb.ac.in; rbalaji@iitb.ac.in

V. Suneel
CSIR-National Institute of Oceanography, Dona Paula, Goa 403004, India

P. Vethamony
Environmental Science Center, Qatar University, Doha, Qatar

V. Sundar et al. (eds.), *Proceedings of the Fifth International Conference in Ocean Engineering (ICOE2019)*, Lecture Notes in Civil Engineering 106,
https://doi.org/10.1007/978-981-15-8506-7_25

1 Introduction

India produced of about 35.68MMT of crude oil and imported of about 220.43MMT for the year 2017–18, and the import quantity is gradually increasing every year [1]. In addition, the increasing oil exploration and production activities along the Indian continental shelf are also enhancing the possibilities of oil spill incidents. The various oil spill sources include natural seepage of oil from seabed, operational or accidental spill from ships, spill due to offshore exploration and productions, leakage during conveyance of oil to nearshore and spill due to accidents near ports and harbours. Generally, ship accidents can cause spilling of fuel oil, and it would be devastating to the marine environment, if the ship is of an oil tanker. Sivadas et al. [2] compared the number of oil spill accidents that have occurred around the world and in India, showing that incidents have increased since 1982 and peaked in 1991–95. Additionally, West Coast of India encountered more number of oil spill incident compared to East, which is because of high ship traffic, increase in oilfields and increase in number of minor/major ports. In which, Gujarat coast, especially Gulf of Khambhat, houses number of oil and gas fields than other places in India. In the present study, a two-dimensional finite element-based numerical model developed to estimate the spilled oil spatial dispersion on the marine water surface for Gulf of Khambhat, West Coast of India.

2 Experimental Study

The methodology of oil-sediment aggregates (OSAs) preparation procedure was described by Khelifa et al. [3] and Sun et al. [4]. The modified methodology used in the present study is as follows: OSAs are prepared under a controlled temperature (25 °C) using a reciprocating shaker at a constant mixing speed of 120 rpm at two different mixing period of 5 and 10 h. For the formation of OSAs, three different crude oils (Arabian light, Kuwait and Murban), dry sediment (SRM 1944) and a artificial sea water with the salinity of 33 ppm are used. Three oil sediment ratios (OSR) are considered, assuming that the ambient oil to sediment ratio is 1:1, 1:2 and 2:1, and further, 200 mg/L of sediment is added manually on the formed OSAs (under ambient condition) to investigate the influence on the formation of OSAs. The formed OSAs samples are analysed using microscope (OLYMPUS SZX2-ILLT) to measure the size of the OSAs and that size will be used as an input to the numerical model to estimate the OSAs spatial dispersion on the marine waters. Arabian light, Kuwait and Murban crude oils with different OSR vary between 0.21 to 1.66 mm, 0.26 to 1.19 mm and 0.26 to 1.06 mm, respectively.

3 Study Area

Many major, minor ports and many oil-exploring units are situated along Gulf of Khambhat (GoK) which is located in West Coast of India. It is one of the busiest waterways in India, so the chances for the oil spill accidents are comparatively more. According to Gujarat maritime Board (GMB), the state is handling 150 million tons of oil imports per annum inclusive of the crude oil exploration by ONGC in Gulf of Khambhat. The crucial part is the physical processes of the gulf which is really complex in the coastal features like bays, gulfs and estuaries. But gulf of Khambhat is one of the complex locations to study compare to other location in India [5–7]. GoK is facing high tidal range of around 10 m which is nowhere available in any other coastal region in India, and the current is also high reach around 4 ms^{-1} [8–11]. In the present study, attempt is made to give an overall understanding of the tidal hydrodynamics along GoK as well as it is important to study the hypothetical spilled oil trajectory modelling. Chandramohan et al. [12] state that highest long-term sediment deposition in Gulf of Khambhat is 0.03 m at Sandheads and it is the occurrences of spits and shoals. Sources of the sediment deposits are transported through rivers. It clearly states that Gulf of Khambhat is one of the regions where the suspended sediment concentrations are really high. Thus, Gulf of Khambhat is the ideal location to investigate the OSAs trajectory modelling.

4 Numerical Modelling

The present study involves development of a hydrodynamic model, validates with observed tidal level and currents and to use the same to estimate the spread of spilled oil.

4.1 Model Description

Hydrodynamic Model

In order to estimate the ambient hydrodynamic conditions along Mumbai coastline, a two-dimensional numerical model, based on finite element method (TELEMAC-2D—Hervouet [13]), developed by solving shallow water equation.

The vertically averaged form of the continuity equation is given as

$$\frac{\partial h}{\partial t} + \frac{\partial (hu)}{\partial x} + \frac{\partial (hv)}{\partial y} = 0 \tag{1}$$

The vertically averaged form of momentum equation is

$$\frac{\partial(hu)}{\partial t}+\frac{\partial(huu)}{\partial x}+\frac{\partial(huv)}{\partial y}=-gh\frac{\partial z}{\partial x}+\frac{\partial}{\partial x}\left(hv_e\frac{\partial u}{\partial x}\right)+\frac{\partial}{\partial y}+\left(hv_e\frac{\partial u}{\partial y}\right)+hF_x \tag{2}$$

$$\frac{\partial(hv)}{\partial t}+\frac{\partial(huv)}{\partial x}+\frac{\partial(hvv)}{\partial y}=-gh\frac{\partial z}{\partial y}+\frac{\partial}{\partial x}\left(hv_e\frac{\partial v}{\partial x}\right)+\frac{\partial}{\partial y}+\left(hv_e\frac{\partial u}{\partial y}\right)+hF_y \tag{3}$$

where h is the depth of water (m), u and v are depth averaged velocity components (ms^{-1}) in x and y directions, g is the gravity acceleration (ms^{-2}), v_e is the momentum diffusion coefficient (m^2s^{-1}), Z is the elevation of free surface (m), t is the time (s), x, y are the horizontal space coordinates (m), F_x, F_y are source or sink terms in the dynamic equations in u and v, respectively, which include wind and atmospheric pressure, Coriolis force and bottom friction.

Oil Spill Model

A Lagrangian/Eulerian oil spill model, using TELEMAC hydro-informatic system, is used to estimate the spatial dispersion of the spilled oil. In this model, Lagrangian approach predicts the spilled surface oil slick transport, whereas the oil dissolution is governed by Eulerian advection–diffusion equation. In this present study, the processes of advection, turbulent diffusion, evaporation, volatilization and dissolution in the water column are considered for modelling. These transport and weathering processes are treated successively in the same time step using the fractional step method [14, 15].

4.2 Model Setup

A relatively large model domain between 16–22 °N and 68–74 °E, covering entire Gulf of Khambhat (GoK) and part of Arabian Sea, is considered for the model with a size of 650 kms × 750 kms. The bathymetry of the study region was extracted from the Admiralty Charts and the depth contours varying from 1 to 3000 meters. As discussed in the earlier Mumbai case study, BlueKenue used to create a triangular mesh over the gulf domain. Initially, equal size of triangular elements is created, and then, the nearshore boundary node density is increased than the offshore boundary. The distance between the nodes varies from 0.5 km to 20 kms from nearshore to offshore boundary, respectively. The whole domain is spatially discretized with the total node numbers of 84,455 and total triangular elements of 165,921 (Fig. 1) with the connecting neighbour nodes of 2 (min.) to 7 (max.). Final mesh nodes are interpolated with the derived bathymetry data.

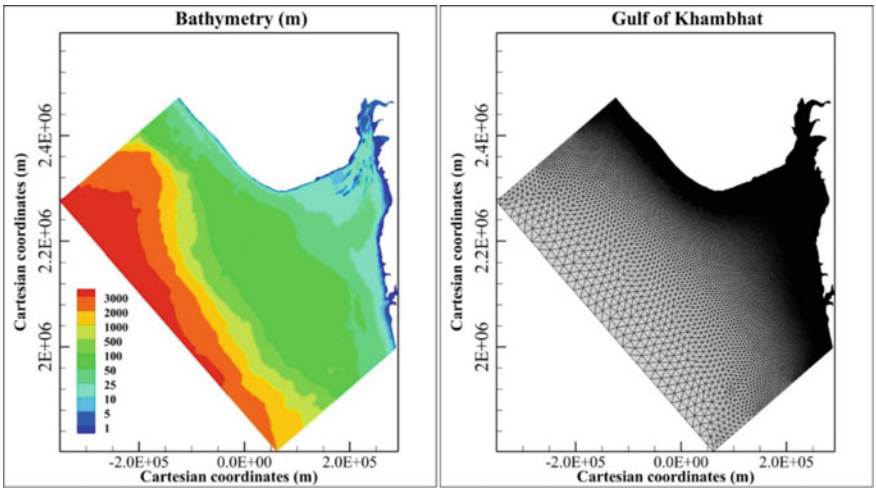

Fig. 1 Typical view of the Gulf of Khambhat domain with the bathymetry and mesh

5 Model Results

5.1 Hydrodynamic Modelling

For the initial boundary condition, a global inverse barometric tidal model TPXO 7.2 [16, 17] combined of ten major tidal constituents. Offshore boundary nodes (North, South and West) selected as an open boundary with prescribed water surface elevation to force the boundary condition on the model and the nearshore boundary nodes (East) given as a solid boundary condition. Tidal flat keyword activated in this study to consider the areas that are periodically wet and dry during high and low tide, respectively, and the Coriolis force activated since the model domain is large.

In this model, model domain is divided into multiple friction zones [18] to apply spatially varying friction coefficient values. Several trail run simulations carried out and the model predicted tidal level and currents compared with the field measured data, and then, the friction values (either increased or decreased) area adjusted based on the comparison. The friction coefficient values vary from 50 to 160 at the water depth of >100 m to <5 m, respectively. Calibration of the model by comparing the tidal levels, currents with the observed data shows good agreement. In order to improve model prediction, the least square fitting was used between the observed and the model results as shown in Fig. 2. Based on the model calibration, the friction coefficient values for the model domain are fixed for any further hydrodynamic simulation. The rest of the field measurement data is used for the model validation.

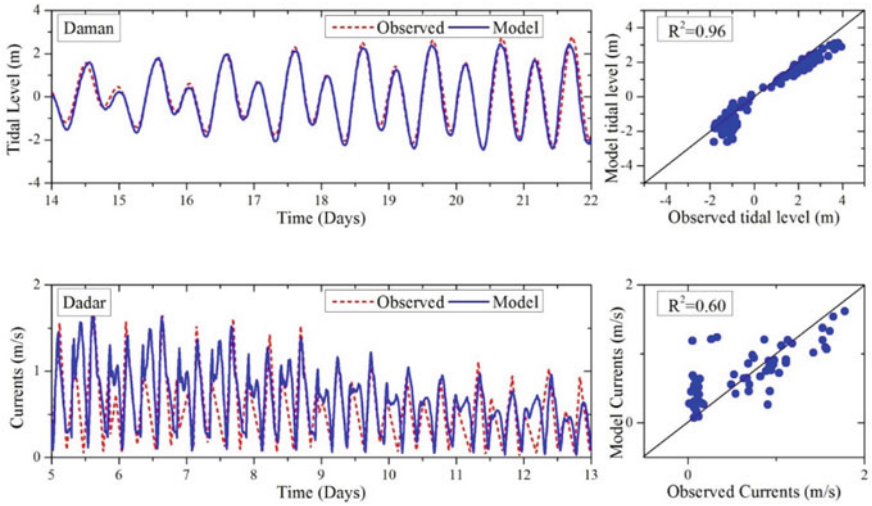

Fig. 2 Typical comparison of the numerical model results with observed data

Table 1 Overview of the inputs for Gulf of Khambhat oil spill model

Spill location (UTM)	231,112.453, 2,344,484.250 (near Hazira) 232,518.438, 2,402,624 (near Ghoga)
Simulation period	13/07/2018 to 17/07/2018 (Spring tide) 21/07/2018 to 25/07/2018 (Neap tide)
Start spill date	13/07/2018 23:00:00 (Spring tide) 21/07/2018 23:00:00 (Neap tide)
Spreading model	Fay's model

5.2 Oil Spill Modelling

Oil spill is introduced into Gulf of Khambhat model at two locations near Hazira and Ghoga that situated near the oilfields. A hypothetical oil spill accident was introduced, and the trajectories are estimated, using the numerical model. Table 1 shows the location, period of model simulation, spill release and other input data for spilled oil trajectory model for Gulf of Khambhat. Figure 3 illustrates the movement of spilled oil at every 24 h typically for Hazira during spring tide.

5.3 OSA Trajectory Model

After spilled oil trajectory simulation, the same model used to estimate the movement of oil sediment aggregates (OSAs). As explained earlier, the experimental results are

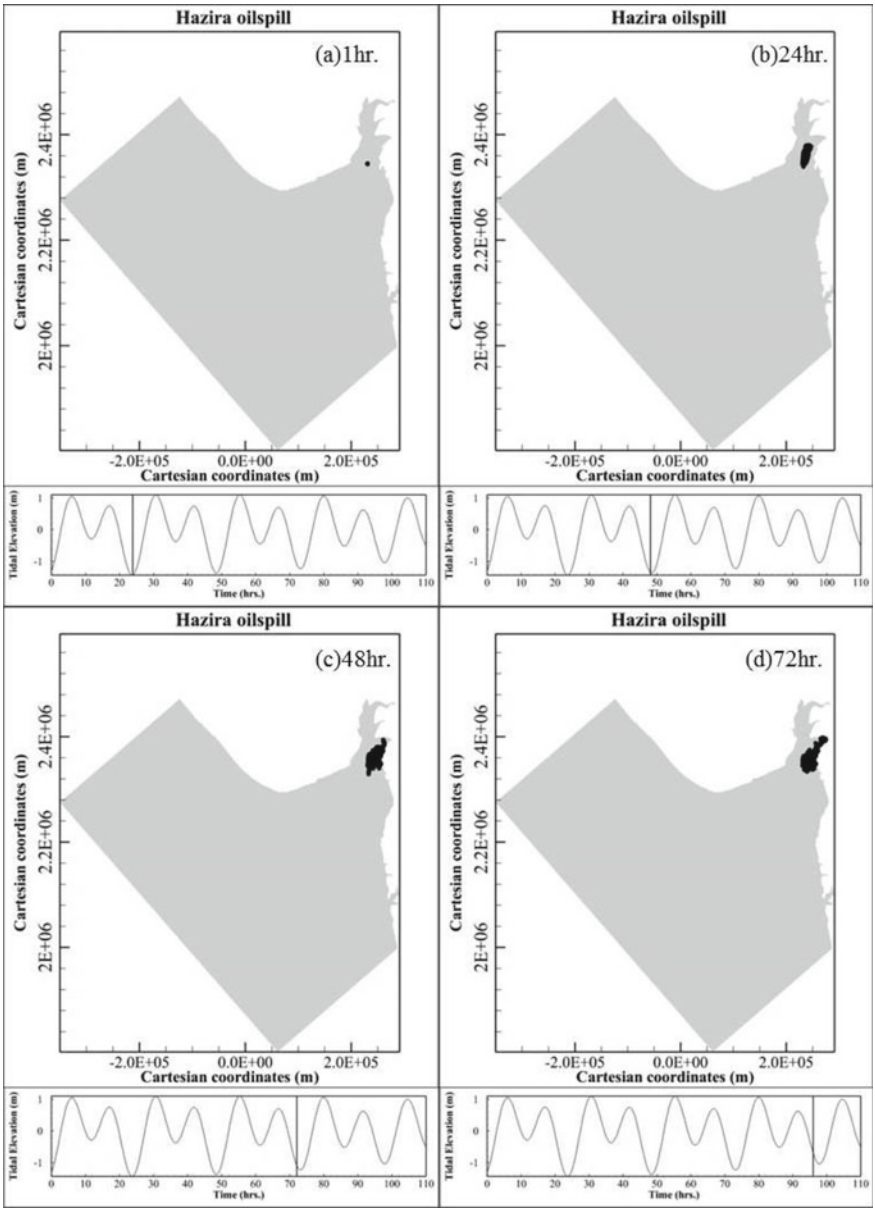

Fig. 3 Typical snapshots of the estimated oil spill trajectories near Hazira during spring tide

used on the model as an input to predict the movement of OSAs. Typical Arabian light crude oil sample OSA size of 1.25 mm is used as a particle diameter in the numerical model, and OSA movement is estimated during the spring and neap tide near Hazira and Ghoga. Figure 4 illustrates the movement of OSA at every 24 h typically for Ghoga during neap tide.

Approximate area influenced by spilled oil and OSAs are estimated for two locations during spring tide and neap tide (Table 2). During the spring tide, the spilled oil near Hazira influences about 1989 km^2, whereas the OSA covers 1/8th of the area is about 237 km^2. However, during the neap tide, the OSA may influence (1088 km^2) as half as the area of spilled oil (1797 km^2). During the spring and neap tide, near Ghoga location, the spilled oil influences of about 2198 km^2 and 1783 km^2, whereas the OSA influences about 1100 km^2 and 858 km^2, respectively. It is observed from the numerical investigation, the area of influence by OSA is much less than spilled oil influenced area on the marine waters.

6 Conclusion

An oil spill accident in the marine waters is a great threat to the marine ecosystem as well as socio-economic impact. To encounter the spilled oil, a countermeasure technique without affecting the marine environment has to be implemented based on the numerical model estimation about the spilled oil spatial dispersion on the marine water surface. In the present study, experimental study is carried out to study the natural mitigation technique (oil sediment aggregates formation) against the spilled oil and developed a location-specific numerical oil spill trajectory prediction model for Gulf of Khambhat. Hypothetical oil spill cases, tested in the Gulf of Khambhat regions, near the oilfields—Hazira and Ghoga, revealed that the area of influence by the OSA is less than the spilled oil, as estimated by the numerical model. The spatial dispersion of the spilled oil is significantly influenced by the tidal conditions. The hypothetical estimate of area of influence of OSA is half of the spilled oil influenced area, at the two different tested locations. The developed oil spill trajectory prediction numerical model to estimate the dispersion of the oil on the water surface along the Gulf of Khambhat found to be effective tool during the mitigation measures.

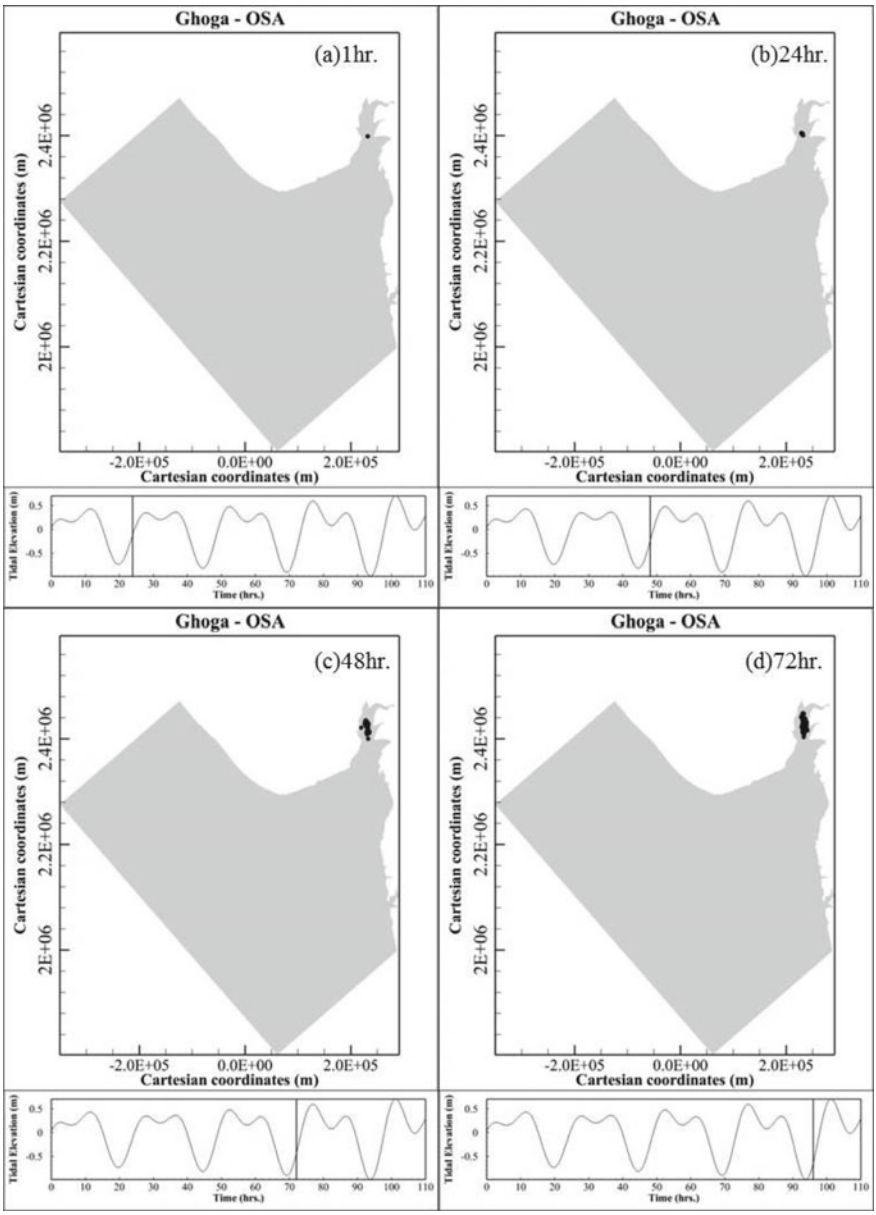

Fig. 4 Typical snapshots of the estimated OSA trajectories near Ghoga during neap

Table 2 Area of influence by spilled oil and OSAs along the Gulf location

Location	Tide	Approx. area of influence by spilled oil (km^2)	Approx. area of influence by OSA (km^2)
Near Hazira	Spring	1989	237
	Neap	1797	1088
Near Ghogha	Spring	2198	1100
	Neap	1783	858

Acknowledgements Authors thank the Director of the CSIR-National Institute of Oceanography, Goa, for permitting to carry out the experimental work.

References

1. Ministry of Petroleum and Natural Gas (2018) Indian Petroleum and Natural Gas Statistics 2017–18
2. Sivadas S, Gregory A, Ingole B (2008) How vulnerable is Indian coast to oil spills? Impact of MV Ocean Seraya oil spill. Curr Sci 95:504–512
3. Khelifa A, Fieldhouse B, Pjontek D, Wang Z, Yang C, Fingas M, Brown CE, Gamble L (2007) A laboratory study on formation of oil-SPM aggregates using the NIST standard reference material 1941b. In: 30th Arctic and Marine Oil spill Program. AMOP Technical Seminar, Environment Canada, Ottawa, ON, pp 35–48
4. Sun J, Khelifa A, Zheng X, Wang Z, So LL, Wong S, Yang C, Fieldhouse B (2010) A laboratory study on the kinetics of the formation of oil-suspended particulate matter aggregates using the NIST-1941b sediment. Mar Pollut Bull 60:1701–1707. https://doi.org/10.1016/j.marpolbul.2010.06.044
5. Kunte PD (2008) Sediment concentration and bed form structures of Gulf of Cambay from remote sensing. Int J Remote Sens 29:2169–2182. https://doi.org/10.1080/01431160701422221
6. Siddiquie HN, Rao DG, Wagle BG, Vora KH, Gujar AR, Karisiddaiah SM (1981) The continental shelf in the southern Gulf fo Khambhat—an evaluation of the sea bed for constructions. In: Proceedings first Indian national conference on harbour and ocean engineering. Central Water and Power Research Station, Pune, India, pp 35–42
7. Vora KH, Gujar AR, Karisiddaiah SM (1980) Sandwaves of the Gulf of Khambhat. Indian J Mar Sci 9:90–93
8. Giardino A, Elias E, Arunakumar A, Karunakar K (2014) Tidal modelling in the Gulf of Khambhat based on a numerical and analytical approach. In: Proceedings 5th Indian national conference on harbour and ocean engineering, 5–7 February 2014, CSIR-NIO Goa, India, pp 106–111
9. Kumar VS, Kumar KA (2010) Waves and currents in tide-dominated location off Dahej, Gulf of Khambhat. India Mar Geod 33:218–231. https://doi.org/10.1080/01490419.2010.492299
10. Kumar VS, Pathak KC, Pednekar P, Raju NSN, Gowthaman R (2006) Coastal processes along the Indian coastline. Curr Sci 91:530–536
11. Sathish Kumar S, Balaji R (2015) Tidal hydrodynamics along Gulf of Khambhat, West Coast of India. In: Aquatic Procedia Elsevier B.V., pp 41–48
12. Chandramohan P, Jena BK, Kumar VS (2001) Littoral drift sources and sinks along the Indian coast. Curr Sci 81:292–297
13. Hervouet J-M (2007) Hydrodynamics of free surface flows. Wiley, Chichester, UK

14. Joly A, Goeury C, Hervouet J-M (2014) Adding a particle transport module to Telemac-2D with applications to algae blooms and oil spills. Report
15. Goeury C, Hervouet J-M, Baudin-Bizien I, Thouvenel F (2014) A Lagrangian/Eulerian oil spill model for continental waters. J Hydraul Res 52:36–48. https://doi.org/10.1080/00221686.2013.841778
16. Haigh ID, Eliot M, Pattiaratchi C (2011) Global influences of the 18.61 year nodal cycle and 8.85 year cycle of lunar perigee on high tidal levels. J Geophys Res 116:1–16 https://doi.org/10.1029/2010JC006645
17. Le Provost C, Bennett AF, Cartwright DE (1995) Ocean tides for and from TOPEX/POSEIDON science 267:639–642 https://doi.org/10.1126/science.267.5198.639
18. Sathish Kumar S, Balaji R (2015) Effect of bottom friction on tidal hydrodynamics along Gulf of Khambhat. India Estuar Coast Shelf Sci 154:129–136. https://doi.org/10.1016/j.ecss.2015.01.012

High Pressure Rheology of Gas Hydrate in Multiphase Flow Systems

Gaurav Pandey and Jitendra S. Sangwai

Abstract The measurement of the rheological properties of gas hydrate slurries necessitates the high pressure rheometer that can provide a proper mixing inside the pressure cell during hydrate formation from two multiphase fluids, water and gas. However, the hydrate formation is highly challenging in conventional cup and bob geometry due to its plane surface. To overcome this, the present work focuses on the study of high pressure rheology for hydrate slurries formed from water-heptane (C_7H_{16}) system using a high pressure cell in Anton-Paar® (MCR-52) rheometer and a modified Couette geometry which enables the measurement of rheological studies of multiphase hydrate system. It was observed that the hydrate slurries exhibit shear thinning behavior. The present study provides an important information about the rheology of methane hydrate slurries formed from multiphase systems for flow assurance applications.

Keywords Gas hydrates · High pressure rheometer · Multiphase · Viscoelastic properties

1 Introduction

In subsea operations, there are several flow assurance issues which hinder the flow and/or block the oil and gas pipelines. The main challenges in a subsea pipeline

G. Pandey
Department of Petroleum Engineering and Earth Sciences, University of Petroleum and Energy Studies, Dehradun 248007, India
e-mail: gauravpandey@u.nus.edu

G. Pandey · J. S. Sangwai (✉)
Gas Hydrate and Flow Assurance Laboratory, Petroleum Engineering Program, Department of Ocean Engineering, Indian Institute of Technology Madras, Chennai 600036, India
e-mail: jitendrasangwai@iitm.ac.in

G. Pandey
Department of Chemical and Biomolecular Engineering, National University of Singapore, Singapore 117585, Singapore

V. Sundar et al. (eds.), *Proceedings of the Fifth International Conference in Ocean Engineering (ICOE2019)*, Lecture Notes in Civil Engineering 106,
https://doi.org/10.1007/978-981-15-8506-7_26

include scale formation, wax deposition, asphaltene precipitation, sanding, and hydrate deposition, which terminologically are represented as flow assurance issues [1].

The natural gas hydrates are solid ice like crystalline compounds which consist of guest gas molecules (e.g., methane, ethane, propane, carbon dioxide) and host (water) molecules which forms cages by hydrogen bonding. The guest molecules are entrapped in the cages formed by the water molecules. Hydrates are classified into three types of crystal structures, viz. structure SI, (formed from methane, carbon dioxide, ethane, etc.), structure SII, (formed from propane, isobutane, hydrogen, etc.), and structure SH (formed from methane + neohexene, etc.) [2, 3]. The hydrate formation is primarily much more strong and favorable at low temperature and high pressure conditions. These solid crystalline compounds are formed and accumulate in crude oil and gas pipeline systems which leads to the complete flow blockage of pipelines [1, 2]. To overcome the hydrate problems, various types of studies (flow loop studies, thermodynamic and kinetic studies) using chemical inhibitors, anti-agglomerants, etc., have been reported in the literature [4–8]. However, it is more important for the oil pipeline operators to determine the occurrence of hydrate formation and the extent to which the flow gets stuck in the pipeline. Therefore, the investigations on rheological properties of hydrate slurries formed from multiphase systems play a crucial role in determining the flow ability of hydrate slurries. Rheology is the study of flow and deformation of matter. From the rheological measurements, we can get the information about the viscosity, flow curve, viscoelastic properties, yield stress, shear stress of hydrate slurries at pipeline conditions (temperature and pressure) which can be helpful for designing the operation to ensure the smooth flow of oil and gas in the pipelines [9, 10].

The better knowledge about the rheological properties of hydrate slurries in flow lines is highly essential for hydrates management in the subsea pipeline. Few researchers used external mixing cell and carried out the rheological studies on methane hydrate systems but were not able to achieve high viscosities (due to poor mixing) [11–13]. To overcome this and achieve proper mixing of gas and water, recently, we have carried out rheological measurements on pure methane hydrate slurries by using novel modified Couette geometry [14]. The present work, which is the extension of the earlier work, focuses on the study of high pressure rheology for methane hydrates slurries formed from water-heptane (C_7H_{16}) system using a high pressure cell in Anton-Paar® (MCR-52) rheometer and a modified Couette geometry which enable the measurement of rheological studies of multiphase hydrate system.

2 Experimental Section

2.1 Experimental Setup

The schematic of the experimental setup used in the present work is shown in Fig. 1. The details on the conventional bob and modified bob (Fig. 2) are available in our

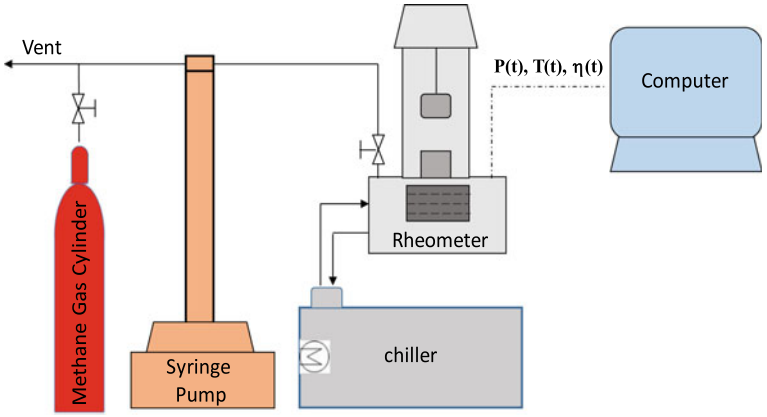

Fig. 1 Schematic diagram of the experimental setup

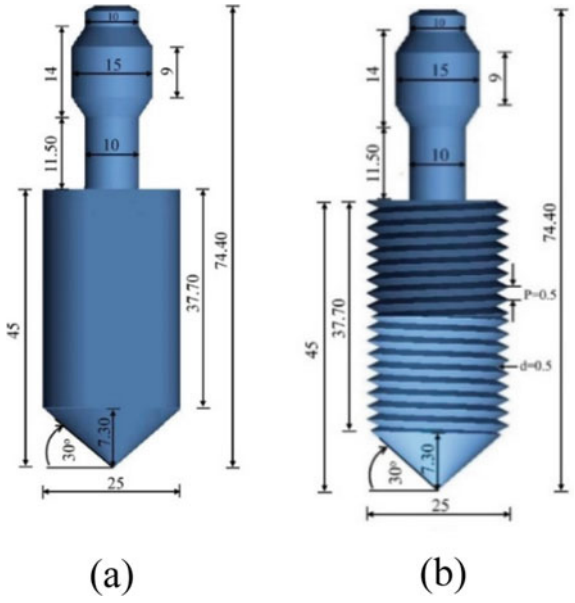

Fig. 2 Schematic of the: (**a**) standard bob, (**b**) modified bob, (P = pitch, d = depth, all dimensions are in mm (adapted from Pandey et al. [14]))

previous work [14]. The rheometer is an Anton-Paar (MCR-52) rheometer instruments and is used for examining the rheological properties of the methane hydrate slurries. The working pressure of the rheometer is 15 MPa. The maximum torque limit and the angular velocity limit are 200 mNm and 314 rad/s, respectively. The concentric cylinder geometry (cup and bob) has been used for the experiments. The cup and bob geometry has an annular gap of 1 mm. The cup and bob geometry has maximum shear rate and shear stress of 1550 s^{-1} and 3000 Pa, respectively. Syringe pump (Teledyne ISCO 500D) has a capacity of 507 ml volume and hold up to a

maximum pressure of 25.86 MPa. Syringe pump has been used to pressurize the pressure cell with methane gas for the hydrate formation experiments.

2.2 Experimental Procedure

Before the experiment, the modified Couette geometry has been calibrated with the silicone fluids having viscosities 0.977 and 9.256 Pa.s. Subsequently, the experimental investigations have been carried out for methane hydrates slurries which are formed in situ from water-heptane (50:50 v/v) mixture in the rheometer cell. Water and ethylene glycol mixture from the chiller has been circulated at the desired temperature through the jacket of the rheometer cell to attain the temperature of 275.15 K. Once the temperature is attained, the pressure cell is purged twice with the methane gas and then pressurized at 10 MPa with the help of syringe pump. The rheological properties of methane hydrate slurries formed from multiphase system are measured at 1000 s^{-1} shear rate during the hydrate formation and dissociation. A sampling time of 10 s was employed for the data collection. The rheological experiments were conducted twice to check for the repeatability.

3 Results and Discussion

Methane hydrate slurries were formed from water-heptane multiphase systems at a shear rate of 1000 s^{-1} at 10 MPa and 275.15 K. Figure 3 represents the viscosity and pressure profiles during formation of methane hydrate slurries with respect to time (after hydrate nucleation) and upto 24 h. It was found that the viscosity of the water-heptane mixture is about 0.001 Pa.s initially. As soon as the hydrate nucleation takes place, the viscosity of hydrate slurries increases above 0.001 Pa.s and stabilizes to 0.131 Pa.s. Initially, after the injection of methane gas in the pressure cell, the dissolution of the methane gas into heptane has been observed which is marked by small decrease in the pressure. The sudden increase in the viscosity has been observed from 0.001 to 0.968 Pa.s in few minutes at around 7 min, which indicate hydrate nucleation. At the same time, the pressure drop was also observed from 10 to 9.23 MPa. This increase in viscosity is due to the formation of methane hydrate in the system. Further, the viscosity of the hydrate slurry is found to decrease, and then, the viscosity stabilizes at 0.131 Pa.s. During this time, the pressure of the cell is reduced to 8.35 MPa, and then, there is no further change in the viscosity and the pressure.

Subsequently, the flow curve was also measured at the end of hydrate formation for 10 min by using shear ramp profile for a shear rate range of 1–1000 s^{-1}. Figure 4 represents the flow behavior of methane hydrate slurries formed from water-heptane multiphase systems at 10 MPa, 275.15 K. It was observed that the hydrate slurry exhibits the shear thinning behavior. Cross model found to fit the flow profile suitably

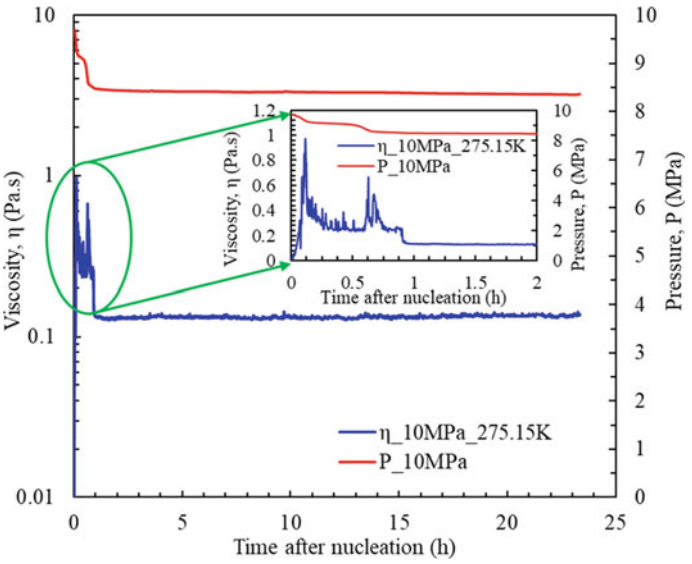

Fig. 3 Viscosity and pressure profile of methane hydrate formed from water-heptane multiphase systems at 10 MPa, 275.15 K, and at 1000 s^{-1}

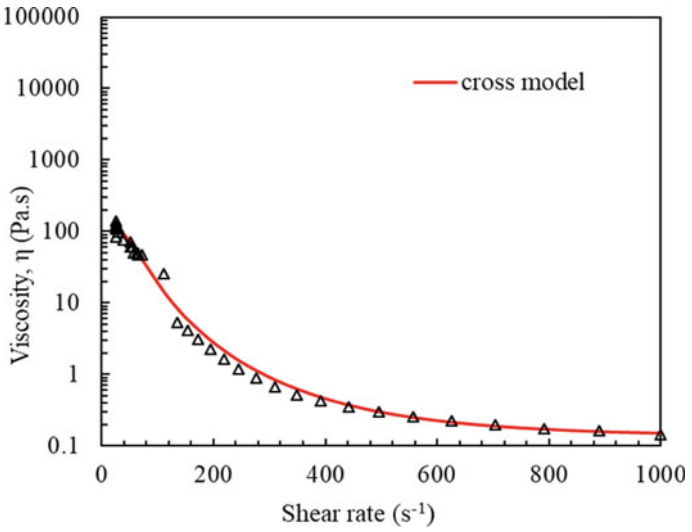

Fig. 4 Flow curve profile of methane hydrate slurries formed from water-heptane multiphase systems at 10 MPa, 275.15 K

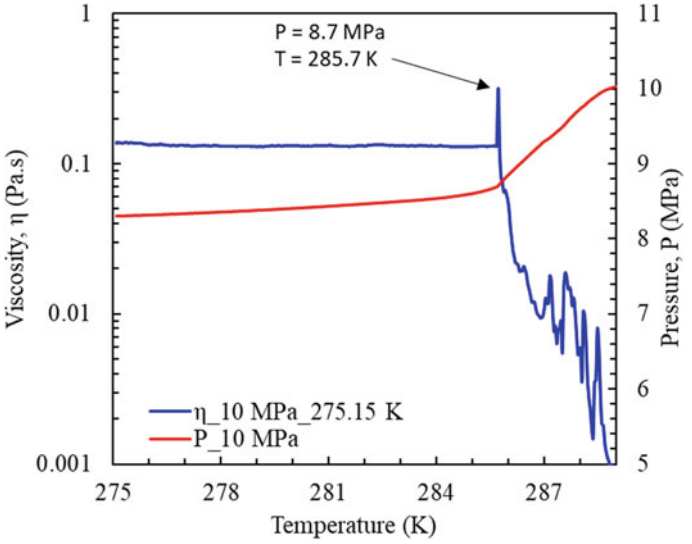

Fig. 5 Viscosity and pressure profile during dissociation of methane hydrate formed from water-heptane multiphase systems at 10 MPa, 275.15 K, 1000 s^{-1}

[15]. The zero shear viscosity (η_o) and the infinite shear viscosity (η_∞) calculated from the cross model are observed to be 120.84 and 0.13 Pa.s, respectively.

Rheological studies during hydrate dissociation have also been investigated using thermal stimulation. A rate of 0.5 K/min in temperature, from 275.15 to 298.15 K, was employed to dissociate the hydrate slurries. Figure 5 represents the viscosity profile during the dissociation of methane hydrate slurries formed from water-heptane system at 10 MPa, 275.15 K. During hydrate dissociation, an abrupt change in the viscosity from 0.131 to 0.318 Pa.s has been observed, which is close to the near hydrate equilibrium dissociation temperature and pressure. The increase in the viscosity is due to the possibility of ballooning of the hydrate crystals near hydrate equilibrium condition.

4 Conclusion

Methane hydrate slurries were formed in situ from (water–gas-heptane) multiphase systems in the high pressure rheometer at a shear rate of 1000 s^{-1}. The modified geometry of bob provides the good mixing to form methane hydrates in situ and measures the rheological properties of the hydrate slurries during hydrate formation and dissociation. Initially, increase in the magnitude of viscosity was observed during the time of hydrate nucleation, and once the hydrate crystals grow and aggregate, the viscosity decreases and stabilizes at 0.131 Pa.s. Other rheological tests have

also been performed to understand the properties of methane hydrate slurries such as yield stress. Methane hydrate slurries represent the non-Newtonian and shear thinning behavior. A peak in the viscosity was also observed just near the hydrate equilibrium temperature during the hydrate dissociation. The present study provides an important information about the rheology of methane hydrate slurries formed from multiphase systems for flow assurance applications.

Acknowledgements Gaurav Pandey acknowledges the support from the joint NUS-IITM Ph.D. program.

References

1. Sloan ED (2010) Natural gas hydrates in flow assurance. Gulf Professional Publishing, USA
2. Sloan ED Jr (2003) Fundamental principles and applications of natural gas hydrates. Nature 426:353
3. Sloan Jr, ED, Koh C (2007) Clathrate hydrates of natural gases. CRC Press
4. Delahaye A, Fournaison L, Marinhas S, Martínez MC (2008) Rheological study of CO_2 hydrate slurry in a dynamic loop applied to secondary refrigeration. Chem Eng Sci 63:3551–3559
5. Peng BZ, Chen J, Sun CY, Dandekar A, Guo SH, Liu B, Mu L, Yang LY, Li WZ, Chen GJ (2012) Flow characteristics and morphology of hydrate slurry formed from (natural gas+ diesel oil/condensate oil+ water) system containing anti-agglomerant. Chem Eng Sci 84:333–344
6. Jerbi S, Delahaye A, Oignet J, Fournaison L, Haberschill P (2013) Rheological properties of CO_2 hydrate slurry produced in a stirred tank reactor and a secondary refrigeration loop. Int J Refrig 36(4):1294–1301
7. Mech D, Pandey G, Sangwai JS (2015) Effect of NaCl, methanol and ethylene glycol on the phase equilibrium of methane hydrate in aqueous solutions of tetrahydrofuran (THF) and tetra-n-butyl ammonium bromide (TBAB). Fluid Phase Equilib 402:9–17
8. Pandey G, Veluswamy HP, Sangwai JS, Linga P (2019) Morphology study of mixed methane-tetrahydrofuran hydrates with and without the presence of salt. Energy Fuels 33:4865–4876
9. Deshpande AP, Krishnan JM, Kumar PS (2010) Rheology of complex fluids. Springer Science & Business Media, Berlin
10. Macosko CW (1994) Rheology Principles. Measurements and Applications. Wiley-VCH, New York
11. Webb EB, Rensing PJ, Koh CA, Dendy Sloan E, Sum AK, Liberatore MW (2012) High pressure rheometer for in situ formation and characterization of methane hydrates. Rev. Sci. Instru. 83(1):015106
12. Webb EB, Koh CA, Liberatore MW (2013) Rheological Properties of Methane Hydrate Slurries Formed From AOT + Water + Oil Microemulsions. Langmuir 29(35):10997–11004
13. Webb EB, Koh CA, Liberatore MW (2014) High pressure rheology of hydrate slurries formed from water-in-mineral oil emulsions. Ind Eng Chem Res 53(17):6998–7007
14. Pandey G, Linga P, Sangwai JS (2017) High pressure rheology of gas hydrate formed from multiphase systems using modified Couette rheometer. Rev. Sci. Instru. 88(2):025102
15. Cross MM (1965) Rheology of non-Newtonian fluids: a new flow equation for pseudoplastic systems. J Colloid Sci 20:417–437

Temporary Cofferdam Structure for New Dry Dock

R. Sundaravadivelu, S. A. Sannasiraj, S. Sakthivel, and R. Kalpana

Abstract This paper presents the design of temporary cofferdam structure for new dry dock. For this, construction of temporary dewatering has to be done at the dry dock area for excavation and safeguarding the work area and keeping dry. The temporary cofferdam can be built in such a way that the entire length of pile sheet piles can be installed and removed easily. Hence, cofferdam with steel sheet pile and beams is proposed based on geological and site constraints. In this paper, discussion about a temporary dewatering at the dry dock location is necessary to isolate the proposed work area. This method provides safe environment to work, and materials can typically be reused on other projects. The 2D analysis using Staad pro has been carried out.

Keywords Steel pipe pile · Sheet pile · Tie rod · Base plate · ISMB500

1 Introduction

A new dry dock is proposed to be constructed at south west coast of India. The Proposed area should be dewatered before construction. Therefore, temporary cofferdam is introduced for dewatering and for ease of construction. The cofferdam is proposed to be constructed with pile sheet pile wall on the proposed dock side & touch pile wall on sea side. Two rows of piles are interconnected by tie rod. So, there is a need of a cofferdam structure which do not create much pollution and also

R. Sundaravadivelu (✉) · S. A. Sannasiraj · S. Sakthivel · R. Kalpana
Department of Ocean Engineering, Indian Institute of Technology Madras, Chennai 600036, India
e-mail: rsun@iitm.ac.in

S. A. Sannasiraj
e-mail: sasraj@iitm.ac.in

S. Sakthivel
e-mail: enggoecrd@gmail.com

R. Kalpana
e-mail: kalpu.j20@gmail.com

V. Sundar et al. (eds.), *Proceedings of the Fifth International Conference in Ocean Engineering (ICOE2019)*, Lecture Notes in Civil Engineering 106,
https://doi.org/10.1007/978-981-15-8506-7_27

economical. The cost comparison of cofferdam in rectangular or U shape indicates that U shape is economical.

2 Need of the Project

To provide a feasible construction space for the new dry dock by providing a suitable cofferdam.

3 Scope of the Project

- To provide a structurally sound cofferdam to withstand the earth pressure and differential water pressure.
- To suggest a temporary structure that can be easily constructed with less time and cost.
- To check the stability of the sheet pile for differential water pressure and later earth pressure.
- To find out the factor of safety.
- To check the stiffness properties of the provided sheet pile section.

4 General Arrangements of Cofferdam

One row of pile sheet pile wall on proposed dry dock side & one row of discrete pile on river side are provided. The dock side and river side piles are interconnected by tie rod.

For the initial 192 m, the width of the cofferdam is 15 m as dredge depth along this length is (−)10.0 m.

Also, the pile diameter is 1200 mm for both rows of pile. The last 125 m toward south, the width of the cofferdam is 25 m as dredge depth along this length is (−)16.0 m.

Also, the pile diameter is 1600 mm for both rows of pile. The sheet pile of width 500 mm for 1200 mm diameter pile and 300 for 1600 mm piles are proposed (Table 1, Fig. 1).

The top level of cofferdam is proposed as (+) 3.00 m. The dock side and river side piles are proposed to be connected with 80 mm steel tie rod. Longitudinal connection is by ISMB 500 from (+) 2.5 m to (+) 3.0 m. Additional piles are provided at the corners to ensure stability.

The founding level is northern side (−)22 m and southern side (−) 32 m. The proposed sheet pile wall has (−)10 m dredge depth at northern side and (−)16 m at the southern side (Figs. 2, 3, 4 and 5).

Table 1 Structural components of cofferdam

S. No.	Description	Dimension	Direction
1	Pile	1200 mm of 12 mm Thick	Northern side
2	Pile	1600 mm of 16 mm Thick	Southern side
3	Sheet pile	12 mm thick	Land side
4	Tie Rod	80 mm thick	-

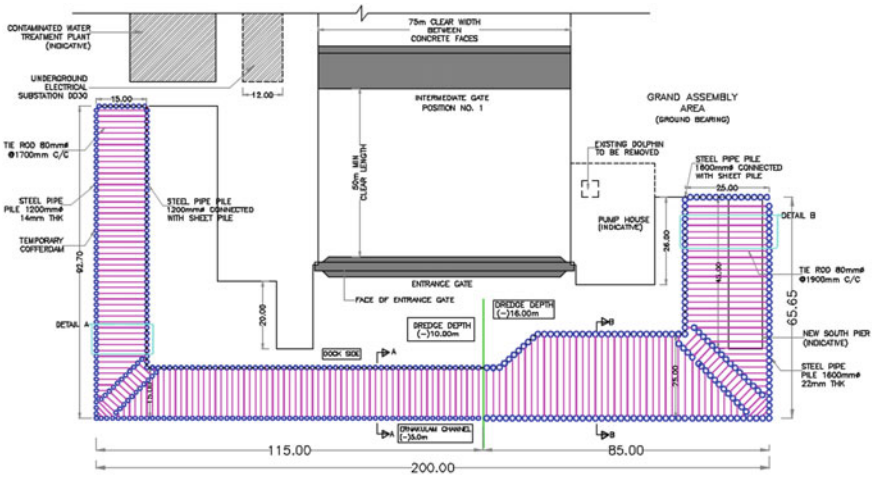

Fig. 1 Plan of temporary cofferdam

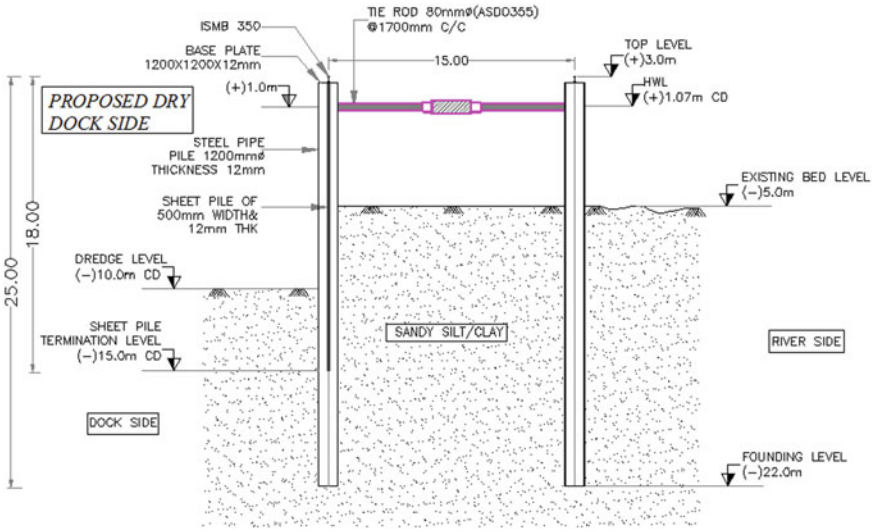

Fig. 2 Cross section of the pile to pile structure (Northern side)

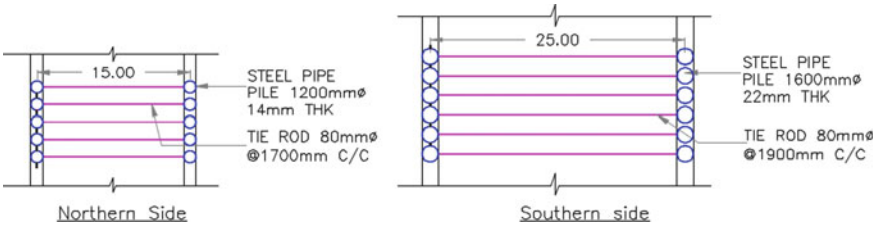

Fig. 3 Tie rod connection plan

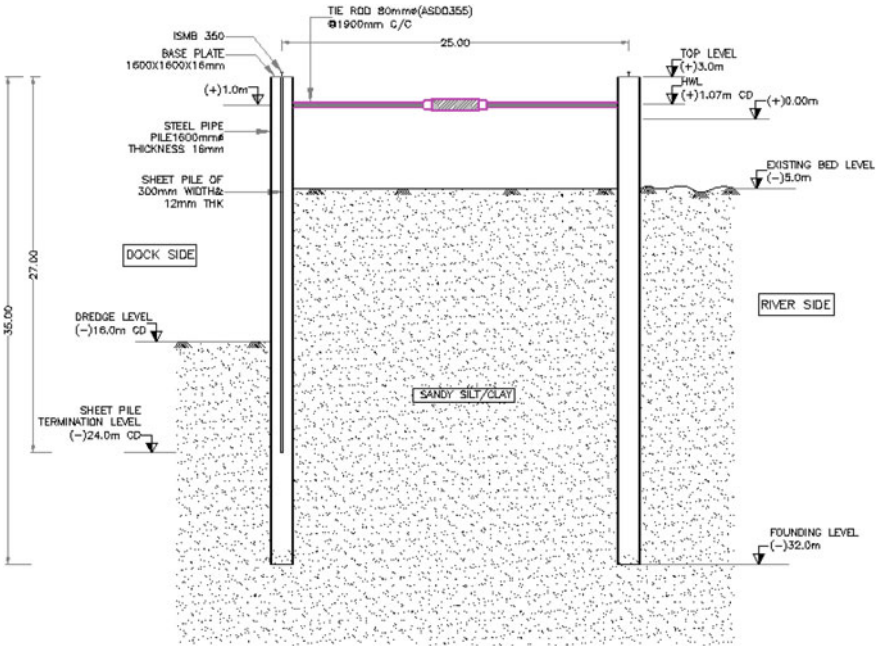

Fig. 4 Land side longitudinal section (Southern side)

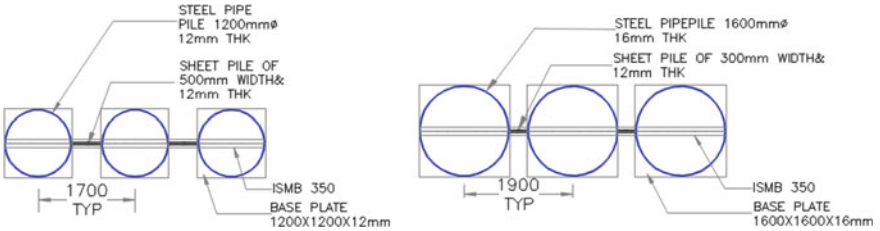

Fig. 5 Land side pile sheet pile arrangements on north and south side

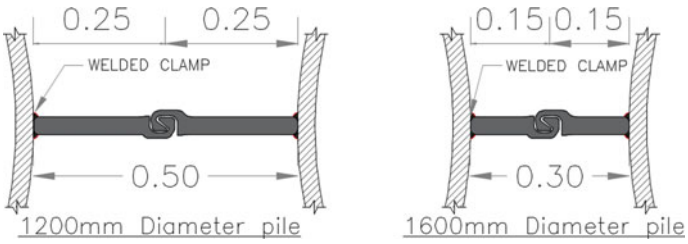

Fig. 6 Pile to Pile interlocking system

Table 2 Tidal data

High water level	(+)1.07 m CD
Highest high water level	(+)1.40 m CD
Low water level	(+)0.30 m. CD
Lowest low water level	(+)0.20 m. CD

The pile sheet pile wall center to center distance of the pile is about 1.7 and 1.9 m on northern and southern side of the land side, respectively. The pile sheet pile wall arrangement system is shown in Fig. 6 for northern and southern side, respectively.

The pile to pile interlocking system of sheet pile is shown in Fig. 6.

5 Oceanograpic Data

5.1 Tidal Data

See Table 2.

6 Soil Data

6.1 Properties of Soil

Borehole No.BH 04 is considered as design borehole for calculations. The location of bore holes is shown in Table 3

Table 3 Properties of soil

Level [m]	Soil	Yunsat KN/m^3	Ysat KN/m^3	ν	Eref KN/m^2	Cref KN/m^2	Ø [°]
+ 3 to −3	Engineered fill material	16	20	0.3	40,000	40	30
−3 to −14	Consolidated sandy silt/clay	14	16	0.3	8000	40	18
−14 to −17	Consolidated sandy silt/clay	16	17.5	0.3	8000	40	18
−17 to −25	Sandy silt/clay	16	17.5	0.3	6000	40	18
−25 to −40	Sandy silt/clay	16	18.5	0.3	8000	40	18
−40 to −50	Dense silty clayey soil	16	20	0.3	50,000	40	39

Table 4 Unit weight of materials

a	Water	10.0 kN/m^3
b	Seawater	10.25 kN/m^3
c	RCC	25 kN/m^3
d	Steel	78.5 kN/m^3

7 Design Criteria of Cofferdam

7.1 Dead Load

Dead loads will consist of the self-weight of the structural components. Unit weight of various materials shall be taken as follows (Table 4)

7.2 Earth Pressure

Earth pressure shall be calculated based on the code IS 2911–2011. The following formulae are used to calculate earth pressure on touch pile,

1. **Active Earth Pressure**

$$P_a = K_a \gamma h - 2C\sqrt{K_a} \tag{1}$$

$$K_a = \frac{1 - sin\varphi}{1 + sin\varphi} \tag{2}$$

Table 5 Active/seismic earth pressure

Steel pile		levels			Active earth pressure		Seismic active earth pressure	
Diameter (mm)	Length (m)	Bed level (m)	Dredge level (m)	Founding level (m)	At top (kN/m@ per m length)	At bottom (kN/m@ per m length)	At top (kN/m@ per m length)	At bottom (kN/m@ per m length)
1200	25	(−)5	(−)10	(−)22	(−)58.07 (assumed as 0 for staad analysis)	(−)36.99 (assumed as 0 for staad analysis)	24.8	0
1600	35	(−)5	(−)16	(−)32	(−)58.07 (assumed as 0 for staad analysis)	(−)11.694 (assumed as 0 for staad analysis)	54.56	0

where γ = Unit weight of the soil in kN/m^3. h = Depth of the soil above the section. φ = Angle of internal factor of the soil. Ka = Coefficient of active earth pressure. C = Cohesion in kN/m^2.

2. **Seismic Earth Pressure**

Seismic load due to earth pressure has been considered as per IS 1893:1984 (Reaffirm 2003) (Table 5).

$$\mathrm{Pa} = \frac{1}{2}\mathrm{wh}^2\mathrm{Ca} \tag{3}$$

where
Paactive earth pressure in kg/m length of wall,
*W*unit weight of soil in kg/m^3,
*h*Height of wall in m.

$$C_a = \left(\frac{C_1 \pm \alpha_y)\cos^2(\Phi - \lambda - \alpha)}{\cos\lambda\cos^2\alpha\cos(\delta + \alpha + \lambda)}\right. \quad X$$

$$\frac{1}{1 + \frac{\{\sin(\phi+\delta)\sin(\Phi-t-\lambda)\}}{\{\cos(\alpha+t)\sin(\underline{\delta}-\alpha-\lambda)\}}}$$

7.3 Spring Calculation

Idealization of soil structure interaction of the substructure is done by springs. The following formulae shall be used to calculate the individual spring constants.

Top spring value

$$K_1 = \frac{BL}{24}(7Ks_1 + 6Ks_2 - Ks_3)$$

Intermediate spring value

$$K_1 = \frac{BL}{12}(Ks_{i-1} + 10Ks_i + Ks_{i+1})$$

Bottom spring value

$$K_1 = \frac{BL}{24}(7Ks_n + 6Ks_{n-1} - Ks_{n-2})$$

where

B = Diameter of pile/Width of the diaphragm wall. L = Segment length of pile (Spacing between springs) Diameter of the pile/thickness of wall = 1.0 m. Ks = Modulus of subgrade

8 Differntial Water Pressure

The differential water pressure is calculated based on IS code 4651–1989—Part 3. The conditions/cases for differential water pressure are shown below

Assuming poor drainage condition, the differential water pressure for a height of (+1 m) to (−10 m) dredge level for 1200 mm diameter piles and (+1 m) to (−16 m) for 1600 mm diameter piles has been considered

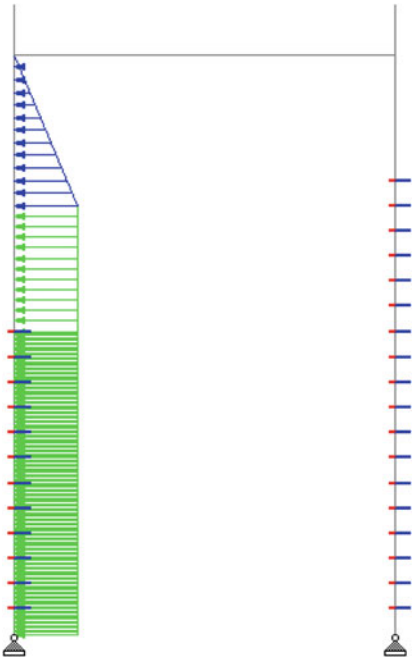

High water level: (+) 1.0 m

8.1 Tie Rod Design

By Anker Schroeder-AS00 Anchors for marine structures (M64—M170) in accordance with EN 1993—5.

8.2 Staad Model

2D analysis shall be carried out using conventional STAAD ProV8i package for various critical load combinations

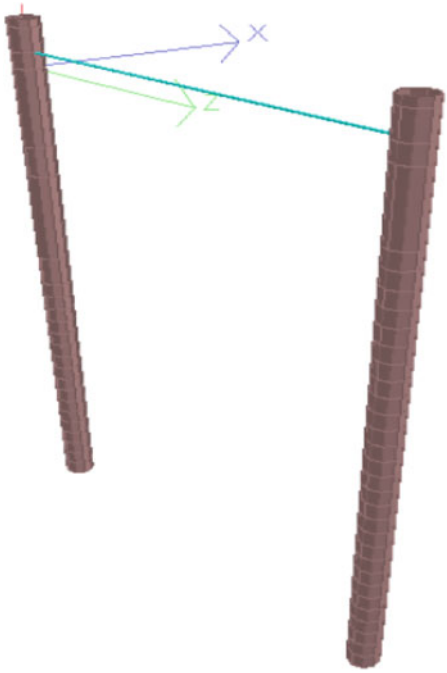

8.3 Model Considered for Design

River side bed level (−) 5.0 m

Dredge level on dock side (−) 10.0 m

Founding level (−) 22.0 m

Water level (+) 1.0 m on dock side pile

1200 mm dia piles of 12 mm thickness with 500 mm sheet pile of 12 mm thickness is considered on dock side

On river side, the below thickness is considered for the corresponding levels

(+)3.0 m to (−)4.0 m − 12 mm thickness
(−) 4.0 m to (−) 14.0 m − 16 mm thickness
(−)14.0 m to (−)22.0 m − 12 mm thickness

Table 6 Stability check

Steel pipe pile	1.2 m dia and 12 mm thick		1.6 m dia and 16 mm thick	
	Dock side	River side	Dock side	River side
Bed level in m	−10	−5	−16	−5
Founding level in m	−22	−22	−32	−32
Passive earth resistance in kN	2972.48	3743.6	5348.9	11,193.52
Differential water pr. in kN	3354.24	–	8111.24	–
Seismic earth force in kN	24.8	–	54.56	–
FOS	1.98		2.02	

9 Stability Analysis

FOS = (Passive earth resistance on dock side + River side)/(Differential water pressure + Seismic earth force) > 1.5 (Table 6).

10 Result

- **Bending moment**

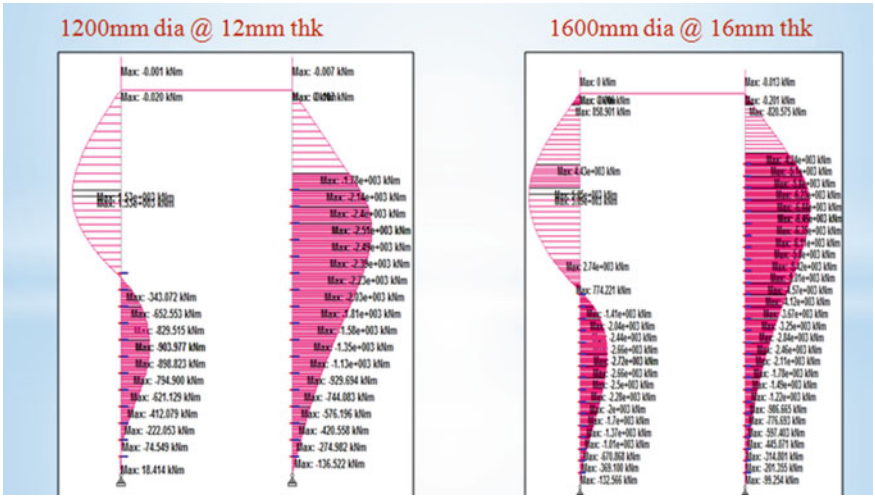

- **Shear Force**

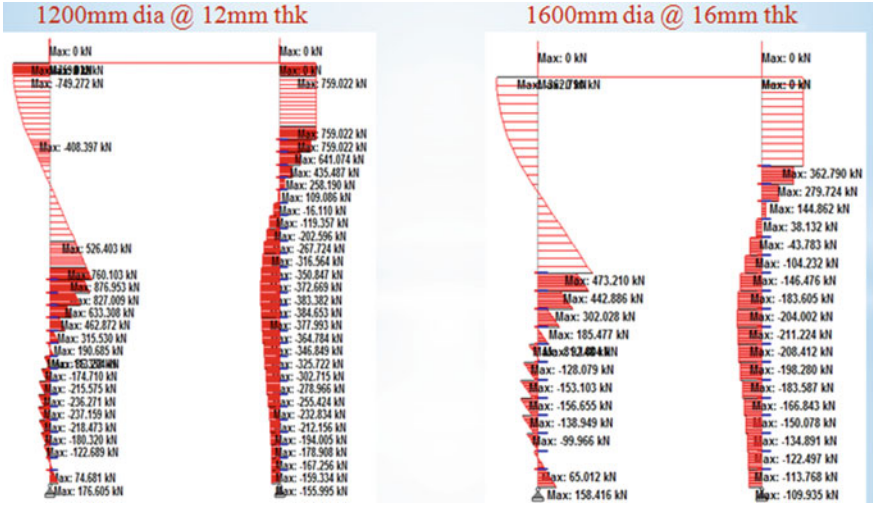

- **Deflection**

Allowable deflection for 1200 mm pile

Allowable deflection: Span/180
= 25000/180
= 138.88 mm

Allowable deflection for 1600 mm pile

Allowable deflection : Span/180
= 35000/180
= 194.40 mm

Deflection in mm			
1200mm pile		1600 mm pile	
Dock side	River side	Dock side	River side
42.58	35.12	47.36	37.86

11 Conclusions

The pile sheet pile wall on the proposed dock side & touch pile wall on river side is proposed for watertight & retaining structure. Two rows of piles are interconnected by tie rod.

The structure was analyzed for critical load conditions, and the results are presented in terms of bending moment, shear force & deflection. Based on the results obtained from analysis, the width of the cofferdam is 15 m with 1200 mm diameter as dredge depth along this length is (-)10.0 m for the initial 192 m. The width of the cofferdam is 25 m with 1600 mm diameter as dredge depth along this length is (−)16.0 m for 125 m toward south. The width of the sheet pile is 500 mm for 1200 mm diameter pile and 300 mm for 1600 mm piles, respectively. The dock side and river side piles are interconnected by 80 mm dia tie rod to keep the structure intact and stable.

The analysis results show that the maximum bending moment is at the mid section on the river side pile from (−)4 m to (−)14 m for the sheet pile wall. Hence, in order to minimize bending moment, the thickness of pipe sheet pile wall has been increased 12 mm to 16 mm thick from (−)4 m to (−)14 m. The increase in sheet pile wall thickness with varying section modulus along the depth is sufficient and found to be economic. The deflection for selected sections is checked for the allowable limits and found to be safe against deflection.

References

1. USACE (1989) Design of sheet pile cellular structures cofferdams and retaining structures. EM1110-2-2503
2. IS: 800: Code of Practice for General construction in steel
3. IS: 1893 Part 1-2016: criteria for earthquake resistant design of structures
4. IS: 4651 Part 4: code of practice for planning and design of ports and harbours-general design considerations
5. IS: 2911Partl/Sec2: Code of Practice for Design and Construction of Pile Foundations-Bored Cast in situ piles
6. BS EN ISO 19902-2007+A1-2013: Petroleum and natural gas industries -- Fixed steel offshore structures

Comparison of PID and LQR Controllers for Dynamic Positioning of an Oceanographic Research Vessel

Kunal Tiwari and P. Krishnankutty

Abstract The purpose of this paper is to compare the performance of proportional-integral-derivative controller(PID), multivariable PID controller and linear quadratic regulator(LQR) applied to a dynamic positioning system of ship by numerical simulation in MATLAB. A square manoeuvre in different sea state is used to test the performance.

Keywords Dynamic positioning · PID · LQR · ORV

1 Introduction

Oceanographic research vessels (ORV) are employed to carry out research on the physical, biological and chemical characteristics of major water bodies. Various equipment's are carried by ORVs. These are used to collect water sample at varied depths, from shallow coastal waters to deep seas. In addition to this they are equipped with instruments for hydro-graphic sounding of seafloor. ORVs often carry unmanned underwater vehicles and divers for exploring the ocean. These activities require vessel to maintain its location or sometimes follow a predetermined trajectory. Dynamic Positioning is the ability of any floating body to maintain its position exclusively by means of active thrust. A dynamically positioned system uses controllers to determine the thrust required in order to overcome the environmental forces. These generalised forces are then allocated to different thrust producing actuator's. Oceanographic research vessels (ORV) are employed to carry out research on the physical, biological and chemical characteristics of major water bodies. Various equipment's are carried by ORVs. These are used to collect water sample at varied depths, from shallow coastal waters to deep seas. In addition to this they are

K. Tiwari (✉) · P. Krishnankutty
Department of Ocean Engineering, Indian Institute of Technology Madras, Chennai 600036, India
e-mail: kt@fourier.in

P. Krishnankutty
e-mail: pkrishnankutty@iitm.ac.in

V. Sundar et al. (eds.), *Proceedings of the Fifth International Conference in Ocean Engineering (ICOE2019)*, Lecture Notes in Civil Engineering 106,
https://doi.org/10.1007/978-981-15-8506-7_28

equipped with instruments for hydro-graphic sounding of seafloor. ORVs often carry unmanned underwater vehicles and divers for exploring the ocean. These activities require vessel to maintain its location or sometimes follow a predetermined trajectory. Dynamic Positioning is the ability of any floating body to maintain its position exclusively by means of active thrust. A dynamically positioned system uses controllers to determine the thrust required in order to overcome the environmental forces. These generalised forces are then allocated to different thrust producing actuator's. The concept of dynamically positioned floating structure can be traced back to [12]. They discussed theory about three legged platform designed for position control using active thrusters. A FORTRAN simulation of DP for *Seaway Eagle* was shown by [1], where proportional-integral-derivative (PID) controller supplemented with a feed forward(FF) compensation for environmental disturbance was shown. A full scale DP experiment involving multipurpose supply vessel *Northern Clipper* is recorded in [10]. LQG feedback controller and a model reference (MR) FF compensator for wave and wind compensation were used. Use of acceleration feedback for derivative control in traditional PID setup was considered by [7]. He demonstrated the superiority of acceleration feedback over conventional feedback for sway manoeuvre of scaled model of *cybership II* an offshore supply vessel. A similar approach for *Cyberrig I* is demonstrated by [13]. DP for *Cybership II* is further explored in [2] with use of model predictive controller. A simulation and its experimental validation was reported in the paper. An instance of LQG control scheme for DP of *OSV Vikings* can be found in [4]. PID with AFB for advanced model of Cybership, *Cybership III* is demonstrated in [9].

The purpose of this paper is to analyse and compare performance of PID and LQR as control scheme for dynamic positioning of an ORV.

2 Mathematical Model

A right handed coordinate system is used in this paper (refer Fig. 1). The positions (x and y) and orientation (ψ) are described with respect to earth fixed coordinate system (O_eX_e, O_eY_e). The origin of earth fixed coordinate system is taken as the starting point of simulation. The velocities (u, v and r) are described with respect to body fixed coordinate system. The origin of body fixed coordinate system is the intersection point of load waterplane, longitudinal central plane and the midship transverse plane .

2.1 ORV Equation of Motion

The equations of motion for vessel can be described as,

$$\boldsymbol{M}\dot{\boldsymbol{v}} + \boldsymbol{D}\boldsymbol{v} = \boldsymbol{\tau} \tag{1}$$

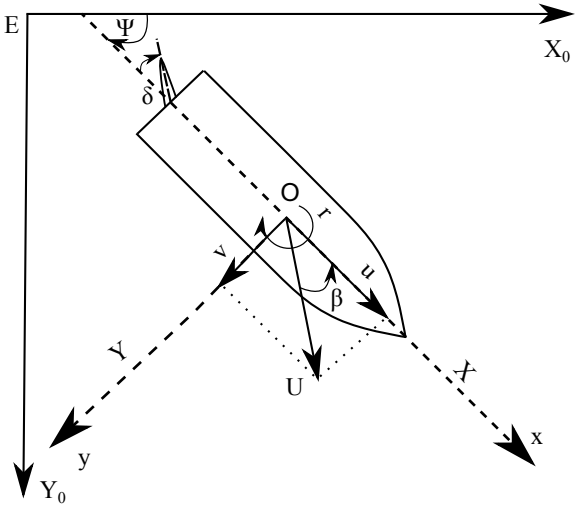

Fig. 1 Coordinate system

where, $\boldsymbol{M}$ is the system inertia matrix and is given as,

$$\boldsymbol{M} = \begin{bmatrix} m - X_{\dot{u}} & 0 & 0 \\ 0 & m - Y_{\dot{v}} & mx_g - Y_{\dot{r}} \\ 0 & mx_g - N_{\dot{v}} & I_z - N_{\dot{r}} \end{bmatrix} \tag{2}$$

$X_{\dot{u}}$,$Y_{\dot{v}}$,$Y_{\dot{r}}$, $N_{\dot{v}}$ and $N_{\dot{r}}$ are added mass. $\boldsymbol{D}$ is the linear damping matrix and is described as,

$$\boldsymbol{D} = \begin{bmatrix} -X_u & 0 & 0 \\ 0 & -Y_v & -Y_r \\ 0 & -N_v & -N_r \end{bmatrix} \tag{3}$$

X_u, Y_v, Y_r, N_v and N_r are damping coefficients. $\boldsymbol{v}$ is velocity matrix and is defined as,

$$\boldsymbol{v} = \begin{bmatrix} u & v & r \end{bmatrix}^T \tag{4}$$

u is surge velocity, v is sway velocity and r is the yaw velocity. $\boldsymbol{\eta}$ is position and orientation matrix written as,

$$\boldsymbol{\eta} = \begin{bmatrix} x & y & \psi \end{bmatrix}^T \tag{5}$$

x is displacement in forward direction, y is linear displacement towards starboard and ψ is rotation about z-axis. $\boldsymbol{\tau}$ is thrust matrix,

$$\boldsymbol{\tau} = \begin{bmatrix} \tau_x & \tau_y & \tau_n \end{bmatrix}^T \tag{6}$$

Table 1 Parameter and hydrodynamic coefficients of ORV (scale 1:17.1)

Parameter	Value	Unit	Parameter	Value	Unit
$X_{\dot{u}}$	−3.57	kg	X_u	−4.27	kg/s
$Y_{\dot{r}}$	−14	kgm	Y_r	19.44	kgm/s
$Y_{\dot{v}}$	−82.99	kg	Y_v	−25.63	kg/s
$N_{\dot{r}}$	−28.0	kgm^2	N_r	−32.65	kgm^2/s
I_z	1.50	Nm	m	123	kg

τ_X, τ_Y and τ_N are the thrust force and moment produced by ship actuator along X, Y and about Z-axis respectively.

In this paper we are simulating a 1:17.1 scaled model of an ORV. The hydrodynamic coefficient used are for a model 2.54m long. The coefficient give in Table 1 are taken from the paper by [6], where numerical simulation of planar motion mechanism was done to estimate these hydrodynamic derivatives.

The mathematical model can be written in standard state space form as,

$$\begin{aligned} \dot{\boldsymbol{x}} &= \boldsymbol{A}\boldsymbol{x} + \boldsymbol{B}\boldsymbol{u} \\ \boldsymbol{y} &= \boldsymbol{C}\boldsymbol{x} \\ \boldsymbol{x} &= \boldsymbol{v} \\ \boldsymbol{A} &= -\boldsymbol{M}^{-1}\boldsymbol{D} \\ \boldsymbol{B} &= \boldsymbol{M}^{-1} \end{aligned} \tag{7}$$

2.2 Wave Forces

In this paper, we are using second order wave transfer function approximation of Pierson-Moskowitz (PM) spectrum which includes a zero mean oscillatory wave frequency motion (first order) induced forces and a non zero slow varying wave drift forces (second order wave induced forces). The wave transfer function is given as,

$$H_i(s) = \frac{2\,K_i\,\lambda\,\omega_0\,\sigma\,s}{s^2 + 2\,\lambda\,\omega_0\,s + \omega_0^2} \tag{8}$$

where,

- $H_i(s)$ is the wave force transfer function. Index i represents force in x-direction or y-direction and moment about z-axis, as 1,2 and 3 respectively.
- K_i is the gain constant. (i = 1, 2, 3 representing K_x K_y K_ψ)
- ω_0 is dominating wave frequency.
- λ is damping factor.
- σ is wave intensity.

3 Controller

Three different control scheme are being compared in this paper and they are briefly explained below.

3.1 PID

Three parallel PID controller are used to compute the corrective thrust force, Fig. 2 shows the blockdiagram. The vessel motion model (refer Eq. 7) is three input three (τ_x, τ_x and τ_n) output system (x, y and ψ). The three inputs are modified using three different PID controller based on error between the measured and setpoint in x, y and ψ respectively. The formula for PID can be written in generalised form as [5],

$$\tau_i^c = K_P^i e^i + K_I^i \int e^i \, dt + K_D^i \frac{de^i}{dt} \tag{9}$$
$$e^i = i_d - i$$

where, e^i is the error between desired and actual output, $i = x, y$ and n, K_P^i is the proportional gain constant, K_D^i is the derivative gain constant and K_I^i is the integral gain constant. For accurate working of PID, finding the correct value of K_P^i, K_I^i and K_D^i is necessary. This process is called tuning of PID.

3.2 Multivariable PID

The coupled nature of yaw and sway subsystems necessitates use of a decoupling mechanism. This can be achieved using a multivariable PID given as,

$$\boldsymbol{\tau}^c = \boldsymbol{K_P e} + \boldsymbol{K_I} \int \boldsymbol{e} \, dt + \boldsymbol{K_D} \frac{d\boldsymbol{e}}{dt} \tag{10}$$

Where, $\boldsymbol{K_P}$, $\boldsymbol{K_I}$ and $\boldsymbol{K_D}$ are proportional, derivative and integral gain matrices and have structure as [8],

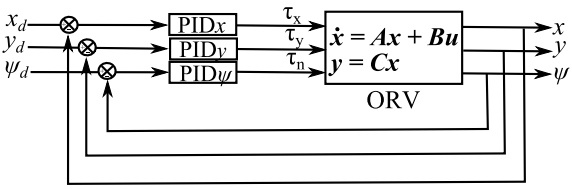

Fig. 2 Block diagram of parallel PID controller

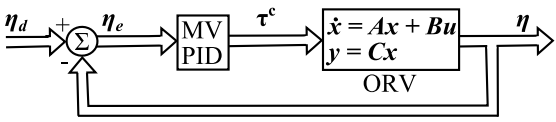

Fig. 3 Block diagram of multivariable PID controller

$$\boldsymbol{K_j} = \begin{bmatrix} K_{j_{11}} & 0 & 0 \\ 0 & K_{j_{22}} & K_{j_{23}} \\ 0 & K_{j_{32}} & K_{j_{33}} \end{bmatrix} \tag{11}$$

where, $j = P, I$ and D. $K_{j_{23}}$ helps to counteract the effect of e^y on ψ and $K_{j_{32}}$ helps to counteract the effect of e^n on y. In absence of these two terms in $\boldsymbol{K_P}$, $\boldsymbol{K_I}$ and $\boldsymbol{K_D}$ matrices, the structure will be similar to three parallel PID as in first case. The schematic diagram for multivariable PID is shown in Fig. 3.

3.3 LQR with Integral Term

Linear quadratic regulator is a state feedback control technique which steers state to zero and keeps it there. This is achieved by introducing feedback given by,

$$\boldsymbol{u^{opt}} = \begin{bmatrix} \boldsymbol{K^{opt}} & \boldsymbol{H^{opt}} \end{bmatrix} \begin{bmatrix} \boldsymbol{x} \\ \boldsymbol{q} \end{bmatrix} \tag{12}$$

where, $\boldsymbol{q} = \boldsymbol{\eta_d} - \boldsymbol{\eta}$ is the error between the desired position and orientation and current position and orientation. $\boldsymbol{K^{opt}}$ and $\boldsymbol{H^{opt}}$ are the feedback gain. The objective is to minimise cost function,

$$J = \int_0^\infty (\boldsymbol{z}^T \boldsymbol{Q z} + \boldsymbol{u}^T \boldsymbol{R u}) \, dt \tag{13}$$

where, $\boldsymbol{Q}_{6\times6}$ and $\boldsymbol{R}_{3\times3}$ are positive definite weight matrices. The matrices are tuned using trial and error method where in you change the values of elements of the matrices until you get acceptable results. The initial guess for matrices is done using Bryson's rule [11] as,

$$Q_{nn} = \frac{1}{\max\langle z_{nn}^2 \rangle} \quad n \in \{1, \cdots, 6\} \tag{14}$$

$$R_{mm} = \frac{1}{\max\langle u_{mm}^2 \rangle} \quad m \in \{1, 2, 3\} \tag{15}$$

where, $\boldsymbol{z}_{6\times1} = \begin{bmatrix} u & v & r & (x_d - x) & (yd - y) & (\psi_d - \psi) \end{bmatrix}^T$

The block diagram for LQR with integral term is shown in Fig. 4. It is physical realisation of Eq. 12.

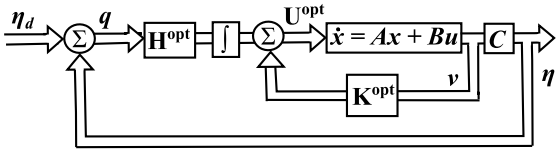

Fig. 4 Block diagram of LQR with integral term

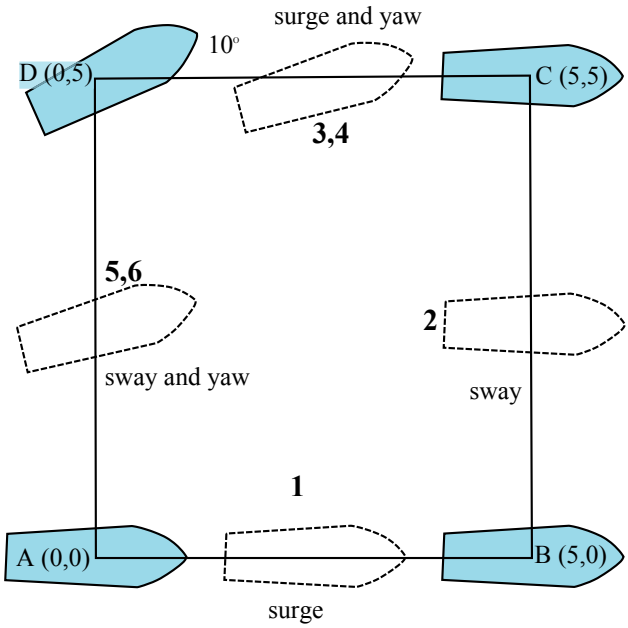

Fig. 5 Square manoeuvre DP test

4 Simulation and Results

The dynamic positioning ability of ORV is simulated in SIMULINK© using Eq. 7 for ship, Eq. 8 for wave forces and Eqs. 9, 10 and 12 for the different controllers. A square manoeuvre is chosen to understand the performance of controller in setpoint tracking. The idea behind this is to test every aspect of motion as vessel returns to its initial position making a square trajectory (refer Fig. 5). The different stages in this manoeuvre are,

- The vessel is initialised with zero heading at point A(0,0).
- A position change 5 m in x-direction is commanded. The vessel experiences surge motion in forward from A to B(5,0).
- A position change 5 m in y-direction is commanded. The vessel experiences port side sway motion from B to C(5,5).
- A position change of −5 m in x-direction and 10° anticlockwise heading change is commanded. The vessel moves in backward direction from C to D(0,5) and turns 10° to port.
- A position change of -5m in y-direction and an clockwise yaw of 10° is commanded. The vessel experiences starboard side sway motion from D to A(0,0) and returns to zero heading.

In the first two arms of square manoeuvre, A-B and B-C, setpoint tracking of surge and sway is tested. In the final two arms, C-D and D-A, two setpoint are tracked simultaneously. This helps us to understand ability of controller in setpoint tracking with different combinations.

Different arms of square manoeuvre are subjected to different sea states. The forward surge motion takes place in calm sea condition (A-B). During port side sway, sea condition changes from calm to moderate (B-C). Sea condition changes from moderate to high during backward surge and anticlockwise yaw (C-D). Starboard side sway and clock wise yaw motion takes place in phenomenal sea state (D-A). The environmental forces are simulated using equation 8 with parameter given for different sea state in Ttable 2 [3].

The simulation results are given in Figs. 6, 7 and 8. Figure 6 is the controller output, Fig. 7 is the tracking of setpoint for x, y and ψ setpoints. The final trajectory of square manoeuvre is shown in Fig. 7.

For setpoint tracking from A-B, we can observe that all the controller are able to achieve setpoint in x (Fig. 7a). For this region of manoeuvre we can conclude from Fig. 6a that parallel PID requires more force than MV PID. The force requirement of LQR is very high. it should be noted that LQR force shown in graph is divided by 50 to plot it with forces from parallel and MV PID.

For region B-C, from Fig. 7b, we can observe smooth tracking of sway setpoint by LQR and parallel PID. The response of MV PID can be termed a bit sluggish. The slight overshoot of MV PID can bee see at point C in Fig. 8. From Fig. 7c at point B, we can see the variation in ψ as result of τ_y^c. It can be easily concluded that

Table 2 Parameters for wave transfer function

Sea State Code	Description of the sea	λ	ω (rad/s)	σ	H_s (m)
1	calm	0.1	3.927	0	0.05
4	moderate	0.1	0.9	0.583	1.875
7	high	0.1	0.4613	1.919	7.5
9	phenomenal	0.1	0.3357	2.630	14

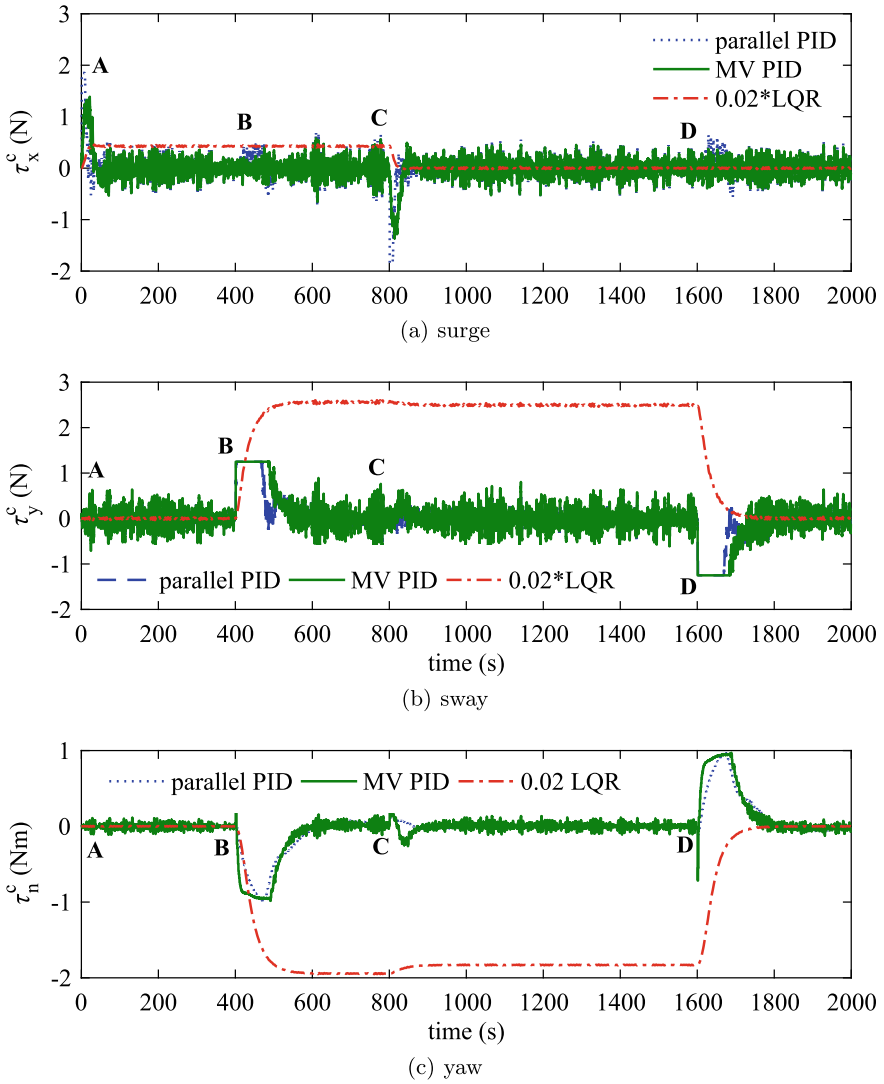

Fig. 6 Controller output

parallel PID structure is incapable of handling such coupled systems. Though LQR is able to track setpoint correctly, the high force requirement evident from Fig. 6b between point B-C suggest that this cannot be used for practical purposes.

Region C-D involves simultaneous tracking of two setpoints, x and ψ. For heading angle setpoint (refer Fig. 7c) we can observe that all controllers are able to perform well. A slight overshoot is observed in parallel PID, but a better tuning can overcome this drawback. For surge setpoint (Fig. 7a), we can see an overshoot for LQR. This

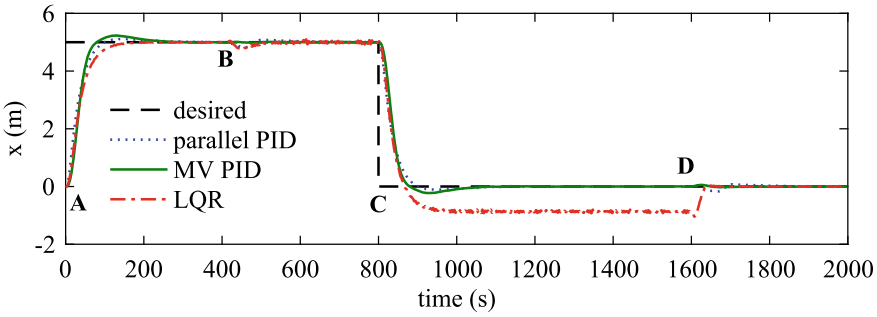

(a) surge

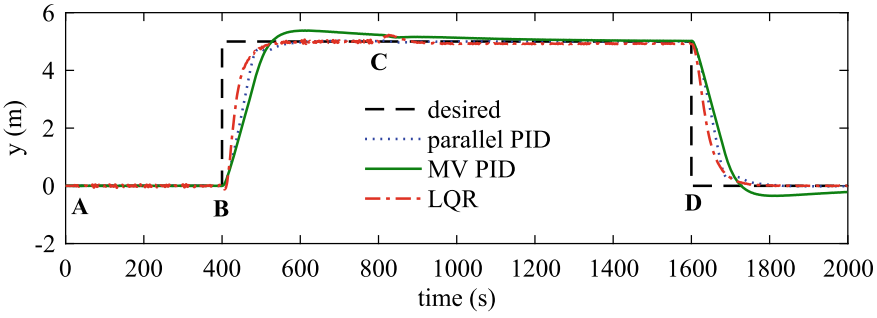

(b) sway

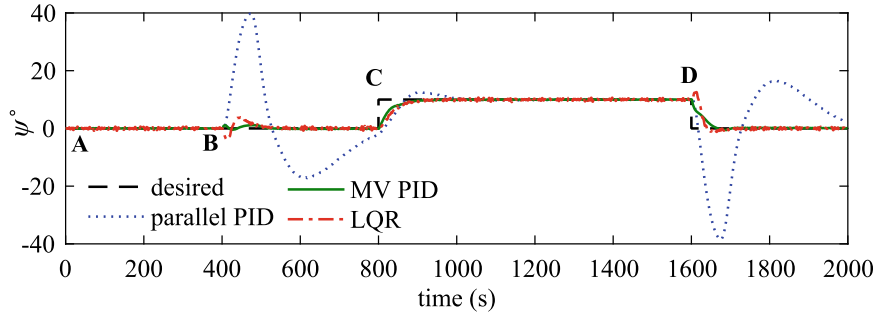

(c) yaw

Fig. 7 Setpoint response

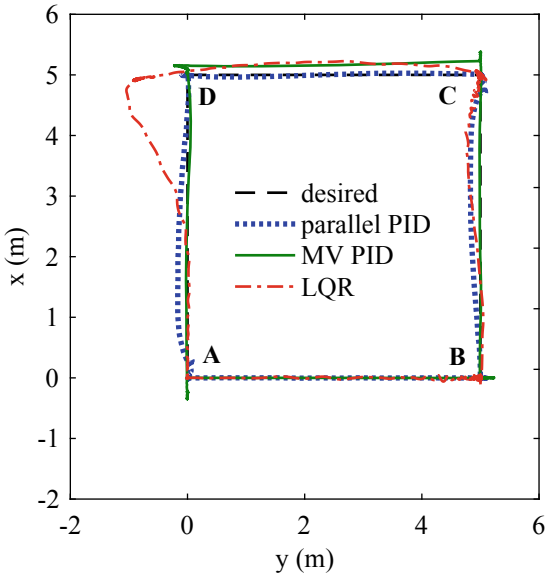

Fig. 8 xy trajectory of ship during square manoeuvre test

can be attributed to either poor tuning or implicit inability of LQR to handle setpoint tracking. The overshoot is visible clearly in Fig. 8 at point D.

Region D-A involves simultaneous tracking of two setpoints, y and ψ. For sway setpoint (Fig. 7b) a slight sluggish performance for MV PID can be seen. This might be due to coarse tuning of MV PID. The inability to handle coupled system for parallel PID is evident in response of ψ in Fig. 7c at point D.

5 Conclusion

The paper attempts to compare performance of three different control schemes, parallel PID, multivariable PID and LQR with integral term for dynamic positioning of an oceanographic research vessel. From the results it can be concluded that out of the three control methods employed in the paper, multivariable PID is the best option. The problem faced by LQR was high control force. This problem can be solved using technique like H_∞ which allow for constrains on the control signal. For further improvement of the controller, advance technique like fuzzy logic controller can be explored. Fuzzy logic allows to design controller using the knowledge of operator and does not require complex tuning like MV PID or LQR with integral term.

References

1. Susbielles G, Martin Y, Vasseur B et al (1974) The first semi-submersible platform specifically designed for dynamic positioning. In: SPE European Spring Meeting. Society of Petroleum Engineers
2. Balchen JG et al (1980) A dynamic positioning system based on Kalman filtering and optimal control. Modeling Identification Control 1(3):135
3. Sorensen AJ, Sagatun SI, Fossen TI (1996) Design of a dynamic positioning system using model-based control. Control Eng Practice 4(3):359–368
4. Lindegaard, K-P (2003) Acceleration feedback in dynamic positioning. PhD thesis. NTNU, Norway
5. Tysso J, Aga A (2006) DP control system design for CyberRig I. MA thesis. NTNU, Norway
6. Fannemel AV (2008) Dynamic positioning by nonlinear model predictive control. MA thesis. NTNU, Norway
7. Hansen SR (2013) LQG Dynamic Positioning for a Supply Vessel. MA thesis. University of California, San Diego
8. Rabanal OMR, Brodtkorb AH, Breivik M (2016) Comparing Controllers for Dynamic Positioning of Ships in Extreme Seas. IFAC- PapersOnLine 49(23):258–264
9. Tiwari KN, Hariharan K, Krishnankutty P (2018) Manoeuvring predication of an oceanographic research vessel using numerical horizontal planar motion mechanism (HPMM) test. In: The RINA international conference on computational and experimental marine hydrodynamics (MARHY), Chennai. RINA, pp 421–426
10. Johnson CD (1999) Process control instrumentation technology. Prentice–Hall, PTR
11. Martin P, Katebi R (2005) Multivariable PID tuning of dynamic ship positioning control systems. J Marine Eng Technol 4(2):11–24
12. Sturgeon WR (1981) Controllers for aircraft motion simulators. J Guid Control Dyn 4(2):184–191
13. Fossen TI (1994) Guidance and control of ocean vehicles. Wiley

Hybrid Functions for Nonlinear Energy Transfers in Third-Generation Wave Models: Application to Observed Wave Spectra

G. Uma and S. A. Sannasiraj

Abstract Hybrid functions (hereafter, HBL) has been newly presented as an efficient method to the full Boltzmann integral (FBI) for quadruplet wave–wave interactions at finite depths and also been tested for idealized wave spectra. Herein, the method is implemented in TOMAWAC, the third-generation wave model, and is validated between the existing approximate methods such as discrete interaction approximation (DIA), multiple discrete interaction approximate method (MDIA) and quasi-exact method, namely Gauss quadrature method (GQM), for observed wave spectra. The measured wave spectra obtained from the off-Kochi, along the southwest coast of India at a water depth of 21 m, are analyzed for southwest monsoon period in the year 2016, with an objective to understand the effect of nonlinear coupling due to quadruplet resonant interactions on composite spectra. The swell and sea components of the spectra are separated using peakedness algorithm, and the analysis shows that most of the spectra are swell dominated. The nonlinear coupling between swell and sea spectra is studied thoroughly, and it is ascertained that coupling is generally much larger in the vicinity of closer intermodal distance and mean directions.

Keywords Composite spectra · Nonlinear interactions · Third-generation wave model

1 Introduction

Nonlinear quadruplet four-wave interactions constitute a primary role in the modern third-generation operational wave models. Most of the wave models such as Wave Analysis Model, WAVEWATCH III and TOMAWAC [1] use discrete interaction approximation method for quadruplet four-wave approximation. Despite its shortcomings, the method is preferred for its computational efficiency [2]. Although there exist several methods for nonlinear four-wave interactions [2], their implementation in 3G models still remains a challenging task. Because the methods when integrated

G. Uma (✉) · S. A. Sannasiraj
Department of Ocean Engineering, Indian Institute of Technology Madras, Chennai, India
e-mail: umasathish82@gmail.com

V. Sundar et al. (eds.), *Proceedings of the Fifth International Conference in Ocean Engineering (ICOE2019)*, Lecture Notes in Civil Engineering 106,
https://doi.org/10.1007/978-981-15-8506-7_29

with other source terms in the wave model either give incorrect results or take more computational time. In order to achieve this task, Uma et al. [3] made an attempt to account for both efficiency and accuracy. In the present paper, the work of Uma et al. [3] has been tested for the spectra, observed in off-Kochi coast located in the west of Arabian Sea during the southwest monsoon (SW) period.

The 2D spectra obtained from direction wave rider buoy, deployed at a water depth of about 21 m, are considered in the present study. The spectra composed of both swell and wind sea components are partitioned in different ways in third-generation wave models, for example, SWAN uses watershed algorithm [4] and WAM model adopts the wind generation formulation [5]. The formulation could be used when the wind information and the two-dimensional spectra are available. Mostly, the model users discard such partition, and the components are in no means computed separately. The need for such partition and their pitfalls can be found in [6]. Further, they also propose a $1 - d$ partitioning algorithm which estimates the ratio (γ^*) between the peak energies of the wave system and Pierson-Minkowski spectrum at the same peak frequency. If the ratio is greater than the threshold value 1.0, the system is identified as sea else swell.

The main objective of the paper is to implement the partitioning algorithm based on spectral peakedness in the TOMAWAC wave model and to validate the methods of nonlinear interactions (NL/Snl) such as DIA, MDIA and GQM with the newly implemented algorithm [3] in the wave model [1] for the observed spectra. Although the methods for NL in the TOMAWAC model hold only for deep water, for finite depth they use the parametrization (scaling relation) proposed by WAMDIG [5].

The organization of the paper is as follows: Sect. 2 presents a description of the observed buoy data and spectral partitioning. Section 3 compares the methods of NL for different/forms of spectra. Finally, the findings are summarized in Sect. 4.

2 Observed Spectra and Spectral Partitioning

Wave measurements were carried out at an interval of 3 h using TriAxys directional wave buoy at Kochi region (9° 58′ 33.00" N, 76° 6′ 45.01" E). In the selected domain, the southwest monsoon prevails during May–September. Wave rider buoy (WRB) was deployed in a depth of about 21 m water depth to measure the wave parameters. WRB provided observations in the Arabian Sea for validating the TOMAWAC model results for nonlinear interactions. The performance of the TriAxys directional wave buoy is ascertained through some computer simulations carried out at the NRC Canadian Hydraulics Centre. The processor on the buoy employs obtains energy spectrum using fast Fourier transform on the wave record. In the wave spectrum, the frequency ranges between 0.05 and 0.64 Hz (129 discrete frequencies), and the directions are linearly spaced with 3° directional resolution in circular grid (0°–360°).

Based on the availability, the spectra obtained during the period from 01 Jul 2016 to 11 Jul 2016 observed at every 3 h interval at a depth of 21 m are used. Much of the buoy data are swell dominated. Following Portilla [6], separation frequency

Table 1 Spectral analysis

Sea state category/ID	Percentage of spectra falling in each category (%)
Type I swell dominated Closer peaks Moderate peaks Far-off peaks	88.2 18.4 69.7 –
Type II spectral peaks of comparable energy Closer peaks Moderate peaks Far-off peaks	5.2 5.2 –
Type III Wind dominated sea Closer peaks Moderate peaks Far-off peaks	2.6 2.6 – –
Type IV pure swell	3.9
Type V pure wind	–

is identified and the sea state is classified using swell-sea energy ratio (SSER) and intermodal distance (ID) proposed by Carlos. The purpose of the study is to analyze the behavior of the methods of NL for different sea state category with respective to their difference in mean direction and intermodal distance. The results of the spectral analysis are presented in Table 1. Figure 1 presents the mean direction of observed, swell and sea spectra.

3 Data Preparation and Application of Methods of NL for the Monsoon Season

The observed directional wave spectra are converted from linear spacing to geometrical spacing to facilitate the comparison among the NL formulations (DIA, MDIA and GQM) in the third-generation wave model, TOMAWAC. The partitioned subspectra for swell and sea have peak frequencies, f_{p1} and f_{p2}, and mean directions θ_{m1} and θ_{m2}, respectively. The observed directional spectrum is smoothened with two parameter (H_s, f_p) JONSWAP spectrum in the wave model, and the directional spreading corresponds to Mitsuyasu which is coded for the purpose of the study.

By performing convergence analysis, a polar grid consisting of 40 frequencies and 24 angles in circular resolution is found to be an optimal one and is considered throughout the study for computation and comparison. The magnitudes of NL are investigated for composite spectra observed during the month of July in the year 2016. The magnitudes of NL increase with decreasing ID and mean directions and eventually force the spectra back to unimodal (Fig. 2c, f). Similarly, when the spectra

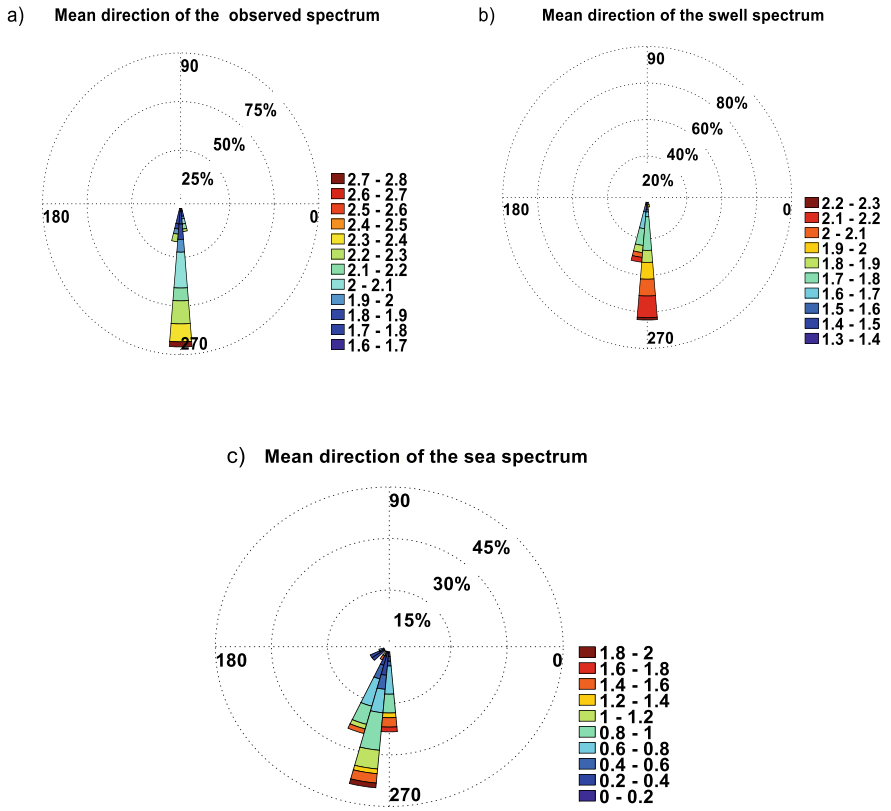

Fig. 1 Mean directions of **a** observed spectrum, **b** swell spectrum and **c** sea spectrum for the month of July 2016

are increasingly separated in their mean direction and ID, the interaction between them is negligible. In such case, the magnitude of NL decreases and bimodality is explicitly visible, in the 1D as well as 2D cases presented in Fig. 2d, f. The presented findings are the response of the input spectrum observed in 00:00 UTC of 4 July 2016 and 18:00 UTC 6 July 2016, presented in Fig. 2a, b, respectively. The presented results confirm the findings of Young et al. [7].

4 Conclusion

An efficient scheme based on Hybrid functions for nonlinear energy transfers applicable for finite depths is incorporated in TOMAWAC, a third-generation wave model. In order to substantiate the performance of the method, it is subjected to the more complicated swell-sea interaction test case [8] together with the existing methods for

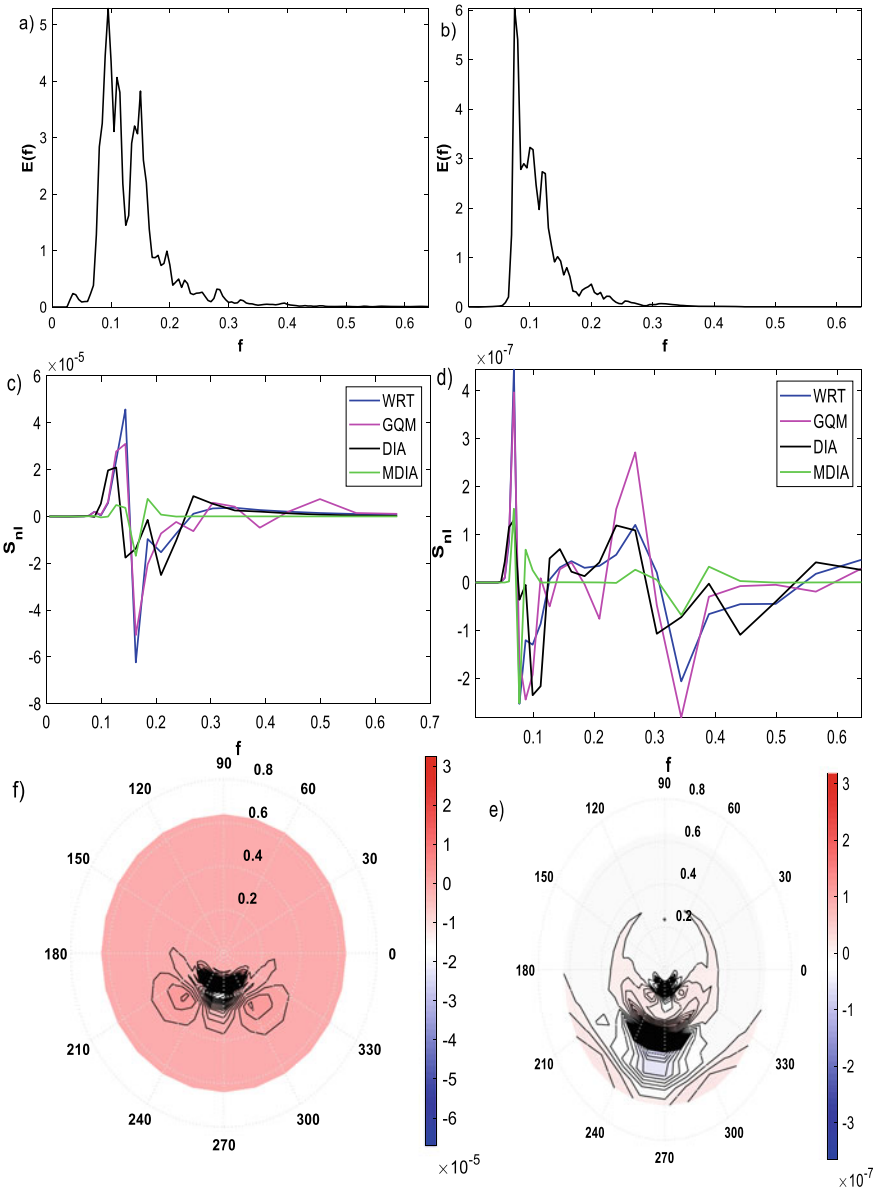

Fig. 2 Upper panels **a** and **b** present the observed spectra at 00:00 UTC of 4 July 2016 and 18:00 UTC of 6 July 2016, respectively. The middle ones (panels **c** and **d**) are their respective 1D nonlinear energy. The lower panels **e** and **f** show the 2D nonlinear energy results

NL in the 3G wave model. To serve the purpose, peakedness algorithm proposed by Portilla for spectral portioning is implemented in the wave model, and the methods are validated for the spectra observed in the Kochi coast for the month of July 2016 which falls in the monsoon season. The response of methods for NL to implemented partition algorithm is similar. The magnitude of NL increases with lesser ID and difference between the mean directions of swell and sea spectra.

Reference

1. Benoit M, Marcos F, Becq F (1996) Development of a third generation shallow-water wave model with unstructured spatial meshing. In: Proceedings of the 25th international conference on coastal engineering, Florida, pp 465–478
2. Cavaleri L, Alves JHGM, Ardhuin F, Babanin A, Banner K, Belibassakis K, Benoit M, Donelan M, Groeneweg J, Herbers THC, Hwang P, Janssen PAEM, Janssen T, Lavrenov IV, Magne R, Monbaliu J, Onorato M, Polnikov V, Resio D, Rogers WE, Sheremet AJ, Smith M, Tolman L, Van Vledder G, Wolf J, Young IR, WISE Group (2007) Wave modelling—the state of the art. Prog Oceanogr 75(4):603–674
3. Uma G, Prabhakar V, Sannasiraj SA (2018) Hybrid functions for nonlinear energy transfers at finite depths. J Ocean Eng Mar Energy 4:187–198
4. Booij N, Haagsma IJG, Holthuijsen LH, Kieftenburg ATMM, Ris RC, Van der Westhuysen AJ, Zijlema M (2004) SWAN user manual, SWAN cycle III, Version 40.41. Delft University of Technology, pp 465–478
5. WAMDIG Group (13 authors) (1988) The WAM model-a third generation ocean wave prediction model. J Phys Oceanogr 18:1775–1810
6. Portilla J, Ocampo-Torres FJ, Monbaliu J (2009) Spectral partitioning and identification of wind sea and swell. J Atmos Oceanic Technol 26:107–122
7. Young IR, Hasselmann S, Hasselmann K (1985) Calculation of the non- linear wave-wave interactions in cross seas. Hamburger Geophys Einzel 74:50 (1985)
8. The SWAMP Group (1985) Ocean wave modeling, 1st edn. Springer US

False Nearest Neighbour Method for the Analysis of Sea Surface Temperature Time Series

Vinayakam Jothiprakash, Bellie Sivakumar, Mohit Udenia, and Himanshu Jotaniya

Abstract Sea surface temperature (SST) plays a key role in the dynamics of the global climate system. Adequate understanding of the SST dynamics is crucial for modelling the land–ocean-atmospheric dynamics and for predicting weather. There exist many different approaches and associated methods for studying the dynamics of SST. Among these, methods developed in the context of nonlinear dynamic and chaos theories are particularly suitable and useful, since there is sufficient evidence as to the presence of chaotic behaviour in SST dynamics. Many past studies have applied the concepts of chaos to analyse the SST time series in different parts around the world and reported interesting results. Encouraged by the outcomes of such studies, the present study applies the concepts of chaos theory to examine the dynamic characteristics of SST in the Arabian sea region. In particular, the False Nearest Neighbour (FNN) is employed to a 30-year SST data series from (1987 to 2016). The implementation of the FNN method involves phase space reconstruction of the SST time series using a delay embedding procedure and identification of the false nearest neighbours in the reconstructed phase space using a neighbour search approach. The effect of delay time on the FNN dimension estimation of the SST series is also investigated by considering different delay time values, including those obtained using the Autocorrelation Function (ACF) method and the Average Mutual Information (AMI) method.

V. Jothiprakash (✉) · B. Sivakumar · M. Udenia · H. Jotaniya
Department of Civil Engineering, Indian Institute of Technology Bombay, Mumbai 400076, India
e-mail: vprakash@iitb.ac.in

B. Sivakumar
e-mail: s.bellie@unsw.edu.au; b.sivakumar@iitb.ac.in

M. Udenia
e-mail: mohit.udenia@gmail.com

H. Jotaniya
e-mail: himanshuj1370@gmail.com

B. Sivakumar
UNSW Water Research Centre, School of Civil and Environmental Engineering, The University of New South Wales, Sydney, NSW 2052, Australia

V. Sundar et al. (eds.), *Proceedings of the Fifth International Conference in Ocean Engineering (ICOE2019)*, Lecture Notes in Civil Engineering 106,
https://doi.org/10.1007/978-981-15-8506-7_30

Keywords Sea surface temperature · Time-series analysis · Nonlinear dynamics · Chaos · False nearest neighbours method

1 Introduction

Sea Surface Temperature (SST) is the ocean temperature that is a measure of heat near the surface of the ocean. SST broadly affects the variation of energy between the ocean and the atmosphere. For the study of marine ecosystems, weather prediction, and atmospheric model simulations, SST provides fundamental information on the global climate system. The SST has an enormous influence on the Indian monsoon rainfall and the wind patterns over India. Hence, SST is a necessary element in ocean engineering operations. In the existing study, we have attempted to analyse the nonlinear behaviour of the SST time series at a station Arabian Sea using the long-term daily data records of 30 years from 1987 to 2016. The scope of this research is to acquire some insight into the chaotic nature of the SST time series. SST was measured through by computing water flowing of ocean-faring ships through the input ports. Later the information about global SST is obtaining from satellite observation, infrared radiometer and using moorings and drifters buoys. Time series of one particular location is usually measured by moorings, and the data for the deeper ocean temperature are measured from drifters. Data recorded at time T (it could be discrete, $T = 1, 2, 3$, or continuous $T > 0$). A data point can be observed at a particular location over time or at a specific time in different areas or at different places over time. A nonlinear hydrologic time-series analysis is carried out to extract the broad range of characteristics and dynamics information.

Chaotic systems typically have a 'random-looking' structure that is a typical encounter in various methods, the concepts of chaos theory have expanded substantial growth in various scientific fields. System showing chaotic nature is irreproducible and unpredictable in the long term (due to sensitivity to initial conditions) but reproducible and predictable in the short term (due to determinism. Sum of leading variables affecting any particular time series (SST) recognized by analysing the chaotic nature of SST, which is a so-far unexplored field that can help in better understanding and forecasting of the Climate process.

2 Study Area and Data Description

This study presents nonlinear analyses for the determination of chaotic behaviour of SST over the region of the Arabian Sea. Required daily SST data for the chosen location in the Arabian Sea is collected from European Centre for Medium-Range Weather Forecast (ECMWF). For explaining the methodology, initially a station is selected and analysed. The Arabian Sea being the north-western wing of Indian Ocean is the main sea route, connecting Asia with America and Europe. To study the

climatology of Arabian Sea SST and its relationship with other climatic parameters is necessary as it has a significant influence on India climate. The daily data available from 1/1/1987 to 31/12/2016 has been used in this study.

3 Material and Method

Various methods for identification and prediction of chaos has been developed due to significant interest in studying the chaotic behaviour of natural systems. Some of the most common methods for chaos identification involve phase space reconstruction, surrogate data method, correlation dimension method, FNN method, Kolmogorov entropy method, Lyapunov exponent method, and nonlinear local approximation prediction method; these methods have different bases and approaches especially with the applications in hydrology and often aim to identify various measures of chaos. In the present research, we have used the following tools and method given in Fig. 1.

3.1 Internal Characteristics

Several tests have been conducted for analysing the internal characteristics of SST. As SST time series is may be of the non-parametric form (not following the normal distribution), trend analysis is carried out by two commonly used method Mann–Kendall and Sen slope trend test. For homogeneity check-Standard Normality test, Buishand Range test and petite test are utilized while the stationarity analysis has carried out by Augmented Dickey Fuller (ADF) and Kwiatkowski–Phillips–Schmidt–Shin (KPSS) test respectively.

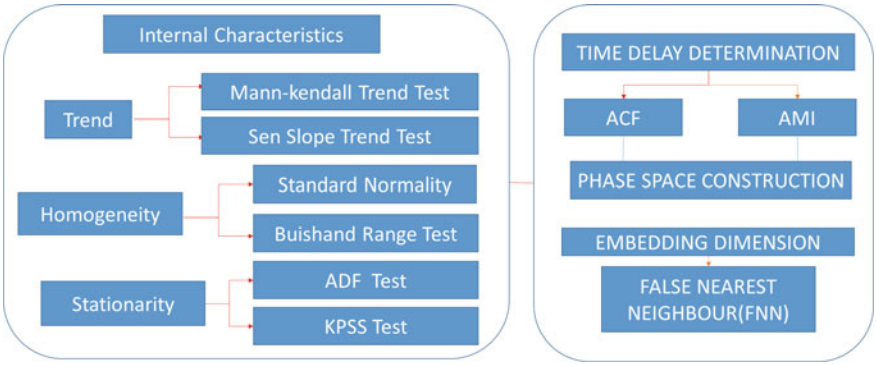

Fig. 1 Tools and methods used in the present study

3.2 Phase Space Reconstruction

Dynamics system can be deterministic or low deterministic (chaotic) or may be stochastic. The specific state of the system has represented on co-ordinate diagram called phase space. The trajectories of the phase space diagram describe the evolution of the system from some initial state, which is assumed to be known, and hence represent the history of the system. To reconstruct phase space, choice of correct embedding dimension is required by any global model that can be estimated using FNN method. The FNN algorithm uses standard delay time value to provide information about optimal embedding dimension of the phase space for representing the system dynamics by inspecting percentage of false neighbour for a particular dimension. For example, the neighbours of particular vector '*v*' will be false for a low dimension while at optimum higher dimension neighbours are genuine. There are several methods and guidelines for the selection of an appropriate delay time (s) for phase space reconstruction and any subsequent chaos analysis. The ACF and AMI are commonly used method. ACF is a primary linear tool that used for data manipulation in the analysis of time series for identification of system properties. It measures the direct relation between consecutive values of time series, determining the degree of dependence present between the values. Strong relationship exist between values that repeat over and over again. For a purely random process, the ACF fluctuates about zero, meaning that the process at any particular instance has no 'memory' of the past at all. There is another method called AMI, a tool to determine a reasonable delay time. The AMI function measures the linear as well as general dependence, between successive points [1–10].

4 Result

4.1 Statistical Analysis

Statistical analysis is carried out to know the variation of data over time. Daily data provided by European Centre for Medium-Range Weather Forecasts during the 30 years as shown in Fig. 2 is analysed. Result for the following statistical analysis is given in Table 1.

4.2 Internal Characteristics

Several tests have been used for examining stationarity, homogeneity and trend analysis over a 30 year's data set to find the possible characteristics of SST. The trend analysis was made based on the following criteria.

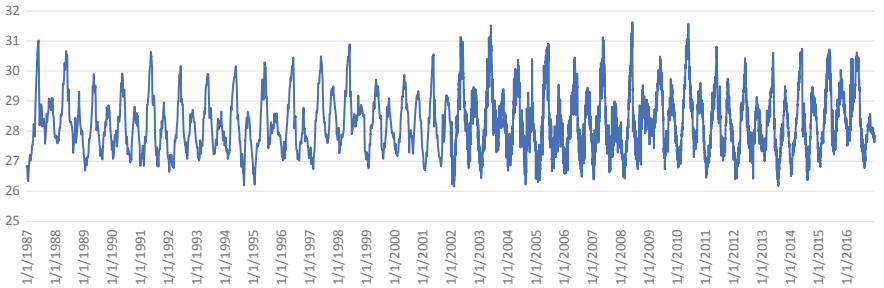

Fig. 2 Time-series plot of SST

Table 1 Descriptive statistics result

Mean (°C)	Median (°C)	Standard deviation (°C)	Kurtosis	Skewness	Minimum (°C)	Maximum (°C)
28.27	28.16	0.95	−0.18	0.53	26.16	31.62

- 1/−1 indicates increasing and decreasing trend respectively.
- Mean 1/2 = average of data values before/after time *T*.
- If the p value is less than 0.05, rejecting null hypothesis that there, is no difference between the means and conclude that a significant difference does exist. If the *p*-value is larger than 0.05, we cannot conclude that a significant difference exists.

Mann–Kendall trend analysis test result gave S value = 2,090,692 and Z value = 5.47 having p value less than 0.05. A Positive Sen value of 1.58E−05 is obtained from Sen Slope trend test. Also, The Pettitt Homogeneity Test and Buishand Range Homogeneity Test at Time (3728) gave Mean1 and Mean2 value of 28.14 and 28.33 respectively.

4.3 Time Delay Estimation

The FNN method use the standard delay time values picked up from ACF and AMI analysis. Descriptive analysis is carried out to determine cyclic pattern. The ACF plot is shown in Fig. 3.

The value of the ACF lies between +1 and −1, with +1 representing complete correlation, and −1 indicative of a negative correlation. The point on X axis where ACF plot crosses zero for the first time is taken as standard delay time value of ACF, 54 days as a standard delay time value. However, AMI has greater advantage over ACF as it also consider nonlinear correlations. We will prefer AMI delay time value over ACF delay for better nonlinear analysis. For the determination of delay time value AMI function is run to get AMI vs time lag graph with lag of one day over 30 years of data. The lag time where AMI curve get its first minimum is taken as

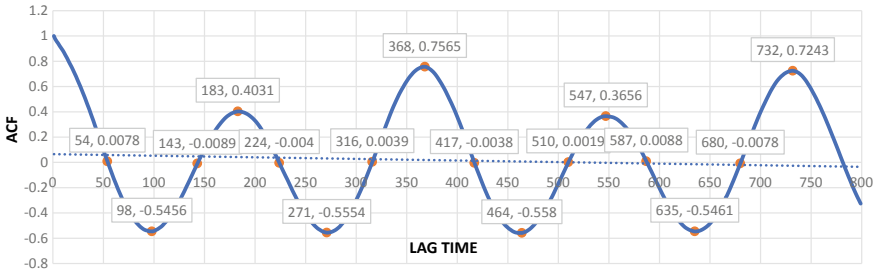

Fig. 3 ACF plot

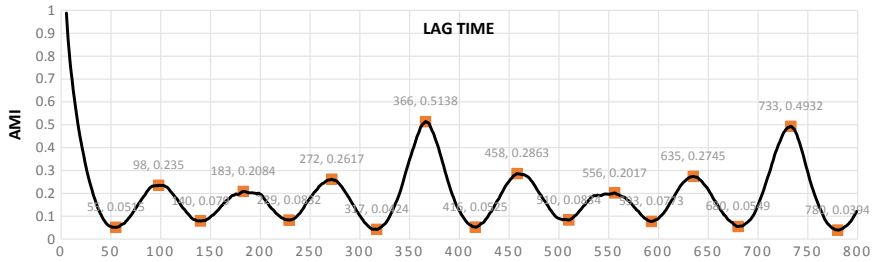

Fig. 4 AMI curve

standard delay time value, that comes out to be 54 days as shown in Fig. 4. It is not necessary to get same delay time from both the tools, the value may differ for different parameter time series.

4.4 Phase Space Construction

Phase space is essentially a graphical representation, whose coordinates represent the variables necessary to effectively describe the state of the system at any instant. In the present study, Takens' delay embedding theorem has been used for phase space (or state space) reconstruction. Given a single variable series, Xi, where $i = 1, 2, \ldots N$. A graph between Xi versus $Xi + 1$ and Xi versus $Xi + \tau$ plotted where τ denotes delay time (54) to obtain important qualitative information about the trajectory of the system evolution and complexity of the attractor. The phase space plot with delay time $\tau = 1$ and $\tau = 5$ is given in Fig. 5a, b respectively.

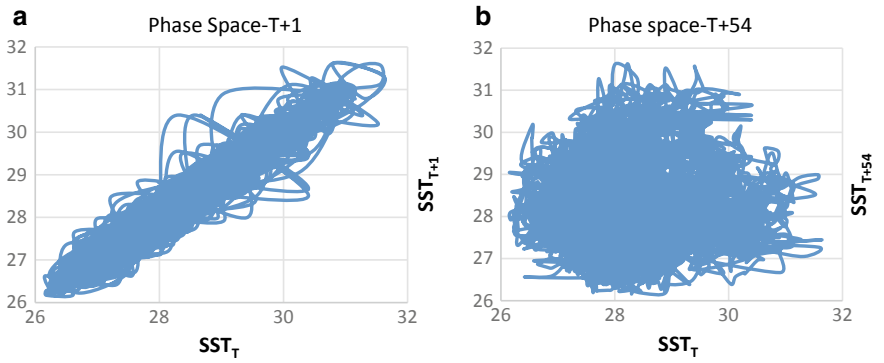

Fig. 5 a Attractor (phase plot $\tau = 1$), **b** attractor (phase plot $\tau = 54$)

4.5 Estimating Embedding Dimension

The time series of the selected data are analysed in detail to get their basic governing dynamics. The FNN algorithm used as a method to determine the optimal embedding dimension required for recreating or unfolding nonlinear system dynamics. The delay time obtained from ACF and the AMI method employed to use FNN analysis. The plot between the embedding dimensions number on the x-axis and the percentage of false neighbours on the Y-axis is obtained by using FNN algorithm. The shape of the plot and the FNN number are both equally important. Starting Dimension at which there is no change in percentage FNN is our required embedding dimension. Figure 6 shows the FNN plot for different delay time values. The embedding dimensions arrived

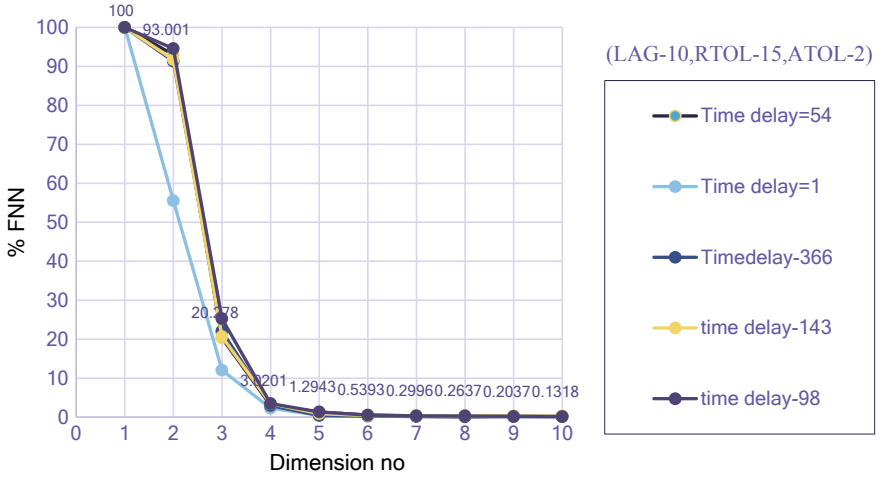

Fig. 6 FNN plot

Table 2 Embedding dimension corresponding to different delay time value

Method	Delay time	Embedding dimension
Measured time step	1	4
The autocorrelation function (ACF)	54	5
The average mutual information (AMI)	54	5
Second zero (ACF)	143	5
Time period (annual, periodic)	366	5

using FNN with different delay time is given in Table 2, all shows an embedding dimension around five.

5 Conclusions

In the current study, several tests has been performed to know the nonlinear dynamic behaviour of the SST time series. The long-term SST time series has been analysed by using different statistical tools. Statistical parameters such as mean, standard deviation, skewness, kurtosis are indecisive, but it helps to give some understandings. The trend is a useful property to identify system changes and to make future predictions. As our input data may or may not follows the normal distribution, the trend analysis for non-parametric data is carried out by a commonly used test like the Mann–Kendall Test and Sen Slope Test. The result (Z and Sen value) shows positive significance and increasing trend indicate a gradual increase in SST (global warming). Pettitt, Buishand range and Standard Normal Homogeneity test show a significant difference in average mean-1 of the data before time T and mean-2 after time T, in other words, there is a sudden jump in the data series at a time T concluding non-homogeneous behaviour of SST time series. Further due to a distinctive result from ADF and KPSS stationarity test we are unable to comment on the stationarity of the SST.

Both the ACF and AMI plot showed a strong relation between values that repeat over and over again indicating the cyclic nature of time series with the period of 366 days (1 year). Phase space plot obtained using delay time value from AMI (54 days) gave essential qualitative information about the trajectory of the system evolution and nature and complexity of the attractor. It can be concluded that there is a gradual change in the consecutive value of time series whose extreme values lies within limits. The FNN plot is not fluctuating and decreasing to zero monotonically for different value of delay time indicates that the noise level is much less in the deterministic chaos signal. In addition, the value of the embedding dimension is constant for the long range of delay time value too. FNN results show chaotic behaviour of SST which is influenced mainly by five dominant processes. From the

gained optimum value of delay time 54 and an embedding dimension of five, we can process a short-term prediction or forecasting using a different method like local approximation and inverse approach.

References

1. Lambrakis N, Andreou AS, Polydoropoulos P, Georgopoulos E, Bountis T (2000) Nonlinear analysis and forecasting of a brackish karstic spring. Water Resour Res 36(4):875–884
2. Sivakumar B, Berndtsson R, Persson M (2001) Monthly runoff prediction using phase-space reconstruction. Hydrol Sci J 46(3):377–387
3. Sivakumar B, Jayawardena AW, Li WK (2007) Hydrologic complexity and classification: a simple data reconstruction approach. Hydrol Process 21(20):2713–2728
4. Jothiprakash V, Fathima TA (2013) Chaotic analysis of reservoir inflow series-a case study on Koyna reservoir inflow. J Inst Eng India 94(2):89–97
5. Islam MN, Sivakumar B (2002) Characterization and prediction of runoff dynamics: a nonlinear dynamical view. Adv Water Resour 25:179–190
6. Regonda S, Sivakumar B, Jain A (2004) Temporal scaling in river flow: can it be chaotic? Hydrol Sci J 49:373–385
7. Salas JD, Kim HS, Eykholt R, Burlando P, Green TR (2005) Aggregation and sampling in deterministic chaos: implications for chaos identification in hydrological processes. Nonlinear Proc Geophys 12:557–567
8. Kim HS, Lee KH, Kyoung MS, Sivakumar B, Lee ET (2009) Measuring nonlinear dependence in hydrologic time series. Stoch Environ Res Risk Assess 23:907–916
9. Khatibi R, Sivakumar B, Ghorbani MA, Kisi O, Koçak K, Farsadi Zadeh D (2012) Investigating chaos in river stage and discharge time series. J Hydrol 414–415:108–117
10. Tongal H, Demirel MC, Booij MJ (2013) Seasonality of low flows and dominant processes in the Rhine River. Stoch Environ Res Risk Assess 27:489–503

Estimation of Ship Heave and Pitch Under Wave Loads Using Kalman Filtering

Kaustubh Joshi and Nilanjan Saha

Abstract Ships or any marine vessels experience loads in form of dynamic wave and wind forces. These affect the motion of ships in both transverse and longitudinal direction. The motions of ship are an important parameter to be controlled as well as to be known in order to prevent any failures like capsizing or structural instability. Therefore, it is of utmost importance to predict the ship motions. This paper attempts to study the ship motions using Kalman filter (KF) considering a regular sea state. Initially, the dynamic longitudinal loads are obtained by the long-term prediction method on basis of ship motion calculations using strip theory. The measurements are then corrupted via noise to simulate practical observations. The unknown parameters like sectional wave exciting force and sectional hydro-mechanic force are then estimated using KF by analysing the problem as a 2D problem using linear Airy wave theory under assumption that the body is a rectangular floating frame. The problem can then be extended to actual load conditions and sea states.

Keywords Kalman filter · Parameter estimation · Ship motions · Noisy measurements

1 Introduction

Marine vessels are subjected to various forces due to waves, winds and currents. Such extraneous forces affect the motion of ship. Ship motions play a crucial role in understanding the dynamic loading on the ship structures and components. In case of aircraft carriers and similar vessels, unstable ship motions can hamper the process of recovery and deployment of aircraft or vessel. Unstable ship motions also have an adverse effect on the passengers as well as crew of the vessel like motion sickness.

K. Joshi (✉) · N. Saha
Indian Institute of Technology Madras, Chennai, Tamil Nadu 600036, India
e-mail: kaustubh.joshi1997@gmail.com

N. Saha
e-mail: nilanjan@iitm.ac.in

V. Sundar et al. (eds.), *Proceedings of the Fifth International Conference in Ocean Engineering (ICOE2019)*, Lecture Notes in Civil Engineering 106,
https://doi.org/10.1007/978-981-15-8506-7_31

The design of ships is also heavily dependent on the motions of the ship. For example, it would be difficult to have loose machinery at parts of the ship which experience the most movement. Hence, it is of utmost importance to have an estimate of ship motions in order to avoid similar circumstances. A ship model can be represented through six degrees of motions (DoF). Figure 1 shows the brief explanation of motion direction, and the other axis details are reported in Table 1.

The previous works have been reported by Triantafyllou [1] in estimating the real-time ship motions using Kalman filter in order to land aircraft on a ship. Through this paper, an attempt is to effectively use the Kalman filter (KF) estimation algorithm to obtain these ship motions so as to find the forces acting on the structure of the ship. Assuming only head waves are being encountered by the ship, herein only the wave loads are considered and the wind loads are ignored. Lewis [2] had contributed towards obtaining the equations of motion. Using the strip theory, which was developed by [3] based on slender body assumption, the ship body is divided into many sections and wave loads will be found at each section of the ship. It will subsequently be integrated to find it on the structure as a whole. Strip theory has introduced coefficients of ship motions like added mass coefficients and damping

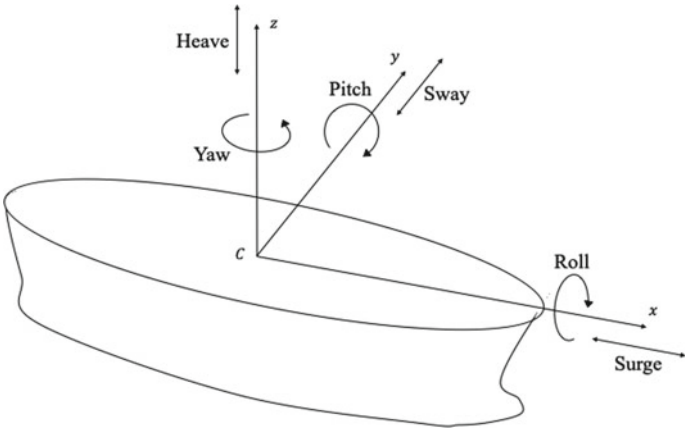

Fig. 1 Degrees of freedom of a ship

Table 1 Notations for ship motions and descriptions

Number	Motion	Description	Symbols
1	Surge	Linear motion in x direction	x
2	Sway	Linear motion in y direction	y
3	Heave	Linear motion in z direction	z
4	Roll	Angular motion about x axis	ϕ
5	Pitch	Angular motion about y axis	θ
6	Yaw	Angular motion about z axis	ψ

coefficients. The added mass coefficients can be found out through the recent work by [4].

In this paper, attempt is made to estimate the ship motions using the extended Kalman filter [5, 6]. For this study, the sea conditions are assumed to be defined by Airy wave theory (also known as linear wave theory) and the vessel to be a slender rectangular frame. The equation of motion is obtained by using simple free-body diagrams and then modelled into a state-space equation as given in [7] as to create the foundation for KF algorithm which requires the description of states of the system. The parameters to be estimated are the ship motion, its velocity and the damping factor.

Hence, the first part of this paper will deal with forming the equations of motions for uncoupled heave and pitch when subjected to head waves. Next, the equations will be modelled as state-space equations, and the later part will be the implementation of KF to these equations so as to get the estimate of required parameters. The problem can also be extended to regular sea state in order to solve for coupled ship motions under nonlinear waves using Stokes wave theory. This data can be used to estimate the forces acting on the structure of the ship and hence giving the required feedback to the system in order to ensure that the integrity of the structure is not compromised.

2 Problem Formulation

Off late knowing *apriori* the structural health of the ships is important for the safety of the vessels. Ship motions play a huge roll in load carrying capacity and hence it is crucial to know these motions. In this paper, we will attempt to estimate the ship motions when the ship structure is subjected to wave loading. The estimation will be done by using Kalman filtering [8]. The problem will be handled in framework of linear wave theory and keeping parameters other than those to be estimated as constant. The damping factor is considered to be an unknown parameter, which will be estimated.

3 Equations of Ship Motion and Modelling

For obtaining the equation of motion for the ship, we will be taking 2D cross sections and analysing them section by section to obtain the equation of motion for the complete body. As we have assumed a slender cuboidal shape, each longitudinal cross section will be similar and the same applies to each transverse cross section as well. The forces acting on the each section and consequently, the whole body will be its weight, buoyant force and wave loads.

3.1 Wave Loading Under Linear Waves

Wave motion will result in loading on the body. Here, we will be assuming that wave motion follows small amplitude wave theory (or Airy wave theory). Waves will exhibit a local fluid particle acceleration [9] which will exert force on each "strip" of the body in both horizontal and vertical directions. The formula for the local fluid particle acceleration (a_z) in vertical direction is

$$a_z = -agk\frac{\sinh(k(d+z))}{\cosh(kd)}\cos(kx - \omega t) \tag{1}$$

where a is the wave amplitude, g is the acceleration due to gravity, k is the wave number, ω is the wave frequency and d is the depth of water. The local fluid particle acceleration (a_x) in the horizontal direction is

$$a_z = -agk\frac{\cosh(k(d+z))}{\cosh(kd)}\sin(kx - \omega t) \tag{2}$$

3.2 Uncoupled Heave Motion

Given that it is an uncoupled heave motion, we will be considering only the vertical forces in this case. The free-body diagram of the body is as below (see Fig. 2).

The total vertical force F_z on the body will be

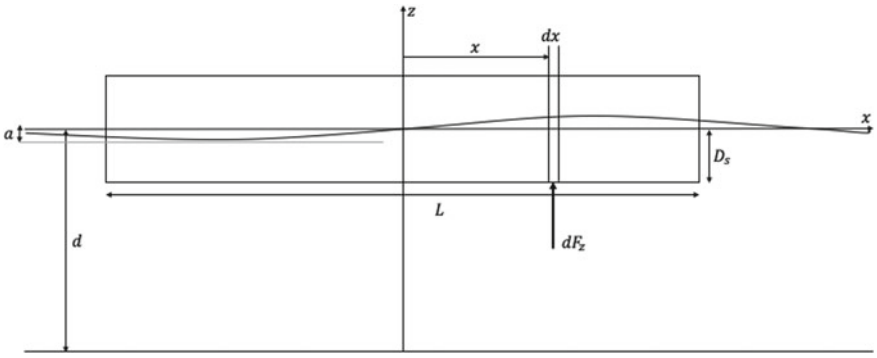

Fig. 2 Vertical forces on the body, (here, L, B, H and D_s are the length, breadth, height and draft of the ship, respectively)

$$F_z = \int_{-L/2}^{L/2} \rho_{\mathrm{m}} \mathrm{BH}(agk) \frac{\sinh(k(d+D_{\mathrm{s}}))}{\cosh(kd)} \cos(kx - \omega t)\mathrm{d}x \tag{3}$$

Hence, the exciting force term after solving Eq. (3) is

$$F_z = \rho_{\mathrm{m}} \mathrm{BH}(agk) \frac{\sinh(k(d+D_{\mathrm{s}}))}{\cosh(kd)} * 2 \sin\left(\frac{kL}{2}\right) \cos(\omega t)$$

According to (Fig. 2), the equation of motion for uncoupled heave motion will be

$$(M + A_{33})\ddot{z} + B_{33}\dot{z} + K_{33}z = \rho_{\mathrm{m}} \mathrm{BH}(agk) \frac{\sinh(k(d+D_s))}{\cosh(kd)} \cos(kx - \omega t)\mathrm{d}x \tag{4}$$

where $M = \rho_{\mathrm{m}}(\mathrm{LBH})$ is the mass of the ship, A_{ij} is the added mass, B_{ij} is the damping coefficient, K_{ij} is the restoring factor where the subscript ij refers to the effect of parameter on the body in i direction due to motion of body in j direction. For the sake of ease in calculations, the following are assumed.

$$\rho_{\mathrm{m}} \mathrm{BH}(agk) \frac{\sinh(k(d+D_{\mathrm{s}}))}{\cosh(kd)} \times 2 * \sin\left(\frac{kL}{2}\right) = F_z(M + A_{33})\ddot{z} + B_{33}\dot{z} + K_{33}z = F_3 \cos(\omega t)$$

which is reformulated after dividing Eq. (4) by $(M + A_{33})$

$$\ddot{z} + C_z\dot{z} + K_z z = \mathrm{F_z} \cos(\omega t) \tag{5}$$

3.3 Uncoupled Pitch Motion

Similarly, the pitch equations can be written based on the notations as explained in the Fig. 3.

From Eq. (2), the moment due to vertical force can be calculated as

$$M_z = \int_{x=-\frac{L}{2}}^{x=\frac{L}{2}} \int_{z=0}^{z=D_{\mathrm{s}}+x\theta} [\rho_m B(\mathrm{d}z)(\mathrm{d}x)] \left[(agk)\frac{\sinh(k(d+z))}{\cosh(kd)} \cos(kx - \omega t)\right] x \tag{6}$$

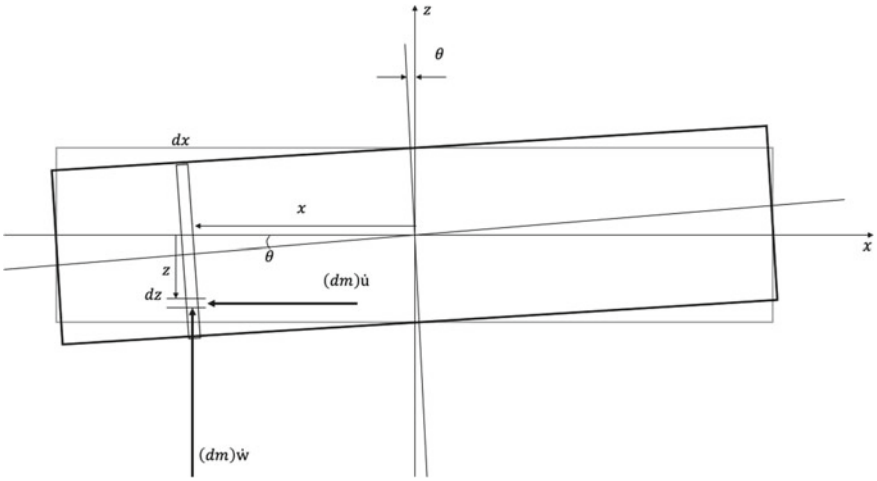

Fig. 3 Forces acting in pitch motion

From Eq. (1), the moment due to horizontal force can be calculated as

$$M_x = \int_{x=-L/2}^{x=L/2} \int_{z=0}^{z=D_s+x\theta} [\rho_m B(\mathrm{d}z)(\mathrm{d}x)] \left[(agk)\frac{\cosh(k(d+z))}{\cosh(kd)}\sin(kx-\omega t)\right] z \tag{7}$$

The equation for the pitch motion is

$$\left(I_y + A_{55}\right)\ddot{\theta} + B_{55}\dot{\theta} + K_{55}\theta = M_x + M_z$$

Equation (8) is derived and reformulated from Eqs. (6), (7) and Appendix B

$$\ddot{\theta} + C_\theta\dot{\theta} + K_\theta\theta = C_1\theta^2\sin(\omega t) + C_2\theta\cos(\omega t) + C_3\sin(\omega t) \tag{8}$$

where $C_\theta = \frac{B_{55}}{I_y+A_{55}}$ and $K_\theta = \frac{K_{55}}{I_y+A_{55}}$. The values of C_1, C_2 and C_3 are given in Appendix A.

3.4 State-Space Modelling

State-space modelling is a representation of a system as a mathematical model for first-order differential equations. The state variables are the parameters whose value

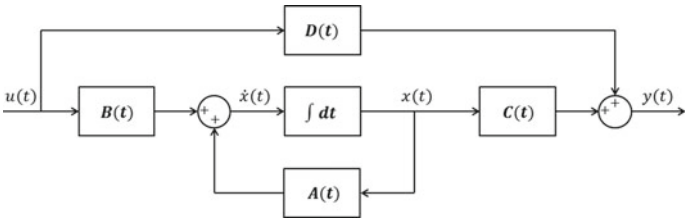

Fig. 4 State-space representation

(or state) keeps changing with respect to time. The variables can be dependant or independent of each other, and the state-space model is the one with least number of parameters involved. The state-space representation and general equation are shown below [see Fig. 4 and Eq. (9)].

$$\begin{aligned} \dot{x}(t) &= A(t)x(t) + B(t)u(t) \\ y(t) &= C(t)x(t) + D(t)u(t) \end{aligned} \tag{9}$$

Here, x is state vector, y is output vector, u is control or input vector, A is state transition matrix, B is input matrix, C is output matrix, and D is feed-forward matrix (zero if the system does not have direct feed-through). The discrete form of the same can be taken at different states being, state $k + 1$ at time $t + \Delta t$ and state k at time t leading to the following relation

$$x_{k+1} = [I + \Delta t A_k]x_k + B_k u_k \Delta t$$

4 Kalman Filter

Kalman filtering is an algorithm used to estimate the state of a system at a given time based on the past measurements. KF, being an optimal filter, is a linear one and does an excellent job in minimizing the mean square estimation error. It is a recursive algorithm which obtains the estimate from a very noisy data but what makes it even more useful is that it gives an even better estimate than other filtering techniques because it also takes state estimates into account while calculating the estimate.

The algorithm involves two recursive steps, prediction and updating. The prediction step involves rough estimates which are produced by KF, with the initial prediction given by the user. In the next stage, the actual state is measured by sensors on the system. The measurement contains some amount of error and is accompanied by random noise. The next step involves updating these estimates. The concept of weighted average will be used here in which the measurement values hold more importance. After this, the state is changed and a new prediction is made for that

state. This algorithm runs recursively. The KF algorithm is represented in a discrete form [10], based upon the assumption that the state of system (k) at a particular time t is related to its prior state ($k-1$) at time $t-\Delta t$ using

$$x_k = A_k x_{k-1} + B_k u_k + w_{k-1}$$

Here, x_k is state vector which has the information about the state of system at a given point of time t, A_k is state transition matrix which gives the dependence of the next state, k, parameter on the parameters in the previous state, $k-1$. B_k is input matrix which gives the relation of given inputs on the state vector, u_k is input vector, which contains the inputs given to the system, and w_k is process noise term

$$z_k = H_k x_k + v_k$$

Again, z_k is measurement vector which contains the measurements of quantities measured, H_k is transformation matrix which relates the measured quantities to the state parameters, and v_k is measurement noise, which is the random noise obtained due to errors in measuring the required quantities. As mentioned earlier, the KF works in two steps: predict and update [11]. The probability distribution functions (pdf) of the state variables play the most important role in the prediction and estimation of variables. The expected value and the variances as well as co-variances at a given state of a variables quantify the state parameters. This information is stored in the co-variance matrix P_k where the diagonal elements are the variances of the state variables and the remaining elements of the matrix are the co-variances between the corresponding terms of the state vector.

$$P_{k|k-1} = \boldsymbol{E}\Big[\big(x_k - \hat{x}_{k|k-1}\big)\big(x_k - \hat{x}_{k|k-1}\big)^{\mathrm{T}}\Big]$$

The KF equations for predictions constitute of the following

$$\hat{x}_{k|k-1} = A_k \hat{x}_{k-1|k-1} + B_k u_k$$
$$P_{k|k-1} = A_k P_{k-1|k-1} A_k^T + Q_k$$

where $\hat{x}_k$ is the predicted state vector and Q_k is the process noise co-variance matrix due to the noise from control inputs.

$$Q_k = \boldsymbol{E}\big[w_k w_k^T\big]$$

The equations for the measurement update are:

$$K_k = P_{k|k-1} H_k^T \big(H_k P_{k|k-1} H_k^T + R_k\big)^{-1}$$
$$\hat{x}_{k|k-1} = \hat{x}_{k|k-1} + K_k\big(z_k - H_k \hat{x}_{k|k-1}\big)$$

$$P_{k|k} = (I - K_k H_k) P_{k|k-1}$$

where K is the Kalman gain and R is the measurement noise co-variance matrix given as

$$R_k = \boldsymbol{E}\left[v_k v_k^T\right]$$

Once the measurement update is done, the state is updated as well from $(k-1) \rightarrow k$ recursively and the prediction step is carried out.

4.1 Extended Kalman Filter

The above-mentioned algorithm is for a linear system. In our case, the Eqs. (5) and (8) are continuous and nonlinear. The nonlinearity is handled by an extension of the KF algorithm called as the extended Kalman filter (EKF). The algorithm for continuous time EKF involves the steps as shown below [12]

$$\dot{x}(t) = f(x(t), u(t)) + w(t)$$
$$z(t) = h(x(t)) + v(t)$$

$f(\cdot)$ being nonlinear is expanded using Taylor series and then linearized about $\hat{x}(t)$ as:

$$f(x(t), u(t)) = f\left(\hat{x}(t), u(t)\right) + \frac{\partial f}{\partial x}|_{\hat{x}(t),u(t)}\left[x(t) - \hat{x}(t)\right]$$

$$A(t) = \frac{\partial f}{\partial x}|_{\hat{x}(t),u(t)} = \begin{bmatrix} \frac{\partial f_1}{\partial x_1} & \cdots & \frac{\partial f_1}{\partial x_n} \\ \vdots & \ddots & \vdots \\ \frac{\partial f_n}{\partial x_1} & \cdots & \frac{\partial f_n}{\partial x_n} \end{bmatrix}$$

where $A(t)$ is known as the Jacobian matrix of $f(\cdot)$. Similarly, one may write for the measurement transformation matrix $H(t) = \frac{\partial h}{\partial x}|_{\hat{x}(t)}$. The equations for Kalman gain are

$$K(t) = P(t)H^T(t)R^{-1}(t)$$
$$\dot{P}(t) = F(t)P(t) + P(t)F^T(t) + G(t)Q(t)G^T(t) - K(t)R(t)K^T(t)$$

This again just like KF goes on recursively and one obtain the estimated states of the system. In order to get an even more optimized solution, another extension

of KF, i.e. the ensemble Kalman filter (EnKF), is used in which one run the whole KF algorithm for a given number of times to get a mean of the estimate at any given point of time and the covariance matrices are generated through the ensemble equations [13]. This helps in optimizing the algorithm when noisy quantities may result in singular matrices which may give very large estimates by producing singular matrices which do not have defined inverse matrices. Hence, EnKF proves to be a very useful tool in getting better estimates.

5 Implementing the Kalman Filter

With reference to the equation of motion we derived [see Eq. (5)], our parameters to be estimated are heave position z, heave velocity $\dot{z}$ and damping coefficient C_z. The equation is a continuous nonlinear equation which results in the following state space.

$$\frac{\mathrm{d}}{\mathrm{d}t}\begin{bmatrix} z \\ \dot{z} \\ C_z \end{bmatrix} = \begin{bmatrix} \dot{z} \\ -C_z\dot{z} - K_z z + F_z \cos(\omega t) \\ 0 \end{bmatrix} + w(t) \tag{10}$$

We have taken the initial values and prediction of position and velocity to be zero for both heave and pitch motions.

Similarly, the state space for pitch motion [Eq. (8)] is

$$\frac{\mathrm{d}}{\mathrm{d}t}\begin{bmatrix} \theta \\ \dot{\theta} \\ C_\theta \end{bmatrix} = \begin{bmatrix} \dot{\theta} \\ -C_\theta\dot{\theta} - K_\theta\theta + C_1\theta^2 \sin(\omega t) + C_2\theta\cos(\omega t) + C_3 \sin(\omega t) \\ 0 \end{bmatrix} \tag{11}$$

The results obtained after implementing the EKF on the above equations (Eqs. 10 and 11) are depicted in Fig. 5 for heave motion and Fig. 6 for pitch motion.

As it can be seen in the results, the measurement follows the equation of motion which varies with some random noise. The estimated values try to converge with the true state. The convergence is dependent on Q and R matrices. A higher value of Q and a lesser value of R are highly suitable for a better convergence of the estimate. The results clearly show that the ensemble version of Kalman filter can be used as a tool to estimate the motions (translational and rotational) along with estimation of damping parameter for the ship motions.

6 Conclusion

The motion and control of ships are important for carrying out marine operations successfully. Since there are various forces acting on the ship in all directions, it becomes really necessary to have an accurate estimate of ship motions in order to

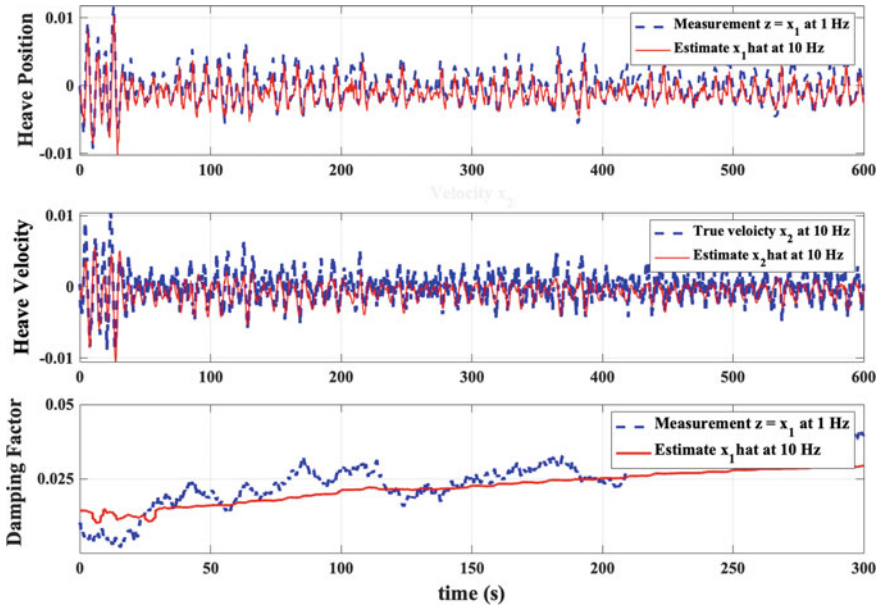

Fig. 5 Results for heave position, velocity and damping factor

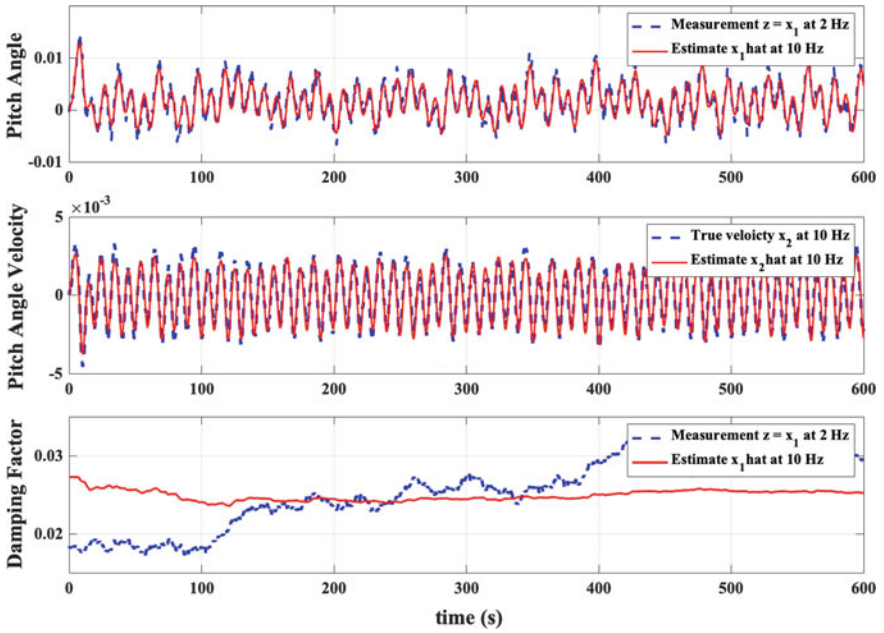

Fig. 6 Results for pitch angle, velocity and damping factor

Table 2 Notations and assumed values for ship dimensions and obtained values of coefficients

Quantity	Value	Quantity	Value	Quantity	Value
L	175 m	a	5 m	K_z	0.7664
B	25.4 m	g	9.81	F_z	0.0285
H	16 m	k	0.0402	K_θ	0.0403
D_s	8 m	ω	0.628 s−1	C_1	0.0318
ρ_w	1030 kg/m^3	d	2000 m	C_2	0.1193
ρ_m	515 kg/m^3			C_3	0.0142

have an idea about the movement of ship and forces acting on the structure of the ship. Once the time series of position and velocity is known, acceleration can be found out which can give us an estimate of forces acting on the ship. It becomes an integral part of structural health monitoring. Kalman filter does an excellent job in estimating the required quantities with respect to the noisy measurements.

In this paper, an attempt is made to estimate the position, velocity and the damping factor for the heave and pitch directions of a ship. Initially, the forces are calculated on the ship by dividing it into small cross sections throughout its length and derived from their respective equations of motion. The equations of motions were written into state-space representation as to aid the KF algorithm. Since these equations are nonlinear, one had to use the extended Kalman filter form. Thus, this paper provides a basic formulation and tutorial on how ship motion can be modelled under wave loads and estimated by Kalman filtering techniques.

7 Appendix

7.1 Appendix A

The adjoining table gives the values of quantities taken for this problem (Table 2).

7.2 Appendix B

$$M_z = \int_{x=-\frac{L}{2}}^{x=\frac{L}{2}} \int_{z=0}^{z=D_s+x\theta} [\rho_m B(\mathrm{d}z)(\mathrm{d}x)] \left[(agk) \frac{\sinh(k(d+z))}{\cosh(kd)} \cos(kx - \omega t) \right] x$$

$$= C_p \int_{x=-\frac{L}{2}}^{x=\frac{L}{2}} \int_{z=0}^{z=D_s+x\theta} x \frac{\sinh(k(d+z))}{\cosh(kd)} \cos(kx - \omega t)(\mathrm{d}z)(\mathrm{d}x)$$

$$= C_p \int_{x=-\frac{L}{2}}^{x=\frac{L}{2}} \int_{z=0}^{z=D_s+x\theta} e^{kz} x \cos(kx - \omega t)(\mathrm{d}z)(\mathrm{d}x)$$

$$= \frac{C_p}{k} \int_{x=-\frac{L}{2}}^{x=\frac{L}{2}} x \cos(kx - \omega t)\left(e^{k(D_s+x\theta)} - 1\right)\mathrm{d}x$$

$$M_x = \int_{x=-\frac{L}{2}}^{x=\frac{L}{2}} \int_{z=0}^{z=D_s+x\theta} [\rho_m B(\mathrm{d}z)(\mathrm{d}x)]$$

$$\left[(agk)\frac{\cosh(k(d+z))}{\cosh(kd)} \sin(kx - \omega t)\right] z$$

$$= C_p \int_{x=-\frac{L}{2}}^{x=\frac{L}{2}} \int_{z=0}^{z=D_s+x\theta} z \frac{\sinh(k(d+z))}{\cosh(kd)}$$

$$\cos(kx - \omega t)(\mathrm{d}z)(\mathrm{d}x)$$

$$= C_p \int_{x=-\frac{L}{2}}^{x=\frac{L}{2}} \int_{z=0}^{z=D_s+x\theta} e^{kz} z \cos(kx - \omega t)(\mathrm{d}z)(\mathrm{d}x)$$

$$= \frac{C_p}{k} \int_{x=-\frac{L}{2}}^{x=\frac{L}{2}} \sin(kx - \omega t)$$

$$\left[1 + [k(D_s + x\theta) - 1]e^{k(D_s+x\theta)}\right]\mathrm{d}x$$

Both the equations are further integrated using symbolic integration in MATLAB and then added together to give

$$M_{\text{total}} = C_1\theta^2 \sin(\omega t) + C_2\theta \cos(\omega t) + C_3 \sin(\omega t)$$

Acknowledgements The MATLAB codes for the Kalman filtering algorithm have been referred from the MSS Toolbox [14] and modified suitably to the needs of this problem.

References

1. Triantafyllou M, Bodson M, Athans M (1983) Real time estimation of ship motions using Kalman filtering techniques. IEEE J Ocean Eng 8(1):9–20
2. Lewis EV (1989) Principles of naval architecture. 3. Motions in waves and control ability; Estimation of ship motions under wave loads using Kalman Filtering. Soc Naval Arch Mar Eng
3. Ogilvie TF, Tuck EO, Faltinsen OM (1969) A University of Michigan, Department of Naval Architecture and Marine Engineering
4. Sen DT, Vinh TC (2016) Determination of added mass and inertia moment of marine ships moving in 6 degrees of freedom. Int J Transp Eng Technol 2(1):8–14
5. Perez T (2006) Ship motion control: course keeping and roll stabilisation using rudder and fins. Springer Science and Business Media
6. Chui CK, Chen G (2017) Kalman filtering. Springer
7. Brogan WL (1974) Modern control theory. Quantum Publishers
8. Kalman RE (1960) A new approach to linear filtering and prediction problems. Trans ASME J Basic Eng 82(Series D):35–45
9. Dean RG, Dalrymple RA (1991) Water wave mechanics for engineers and scientists. Adv Ser Ocean Eng
10. Faragher R (2012) Understanding the basis of the kalman filter via a simple and intuitive derivation [Lecture Notes]. IEEE Signal Process Mag 29:128–132
11. Welch G, Bishop G (1995) An introduction to the Kalman filter. University of North Carolina at Chapel Hill
12. Grewal MS, Andrews AP (1993) Kalman filtering: theory and practice. Prentice-Hall, Inc.
13. Evensen G (2009) Data assimilation: the ensemble Kalman filter. Springer Science and Business Media
14. Perez T, Fossen TI (2009) A matlab tool for parametric identification of radiation-force models of ships and offshore structures. Model Identif Control MIC30(1):1–15

3D Simulation of Wave Slamming on a Horizontal Deck Using WCSPH

N. Sasikala, S. A. Sannasiraj, and Richard Manasseh

Abstract Wave slamming induces extremely high loads to offshore structures and ships whether, due to wave impact on the deck of offshore structure or due to moving bodies such as ships and air crafts hitting the water surface. During slamming wave impact, a localized high pressure will generate at the point of incidence. This very high pressure experienced by the bottom of deck plate is difficult to predict. In this paper, numerical simulation of wave slamming on offshore platform deck structures in incident waves is carried out using weakly compressible smoothed particle hydrodynamics (WCSPH). Pressure values in SPH are very sensitive to errors in the treatment of boundary conditions. Hence, two types of boundary conditions are tried for this slamming problem: repulsive and dynamic boundary conditions. The pressure values on the center regions of the structure are observed from the SPH generated pressure contour lines, to be larger than the values on the surrounding parts.

Keywords Wave impact · Wave slamming · SPH · Pressure contours

1 Introduction

In general, wave slamming is a fluid—structure interaction problem, but what makes the slamming problem challengeable computationally is the prediction of highly localized pressures exerted on the ocean structures. Though the local peak pressure lasts only for short duration, it causes very high damage to offshore structures. For the past two decades, numerous works have been done regarding the wave impact upon

N. Sasikala (✉) · S. A. Sannasiraj
Department of Ocean Engineering, Indian Institute of Technology Madras, Chennai, India
e-mail: oe15d006@smail.iitm.ac.in

N. Sasikala · R. Manasseh
Fluid Dynamics, Swinburne University of Technology, Melbourne, Australia

V. Sundar et al. (eds.), *Proceedings of the Fifth International Conference in Ocean Engineering (ICOE2019)*, Lecture Notes in Civil Engineering 106,
https://doi.org/10.1007/978-981-15-8506-7_32

the structures. Two-dimensional simulation of the regular wave impact on the horizontal deck structure using BEM was done by Faltinsen [1]. In many offshore structures such as wave energy converters, where the surface can be allowed to deform, the local pressures need to be calculated accurately to understand the influence of slamming loads on the structure [8].

The interaction of forward face of the wave crest with the flat plate leads to the disadvantages of creation of regions with sharp curvatures. This makes the mesh stability a problematical in the conventional mesh-based methods. But the lagrangian particle nature of SPH captures highly deforming flows undergoing severe topology change automatically, thus enabling all aspects of the slam event (before, after and during impact). In the conventional mesh-based methods, the mesh connectivity faces complications in dealing deformable boundaries, complex geometries and moving interfaces, and when the mesh is tangled or regenerated, the numerical operators no longer give correct results. The aim of this paper is to study the impact of a single wave cycle on a flat horizontal deck plate using SPH in 3D space.

2 SPH Methodology

The method that has been used to model the wave slamming on a deck is called smoothed particle hydrodynamics (SPH), a meshfree lagrangian particle method which was first originally suggested for solving astrophysical problems without any solid boundaries in 3D by Lucy [4] and Gingold and Monaghan [2], later applied to free surface flows, especially wave propagation [5]. As the methodology has been in use for free surface flows for many years, it is well documented already (e.g., [5]); thus, merely, a brief review is provided here.

SPH is an interpolation method that has a great ability to handle hydrodynamic problems with highly complex phenomena in which the fluid domain is discretized using particles. Each particle carries some fluid mass, density and pressure. In SPH, each particle moves with its own velocity and follows its own trajectory.

In SPH, the fundamental principle is to approximate any function $A(r_i)$ by summing up contribution of neighboring particles j.

$$A_i = \sum_j \frac{m_i}{\rho_i} A_j W(r_i - r_j, h) \tag{1}$$

where r being the distance between particles, the parameter h, often called influence domain or smoothing length and $W(r_i - r_j, h)$ is the weighing function or kernel. The choice of the type of kernel function is significant as it affects the stability, accuracy and computational efficiency of the SPH method. The basic equations such as conservation of momentum and continuity can be represented in SPH notation.

The fluid in the standard SPH formulation is treated as weakly compressible, which facilitates the use of an equation of state to determine pressure, which is much

faster than solving the Poisson's equation, i.e., the particle motions are driven by the pressure gradient, while the pressure is explicitly calculated by the local particle density, known as Tait's equation of state (Eq. 2).

$$\begin{aligned} P &= B\left[\left(\frac{\rho}{\rho_o}\right)^{\gamma} - 1\right] \\ B &= c_o^2 \rho_o / \gamma \\ c_o^2 &= C_{\text{coeff}}^2 g d \end{aligned} \tag{2}$$

where c_o is the speed of sound at the reference density; C_{coeff} is a coefficient with the limit 10 – 40; ρ_o is the reference density, 1000 kg/m^3; γ is a constant, i.e., chosen as 7 for fluid motion; and d is the mean water level.

The fully tested toolbox of SPHysics is adopted to build the model for the present study. The combination of the methods is chosen based on the experience gained during the project. The initial SPH model of the wave slamming problem is depicted in Fig. 1b. Initially, fluid particles follow simple cubic arrangement with zero initial velocity, and boundary particles are arranged in staggered manner (BCC) and detailed in the next subsection.

3 Wave Slam on a Horizontal Deck

3.1 Problem Description and Numerical Settings

The wave slamming process on a deck is modeled similar to the schematic shown in Fig. 1b, where x is the horizontal coordinate positive in the wave propagating direction with $x = 0$ m and z is the vertical coordinate positive upward. The geometry is three dimensional. Slam plate is modeled as a simple non-rotating rigid body, constructed using a line of incompressible particles. Any deformation or elastic responses in the plate that may occur during impact is not considered. A rigid slam plate of size 8 cm $\times$ 8 cm $\times$ 0.1 cm is initially positioned at 1.8 cm above the still water level. The deck plate is placed at a distance 1 m from the wave maker. The numerical wave tank is of size 6 m $\times$ 0.4 m $\times$ 0.36 m with a sloping beach at its right end. The still water depth of the tank is 0.16 m. Using this numerical wave tank of particle spacing 0.02 m, the simulation of regular wave of height 4.8 cm with a period of 0.6 s is conducted. The physical behavior of wave impact on plate for one wave cycle includes the following stages: partial submergence, complete submergence, wave recession and wave drainage. The present numerical model (Fig. 1c) is able to simulate these stages properly. The particle approximation is done using cubic spline kernel function which is defined as nonzero for $q < 2$, i.e., $r < 2$ h where h is the smoothing length [7].

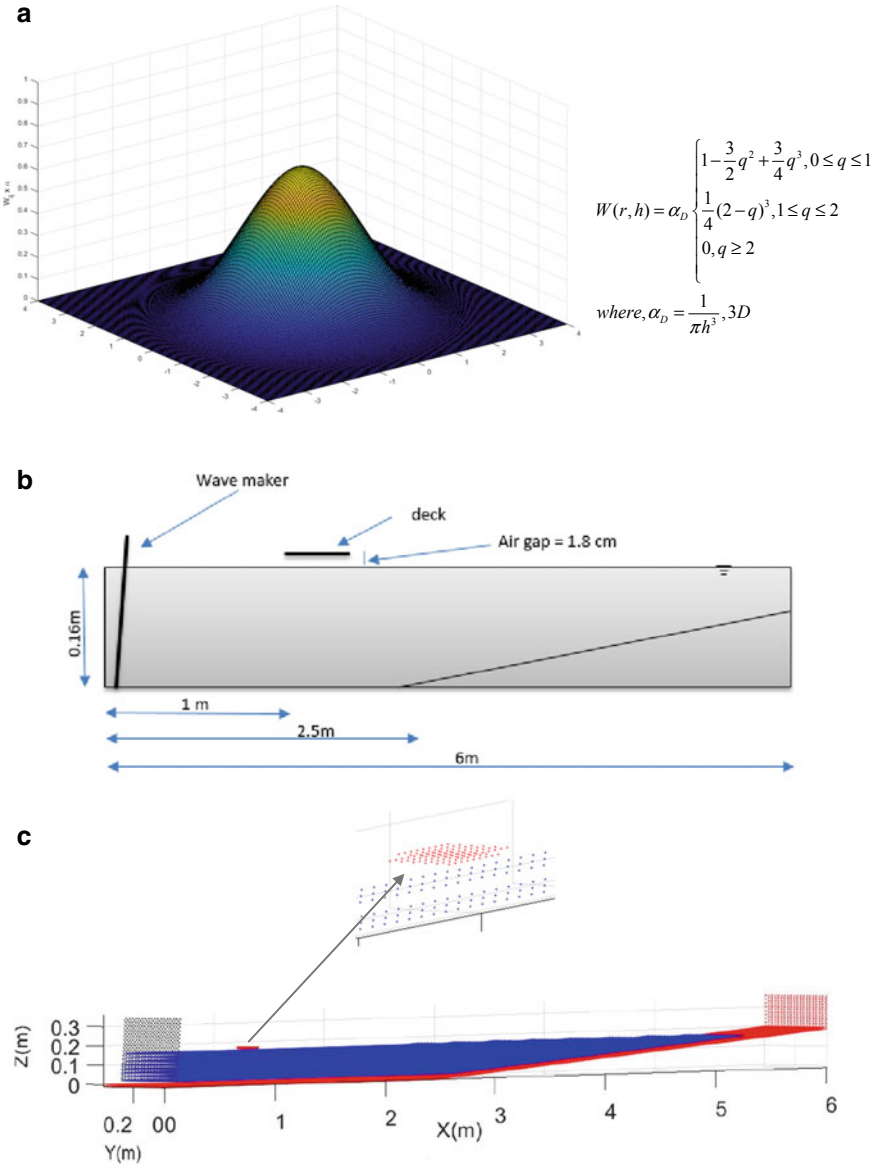

Fig. 1 **a** Cubic spline kernel function in three-dimensional space, **b** schematic representation of the wave slamming problem (not to scale), **c** initial numerical model setup in 3D

3.2 Solid Boundary Treatment (SBT)

Different types of boundary conditions are developed for SBT in SPH. Among them, only two popular boundary conditions (which are inspired from their success) are tried for this slamming problem.

Repulsive Boundary Condition (RBC). The boundary wall is described by a set of discrete boundary particles which exert a repulsive force on water particles when they approach. And RBC demands only one layer of solid particles to fit the geometry. The repulsive boundary condition (RBC) was developed by Monaghan [5] to ensure that a water particle would never enter into a solid boundary.

The forces exerted by the solid boundary particles are similar to intermolecular forces that have the form given by Lennard–Jones potential. This method was refined in Monaghan and Kos [6]. There is a small gap (2 h) created between the layer of repulsive solid particles and fluid particles (Fig. 2) to avoid particle mixing. But this SBT fails to mimic the effect of real physical behavior of wave slamming on a rigid plate because of the great resistance offered by the solid boundary particles when it experiences fluid particles.

Dynamic Boundary Condition (DBC). In DBC, two layers of stationary fluid particles need to be deployed along the solid boundary while initializing the model, i.e., boundary particles remain at rest with zero velocities during simulation. However, these boundary particles are involved in the calculation of fluid particle accelerations during fluid solid interaction. This treatment also gives pressure calculations at boundary points. When a fluid particle approaches boundary wall, the density of the boundary particles increases, resulting in a pressure increase. Thus, the force exerted on the fluid particles increases due to the pressure term in the momentum equation.

It is also evident from Fig. 2c that the RBC fails to mimic the effect of real physical behavior of wave slamming on a rigid plate; thus, dynamic boundary condition is considered in this study. The deck plate is made up of two layers of quasi-fluid particles, consisting of 72 boundary particles arranged in staggered manner.

4 Results

The focal phases of impacting pressure on the subsurface can be observed in Fig. 3a. The presence of a deck plate inside a computational domain gives high density gradients near deck. To minimize this effect, the density calculated from the continuity equation is buffered using Eq. (3) [3]. And the pressure is recalculated from the new density using the state Eq. (2).

$$\rho_{\text{new}} = \rho_{\text{calculated}} + 0.3 * (\rho_o - \rho_{\text{calculated}}) \tag{3}$$

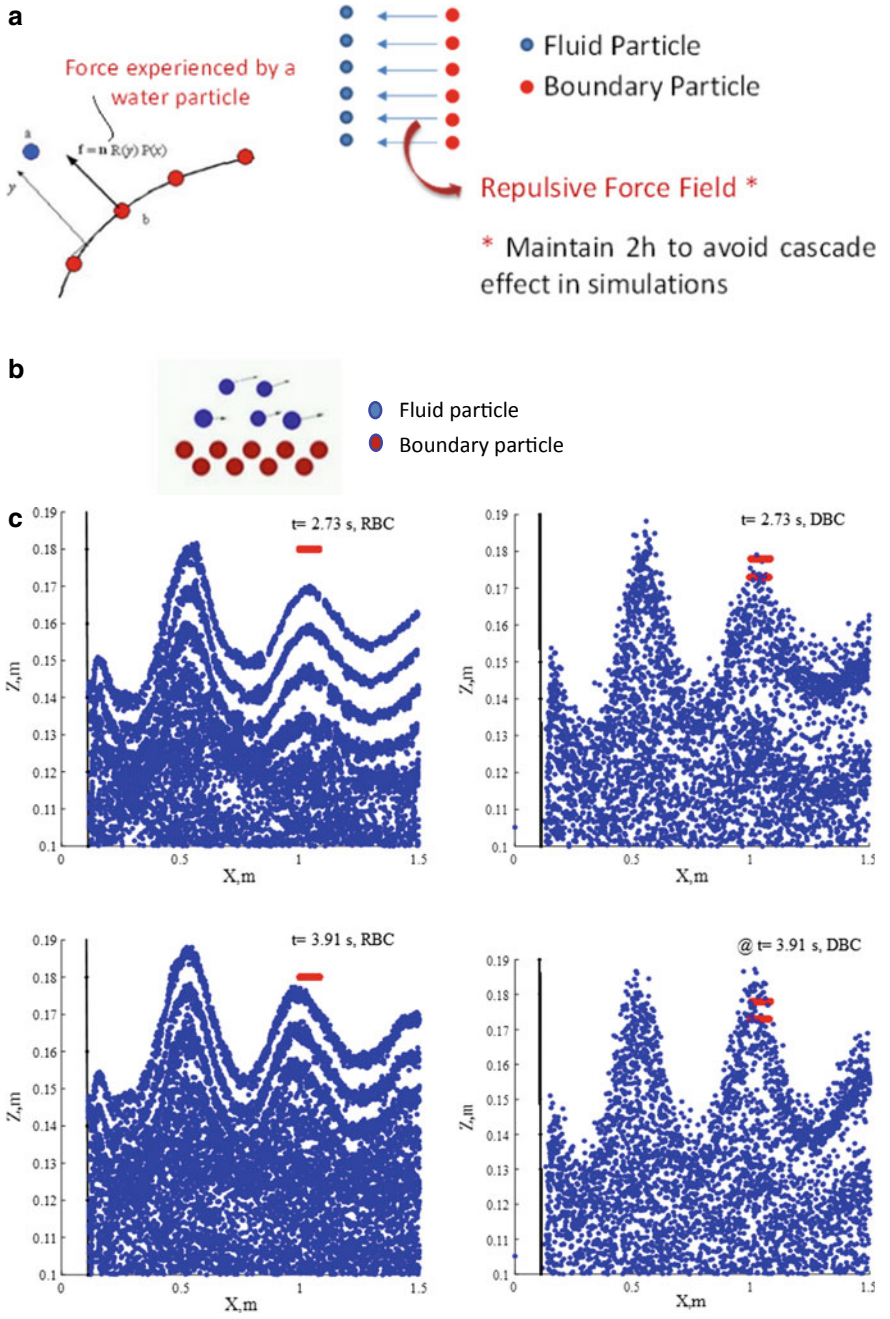

Fig. 2 **a** 2D sketch of the interaction between fluid particles and a set of repulsive boundary particles, **b** 2D sketch of dynamic boundary layer, **c** snapshots showing the difference between the usages of two boundary conditions

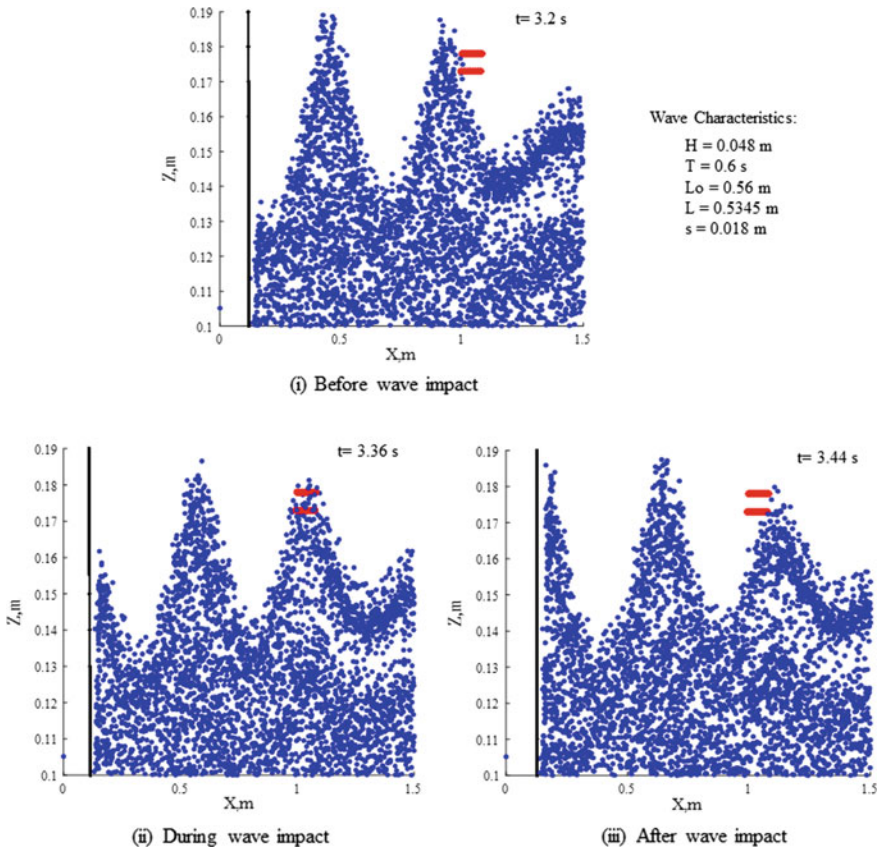

Fig. 3 Particle positions showing focal phases of wave impact on deck for one wave cycle

The two main stages of wave impact on plate during one wave cycle are shown in Figs. 4a and 5a representing particle positions for plate under complete submergence at 3.95 s and water drainage after submergence at 4.05 s, respectively. During slamming wave impact, a localized high pressure will generate at the point of incidence. And this wave impact pressure is a highly localized phenomenon in time and space. So, pressure analysis is done on the basis of an area rather than on a discrete point. In this study, the SPH methodology adopted from SPHysics is further enhanced to better capture the physics of the wave slamming phenomenon by using an additional post-processing procedures.

In Figs. 4b and 5b, the values of the density and pressure on the bottom of the deck are plotted as contour lines in left and right column, respectively, for the relative clearance, $s/H = 0.375$. The abscissa represents the length of the plate along the direction of wave propagation, and the ordinate represents the breadth of the deck plate across the wave propagating direction. The horizontal arrow indicates the direction of wave propagation. It can be seen from the contour lines of recalculated

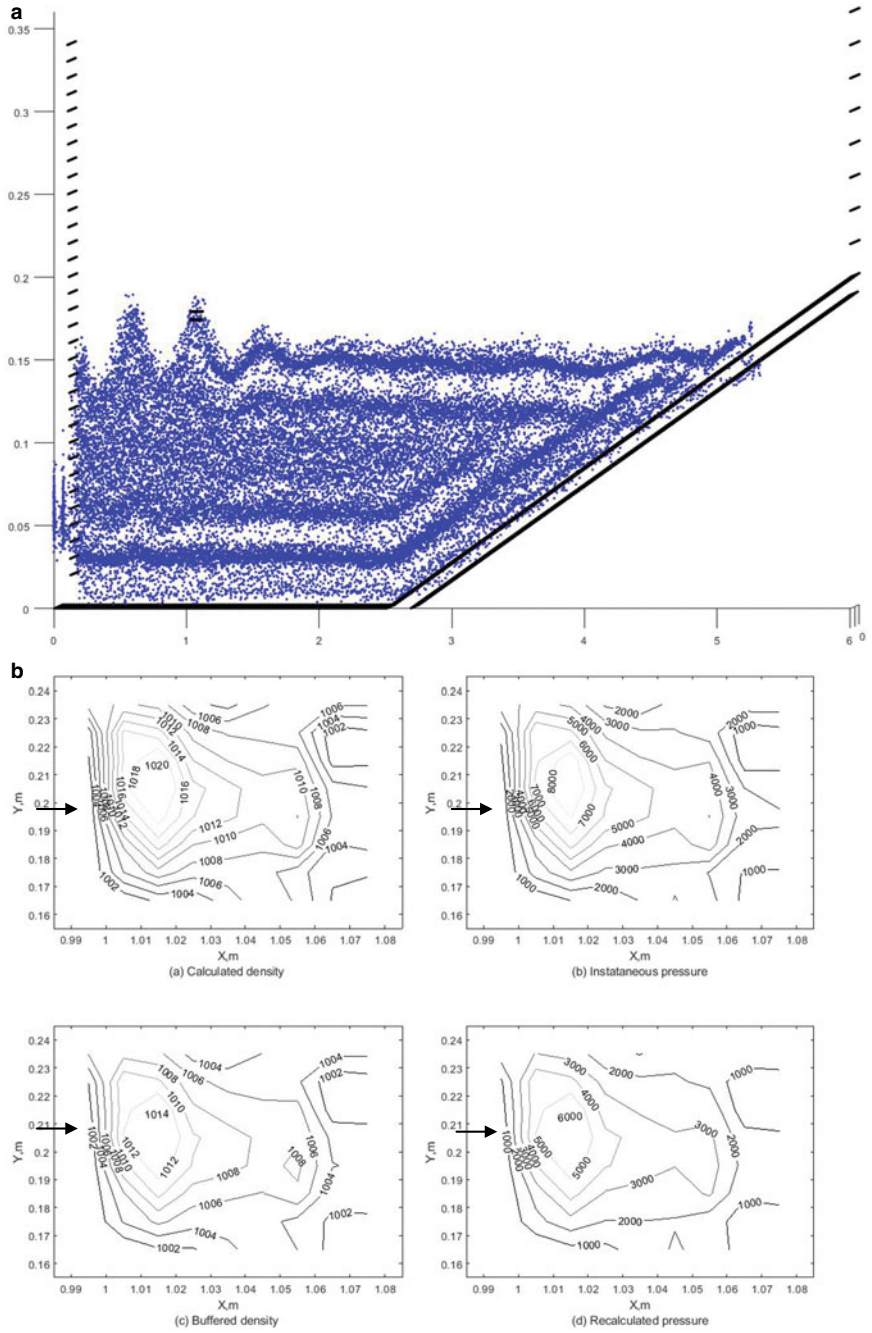

Fig. 4 **a** Snapshot showing particle distributions for deck plate under complete submergence at 3.95 s, **b** distribution of the wave impact pressures (right column) on the underside of the deck structure at 3.95 s for $H = 4.8$ cm, $s/H = 0.375$

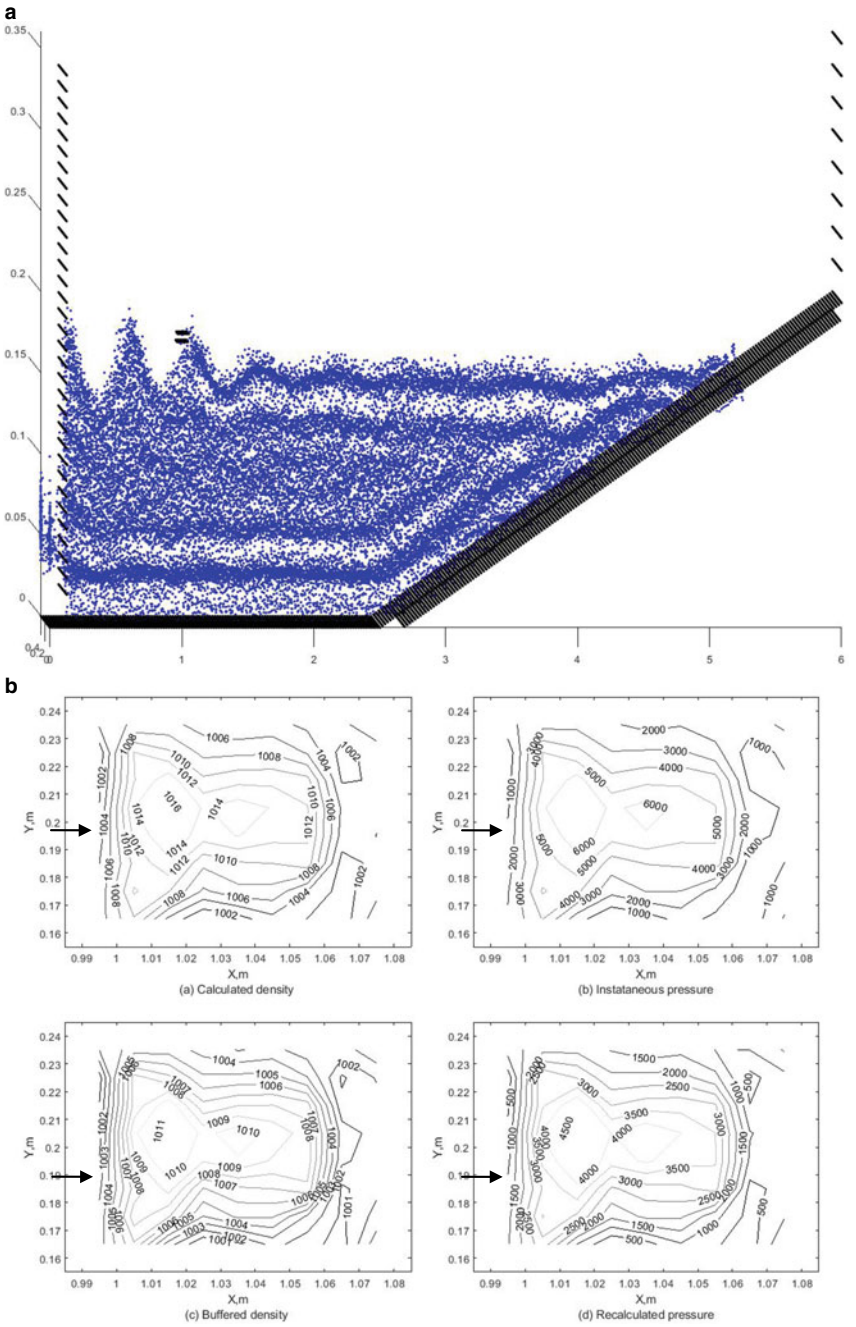

Fig. 5 **a** Snapshot showing particle distributions for wave recession after submergence at 4.05 s, **b** distribution of the wave impact pressures (right column) on the underside of the deck structure at 4.05 s for $H = 4.8$ cm, $s/H = 0.375$

pressure that the impact pressures have symmetrical distributions about the wave rays, and during the complete submergence of deck, the central parts of the plate experience more impact pressure than the surrounding regions.

5 Summary and Conclusions

The mesh-based numerical models developed for various hydrodynamic problems have however certain disadvantageous compared with meshfree methods. The large discontinuities that do not coincide with the model grid could not be modeled with mesh methods. Thus, the truly meshless character of smoothed particle hydrodynamics (SPH) and no treatment on the free surface ease the three-dimensional simulation of water waves which are slamming on a simple rigid plate, in a straightforward way compared to mesh-based solvers.

We demonstrated in this paper that the wave slamming SPH model performs better in dynamic boundary treatment. Although two boundary treatments are used in this paper, all other types of boundary conditions can also be trialed. The present 3D SPH model can be used to investigate wave—in deck forces on a flat horizontal plate of offshore structures under regular waves.

References

1. Baarholm R, Faltisen OM (2004) Wave impact underneath horizontal decks. J Mar Sci Technol: 1–13
2. Gingold RA, Monaghan JJ (1977) Smoothed particle hydrodynamics. Mon Not R Astron Soc 235:911–934
3. Gomez-Gesteira M, Cerqueiro D, Crespo C, Dalrymple RA (2005) Green water overtopping analyzed with a SPH model. Ocean Eng:223–238
4. Lucy LB (1977) A numerical approach to the testing of fusion process. Astron J 88:1013–1024
5. Monaghan JJ (1994) Simulating free surface flows with SPH. J Comput Phys 110:399–406
6. Monaghan JJ, Kos A (1999) Solitary waves on a cretan beach. J Waterw Ports Coast Ocean Eng 125:145–154
7. Monaghan JJ, Lattanzio JC (1985) A refined particle method for astrophysical problems. Astron Astrophys 149:135–143
8. Van PaepegemW, Blommaert D, De Baere I, Degrieck J, De Backer J, De Rouck J, Degroote J, Vierendeels J, Matthys S, Taerwe L (2011) Slamming wave impact of a composite buoy for wave energy applications: design and large-scale testing. Polymer Compos

Investigation of a Surfactant for Reducing Friction in Different Pipeline Sizes

D. Mech, F. Jameel, and S. P. Gowardhan

Abstract The loss or drop of pressure or head which occurs in pipelines or in duct flow due to the fluid's viscosity in or inside the surface of the pipeline or duct is known as friction loss (or skin friction). Pressure drop occurs along the flow direction inside a pipe which is triggered by friction due to fluid, both internal within the fluids and with the piping surfaces, piping restrictions or sudden changes in the geometry of the flow path. Surfactants are used in the oil and gas industries for flow assurance purpose since years, but using the same for reducing friction in pipelines is still rare available in the literatures. In addition, surfactants are the chemicals which are used to get adsorbed and coated on the walls of the pipeline for reducing the friction and also affect the drag reduction. Therefore, surfactant as a friction reducing agent is having lot of scope to explore and a necessary requirement for studying to reduce friction in the pipelines. In this work, sodium lignosulfonate (SLS) is used for the studies of friction in the different diameter of pipelines for measuring the head loss. Two pipe diameters which have been used in this study are ¾ inches and ½ inches. The head loss due to friction has been determined using Darcy–Weisbach equation. It has been found that the surfactant helps to reduce the friction in the pipelines. This work provides a precursor for further studies involving surfactant to reduce friction in the pipelines for various industrial processes.

Keywords Discharge · Friction · Sodium lignosulfonate (SLS) · Velocity

1 Introduction

Friction is the force which restricts the relative motion of fluid layers, solid surfaces and material elements which are sliding against each other. There are many types of friction: Dry friction is a force that stops the relative lateral motion of two solid surfaces which are in contact. Dry friction is further divided into static friction which is between non-moving surfaces also known as stiction and kinetic friction between

D. Mech (✉) · F. Jameel · S. P. Gowardhan
Department of Petroleum Engineering, Presidency University, Bengaluru 560064, India
e-mail: deepjyotimech@presidencyuniversity.in

V. Sundar et al. (eds.), *Proceedings of the Fifth International Conference in Ocean Engineering (ICOE2019)*, Lecture Notes in Civil Engineering 106,
https://doi.org/10.1007/978-981-15-8506-7_33

the moving surfaces. Dry friction is due to surface features and not due to molecular or atomic features. This is known as asperities. Fluid friction tells us about the friction which is present between the layers of a viscous fluid that are moving relative to each other [3, 9, 10]. Lubricated friction is the fluid friction where the lubricant fluid separates the two solid surfaces [7, 15, 16]. Skin friction is related to drag and is defined as the force which restricts the motion of a fluid across the surface of a body. Internal friction is the force which restricts motion between the elements which make up a solid material during its deformation [9, 10].

Viscosity is known by the measurement of the frictional force which arises between two adjacent layers of fluid that are in relative motion. For example, when a fluid is being forced through a tube, the fluid flows more quickly at the center (near the tube's axis) and more slowly near the walls of the tube. In such instance, it is noticed that stress (such as a pressure difference between the two ends of the tube) is required to maintain the flow through the tube. This is solely because of the necessity of a force to overcome the friction between the different layers of the fluid which are in relative motion: The strength of this force is directly proportional to the viscosity of the liquid. An ideal or inviscid fluid is a fluid that has no resistance to shear stress. In superfluids, at very low temperatures, zero viscosity is observed. Otherwise, the second law of thermodynamics requires all fluids to have positive viscosity; such fluids are technically said to be viscous or viscid. A fluid having a relatively high viscosity, such as pitch, may appear to be a solid [2].

Loss in energy due to friction, mainly due to fluid molecules bombarding against each other or having contact with the walls (of the pipe it is flowing through), is termed as 'Major Losses.' Here, it is greatly affected by whether the flow is laminar ($Re < 2000$) or turbulent ($Re > 4000$) [11]. It is essential to consider the energy losses due to friction in pipelines of fluids having different velocities and distances to travel. The fluid experiences some loss in energy due to resistance when it is flowing in a pipe. This loss of energy in the fluid when it flows through pipes can be classified as major energy and minor energy losses. In long pipelines, there is a lot of loss due to friction which is much larger than the minor losses, and hence, the minor losses are often neglected. The losses because of friction in the pipelines are known as major energy losses. The friction in the pipeline is caused by a viscous drag which is between the stream bends of fluid. The stream bends of adjacent to the solid surface are always at rest with respect to the wetted surface. The molecular attractions between the molecules of the fluid are the reason for this viscous drag. It is found that the total friction resistance to fluid flow depends on the wetted surface area, fluid density and roughness of the surface. Friction resistance is also independent of the fluid pressure and increases with the square of the velocity.

In oil and gas industry, friction reducing agent or surfactant or drag reducing agent is used nowadays to minimize friction inside the pipelines. It is a chemical which usually gets absorbed at the interface which is used to lower the surface tension or interfacial tension between fluids or between a fluid and a solid. Surfactants include myriad things that function as oil-wetters, defoamers, emulsifiers, water-wetters, foamers and dispersants. The structural groups on the molecule (or mixture

of molecules) correspond to the type of surfactant. The function that a molecular group will perform depends on the hydrophile-lipophile balance (HLB) number.

For a surfactant to work more efficiently for the process of enhanced recovery from an oil reservoir, it must be properly selected based on the environmental variables such as temperature, pressure and salinity. If the selection is not done properly, then it may result in low recovery and may even cause harm to the reservoir due to undesirable wettability change and dissolution of rock resulting in a chemical reaction with the displacing fluid and plugging of the pore spaces.

Also, choosing the wrong surfactant without considering the rock mineralogy may result in high adsorption on the pore surface of the rock and unnecessary waste of resources. It is also worthy to note that surfactants are some of the most expensive chemicals used during EOR. The extensive literature review suggests that anionic surfactants are the preferred surfactant category for EOR especially when it comes to sandstone reservoirs. Occasionally, in specific situations, a better performance has been reported after injecting cationic, non-ionic or mixtures of both surfactants, particularly when dealing with carbonate reservoirs [13].

Surfactants consists of a hydrophilic part that forms hydrogen bonding and a hydrophobic part which is a non-polar of long hydrocarbon chain. The surfactant molecules prefer to present at the water surface or at the interface, thereby reducing the surface tension. The hydrophobic part combines with water to reduce the contact with the water and simultaneously, and the hydrophilic head part surrounds the hydrocarbon group, where it makes the direct contact with the water molecules. The structure of this surfactant accumulation is known as micelle. Mysels [12] is the first one to research in the drag reduction effect using surfactant in the presence of turbulent flow. However, Dodge and Metzner [4] also conducted study on drag reduction effect that acknowledged sufficient consideration. Surfactants provided more resistance for mechanical degradation as compared to polymers, and most of the surfactants are friendly chemicals for the environment [5, 6, 17, 19]. Micelles are formed by the surfactants which are essential for increasing the drag reduction in the pipelines via surfactant aqueous solutions [14, 18, 19]. The morphology of micelles can be changed from spherical to thread-like by adding ionic solutions which is an oppositely charged surfactant and also by adding organic counterions, or even uncharged small compounds like alcohols. In addition, the micelle can be spherical, disk-like, cylindrical, thread-like, bilayer spherical (vesicle), hexagonal, lamellar and cubic crystal depending on the system conditions [18, 20].

In this work, the sodium lignosulfonate (SLS) is used for friction studies in different pipeline diameters for measuring the head loss. Two pipe diameters which have been used in this study are ¾ inches and ½ inches. The friction factor (f) is determined for both the pipeline diameters using 1 weight (wt%) of SLS and pure water. The head loss due to friction or f has been determined using Darcy–Weisbach equation. It has been found that the surfactant (SLS) helps to reduce the friction in the pipelines as compared to pure water. This work provides a precursor for further studies involving surfactant to reduce friction in the pipelines for various industrial processes.

2 Experimental Section

2.1 Materials

Materials used in this study are pure water and SLS with purity mass fraction of 95%. A standard mass balance (RADWAG AS-220/X) has used to weigh the materials with an accuracy of ±0.00004 mass fraction. Deionized or pure water of 'Type 3' grade has used from Labostar (SIEMENS, Germany) to prepare aqueous solutions.

2.2 Experimental Setup

The apparatus consists of a sump tank with centrifugal pump as shown in Fig. 1. Two pipes of different diameters (½″ and ¾″) for which common inlet connection is provided with control valve to regulate the flow, near the downstream end of the pipe. Pressure tapings are taken at suitable distance apart between which a manometer is provided to study the pressure loss due to the friction. Discharge is measured with the help of measuring tank and stopwatch.

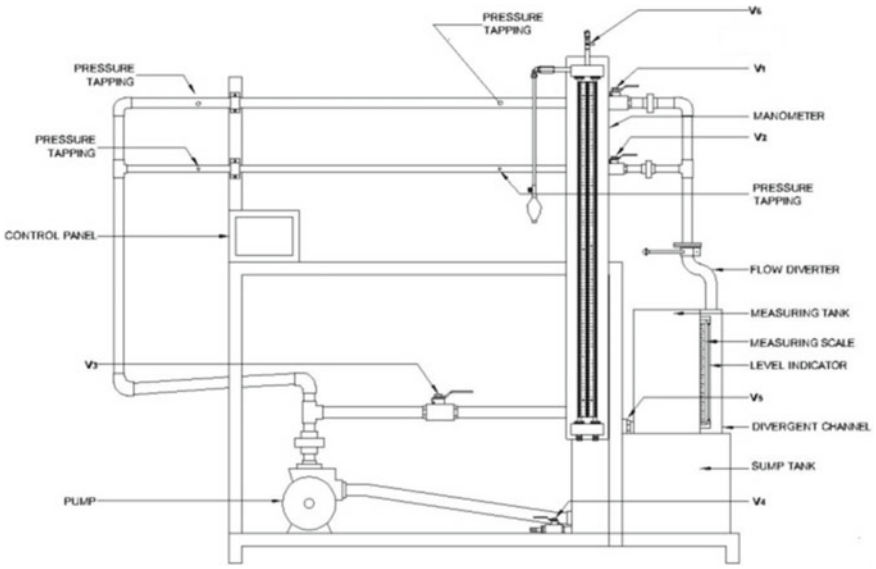

Fig. 1 Experimental setup

2.3 Experimental Procedure

All the valves provided in the setup (V1–V6) are closed initially. We fill the 75% of the sump tank with distilled water and make sure that there are no foreign particles/impurities in it. We open the bypass valve V3 which opens an additional path for flow from the main supply line to the tank. This valve can be later adjusted for vary the amount of water being flowed in the main supply line by diverting some fluid toward the sump tank.

All the switches given on the panel are in switched off mode before starting the experiment. To start the experiment, the main supply is switched on to start the setup and also, switch on the centrifugal pump. As we are studying the losses due to friction in different pipeline sizes, we have a designated valve situated before each pipe to ensure the flow of fluid in a specific pipeline under study. The pipeline being considered for study is called test section. We operate the flow control valve V1 for ¾″ pipe or V2 for ½″ pipe and bypass valve V3 to regulate the flow of water in the desired test section. There are pressure taps at each test section which can be connected to the manometer to check the pressure differences. To check the same, we must open the valve V6 provided on the manometer to release the air in manometer. We close the air release valve V6 when there is no air in the manometer. We adjust flow rate of water in the desired section with the help of control valve V1 and V2. We record the manometer reading; in case the pressure goes above scale in any tube and the reading is difficult, then we apply air pressure by hand pump to get readable reading. We measure the flow rate which is discharged through the desired test section by using a stop watch and measuring tank. We repeat the experiment for different flow rates of water by operating the control valve V1 or V2 and bypass valve V3. After the experiment is conducted for each test section, we open the bypass valve V3 completely and close the flow control valve of running test section V1 or V2 and open the control valve of secondly desired test section V2 or V1. We repeat the same procedure for the other test section.

After conducting the experiment for both the test sections with a particular weight percentage of surfactant, we vary the amount of surfactant and repeat the entire procedure again for both the test sections (both the pipelines). After the completion of experiment, we switch off the pump and the power supply to the setup, and drain the fluid in the tanks with the help of the drain valves provided in the setup.

2.4 Calculation

The loss of head in pipe due to friction is calculated from Darcy–Weisbach equation which has been given by:

$$h_{\mathrm{f}} = 4fLV^2/2\mathrm{gd},$$

where

h_f loss of head due to friction;
f friction factor;
L distance between pressure point;
V velocity of fluid;
d diameter of pipe and
g acceleration due to gravity.

3 Results and Discussion

It is evident that the velocity of both the fluids, (1 wt% concentration) SLS surfactant solution and pure water is higher in ½″ pipe when compared to the velocity of the aforementioned fluids in ¾″ pipe due to the restricted flow path in terms of the area of flow.

The area of cross section of a ½″ pipe is less than that of a ¾″ pipe. This would result in a comparably constricted flow area and helps in increase in velocity of the fluid passing through it. It is also observed from Fig. 2 that the velocity of the SLS surfactant solution is much more than the velocity of pure water flow in their respective pipeline. This could be because surfactant prevents turbulence in the

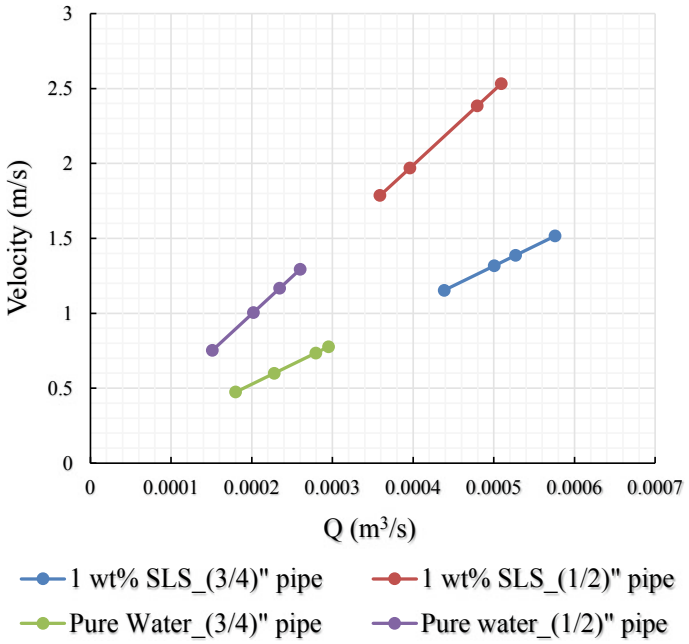

Fig. 2 Effect of flow rate on velocity with respect to discharge in ¾″ and ½″ I.D. pipes

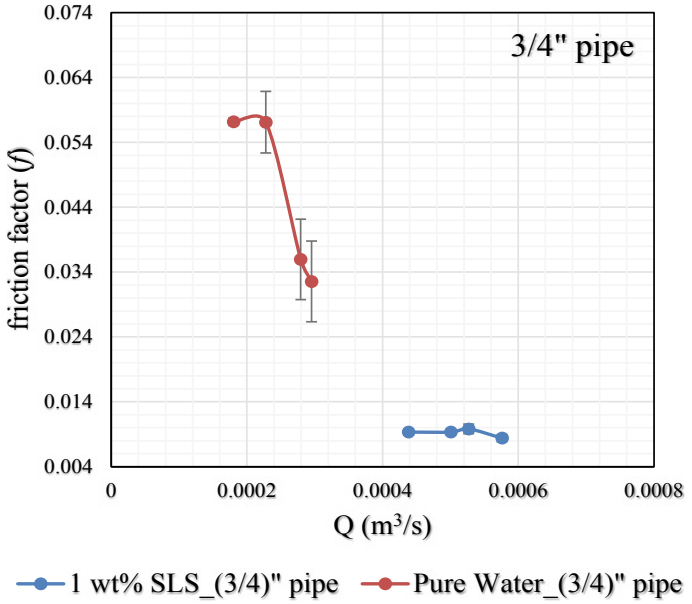

Fig. 3 Effect of flow rate on friction factor (f) in ¾″ I.D. pipe for different aqueous solutions

pipelines. Turbulent flow in the pipeline would reduce the velocity of the flowing fluid through the length of the pipe. SLS surfactant fluid hence reduces the intensity of turbulence and thereby increases the velocity of flow through the pipeline [1].

Figure 3 shows the friction factor of both the fluids (pure water and fluid containing 1% weight concentration of SLS surfactant) which is studied for different flow rates in a ¾″ pipeline. In addition, the standard error has been plotted in Fig. 3 for all the different discharge runs mentioned in the x-axis, and it has shown that the observed experimental data is correct. It is observed that the friction factor was remarkably high for pure water flowing in a ¾″ pipeline, and it drastically decreases in the solution containing surfactant. This could be because of the property of surfactant which prevents the formation of eddies in the pipelines and hence makes the fluid flow with relatively lower friction through the length of the pipeline [8].

Individually, pure water and surfactant solution have a friction factor which decreases with the increase in the flow rate. Friction factor is indirectly proportional to the flow rate of the fluid, i.e., with the increase in flow rate of the fluid in the pipeline, the friction factor decreases. With the decrease in flow rate the friction factor decreases.

The friction factor of both the fluids (pure water and fluid containing 1% weight concentration of SLS surfactant) is studied for different flow rates in a ½″ pipeline as shown in Fig. 4. The graph (Fig. 4) shows the plots of standard error with respect to their discharges mentioned in the x-axis and shows the correctness of f values. As mentioned earlier, surfactant decreases the friction factor of the fluid flowing through

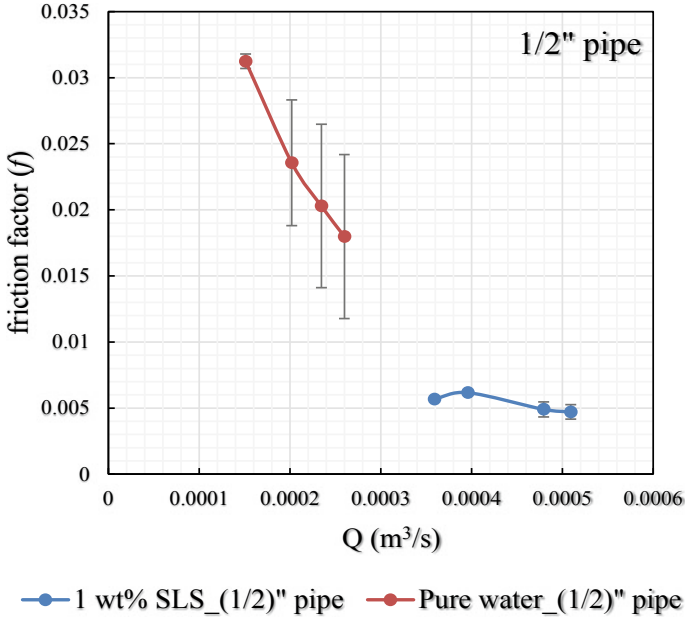

Fig. 4 Effect of flow rate on friction factor (f) in ½″ I.D. pipe for different aqueous solutions

the pipe, and hence, the friction factor of the fluid containing surfactant is less than that of pure water.

As compared to the ¾″ pipe, the ½″ pipe offers less friction factor. Friction factor (f) is directly proportional to the diameter to the pipeline, i.e., with increase in the pipeline diameter, there would be an increase in the friction factor, and with decrease in the pipeline diameter, there would be a decrease in the friction factor.

Surfactant is a drag reducing agent which decreases the friction of the fluid flowing in the pipe in turbulent type of flow. The presence of surfactant reduces the friction caused due to turbulence in the solution. This hence results in the reduction in the pressure drop across the length of the pipeline due to which a lower energy requirement to transmit the fluid through the pipe.

It is evident from Fig. 5 that the drag reduction percentage is higher in ¾″ pipe. Usage of surfactant causes around 70–80% of drag reduction and is hence successful in providing a smooth flow of fluid in the pipeline by minimizing reduction in flow energy.

4 Conclusion

The effect of sodium lignosulfonate (SLS) aqueous solution has been investigated for friction studies in different pipeline diameters for measuring the head loss. Friction

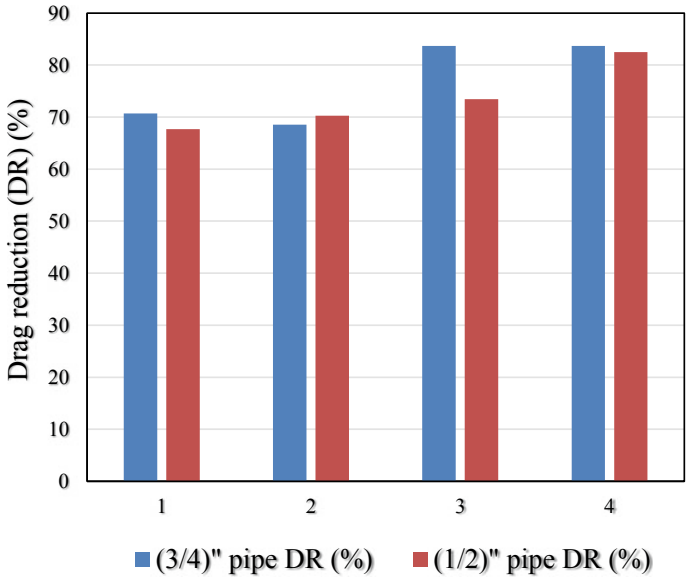

Fig. 5 Variation in drag reduction (DR) percentage (%) for different velocities and discharges

is observed to reduce in low size of pipe diameter is more as compared to the high size of pipe diameter in the presence of SLS aqueous solution. The friction factor (f) is observed to reduce for both the pipeline diameters using 1 weight (wt%) of SLS as compared to pure water. It has been found that the surfactant (SLS) helps to increase the drag reduction (%) in the pipelines satisfactorily. This work provides a basis for future studies involving application of surfactant to reduce friction in the oil and gas pipelines for various industrial processes.

References

1. Abdul-Hadi AA, Khadom AA (2013) Studying the effect of some surfactants on drag reduction of crude oil flow. Chin J Eng 321908: 6
2. Balescu R (1975) Equilibrium and nonequilibrium statistical mechanics. Wiley, pp 428–429
3. Beer FP, Johnston ER (1996) Vector mechanics for engineers, 6th edn. McGraw-Hill, p 397
4. Dodge D, Metzner A (1959) Turbulent flow of non Newtonian systems. AIChE J 5(2):189–204
5. Gardon JL, Mason SG (1955) Physicochemical studies of lignosulfonates: preparation and properties of fractionated samples. Can J Chem 33:1477
6. Harwigsson I, Hellsten M (1996) Environmentally acceptable drag-reducing surfactants for district heating and cooling. J Am Oil Chem Soc 73(7):921–928
7. Hibbeler RC (2007) Engineering mechanics, 11th edn. Pearson, Prentice Hall. p 393
8. Huang W (2005) Drag reduction in pipeline by polymer-surfactant and polymer-polymer mixtures. In: Master of applied science thesis
9. Meriam JL, Kraige LG (2002) Engineering mechanics, 5th edn. Wiley, p 328
10. Meriam JL, Kraige L, Palm G, John W (2002) Engineering mechanics: statics. Wiley, p 330

11. Munson BR (2006) Fundamentals of fluid mechanics, 5th edn. Wiley, Hoboken, NJ
12. Mysels K, Napalm J (1949) Mixture of aluminum disoaps. Ind Eng Chem 41(7):1435–1438
13. Negin C, Ali S, Xie Q (2017) Most common surfactants employed in chemical enhanced oil recovery. Petroleum
14. Qi Y, Zakin JL (2002) Chemical and rheological characterization of drag-reducing cationic surfactant systems. Ind Eng Chem Res 41(25):6326–6336
15. Ruina A, Pratap R (2002) Introduction to statics and dynamics. Oxford University Press. p 713
16. Soutas-Little RW, Inman B (2008) Engineering mechanics. Thomson, p 329
17. Zakin JL, Lui HL (1983) Variables affecting drag reduction by nonionic surfactant additives. Chem Eng Commun 23(1):77–88
18. Zakin JL, Lu B, Bewersdorff HW (1998) Surfactant drag reduction. Rev Chem Eng 14(4–5):253–320
19. Zakin JL, Myska J, Chara Z (1996) New limiting drag reduction and velocity profile asymptotes for nonpolymeric additives systems. AIChE J 42(12):3544–3546
20. Zhang Y (2005) Correlations among surfactant drag reduction, additive chemical structures, rheological properties and microstructures in water and water/co-solvent systems. The Ohio State University, Ph.D. Thesis

Phase Equilibria and Kinetics of Methane Hydrate Formation and Dissociation in Krishna–Godavari Basin Marine Sediments

Dnyaneshwar R. Bhawangirkar, Vishnu Chandrasekharan Nair, and Jitendra S. Sangwai

Abstract Understanding the formation and dissociation behavior of methane gas hydrate in marine sediments is one of the important precursors for methane gas production from the hydrate deposits. The phase behavior of gas hydrates is influenced by the presence of sediments, composition of salts and water present in it. Krishna–Godavari (KG) Basin in India is one such reservoir which has a huge potential of methane gas hydrates. Here, we have investigated the phase equilibria, and the kinetics of methane hydrate formation, and dissociation in the presence of pure water, and in aqueous solution of 10 wt% (KG) basin sediment. We observed that the phase equilibrium conditions of methane hydrate in presence of 10 wt% sediment solution got shifted to slightly higher pressures at given temperature as compared to that in the bulk phase. It has also been observed that more number of methane gas molecules are consumed in 10 wt% sediment solution in the initial 30 minutes of time than in the pure water system, revealing the promotion effect of sediment surface. The number of moles of methane gas released during the dissociation of hydrate has found to be lesser in sediment solution than in pure water at any given time after initial 55 min of the start of dissociation.

Keywords Kinetics · KG Basin sediments · Marine gas hydrates · Thermodynamics

1 Introduction

Clathrate hydrates or gas hydrates are solid, non-stoichiometric compounds that are formed when hydrogen-bonded water molecules (host) and gas molecules (guest)

D. R. Bhawangirkar · V. C. Nair · J. S. Sangwai (✉)
Petroleum Engineering Program, Gas Hydrate and Flow Assurance Laboratory, Department of Ocean Engineering, Indian Institute of Technology Madras, Chennai 600036, India
e-mail: jitendrasangwai@iitm.ac.in

D. R. Bhawangirkar
Department of Chemical Engineering, Indian Institute of Technology Bombay, Powai, Mumbai 400076, India

V. Sundar et al. (eds.), *Proceedings of the Fifth International Conference in Ocean Engineering (ICOE2019)*, Lecture Notes in Civil Engineering 106,
https://doi.org/10.1007/978-981-15-8506-7_34

come into contact at low temperatures and high pressures [1, 2]. Clathrate hydrates form different crystal structures depending upon the size of the guest molecules. The most common structures are structure I (sI), structure II (sII), and structure H (sH), and unit cells of this crystal contain small, medium, and large cavities. Large deposits of methane hydrates are found in the seafloor or permafrost region and are considered as a huge source of fossil fuel. The amount of methane that can be extracted from these deposits is considered to be more than the energy of all other fossil fuels combined. It is estimated that around ~200 000 trillion cubic feet (TCF) of the methane gas is present in the hydrate form which can provide sufficient energy for several years [3]. India too has few proven methane hydrate reservoirs as in Krishna–Godavari Basin, Andaman Basin, and Mahanadi Basin collectively representing around 1900 TCM methane gas trapped in the form of hydrates [4]. Sufficient work has already been done in the literature for understanding the phase behavior of methane gas hydrates in the presence of pure water [5, 6].

Understanding the thermodynamic and kinetic behavior of gas hydrates in the presence of actual marine sediment systems is very crucial to know whether the sediment promotes or inhibits the formation of gas hydrates. Sediment minerals containing clay has pores and can cause a confining effect on the gas–water system, and they can change the properties of the hydrates [7–12]. Sediments containing pores can absorb water and can swell. Therefore, water content in the sediment can also alter the phase equilibria. Krishna–Godavari Basin in India is dominated by the sediments (with varying percent of clay) [13], and understanding the formation and dissociation behavior of methane hydrates in KG Basin marine sediment is very important from the methane gas recovery point of view.

In this work, we have performed the thermodynamic and kinetic studies to understand the behavior of methane hydrate formation and dissociation in pure water, and in the aqueous solution of 10 wt% sediment. The experimental part has been provided in the next section, followed by results and discussions, and conclusions at the end.

2 Experimental Section

2.1 Materials

The different materials used in this study are given in Table 1 with their purity in mass fraction and suppliers. An accurate mass balance (RADWAG AS-220/X)

Table 1 Purities and suppliers of materials

Chemical/purity in mass fraction	Suppliers
Methane (0.995%)	Bhuruka Gas Agency, Bangalore
KG Basin sediment	NIOT, Chennai

with an accuracy of ±0.00004 has been used to weigh materials used in this study. Aqueous solutions are prepared using the distilled water.

2.2 Experimental Setup

The thermodynamic phase equilibrium and kinetic studies of methane hydrate formation and dissociation in the presence of aqueous solutions formed from the KG Basin sediment and distilled water are carried out by using the experimental setup as shown in Fig. 1. The high-pressure reactor (200 ml of capacity) which is made up of stainless steel (SS-316) has a maximum working capacity of 13 MPa. A temperature sensor (Pt-100) and a pressure transducer are connected to the reactor to measure the reactor variables. A magnetic stirrer at 400 rpm (revolutions per minute) is used to mix the solution properly. The magnetic stirrer helps in minimizing the heat and mass transfer resistances, and helps in reaching the desired hydrate equilibrium conditions. The gas cylinder contains highly pressurized pure methane gas, and its pressure is noted at the pressure transmitter connected to the cylinder. Water bath maintains the temperature of the reactor by circulating the glycol–water mixture through the jacket of the reactor. The data generated during the experimental run is being stored inside the data acquisition system.

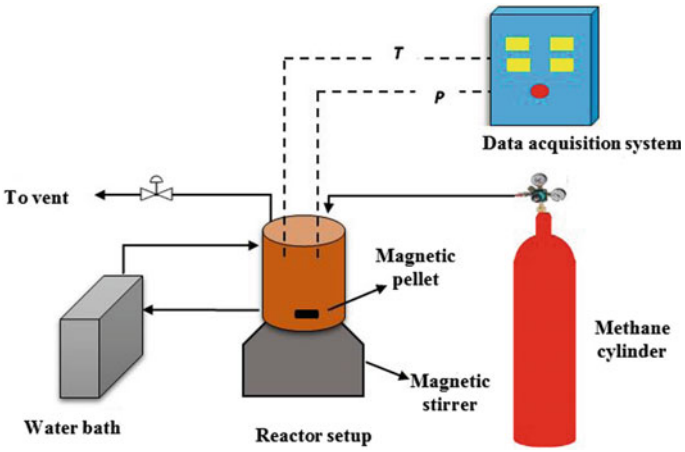

Fig. 1 Schematic of the experimental setup

2.3 Experimental Procedure

The thermodynamic and kinetic studies have been carried out on the formation of methane hydrate in the presence of pure water, and in aqueous solution of water and KG basin sediment. A 60 ml aqueous solution on a 10 wt% basis of the sediment is prepared. The solution is then filled into the reactor after cleaning the reactor with distilled water. To remove the dissolved gases in the solution, and also to ensure no air remains inside the reactor, methane gas at a pressure of around 0.5 MPa is injected into the reactor and then pre-flushed twice. Now, the methane gas is reinjected into the reactor at 9 MPa pressure and at atmospheric temperature (for thermodynamic study) in the remaining 140 ml volume of the reactor. The temperature of the reactor is now lowered by circulating the glycol–water mixture around the reactor through jacketed wall such that the hydrate formation should occur. The isochoric pressure search method is used to obtain the thermodynamic three phase (H–L–V) equilibrium point. However, for the kinetic studies, the temperature of the reactor is first brought to 273.15 K, and then, the methane gas is injected at 9 MPa pressure in the reactor. For the dissociation of the kinetic experiment, the temperature has been increased from 273.15 to 298.15 K.

3 Results and Discussion

The isochor for the methane hydrate formed in the aqueous solution of sediment (10 wt% basis) is shown in Fig. 2.

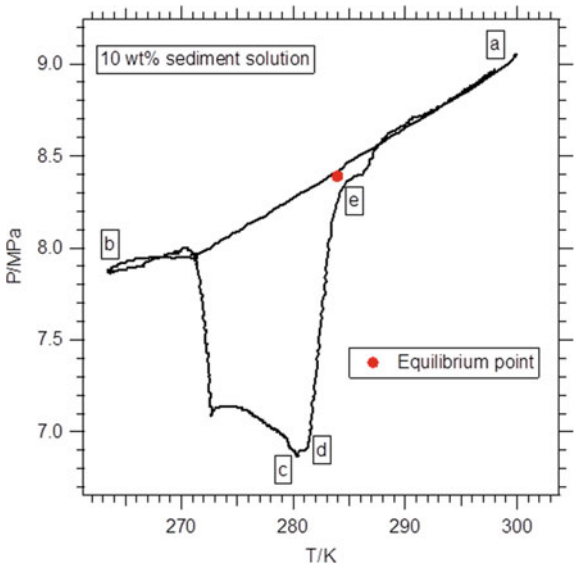

Fig. 2 Isochoric *P–T* curve for the methane hydrate in aqueous solution (10 wt% sediment)

As seen in the plot (Fig. 2), the pressure starts decreasing from the point a–b due to the decrease in reactor temperature. However, there seems a sudden decrease in pressure from point b to c as the nucleation of hydrate formation starts at point b with a marginal increase in temperature as well. At point c, sufficient amount of hydrate has formed, and no more decrease in pressure is observed. Now, from point c to d, the temperature of the reactor is slowly increased with a heating rate of 2 K/h, followed by a rate of 0.5 K/h (from d to e). Point 'e' is referred to as the equilibrium point, and also at this point the hydrate formation and hydrate dissociation curves are close enough to intersect.

Several of such isochors are generated at different initial pressures. It has been observed that the equilibrium condition for the isochor generated here for the aqueous solution of 10 wt% sediment for an initial pressure of 9 MPa is $T_{eq} = 283.95$ K and $P_{eq} = 8.39$ MPa. However, the equilibrium condition for pure methane for the same initial gas pressure of 9 MPa has found to be $T_{eq} = 283.8$ K and $P_{eq} = 8.25$ MPa as given in Table 2.

The kinetic studies have been performed to understand the behavior of methane hydrate formation and dissociation in the presence of pure water and in aqueous solution of 10 wt% sediment. Figure 3 represents the profile of 'moles of methane gas consumed *vs.* time' at 273.15 K. It can be observed that the consumption of

Table 2 Equilibrium *P*–*T* experimental data

System	T_{eq} (K)	P_{eq} (MPa)
CH_4 hydrate in aqueous solution of 10 wt% sediment	283.95	8.39
CH_4 hydrate in pure water	283.8	8.25

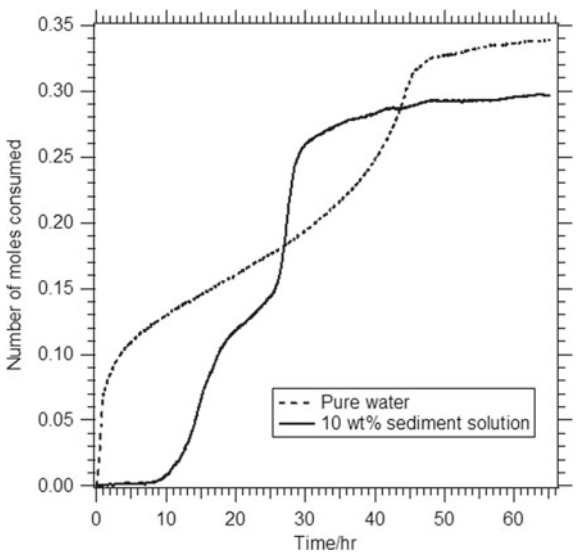

Fig. 3 Moles of methane gas consumed during the hydrate formation in pure water, and in 10 wt% sediment solution

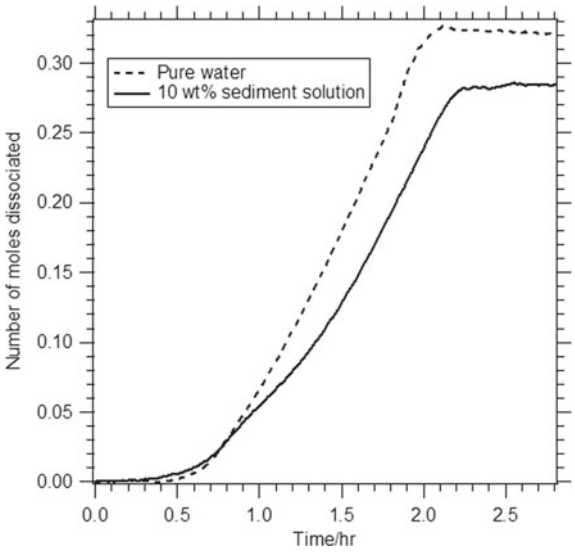

Fig. 4 Moles of methane gas dissociated from the hydrate formed in pure water, and in 10 wt% sediment solution

methane gas during the formation of methane hydrate increases with time in both pure water as well as in 10 wt% sediment solution.

The total number of moles consumed in pure water has found to be more than that in sediment solution. However, the time required to consume 0.25 moles of methane gas in sediment solution is less than in pure water because of the availability of more surface in sediment solution. Here, the sediment surface is promoting the formation of methane hydrate.

Figure 4 represents the moles of methane gas dissociated from the hydrate with time. Thermal stimulation is used (by increasing the temperature of the reactor with the rate as specified in experimental procedure) to dissociate the hydrate, and hydrates are dissociated to release the methane gas.

From Fig. 4, it has been observed that as the time increases the dissociation progresses. However, it takes some time for the dissociation to start as in the initial time; the gas molecules are strongly entrapped inside the hydrate cages. Number of moles of gas from the dissociation process starts increasing rapidly as the hydrate cages starts dissociating. The availability of the water in pure water system is high as compared to that in aqueous sediment solution for the gas molecules to be entrapped; therefore, the number of methane gas molecules released from the hydrate cages formed from pure water is higher than in aqueous sediment solution.

4 Conclusion

The thermodynamic and kinetic studies have been carried out for the methane hydrate formation in presence of pure water and in aqueous solutions of 10 wt%

KG Basin sediment. From thermodynamic studies, it has been observed that the methane hydrate equilibrium point in aqueous sediment solution has shifted slightly to higher pressures at the same temperature compared to that in pure water.

Kinetic studies revealed that it takes less time for the formation of methane hydrate in an aqueous sediment solution as compared to that in pure water for the initial 30 minutes because of the more surface availability in sediment solutions, which mean sediment surface is promoting the hydrate formation. In addition, the dissociation of methane gas molecules has found to be higher in pure water than in aqueous sediment solutions. The understanding of this study can be accounted for a better exploitation of methane gas from Krishna–Godavari hydrate reservoirs.

References

1. Sloan ED (2000) Clathrate hydrates: the other common solid water phase. Ind Eng Chem Res 39(9):3123–3129
2. Dendy SE, Carolyn K (2007) Clathrate hydrates of natural gases, 3rd edn. CRC Press, Boca Raton, New York
3. Sloan ED (2003) Fundamental principles and applications of natural gas hydrates. Nature 426(6964):353–363
4. Vedachalam N, Ramesh S, Jyothi VBN, Thulasi Prasad N, Ramesh R, Sathianarayanan D, Ramadass GA, Atmanand MA (2016) Assessment of methane gas production from indian gas hydrate petroleum systems. Appl Energy 168:649–660
5. Bhawangirkar DR, Adhikari J, Sangwai JS (2018). Thermodynamic modeling of phase equilibria of clathrate hydrates formed from CH_4, CO_2, C_2H_6, N_2 and C_3H_8, with different equations of state. J Chem Thermodyn 117:180–192
6. Bhawangirkar DR, Sangwai JS (2019). Insights into Cage Occupancies during Gas Exchange in CH_4+CO_2 and CH_4+N_2+CO_2 Mixed Hydrate Systems Relevant for Methane Gas Recovery and Carbon Dioxide Sequestration in Hydrate Reservoirs: A Thermodynamic Approach. Ind Eng Chem Res 58(31):14462–14475
7. Guggenheim S, August F, Koster VG (2003) New gas-hydrate phase: synthesis and stability of clay-methane hydrate intercalate. Geology 31:653–656
8. Uchida T, Takeya S, Chuvilin EM, Ohmura R, Nagao J, Yakushev VS, Istomin VA, Minagawa H, Ebinuma T, Narita H (2004) Decomposition of methane hydrates in sand, sandstone, clays and glass beads. J Geophys Res Solid Earth 109(B5):1679
9. Seo YJ, Seol J, Yeon SH, Koh DY, Cha MJ, Kang SP, Seo YT, Bahk JJ, Lee J, Lee H (2009) Structural, mineralogical, and rheological properties of methane hydrates in smectite clays. J Chem Eng Data 54:1284–1291
10. Yeon SH, Seol J, Koh DY, Seo YJ, Park KP, Huh DG, Lee J, Lee H (2011) Abnormal methane occupancy of natural gas hydrates in deep sea floor sediments. Energy Environ Sci 4:421–424
11. Nair VC, Ramesh S, Ramadass GA, Sangwai JS (2016) Influence of thermal stimulation on the methane hydrate dissociation in porous media under confined reservoir. J Pet Sci Eng 147:547–559
12. Nair VC, Prasad SK, Kumar R, Sangwai JS (2018) Energy recovery from simulated clayey gas hydrate reservoir using depressurization by constant rate gas release, thermal stimulation and their combinations. Appl Energy 225:755–768
13. Basu S (2002) Clay mineralogy and pressure analysis from seismic information in Krishna-Godavari Basin, India. Geophysics 55(11):1447–1454

Effect of Sodium Hydroxide on the Interfacial Tension of Hydrocarbon—Water System

Gomathi Rajalakshmi Seetharaman and Jitendra S. Sangwai

Abstract An ultra-low IFT (interfacial tension) is required between the liquid–liquid systems to dislodge the crude oil completely from the pores of the formation. As a huge amount of alkali is used for this purpose, scale formation and formation damage near wellbore region is a common issue. To perform an economically and environmentally viable process, it is obligatory to design the process with low and optimum concentration of alkali. Moreover, if the concentration of alkali is properly designed according to the oil chemistry, the alkali flooding alone could result in a favorable recovery for high acid number crude oil. So, the present study utilized low concentration of NaOH, to understand the behavior of alkali at the IFT of hydrocarbon–water system. Hydrocarbons like heptane and benzene were selected to understand the influence of hydrocarbon type on the IFT reduction. It was found that the IFT between the hydrocarbon–water system continuously decreases with an increase in NaOH concentration; moreover, a minimum concentration of 100 ppm is required to initiate reduction reaction. It is evident to state that IFT is dependent upon type of the hydrocarbon, because the enhanced reduction is observed in aromatics–water system using NaOH due to stronger cation-π interaction.

Keywords Alkali · Hydrocarbons · Interfacial tension · Low concentration

1 Introduction

Approximately world's 60% of remaining oil which got wedged in the pores of formation after primary and secondary recovery can be recovered by lowering the interfacial tension [1]. Lowering the interfacial tension (IFT) is accomplished by injecting various chemical agents like alkali or surfactants into the reservoir. In the alkali flooding, the injected alkali is allowed to react with acid groups present in the

G. R. Seetharaman · J. S. Sangwai (✉)
Petroleum Engineering Program, Gas Hydrate and Flow Assurance Laboratory, Department of Ocean Engineering, Indian Institute of Technology Madras, Chennai 600036, India
e-mail: jitendrasangwai@iitm.ac.in

V. Sundar et al. (eds.), *Proceedings of the Fifth International Conference in Ocean Engineering (ICOE2019)*, Lecture Notes in Civil Engineering 106,
https://doi.org/10.1007/978-981-15-8506-7_35

crude oil to produce in-situ surfactants which reduces the IFT and helps to mobilize the oil [2], because reducing the IFT increases the capillary number, which in turn increases the recovery percentage. The IFT is defined as the work to create a unit of the new surface between two immiscible liquids [3]. An ultra-low IFT of the order of 10^{-2} mN/m is desired to mobilize the oil completely from the reservoir [4]. This ultra-low surface tension was easily obtained for a heavy (or) acidic crude oil using alkaline-based enhanced oil recovery. Since crude oil is a complex mixture of hydrocarbons with various surface active components, researchers believed that utilization of pure hydrocarbons is immensely required to understand the basic mechanism in altering the interfacial behavior of these components. Cai et al. [5] investigated the effect of temperature, pressure, and salt concentration on the IFT between hydrocarbon + water/brine system. It was found that IFT depends on the molecular weight of the hydrocarbon used and not on the salt type. The IFT found to increase with an increase in the pressure and salt concentration. Goebel and Lunkenheimer [6] presented the experimental data for alkane/water system and reported that IFT increases with an increase in carbon number in a water/alkane interface. They also stressed the importance of using the pure solvent for conducting the IFT measurements. Amin and Smith [7] studied the IFT of three gas–liquid binary systems such as methane–pentane, methane–heptane, and methane–decane. It was found that, with an increase in pressure and temperature, IFT is decreased. Zeppieri et al. [8] investigated the IFT of water–alkane system and showed that IFT depends on the temperature. Recent studies by Kakati and Sangwai [9] reported a minimum IFT for a minimum in salt concentration. They inferred that the reduction in IFT is due to accumulation of cations at the interface. Zhao et al. [10] studied the effect of NaOH on lowering the IFT of oil/alkyl benzene sulfonates solution. It has been found that, in the case of paraffin and alkyl benzene sulfonates, NaOH is used as an electrolyte which changed the ionic strength of the aqueous phase and compressed the electrical double layer of alkyl benzene sulfonates. Though several studies are available for the interaction of salts on the IFT of pure hydrocarbons–water systems, there are no studies available on the interaction of alkali on these studies. Since the optimum concentration of alkali provides a suitable level of OH^- ion at the oil–water interface, it is important to analyze the performance of NaOH against pure hydrocarbons–water system for the reduction of IFT. In this study, the effect of concentration of NaOH in reducing the IFT of pure hydrocarbons like heptane–water and benzene–water systems has been studied and discussed.

2 Experimental Section

2.1 Experimental Setup

The surface tension and IFT of the pure hydrocarbons were measured by dynamic contact angle tensiometer (Data physics DCAT 11EC, Germany), which works on

both Dunuoy ring and Wilhelmy plate. The value of IFT is calculated using a predefined equation $\gamma = F/(P \cos \theta)$, where γ is the IFT (N/m), F is the force measured to breakdown the liquid film using Wilhelmy plate, P is the wetted perimeter, and θ is the contact angle between plate and liquid. The Wilhelmy plate is an alloy of platinum and iridium (type PT-11; thickness 0.2 mm; area 3.98 mm^2; with the accuracy of $\pm 1.5\%$ of the measured values) which is an excellent corrosion-resistant material. Before starting the measurement, proper precaution was taken to saturate the air with hydrocarbon concern and reduce the humidity. The tensiometer consists of a sample holder attached to a motorized platform and a temperature sensor, and the Wilhelmy plate is used as a probe to measure the IFT. All measurements were performed at a temperature of 25 °C. A Brookfield water bath (model number TC-650AP, temperature range −20 to +200 °C) was used for this purpose. An inbuilt program SCAT was used to run the experiment. The apparatus is working by balancing the buoyancy force. Initially, the plate is immersed in the lighter density liquid, and the inbuilt weighing balance is allowed to tare automatically. In order to create an interfacial lamella, a heavier density liquid is used, and the plate is partially submerged. Now on the top of heavier phase, a lighter density liquid is poured. The instrument itself will collect 20–30 points until saturation was attained with a minimum standard deviation. For better accuracy, the experiment is repeated three times, and the results that are presented in this paper are the average of three set of data points.

3 Results and Discussion

3.1 Effect of NaOH on the IFT of Heptane–Water System

The effect of various concentrations of NaOH on the IFT of heptane–water system is shown in Fig. 1. The corresponding values of IFT with an increase in NaOH

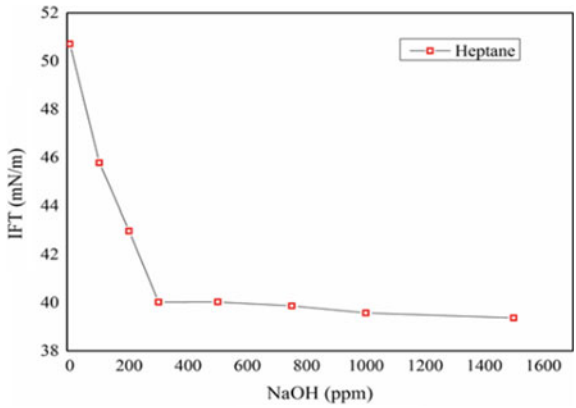

Fig. 1 Effect of concentration of NaOH on the IFT of heptane–water system at 25 °C

Table 1 IFT of NaOH on the interface of pure hydrocarbons (heptane, benzene)–water system at 25 °C

S. No.	NaOH (ppm)	IFT (mN/m)	IFT (mN/m)
		Heptane	Benzene
1	0	50.71	35.00
2	100	45.78	33.57
3	200	42.97	30.98
4	300	40.02	30.33
5	500	40.03	29.46
6	750	39.87	28.86
7	1000	39.57	28.09
8	1500	39.37	26.52

concentration is presented in Table 1. The IFT between the hydrocarbon (heptane) and water is found to decrease with increase in NaOH concentration. In order to evaluate the minimum alkali required to initiate the reduction in IFT, experiments were also conducted at a minimum concentration of 25, 50, and 75 ppm. However, the obtained reduction in IFT at these minimum concentrations is found to be insignificant. At the NaOH concentration of 100 to 300 ppm, the IFT reduced significantly from 50.71 to 40.02 mN/m. However, further increase in the NaOH concentration did not help to decrease the IFT significantly.

3.2 Effect of NaOH on the IFT of Benzene–Water System

The effect of different concentrations of NaOH on the IFT of benzene–water is shown in Fig. 2, and the corresponding values of IFT along with NaOH concentration has been presented in Table 1. The aromatics are cyclic but unsaturated compound due

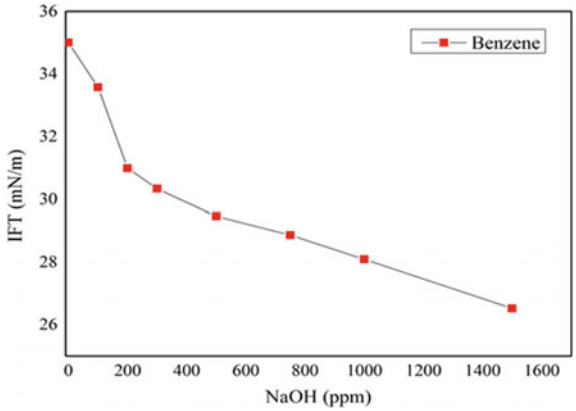

Fig. 2 Effect of low concentration of NaOH on IFT between benzene versus water at 25 °C

to their alternating double bond. They are omnipresent in crude oil and can give information about geological accumulation [11]. Figure 2 shows that, with increase in the concentration of NaOH, the IFT of the system continuously decreases. Like alkanes, the experiments were also conducted at a minimum concentration of 25, 50, and 75 ppm of NaOH concentration for aromatics, but no significant reduction has been observed. Unlike heptane, above 300 ppm of NaOH, a steep reduction in IFT is observed in benzene–water system. Moreover, as compared to alkane–water system, the extent of reduction in IFT is significantly high for aromatics–water systems in the presence of NaOH. This indicates that NaOH are very effective for the reduction of IFT in case of aromatics than alkanes.

It has been understood that the adsorption of moieties at the interface of hydrocarbon–water system will influence a number of factors which results in the reduction in IFT. Since NaOH is a strong alkali, dissolving the NaOH in water completely dissociates it into Na^+ and OH^- ions. The hydroxide ion in the alkali is normally meant for increasing the pH of the solution. Since heptane and benzene are pure hydrocarbons, interaction with NaOH does not produce any in-situ surfactants as in the case of crude oil. Literature shows that increasing the pH of the solution reduces the IFT [12]. In this study, we have seen a similar trend confirming the ability of high pH solution (in the presence of NaOH) to decrease the IFT of hydrocarbon–water system than salt system (in the presence of NaCl). Though the trend of reduction in IFT is same in alkane and aromatics (with water), the extent of reduction is high for aromatics than alkanes. This is due to the interaction between cation of NaOH with aromatics, which is a cation-Π interaction and is stronger than cation induced dipole interaction in the case for alkanes and cation [13].

4 Conclusion

Due to strict environmental constraints, it is always preferable to use a low concentration of chemicals in the reservoir for oil recovery operation. A brief study has been done in the field of alkali flooding using pure hydrocarbons to understand the role of low concentration of alkali on the IFT reduction. It has been found that a minimum concentration of alkali (NaOH) can initiate the reduction in IFT between pure hydrocarbons–water system, and the obtained reduction in IFT is high in case of aromatics than alkanes.

References

1. Herd MD, Lassahn GD, Thomas CP, Bala GA, Eastman SL (1992) Interfacial tensions of microbial surfactants determined by real-time video imaging of pendant drops. In: SPE/DOE enhanced oil recovery symposium. Society of Petroleum Engineers
2. Hunter RJ (1987) Foundations of colloid science Clarendon. New York, pp 244–250

3. Saha R, Uppaluri RV, Tiwari P (2018) Influence of emulsification, interfacial tension, wettability alteration and saponification on residual oil recovery by alkali flooding. J Ind Eng Chem 59:286–296
4. Li HR, Li ZQ, Song XW, Li CB, Guo LL, Zhang L, Zhang L, Zhao S (2015) Effect of organic alkalis on interfacial tensions of surfactant/polymer solutions against hydrocarbons. Energy Fuels 29:459–466
5. Cai BY, Yang JT, Guo TM (1996) Interfacial tension of hydrocarbon+ water/brine systems under high pressure. J Chem Eng Data 41:493–496
6. Goebel A, Lunkenheimer K (1997) Interfacial tension of the water/n-alkane interface. Langmuir 13:369–372
7. Amin R, Smith TN (1998) Interfacial tension and spreading coefficient under reservoir conditions. Fluid Phase Equilib 142:231–241
8. Zeppieri S, Rodríguez J, López de Ramos AL (2001) Interfacial tension of alkane+ water systems. J Chem Eng Data 46:1086–1088
9. Kakati A, Sangwai JS (2017) Effect of monovalent and divalent salts on the interfacial tension of pure hydrocarbon-brine systems relevant for low salinity water flooding. J Petrol Sci Eng 157:1106–1114
10. Zhao C, Jiang Y, Li M, Cheng T, Yang W, Zhou G (2018) The effect of NaOH on lowering interfacial tension of oil/alkylbenzene sulfonates solution. RSC Adv 8:6169–6177
11. Jinggui L, Philp P, Zifang M, Wenhui L, Jianjing Z, Guojun C, Mei L, Zhaoyun W (2005) Aromatic compounds in crude oils and source rocks and their application to oil–source rock correlations in the Tarim basin, NW China. J Asian Earth Sci 25:251–268
12. Anand V, Vashishtha M, Shown B, Patidar P, Malhotra A, Ghosh S, Jaguste S, Naik VM, Thaokar RM, Juvekar VA (2018) Interrelationship between electrocoalescence and interfacial tension in a high acidity crude: effect of pH and nature of alkalinity. Colloids Surf A 555:728–735
13. Orabi EA, Lamoureux G (2011) Cation-π and π–π interactions in aqueous solution studied using polarizable potential models. J Chem Theory Comput 8:182–193

Effect of Nanoparticles on the Viscosity Alteration of Vacuum Residue

Rohan M. Jadhav, Gaurav Pandey, N. Balasubramanian, and Jitendra S. Sangwai

Abstract Heavy oil reservoirs are one of the largest remaining crude oil reserves in the world. Often, the inherent properties of heavy and extra-heavy oils cause major problems in production and transportation processes. The viscosity of these oils makes their treatment difficult with conventional means. Use of solvents to dissolve the heavy oils has been a traditional method to deal with these problems. Improvement in flow through solvent treatment can be further optimized through the use of nanoparticles. Literature works have suggested that nanoparticles have catalyzing effects which affect the polar species of heavy oils. This study is aimed at examining the effects of metallic nanoparticles in altering the viscous property of heavy fraction. Use of thermal stimulation in association with solvents are explored as a means to achieve viscosity reduction. These applications can be further extended into the areas of flow assurance.

Keywords Heavy oil · Nanoparticles · Viscosity · Solvent

R. M. Jadhav · N. Balasubramanian
Department of Chemical Engineering, AC Tech Anna University, Chennai 600025, India
e-mail: rohanj61@gmail.com

G. Pandey
Department of Petroleum Engineering and Earth Sciences, University of Petroleum and Energy Studies, Dehradun 248007, India
e-mail: gauravpandey@u.nus.edu

G. Pandey · J. S. Sangwai (✉)
Gas Hydrate and Flow Assurance Laboratory, Petroleum Engineering Program, Department of Ocean Engineering, Indian Institute of Technology Madras, Chennai 600036, India
e-mail: jitendrasangwai@iitm.ac.in

G. Pandey
Department of Chemical and Biomolecular Engineering, National University of Singapore, Singapore 117585, Singapore

V. Sundar et al. (eds.), *Proceedings of the Fifth International Conference in Ocean Engineering (ICOE2019)*, Lecture Notes in Civil Engineering 106,
https://doi.org/10.1007/978-981-15-8506-7_36

1 Introduction

Unconventional oil reservoirs which constitute of heavy and extra-heavy oil have been an area of special interest in upstream processes due to their untapped potential for energy production [1, 2]. They constitute the majority of the world's unconventional reservoirs. The processing of these fractions has been a challenge due to their highly viscous nature and complex molecular structure which makes it difficult to process them by conventional means [3]. The upgrading process of heavy fractions to lighter ones is a crucial process in order to cater to the requirements of rising fuel demands.

Use of methods such as steam stimulation and in-situ combustion has been continuously optimized to improve heavy oil production [4, 5]. This study focuses on the thermal treatment of the vacuum residue with the help of a hydrogen donor (tetralin) and metallic nanoparticles (nickel) as a catalyst. The objective of the first set of experiments is to obtain an understanding of how the hydrogen donors and nanoparticles impart changes in the viscosity of the residue. These experiments were carried out to confirm any cooperative effects of the hydrogen donor and nanoparticles on the residue. Experiments were carried out at 90 °C to observe the effects of the thermal activity. Rheometric measurements under low and high shear were made to understand the changes in the viscosity of the residue due to the concentration of the particles.

Studies have demonstrated that metallic nanoparticles have a catalyzing effect on the viscosity reduction of oil when used in the presence of a hydrogen donor [6, 7]. Upgrading processes are an effective way to enhance the residual oil fractions to gather lighter units. Hydrogen donors improve the hydrogen–carbon ratio converting more units to lighter fractions. Nanoparticles essentially provide a surface area for the adsorption of asphaltene particles. As asphaltene particles continue to coalesce on the surface of nanoparticles, it removes them from the bulk oil thereby improving the upgrading processes. Further improvements in flow assurance fields can extend these implementations of nanoparticle and solvent processes. Transportation and upgrading problems can be addressed more effectively allowing a better efficiency in heavy oil treatments.

2 Experimental Section

2.1 Materials

Vacuum residue used for all the measurements was provided by CPCL (Chennai Petroleum Corporation Limited). Solvent (tetralin) used in the study was purchased from Alfa Aesar (purity 97%). Commercially available nickel nanoparticles with a size distribution of (<100 nm) were purchased from Sigma-Aldrich. The viscometer was used for the measurement of viscosity at low shear (DV2T spindle viscometer

Brookfield). The rheometer was used for high shear experiments (MCR 52, Anton Paar). Rheoplus software was used to collect and analyze the data from the rheometer.

2.2 Sample Preparation

Nickel nanoparticle of fixed concentrations (0.1 and 1.1 wt.%) was added to a fixed amount of vacuum residue sample. Tetralin concentration was fixed in all cases (20 wt.%). The mixture was then heated and sonicated in a sonicator bath with temperature control to ensure that the nanoparticles disperse inside the sample.

2.3 Thermal Stimulation

Three samples of the composition given in Tables 1 and 2 were used to study the effects of low and high shear variations after the thermal stimulation at 90 °C. Samples were kept at 90 °C for 8 h in the water bath to assess the effects of thermal stimulation when subjected to high and low shear.

3 Results and Discussion

Preliminary viscosity tests were carried out at a range of temperatures to estimate the flow behavior of the residue sample. It was observed that at the temperature range of 65 to 80 °C, the residue shows a semi-solid behavior with little flow behavior. At 90 °C, the residue exhibited flow characteristic showing more fluidic behavior

Table 1 Composition of samples for low shear tests

S. No.	Composition	Test
1	Vacuum residue (VR): nanoparticle (Ni) (0.1 wt.%)	Low shear
2	Vacuum residue (VR): nanoparticle (Ni) (0.1 wt.%): Tetralin (T)	Low shear
3	Vacuum Residue (VR): Tetralin (T)	Low shear

Table 2 Composition of samples for high shear tests

S. No.	Composition	Tests
1	Vacuum residue (VR): nanoparticle (Ni) (0.1 wt.%)	High shear
2	Vacuum residue (VR): nanoparticle (Ni) (1.1 wt.%)	High shear
3	Vacuum residue (VR): Tetralin (T) (0 wt.% particles)	High shear

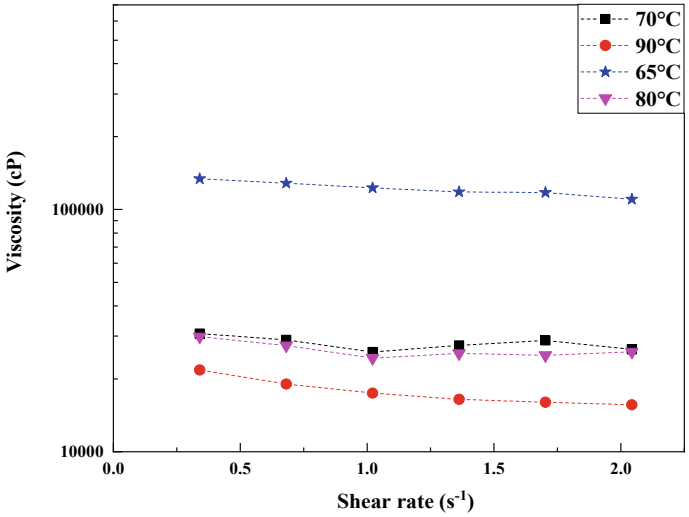

Fig. 1 Variation of vacuum residue viscosity with the shear rate at various temperatures

[8]. Viscosity curve in Fig. 1 shows the flow of vacuum residue with increasing temperature. It can be noticed that the measurements were made at low shear to minimize the deformation of the residue structure and give a good estimate of the viscosity of the vacuum residue. As these are complex fluids, it is important to identify how their flowability alters.

3.1 Low Shear Measurements

Low shear measurements are important to understand because these are helpful in explaining the effects of nanoparticles without causing any notable structural deformation. Effects of thermal stimulation on the viscosity of residue structure and contribution of nanoparticles are evident in Fig. 2. It was observed that the addition of nanoparticles produced better results when compared with the addition of the solvent alone. The combined effects of nanoparticle and tetralin can cause viscosity reduction at moderately high temperatures.

3.2 High Shear Measurements

High shear measurements were performed in a rheometer (MCR52, Anton Paar) at 90 °C. Shear rates were varied from 1–1000 s^{-1} to find the impact of high shear on the structure of residue. Effect of concentration of nanoparticles was observed at 1.1

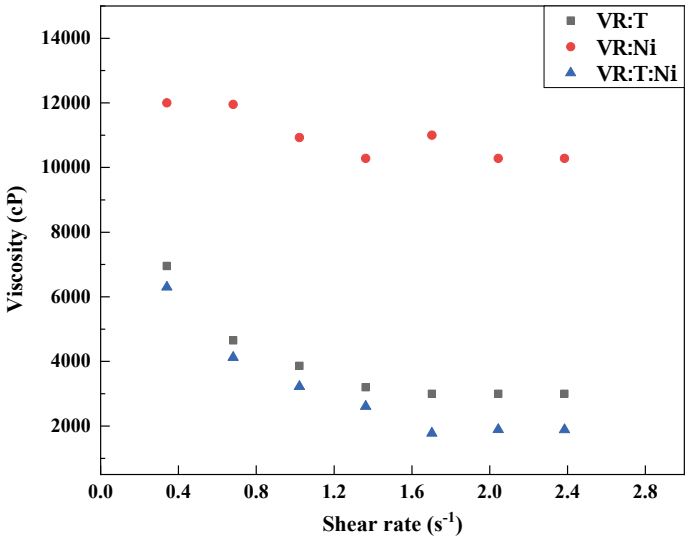

Fig. 2 Variation of the viscosity of various samples at low shear rate. VR: Vacuum residue; Ni: Nickel nanoparticles; T: Tetralin

and 0.1 wt.%. Figure 3 depicts the variation of concentrations. It was observed that 0.1 wt.% nanoparticle concentration achieved high viscosity reduction than samples without nanoparticles. Sample with 1.1 wt.% nanoparticles was observed to have increased viscosity of the residue.

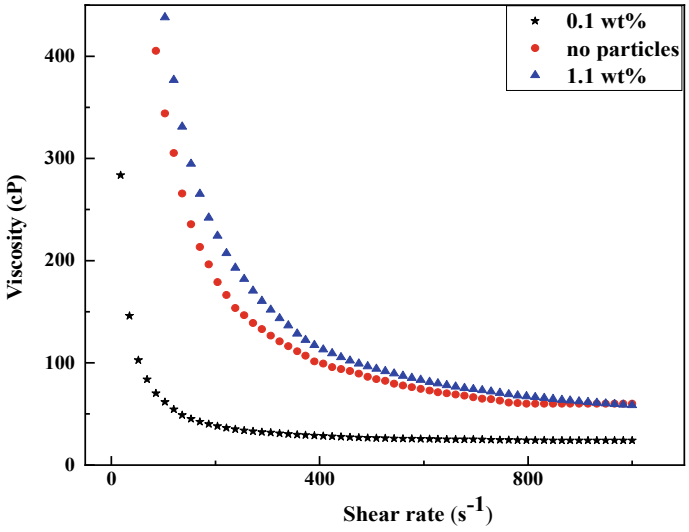

Fig. 3 Variation of viscosity at high shear rate of different composition of residue samples

Increase in concentration of nanoparticles in the residue causes it to form aggregate structures with individual particles which overcomes its effects of adsorbing asphaltenes on its surface. At low concentrations, the asphaltenes can easily get adsorbed on the surface without the formation of aggregates of the individual nanoparticles [9]. Nickel nanoparticles provide a surface for adsorption of the asphaltenes which initiates the reduction of viscosity in the residue. From an application point of view, these can be effectively be used as dispersions which can allow an economical way to perform upgrading process.

4 Conclusion

A series of low and high shear experiments were conducted in this study to observe the effects of metallic nanoparticles and solvent on the flow behavior of vacuum residue. Nanoparticles accompanied by solvent can provide viscosity reduction in the residue. Low concentrations were found to be more effective in reducing the viscosity of vacuum residue. Metallic nanoparticles can effectively increase the effects of thermal stimulation at lower concentrations. The insight of these mechanisms can further the applications for upgrading processes of heavy fractions and field of flow assurance.

References

1. Shokrlu YH, Babadagli T (2014) Kinetics of the in-situ upgrading of heavy oil by nickel nanoparticle catalysts and its effect on cyclic-steam-stimulation recovery factor. SPE Reserv Eval Eng 17:355–364
2. Hashemi R, Nassar NN, Pereira Almao P (2014) Nanoparticle technology for heavy oil in-situ upgrading and recovery enhancement: opportunities and challenges. Appl Energy 133:374–387
3. Taborda EA, Alvarado V, Franco CA, Cortés FB (2017) Rheological demonstration of alteration in the heavy crude oil fluid structure upon addition of nanoparticles. Fuel 189:322–333
4. Mironenko OO, Sosnin GA, Eletskii PM, Gulyaeva YK, Bulavchenko OA, Stonkus OA, Rodina VO, Yakovlev VA (2017) Catalytic steam cracking of heavy crude oil with molybdenum and nickel nanodispersed catalysts. Catal Ind 9:221–229
5. Fathi MM, Pereira-Almao P (2011) Catalytic aquaprocessing of arab light vacuum residue via short space times. Energy Fuels 25:4867–4877
6. Hendraningrat L, Souraki Y, Torsater O (2014) Experimental investigation of decalin and metal nanoparticles-assisted bitumen upgrading during catalytic aquathermolysis. Presented at SPE/EAGE European unconventional resources conference and exhibition, Vienna, Austria, 25–27 Feb
7. Nassar NN, Hassan A, Carbognani L, Lopez-Linares F, Pereira-Almao P (2012) Iron oxide nanoparticles for rapid adsorption and enhanced catalytic oxidation of thermally cracked asphaltenes. Fuel 95:257–262
8. Ghaffari A, Sharifi K, Ivakpour J (2017) An experimental study on the effects of temperature and asphaltene content on the rheological behavior of vacuum residues. Pet Sci Technol 35:768–774
9. Kazemzadeh Y, Eshraghi SE, Kazemi K, Sourani S, Mehrabi M, Ahmadi Y (2015) Behavior of asphaltene adsorption onto the metal oxide nanoparticle surface and its effect on heavy oil recovery. Ind Eng Chem Res 54:233–239

Development of a Single Buoy Anchored Fish Aggregating Device in Mauritius

V. Senedhun, Y. Basant-Rai, S. P. Beeharry, R. D. C. Mohit, D. Lutchmanen, N. Dussooa, and D. Bhunjun

Abstract The development of the Mauritius FAD Fishery started in 1985. The designed FAD is the rosary type comprising trawl floats mounted on a single or double-string polyamide rope, anchored in the open sea with polypropylene ropes, at depths ranging from 400 to 3500 m. Yet, FAD losses are high and mostly due to damages caused by navigating vessels and entanglement of fishing lines and hooks with the mooring rope of fishermen boats fishing close to the FADs. Moreover, it was observed that the rosary type FAD sinks to >200 m during strong surface current; hence, the use of trawl floats, which are resistant to pressure and resurfaces during slack current. Consequently, these FADs can neither be fixed to a light device for easy detection at night nor can they be equipped with satellite buoys as these would implode due to high pressure during sinkage. To reduce FAD losses, a sturdy, unsinkable and traceable fibreglass reinforced plastic single buoy FAD has been designed, equipped with a solar-powered flashlight, and a satellite buoy to track and collect biological and oceanography information. The mooring line consists of a mixed of steel wire (Ø 14 mm) and of polypropylene rope (Ø 20 mm). Based on the law of static equilibrium, the buoyant force on the buoy was calculated at 2,441.0 N. Turbulent flow models with speed of ocean current at 1, 2 and 3 knots were used to calculate the overall drag force (52,656.6 N) on both the mooring rope and the submerged portion of the buoy. Additional improvements made on the single buoy FAD were the (a) net-wrapping technique that proved to reduce the surface tension by as much as three times; and (b) shackle connection coupled with the formation of the catenary loop that provided full scope for rotation, thereby, reducing significantly the tensile force on the main line. Assuming a contingency anchorage of 130% on the total drag force, the minimum anchorage weight was 2,080.2 kg for metal and 3,578.4 kg for concrete.

Keywords FAD · Buoy · Force · Anchorage

V. Senedhun (✉) · Y. Basant-Rai · S. P. Beeharry · R. D. C. Mohit · D. Lutchmanen · N. Dussooa · D. Bhunjun
Ministry of Ocean Economy, Marine Resources, Fisheries and Shipping (Fisheries Division), Albion Fisheries Research Centre, Albion, Petite Rivière, Mauritius
e-mail: senedhunv@gmail.com

V. Sundar et al. (eds.), *Proceedings of the Fifth International Conference in Ocean Engineering (ICOE2019)*, Lecture Notes in Civil Engineering 106,
https://doi.org/10.1007/978-981-15-8506-7_37

1 Introduction

The aim of developing the FAD fishery in Mauritius was concurrently to diversify and increases the income of the coastal artisanal fishermen and divert fishing effort from the heavily exploited lagoon to the outer lagoon to allow the lagoon marine ecosystems to recuperate. A typical Mauritian-designed FAD is made of 70 pressure resistant plastic floats of 200 mm diameter or 28 pressure resistant plastic floats of 280 mm diameter and mounted on a single or double-string polyamide rope Fig. 1. The floats are anchored in the oceanic sea by a polypropylene mooring rope and about one tonne of scrap iron as anchor Fig. 2. FADs are set in consultation with fishermen at 28 dedicated sites around Mauritius at depths varying from 400 to 3000 m and distances from 2 to 12 nautical miles from the shore Fig. 3. The average lifetime of the FAD is estimated to be around 500 days [12]. However, constant maintenance and repairs are necessary to compensate for wear and tear [15]. The cost for setting one FAD at a depth of 1000 m is around US$4000. Subsequent paragraphs, however, are indented.

The common fishing techniques used to fish around FADs is by vertical longline, trolling, driftline and handline [2]. The main pelagic fish caught around FADs are tuna and tuna-like species with predominance of the albacore tuna (*Thunnusalalunga*), which is abundant during the austral summer and is the targeted fish [3].

Fig. 1 A rosary-type FAD mounted on a double-string polyamide rope

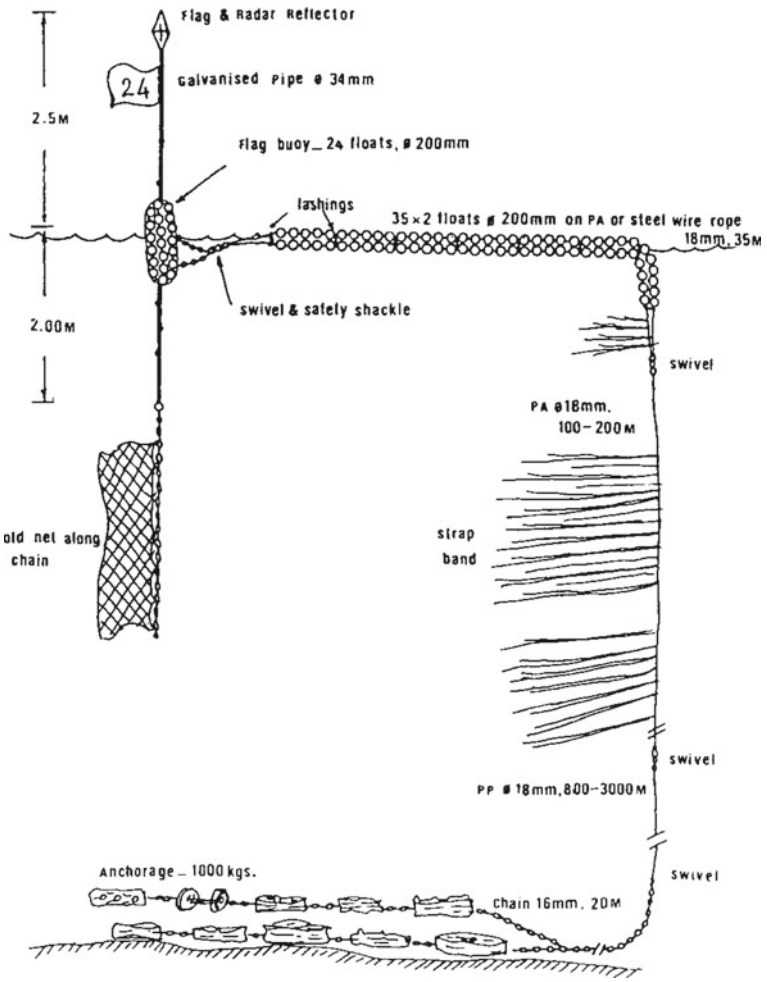

Fig. 2 Schematic diagram of the mooring structure of a rosary-type FAD in the off-lagoon

1.1 Background

It is common knowledge that drifting objects at sea such as logs, floats, ropes and even dead whales attract fish around them. Fishermen, aware of this phenomenon, have long been fishing around drifting flotsams. Subsequently, they have been mooring floating objects such as tree trunks, bamboos and coconut fronds at sea to aggregate pelagic fish and increasing their catch [11]. These structures are commonly known as Fish Aggregating Devices (FADs) or Payaos in South-East Asian countries [5].

In Mauritius, attempts to set FADs date, as far back, as 1974 [14]. Two FADs made of bamboo were anchored in the North of Mauritius at respective depths of

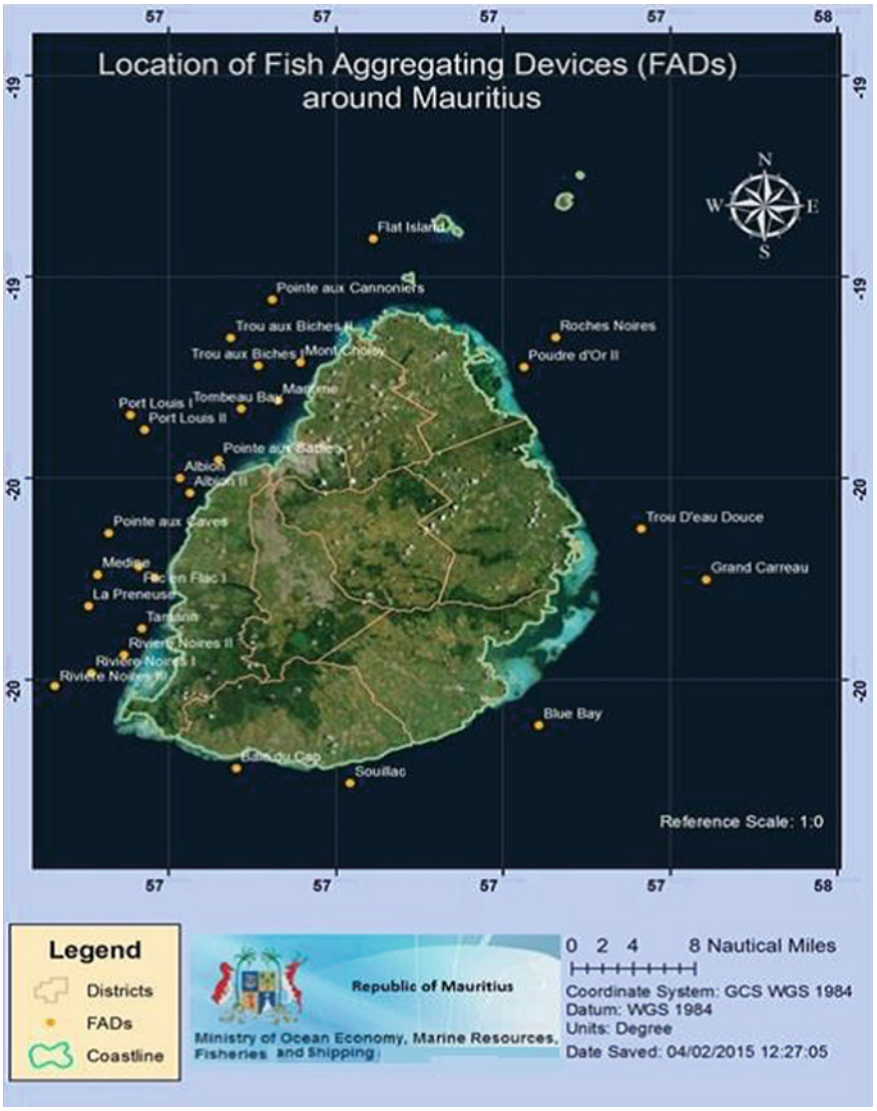

Fig. 3 The twenty-eight FAD locations around Mauritius

200 m and 400 m Fig. 4. No catch was reported from these FADs, and they were lost during the passage of a cyclone. New attempts to deploy FADs were carried out in 1983 under the South-West Indian Ocean Project. Two FADs made of tyres filled with polyurethane foam, were deployed on the western coast off Port Louis at a depth of about 2000 m. One did not float up after deployment while the other was vandalized within three days.

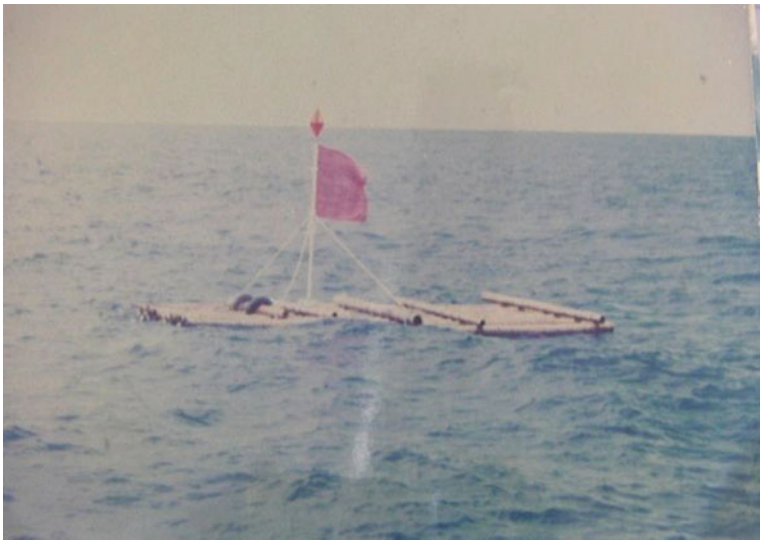

Fig. 4 Typical bamboo raft FAD from the 1970s

The first significant results were obtained during 1985 and 1988 when several FAD models were tried with assistance from FAO/UNDP [12]. FADs made of plastic drums and polystyrene foam and moored using 6 mm polypropylene rope gave encouraging catch rates but their lifespan was still too short. A FAD made of steel buoy, cylindrical in shape and measuring 3.6 m long and 0.9 m diameter was set off the north-west coast using 16 mm steel wire and 1300 kg mooring weights. Though it lasted about 3 months, good catch were reported from big-game fishermen.

The rosary-type FADs were developed in early 1986. These are still in use with some improvement rates in their construction to increase their longevity and to cut down on cost. Currently, such FADs have been moored at 28 sites around Mauritius. About 350 fishermen are regularly fishing around them with catch rates of about 25 kg per fisherman day.

Between 1992 and 1993, under the Outer Lagoon Fisheries Development Project assisted by the Overseas Fishing Cooperation Foundation (OFCF) of Japan; payao-type FADs made of bamboo poles were set at three locations. Two were deployed off Flat Island in the north and one off La Preneuse in the west. The FADs were short-lived (between 4 and 6 months), nevertheless fishermen concurred that catches were better around these FADs.

A single buoy FAD was obtained under the South-West Indian Ocean Fisheries Project (SWIOFP), (developed by PLK Marine in Guadeloupe). The FAD was anchored in March 2013 at a depth of 2400 m and 4 nm off Pointe aux Caves in the west, on a pilot basis. The FAD was made of fibreglass reinforced plastic and spherical in shape of a volume of 600 L. It was fitted with a mast bearing a solar-powered

flashlight and a tube-type radar reflector. It lasted 5 months, and the real cause of its loss is still unknown but may have been destroyed purposefully.

1.2 Objectives of the Study

The rosary-type FAD has been used in Mauritius for more than 30 years and has considerably enhanced the livelihood of the FAD fishermen. However, the rate of loss of FADs are on the high side mainly due to entangling of hooks and line with the mooring ropes, wear and tear and damage caused by large vessels navigating close to the shore while calling or leaving Mauritius. Moreover, the rosary FAD made of trawl floats sinks to more than 200 m during strong surface current and resurfaces when the current slacks down. Thus, the FADs cannot be fitted with light for their detection at night, satellite buoy for transmission of in-situ data and other instruments for data collection as these would be damaged due to pressure when the FAD sinks. There is a need to develop a FAD that is:

i. Sturdy and unsinkable to increase its life span;
ii. easily deployable using available logistics;
iii. mounted with light and radar reflector for ease of detection and safety of navigation;
iv. trackable using global positioning system;
v. equipped with instruments for collection of biological and oceanographic data and
vi. cost-wise comparable to the rosary-type FAD.

2 Methodology

The assumption for all the models validated was based on the law of static equilibrium,

$$F_B = F_G \tag{1}$$

whereby F_B is the upward buoyant force, and F_G is the force due to gravity (gravity (g) is assumed to be 9.81 m/s^2).

Any object at *equilibrium* must have an acceleration of 0 m/s^2. This extends from Newton's first *law* of motion. However, in real situation, an acceleration of 0 m/s^2 does not mean the object is at rest, as it is the case of the FAD at sea.

The models compared the rosary-type FAD which consisted of 28 Fibreglass Reinforced Plastic (FRP) buoys (Ø 280 mm) and the single buoy FAD (Ø 1000 mm).

The main calculations involved were the calculation of (1) overall buoyant force, (2) the drag force on the buoy due to current, (3) drag force on the rope due to current

and the determination of the minimum 'safe' anchor load required to moor the FAD. Two materials were modelled for testing, namely concrete and metal.

2.1 Rosary-Type FAD

The total volume of the rosary-type FAD consisting of 28 buoys (Ø 280 mm) was estimated at 308 L, and the buoyant force acting on the buoys was calculated using:

$$F_{\mathrm{B}} = \rho_{\mathrm{f}} V_{\mathrm{f}} g \tag{2}$$

where F_{B} is the buoyant force, ρ_{f} is the density of the displaced fluid, V_{f} is the volume of the fluid displaced, and g is acceleration due to gravity, 9.8 m/s^2. The equation assumed that one third of the buoys were submerged based on real-time visual estimation. The total volume was thus reduced to 102.67 L.

Hence, the F_{B} on the rosary-type FAD was calculated to be 1036.4 N.

(ρ_{f} of seawater = 1029 kg/m^3, $V_{\mathrm{f}} = 0.10267$ m^3).

The drag force on the buoy due to current was calculated from the equation:

$$F_{\mathrm{Db}} = {}^1\!/_2\, \rho\, v^2 C_d A \tag{3}$$

whereby: $\rho = 1019$ km/m^3, v^2 = velocity of current, C_d = Drag coefficient assumed to be 0.47 for fluids, A = cross–sectional area of all 28 buoys (assuming 1/3 submerged).

The other force which is significant was determined to be the drag force underwater on the mooring rope due to current, F_{Dr}. The same equation at (3) was used taking into account that for the average FAD mooring rope; the length was assumed to be 200 m and the cross–sectional area 0.018 m. C_d for the rope was categorized as short cylinder and was taken as 1.15.

2.2 Single Buoy FAD

The challenge was to develop an unsinkable FAD which would be resistant to ocean currents and reduce the intensity of fishing lines twining with the upper mooring rope of the FAD. The mixed wire consisting of steel and polypropylene rope was deemed best to safeguard against wear and tear due to entangling of fishing lines and hooks.

The equations used to test the rosary-type FAD were applied to the single buoy FAD; with similar assumptions notably, one third of the total volume was submerged, and coefficients of drag for the buoy and the rope were 0.47 and 1.15, respectively.

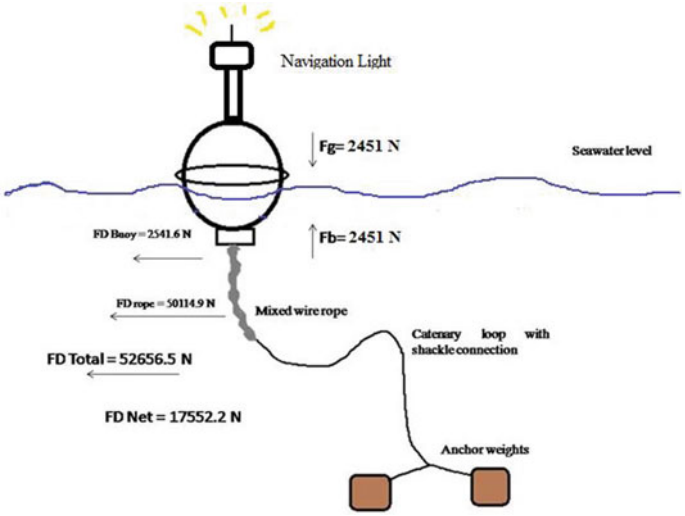

Fig. 5 Interaction of forces to determine the resultant net drags force on the buoy

A graphical representation of all the significant forces acting on the buoy is described in Fig. 5.

In order to reduce drag force caused by the current, an experiment was conducted using a 280 mm Ø buoy towed at a constant speed of 1 knot. The hypothesis tested was to determine as whether wrapping the buoy in netting would reduce the surface tension force, hence, reducing the effect of the resulting drag force of the surface current. It was observed that the buoy wrapped in a net yielded three times lesser surface tension than the one without any netting. This observation was replicated to the single buoy FAD to reduce the effect of drag force due to current at the surface.

Due to various densities and composition of materials, metal and concrete have individual weight underwater. The weight in water was determined using the Equ.

$$W_{\text{sea}} = W_{\text{air}}[\,1 - \rho_{\text{f}}]\rho_{\text{m}}$$

whereby W_{air} = weight of material in air, ρ_{f} = density of seawater, ρ_{m} = density of material.

The coefficients for weight of metal and concrete underwater were calculated as 0.86 and 0.5, respectively, in all calculations used for determining the minimum anchor weight required.

The minimum anchor weight was determined using the net force on the buoy (F_{DNet}). To balance forces, another opposing force of same magnitude had to be applied to sustain the model in equilibrium. Hence, an anchor weight of 2080.2 kg of iron or a weight of 3600 kg of concrete would be suited to safely moor the FAD. A contingency of 130% of the overall weight was applied to the model.

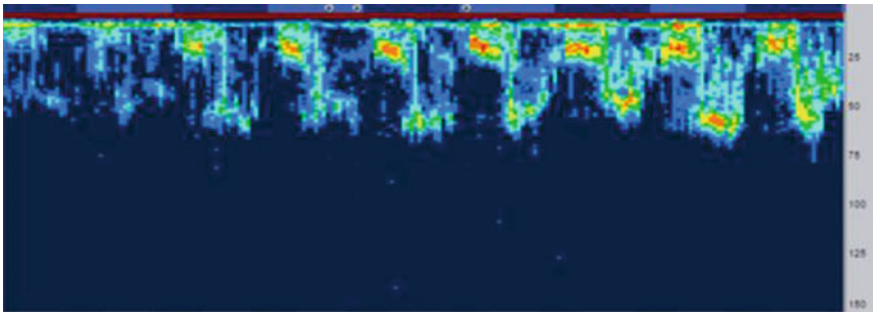

Fig. 6 Sonar image depicting a fish school diving movement below a FAD during a week

2.3 Experimental Satellite Buoys

Two currently used rosary-type FADs were each equipped with a satellite buoy (Make: Thalos), working under the constellation of Iridium and were used to test various parameters such as aggregation of fish under the buoy, wave altimetry, speed of current, sea surface temperature and conductivity. Moreover, the satellite buoy permits the location of the FAD near real time [8]. The satellite buoy uses a transducer which produces sonar image. The sonar image can be fine-tuned to remove noise and interpreted in specialized software (OceanSense). Diurnal movement of fish or aggregation and incidence of primary productivity can also be worked out from the sonar image in Fig. 6 [9]. Some studies using satellite buoys have been used to determine the behavioural variability displayed by tuna near FADs [10].

3 Results and Discussion

The maximum mean current velocity observed around existing sites where FADs are moored around the Island of Mauritius is 3 knots. Based on the findings, the single buoy was conceived and designed to resist to ocean currents. Table 1 shows the comparison of the resistance of the two types of FADs with respect to ocean currents. It can be inferred that the single buoy is less dominated by drag force on the rope and the buoy due to the current. This can be attributed to the shape of the single buoy. The main drag forces taken into consideration were that on the buoy and on the rope.

The deduction of the minimum safe anchor weight was based on the law of static equilibrium. Hence, a 2080.2 kg of iron or a weight of 3600 kg of concrete was theoretically calculated to safely moor the FAD.

The single buoy FAD made up of FRP is 2496 mm in height, with a diameter of 1330 mm and weighs 250 kg. It is equipped with a tube type radar reflector, a solar powered navigational beacon light and belted with a rubber fender Figs. 7 and 8.

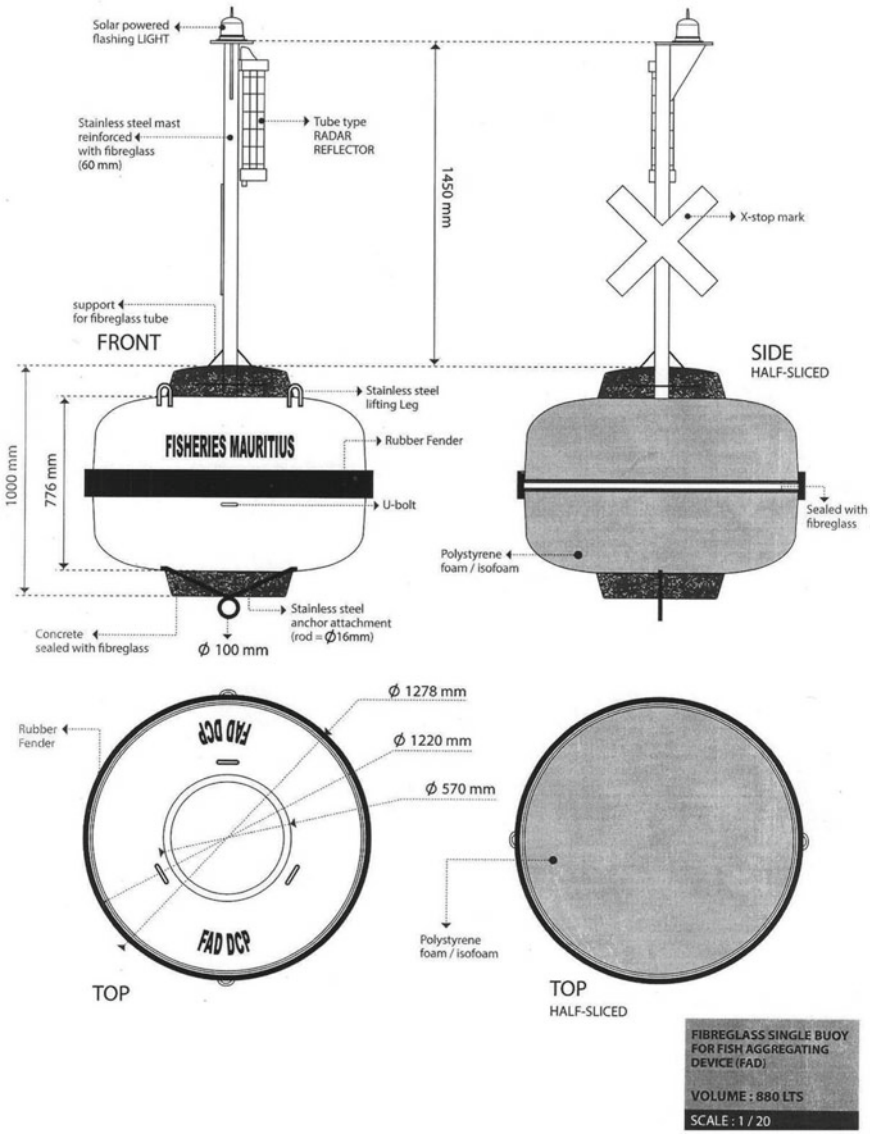

Fig. 7 The schematic design of the single buoy FAD including slice view showing the completely filled up interior space with polystyrene/isofoam

Moreover, the interior is filled with polyurethane foam to prevent water ingress in the event of any cracks induced from collision.

The single buoy FAD was conceptualized by the Fisheries Training and Extension Centre (FiTEC) of the Ministry of Ocean Economy, Marine Resources, Fisheries and Shipping as described in the methodology. A local company specialized in FRP

Fig. 8 Two of the newly constructed single buoy FADs in the compound of the fisheries training and extension centre, Pointe aux Sables, Mauritius

built the buoy. The design also meets the navigation safety requirements of the International Association of Marine Aids to Navigation and Lighthouse Authorities (IALA).

Three sites have been earmarked for deployment of the single buoy FAD on a pilot basis, namely: Pointe aux Caves, Baie du Tombeau and Tamarin. Pointe aux Caves and Baie du Tombeau were selected as they were within the navigational route. The visibility of the FAD and potential collision with large vessels would be observed. The efficacy of the rubber fender would also be tested. The site of Tamarin was selected since it has intensive big-game fishing activities. All the three FADs would be equipped each with a satellite buoy.

The FiTEC has already initiated a sensitization programme to fishermen on the single buoy FAD. The aim is to make fishermen aware of the single buoy, its advantages, and how it will beneficiate the fishermen community. The awareness campaigns have been carried out at various coastal locations around the Island, namely at Trou aux Biches, Roche Bois, Baie du Tombeau, Bain des Dames, Pointe aux Sables, Albion, Tamarin, La Preneuse and Black River.

Use of new satellite technology (GPS, Smart phone) has also been included in the awareness campaign as more and more entrants in the FAD fishery are fishermen of new generation and well versed with mobile applications. The development of an android application to transmit certain data from the satellite buoy is in the pipeline. Fishermen at sea would no longer require to constantly telephone at the FiTEC to inquire of the position of a FAD, as it is the case presently. Instead, the GPS position along with other information would just be a touch away from their smart phone, within their reach.

Based on thoughts gathered from fishermen, they are enthusiastic and keen to adopt the project on the single buoy and to collaborate and share additional information such as daily catch rates with FiTEC.

Depending on the results obtained and feedback from fishermen, the project would then be replicated and all other rosary-type FADs would be replaced by the single buoy FAD. Furthermore, potential new sites as per demand of fishermen community could also be entertained.

Acknowledgements This work was supported by the officers of the Fisheries Training and Extension Centre (FiTEC) and the Ministry of Ocean Economy, Marine Resources, Fisheries and Shipping. The local company, Resiglas Co. Ltd. also extended its support in constructing andmaterializing the prototype of the Single buoy FAD.

References

1. Barbaro A (2009) Modelling and simulations of the migration of pelagic fish. ICES J Mar Sci 66(5):826–838
2. Beeharry SP(2011) International symposium on fish aggregating device (Tahiti)
3. Chooramun V, Senedhun V (2013) Seasonal abundance of tropical tunas around fish aggregating devices (FADs). IOTC WPTT15, pp 1–15
4. Dagorn L, Bach P, Jose E (2000) Movement patterns of large bigeye tuna (*Thunnusobesus*) in the open ocean, determined using ultrasonic telemetry. Mar Biol 136(2):361–371
5. Desurmont A, Chapman L (2001) The use of anchored FADs in the area served by the Secretariat of the Pacific Community (SPC). Tuna fishing and FADs, Martinique
6. Fonteneau A, Pallares P (2000) A worldwide review of purse seine fisheries on FADs. Le Gall J.Y, pp 15–35
7. Franco J, Dagorn L, Sancristobal L (2009) Design of ecological FADs. WPEB-IOTC
8. Hampton J (2010) Tuna fisheries status and management in the western and central Pacific Ocean, Secretariat of the Pacific Community
9. Malig J (1991) Deep-sea aggregating devices in the Philippines, pp 214–228
10. Robert M, Dagorn L, Filmalter JD, Deneubourg JL, Itano D, Holland K (2013) Intra-individual behavioral variability displayed by tuna at fish aggregating devices (FADs). Marine Ecol Program Ser 484:239–247

11. Rohit R (2013) Fish aggregating devices (FADs). CMFRI Research Centre, pp 23–26
12. Roullot J, Venkatasami A, Soondron S (2006) The first three years' experience in the use of fish aggregating devices in Mauritius
13. Roullot J, Venkatasami A (1986) Dispositifs de concentration de poissons, L'expérienceMauricienne—expert consultation on the stock assessment of tunas in the Indian Ocean—Colombo, Sri Lanka, 4–8 Dec 1986, 20 pp
14. Venkatasami A (1990) Introduction of fish aggregating devices in the south west Indian Ocean (a case study). SWIOP Document OISO, Colombo Sri Lanka
15. Yamane T (1989) Status and future plans of artificial reef projects in Japan. Bull Mar Sci 44:1038–1040

Coastal Protection Using Geosynthetic Containment Systems—An Indian Timeline

Tom Elias and Kiran G. Shirlal

Abstract Maritime countries like India face serious coastal erosion issues. Over 1200 km of Indian coastline is identified as eroding. Unavailability and high cost of natural rocks remain as a major hindrance for construction of conventional hard options like breakwaters, seawalls and groynes. This has forced coastal engineers to find nature friendly and economical alternatives. Experiences from Australia, Germany and United States prove the efficacy of geotextile containment systems in coastal protection. This chapter aims at reviewing Indian examples of protection works using geosynthetic and geotextile containment systems from early 1980s. Geosynthetic protection structures include groynes, submerged reefs, seawalls and breakwaters. Benefits and difficulties in implementation of protection works are identified by reviewing prominent works conducted in the east and west coast of India. Experiences at Hamla, Dahanu and Pentha helped in replacing conventional structures with geotubes. Equilibrium beach profile is attained using near-shore geotube reef system at Hamla and Dahanu, Maharashtra, whereas reef constructed using geotextiles at Candolim, Goa suffered serious damage due to vandalism and toe scour. Geosynthetic systems along with gabions and rock armours improve the stability, wave dissipation and reflection characteristics as seen in Pentha, Odisha and Uppada, Andhra Pradesh. Lack of proper design criteria and deliberate destruction by vandals remains as the major threat. Countering these challenges, geosynthetic containment systems offer a cost-effective alternative to conventional coastal protection methods in India.

Keyword Geotextiles · Coastal protection · Geotubes · Geosynthetics · Erosion control

T. Elias (✉) · K. G. Shirlal
Department of Applied Mechanics and Hydraulics, National Institute of Technology Karnataka, Surathkal, Mangaluru 575025, India
e-mail: tomelias00@gmail.com; tom.177am010@nitk.edu.in

K. G. Shirlal
e-mail: kshirlal@gmail.com

V. Sundar et al. (eds.), *Proceedings of the Fifth International Conference in Ocean Engineering (ICOE2019)*, Lecture Notes in Civil Engineering 106,
https://doi.org/10.1007/978-981-15-8506-7_38

1 Coastal Protection

Coastal areas constitute a major part of global geography, and out of which, more than 60% is facing serious erosion over past decades [1]. According to Kudale et al. [2], 1200 km of Indian coastline is under threat of acute erosion. This erosion trend is assumed to be increasing as a result of sea level rise, storm frequency and storm intensity. As a result, coastal protection has become a serious concern, and coastal engineers are forced to find out novel and eco-friendly coastal defences. Over years, there had been massive innovations in coastal protection methods. Coastal engineers came up with hard and soft methods of coastal protection. When hard structures are engineered options like breakwaters, groynes, revetments, seawalls, etc., soft methods comprise of sand nourishment, sand dune care, vegetation and sand bypassing. Rubble mound structures have been widely used for coastal defence both globally and locally. This is because of the availability of rock and extensive research carried out in this area. Established relationships and equations like 'Hudson' and 'Van Der Meer' are helpful in designing hard structures. But in the present scenario, non-availability of natural rocks and prohibition of quarrying in many parts of the country, forced us to find alternatives for the conventional rubble mound structures [3, 4]. These alternatives should be economical as well as eco-friendly [5]. In this regard, sand encapsulated geotextile containment system emerges as the future concept of coastal protection. Applications of geosynthetics in coastal engineering problems are immense. Geosynthetics sand containers (GSCs) as a 'Soft Rock' for coastal defence was first introduced in 1950s at Pluimpot, the Netherlands for the construction of an inlet dike [6]. Since then, there have been numerous improvements in the geosynthetic-based coastal protection technologies with regard to their durability, UV resistance, long-term performance, hydraulic stability and failure modes [4, 7–11]. According to Pilarczyk [12], GSCs offer a band of advantages, like reduction of construction cost, time and volume, usage of locally available material and ease of modification or reshaping if subjected to damage or vandalism.

1.1 A Geosynthetics and Geotextiles in Coastal Engineering Applications

The word 'Geo' stands for soil or earth and 'synthetics' means artificial products. So, man-made products used for geotechnical engineering applications are widely termed as geosynthetics. It consists of a wide spectrum of products made out of natural and artificial polymers or fibres. Natural polymers used in geosynthetics are coir, jute, etc. while artificial polymers include Polyester (PET), Polyethylene (PE), Polypropylene (PP) and Polyamide (PA) [13]. The most commonly available geosynthetic products are in the form of geotextiles, geogrids, geonets, geomembranes, geo-composites, geocells and geofoams. Out of which, geotextiles find major application in coastal engineering field. Geotextiles are continuous sheet of fibres which

are flexible and permeable. It possess a fabric appearance and are often available in the market in big rolls. Geotextiles are again classified into woven and non-woven, based on the method they are manufactured. Woven geotextiles are made by the weaving of fabric looms. They are generally thin, fine textured and possess uniform apparent opening size. They have larger tensile strength and less elongation. Woven geotextiles are comparatively costlier because of the weaving process. Non-woven geotextiles, on the other hand, are made like felts. The raw materials used for manufacture are taken to a binding process through a conveyor belt, where the mass of raw materials is bonded into a single fabric. This binding process can be chemical bonding, needle punching or heat binding, with needle punching being widely practiced [14]. Non-woven geotextiles remain thicker and cheaper than woven and are more puncture resistant. They exhibit slightly more elongation than woven textiles and possess comparatively lower tensile strength. However, non-woven geotextiles are more favoured in coastal engineering applications because of its durability and cost-effectiveness [12, 15].

Geotextiles, when used for coastal protection structures, are generally encapsulated with sand to form units of different dimensions. These units are generally — bags, tubes and containers [13]. Geotextiles bags are small units in the range of 0.05–5 m^3 in volume. Geotextile tubes are long cylindrical units generally 1–5 m in diameter and length up to 200 m [16]. Indian experiences show a general dimension of 3 and 1 m diameter tube with 20 m length. Tubes are usually filled at site with a mixture of sand and water, pumped using high-powered motors. When the volume of geobags is sufficiently large, i.e. in range of 100–700 m^3, they are termed as geotextile containers [6]. These containers are filled onshore and are transported to site using split bottom barges [17].

2 Coastal Protection Works with Geotextiles Indian Timeline

In a global context, geotextile coastal protection works began by 1950s. These textiles were used for various other engineering projects even before, but not known by the specific name of geotextiles. Indian experiences in geotextiles coastal protection works date back to early 1980s. Since early 2000, there were no remarkable GSC structures but geotextile coastal protection branch flourished in India during 2000–2010. Over this period, pioneering works of Central Water and Power Research Station (CWPRS), Pune, National Institute of Ocean Technology (NIOT), Chennai and Indian Institute of Technology, Madras have contributed to the growth of GSC structures. Some of the major projects in the east and west coast of India is reviewed in the present study.

2.1 Coastal Erosion Control, Mumbai

City of New Mumbai witnessed massive expansion during 1970s and 1980s. Expansion of city by reclaiming the marine land-created problems of coastal erosion. This problem of shoreline erosion was countered by constructing geocells using High-Density Polyethylene (HDPE) geogrids. The first two rows were filled with stones and the other layers with sea sand at site. The interconnection of geocells made the structure massive, which in turn helped in reducing dislodgement due to sea waves [18].

2.2 Geotextiles Tubes, Shankarpur, West Bengal

Shankarpur is a village in West Bengal, situated at the east coast of India. Many parts of its coastal stretch were subjected to severe erosion, and a 900 m long stacked geotextile reef was constructed to protect the eroding coast. The construction of geotube protection structure was completed in 2007 [19]. It consisted of two 3 m diameter geotubes at the bottom and one 3 m diameter tube at the top (Fig. 1). A non-woven cover of polypropylene is provided for additional UV protection (black colour). The structure is subjected to extreme wave action and got damaged (200 m length) in August 2007 and subsequently (400 m length) in monsoon 2008. In order to provide additional protection, two rows of wooden bullies filled with laterite stones were provided at 20–25 m seaward of the structure. It helped by breaking and reflecting waves in the wooden bullies, thus reducing effect on the geotubes [2, 20]. Post-construction, polypropylene protection layer was damaged due to subsequent cyclones and high tide level, but the main tube structure remained intact.

Fig. 1 Geotextile tubes at Shankarpur [21]

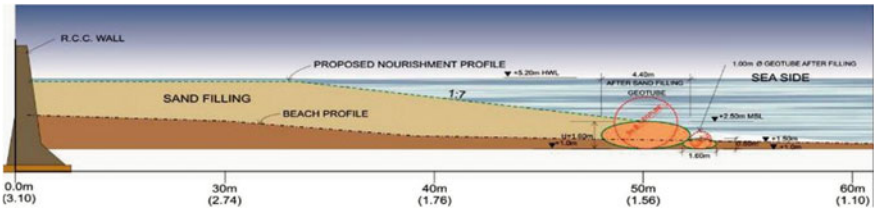

Fig. 2 Geotextile tubes at Hamla, Maharashtra [22]

Fig. 3 Geotextile reef at INS Hamla, Maharashtra [22]

2.3 Nearshore Reef at INS Hamla, Mumbai:

INS Hamla is a Naval Base located at Malad, Mumbai, Maharashtra State. The beach at Hamla was experiencing serious erosion. As a protection measure, a 900 m RCC vertical retaining wall was constructed on the coast supplemented with beach nourishment. To hold the nourished sand, a geotube reef was constructed 50 m away from the retaining wall (Figs. 2 and 3). The reef consisted a layer of 3 m diameter geotextile tube with top at mean sea level (+2.6 m) along with a scour protection layer of 1 m diameter geotextile tube at the toe of 3 m tube. The construction and nourishment were completed by March 2010. Beach stabilised after a couple of months, and tubes were buried up to a level of +1.5 m, directly pointing to the efficiency of structure [2, 22].

2.4 Nearshore Reef, Candolim Goa

Candolim beach lies 15 km north of Panjim, Goa. Grounding of a 300 m long ship named 'River Princess' in 2008, 150 m away from the beach created erosion in the southern part and accretion in the northern part of the beach [2]. A nearshore geotextile tube was proposed as the solution for the erosion problem. The reef consisted of two layers of 3 m diameter geotubes and one layer of 1 m diameter tube at seaside toe of the main tube. Beach nourishment was carried out behind the reef structure (Fig. 4). The reef with a length of 800 and 50 m distance from the coastline was

Fig. 4 Nearshore reef at Candolim, Goa [2]

completed in April 2010. Soon after the construction, sand accretion took place in the beach and continued till monsoon 2010. But the monsoon storm and larger waves resulted in the scouring of sand beneath the geotextile tubes. Scattered debris and stones punctured the geotextiles resulting in the damage of the structure [23].

2.5 Nearshore Reef, Dahanu, Maharashtra

Dahanu is located 110 km north of Mumbai, Maharashtra state. Dahanu beach is being widely used by tourists. A PCC retaining wall was constructed for a length of 400 m, which is stepped towards the seaside. Beach nourishment was also adopted as a soft protection method. Number of offshore reefs with geotubes was constructed to hold the nourished sand. Construction was carried out in the year 2010–2011. It consisted of a 3 m diameter tube supplemented with a 1 m diameter tube as toe protection, placed at 120 m away from the coast (Fig. 5). The reef with its top layer placed at the mean sea level helped in arresting the sand on beach, and its performance was impressive [2].

Fig. 5 Nearshore reef at Dahanu, Maharashtra [2]

2.6 Seawall, Uppada, Andhra Pradesh

Nearly, 1.5 km stretch of coastline in Uppada village, East Godavari District of Andhra Pradesh state had been experiencing severe erosion in last 2–3 decades. Since it posed a serious threat to the life of villagers and some important monuments, Irrigation Department, Government of Andhra Pradesh decided to adopt a protection plan for Uppada coast. A seawall constructed with geotextile tube and bags covered with rock gabions emerged as the solution [24]. The core of the sea wall was made of woven polypropylene geotubes with 3 m diameter and 20 m length. 92 geotubes have been used for the entire construction along with 3,50,000 small Geobags placed over the core layer. The outer layer of the sea wall constitutes rock gabions made of polypropylene ropes (Fig. 6).

The construction of 1 km long seawall was completed in the year of 2011. It helped in reducing the erosion rate, and till 2014 accretion rates showed a positive trend [25]. After Hud Hud cyclone in 2014, studies indicated massive erosion in Uppada coast as result of destruction of the protective structure.

Fig. 6 Construction stages of seawall at Uppada, Andhra Pradesh [24]

Fig. 7 Coastal protections using geobags in Ullal, Karnataka [4]

2.7 Nearshore Berms, Ullal, Karnataka

Ullal at Mangaluru in Karnataka state is located on the south coast of India. It lies adjacent to the combined river mouth of Nethravathy and Gurupur River. Ullal coast had been suffering from severe erosion over decades. After 2010, erosion was so severe that many of the local fishing communities lost their houses. In order to bring down erosion, a series of shore-parallel berms made of geotextile bags were proposed. As a result, construction started using new methodologies to fill the bags in site. The 'Grab' methodology and 'J-Bin' technology have been adopted to fill the geobags (Fig. 7). These technologies were earlier used to fill bags in various coastal protection projects in Australia [4]. Both methods use crane and specialised equipment to fill and place the bags, with improved precision and pace of construction. Structures stacked with non-woven geotextile bags with 1 and 2.5 m^3 volume were constructed and completed by 2014 [25].

2.8 Geotube and Gabion Seawall, Pentha, Odisha

The coastal stretch of Odisha state is protected with saline embankment for a length of nearly 475 km made of locally available soil. The erosion of these saline embankments poses a threat to livelihood of coastal communities. Pentha coast in Kendrapara District, Odisha is protected by Rajnagar Gopalpur saline embankment. The retarded embankment is also susceptible for erosion; therefore, it has become essential to protect the retarded embankment. Thus, central government proposed to construct a geotube embankment in the seaside of the retarded embankment. Thus, a standalone geotube embankment with 30 m base width, 675 m length with a design wave height of 5 m was designed by IIT Madras, Department of Ocean Engineering, in 2011 [26]. The construction was started by September 2013, and soon on October 12th, 2013 Pentha coast was hit by a cyclonic storm, Phailin accompanied by torrential rain. Pentha coast was severely eroded; as result, IIT Madras was forced to

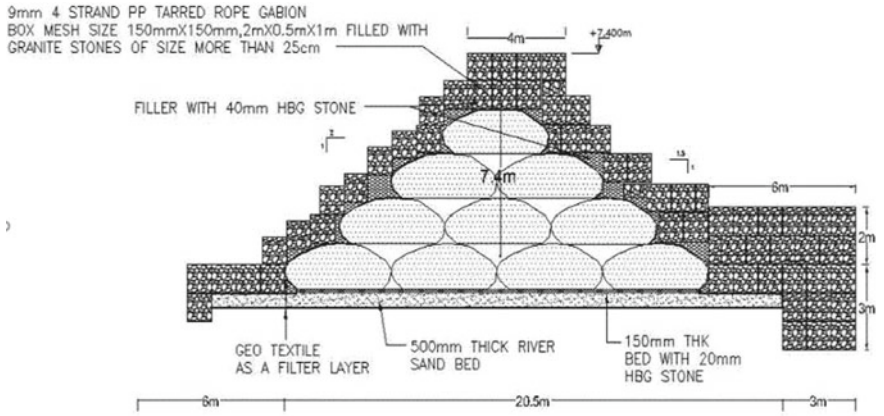

Fig. 8 Cross section of geotube embankment at Pentha Coast, Odisha [26]

redesign the geotube embankment because of space limitation. The newly formulated design reduced the length of geotube embankment from 675 to 505 m (Fig. 8). The construction was completed in the year of 2016 [7].

The structure consists of geotubes of 3 m diameter and 20 m length as the core and polypropylene rope gabions as the outer layer. 16 and 9 mm diameter ultraviolet stabilised ropes were used for gabions. Hard granite stones were used to fill the gabions. Finally, gabions boxes of 2 m $\times$ 1 m $\times$ 1 m size were used. While construction, the structure faced Hud Hud cyclone 2014. The seaside gabion boxes of the embankment were not disturbed even after exposing to huge tidal surge and waves, keeping the structure intact. Accretion of sand started building up in front geotube tube embankment, and the structure is still serving its purpose [27, 28].

2.9 Island Reclamation, Cheruvattor, Kerala

Cheruvattor coastal village is situated in northern part of Kerala in the district of Kasaragod. Cheruvattor fishing harbour is very prominent both in terms of seafood trade as well as tourism. The harbour basin contains a small Island formed due to the deposition of sediments supplemented by Tejaswini River and Oripuzha. The Island faced severe erosion in monsoon season, and the government decided to reclaim the Island using geotextile tubes. Thus, the Island is provided with two layers of geotubes in three sides and one layer of geotubes in the remaining side. Woven geotubes of 3 m diameter and 20 m length were used (Fig. 9). Tubes are filled up to 80% of its capacity with sand slurry containing 30% sand and 70% water. The construction was started by December 2017 and is still ongoing. (Details collected during Cheruvattor fishing harbour visit (2018), Department of Harbour Engineering, Kerala state).

Fig. 9 Geotube Island reclamation, Cheruvattor, Kerala (photographs taken during field visit)

3 Summary

Detail reviewing of coastal protection works involving geotextiles leads to important observation that geotextile is a promising future engineering material. Since geotextiles are cheaper and nature friendly, its use is more promoted in a developing country like India. As the review suggests, the design of structures is usually site specific. One should be very keen in coastal processes, soil behaviour and natural disaster vulnerability of a particular site, even at the pre-design stage. Site-specific nature of geotextile coastal protection works makes it very difficult to provide unified codes of design practice. Beginning from 1980s to 2019, the number of geotextile structures used for coastal protection works found an exponential rise. Indian experiences certify the efficacy of the structures and Indian engineers in undertaking major protection works across the Indian coast. In certain instances, various factors have lead to the failure of structures, especially in Candolim Goa. Geotube structure at Shankarpur, in spite of losing its UV protection cover, served its purpose. The review shows a positive approach in India towards geotextile coastal protection in recent years and is works carried out after 2005. As evident from the recent examples, geotextiles prove to be a very promising future engineering material, with adequate designs and vandalism control of such structures.

Acknowledgements The authors are thankful to the Department of Applied Mechanics and Hydraulics, National Institute of Technology, Karnataka for extending all the necessary support to conduct the present study.

References

1. Corbella S, Stretch DD (2012) Geotextile sand filled containers as coastal defence: South African experience. Geotext Geomembr 35:120–130. https://doi.org/10.1016/j.geotexmem.2012.09.004

2. Kudale MD, Mahalingaiah AV, Tayade BR (2014) Use of sand-filled geotextile tubes for sustainable coastal protection-case studies in Indian scenario. Indian J Geo-Marine Sci 43:1241–1246
3. Pilarczyk K (2008) Alternatives for coastal protection. J Water Res Environ Eng 181–188
4. Jackson LA (2016) Coastal stabilisation—advancement in geotextile design & construction methods as an alternative to rock. In: Proceedings of 3rd international conference on coastal zone engineering and management in the middle east (Arabian Coast 2016), 20th to 23rd Nov, pp 321–342
5. Shin EC, Oh YI (2007) Coastal erosion prevention by geotextile tube technology. Geotext Geomembr 25:264–277. https://doi.org/10.1016/j.geotexmem.2007.02.003
6. Oumeraci H, Recio J (2010) Geotextile sand containers for shore protection. In: Handbook of coastal and ocean engineering, pp 553–600. https://doi.org/10.1142/9789812819307_0021
7. Prem NS, Sundaravadivelu R, Saha N (2018) Geotextile tube and gabion armoured seawall for coastal protection an alternative. In: PIANC-World Congress Panama City, Panama
8. Faraci C (2018) Experimental investigation on hydro-morphodynamic performances of a geocontainer submerged reef. J Waterway Port Coast Ocean Eng 144:1–10. https://doi.org/10.1061/(ASCE)WW.1943-5460.0000434
9. Shirlal KG, Mallidi RR (2015) Physical model studies on stability of geotextile sand containers. In: 8th international conference on Asian and Pacific coasts (APAC 2015) procedia engineering. Elsevier, pp 567–574
10. Dassanayake DT, Oumeraci H (2012) Engineering properties of geotextile sand containers and their effect on hydraulic stability and damage development of low-crested/submerged structures. Int J Ocean Clim Syst 3:135–150. https://doi.org/10.1260/1759-3131.3.3.135
11. Nasar T, Balaji R, Sundar V (2004) Hydrodynamic characteristics and stability of rubble mound breakwater with geobags as the core. In: 3rd Indian national conference on harbour & ocean engineering, pp 492–497
12. Pilarczyk KW (2000) Geosynthetics and geosystems in hydraulic and coastal engineering, Taylor and Francis
13. Ashis M (2015) Application of geotextiles in coastal protection and coastal engineering works: an overview. Int Res J Environ Sci 4:96–103
14. Oyegbile BO, Oyegbile BA (2017) Applications of geosynthetic membranes in soil stabilization and coastal defence structures. Int J Sustain Built Environ 6(2):636–662
15. Saathoff F, Oumeraci H, Restall S (2007) Australian and German experiences on the use of geotextile containers. Geotext Geomembr 25:251–263. https://doi.org/10.1016/j.geotexmem.2007.02.009
16. Kiran AS, Ravichandran V, Sivakholundu KM (2015) Stability analysis and design of offshore submerged breakwater constructed using sand filled geosynthetic tubes. Proc Eng 116:310–319. https://doi.org/10.1016/j.proeng.2015.08.295
17. Lawson CR (2008) Geotextile containment for hydraulic and environmental engineering. Geosynthetics Int 15:384–427. https://doi.org/10.1680/gein.2008.15.6.384
18. Rajagopal K (2010) Different geosynthetic solutions for coastal erosion control. In: Proceedings of international workshop on geosynthteic and modern materials in coastal protection and related applications. IIT Madras, pp 202–208
19. Sundar V, Maiti DK, Sannasiraj SA, Venkatraman M (2009) Geosynthetic application for coastal protection at Shankarpur, West Bengal, India. In: Asian and Pacific Coasts, pp 58–64
20. Satyakumar S, Deepa V, Venkataraman M (2010) Indian experience in using geosynthetics for coastal protection and beach restoration works. In: Proceedings of international workshop on geosynthetic and modern materials in coastal protection and related applications. IIT Madras, pp 262–270
21. Sundar V, Sannasiraj SA (2013) Coastal protection using geosynthetic at Shankarpur, West Bengal, India. In: Second international workshop on geosynthetic and modern materials in coastal protection and related applications, pp 159–167
22. Tayade BR, Mahalingaiah AV, Gokhale NV, Kudale MD (2015) Importance of location and alignment of geotextile tubes for the coastal protection measures. Aqua Proc 4:190–197. https://doi.org/10.1016/j.aqpro.2015.02.026

23. Hegde AV (2010) Coastal erosion and mitigation methods—global state of art. Indian J Marine Sci 39:521–530
24. Sundar V (2013) Coastal protection measures along few stretches of Indian coast. In: Second international workshop on geosynthetic and modern materials in coastal protection and related applications, pp 147–158
25. Kannan R, Abhrankash K, Ramanamurty MV, Ramana KV (2018) Shoreline evolution along Uppada coast in Andhra Pradhesh using multi temporal satellite images. In: Proceedings of seminar on geosynthetics for erosion control and coastal protection. Bhuvaneswar, Odisha, pp 25–32
26. Sundaravadivelu R (2013) Design and construction of geotube saline embankment at Pentha, Orissa. In: second international workshop on geosynthetic and modern materials in coastal protection and related applications, pp 143–147
27. Jugal KT (2018) Construction of Geo-tube embankment at Pentha in Kendrapara district of Odisha—a case study. In: Proceedings of seminar on geosynthetics for erosion control and coastal protection. Bhuvaneswar, Odisha, pp 33–40
28. Mahalingaiah AV, Tayade BR, Gokhale NV, Kudale MD (2015) Hydraulic model studies for the design of submerged offshore reefs for the coastal protection measures. Proc Eng 116:350–357. https://doi.org/10.1016/j.proeng.2015.08.298

Stability of Groynes Built Using Geo Systems

S. PavanKumar, Vallam Sundar, and S. A. Sannasiraj

Abstract In general, the groyne sections are made of rubble stones of different sizes. To conserve the ecosystem and also due to the scarcity of natural rocks around certain locations, the reliance on these hard materials for the construction of groyne sections becomes questionable forcing us to look for alternate eco-friendly soft materials, for example, geo systems. In order to evaluate the feasibility and advantages of geo systems for groyne construction and to test their hydrodynamic stability, the core section of rubble stones was replaced by geo-bags filled with sand. The objective of this study is to assess the wave transmission, hydrodynamic stability and wave overtopping of a groyne section with a geo-bags filled core section through physical model studies. The tests were conducted in a wave flume in Department of Ocean Engineering, Indian Institute of Technology Madras, India. A model scale of 1:15 is adopted based on Froude's scaling law and dimensional limitations of the testing facility. The aforementioned cross sections were tested simultaneously in a wave flume that was partitioned longitudinally. The transmission and hydrodynamic stability of both the sections have been analysed by subjecting the corresponding sections to the action of random waves defined by JONSWAP spectrum through a well-controlled experimental programme. The details of test set-up, testing facility, parameters of model, test procedure, analysis of results and discussion will be reported in this chapter.

Keywords Geo-bags · Wave overtopping · Wave transmission

1 Introduction

The state of Kerala, India has a coastline of about 500 km long being effectively utilized for various activities and fishing being most dominant. The coast has been protected with seawall structures over several decades. However, the continuous wave action requires the rehabilitation/reconstruction of seawalls in frequent intervals.

S. PavanKumar (✉) · V. Sundar · S. A. Sannasiraj
Department of Ocean Engineering, Indian Institute of Technology Madras, Chennai 600036, India
e-mail: spavankumar235@gmail.com

V. Sundar et al. (eds.), *Proceedings of the Fifth International Conference in Ocean Engineering (ICOE2019)*, Lecture Notes in Civil Engineering 106,
https://doi.org/10.1007/978-981-15-8506-7_39

Further, over the last decade, the importance of groynes has grown in this state, and in particular, at locations dominated by longshore drift, groyne fields have proved its worth in protecting as well as winning the lost beach. The coastal stretch of Perumpally (9°50′42.69″N 76°21′44.36″E) is one such location, which stands as an example to the efficiency of the performance of the groyne field. Conservatively, the groyne sections are composed of rubble stones. Due to the advantages of using modern materials such as geotextiles for the groyne construction, a feasibility study was conducted adopting geosynthetic products for its hydrodynamic stability. A physical model study was conducted to test the hydrodynamic stability of groyne sections with the core replaced by geosynthetic bags. Accordingly, a detailed physical model study has been conducted, and this paper details the salient aspects of this study. The objective of this study is to assess the wave transmission, hydraulic stability and wave overtopping over two trunk sections in a water depth of 3 m through physical model studies. The core of one of the trunk section is made up of rubble stones, and the other is made up of geo-bags. The present two-dimensional physical model tests were carried out on the scaled down model corresponding to the Froude's scaling law of scale of 1:15. The model scale is adopted based on the wave generation capability of the wave maker and minimum requirement of water depth at the model scale.

2 Experimental Setup

2.1 Experimental Facility

The present experimental setup consists of a flume of dimension 72.5 m long, 2 m wide and 2.5 m deep wave flume in Department of Ocean engineering, Indian Institute of Technology, Madras. A wave maker is installed at one end of the flume, and the rubble mound beach to dissipate the wave energy exists at the other end of the flume. Wave maker is operated in piston mode to simulate intermediate and shallow water waves. For the present study, random wave generation through a servo actuator with remote control system is adopted. The servo actuator is connected to a personal computer through which wave climate is given as input, and data is acquired. The wave synthesizer, application software package along with analogue–digital and input/output modules are installed in the PC. The software is capable of controlling the wave paddles and acquires the data during the test period. This software can be used for analysis of data in frequency as well as time domains. In the present study, JONSWAP spectrum is adopted. The tests were carried out for the following water levels by both considering the situation with and without storm surge for section. Table 1 presents the water level testing criteria.

Table 1 Different loading conditions adopted for stability tests

Loading conditions	Water level	Remarks
75% of H_s	4.2	Consolidation
100% of H_s	4.2	Operational condition
125% of H_s	4.2	Overload condition

Table 2 Loading conditions for the groyne section at −3 m CD

Loading	Prototype wave height (m)	Prototype wave period (s)	Model wave height (m)	Model wave period (s)
75% of H_s	1.33	7.75	0.087	2
100% of H_s	1.63	7.75	0.109	2
125% of H_s	2.07	7.75	0.138	2

2.2 Test Conditions

The details of wave climate in prototype and in model are provided in Table 2. All the tests were carried out for 1000 waves corresponding to prototype scale which could approximately represent two to three hours storm duration.

2.3 Prototype and Model Details

In prototype, the filter layer consists of blasted granite stones with the weight of the individual unit ranging between 5 and 10 kg. The core layer consists of blasted granite stones with the weight of the individual unit ranging between 10 and 200 kg. The primary armour layer is formed by two layers of quarried stone of each unit weight ranging from 1250 to 2000 kg with the thickness of 1.7 m. The slope given to the trunk section is 1 in 2 on the sea side and on the channel side. The upstream and downstream slopes are 1V and 2H.

The model scale adopted for quarry stone armoured section is 1:15. The details of the geometrically similar model section for conventional system adopted are as shown in Table 3, which represents the details of geometrically similar model section for conventional and the proposal with geo-bags along with the prototype layer specifications.

In the model, the size grading of the layer materials and specific gravity is reproduced as closely as possible. The filter layer consists of quarried rubble with the weight of the individual unit ranging between 1.5 and 3 g. The core layer consists of quarried rubble with the weight of the individual unit ranging between 3 and 6 g. The primary armour layer is formed by two layers of quarried stone unit weight ranging from 0.370 to 0.590 kg with a thickness of 0.11 m. The slope given to the trunk section is 1 in 2 on the sea side and channel side. The details of the cross

Table 3 Prototype and model details of the trunk section by conventional and with geo-bags

Layer	Conventional (core with rubble stones)		Core with geo-bags	
	Prototype (kg)	Model (g)	Prototype (kg)	Model (g)
Armour	1250–2000	370–590	1250–2000	370–590
Toe mound	300–500	90–140	300–500	90–140
Core	10–200	3–6	1 m × 0.7 m geo-bags	6.6 cm × 4.6 cm
Filter	5–10	1.5–3	5–10	1.5–3

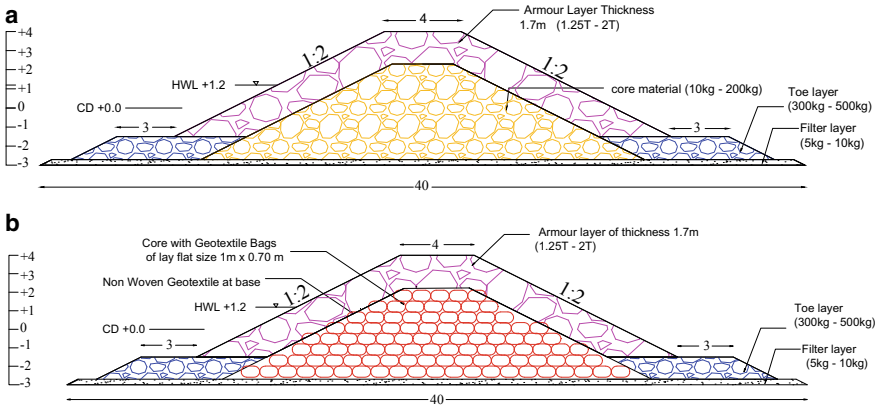

Fig. 1 **a** Cross section of the prototype groynes for 3 m water depth in conventional system. **b** Cross section of the prototype groyne for 3 m water depth with geo-bags

section of groyne of prototype in which core as rubble stones and as geo-bags at 3 m are shown in Fig. 1a, b, respectively. The details of the cross section of model groynes corresponding to the above specified prototype in conventional system and with geo-bags section are shown in Fig. 2a, b, respectively. The bed of the model is at an elevation of 3 m below CD. The crest level of the groyne is at 4 m above CD.

3 Methods for Hydraulic and Damage Assessment of Armour Units

The total percentage of damage of any groyne cross section can be assessed either by profiling the damaged portion or by counting number of units displaced. Both the methods are explained below.

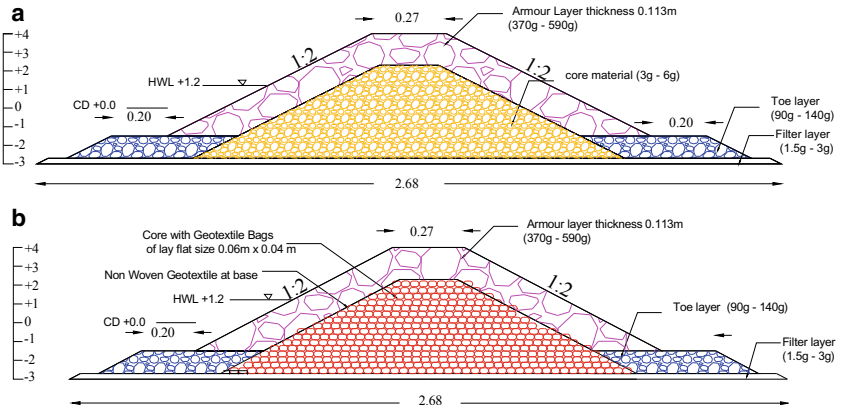

Fig. 2 **a** Cross section of the model groyne for 3 m water depth in conventional system. **b** Cross section of the model groyne for 3 m water depth with geo-bags

3.1 Area Method

The damage to the armour layer can be given as a percentage of displaced blocks related to a certain area (the whole or a part of the layer). Damage can be defined as the relative damage, N_o, which is the actual number of units displaced or rocking related to a width along the longitudinal axis of the structure of one nominal diameter D_n. An extension of the subscript in N_o can give the distinction between displaced out of the layer, units rocking within the layer (only once or more times). The actual number is related to a width of one D_n.

N_{od} = units displaced out of the armour layer (hydraulic damage).

N_{or} = rocking units and

3.2 $N_{omov} = N_{od} + N_{or}$

3.3 Number of Units Method

This method damage assessment follows the procedure of Owen and Allsop [1]. The damage to the groyne section is in terms of the number of armour units, which have been totally dislodged from the armour layer. This can be expressed as a percentage of the total number of units on the armour layer. The movement of armour units can assess the damage, and four categories of armour unit movements are given below.

P Unit seen to be rocking, but not permanently displaced.
Q Unit displaced by up to 0.5*D*.

R Unit displaced between 0.5 and 1.0*D*.
S Unit displaced by more than 1.0*D*.

where *D* is the equivalent diameter of an individual armour unit. The order of damage for armour layer has been assessed using the formula.

$$\%\ \text{of damage} = \frac{\text{Number of armour units dislodged}}{\text{total number of units in armour layer}} \times 100$$

The total is P + Q + R + S which it is less than 5%; the section is accepted to be safe. For the groyne sections, the assessment of damage by the number of units method was adopted; in which case, the units are continuously monitored during the propagation of waves over the section 1-1 armoured with quarry stone. The study on the stability of groyne sections and their analysis was based on visual observations of its physical behaviour. As stated in this section, the number of unit's method is adopted for assessing damage of the groyne sections.

3.4 Prototype and Model Details

For the stability, the following criteria is adopted,

In the design wave conditions, the toe must maintain its function of sustaining armour. The reshaping of the toe should not reach the toe of the armour. The rocks of the toe must not be projected to the armour layer. The criteria for the design of toe is $N_{od} = 0.5$ corresponding to the start of damage as per Van der Meer formula [2],

$$N_{od} = \frac{\text{Number of units displaced}}{\text{Width of test section in} D_{n50}} \times 100$$

The Rock Manual [3] proposes the following percentage of damage and is adopted here,

0–3%: No movement of stones (or only few) in the toe.

3–10%: The toe flattened out a little but still functioning (supporting the armour layer). Acceptable damage >20%: Failure. The toe lost its function and unacceptable.

4 Results and Discussions

In the present studies, it was 0% failure and found to be stable. The summary results of the comprehensive tests on the stability assessment of trunk section armoured with quarried stone in 3 m water depth (Trunk slope 1 in 2) are presented in Table 4. The details on the results on the stability assessment of trunk section armoured with

Table 4 Stability assessment of trunk section armoured with quarried stone in −3 m water depth

Loading	Observations
75% of H_s	No rocking of armour units
100% of H_s	No rocking of armour units and splashing of water drops towards lee side
125% of H_s	No rocking of armour units and splashing of water drops towards lee side

Trunk slope 1 in 2

quarried stonein 3 m water depth established after being subjected to 1000 waves are reported in Table 5.

4.1 Wave Over Topping

As the groyne section has been designed as a non- overtopping section, no overtopping was observed to any of the wave conditions to which the sections were exposed. Hence, it is inferred that wave overtopping is zero, and the sections are safe against overtopping. The details of the results are provided in Table 6.

4.2 Wave Transmission

The performance of stone armour units, due to the action of waves in the flume for the water depths of 0.28 m for trunk slope of 1 in 2, is determined in hydraulic model tests. Figure 3a, b shows the views of the groyne model section before and after being subjected to 125% of H_s, respectively. The summary of the results from the model testing of conventional system and with geo-bags is provided in Tables 7 and 8, respectively. The results show that the wave transmission is a minimum for both the models.

5 Conclusions

The transmission and hydraulic stability of the trunk section in water depths of 3 m have been analysed by subjecting the corresponding sections to the action of random waves through a well-controlled experimental programme. The wave loading conditions 75% of H_s, 100% of H_s and 125% of H_s adopted for a design water depth. A maximum transmission of 5.17% was observed for the groyne trunk section in 100% of H_s in a water depth of 3 m in conventional section. Under stability tests, there was neither rocking nor sliding of armour units. There was no wave overtopping in the above tests. Based on the above investigations, the percentage of transmission

Table 5 Stability assessment of trunk section armoured with quarried stones in −3 m water depth

Wave period, T		Wave height, H		Water depth		Loading	Movement of armour blocks			Remarks
P (s)	M (s)	P (m)	M (m)	P (m)	M (m)		Category	No. of units	% of damage	
7.75	2	1.33	0.088	4.2	0.28	75% of H_s	P Q R S	0 0 0 0	0	No rocking of armour units
7.75	2	1.63	0.109	4.2	0.28	100% of H_s	P Q R S	0 0 0 0	0	No rocking of armour units and splashing of water drops towards lee side
7.75	2	2.07	0.138	4.2	0.28	125% of H_s	P Q R S	0 0 0 0	0	No rocking of armour units and splashing of water drops towards lee side

Scale adopted: 1:15. Number of waves = 1000

Table 6 Wave overtopping over the trunk section armoured with quarried stones in −3 m water depth scale adopted: 1:15

Wave period, T		Wave height, H		Water depth		Loading	Overtopping		Remarks
P (s)	M (s)	P (m)	M (m)	P (m)	M (m)		Prototype *l/s/m*)	Model (*l/s/m*)	
7.75	2	1.33	0.887	4.2	0.28	75% of H_s	Nil	Nil	Nil
7.75	2	1.63	0.109	4.2	0.28	100% of H_s	Nil	Nil	Splashing of waves observed during few occurrences
7.75	2	2.07	0.138	4.2	0.28	125% of H_s	Nil	Nil	Splashing of waves observed during few occurrences

Number of waves = 1000

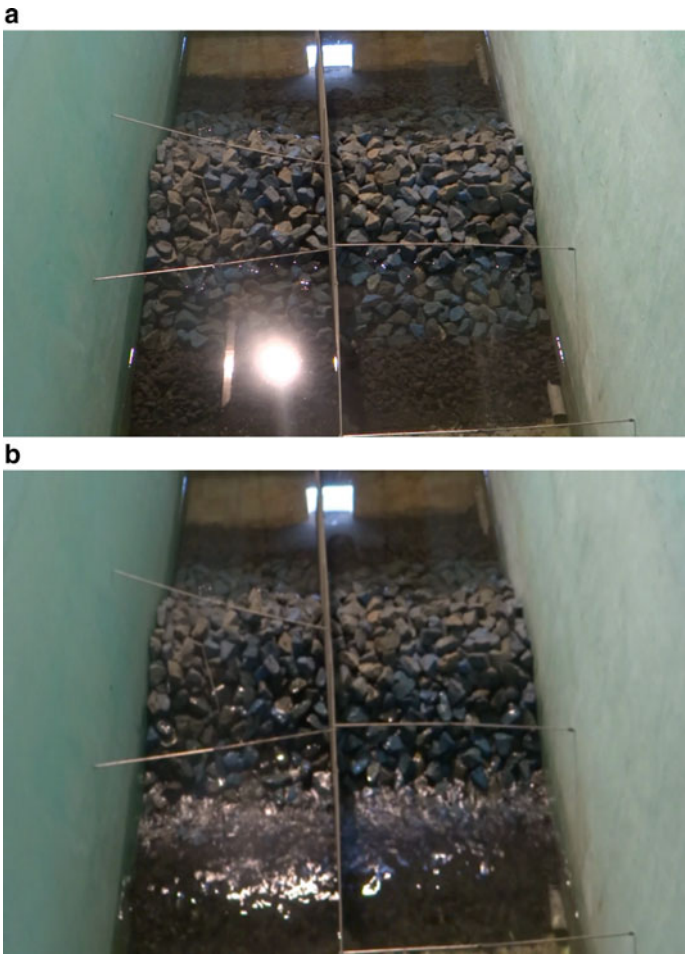

Fig. 3 **a** View of 125% H_s test condition on breakwater section in 3 m water depth prior to the tests. **b** View of 125% H_s test condition on break water section in 3 m water depth after the tests

is found to be less in groyne section with core as geo-bags compared to conventional system. Hence, the design is quite safe from hydrodynamic performance point of view and can adopt for construction after ascertaining the sea bed conditions through a borehole survey.

Table 7 Wave transmission over trunk section armoured with quarried stones in −3 m water depth (conventional section) scale adopted: 1:15

Wave period, T		Wave height, H		Water depth		Loading	Transmission		Remarks
P (s)	M (s)	P (m)	M (m)	P (m)	M (m)		P	M	
7.75	2	1.33	0.0887	4.2	0.28	75% of H_s	0.54	0.0360	Nil
7.75	2	1.63	0.109	4.2	0.28	100% of H_s	0.775	0.0517	Splashing of waves observed during few occurrences
7.75	2	2.07	0.138	4.2	0.28	125% of H_s	0.675	0.045	Splashing of waves observed during few occurrences

Number of waves = 1000

Table 7

Wave period, T		Wave height, H		Water depth		Loading	Transmission		Remarks
P (s)	M (s)	P (m)	M (m)	P (m)	M (m)		P	M	
7.75	2	1.33	0.887	4.2	0.28	75% of H_s	0.475	0.0317	Nil
7.75	2	1.63	0.109	4.2	0.28	100% of H_s	0.735	0.049	Splashing of waves observed during few occurrences
7.75	2	2.07	0.138	4.2	0.28	125% of H_s	0.645	0.0433	Splashing of waves observed during few occurrences

Number of waves = 1000

References

1. Owen MW, Allsop NWH (1983) Hydraulic modelling of rubble mound breakwaters. In: Proceedings of ICE conference on breakwaters: design and construction, publication. ICE, London, pp 71–78
2. Van der Meer JW (1988) Rock slopes and gravel beaches under wave attack. PhD thesis, Delft University, The Netherlands
3. The Rock Manual "The use of rock in hydraulic engineering", CIRIA-CUR-CETMEF (2007)

Optimization in Selecting Member Size in an Approach Jetty, Mormugao, Goa

R. Sundaravadivelu, S. Sakthivel, and H. Balaji

Abstract This paper presents the design optimization for reinforced concrete structure done in order to minimize the cost of the concrete and steel for pile by selecting different span length in marine approach jetty, POL berth, Mormugao, Goa. Dimensions of approach jetty is 200 m length × 15 m width. The purpose of the approach jetty is to carry vehicles and oil pipelines. Live load of 30 kN/m^2/Class 70R (wheeled) from IRC is considered for the jetty design. The proposed location falls under seismic zone III. Piles are founded in sandstone at a depth of (−)32 m CD. Two options (I and II) were explored for the above considerations, and the feasible alternative has been arrived at cost-effective, robust design, and time-sensitive manner.

Keywords Approach jetty · Tide levels · Optimization · Piles · Berth

1 Introduction

The growth in the economy and the cargo traffic for MPT becomes necessary to develop a new POL (Petroleum, Oil, and Lubricant) Jetty toward east of existing cargo berth. The liquid jetty is non-polluting, and hence, shifting may not cause any public unrest. The optimistic situation will further enhance the traffic position and the necessity to utilize the berths for the optimal use. Approach jetty is proposed adjacent to the existing cargo berth for access of vehicles and for laying oil pipelines.

R. Sundaravadivelu (✉) · S. Sakthivel · H. Balaji
Department of Ocean Engineering, Indian Institute of Technology Madras, Chennai 600036, India
e-mail: rsun@iitm.ac.in

S. Sakthivel
e-mail: enggoecrd@gmail.com

H. Balaji
e-mail: balaji098123@gmail.com

V. Sundar et al. (eds.), *Proceedings of the Fifth International Conference in Ocean Engineering (ICOE2019)*, Lecture Notes in Civil Engineering 106,
https://doi.org/10.1007/978-981-15-8506-7_40

Fig. 1 Proposed approach jetty

2 Need for the Project

Approach jetty will be constructed for developing the POL Berth at Vasco Bay, Mormugao Port Trust (MPT). At present, existing liquid cargo berth has reached its optimum capacity utilization. Hence, there is no option left for the port other than developing a new POL/liquid cargo berth to handle the liquid cargos. Lest, the port may lose the cargos due to lack of berth (Fig. 1).

3 Structural Arrangement of Approach Jetty-I

Dimensions of approach jetty is 200 m length × 15 m width. Approach jetty is provided for vehicles approach of 10 m width and for laying oil pipelines of 5 m width.

- Initially, it has been considered with three rows of 800 mm diameter piles with spacing of 6 m in transverse direction and 5 m in longitudinal directions.
- Pre-cast pile muff of 1200 mm × 1200 mm × 450 mm has been considered for each pile.
- The transverse and longitudinal beams of size 1000 mm × 1200 mm and 300 mm thick slab with precast of 200 mm thick and
- in-situ of 100 mm thick have been considered. As per these structural arrangements, required number of piles is 120. The time period for construction of 120 piles shall cover 18 months which will lead to delay of project completion and berth operation (Figs. 2, 3 and 4).

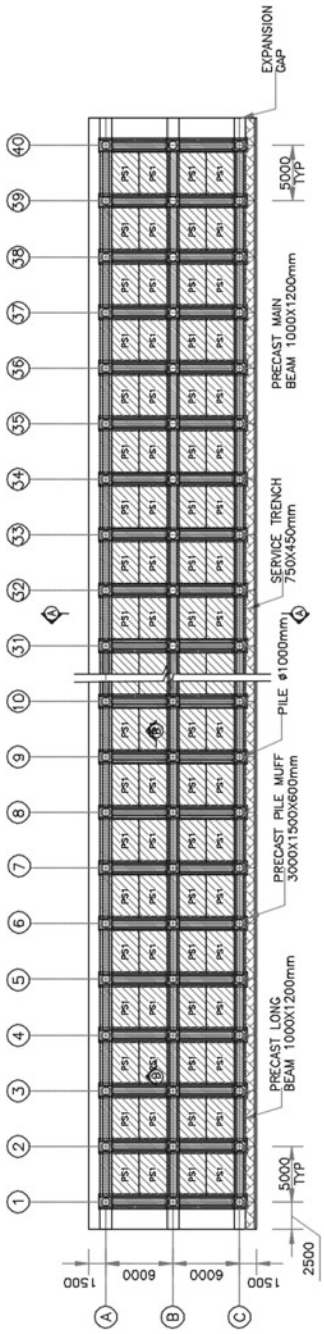

Fig. 2 Plan of approach jetty

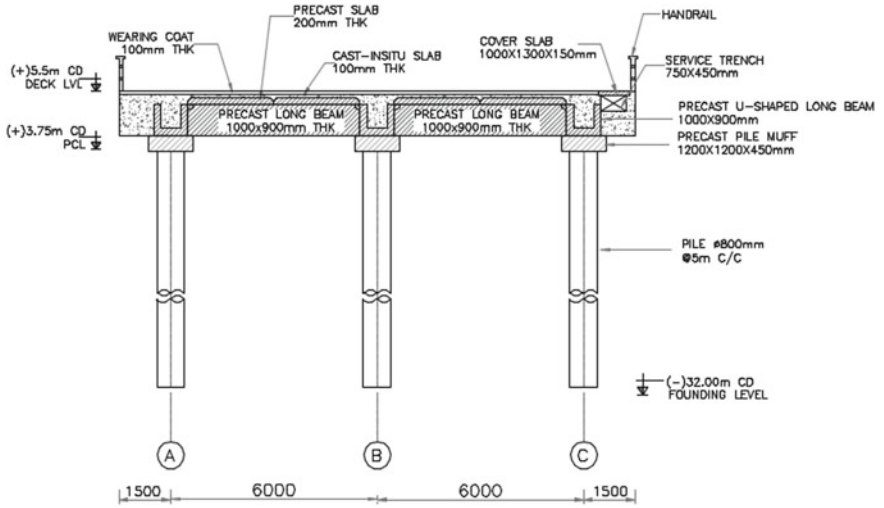

Fig. 3 Cross section of approach jetty

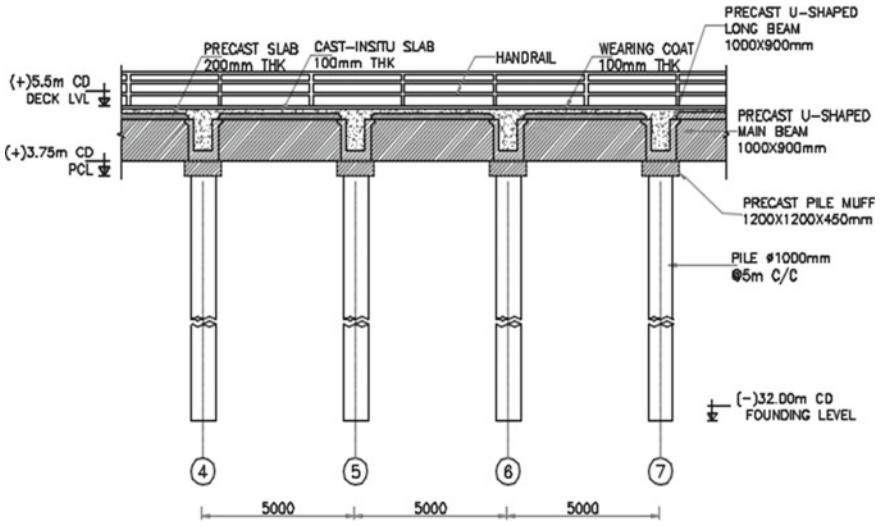

Fig. 4 Longitudinal section of approach jetty

4 Revised Structural Arrangement of Approach Jetty-II

Dimension of approach jetty is 200 m length × 15 m width.

- It has been considered with two rows of 1000 mm diameter piles with spacing of 12 m in transverse direction and 5 m in longitudinal direction.

- Precast pile muff of 3000 mm × 1500 mm × 600 mm has been proposed for each pile.
- The transverse and longitudinal beams of size 1000 mm × 1500 mm are considered.
- 300 mm thick slab with precast of 200 mm thick and
- in-situ of 100 mm thick have been considered (Figs. 5, 6 and 7).

5 Governing Factors

5.1 Oceanographic Data

See Table 1.

5.2 Loads on Berthing Structure

Loads considered on approach Jetty.

a. Dead load
b. Live loads on deck
c. Vehicular load
d. Earth pressure
e. Seismic load.

Based on the above factors, the berth is designed.

5.3 Soil Profile

Soil profile at the proposed site is as shown in Fig. 8.

5.4 Materials and Cover

The following materials and covers used in different structural members are mentioned below (Table 2).

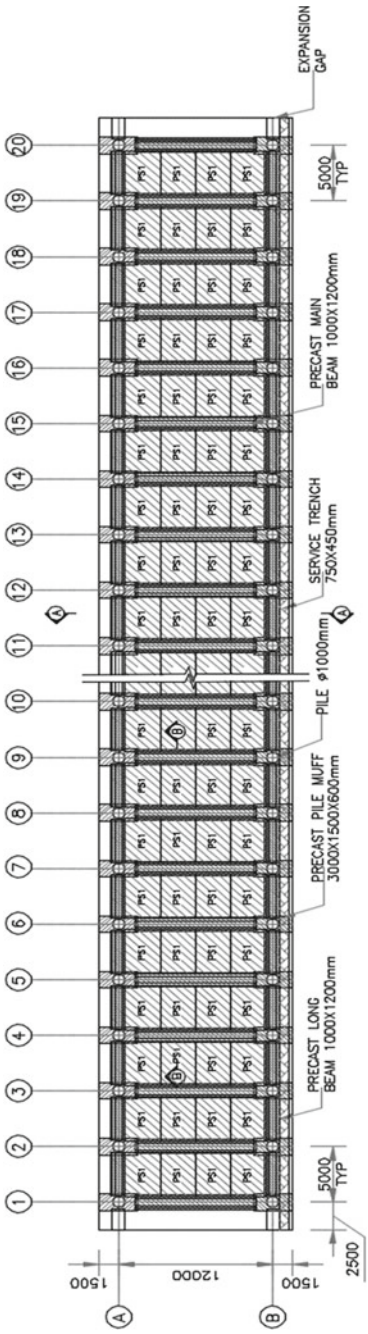

Fig. 5 Plan of approach jetty

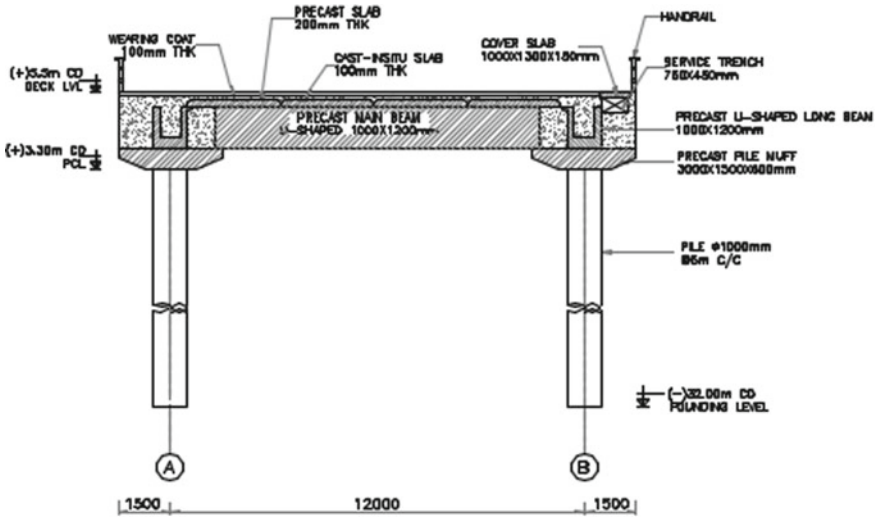

Fig. 6 Cross section of approach jetty

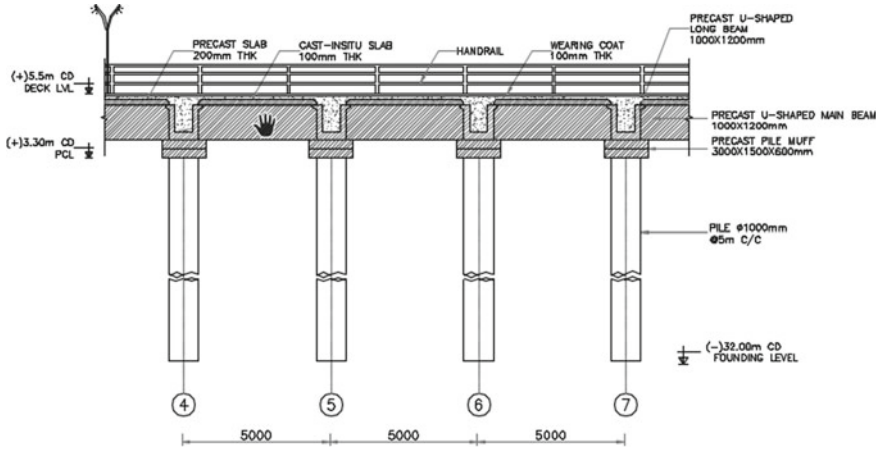

Fig. 7 Longitudinal section of approach jetty

Table 1 Tidal data

Higher high water at springs	(+)2.30 m CD
Mean higher high-water	(+)1.90 m CD
Mean sea level	(+)1.03 m CD
Mean higher low water	(+)1.00 m CD
Mean lower low water	(+)0.50 m CD

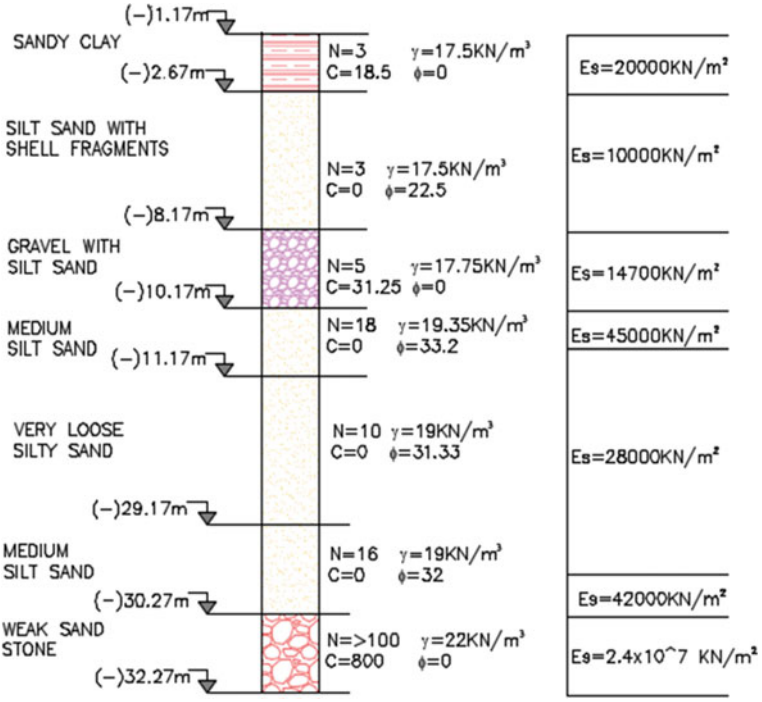

Fig. 8 Borehole details

Table 2 Materials and cover

Structural members	Materials used		Clear cover (mm)
	Concrete	Steel	
Piles	M40	Fe500D	75
Pile muffs	M40	Fe500D	60
Beams	M40	Fe500D	40
Deck slab	M40	Fe500D	40

6 Modeling and Analysis

A 3D analysis is carried out using conventional STAAD Pro software. The pile and beam are modeled as beam element, and offset option is used to model the slab as beam element. The soil–structure interaction analysis is performed by using springs as a representation of soil. The loads are applied as per the guidelines of IS 4651 part IV 2014. The critical load case for limit state of collapse and limit state of serviceability is considered for the design (Figs. 9 and 10).

Fig. 9 2D rendered view

Fig. 10 3D rendered view

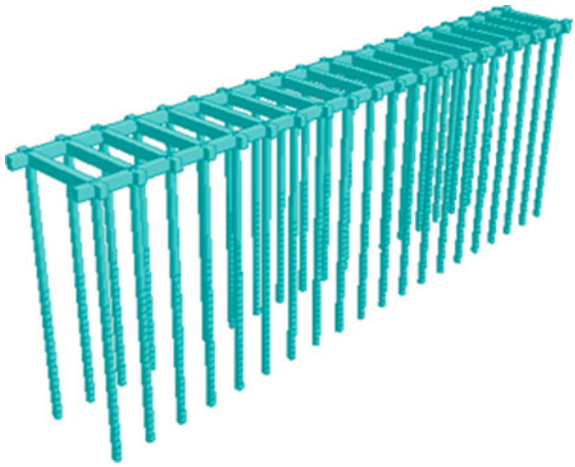

The analysis of the structure is carried out using STAAD PRO, by idealizing the soil support using springs for piles (Fig. 11).

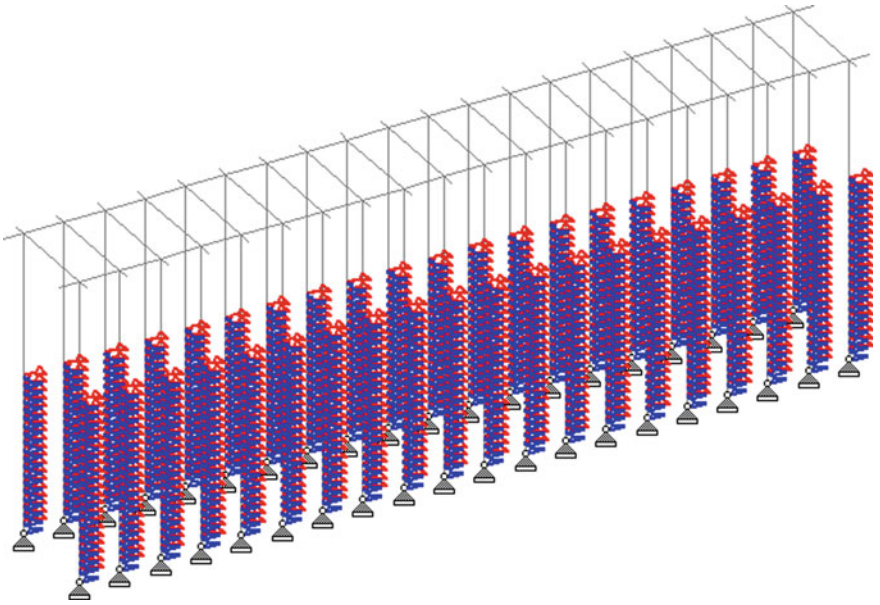

Fig. 11 Spring representation on structure

6.1 Dead Loads

Dead loads consist of the self-weight of the structure. Unit weight of various materials considered in the structural members shall be taken as follows (Fig. 12):

a. Water: 9.81 kN/m^3
b. Sea water: 10.3 kN/m^3
c. Reinforced concrete: 25.0 kN/m^3
d. Plain cement concrete: 24.0 kN/m^3
e. Steel: 78.5 kN/m^3.

6.2 Live Loads

Live load of 30 kN/m^2 is considered as per IS 4651(Part 3-1974) (Fig. 13).

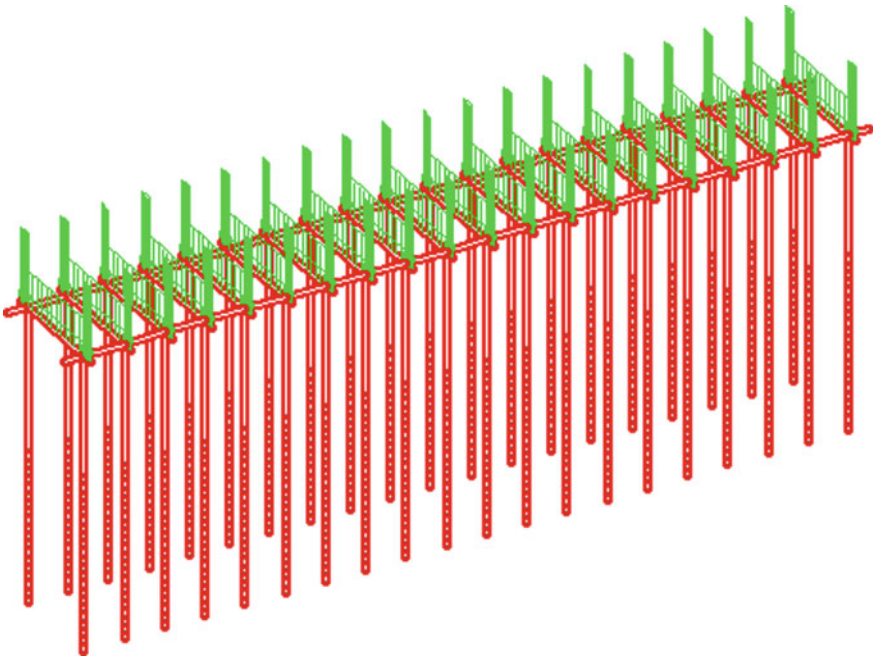

Fig. 12 Dead load representation on structure

6.3 Seismic Load

Seismic force is calculated according to IS 1893-2016 (part-I), considering 100% dead load +50% live load acting on the structure. As per IS 1893-2016, the proposed location falls under seismic zone III, and the basic horizontal seismic coefficient shall be calculated accordingly (Table 3).

Horizontal seismic coefficient

$$A_h = Z/2 \times I/R \times S_a/g$$

where

6.4 Vehicular Load

The following vehicular loads as per IRC-6 are considered for analysis:

IRC 70-R loading.

- Wheeled (Fig. 14)

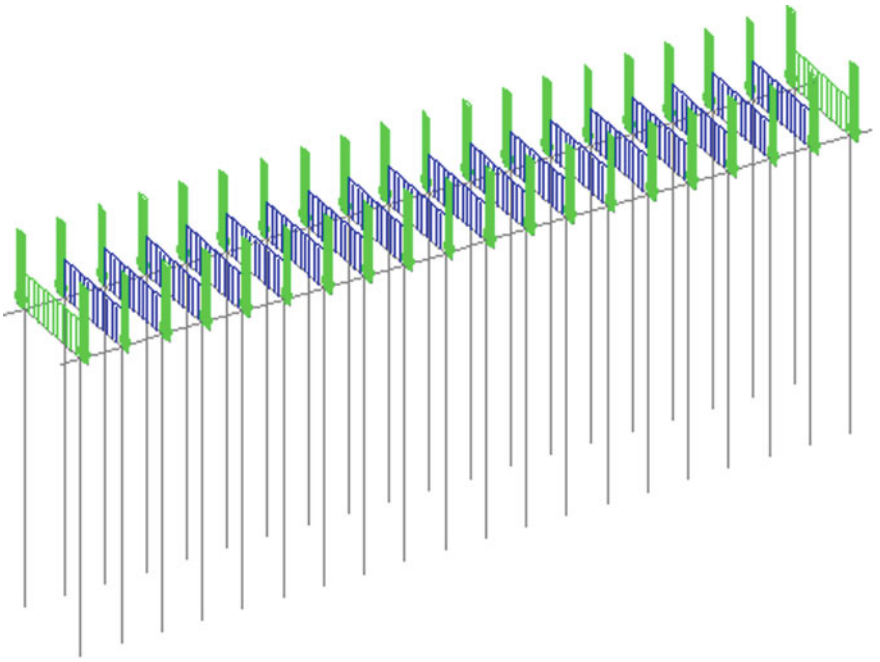

Fig. 13 Live load representation on structure

Table 3 Seismic coefficient

Zone factor	$Z = 0.16$	(Table 3—IS 1893 (Part-I) 2016)
Importance factor	$I = 0.15$	(Table 8—IS 1893 (Part-I) 2016)
Response reduction factor	$R = 3.0$	(Table 9—IS 1893 (Part-I) 2016)
Avg. response acceleration coefficient	S_a/g	(Depends on natural time period of structure)

6.5 Design Methodology

The various components of the structure has been designed according to Indian standards. All the elements has been designed as per limit state of collapse and checked for limit state of serviceability. The structural members are designed for the critical load combinations furnished in Fig. 15.

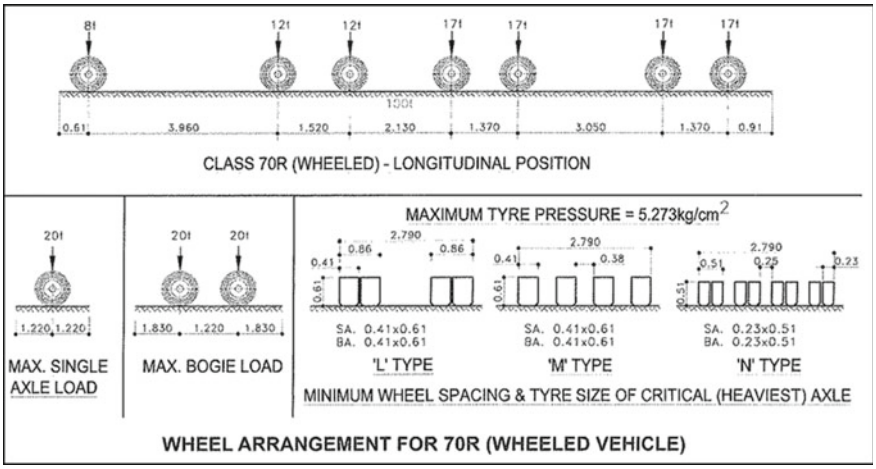

Fig. 14 Wheel arrangement for 70R wheeled vehicle

Table 1 Partial Load Factors for Loads in Limit State Design
(*Clauses* 5.1 and 7.1.2)

Sl No.	Loading	Partial Load Factor					
		Limit State of Serviceability		Limit State of Collapse			
		Short Term	Long Term	Normal	Extreme/ Survival	Temporary	Reversal
(1)	(2)	(3)	(4)	(5)	(6)	(7)	(8)
i)	Dead load (DL)	1.0	1.0	1.5	1.2	1.2	0.9
ii)	Vertical live load:						
	a) Impact or dynamic load (DyL)	1.1	0.5	1.5	1.2	1.2	0.9
	b) Static(LL)	1.0	0.5	1.5	1.2	1.2	0.9
iii)	Earth pressure (EP)	1.0	1.0	1.2	1.0	1.0	1.0
iv)	Hydrostatic force (HyF)	1.0	-	1.0	1.0	1.0	1.0
v)	Wave and current force (WL and CL)	1.0	-	1.2	1.0	1.0	1.0
vi)	Berthing force(BF)	1.0	-	1.5	1.0	-	1.5
vii)	Mooring force(MF)	1.0	-	1.5	-	-	1.5
viii)	Working wind force (WWiF)	1.0	-	1.0	-	-	-
ix)	Extreme wind force (EWiF)	-	-	-	1.2	-	1.5
x)	Shrinkage	-	1.0	-	-	-	-
xi)	Creep	-	1.0	-	-	-	-
xii)	Temperature (TempL)	-	1.0	-	-	-	-
xiii)	Seismic force (EL)	1.0	-	-	1.2	-	1.5
xiv)	Tsunami force (TL)	-	-	-	1.2	-	-
xv)	Secondary stresses (SS)	1.0	-	-	-	-	-

Fig. 15 Load combinations

6.6 Results of Analysis

The following results are obtained from P-δ analysis using STAAD Pro software. The structural members are designed for the moments and axial force given in Table 4.

Table 4 Result of analysis

S. No.	Members	Limit state of serviceability		Limit state of collapse	
		Axial force (kN)	Moment (kN m)	Axial force (kN)	Moment (kN m)
1	Pile	3484	1528.0	4434	1788.0
2	Main beam	58.7	3620	68.36	6910
3	Long beam	119.0	966	177	1570
4	Slab	–	125	–	170.5

Table 5 Required construction materials

Description	Unit	Option-I	Option-II
Liner	T	501	413
Boring	RM	3840	2560
Concrete	Cu.m	4532	4718
Steel	MT	1077	1044

7 Impact on Project Execution and Cost

- The pile, beam, and pile muff sizes are optimized to meet the project and design requirements as well as to reduce number of piles.
- Based on structural arrangement-I analysis and results, if beams of 1000 mm × 1200 mm are considered, three rows of 800 mm dia pile and pile muff of 1200 × 1200 × 450mm are required.
- As per structural arrangement-II, if beam size of 1000 mm × 1500 mm with spanning 12 m c/c considered, two rows of 1000 mm dia pile and pile muff of 3000 × 1500 × 600mm is required.

Table 5 shows the comparison of required construction materials between option-I and option-II.

8 Conclusion

- Two structural arrangement were considered for structural member size optimization. Also, the construction cost is taken into account for structural optimization.
- Structural arrangement-I: Beams of 1000 mm × 1200 mm, three rows of 800 mm dia pile, and pile muff of 1200 × 1200 × 450mm are required
- Structural arrangement-II: Beam size of 1000 mm × 1500 mm with spanning 12 m c/c, two rows of 1000 mm dia pile, and pile muff of 3000 × 1500 × 600mm are required.

- Structural arrangement-II is safe and robust as per design requirement and construction cost is reduced by 8% when compared to the Structural arrangement-I.
- The structural arrangement-II found to be cost effective
- Less execution time when compared to structural arrangement-I, reducing construction time by almost 6 months. Hence, structural arrangement-II is recommended.

Effect of Porous Curtain Wall on the Internal Hydrodynamics of an Offshore Intake Well

V. Prabu Kumar, R. Sundaravadivelu, and K. Murali

Abstract The purpose of offshore seawater intake is to provide a continuous supply of seawater with proper quantity and quality. The large volume and specified water quality requirements, offshore intake wells are preferred. The adequate and economical supply of seawater from the offshore intake well depends on the performance of the pumping system. In a typical intake well, the pumping equipment is placed below the water surface based on the free surface water oscillation inside the well. The loads exerted by the incoming waves and the free surface water oscillation will affect the pumping performance. This phenomenon should be reduced for smooth and efficient pumping operation. To achieve this, some auxiliary equipment like curtain wall is introduced into the intake well. This type of internal structure can regulate the flow and dissipate the incident wave energy up to some extent. Moreover, they can obstruct the formation of vortices and eddying. The present study focuses on the internal hydrodynamics of an offshore intake well with a porous curtain wall. A 1:20 scale model is tested with regular waves in the shallow wave basin and wave run-up, rundown, free surface water oscillation inside the well and the pressure acting on the curtain wall is measured. Then, the influence of the porosity on the free surface water oscillation is investigated by changing the porosity.

Keywords Offshore intake well · Wave run-up · Rundown · Curtain wall · Pressure force · Free surface water oscillation · Porosity

Notations

d	Water depth (m)
D	Outer diameter of the intake well (m)
T	Wave period (s)
L	Incident wavelength (m)

V. Prabu Kumar (✉) · R. Sundaravadivelu · K. Murali
Department of Ocean Engineering, Indian Institute of Technology Madras, Chennai 600036, India
e-mail: vprabuoptimist@gmail.com

V. Sundar et al. (eds.), *Proceedings of the Fifth International Conference in Ocean Engineering (ICOE2019)*, Lecture Notes in Civil Engineering 106,
https://doi.org/10.1007/978-981-15-8506-7_41

H Incident wave height (m)
H_{ic} Free surface water oscillation in the inlet chamber (m)
H_{pc} Free surface water oscillation in the pumping chamber (m)
k Wave number (2π/L)
R_u Wave run-up (m)
R_d Wave rundown (m)
P_{CF} Pressure on curtain wall front side (N/m^2)
P_{CB} Pressure on curtain wall back side (N/m^2)
P Porosity
H/d Relative water depth
d/L Relative water depth
H/L Wave steepness

1 Introduction

The seawater intake wells are the primary source of water to many coastal aligned industries for various purposes. In general, the intake wells are installed away from the shore in shallow or intermediate water depths. The interaction between the well and the incoming waves offers many design parameters like wave force, wave run-up, rundown, etc. The water surface oscillation inside the well plays a significant role in the continuous and efficient pumping. The wave forces and moments on a seawater intake well studied experimentally and found that the moment on the intake well increases due to the consequence of inlet opening [1]. The wave interactions with single and double vertical slotted barriers are numerically studied based on eigenfunction expansion and validated with the experimental outcomes [2, 3]. The vertical cylinder with perforated vertical and slotted barriers was experimentally investigated and showed that the wave force on the cylinder reduced when the relative wave height increased to the maximum value [4]. The physical modal study on a seawater intake caisson with perforated square caisson shows that the wave force ratios reduced up to 60% by increasing the porosity from 1.6 to 16.9% [5]. The predictive formulas were developed based on the experimental outcomes to compute the wave run-up on a circular cylinder with an outer perforated cylinder cover [6]. The experimental measurement of dynamic pressure on a single and twin vertical slotted wave barrier shows that the porosity influences the dynamic pressure near the free surface [7]. The double vertical slotted walls were used as effective wave energy-dissipating element and found that maximum wave reflection occurs compared to the wave transmission [8]. The wave run-up, rundown, and free surface water oscillation in a seaward offshore intake well were investigated through experiments and found that the free surface water oscillation in the pumping chamber is higher than the inlet chamber for the d/L range 0.26–0.105 [9].

This chapter discusses the study of internal hydrodynamics mainly focuses on the free surface water oscillation inside the seawater intake well with a porous curtain wall.

2 Experimental Arrangement

2.1 Test Model and Facilities

An offshore caisson-type intake well having a diameter of 25 m and height of 17 m is considered for the model study. The intake well is installed at a depth of 11 m and exposed to breaking and non-breaking waves in the field. A concrete central wall divides the well into two half-sections. The incoming waves enter into the well inlet chamber through the inlet openings and directed to the pumping chamber. Each section has a pump with pumping capacity 45,000 m^3/h. The modal studies were carried out in the shallow wave basin located at Department of Ocean Engineering, IIT Madras, India. The size of the shallow basin is 17 m × 15 m × 1.0 m. A piston-type wavemaker connected with LVDT actuators which is controlled by a computer can generate random and regular waves. The maximum working water depth is 0.6 m, and the wave period can be changed from 1 to 3 s. The wave height can be generated in the range 0.03–0.4 m in both the wave climates. The resistance-type wave probes and run-up gauges are used to capture the field values. The data accession is done by a dedicated computer system which gets input from the sensors through wavemeter and eight-channel spider system.

2.2 Experimental Setup

A 1:20 scale is selected to fabricate the intake well model based on the available facility limitations. A water depth 0.55 m is maintained as constant, and the incident wave height is changed from 0.05 to 0.15 m with a 0.025 m interval. The d/L value ranges from 0.105 to 0.36. The regular waves were generated in the wave period range 1–2.4 s with an interval of 0.2 s. The H/d ranges from 0.091 to 0.273. Figure 1a shows the illustrative plan view of the shallow wave basin with the intake well, and Fig. 1b shows the detailed experimental setup with the instruments. The wave probe 1 (WP1) measures the incident wave height.

The run-up gauges RG1, RG2, RG3, and RG4 fixed around the outer wall of the well measure the wave run-up and rundown. The wave probes WP2, WP3, WP4, and WP5 fixed in well inside measure the free surface water oscillation. The pressure sensors set on the curtain wall measures the pressure values when the incoming wave interacts with the curtain wall. Figure 2 shows the layout of the curtain wall with different porosities. The curtain wall of size 280 × 450 mm with two different

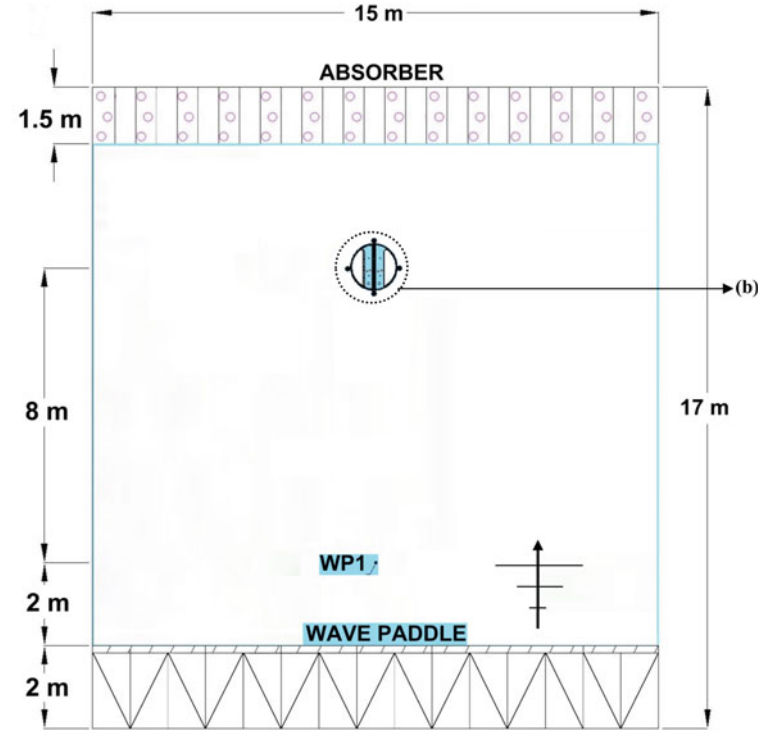

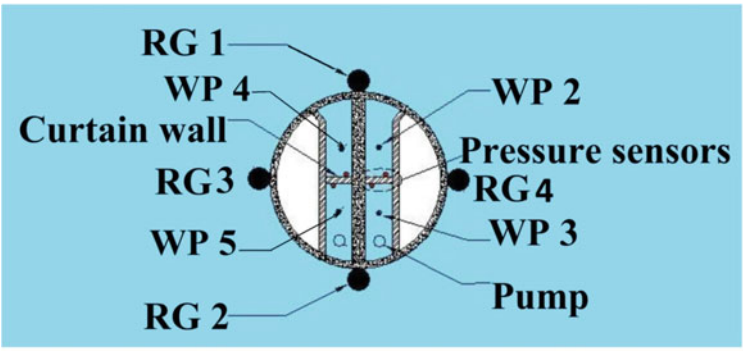

Fig. 1 Demonstrative plan view **a** the shallow wave basin; **b** the intake well with the instrumentation

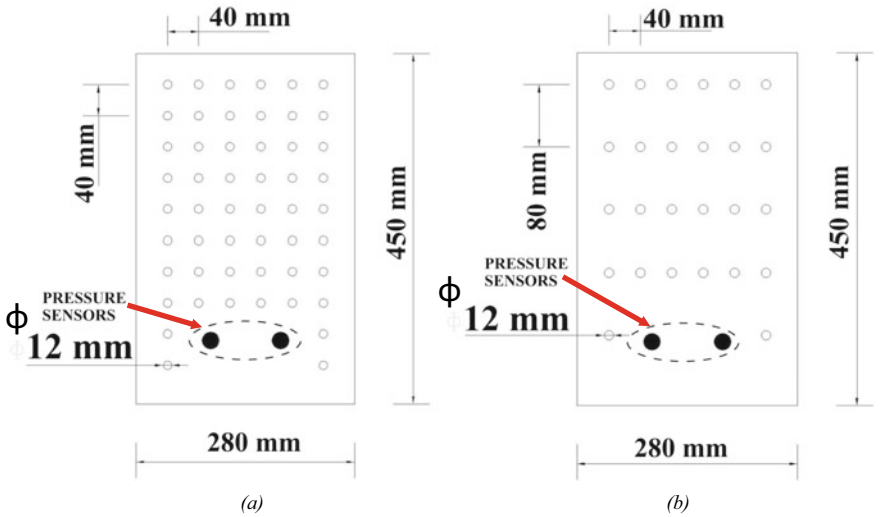

Fig. 2 Layout of the porous curtain wall **a** $P = 9.34\%$; **b** $P = 18.7\%$

porosities is inserted before the pump. The diameter of the porous hole kept constant as 12 mm, and the porosity is changed by increasing the vertical spacing between the holes.

Figure 3a shows the experimental setup of an offshore intake well in the shallow wave basin with instruments, and Fig. 3b shows the detailed inner section of the intake well. The run-up gauges are located around the well such that the incident wave angle is 0° (RG1), 90° (RG3), 180° (RG2), and 270° (RG4). Two wave probes

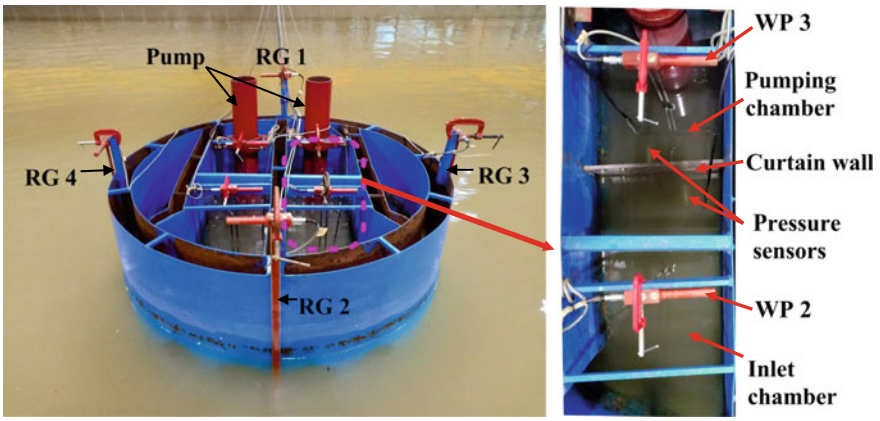

Fig. 3 Experimental setup **a** intake well; **b** detailed view of the inner section

and two pressure transducers are fixed in each section to measure the free surface water oscillation and the pressure on the front and backside of the curtain wall.

3 Results

3.1 Wave Run-Up

The non-dimensional wave run-up profile around the intake well is shown in Fig. 4. The wave run-up on the front side records maximum compared to the other three faces and is highly sensitive to the H/d values. Besides, the run-up on the front side reaches peak value whereas on the backside it reaches the minimum for the maximum d/L value. Moreover, the H/d values do not have a significant influence on wave run-up values on the side faces.

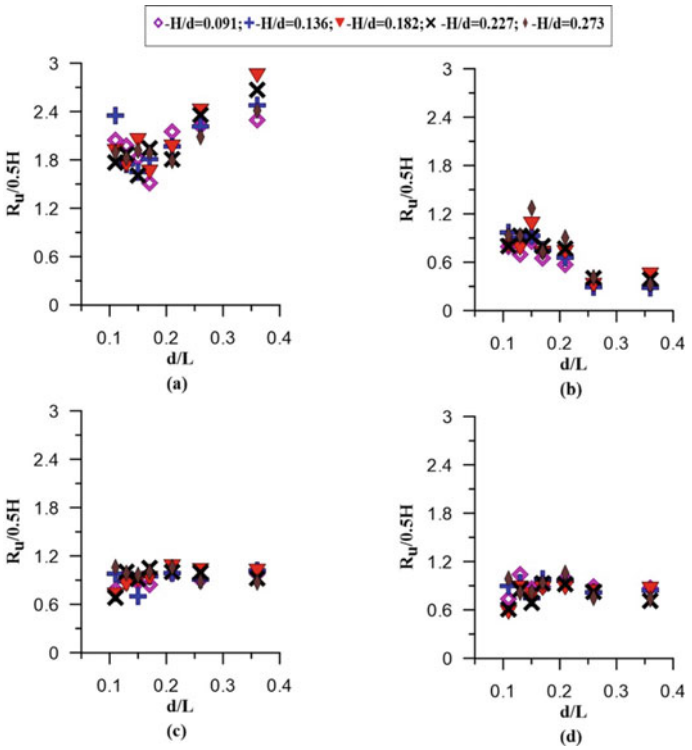

Fig. 4 Non-dimensional wave run-up profile with d/L **a** seaward face; **b** shoreward face; **c** right side face; **d** left side face

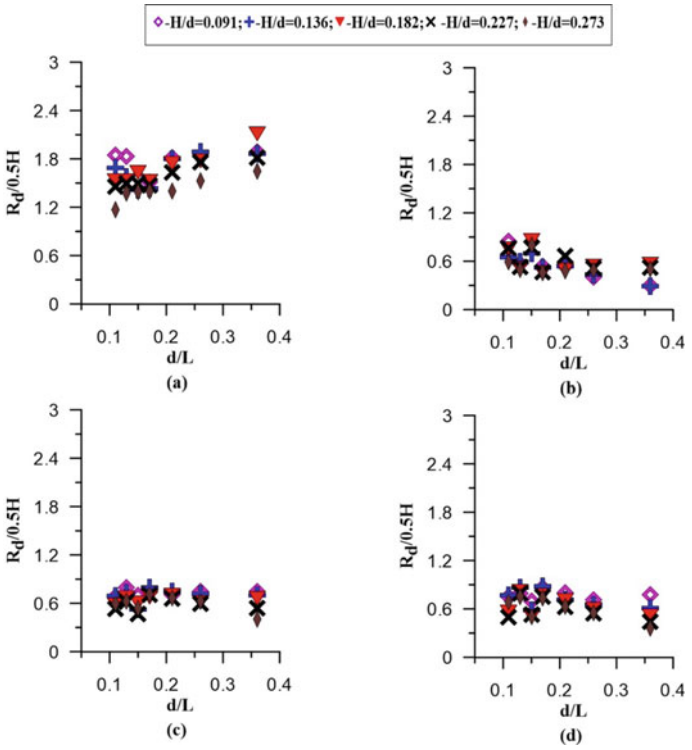

Fig. 5 Non-dimensional wave rundown profile with *d*/*L* **a** seaward face; **b** shoreward face; **c** right side face; **d** left side face

3.2 Wave Rundown

Figure 5 shows the non-dimensional wave rundown profile with *d*/*L* values. The rundown values on the front side increases when the *d*/*L* value approaches to the maximum value while it reaches a minimum on the backside of the well. The rundown on the front side measures minimum when the *H*/*d* is 0.273 for the *d*/*L* range 0.105–0.36. However, the rundown on the side faces has less sensitive to the *H*/*d* values compared to the front face.

3.3 Internal Free Surface Water Oscillations

The free surface water oscillation in the inside well is an influencing parameter of pumping performance. Also, the location of the pumping unit below the free surface water level is fixed based on the inside water oscillation. Figure 6 shows the comparison of the free surface water oscillation at the inlet chamber with a porous

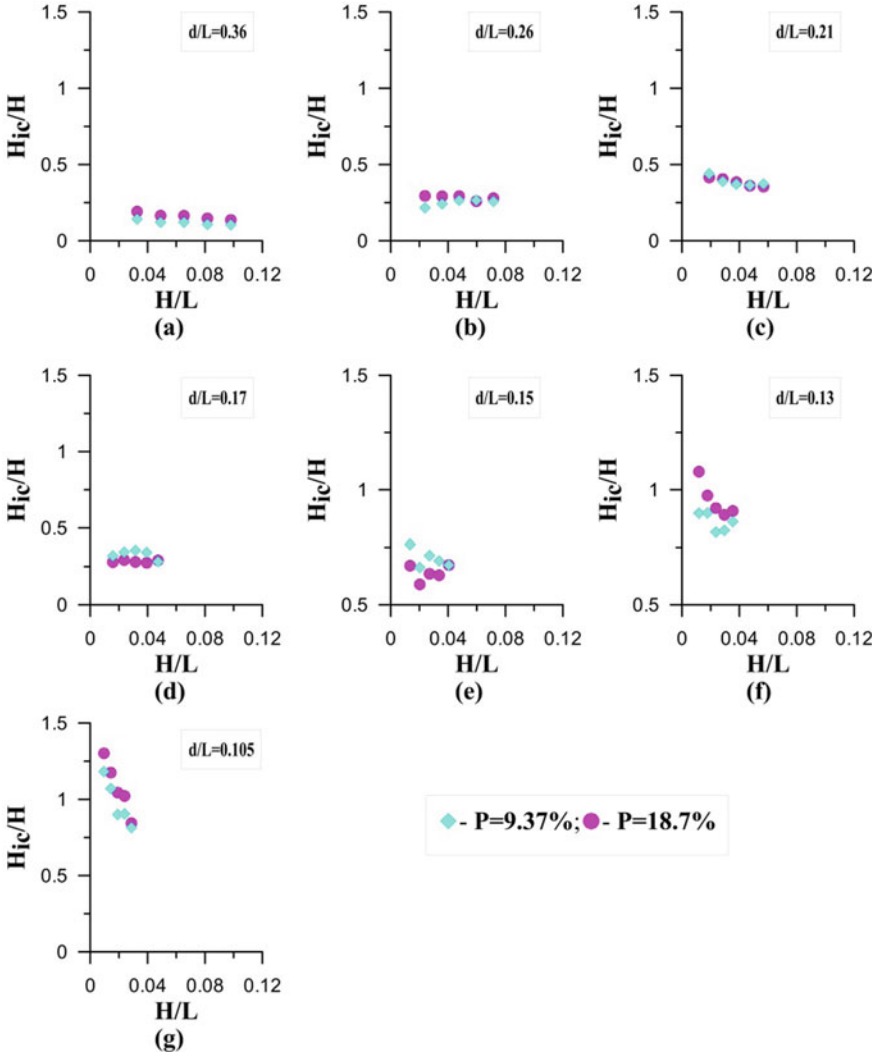

Fig. 6 Comparison of the free surface water oscillation at the inlet chamber for different *d*/*L* values

curtain wall with different porosities. The free surface water oscillation is decreasing with increase in *H*/*L* values for all *d*/*L* values in both cases. Also, it reaches a minimum when the curtain wall porosity is 9.37% for the *d*/*L* values 0.36 and 0.105.

Figure 7 shows the free surface water oscillation at the pumping chamber with *H*/*L*. The free surface water oscillation is decreasing with increase in *H*/*L* value. However, it is increasing when the *d*/*L* approaches to the minimum for all the cases. The curtain wall with 9.37% porosity results in minimum free surface water oscillation for the *d*/*L* range of 0.21–0.36.

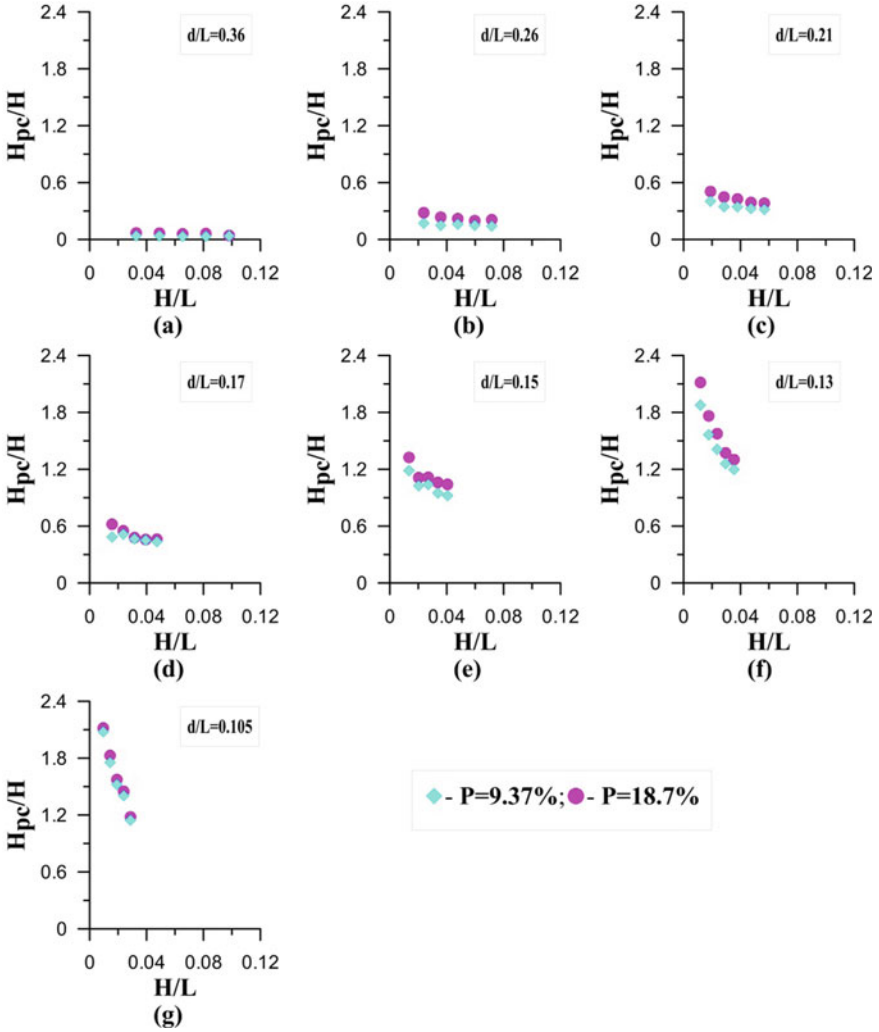

Fig. 7 Comparison of the free surface water oscillation at the pumping chamber for different *d*/*L* values

3.4 The Pressure Acting on the Curtain Wall

The comparison of the normalized pressure acting on the front side of the curtain wall is shown in Fig. 8. The porosity does not have a significant influence on the front-side pressure for the *d*/*L* range 0.36–0.21. Besides, the pressure value measures nearly the same values for all *H*/*L* ranges when the *d*/*L* varies from 0.36 to 0.21. However, the pressure on the front side keeps on increases with decreases in *d*/*L* value, and it

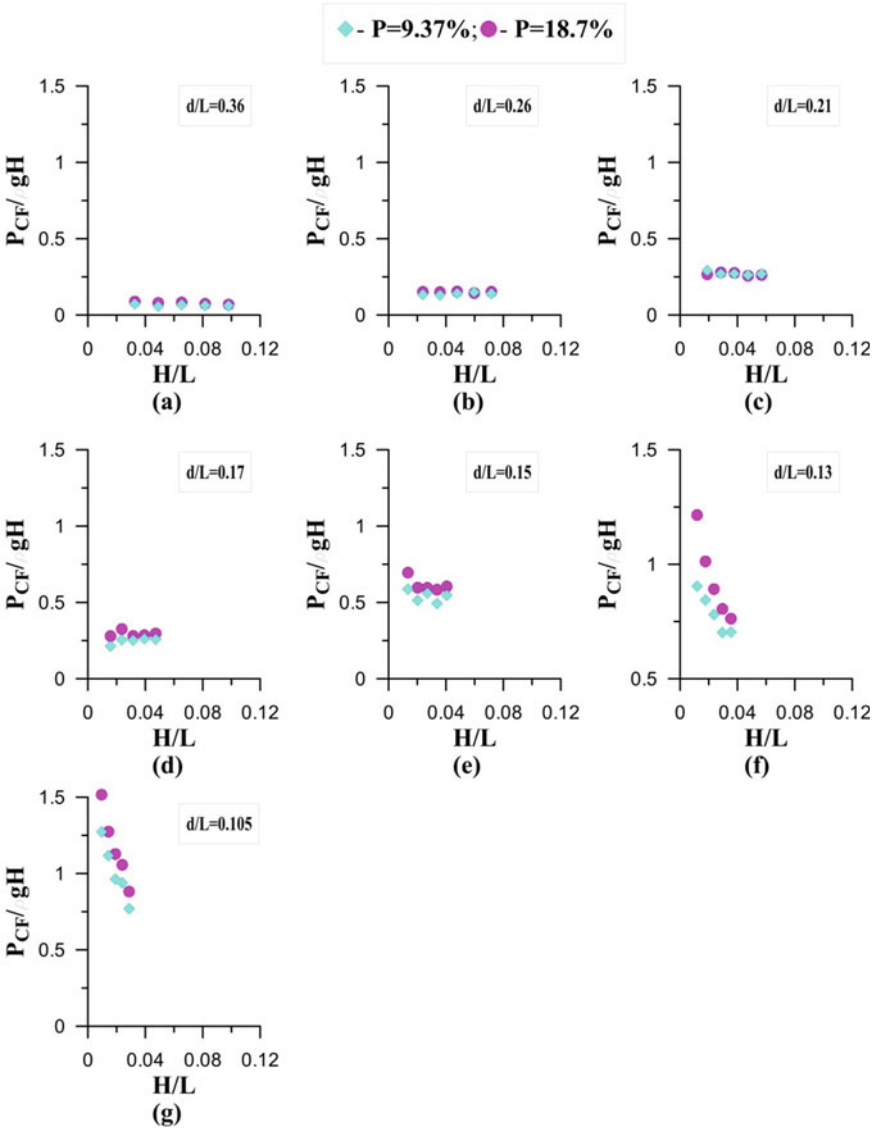

Fig. 8 Comparison of the relative pressure on the front side of the porous curtain wall for different *d*/*L* values

records the maximum for lower *H*/*L* values for all *d*/*L* values. Moreover, the curtain wall with 9.37% porosity measures minimum pressure in the *d*/*L* range 0.17–0.105.

Figure 9 shows the comparison of the relative pressure measured on the backside of the porous curtain wall. The pressure is insensitive to the porosity and estimates the same value for when the *d*/*L* is 0.36. It implies that for short wave periods,

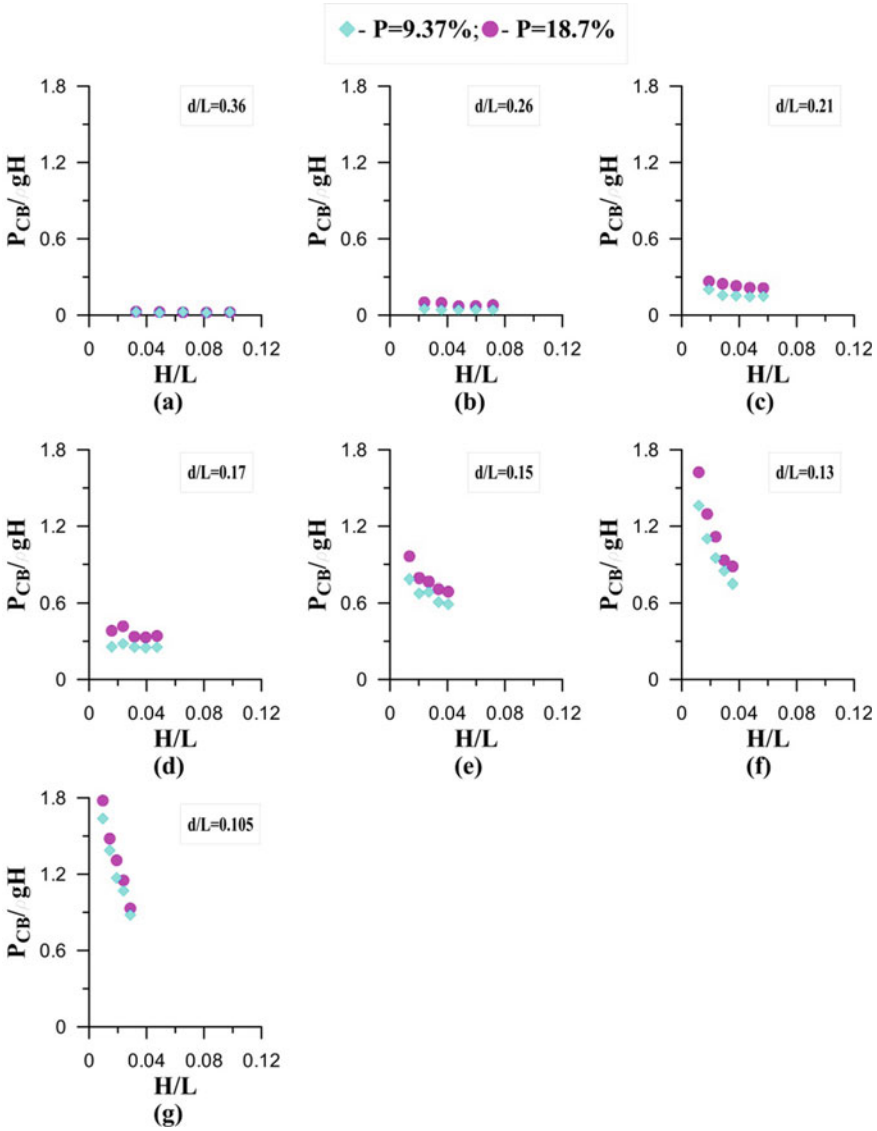

Fig. 9 Comparison of the relative pressure on the backside of the porous curtain wall for different *d*/*L* values

the porosity does not have a significant influence on the pressure values. However, the backside pressure increases when the *d*/*L* decreases from 0.36 to 0.105. Thus, longer wave exerts more pressure on the curtain wall. The pressure on the backside is minimum for the porosity value of 9.37% in the *d*/*L* range 0.26–0.105.

4 Conclusion

An offshore intake well with porous curtain wall is experimentally investigated in a regular wave environment. The porosity of the curtain wall is maintained as 9.37 and 18.4%, and its influence on the internal free surface oscillation is studied. The conclusions are summarized as follows.

1. The wave run-up and rundown values on the well front face are maximum and influenced by the H/d values compared to the other faces.
2. The wave rundown on the front face measures minimum value when the H/d is 0.273 for the d/L range 0.105–0.36.
3. When the porosity is 9.37%, the free surface water oscillation at the inlet chamber is minimum for the d/L values 0.36 and 0.105, whereas at the pumping chamber, it is minimum for the d/L range 0.36–0.21.
4. The free surface oscillation is increasing when the H/L and d/L values approach to minimum values.
5. The pressure on the front and backside keep on increasing with wave steepness, and relative water depth approaches to the minimum value.
6. The curtain wall with 9.37% porosity measures minimum pressure on the front side in the d/L range 0.17–0.105 whereas on the backside in the d/L range 0.26–0.105.

References

1. Sundaravadivelu R, Sundar V, Surya Rao T (1999) Wave forces and moments on an intake well. Ocean Eng 26:363–380
2. Isaacson M, Premasiri S, Yang G (1998) Wave interactions with vertical slotted barrier. J Waterway Port Coast Ocean Eng 124(3):118–126
3. Isaacson M, Baldwin J, Premasiri S, Yang G (1999) Wave interactions with double slotted barrier. Appl Ocean Res 21:81–91
4. Neelamani S, Muni Reddy MG (2002) Wave forces on a vertical cylinder defended by a perforated vertical and inclined barriers. Indian J Marine Sci 31(3):179–187
5. Neelamani S, Uday Bhaskar N, Vijayalakshmi K (2002) Wave forces on a seawater intake caisson. Ocean Eng 29:1247–1263
6. Vijayalakshmi K, Neelamani S, Sundaravadivelu R, Murali K (2007) Wave runup on a concentric twin perforated circular cylinder. Ocean Eng 34:327–336
7. Alkhalidi M, Neelamani S, Haj Assad AI (2015) Wave pressures and forces on slotted vertical wave barriers. Ocean Eng 108:578–583
8. Yueh C-Y, Chih-Hao S, We C-C, Chuan S-H (2016) Analysis of wave interaction with double vertical slotted walls using MBEM. J Marine Sci Technol 24(5):992–1002
9. Prabu Kumar V, Sundaravadivelu R, Murali K (2018) Experimental wave run-up on seaward offshore intake well with regular waves. In: Proceedings of international conference on computational and experimental marine hydrodynamics MARHY 2018. Indian Institute of Technology Madras, Chennai, pp 175–183

Surf-riding and Broaching—A Numerical Investigation on the Vulnerability of Ships

Suresh Rajendran and A. S. Ameer Hassan

Abstract International Maritime Organization's (IMO) recent discussion on the development of second-generation intact stability criterion has emphasized on the instability problems like surf-riding and broaching of ships. Surf-riding and broaching occur when a ship rides in astern seas with the ship velocity close to the wave celerity. It results in loss of stability, sometimes even leading to capsizing. Rudder becomes ineffective in these conditions and ship may lose its manoeuvring abilities. A ship's vulnerability towards surf-riding and broaching is investigated using a numerical method. The numerical method based on strip theory calculates the Froude–Krylov and hydrostatic force for instantaneous wave profile. The numerical study is conducted on the ITTC A2 fishing vessel in regular astern waves and is compared with the measured ones available from the literature.

Keywords Surf-riding and broaching · Loss of stability · Regular astern waves

1 Introduction

A ship in following or stern quartering seas may capsize due to mainly three reasons (1) parametric rolling, (2) pure loss of stability in waves and (3) due to broaching. Parametric rolling happens when the wave period is about half of the roll period, and the wave height is above a threshold limit. The metacentric height of a slender ship with pronounced bow flare reduces when it encounters wave a crest at the midship and troughs at both ends. This results in a reduction in the water plane area which results in the reduction of the metacentric height. On the other side, the metacentric height increases when it encounters the wave trough at amidship. This sets the ship in rolling motion which on resonating with the rolling period of the ship results in parametric rolling. Even though the pure loss of stability in waves and broaching are instability problems like parametric rolling, these are not ship resonance problem like

S. Rajendran (✉) · A. S. Ameer Hassan
Indian Institute of Technology Madras, Chennai, India
e-mail: sureshr@iitm.ac.in

V. Sundar et al. (eds.), *Proceedings of the Fifth International Conference in Ocean Engineering (ICOE2019)*, Lecture Notes in Civil Engineering 106,
https://doi.org/10.1007/978-981-15-8506-7_42

parametric rolling. However, the cause of these problems is similar to the parametric rolling.

Pure loss of stability in waves happens when a large and steep wave hits the ship from the aft. In this case, the wave celerity and the ship speed should be close enough so that the ship rides on the wave crest for a longer time. It results in a reduction in the water plane area and the metacentric height. This phenomenon is purely non-oscillatory, and the ship avoids the risk of capsizing once the steep wave passes. Broaching can also be defined as instability in the steering of the ship. The ship encounters large yaw angle in following waves which cannot be easily corrected by the rudder. Because of this diverging yaw, the ship's orientation changes to beam sea condition and experiences severe rolling which may lead to capsize. Surf-riding is considered to be a prerequisite for broaching. Surf-riding is a phenomenon in which a ship is captured and carried away by a wave. In this condition, the propeller thrust along with the wave surging force enables the ship to move at a higher speed and matches up with the wave celerity.

In the past, many researchers have studied the ship instability problem in stern quartering seas based on (1) theoretical solutions using nonlinear dynamics [1–3], (2) numerical hydrodynamic models [4, 5] and (3) experiments [6]. In this paper, a numerical time domain method is used to predict the instability of a fishing vessel in stern quartering seas. The simulations are carried out for different Froude number and wave headings. The results are compared with the experimental results available with the literature [6] and Sample ship data.

2 Numerical Program

A 6 DoF time domain numerical method based on strip theory is used for calculation of the ship behaviour in regular waves. Surge motion is calculated based on a semi-empirical method, Rajendran et al. [7], 8. Two kinds of frame of reference are followed: (1) an inertial frame which moves with the steady velocity of the ship and fixed on the mean water level and in line with the centre of gravity of ship in static equilibrium position and (2) a body frame fixed on the body and translates and rotates with the ship. The radiation and diffraction forces are assumed to be linear. The Froude–Krylov and restoring forces are considered to be body nonlinear and are calculated for the exact wetted surface. The incident wave motion is represented in the inertial frame. The ship position relative to the incident wave (in the inertial frame) is calculated for the estimation of instantaneous wetted surface area, and associated forces are then transformed into the body coordinates. The equation of motion is solved in the body frame, and the coordinate transformation between the inertial and the body frame is carried out by means of Euler angle.

The time domain model consists of manoeuvring modules, i.e. rudder, propeller, hydrodynamic derivatives in calm water. Rudder forces are calculated based on Son and Nomoto model [9]. In our chapter, ITTC A2 fishing vessel is used for simulating the ship responses. The vessel is used to analyse the capability of the developed time

domain method to predict the instability of the ship in astern waves. The ship data and the corresponding experimental data are publicly available (sample ship data-see reference). The parameters associated with the calm water resistance, propeller thrust, rudder and the hydrodynamic derivate calculations are selected from the publicly available report.

The nonlinear 6 DoF equation of motion can be written as [10], 11.

$$M\dot{V} + CV = F \tag{1}$$

where M, C, F and V are the inertia matrix, matrix associated with centripetal force, the exciting force acting on the body and the generalized velocity expressed as a column matrix $\{uvwpqr\}^T$, respectively. The exciting forces include both the seakeeping and the manoeuvring forces. The seakeeping module includes Froude–Krylov, diffraction, radiation and restoring forces and the manoeuvring module includes rudder, propeller, calm water resistance and viscous forces.

3 Ship and Wave Data

The ITTC A2 fishing vessel (sample ship data-see Ref. [12]) is used for the numerical simulation, and the results are compared with experimental results available in the report. The main particulars of the vessel are given below. Further details of the vessel can also be found in Umeda et al. [6] (Table 1).

The model (1:15 scale) was tested in a wave basin in stern quartering regular waves and for a range of Froude number, Umeda et al. [6]. The numerical simulation is carried out for the same sea states, and the results are compared with the measured responses. The model was tested in regular waves of height 4.47 and 5.65 m with

Table 1 Main particulars of the ship

Length between perpendiculars, L_{pp}(m)	34.5
Breadth, B(m)	7.60
Depth, D(m)	3.07
Fore draught, T_f (m)	2.5
Aft draught, T_a (m)	2.8
Mean draught, T(m)	2.65
Block coefficient, C_B	0.597
Radius of gyration, roll, k_{xx}/L_{pp}	0.108
Radius of gyration, pitch yaw, k_{yy}/L_{pp}, k_{zz}/L_{pp}	0.302
Longitudinal position of buoyancy, LCB(m)	1.31 m aft
Longitudinal position of floatation, LCF(m)	3.94 m aft
Metacentric height, GM(m)	1.00

Table 2 Incident wave characteristics and ship speed

Case	H (m)	λ (m)	λ/L_{PP}	ω (rad/s)	T (s)	Heading	Fn	ω_e (rad/s)
1	4.47	38.88	1.127	1.34	4.69	15	0.15	0.85
2	4.47	38.88	1.127	1.34	4.69	15	0.3	0.36
3	4.47	38.88	1.127	1.34	4.69	15	0.43	-0.06
4	4.47	38.88	1.127	1.34	4.83	30	0.15	0.9
5	4.47	38.88	1.127	1.34	4.83	30	0.3	0.47
6	4.47	38.88	1.127	1.34	4.83	30	0.43	0.08
7	5.65	56.48	1.637	1.09	5.74	15	0.15	0.77
8	5.65	56.48	1.637	1.09	5.74	15	0.3	0.44
9	5.65	56.48	1.637	1.09	5.74	15	0.43	0.16
10	5.65	56.48	1.637	1.09	5.74	30	0.15	0.8
11	5.65	56.48	1.637	1.09	5.74	30	0.3	0.51
12	5.65	56.48	1.637	1.09	5.74	30	0.43	0.26

respective periods 4.69 and 5.74 s. The wave to ship length ratio for these waves are found to be 1.127 and 1.637. The wave frequency is calculated considering the nonlinearity of waves, i.e. $w^2 = gk(1 + k^2a^2)$ [13]. Table 2 gives a detailed description of the test conditions.

4 Results

The numerical simulation is conducted for the 12 cases given in Table 2. The numerical results are compared with experimental ones given by Umeda et al. [6]. The summary on the comparison of the results is given in Table 3. For low Froude number, i.e. Fn = 0.15 and 0.3, the vessel always undergoes periodic motion in both numerical and experimental simulations. The periodic motion of the vessel obtained from numerical is shown in Figs. 1 and 2, respectively, for case 5 and 11 Table 2. For case 5 and 11, the vessel is moving with 0.3 Froude number and encounters waves at 30° heading. Similar kind of numerical responses is obtained for lower Froude number (i.e. 0.15) and wave headings of 15° and 30°.

For case 3, when the heading is 15°, the ship capsizes in the numerical simulation due to broaching Table 3. However, the numerical prediction does not match exactly with the experimental results, where the ship undergoes broaching without capsizing. For the same Froude number, i.e. 0.43, the vessel undergoes different kinds of instability problem in 30° heading (case 6). For case 6, Fig. 3 shows that the vessel is subjected to loss of stability on a wave crest due to insufficient metacentric height. The wave elevation given in figures is with reference to the inertial frame that steadily translates with the ship. When the wave crest is close to the midship,

Table 3 Comparison between the numerical and the experimental results

Case	H (m)	λ (m)	ω (rad/s)	Heading	Fn	ω_e (rad/s)	Experiment	Numerical
1	4.47	38.88	1.34	15	0.15	0.85	Periodic	Periodic
2	4.47	38.88	1.34	15	0.3	0.36	Periodic	Periodic
3	4.47	38.88	1.34	15	0.43	-0.06	Broaching without capsize	Capsize due to broaching
4	4.47	38.88	1.34	30	0.15	0.9	Periodic	Periodic
5	4.47	38.88	1.34	30	0.3	0.47	Periodic	Periodic
6	4.47	38.88	1.34	30	0.43	0.08	Loss of stability on a wave crest	Loss of stability on a wave crest
7	5.65	56.48	1.09	15	0.15	0.77	Periodic	Periodic
8	5.65	56.48	1.09	15	0.3	0.44	Periodic	Periodic
9	5.65	56.48	1.09	15	0.43	0.16	Capsize due to broaching	Capsize due to broaching
10	5.65	56.48	1.09	30	0.15	0.8	Periodic	Periodic
11	5.65	56.48	1.09	30	0.3	0.51	Periodic	Periodic
12	5.65	56.48	1.09	30	0.43	0.26	Periodic	Periodic

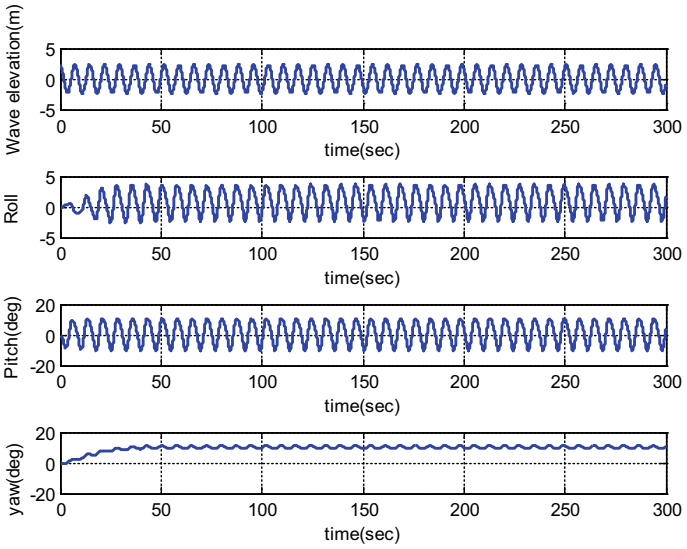

Fig. 1 Time series of the wave elevation and ship responses in a wave of wave height of 4.47 m, wave length of 38.88 m with a heading angle of 15° and for 0.15 Froude number (Case 1)

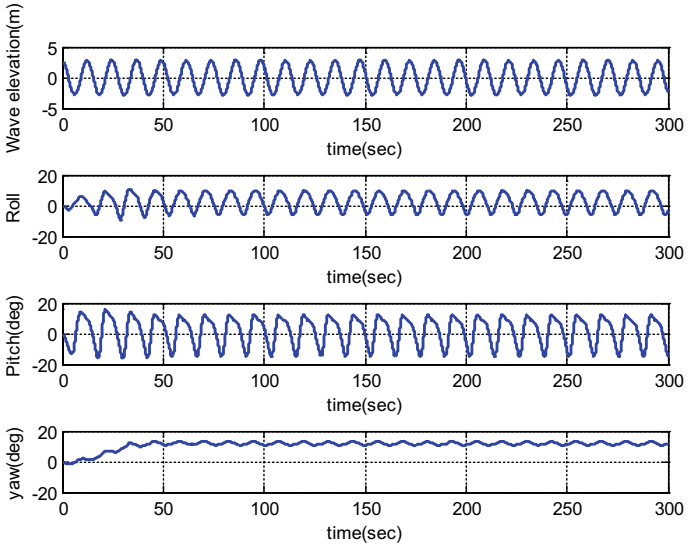

Fig. 2 Time series of the wave elevation and ship responses in a wave of wave height of 5.65 m, wave length of 56.48 m with a heading angle of 30° and for 0.30 Froude number (Case 11)

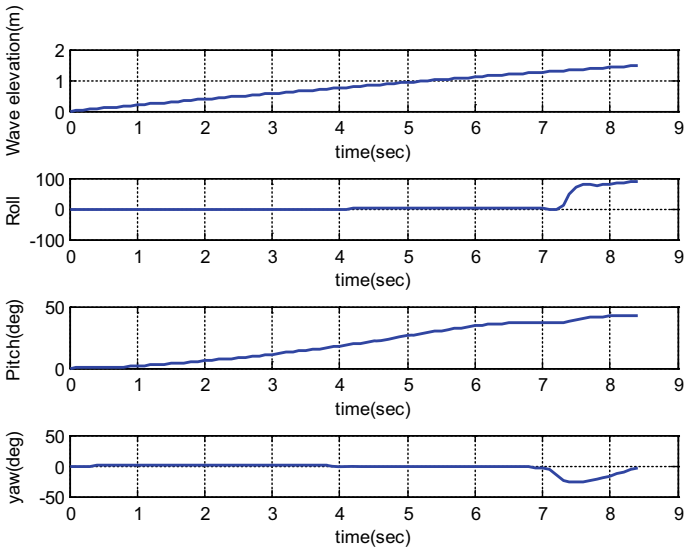

Fig. 3 Time series of the wave elevation and ship responses in a wave of wave height of 4.47 m, wave length of 38.88 m with a heading angle of 30° and for 0.43 Froude number (Case 6)

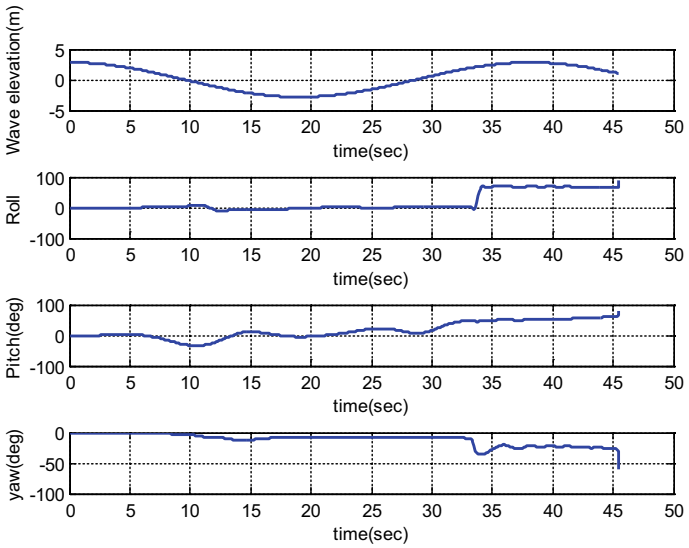

Fig. 4 Time series of the wave elevation and ship responses in a wave of wave height of 5.65 m, wave length of 56.48 m with a heading angle of 15° and for 0.43 Froude number (Case 9)

the ship loses its stability, and the roll angle becomes very high, and subsequently, the vessel capsizes.

For case 9 Fig. 4, i.e. in higher wave height and longer waves, after 45 s, ship undergoes broaching and capsizes (yaw and roll angle shoots up). Here, the numerical result matches with the experiment. For case 12, Table 3, for which the wave height is same as case 9 but encountering frequency is higher, the vessel is stable and undergoes periodic motion in both the numerical and experimental results.

As depicted in the plots, regular periodic motions can be captured at lower Froude numbers such as 0.15 and 0.30. At higher Froude numbers such as 0.43, loss of stability and capsize due to broaching is captured. During capsizing due to broaching phenomenon Fig. 4, the ship tends to make a constant pitch value for a particular time duration. This can be considered as surf-riding. Eventually, the ship's roll and yaw amplitude go beyond the limit and the ship capsizes. In general, it is concluded that that the vessel undergoes instability when the encountering frequency is low, i.e. the ship velocity is close to the wave velocity. For higher encountering frequencies, the vessel undergoes periodic motion. The comparison between the numerical and the experimental results are generally good and the numerical method is able to predict the behaviour of the vessel accurately.

5 Conclusion

A numerical time domain method is used for calculating the instability of a fishing vessel in astern seas. The numerical method combines the seakeeping and manoeuvring modules. The simulations are conducted in regular waves for different speed and headings. The ship undergoes periodic motion for higher encountering frequencies, i.e. when the waves are travelling faster than ships. However, for low encountering frequencies, the vessel undergoes different kinds of instability problem like loss of stability on a wave crest, broaching and capsizing due to broaching. On comparison with the experimental results, it was found that the numerical calculations are able to predict these instabilities accurately except for one of the cases.

References

1. Belenky V, Bassler C, Spyrou K (2011) Development of second generation intact stability criteria, NSWCCD-50-TR-2011/065
2. Motora S, Fujino M, Koyonagi M, Ishida S, Shimada K, Maki T (1981) A consideration on the mechanism of occurrence of broaching-to phenomena. JSNA 150
3. Umeda N (1998) New remarks and methodologies for intact stability assessment. In: 4th international ship stab. workshop, St. Johns
4. de Kat JO, Pinkster D-J, McTaggart KA (2002) Random waves and capsize probability based on large amplitude motion analysis. ASME Conf Proc 36142:685–694
5. Yu L, Ma N, Gu X (2014) Numerical investigation into ship stability failure events in quartering seas based on time domain weakly nonlinear unified model. In: Proceedings of the 14th international ship stability workshop. Kuala Lumpur, pp 229–235
6. Umeda N, Matsuda A, Hamamoto M et al (1999) Stability assessment for intact ships in the light of model experiments. J Mar Sci Technol 4:45–57
7. Rajendran S, Fonseca N, Guedes Soares C (2015) Effect of surge motion on the vertical responses of ships in waves. Ocean Eng 96:125–138
8. Rajendran S, Fonseca N, Guedes Soares C (2015) Simplified body nonlinear time domain calculation of vertical ship motions and wave loads in large amplitude waves. Ocean Eng 107:157–177
9. Son K, Nomoto K (1981) On the coupled motion of steering and rolling of a high speed container ship. J Society Naval Arch Japan 1981(150):232–244
10. Fossen TI (2011) Handbook of marine craft hydrodynamics and motion control. Wiley
11. Sutulo S, Guedes Soares C (2011) Mathematical models for simulation of manoeuvring performance of ships. In: Guedes Soares C, Garbatov Y, Fonseca, Teixeira AP (eds) Marine technology and engineering. Taylor & Francis Group, London, pp 661–698
12. Sample ship data sheet: ITTC A2 fishing vessel: Available online at https://www.naoe.eng.osaka-u.ac.jp/imo/a2
13. Newman JN (1977) Marine hydrodynamics, MIT Press, Cambridge, pp 247–251

Optimization of Gap-to-Chord Ratio of Wells Turbine with Guide Vanes for Wave Energy Conversion

F. A. Varghese and A. Samad

Abstract Wells turbine (WT) used for harnessing wave energy has narrow operating range and poor starting characteristics. To enhance its starting and running characteristics, guide vanes (GV) are installed upstream and downstream of the rotor. This paper studies the effect of the gap-to-chord (G/l_r) ratio of the WT GV on the turbine performance numerically. The work incorporates validation of the numerical simulations with experimental results and application of optimization techniques to find the optimal G/l_r ratio. A range for G/l_r ratio is suitably selected for the analysis and metamodel based on Kriging algorithm is developed. Following this, the optimization algorithm of screening is utilized to find the optimal conditions to achieve the objective function.

Keywords Wells turbine · Guide vanes · CFD · Optimization · Metamodel

1 Introduction

Oceans are an extensive source of energy. Waves and tides are of very large potential. It could be harnessed suitably to cater to the growing energy demand. The unpredictable nature of the oceans makes the process cumbersome. However, several technologies for marine energy conversion have been developed over the years. Oscillating water column (OWC)-based systems are the most promising of the wave energy conversion devices. It uses an impulse or a reaction turbine for power conversion. Wells turbine (WT) is a self-rectifying reaction turbine used for the wave energy conversion. It possesses symmetrical airfoil blades fitted around a hub. It has a stagger angle of 90°. The angles of attack of the fluid flow during the starting conditions are low. It results in poor starting characteristics and high axial force. However, the peak

F. A. Varghese (✉) · A. Samad
Department of Ocean Engineering, Indian Institute of Technology Madras, Chennai, India
e-mail: francisamalvarghese@gmail.com

A. Samad
e-mail: samad@iitm.ac.in

V. Sundar et al. (eds.), *Proceedings of the Fifth International Conference in Ocean Engineering (ICOE2019)*, Lecture Notes in Civil Engineering 106,
https://doi.org/10.1007/978-981-15-8506-7_43

efficiency of a WT is greater than that of an impulse turbine. Also, the simplicity in construction and less mechanical parts because of its self-rectifying nature makes it easier to install and operate. Another limitation of WT is its limited operating range caused by flow separation at high angles of attack.

The use of guide vanes (GV) before and after of the rotor is reported to improve the starting and running characteristics. Takao et al. [1] and Thakker and Hourigan [2] reported that the presence of GV could enhance the turbine efficiency. Sturge [3] Gato and Falcao [4] and Suzuki and Arakawa [5] did a theoretical performance study on the WT with GV. Also, Inoue et al.[6] Arakawa et al.[7] and Gato and Falcao [4] carried out an experimental investigation of WT with GV. Govardhan and Dhanasekaran [8] investigated the effect of GV with variable and constant chord WT rotors. The presence of GV improved the angle of attack at the pressure side of the rotor during starting.

The downstream GV enhanced the recovery of kinetic energy in the swirl component from the exit of the rotor blade. Govardhan and Chauhan [9] carried out a numerical study on the performance of the WT with GV. Computational fluid dynamics (CFD)-based analysis of the turbine was found in agreement with the prediction from the experiments. They reported that the inlet guide vane (IGV) led to the generation of tangential velocity and the downstream guide vane (DGV) led to the recovery of exit kinetic energy. The flow through the turbine is influenced by the mutual interference between the rotor and GV. Setoguchi et al.[10] investigated the effect of the gap between the rotor and GV experimentally. They reported that the optimum gap-to-chord ratio (G/lr) for the is 0.433. It was also found that smaller the gap, the starting characteristics improve. According to previous studies, it was seen that the performance of the WT is improved by introducing GV. Setoguchi et al. [11] carried out an experimental study on the influence of guide vane shape on the performance of WT.

In the past, trial and error methods were generally used for finding the optimal parameters. Of late, mathematical optimization algorithms are being used. Metamodelling is one of the most popular optimization methods used in the research arena. It helps in reducing the time required for the optimization by curtailing the number of CFD simulations to be carried out. In complex flow problems involving three-dimensional geometries like turbines and compressors, CFD solvers take a longer time. In such cases, the metamodels quicken the optimization process with good accuracy. Badhurshah and Samad [12] performed multiple metamodel-based optimization of a bidirectional impulse turbine. Halder et. al [13] performed numerical optimization of WT using a weighted-average metamodel-based genetic algorithm.

In the present work, the effect of the G/l_r ratio between the rotor and guide vane is studied using optimization techniques and numerical simulations. This work highlights the use of CFD simulations coupled with optimization techniques to analyze the performance of the WT for different G/l_r ratios.

2 Computational Methodology and Optimization

2.1 Problem Description

The WT is a self-rectifying air turbine possessing symmetrical airfoil blades arranged around the hub. The turbine rotor blade and the geometry of the GV are shown in Fig. 1. The blade profile of the rotor is a NACA 0021 airfoil, and the chord length is 90 mm. The profile of guide vane is a circular arc with a chord length of 91 mm. The design specification of the WT blade and GV is shown in Table 1. The upstream and downstream lengths were taken as eight and eight times of the chord length, respectively, for the flow domain. The blade thickness is 1 mm, and the ends are of circular arc profiles with a diameter of 1 mm. The gap between rotor and GV was taken as G = 39 mm. The gap was chosen according to the G/l_r ratio (=0.433) reported by [11].

The entire computational domain is split into three parts and is meshed separately. The inlet and downstream guide vanes, IGV, and DGV, respectively, are meshed using Ansys Turbogrid. The computational domains of IGV and DGV spanning a total length of 705 mm each were discretized using a fully structured grid. On the other hand, ICEM CFD was used for the rotor domain. The domain of length 30 mm was discretized using an unstructured grid. Prism layers were defined near the blade walls to capture boundary layer physics in both cases. The rotor domain had 2.3 million elements and 1 million nodes whereas the stator domain had 0.5 million elements and nodes. The entire domain had 2.8 million elements and 1.5 million nodes. Figure 2 shows the meshed domains for CFD analysis.

The commercial code, Ansys CFX 16.1 is used for the CFD analysis. It solves steady, incompressible Reynolds-averaged Navier–Stokes (RANS) equations, discretized by a finite volume approach. The code uses a semi-implicit method for

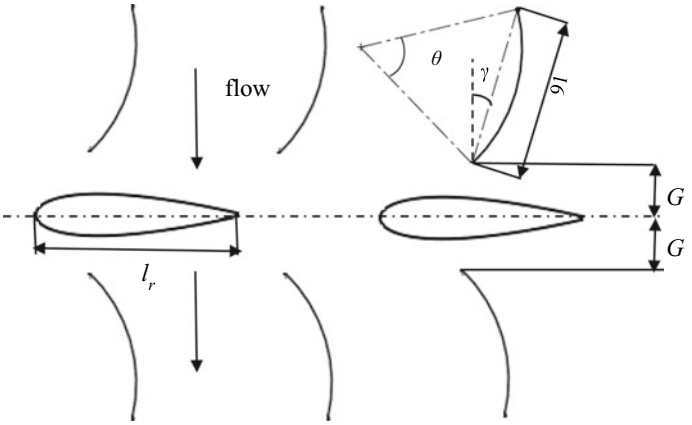

Fig. 1 Configuration of GV and rotor blade

Table 1 Design details of rotor and GV

Rotor/GV	Design parameter	Detail
Rotor	Blade profile	NACA 0020
	Chord length, l_r	90 mm
	Number of blades, Z_r	6
	Solidity	0.67
	Tip diameter	298 mm
	Hub diameter	210 mm
	Tip clearance	1 mm
GV	Chord length, l_g	91 mm
	Blade profile	Circular arc
	Number of blades, Z_g	11
	Camber angle, θ	60
	Stagger angle, γ	16.3°
	Thickness	1 mm

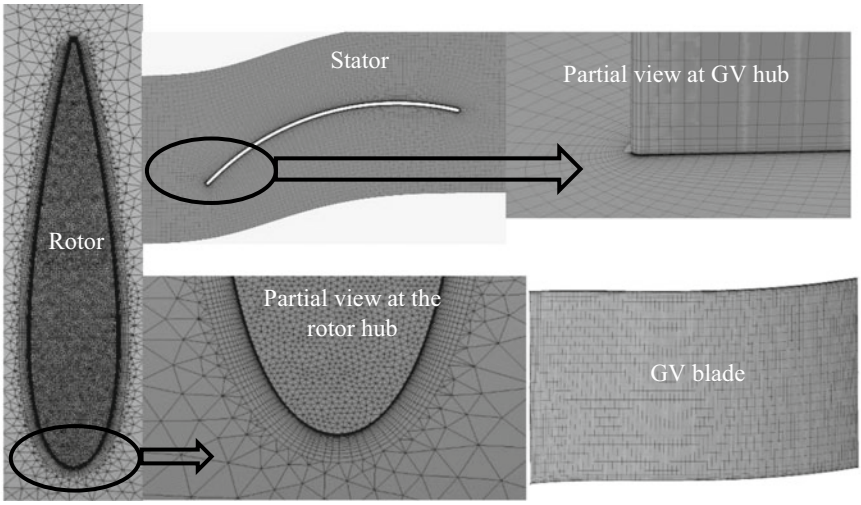

Fig. 2 Meshed rotor and GV

pressure linked equations (SIMPLE) algorithm for pressure–velocity coupling. *k*-ω-based shear stress transport (SST) model is used for the numerical analysis. It takes into account the turbulent shear stress transport and predicts the onset and extent of separated flow during adverse pressure gradients. Figure 3 shows the computational domain for the rotor with GV.

The performance of the WT is investigated based on performance indicators, which are non-dimensional numbers obtained from physical quantities such as torque, pressure, and velocities. These are torque coefficient (C_T), input coefficient

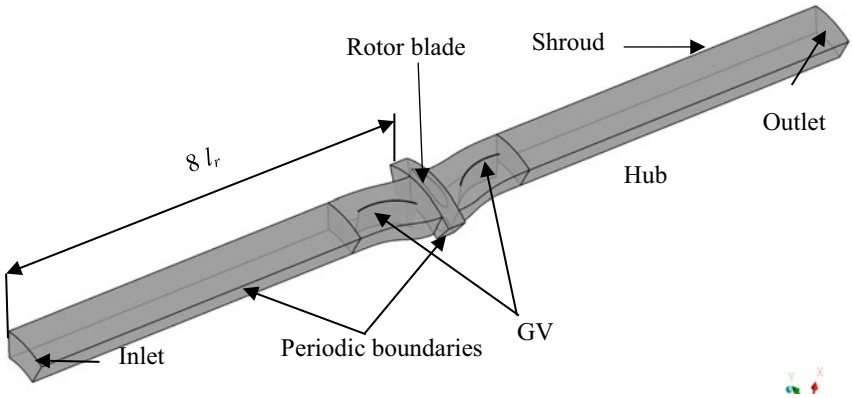

Fig. 3 Computational domain for rotor and GV

(C_A), and flow coefficient (ϕ) and are defined as:

$$C_T = {}^{T_0}\!/\!_{\rho_a\left(v_a^2 + U_R^2\right) b l_r Z_r r_R/2} \tag{1}$$

$$C_A = {}^{\Delta p Q}\!/\!_{\rho_a\left(v_a^2 + U_R^2\right) b l_r Z_r v_a/2} \tag{2}$$

$$\phi = {}^{v_a}\!/\!_{U_R} \tag{3}$$

where T_0 is the output torque, Δp is the total pressure drop before and after the turbine, Q is the flow rate, ρ_a is the density of air, U_R is the blade speed at mean radius, r_R, v_a is the average axial velocity, b represents the blade height, l_r is the chord length of the WT blade and Z_r is the number of rotor blades, respectively.

The target of the present optimization is to maximize C_T of the WT geometry considering the G/l_r ratio. The optimal gap-to-chord ratio which yields the maximum C_T is found out. The optimization problem was formulated as follows.

$$\text{Objective Max} \cdot C_T \tag{4}$$

$$\text{Subject to } 0.267 \leq {}^{G}\!/\!_{l_r} \leq 0.6 \tag{5}$$

2.2 Design of Experiments (DOE)

A reliable metamodel is obtained by carefully selecting the initial design points. The initial design points should accurately represent the design space. DOE is a

technique used to determine the location of these design points in the design space. In the present work, Latin hypercube sampling (LHS) technique [14] was used. The number of samples specified was 6. The LHS algorithm created a 6×1 matrix ensuring that all the points are placed optimally distant between each other and within the design space. 0.267 and 0.6, respectively, were the lower and upper limits of the design parameter.

2.3 Metamodel

Kriging model [15, 16] was used for the present work. Kriging algorithm consists of two terms, a polynomial model and departures.

$$y(x) = f(x) + Z(x) \tag{6}$$

where $y(x)$ is an unknown function of interest and $f(x)$ is a known function of x, and it gives the global approximation of the design space. Whereas $Z(x)$ is the realization of a random Gaussian process with mean as zero and variance of σ^2 and it created localized deviations. In Eq. 6, covariance matrix, $Z(x)$ is defined as,

$$\text{Cov}[Z(x)^i, Z(x)^j] = \sigma^2 R\left[R\left(x_i, x_j\right)\right] \tag{7}$$

where R denotes the correlation matrix and $R\left(x_i, x_j\right)$ represents the correlation function between any two of the initial design points. The term R is an $n \times n$ matrix which is symmetrical and its diagonal is with ones.

2.4 Optimization Strategy

Screening or shifted Hamersley sampling [17] was used for optimization. A non-iterative approach is followed. The Hamersley points for the search space of the kth dimension are given by,

$$H_k(i) = \left[\frac{i}{N}, \phi_{R1}[i], \phi_{R2}[i], \ldots, \phi_{Rk-1}[i]\right] \tag{8}$$

In Eq. 8, N is the number of sample points. A point shifting method was introduced to avoid the inherent unnecessary bias of the technique in the form of skewness toward the cube's origin. To remove the unnecessary bias, the points are moved by a distance of,

$$\Delta = \frac{1}{2}N \tag{9}$$

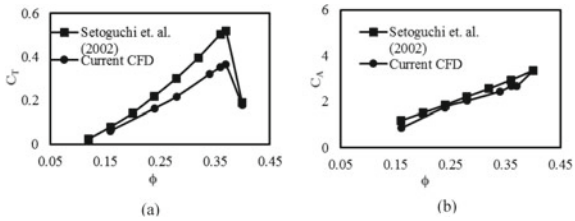

Fig. 4 **a**. C_T versus ϕ **b**. C_A versus ϕ

3 Results and Discussion

3.1 Validation of Numerical Model

To guarantee sufficient accuracy of the numerical model, it has to be validated with a set of experimental or analytical results. Here, the CFD results were validated by comparing it with the experimental results reported by [11]. The geometry and operating conditions of the present study were also taken according to this literature. CFD simulations were carried out for flow coefficients ranging from 0.12 to 0.40. Figure 4 shows the C_T, and C_A plotted against various flow coefficients ϕ. The CFD results were found well matching with the experimental results.

3.2 Optimization Results

DOE created six initial design points within the design space for which CFD simulations were carried out at the flow coefficient of 0.37. This flow coefficient was chosen because this is the flow condition for the reference case at which maximum C_T was obtained. The objective function was found out at the initial design points. Table 2 shows the initial design points and their corresponding C_T values. The results from the DOE was utilized to develop the metamodel. Kriging metamodel was created based on the DOE results from which the response of C_T against various G was obtained. Figure 5 shows the response curve. Finally, the screening algorithm was

Table 2 List of DOE design points and reference design point

No.	G/l_r	C_T
1	0.294	0.376
2	0.35	0.379
3	0.406	0.367
4	0.461	0.359
5	0.517	0.344
6	0.572	0.336
Reference	0.433	0.364

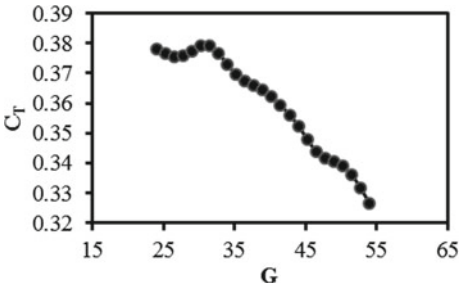

Fig. 5 Response curve of C_T

used to obtain the optimal points from the surrogates. The optimal points were solved using the RANS solver to verify the accuracy of the metamodel. Table 3 shows the candidate points (CP) and the comparison between the predicted and CFD values of C_T. The CP's represent the optimal points at which our objective function is maximized. From the table, candidate point 1 can be chosen as the optimal point since it has the least percentage error between the prediction and CFD result. CP 1 produces an improvement of 3.79% compared to the reference case. The corresponding G/l_r ratio is 0.344.

Figure 6 shows the static pressure (C_P) contours plotted on the suction side (SS) of the rotor blade. The static pressures are calculated with respect to the pressure at rotor inlet and outlet. In the SS, there is a smaller extent of the positive pressure for optimized case than the reference case which is observed near the TE. Positive pressure region near the TE corresponds adverse pressure gradient (APG) as the flow

Table 3 List of candidate points with predicted and CFD results

CP	G (mm)	G/l_r	C_T		
			Predicted	CFD	%error
1	30.998	0.344	0.379	0.378	0.282
2	28.665	0.318	0.377	0.367	2.661

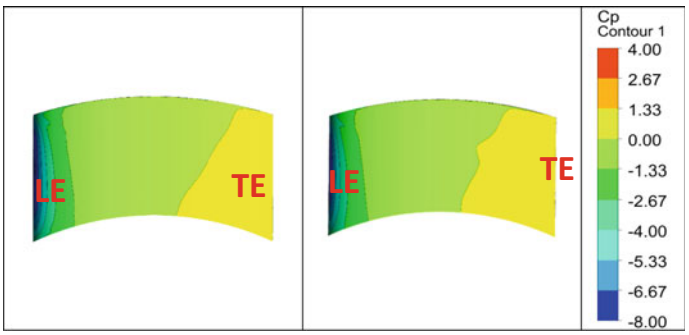

Fig. 6 Static pressure contours on suction side of rotor surface

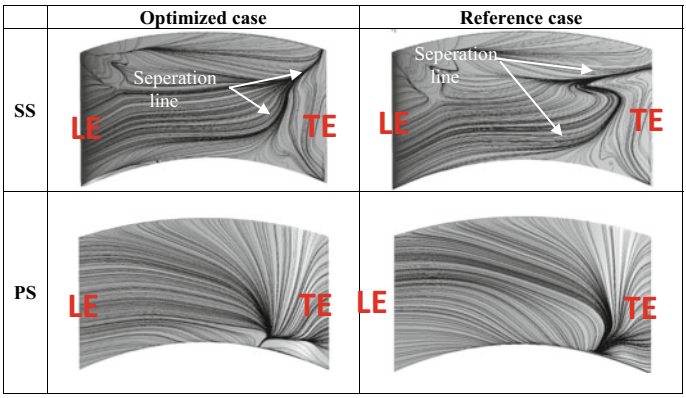

Fig. 7 Streamlines plotted on rotor surfaces

passes from LE to TE. This leads to flow separation. Therefore, lesser extent of the positive C_P region near the TE denotes, lesser region of separated flow and attached flow takes place in that extra area. This is evident in the increase of C_T value for the optimized case when compared to the reference case. Figure 7 illustrates streamlines plotted on the SS and pressure sides (PS) of the blade. It can be noted that the separation line is shifted toward the TE for the optimized case when compared with the reference case. As a result, the flow remains more attached in the optimized case than the reference case leading to higher power output.

4 Conclusions

WT with GV was analyzed numerically for different G/l_r ratios. Steady-state CFD simulations were carried out to obtain the initial design points. Kriging algorithm was used as the metamodel and screening technique was used for the optimization. Three candidate points were predicted by the optimization technique. Out of which, after verification using CFD, the optimal G/l_r ratio was found to be 0.344. An increase in the peak C_T of about 3.79% was obtained at this case.

References

1. Takao M, Setoguchi T, Kim TH, Kaneko K (2000) The performance of Wells turbine with 3D guide vanes. Proceedings of the tenth international of offshore and polar engineering Conference. Seattle, USA
2. Thakker A, Hourigan F (2004) Modeling and scaling of the impulse turbine for wave power applications. Renew Energy 29(3):305–317

3. Sturge DP (1977) Turbine for an oscillating wáter column wave power system. *CEGB Report*, No. MM/MECH/TA41.
4. Gato LMC, Falcao AF, de O (1990) Performance of the Wells turbine with a double row of guide vanes. JSME Int J Series II 33(2):262–271. Author F (2016) Article title. J 2(5):99–110
5. Suzuki M, Arakawa C (2000) Guide vanes effect of Wells turbine for wave power generator. Int J of Offshore Polar Eng 10(2):153–159
6. Inoue M, Kaneko K, Setoguchi T (1985) Studies on Wells turbine for wave power generator. Bull JSME 28(243):1986–1991
7. Arakawa C, Suzuki M, Tagori T (1987) Improvement of performances of Wells turbine. In: Proceedings 6th conference on energy and resources, 39–44.
8. Govardhan M, Dhanasekaran TS (2002) Effect of guide vanes on the performance of a self-rectifying air turbine with constant and variable chord rotors. Renew Energy 26(2002):201–219
9. Govardhan M, Chauhan VS (2007) Numerical studies on performance improvement of self-rectifying air turbine for wave energy conversion. Eng Appl Comput Fluid Mech 1(1):57–70
10. Setoguchi T, Takao M, Kaneko K, Inoue M (1998) Effect of guide vanes on the performance of a Wells turbine for wave energy conversion. Int J Offshore Polar Eng 8(2):155–160
11. Setoguchi T, Santhakumar S, Takao M, Kim TH, Kaneko K (2001) Effect of guide vane shape on the performance of a Wells turbine. J Renew Energy 23:1–15
12. Badhurshah R, Samad A (2015) Multiple surrogate based optimization of a bidirectional impulse turbine for wave energy conversion. Renew Energy 74(2015):749–760
13. Halder P, Rhee SH, Samad A (2015) Numerical optimization of Wells turbine for wave energy extraction. Int J Naval Arch Ocean Eng 9:11–24
14. McKay MD, Beckman RJ, Conover WJ (1979) Comparison of three methods for selecting values of input variable in the analysis of output from a computer code. Technometrics 21:239–245
15. Jeong S, Murayama M, Yamamoto K (2005) Efficient optimization design method using Kriging model. J Aircraft 42:413–420
16. Simpson TW, Mauery TM, Korte J, Mistree F (2001) Kriging models for global approximation in simulation-based multidisciplinary design optimization. AIAA J 39:2233–2241
17. Ansys (2016) Designxplorer user's guide. Ansys Inc

CFD Study of Coupled Flow due to Frigate Airwake and Helicopter Rotor Downwash on Flight Deck

Sumit Kumar and R. Vijayakumar

Abstract This paper discusses the effect of modifying the hangar shape on the dynamic interaction of ship airwake and rotor downwash of the helicopter using computational fluid dynamics (CFD). A traditional 1:100 scaled simplified frigate ship (SFS-2) is modified to obtain trapezoidal and rectangular configurations of the hangar. The coupled interaction of ship airwake formed behind the ship subjected to free stream velocity of 6 m/s with the downwash generated by helicopter rotor hovering at 5000 rpm is simulated using STARCCM + CFD solver. The Reynolds-averaged Navier–Stokes equation is solved with conventional$k$-ω two-equation turbulence model to simulate the flow. The helicopter rotor thrust coefficient on hovering plane and landing plane is calculated for all the three SFS-2 configurations. The resultant velocity flow field of the ship airwake and rotor downwash is surveyed to compare the turbulence intensities at four equidistant lateral planes along the flight deck for a zero wind-over-deck (WOD) angle. The modified hangar configurations are shown to improve the coupled flow aft of the hangar.

Keywords SFS-2 · WOD · CFD · RANS · Hangar shape · Recirculation length · Thrust coefficient · Turbulence intensity

1 Introduction

Shipboards helicopter flight operation in a seaborne environment is considered as a high-risk job for pilots due to the workload being remarkably high, in turn, increases the difficulty associated with take-off and landing on a moving ship as compared to land-based operations. The aerodynamic interaction between the helicopter and the ship airwake is known to play an important role in increasing the pilot workload, thereby reducing aircraft capability and compromises on the safety aspects [2, 12]. The ship airwake is the most important factor considered in limiting the helicopter operations on a ship due to a large region of turbulence [14]. Other factors may also

S. Kumar (✉) · R. Vijayakumar
Indian Institute of Technology Madras, Chennai, India
e-mail: sumit@smail.iitm.ac.in

V. Sundar et al. (eds.), *Proceedings of the Fifth International Conference in Ocean Engineering (ICOE2019)*, Lecture Notes in Civil Engineering 106,
https://doi.org/10.1007/978-981-15-8506-7_44

include bad weather, rough sea conditions, ship rotational and translational motions, and frigates with the smaller landing area. For this reason, knowledge of the airflow around the ship and through the helicopter rotors is necessary to understand the problems that the helicopter encounters as it lands and takes off [15, 5, 20].

Thus, an aft flight deck located behind a hangar (commonly seen on frigates and destroyers) has been a standard configuration for many years (Fig. 1a and b). In modern day, warships such as destroyers and frigates have sharp/inclined superstructure and hanger to meet the stealth requirement. Thus, the top deck arrangement as

(a) US Navy 001112-N-2147W-030 USS Fletcher
(b) (DD 992) (Courtesy US Navy)

(c) (b) Modern-Day Frigate with step-back hangar
(d) (Image courtesy BMTDefense Services site)

Fig. 1 Modern-day ships with helicopter landing spot

shown in Fig. 1 is designed based on stealth considerations and lacks aerodynamics aspects, which is essential for safe onboard helicopter operation.

The present-day configuration of helo landing spot and the helo hangar represents flow over a backward-facing step. The typical flow behind the hangar gets separated and creates vortex shedding composed of large pressure gradient which in turn triggers large region of turbulence [8, 21, 16]. Hangar shape is the key structure that affects the airwake in the helicopter operating area.

The current study focuses on the effect of hangar shape modification on rotor thrust coefficient and the turbulent intensity. By changing the shape of the hangar, there is a smooth gradual pressure change in the helicopter operating area, avoiding the strong vortices and the shear layer caused by the speed jump so as to optimize the ship design.

2 Study Methodology

2.1 Geometry and Mesh Description

Simplified frigate ship (SFS-2) as shown in Fig. 2b is a basic design model of a modern-day frigate. Scientists and researchers have been performing several tests and experiments on this test model. The test geometry adopted for this research work is chosen considering the wide research in both experimental and computational areas performed at the Indian Institute of Technology Delhi. The SFS-2 test geometry is modified at the aft of the hangar to obtain a rectangular prism shape and trapezoidal prism shape as shown in Fig. 2a, c, and d, respectively [10, 16]. A three-bladed propeller of 7-inch diameter with a total pitch of 3-inch is chosen for this research work (Fig. 3e). The ROBIN fuselage is a simplified helicopter fuselage proposed by NASA for helicopter fuselage study as shown in Fig. 3e.

The computation domain is chosen as per the experimental setup by Makkar et al. [6] (Fig. 3a). A three-plane sliding mesh technique is used to create an interface between the background mesh and the rotating mesh (Fig. 3b) [15, 4, 20, 17]. The rotor blade is discretized using unstructured polyhedral mesh elements. Prism layer meshing over the rotor blade captures fine corners and curved edges, and surface remesher is used for meshing (Fig. 3d and e). A control volume is created to gradually increase the mesh size from finer meshes near the geometric model to coarser toward the boundary (Fig. 3c). Grid independence test is performed on 3.2, 3.77, and 4.42 million cells. Observing the difference in thrust coefficient was less than 0.3%, and the grid size of 3.77 million cells was considered to have achieved grid independence.

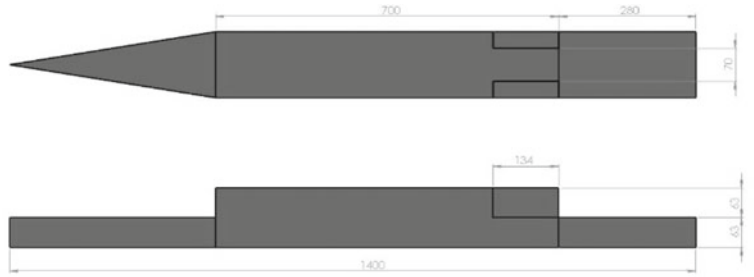

(a) Top and Side View of Rectangular hangar SFS-2

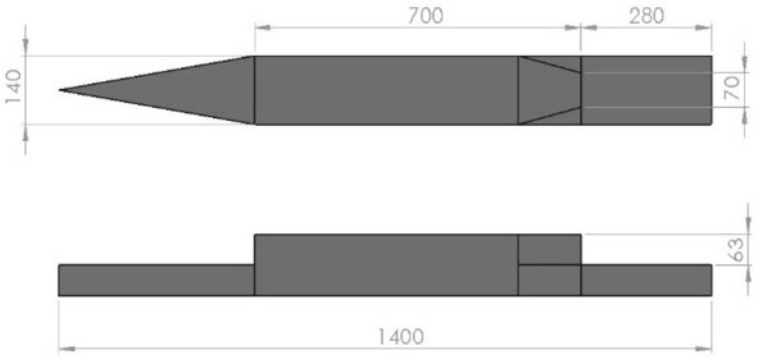

(b) Top and Side View of Trapezoidal hangar SFS-2

Fig. 2 Geometrical description of the models

2.2 Mathematical Formulation and Numerical Technique

The present numerical simulations have been performed using general-purpose commercial CFD code STARCCM + 11, which is based on the finite volume approach. In this method, the entire flow domain is discretized into small volumes, and the equations are integrated over the complete volume. The steady state of modified SFS-2 together with the effect of rotor downwash over the flight deck is simulated using the traditional RANS with SST k-ω two-equation turbulence model.

2.2.1 RANS Equations

In RANS equation, all the scales are averaged out for turbulence steadiness. When averaging the nonlinear term of the Navier–Stokes equation, a term for Reynolds stresses needs to be modeled. This leads to a closure problem which requires some approximation. The time-averaged continuity and momentum equations for steady, incompressible flows without the body forces can be written as [3, 9, 12]:

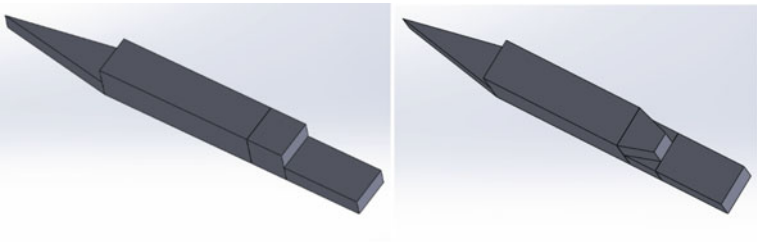

(c) Simple hangar SFS-2 (d) Trapezoidal hangar SFS 2

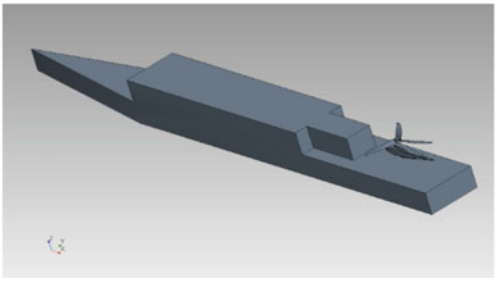

(e) Rectangular hangar shape of SFS-2

Fig. 2 (continued)

Continuity equation

$$\rho \frac{\partial u_i}{\partial u_j} = 0 \tag{1}$$

Momentum equation

$$\rho \frac{\partial}{\partial x_j}\left(\overline{\rho u_i u_j}\right) = -\frac{\partial \overline{p}}{\partial x_i} + \frac{\partial \overline{\sigma}_{ij}}{\partial x_j} \tag{2}$$

where

$$\overline{\sigma}_{ij} = \overline{\mu\left(\frac{\partial u_i}{\partial x_j} + \frac{\partial u_j}{\partial x_i}\right)} \tag{3}$$

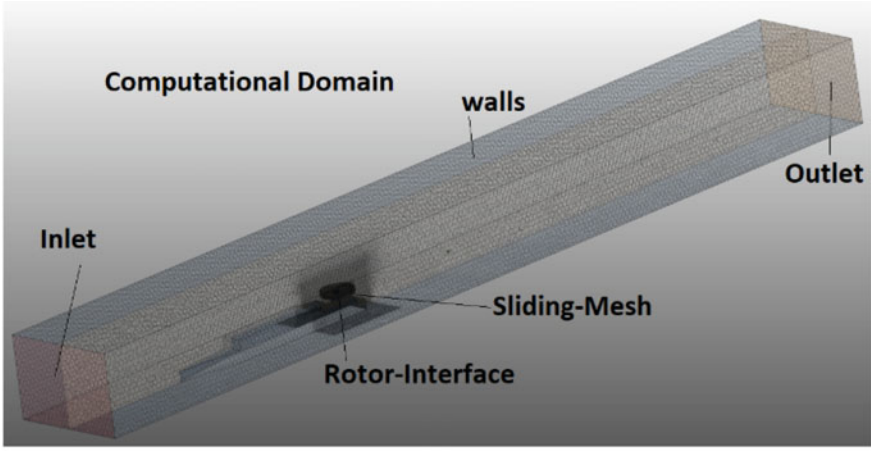

(a) Computational Domain (IIT-Delhi Wind Tunnel Test Section)

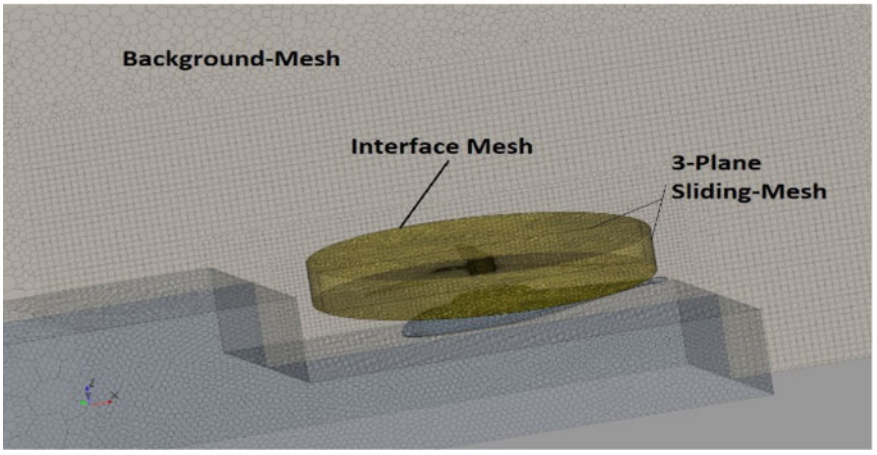

(b) Rotating and Background Mesh (STARCCM+)

Fig. 3 Mesh description generated on the geometrical models

2.2.2 Standard k-ω Turbulent Model

The SST *k-ω* turbulence model Menter (1993) is a two-equation eddy-viscosity model does produce a bit too large turbulence levels in regions with large normal strain, like stagnation regions and regions with strong acceleration. The advantage of the *k-ω* model is that it may be applied throughout the boundary layer without further modification, and the standard *k-ω* model can be used in this mode without computing the wall distance. *k-ω* is a popular model where strong vortices are present

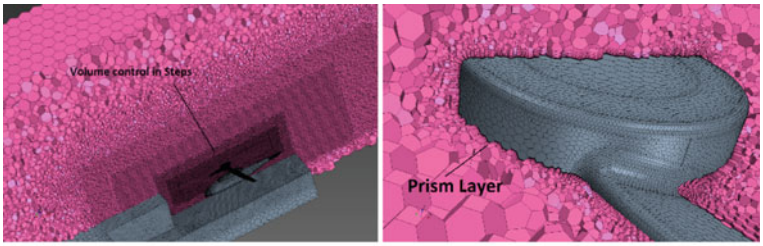

(c) Volume Control mesh (d) Prism Layer on Blade

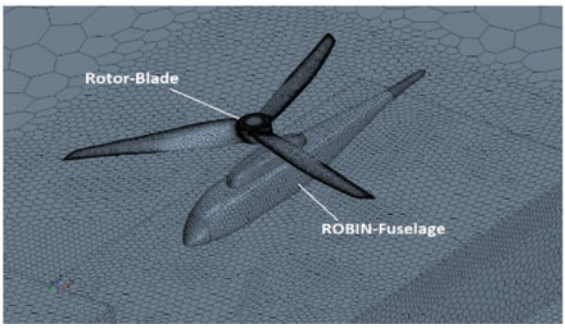

(e) Refined Mesh on Blade

Fig. 3 (continued)

such as those produced from wingtips, perform well for swirling flows and in the near-wall region, but overpredict separation [10].

Turbulent kinetic energy

$$\frac{\partial k}{\partial t} + U_j \frac{\partial k}{\partial x_j} = P_k - \beta^* k\omega + \frac{\partial}{\partial x_j}\left[(v + \sigma_k v_T)\frac{\partial k}{\partial x_j}\right] \tag{4}$$

Specific dissipation rate

$$\frac{\partial \omega}{\partial t} + U_j \frac{\partial \omega}{\partial x_j} = \alpha S^2 - \beta\omega^2 + \frac{\partial}{\partial x_j}\left[(v + \sigma_\omega v_T)\frac{\partial \omega}{\partial x_j}\right] + 2(1 - F_1)\sigma_{\omega^2}\frac{1}{\omega}\frac{\partial k}{\partial x_i}\frac{\partial \omega}{\partial x_i} \tag{5}$$

2.2.3 The Boundary Conditions

For gradient terms, linear interpolation of second-order accuracy was implemented. The second-order upwind scheme was used for the momentum, turbulence kinetic energy, and dissipation rate terms. SIMPLE algorithm is used for momentum–pressure coupling. Details of the same are mentioned in Table 1.

2.3 Measuring Plane

Further, the survey of the coupled flow from ship airwake is done on to the rotor on hovering plane *M* and helicopter landing plane *K* positioned on the z-axis (plane *K* being nearest to flight deck at a distance of 48 mm above flight deck and plane *M* being farthest at a distance of 78 mm above flight deck) as shown in Fig. 4a and b. The grid for measurement consists of four vertical lateral planes A, B, C, and D along the longitudinal axis (plane A being nearest to superstructure at 20% of flight-deck aft of superstructure and plane D being farthest at 80% along flight-deck superstructure) [10, 17].

3 Results and Analysis

3.1 Thrust Coefficient

Mathematically thrust coefficient is defined as below:

$$K_T = \frac{T}{\rho n^2 D^4} \tag{6}$$

where

Table 1 Details of boundary conditions

Parameters	Stationary region boundary conditions	Rotating region boundary conditions
Inlet	$V_\infty = 6$ m/s, Intensity = 1%, turbulent length sale = 7%	Rotation rate = 5000 rpm Advance ratio = 0.4
Domain walls	Stationary wall with zero specified shear	Rotating part wall is stationary
SFS-2 and ROBIN	Stationary wall with no-slip condition turbulence model standard k-ω model	
Discretization method	Momentum, turbulent kinetic energy and dissipation rate: second-order upwind	

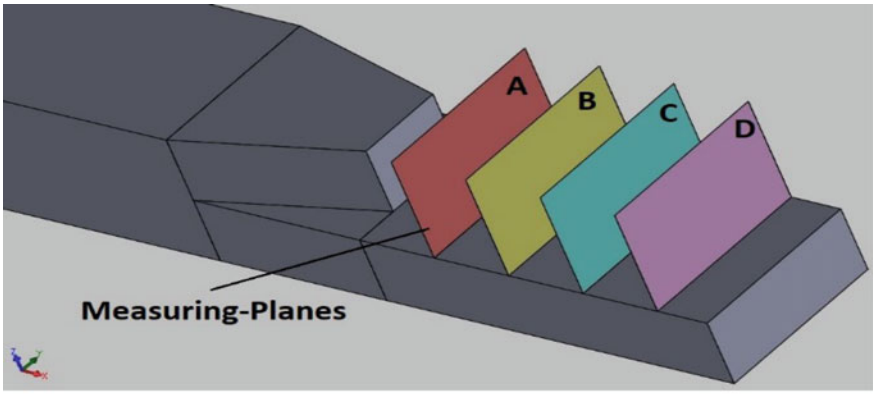

(a) Measuring Plane

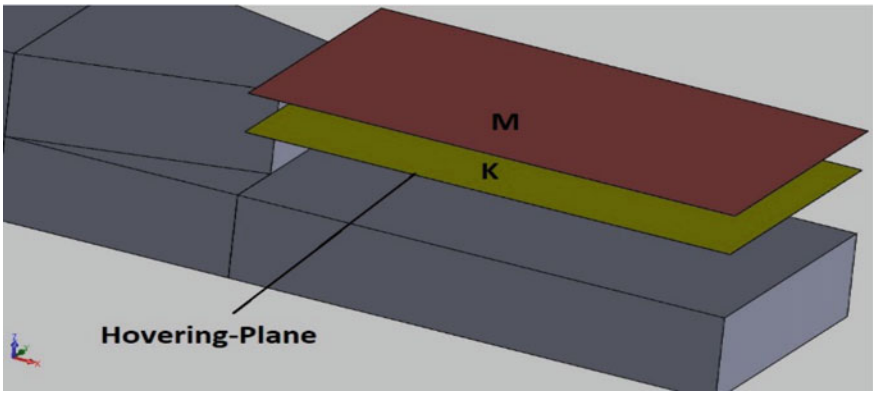

(b) Hovering Plane M and Landing Plane K

Fig. 4 Computation lateral and longitudinal measuring planes

T is thrust generated by rotor (N),
ρ density of air (1.225 kg/m^3).
n is rotational rate (rad/s), and
D is rotor diameter.

Figure 5 represents the velocity vector field for the rectangular hangar shape of SFS-2 on the longitudinal, transverse, and top plane for the position of the rotor at K-plane. The figures below give the physical visualization of the flow, and the flow pattern will remain unaltered for all the three hangar shapes, but the magnitude keeps varying represented by the color bars.

The rotor thrust coefficients are computed for all six cases and are tabulated below in Table 2.

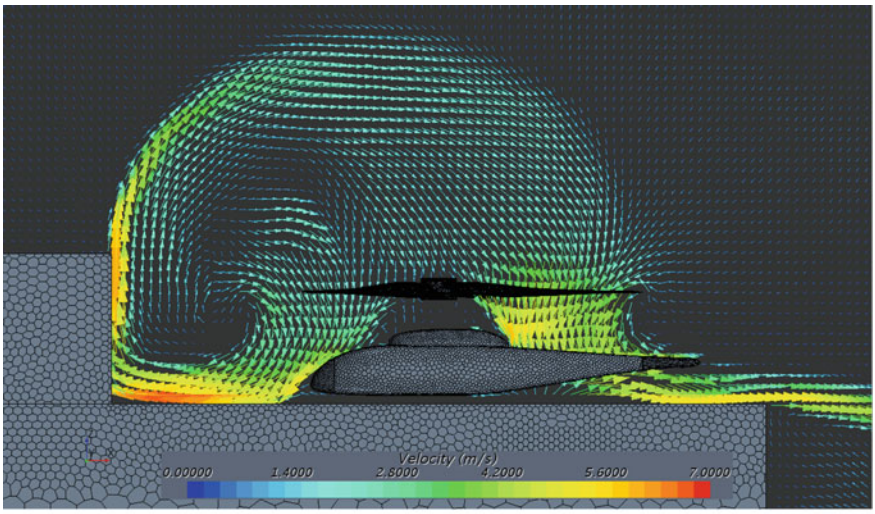

(a) Vector Plot on centreline Plane, Rotor at K-Plane

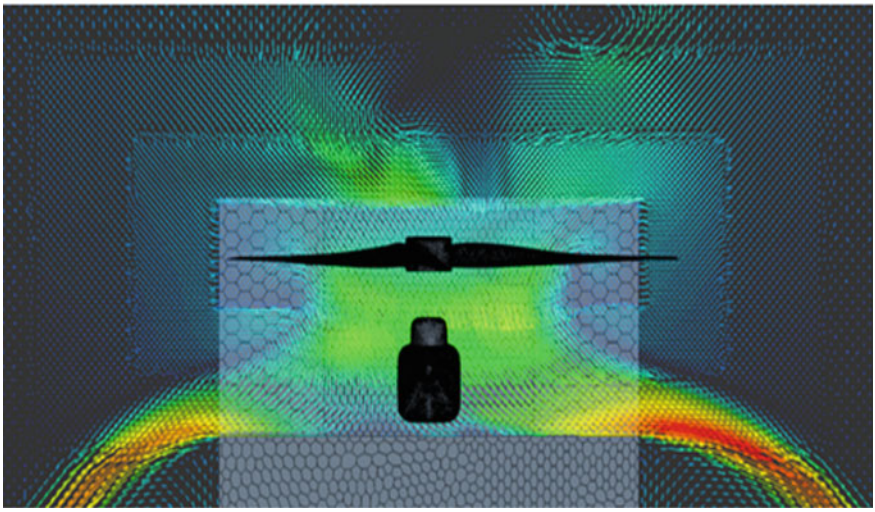

(b) Vector Plot on TransversePlane, Rotor at K-Plane

Fig. 5 Velocity vector flow visualization for rectangular hangar and rotor at K-landing plane

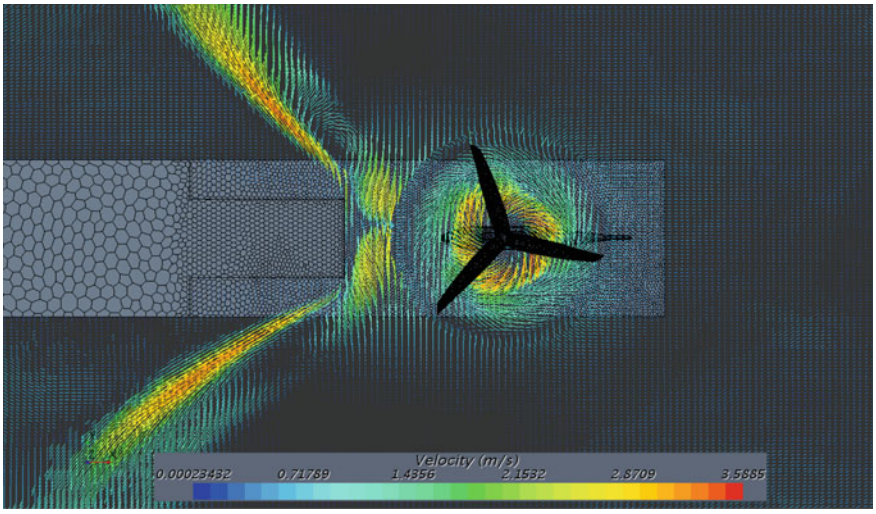

(c) Vector Plot on Top-Plane, Rotor at K-Plane

Fig. 5 (continued)

Table 2 Rotor thrust coefficient on hovering and landing plane

Rotor planes	K-plane (landing)	M-plane (hovering)	Percentage change in K and M
SIMPLE SFS-2	0.00128	0.0015	17.19
Modified SFS-2 (rectangular)	0.00141	0.00153	8.51
Modified SFS-2 (trapezoidal)	0.00142	0.00155	9.15
Percentage change in (simple and rectangular)	10.16	2	–
Percentage change in (Simple and trapezoidal)	10.94	3.33	–
Percentage change in (trapezoidal and rectangular)	0.71	1.31	–

3.1.1 Hovering Plane Observation

From the table, it can be observed that the thrust coefficient increases as the helicopter moves on to hovering plane(K) from landing plane(M) for all the hangar shapes with a maximum change observed in the case of a simple hangar of SFS-2.

K-plane Observation for All Hangar Shapes

The thrust increases by approximately 10% when the hangar shape is changed from simple to rectangular or trapezoidal shape. It is also interesting to note that the increase in thrust in case of trapezoidal shape compared to rectangular shape is only about 0.3%.

M-plane Observation for All Hangar Shapes

The case of M-plane is a little different from the K-plane where the observed increase in thrust coefficient is very less as compared to the K-plane. There is a small decrease in the value of thrust coefficient of about 0.84% as the hangar shape is changed from rectangular to trapezoidal. When the rotor is below the top of the hangar door, the recirculation region has a powerful interaction with the rotor downwash. The rotor thrust is a balance of several influences' vis-a-vis the deleterious effect of reingestion, downwash, the relatively low streamwise flow components, and the positive influence of ground effect.

3.2 Turbulent Intensity

The mathematical formulation for turbulent intensity at a given instant of time can be expressed as below:

$$I = \frac{\sqrt{\frac{3}{2}v_t^2}}{V_\infty^2} \quad \text{where} \quad v_t \text{ is the turbulent velocity scale} \tag{7}$$

Turbulent intensity plot on hovering and landing planes are given below for all computational measuring planes A, B, C, and D located 3 mm below the ROBIN fuselage (Figs. 6 and 7).

K-Plane Observation

Figure 6 shows the turbulence intensity plot on the landing plane K for different hangar shapes of SFS-2 for a qualitative comparison of flow in terms of turbulence intensity. The turbulence intensity on the simple hangar on the K-plane model is maximum just behind the hangar door whereas the trapezoidal and triangular cases have an almost similar pattern with lower magnitudes. Moving on to the planes B and C, the flow gets accelerated in the downward direction increasing the turbulence due to the presence of the rotor. The flow is more disturbed in these planes as compared to planes A and D. The flow dies down as it covers 80% of the flight deck and not much difference is observed among all the hangar shapes.

M-Plane Observation

The variation of turbulence intensity on the flight deck along the beam axis of the ship on all measuring plane for the hovering plane M is represented in Fig. 7. From Fig. 7a,

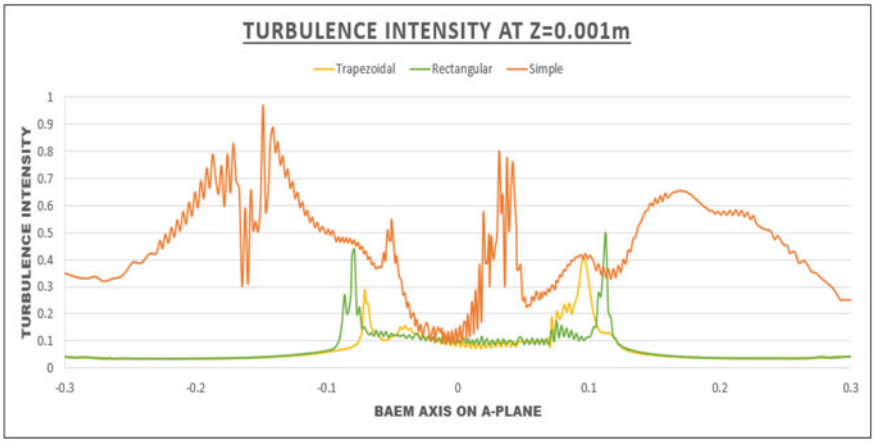

(a) Turbulence Intensity on A-plane

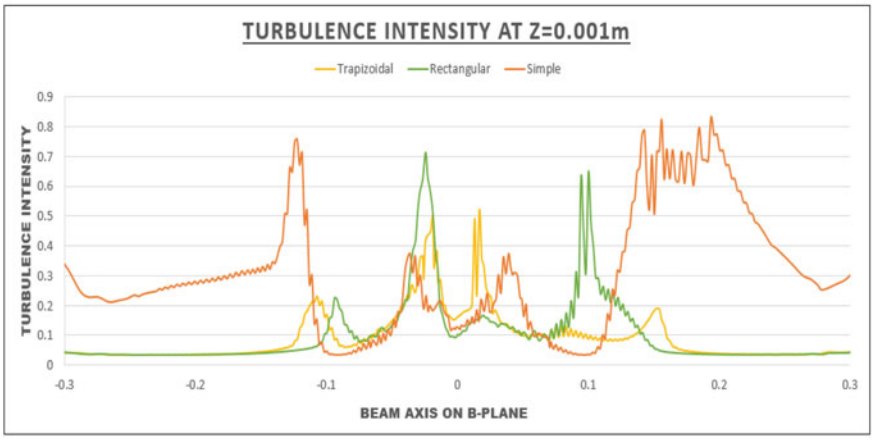

(b) Turbulence Intensity on B-plane

Fig. 6 Turbulence intensity measured for K-landing plane 3 mm below ROBIN fuselage

it can be observed that the turbulence intensity for the rectangular case is maximum and minimum for the simple case. In Fig. 7b and c, the variation in turbulence is almost similar for all hangar shape. In Fig. 7d, it is very interesting to note that the flow dies down on plane D but there is some turbulence on the positive lateral axis (beam axis), that is because of the trailing edge of the rotor blade which induces tip vortices and contribute in the turbulence.

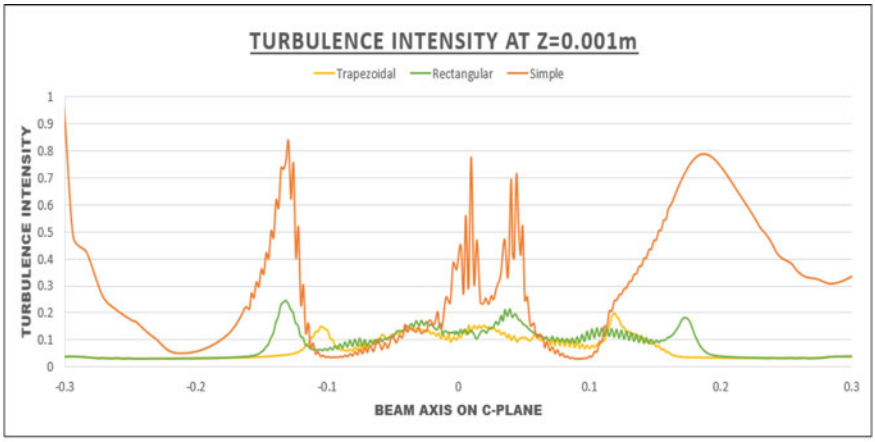

(c) Turbulence Intensity on C-plane

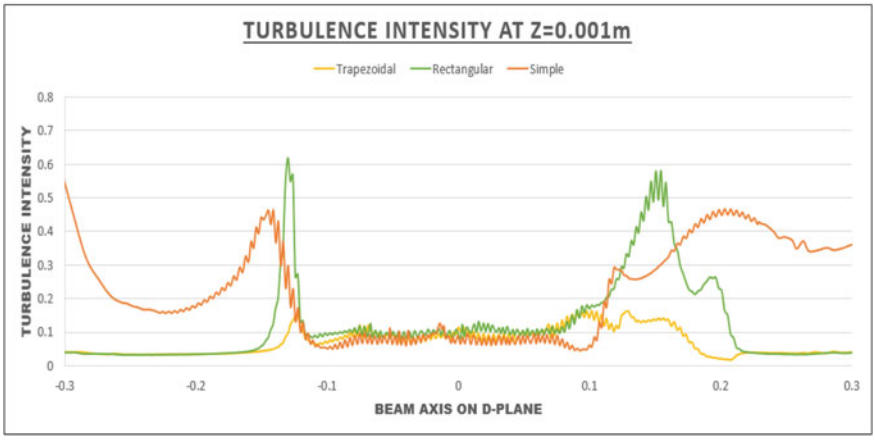

(d) Turbulence Intensityon D-plane

Fig. 6 (continued)

4 Conclusion

Pilots of maritime helicopters face significant challenges when operating on moving platform. The handling of the helicopter is made more difficult as the helicopter enters the ship's airwake, which is the region of separated flow. This study elaborates an unsteady RANS simulation for understanding the coupled behavior of a helicopter rotor downwash and ship airwake in the presence of a simplified helicopter fuselage: ROBIN fuselage.

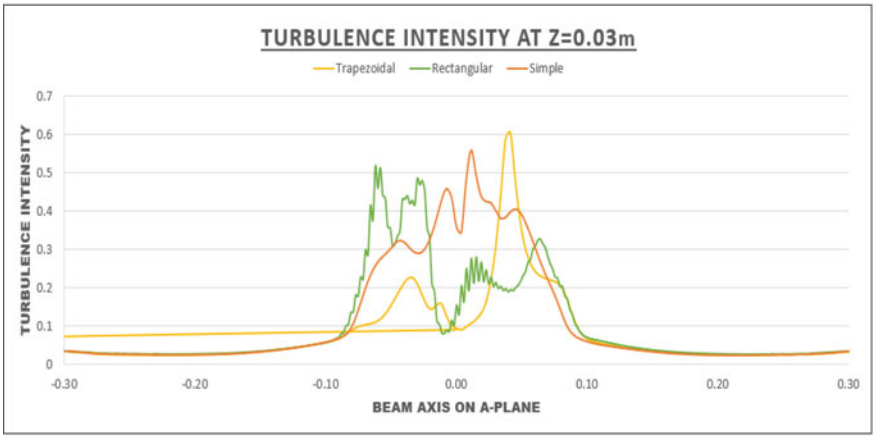

(a)Turbulence Intensityon B-plane

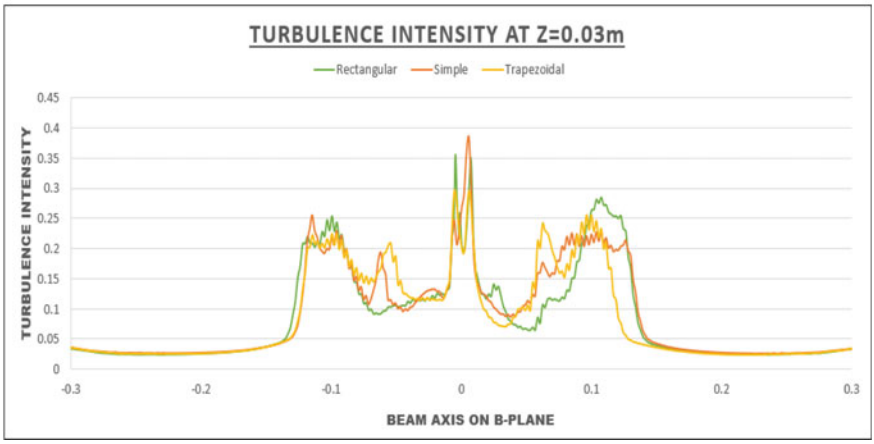

(b) Turbulence Intensity on B-plane

Fig. 7 Turbulence Intensity measured for M-hovering plane 3 mm below ROBIN fuselage

The main effect of change of hangar shape is observed on the landing plane (K-plane) which is in the ship airwake zone. For the simple hangar shape, the recirculation length is almost half the length of the flight deck [1, 15, 19]. For rectangular and trapezoidal hangar shapes, the recirculation length is lesser by approximately 40 and 30%, respectively [11]. There is a significant increase in the thrust coefficient and decrease in the turbulence intensity when the hangar shape is changed from simple to rectangular and then to trapezoidal. This happens because, when the rotor is below the top of the hangar door, the recirculation region has a powerful interaction with the rotor downwash, which from the literature justifies that the modification in the hangar shape can improve the flow toward the aft of the hangar reducing the

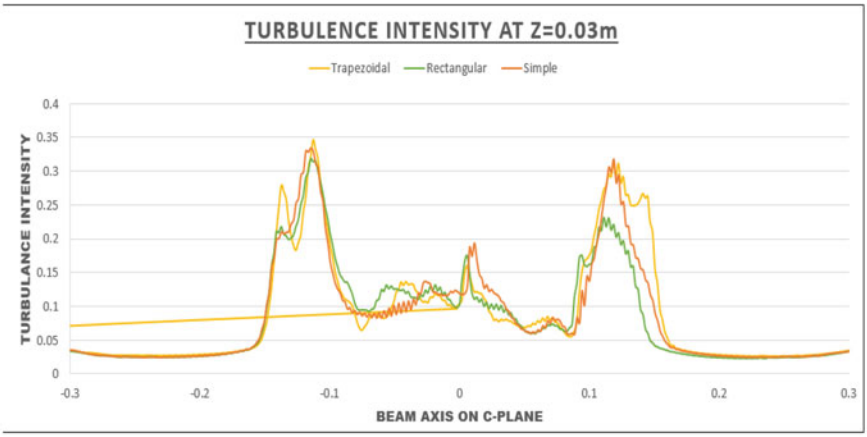

(c) Turbulence Intensity on A-plane

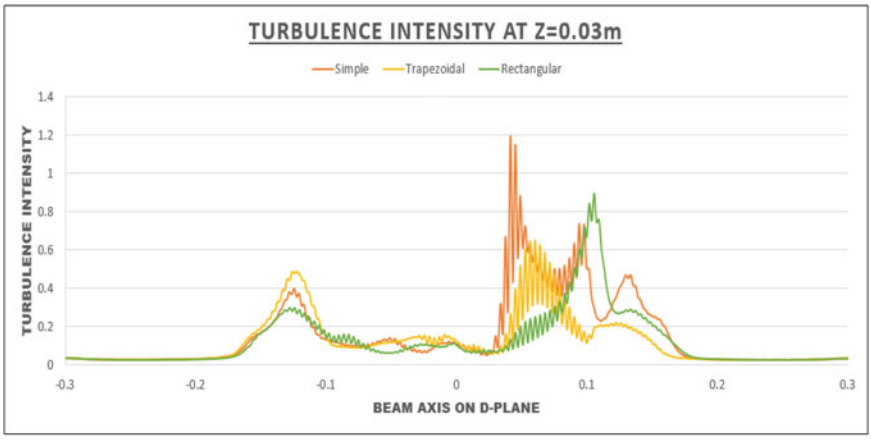

(d) Turbulence Intensity on D-plane

Fig. 7 (continued)

recirculation length. The rotor encounters a higher velocity outer flow from the top of the ship superstructure. Due to the reduced downwash of the airwake and the increased airwake velocity with height, there is an increase in the thrust with the height beyond the hangar. Although the rectangular hangar shape has a significant effect, the above arguments can reasonably conclude that the trapezoidal shape of the hangar of SFS-2 modifies the flow behind the hangar more effectively resulting in increased thrust coefficient and a reduced turbulence intensity ultimately decreasing the pilot's workload.

References

1. Bridges D et al (2007) Coupled flight dynamics and CFD analysis of pilot workload in ship airwakes. In: AIAA atmospheric flight mechanics conference, pp 1–19. https://doi.org/10.2514/6.2007-6485
2. Crozon C, Steijl R, Barakos GN (2014) Numerical study of helicopter rotors in a ship airwake. J Aircraft 51(6):1813–1832. https://doi.org/10.2514/1.C032535
3. Dillmann A et al (2012) and multidisciplinary design 124 new results in numerical and experimental fluid mechanics IX
4. Flash A, The P (2018) A simulation using an overset mesh geometry—region—physics continuum. pp 1–14
5. Harris FD (2011) Introduction to autogyros, helicopters, and other V/STOL Aircraft—Volume 1 Overview and Autogyros. Available at: d:%5Cgali_da%5Cphd%5Creadings%5Cdocs%
6. Makkar IS et al (2016) Study of dynamic flow effects due to ship air wake and rotor downwash interaction on warship helo-decks. In: RINA, royal institution of naval architects—warship 2016: advanced technologies in naval design, construction, and operation, pp 15–16
7. Nacakli Y, Landman D (2011) Helicopter downwash/frigate airwake interaction flowfield PIV surveys in a low speed wind. In: 67th annual forum of the american helicopter society
8. Offline SO, Kääriä CH (2010) Determining the impact of hangar-edge modifications on ship-helicopter operations using offline and piloted helicopter flight simulation. In: 66th annual forum of the american helicopter society, p 11
9. Peir J (2005) Finite difference, finite element and finite volume methods for partial differential. pp 1–32
10. Praveen B et al (2016) Parametric investigation of airflow over helodeck of a generic frigate with introduction of flow modifying device
11. Praveen B (2018) Study of the ship airwake helodeck flow field for safe helo operation. Doctoral Thesis
12. Praveen B, Vijayakumar R, Singh SN, Seshadri V (2019) Flow field on helodeck of a frigate: a review. Int J Marit Eng. In: Proceedings of Royal Institute Naval Architecture, vol 161, pp 401–418, Part A4, Oct–Dec 2019 SCI-19
13. Rodriguez C (2012) CFD Analysis on the main-rotor blade of a scale helicopter model using overset meshing
14. Seddon J (1990). Basic helicopter aerodynamics. https://doi.org/10.1002/9781119994114
15. Sezer-Uzol N, Sharma A, Long LN (2005) Computational fluid dynamics simulations of ship airwake. Proc Instit Mech Eng Part G J Aerospace Eng 219(5):369–392. https://doi.org/10.1243/095441005X30306
16. Shukla S, Singh SN, Suman S, Vijayakumar R (2020) An investigation of ship airwakes by scale adaptive simulation. Int J Mar Navig Saf Sea Transp 14(2):471–475. June 2020
17. Shukla S, Singh SN, Suman S, Vijayakumar R (2020) A conceptual method to assess ship-helicopter dynamic interface. IMechE, Part G: J Aerosp Eng 234(5):1092–1116
18. Steijl R, Barakos G (2008) Computational analysis of rotor-fuselage interactional aerodynamics using sliding-plane CDF Method. In: 34th European Rotorcraft Forum, pp 1–16. https://doi.org/10.1080/00221309.1975.9710851
19. Syms GF (2008) Simulation of simplified-frigate airwakes using a Lattice-Boltzmann method. J Wind Eng Ind Aerodyn 96(6–7):1197–1206. https://doi.org/10.1016/j.jweia.2007.06.040
20. Vijayakumar R, Seshadri V, Singh SN, Kulkarni PR (2008) A wind tunnel study on the interaction of hot exhaust from the funnel with the superstructure of a naval ships. Oceans 2008, Kobe, Japan 18–21. April 2008
21. Wang J, Jiang G, Wang X (2018) Effect analysis of the hangar rear edge curvature on the ship airwake. IOP Conf Series Mater Sci Eng 408:012024. https://doi.org/10.1088/1757-899X/408/1/012024

Experimental Studies of Stern Flap Performance on a Transform Stern High-Speed Displacement Vessel

Y. Hemanth Kumar and R. Vijayakumar

Abstract Hydrodynamic drag of ocean-going vessels imposes severe penalty with regard to exhaust emissions and fuel consumption. Stern flaps have been extensively used as a cost-effective energy saving device, largely by the US Navy. Experimental analysis to identify an optimum stern flap fitted at the transom stern end of a generic high-speed displacement vessel operating at Froude number regime of 0.17–0.48 is described. In this study, twelve different stern flap configurations were studied. Identification of optimum stern flap was based on systematic analysis of extensive model test resistance data of various stern flap configurations over twelve different Froude numbers.

Keywords Ship hydrodynamics · Resistance · Stern flap · Transom stern

1 Introduction

Green ship initiatives to reduce onboard fuel consumption and mitigation of exhaust emissions have taken a center stage in the midst of two conflicting yet vital subjects, the exponential growth in maritime trade on one end of the spectrum and growing concern on maritime pollution on the other end. In order to address these twin concerns, cost-effective energy saving technologies are imperative. Stern flap is one such cost-effective energy saving device which is fitted at the transom end of a vessel to absorb the energy of the stern ward moving flow and thereby increase the pressure force. Flow characteristics at the stern end are strongly dependent on the stern flap geometry. Previous researchers [6] have shown that a suitably designed stern flap fitted at the transom edge of the vessel could reduce the total resistance from 4–10% depending on the vessel type and operating speed. Cave [1] conducted model tests

Y. Hemanth Kumar (✉) · R. Vijayakumar
Department of Ocean Engineering, Indian Institute of Technology Madras, Chennai 600036, India
e-mail: hemanthnavy@gmail.com

R. Vijayakumar
e-mail: vijay2028@iitm.ac.in

V. Sundar et al. (eds.), *Proceedings of the Fifth International Conference in Ocean Engineering (ICOE2019)*, Lecture Notes in Civil Engineering 106,
https://doi.org/10.1007/978-981-15-8506-7_45

of US Navy FFG-7 frigates for determining optimum flap stern angle. Tests were conducted for turning angles ranging from −5° to +20° in steps of 5° and optimum angle was finalized based on the lowest effective power as a result of increase in the pressure on the aft hull. Delivered power ratios for different flap turning angles were plotted against each Froude number and it emerged that flap with turning angle 10° achieved 8.4% power reduction at 26 kn. It was reported that stern flap will produce a larger decrease in delivered power at full scale than shown at model experiments. Karafiath et al. [6] discussed various configurations of Stern flaps fitted on variety of US Navy vessels and explained a general overview of the hydrodynamic mechanism and reported that stern flap produced modification of the near/far field waves, hull pressure, flow velocity, and modification of running attitudes. Following this, [5] conducted model tests of USCG Patrol boat fitted with stern flap as a solution to its engines inability to reach maximum engine RPM and power.

They reported that at low Froude numbers, the transom stern of the vessel and stern flap is submerged, and the flow was attached, while at intermediate Froude numbers, a transitional phase exists where the transom becomes less submerged. In high Froude number range, there is a clean flow separation. Thornhill et al. [10] discussed the performance of stern flaps for various classes of US Navy vessels and Canadian frigates by CFD analysis. It was observed that at a crossover speed where the stern flap began to reduce the overall drag [7].

Taking a lead from the previous work on Stern flaps, [8] conducted experimental and CFD analysis of DTMB 5415 destroyer hull models to determine effect of running attitudes and wave making at stern region on resistance reduction. Coefficient of resistance was analyzed for various groups of stern flaps with configurations of the first group being 1–2% L chord length, single flap angle of 10°, and flap angle w.r.t ship side 0° and 10°. It was observed that flap angle w.r.t ship side does not affect the flow behind the stern and resistance reduction is not sufficiently achieved. It was highlighted that, the reduction in resistance was essentially due to the flow detached from the ship's bottom. Another set of stern flaps with configurations of chord length 1% L, turning angles of 0°, 10° and 18°, and varying span as a percentage (50, 75, and 100%) of transom widths was analyzed. It was reported that the wider span flap was more effective. Authors have undertaken extensive literature survey [2] and preliminary CFD studies [4] and based on the results obtained in these studies, developed physical models comprising of 12 different configurations of Stern flaps for fitment on a generic model of a high-speed transom stern displacement vessel operating in the froude number regime of 0.17–0.48.

2 Description of Hull Form and Flap Geometry

Experimental investigation on scaled ship model in towing tank helps to understand the hydrodynamics of fluid flow over the prototype hull of ships. In the present experimental study, resistance of a scaled hull model of a generic high-speed displacement vessel with a transom stern is investigated to study the effect of stern flap fitted at

Table 1 Details of hull

Parameter	Dimension
Length overall, L_{OA}	4.11 m
Length b/w perpendiculars, L_{BP}	3.87 m
Breadth extreme, B	0.485 m
Transom width, B_T	0.362 m
Draft, T	0.123 m
Displacement	110.74 kg

the transom end with three groups of flap configurations. The main particulars of the hull model are indicated at Table 1.

After finalizing the model dimensions, in order to ascertain the accuracy of the resistance results, simulations of the model hull form with various Stern Flap configurations were undertaken [3] and the resistance values are compared for drag reduction. Once the accuracy of the CFD simulations were established, physical FRP hull model was fabricated with a scale of 1:35. The model scale was selected based on hydrodynamic considerations. The FRP hull model was manufactured to the geometric scale according to ITTC recommended procedures [9]. The photographic details are shown below (Figs. 1 and 2).

The model was marked with the frame numbers and water lines. A trip wire of 3 mm diameter was fixed to the hull at 5% of the hull length aft the forward perpendicular for turbulence stimulation. Parametric investigations for hull model fitted with four groups of stern flap by through comprehensive model tests were undertaken over a Froude number range of 0.17–0.48 with two knot increments. Details of the flap geometry of flap groups considered are indicated at Table 2.

3 Experimental Setup and Procedure

The experimental setup is schematically shown in Fig. 3 and is described in the subsequent paragraphs.

The towing tank is hydrodynamic testing facility consisting of resistance testing module (including two pivot levers, support frame and pulley mechanism), load cell, experimental data collecting and processing system, towing carriage, carriage control unit, and testing tank. Towing tank available at IITM has a cross section of 3.2 × 2.5 m with a length of 85 m. The towing tank carriage is driven by 4 × 3.5–7.5 kW motors for towing the model. The maximum velocity attainable in the towing tank is 5 m/s. Different Froude numbers can be attained in the towing tank by controlling the carriage speed through an onboard carriage control unit. A standard 50 kg load cell was mounted on the support frame of the resistance testing module to measure the drag values. The high-speed displacement vessel model was mounted on the towing carriage by using two pivot levers and supported by a brake pad. A motion reference

Fig. 1 Various stages of model preparation

unit (MRU) was mounted on the model, which allowed the measurement of dynamic trim of the model.

4 Experiment Procedure

Stern flaps with varying configurations (Table 2) were installed on the transom stern of the hull. Stern flap was installed such that the flap trailing edge coincided with the transom-end curvature of the hull. The centerline buttock of the transom hull was to coincide with the centerline of the stern flap. The inlet flow to the hull was attained by towing the model in a towing tank. During each test run, the model was towed at steady speed in calm water as per the desired speed. The range of speeds in which the tests are conducted is from Froude no. 0.17–0.48. The drag experienced

Fig. 2 Flap arrangement at the stern

Table 2 Details of stern flaps

Parameter	Type A	Type B	Type C	Type D
Chord length	1% L_{OA}	1.5% L_{OA}	1.5% L_{OA}	1% L_{OA}
Span	58% B_T	58% B_T	42% B_T	42% B_T
Turning angle	5°, 10°, 15°	5°, 10°, 15°	5°, 10°, 15°	5°, 10°, 15°

by the hull is measured using the load cell and trim angle my motion reference unit (MRU) continuously on a time base. The time duration of data collection for each run consists of stationary, accelerating, and steady phase of carriage movement. The model was ballasted and fitted with towing point at the bottom, brake pads, fore, and aft pivot holders and prepared for the towing tests. The ballast weights were added for correct simulation of the LCG position as in prototype. The tow string was connected to the towing point so that the line tension is a direct measure of the drag of the model. The model was fixed to the towing carriage and held with a brake in various conditions while the carriage is at rest, accelerating phase or reversing after a run. The towrope is connected to the hull tow point and the other end is connected to the sensing end of a load cell; the towrope runs through a vertically adjustable pulley and a fixed pulley before the load cell. The adjustable pulley was fixed so that the towrope is parallel to the still water line to ensure that only the drag force on the hull is transmitted to the load cell. The model was connected to the carriage and towed in such a way that during the test, when the brake holding the model is released, it is free to take its natural trim and heave attitude while the carriage tows the model along the centerline without any drift or sway. The brake pad was released after the acceleration phase as the set speed is achieved by the carriage and load cell readings were recorded for the total duration of the steady speed in the run. The dynamic force

Fig. 3 Experimental setup in towing tank

of the towed model was measured using a beam-type load cell having a sensitivity of 0.076 N and the trim angle was measured using a motion reference unit (MRU).

The error in the measurement of force was of the order $\pm 0.4\%$ whereas the error in the measurement of trim was of the order $\pm 0.8\%$, which are connected to a data acquisition system. The data acquisition system was configured for the experiment

using data processing software, which manages the settings and calibration data of the measuring instruments. The load cell used was of nominal rated load 50 kg (≈490 N of force), which was calibrated for the measurement range of the experiment. During the experiment, the signal data from the load cell through data acquisition system is processed to display the measured force plots in real time on the computer considering the zero corrections, calibrations data, and 50 Hz sampling rate as per the settings. Sufficient waiting time was provided between the consecutive runs, performed over the required range of speed, for the disturbed water to settle down and achieve consistent conditions for all the speeds. The recorded data of the measured force for each run was processed to obtain the average tow force value & trim by selecting the data window for the constant speed duration from the time series plot corresponding to the particular speed.

5 Results and Discussion

Resistance model test in bare hull condition and hull fitted with flaps condition was conducted and presented for Froude numbers 0.17–0.48, where Fn = 0.17–0.28 is the wet transom regime and Fn = 0.31–0.48 is the dry transom regime. The hull model was observed to ventilate/become dry at Fn = 0.31. Ballast loading condition at 0.123 m draft in even keel was maintained throughout the tests. A total of 144 runs in the towing tank was performed. The results are summarized in Tables 3, 4, 5 and 6 and are discussed subsequently. Model resistance acquired in the model tests have been tabulated in four groups Type A, Type B, Type C and Type D for ease of

Table 3 Details of stern flaps-Type A

Flaps-Type A			5°	10°	15°
	Froude No	Bare hull	1L58%	1L58%	1L58%
Wet transom	0.17	4.28	4.18	4.43	4.45
	0.20	5.83	5.59	5.90	6.18
	0.23	7.88	7.29	7.76	8.13
	0.25	10.42	9.96	10.38	10.36
	0.28	13.81	13.25	13.74	13.59
Dry transom	0.31	17.40	17.02	17.18	17.28
	0.34	21.24	20.66	21.20	20.99
	0.37	27.12	25.83	26.58	26.08
	0.40	34.34	33.42	33.31	33.44
	0.42	43.03	41.96	41.38	41.82
	0.45	50.51	50.06	50.59	50.76
	0.48	57.83	57.54	58.20	57.12
Average % teduction			−3.2%	−0.6%	−0.09%

Table 4 Details of stern flaps-Type B

Flaps-Type B			5°	10°	15°
	Froude No	Bare hull	1.5L58%	1.5L58%	1.5L58%
Wet transom	0.17	4.28	4.08	4.36	3.95
	0.20	5.83	5.86	5.86	5.92
	0.23	7.88	7.81	7.86	7.93
	0.25	10.42	10.50	10.29	10.33
	0.28	13.81	13.48	13.30	13.49
Dry transom	0.31	17.40	17.59	17.03	17.22
	0.34	21.24	20.54	21.61	20.57
	0.37	27.12	25.84	26.59	25.06
	0.40	34.34	33.41	33.02	32.85
	0.42	43.03	42.41	41.84	41.56
	0.45	50.51	49.73	49.63	49.47
	0.48	57.83	57.40	56.35	56.82
Average % reduction			−1.7%	−1.3%	−2.7%

Table 5 Details of stern flaps-Type C

Flaps-Type C			5°	10°	15°
	Froude No	Bare hull	1.5L42%	1.5L42%	1.5L42%
Wet transom	0.17	4.28	3.53	3.76	4.05
	0.20	5.83	5.46	5.55	6.04
	0.23	7.88	6.81	6.87	8.13
	0.25	10.42	9.89	10.05	10.45
	0.28	13.81	13.15	13.33	13.71
Dry transom	0.31	17.40	16.83	17.22	17.37
	0.34	21.24	21.74	21.01	21.65
	0.37	27.12	26.16	26.10	26.79
	0.40	34.34	32.81	32.85	33.75
	0.42	43.03	41.39	42.44	41.91
	0.45	50.51	49.12	50.22	50.34
	0.48	57.83	56.31	56.77	56.90
Average % reduction			−5.4%	−4.7%	−0.4%

analysis. Average percentage resistance reduction relative to bare hull resistance was taken as a metric to quantify the performance of each flap.

Table 6 Details of stern flaps-Type D

Flaps-Type D			5°	10°	15°
	Froude No	Bare hull	1L42%	1L42%	1L42%
Wet transom	0.17	4.28	4.04	4.09	4.20
	0.20	5.83	5.54	6.06	5.88
	0.23	7.88	7.49	8.01	7.20
	0.25	10.42	9.98	10.30	10.26
	0.28	13.81	13.32	13.63	13.52
Dry transom	0.31	17.40	17.16	17.24	17.35
	0.34	21.24	20.32	20.91	21.20
	0.37	27.12	26.52	26.57	26.72
	0.40	34.34	33.29	33.96	33.71
	0.42	43.03	42.65	41.59	41.75
	0.45	50.51	49.54	50.45	49.65
	0.48	57.83	56.87	55.89	56.50
Average % reduction			−3.2%	−1.1%	−2%

5.1 Analysis

Model resistance data recorded in towing tank model tests in with and without flap conditions was arranged in four groups, namely Type A, Type B, Type C, and Type D. Typical feature of each of these groups was that, each group comprised of stern flaps with constant chord length and constant span with varying flap angles. In order to systematically investigate, capture coherent patterns in the resistance data, consider all the variables (chord length, span, flap angle, and Froude number) and to evaluate the flap performance, analysis was undertaken in two modes of operation for ease of examination. In operation-1, the starting point was flap Type-A data. The flap performance in terms of average percentage resistance reduction in Type-A group was first compared to corresponding Type-B flaps, i.e., an increase in chord length keeping the span constant (varying flap angles). Thereafter, performance of Type-B flaps were compared to Type-C flaps, i.e., decrease in span and keeping the length constant. Analogous to operation-1, operation-2 also starts by first considering Type-A flaps. However, this time, first the flaps performance in Type A are compared to Type D, i.e., a decrease in Span keeping the chord length constant. Thereafter, Type-D flaps are compared to Type-C flaps, i.e., increase in chord length by keeping the span constant. Findings of both the operations are explained in the subsequent paragraphs.

5.2 Operation-1: Increase in Chord Length Followed by Decrease in Span

Analyzing the resistance data by increasing the chord length of the flap from 1 to 1.5% L and keeping the span constant at 58% B_T, it was observed that there was a decrease in average performance for 5° flap angle from 3.2 to 1.7% and a considerable increase of 0.6 to 1.3% and 0.09 to 2.7% for 10° and 15° flap angles, respectively. Thereafter, reduction in span to 42% for the 1.5% L flap, led to an increase in average performance from 1.6 to 5.4% and 1.3 to 4.7% for 5° and 10° flaps, respectively, while there was a decrease from 2.6 to 0.4% in the case of 15° flap.

5.3 Operation-2: Decrease in Span Followed by Increase in Chord Length

Analyzing the resistance data by decreasing the flap span from 58% B_T to 42% B_T and keeping the chord length constant at 1% L, an increase in the average performance was observed for all the three flap angles (5°, 10°, 15°), i.e., 3.2 to 3.4%, 0.6 to 1.1%, and 0.09 to 2%, respectively. Thereafter, an increase in chord length to 1.5 from 1% L flap led to an increase in average performance from 3.2 to 5.4% and 1.1 to 4.7% for 5° and 10° flaps, respectively, while there was a decrease from 2 to 0.4% in the case of 15° flap.

From the above operations conducted throughout the operating Froude number range for this model, following inferences can be made:

- From the point of view of operation-1, there is an increase of 3.8% and 3.4% in average performance of 5° and 10° flaps, respectively.
- From the point of view of operation-2, there is an increase of 2.2% and 3.6% in average performance of 5° and 10° flaps, respectively.
- In both the operations, it was observed that there was a decrease in the average performance of 15° flap, i.e., 2.2% and 1.6%, respectively.
- From the above analysis, it can be observed that an increase in the chord length accompanied by a decrease in span resulted in an increase in the average performance. Further, flaps 5° and 10° with chord length 1.5% L and 42% B_T span were observed to be promising candidates in terms of resistance reduction.
- After having identified 5° and 10° flaps (1.5% L and 42% B_T) as promising candidates, the task was to identify an optimum stern flap between 5° and 10° flap. Analysis of their performance in wet transom regime revealed that there was an average decrease in the resistance by 9.5 and 8.4% for 5° and 10° flaps, respectively. Similarly, in the dry transom regime (i.e., from Froude number 0.31 onwards), there was an average decrease in resistance by 2.6 and 2.1% for 5° and 10° flaps, respectively. This clearly shows that 5° flap performed better than 10°

flap in both the regimes, which is evident from decrease in the resistance relative to bare hull condition, i.e., 5.5 and 4.7%, respectively.

6 Conclusions

Comprehensive analysis mechanism of resistance reduction by a stern flap fixed to a transom stern high-speed displacement vessel is extremely complicated since the phenomenon is affected by a large number of parameters like local transom shape, flow velocity, pressure variation, modification of stern wave system, stern flap geometry, transom immersion, running attitude, effective lengthening, etc. Varying one these parameters, i.e., stern flap geometrical features and investigating a total of 144 cases using experimental model resting testing has provided preliminary insight into resistance reduction. The following conclusions are drawn from the experimental investigations:

(a) An increase in the chord length accompanied by a decrease in span resulted in an increase in the resistance reduction for the present case.
(b) Flap angle 5° with chord length 1.5% L and 42% B_T was observed to be the most efficient flap, based on average resistance reduction in the entire Froude number regime.
(c) Flap angle 15° was not efficient in comparison to 5° and 10°.
(d) Parametric investigations in to the effect of stern flap geometrical features on the resistance is a starting point in understanding the stern flap hydrodynamics. Detailed studies are required to investigate effect of flap on other components that effect the resistance.

In the future, it is aimed to conduct detailed flow analysis on the transom stern to investigate the physics of resistance reduction and effect of stern flap geometry. Experimental studies on pressure recovery on hull and flow visualization studies in the vicinity of the stern are planned to be undertaken.

Acknowlegments The authors acknowledge the support and guidance given by Prof. Ananthasubramanian, Department of Ocean Engineering, Indian Institute of Technology (Madras), India.

References

1. Cave C (1993) Effect of stern flaps on powering performance of the FFG-7. Class 30(1):39–50
2. Hemanth Kumar Y, Vijayakumar R (2018) Stern flaps : A cost-effective technological option for the Indian shipping industry. Maritime Aff J Natl Maritime Foundat of India 14(2):26–37
3. Hemanth Kumar Y, Vijayakumar YH (2018a) Review of hydrodynamic performance of stern flap. In: International conference on computational and experimental marine hydrodynamics MARHY 2018, 26–27 November 2018, IIT Madras, Chennai, India, pp 104–116

4. Hemanth Kumar Y, Vijayakumar R (2020) Effect of flap angle on Transom stern flow of a High-speed displacement Surface combatant. Ocean Syst Eng 10(1):1–23, SCI-24. DOI: https://doi.org/10.12989/0se.2020.10.1.001
5. Karafiath G, Cusanelli DS, Jessup SD, Surface N, Barry CD, Guard USC (2001) Hydrodynamic Efficiency Improvements Ft WPB ISLAND Class Patrol Boats to the USCG 110(109):197–220
6. Karafiath G, Cusanelli DS, Lin CW (1999) Stern wedges and stern flaps for improved powering–US Navy experience. Trans Soc Naval Archi Marine Eng 107:67–99
7. Kumar YH, Kumar RV (2020) Development of an energy efficient stern flap for improved EEDI of a typical high speed displacement vessel. Def Sci J 70(1):95–102. https://doi.org/10.14429/dsj.70.14669
8. Maki A, Arai J, Tsutsumoto T, Suzuki K, Miyauchi Y (2016) Fundamental research on resistance reduction of surface combatants due to stern flaps. J Marine Sci Technol (Japan) 21(2):344–358. https://doi.org/10.1007/s00773-015-0356-8
9. Resistance Committee of the 28th ITTC. ITTC – Recommended Procedures and Guidelines Ship Models, Pub. L. No. 7.5–01–01–01, 9 (2017).
10. Thornhill E, Cusanelli D, Cumming D (2008). Stern flap resistance reduction for displacement hulls. In: 27th symposium on naval hydrodynamics, 3, 10p.

Corrosion of Bare and Embedded Reinforcement Exposed to Simulated Sea Tide

Hansraj Kumar Dhawatal and Sailesh Kumar Singh Nunkoo

Abstract This degree project investigated on the corrosion rate of distinct steel reinforcement diameters exposed to urban atmosphere, coastal atmosphere, tidal and submerged zone and compared the corrosion rate for the different exposure conditions. The corrosion rate of steel reinforcement embedded in different concrete cover thicknesses was evaluated and discussed. The methodology involved exposing samples of 6, 8, 10 and 12 mm diameter bare steel reinforcement to urban atmosphere, coastal atmosphere, tidal zone and submerged zone for 60 days. Similarly, 10 mm diameter steel reinforcement embedded in concrete with cover thicknesses of 25 and 50 mm was exposed to tidal actions. The research findings showed that the corrosion rate for steel reinforcement exposed to tidal zone experienced structurally significant metal loss and a corrosion rate of 131.229 μm/yr over the 60-day exposure period, whereas specimens exposed to the submerged zone experienced a corrosion rate of 34.781 μm/yr over that same exposure period. The corrosion rate of steel samples exposed at Mahebourg was 66.940 μm/yr and the corrosiveness for this location was high and classified under category C4 corrosion. However, the corrosion rate for specimens exposed to Vacoas was 48.783 μm/yr and the corrosion activity for Vacoas falls under category C3 corrosion since the corrosiveness was medium. The percentage mass losses for 10 mm diameter bare steel reinforcement exposed to sea tides for 60 days were 0.897%, while for steel reinforcement embedded in 25 and 50 mm concrete cover, the percentage mass losses decreased to 0.092% and 0.017%, respectively. The cost assessment based on the proposed case study was cost-effective when the repairs were performed during construction phase. It consisted of increasing the cover thickness to 50 mm for reinforced concrete piles exposed to splash and tidal zones.

Keywords Corrosion · Bare steel reinforcement · Steel reinforcement embedded in concrete · Atmospheric corrosion · Alternate and continuous immersion corrosion testing · Cost assessment

H. K. Dhawatal (✉) · S. K. S. Nunkoo
Civil Engineering Department, University of Mauritius, Reduit, Mauritius
e-mail: hansrajdhawatal@umail.uom.ac.mu

V. Sundar et al. (eds.), *Proceedings of the Fifth International Conference in Ocean Engineering (ICOE2019)*, Lecture Notes in Civil Engineering 106,
https://doi.org/10.1007/978-981-15-8506-7_46

1 Introduction

Corrosion is simply defined as a chemical or electrochemical reaction between a material (typically a metal) and its local environment, resulting in deterioration in the physical appearance and a rapid decline in the material's properties [1]. When steel reinforcements are manufactured, the metal is in a stable state. Depending on the environmental exposure conditions, steel reinforcements are susceptible to corrosion as they will attempt to regress to their equilibrium state by transforming into lower energy compound. The Mauritian economy is affected as the cost of corrosion in the island is expected to amount up to one billion rupees [2] and amount up to 0.38% of the country's GDP [3].

Nowadays, numerous concrete structures such as buildings, bridges and highways built in the last century are crumbling and will become obsolete before its life cycle ends. This may seem curious given the survival of ancient structures. The main difference is the present use of steel reinforcement inside the concrete. Steel is mainly made of iron and one of the unchanging properties of iron is that it corrodes when exposed to severe environmental conditions, for example, splash and sea-tide zones [4].

The structural effect of corrosion of steel reinforcement is the reduction in effective cross-section area that will reduce axial and flexural strength of reinforced concrete elements and make them structurally weak. The rapid propagation of fatigue crack propagation introduces points of stress concentrations at which further cracking may develop and reduce the fatigue strength. The significant reduction in overall bond strength between the solid concrete and steel reinforcement interface and anchorage or lap length may result in failure of certain sections of a structure and also lead to reduced shear capacity and ductility [5].

Therefore, the study of the process of corrosion of steel reinforcement in different coastal exposure zones is a very important knowledge for civil engineers as it will enable them to give possible recommendations to adapt to either control or prevent corrosion.

2 Methodology

The atmospheric corrosion test is performed on different diameters of bare steel samples to determine the rate of corrosion under urban (Vacoas) and coastal (Mahebourg) atmospheric conditions. The simple immersion test involves the continuous immersion of steel reinforcement specimens in 3.5% NaCl solution for a period of time. This test was used to simulate exposure to the submerged zone. The alternate immersion test is a form of accelerated corrosion test and involves the alternate immersion of specimens in 3.5% NaCl or any other corrosion solution for a defined period of time. This method is truly representative of tidal condition and take into consideration the corrosive effects of the marine tidal zone. These specimens were

immersed in the solution during high tide and then withdrawn from the solution for a period of drying during low tide. In this case, this alternate immersion test will simulate sea-tides conditions.

The bare steel specimens are removed, dried and examined before immersing them again after 15, 30, 45 and 60 days and steel reinforcement specimens embedded in concrete cover thickness of 25 and 50 mm were pull-out after 60 days of exposure and excess concrete were removed with a metallic brush [6]. The mass of specimens is measured before each immersion and the mass loss is calculated and corrosion rate (CR) is determined using the formula below [7].

$$CR = (k \times \Delta w)/(A \times T \times \rho) \tag{1}$$

where CR = Corrosion rate (mm/year),
Δw = Mass loss (g),
A = Exposed surface area of specimen (cm^2),
ρ = Density of steel reinforcement (7.86 g/cm^3),
T = Time of exposure (hr),
k = Constant for unit conversion (8.76 × 107 μm/yr).

3 Analysis and Discussions

Following a visual assessment, the following signs of corrosion were observed on bare steel reinforcement specimens exposed to urban atmosphere, coastal atmosphere, tidal zone and submerged zone (Table 1).

The mass loss of samples exposed to different exposure environments is expected to increase exponentially over the 60 days of exposure as shown by the trend of the graph in Fig. 1.

The corrosion rate of samples exposed to different exposure environments is expected to remain almost constant after 60 days of exposure as shown by the general trend of the graph in Fig. 2.

During the 60 days of exposure, the steel reinforcement specimens exposed to the tidal zone experienced the highest mass loss and corrosion rate as shown in Fig. 1 and Fig. 2, respectively. The justification for such an observation accounted for the evaporative effect of NaCl solution, varying temperature and moisture during wet and dry cycles roughly equivalent to high and low tide conditions. These allowed the optimum exposure to oxygen and chloride ions and thus increased the corrosion rate. However, steel reinforcement specimens exposed to submerged zone experienced the lowest corrosion rate during the 60 days of exposure. The obvious reason of this is that the area is already saturated with seawater and there is a low level of oxygen in the submerged area, and therefore, corrosion proceeds at a much slower rate. The submerged zone can be regarded as one which is protected from variations in temperature and moisture, which are important parameters for influencing the initiation and propagation of corrosion.

Table 1 Observations on specimens exposed to different environments

Exposure environment	Observations and comments	Contributing factors
Urban atmosphere	• First sign of corrosion was observed after three days of exposure • No sign of other forms of corrosion were observed • Uniform corrosion mainly occurred • Minor metal loss was recorded	• Duration of dryness and wetness depended on rainfall activity • Lower temperature recorded at Vacoas compared to coastal atmosphere • Presence of atmospheric oxygen • Concentration of electrolyte was low because of absence of salt spray in atmosphere
Coastal atmosphere	• First sign of corrosion occurred after two days of exposure • Pitting corrosion were observed during the initial stage • Uniform corrosion mainly occurred • Significant and measurable metal loss were obtained	• Duration of dryness and wetness depended on speed of wind blowing salt spray from sea and also on rainfall activity • Higher temperature recorded at Mahebourg compared to urban atmosphere • Presence of atmospheric oxygen • Concentration of electrolyte was high in NaCl content because of salt spray from seawater
Tidal zone	• First sign of rust was observed after one day of exposure • Pitting corrosion were initially observed • Uniform corrosion mainly occurred • Structurally significant metal loss was recorded	• Duration of dryness and wetness depended on low and hide tide • High temperature during low tide and lower temperature during high tide • High amount of atmospheric oxygen during low tide and dissolved oxygen during high tide • Concentration of electrolyte was high in NaCl content because tidal actions of seawater and salt spray
Submerged zone	• First sign of corrosion occurred after four days • Pitting corrosion was initially seen • Uniform corrosion mainly occurred • Insignificant metal loss was recorded	• No alternate duration of dryness and wetness because of continuous immersion • Lower temperature measured due to continuous immersion in solution • Very low amount of dissolved oxygen due to complete immersion in solution • Concentration of electrolyte was high in NaCl content due to continuous immersion in solution

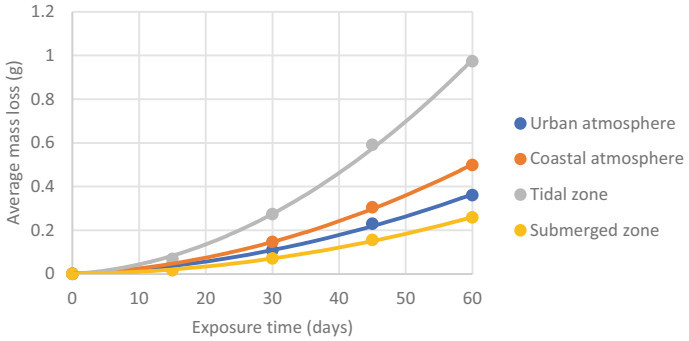

Fig. 1 Average mass loss against exposure time

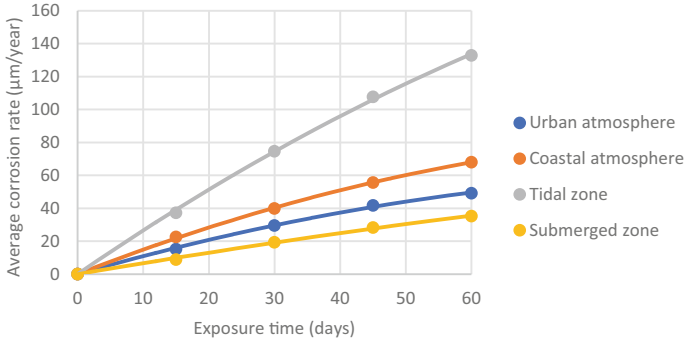

Fig. 2 Average corrosion rate against exposure time

The bare steel reinforcement specimens exposed at Mahebourg experienced a higher mass loss and corrosion rate compared to specimens exposed at Vacoas. The high corrosion rate measured for samples exposed at Mahebourg is due to an increased in the percentage of salinity in the atmosphere caused by seawater salt spray. Mahebourg has a coastal and rural atmosphere that is known to be a very corrosive environment. The corrosive effect of this environment depends on numerous factors such as wave action, winds, relative humidity and shore topography [8]. The deposition rate of sodium chloride by marine fog and windblown spray droplets was always very high near the shore, but the corrosiveness decreased significantly as we moved inland (Vacoas) from the shore (Mahebourg). Vacoas is an urban region with similar characteristics to rural atmosphere and the corrosion rate is influenced by emissions of sulfur and nitrogen oxides characterized by low industrial activity. However, sodium chloride and sulfur dioxide emissions from motor vehicles may also have a higher deposition rate and increase the corrosion rate of the area [9].

It was observed that as the thickness of the concrete cover increased from 0 to 50 mm, the mass loss and corrosion rate for steel reinforcement decreased significantly as shown in Fig. 3 and Fig. 4, respectively. The reason behind this

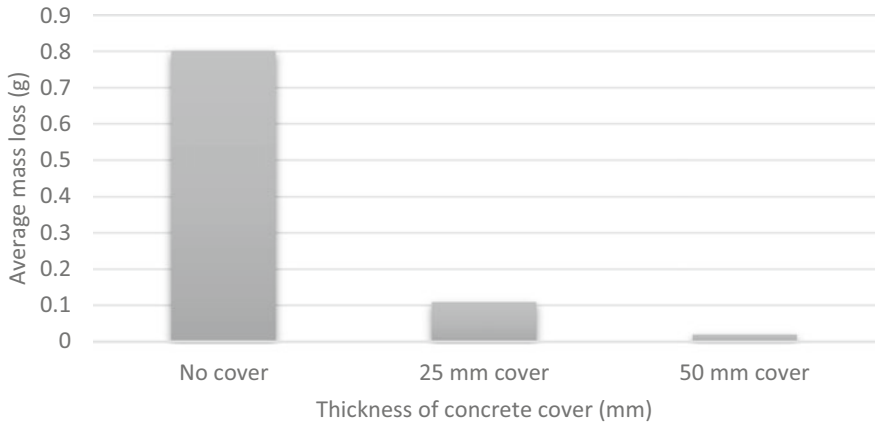

Fig. 3 Variation of average mass loss (g) with thickness of concrete cover (mm)

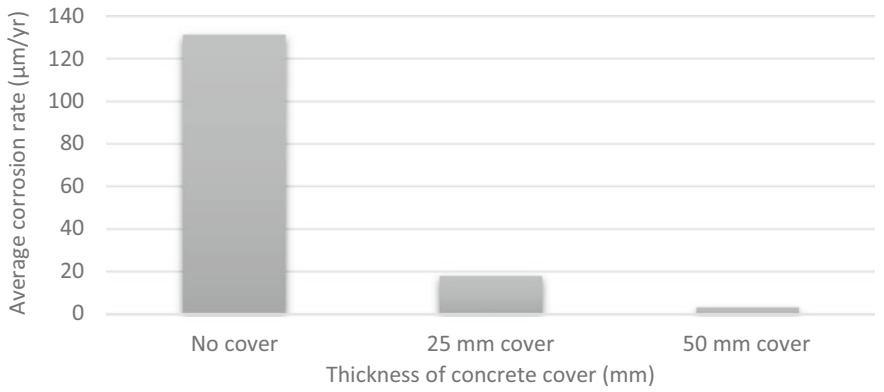

Fig. 4 Variation of average corrosion rate (μm/year) with thickness of concrete cover (mm)

decrease in the corrosion rate is due to the protective nature of the concrete, which increases corrosion initiation and propagation time in steel reinforcement even under extremely corrosive exposure conditions. The high alkalinity content of the concrete surrounding the steel reinforcement acts as a protective layer and the corrosion rate decreases with pH increase.

When reinforced concrete structures are exposed to the marine environment, chloride ions penetrate through the concrete cover and break down the passive layer to initiate corrosion. Structural concrete has three states; solid state (hardened concrete), liquid state (fluid concrete inside) and gas state (air voids in the concrete). The corrosion rate of steel reinforcement is greatly influenced by the thickness of the concrete cover used. The larger the concrete cover, the thicker the fluid concrete layer, and thus, the corrosion proceeds at a slower pace as chlorine ions take more time to diffuse

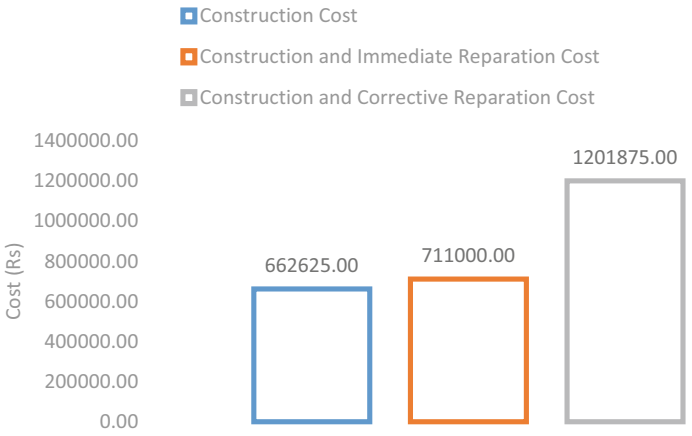

Fig. 5 Cost assessment

the 50 mm cover in order to reach the steel reinforcement than the 25 mm cover. This investigation validates the use of the 50 mm cover to meet the durability requirements for the most severe exposure conditions, i.e., sea-tide conditions. It should be highlighted that a higher quality concrete for cover coupled with an increase in cover thickness would result in a further decrease in mass loss and corrosion rate of embedded steel reinforcement.

The cost assessment proved to be cost-effective only when the cover thickness was increased from 25 to 50 mm for splash and tidal zones during construction. Figure 5 clearly showed that construction costs for protection of steel reinforcement corrosion in coastal structures exposed to splash and tidal zones were significantly lower than the cost of construction and increasing the thickness of concrete cover to 50 mm after concreting of piles has been done.

The construction and corrective repair costs were significantly higher because of the high excavation cost and were therefore not cost-effective. This case study again proved the importance of the studying the corrosion rate of steel reinforcement exposed to different conditions and providing the most economical solution to problems related to corrosion. The cost assessment did not consider transportation, workmanship and equipment-related costs.

4 Conclusion

The aim of this research work was to assess the corrosion of bare and embedded in concrete steel reinforcement exposed to marine environment. It has been successfully achieved though the implementation of the objectives by following a clearly defined and step-by-step methodology. The visual assessment performed on samples exposed to different exposure conditions proved that specimens exposed to tidal zone

showed the first sign of corrosion within the first day of exposure, whereas specimens exposed to submerged zone took almost five days before the first sign of rusting could be seen. The experimental findings showed that the corrosion rate for steel reinforcement exposed to sea-tide zone endured structurally significant metal loss and experienced the highest corrosion rate over the 60-day exposure period. However, steel reinforcement specimens of different diameters exposed to the submerged zone encountered the lowest corrosion rate among the different exposure environments over the same period. The findings also showed that the average corrosion rate of steel samples exposed at Mahebourg correlated with a rate of corrosion experienced in coastal region with moderate level of salinity in the atmosphere. The corrosive activity for this location was high and classified under category C4 corrosion. However, the average corrosion rate of steel specimens exposed at Vacoas corresponded to that of an urban region with moderate level of pollution. The corrosion activity for Vacoas was classified under category C3 corrosion as the corrosive activity is medium. The percentage mass loss for 10 mm diameter bare steel reinforcement exposed to sea tides for a period of 60 days was 0.897% and for steel reinforcement embedded in 25 and 50 mm cover was 0.092% and 0.017%, respectively. The cost assessment was cost-effective when the increase in the cover thickness from 25 to 50 mm for splash and tidal zones was carried out during concreting of piles. The construction and corrective repair costs were approximately two times higher than the cost construction of because of the high cost excavation involved in corrective reparation and was therefore not cost-effective, thereby emphasizing on good knowledge of consulting engineer on the negative effects of exposure to the tidal zone.

5 Recommendations

This research work has been carried out to raise awareness among major stakeholders in the construction industry about the detrimental effect of steel reinforcement corrosion exposed to atmospheric, tidal and submerged zones in the coastal environment. It can be applied to the study of the corrosion rate of steel reinforcement bars in reinforced concrete piles, seawalls, breakwaters and foundations of houses located next to the sea.

The thickness of concrete cover is important for prolonging the durability of buildings. The corrosion activity and category of the environment can be clearly identified using relevant standards and the thickness of concrete cover should be provided with respect to that exposure environment. For example, the tidal and splash zones experienced the highest corrosion rate and the concrete cover thickness would be higher for these exposure zones compared to the atmospheric and submerged zones where the concrete cover thickness could be minimal.

The use of reinforcing materials for example epoxy coated reinforcement, stainless steel reinforcement or galvanized steel reinforcement can be alternative to replacement of carbon steel reinforcement. These alternatives can also be combined with conventional reinforcement to increase economical, durability and sustainability

benefits. These materials are recommended for their corrosion-resistant surface in severe exposure environments such as the tidal and splash zones.

The research work is applicable to study the corrosion of steel reinforcement used to strengthen wooden beams or columns and other structural members. Wooden structures are mostly used in hotel located near coastal areas of the island of Mauritius. Therefore, in addition to repeated wetting and drying cycles, steel reinforcement embedded in wood is affected by the salt spray from seawater, culminating in subsequent loss of the shear and flexural strength of these members and exposure to high temperatures in tropical climate make them susceptible to buckling. The structural integrity of the reinforced wooden structure is affected as the mechanical properties of reinforced timber are dependent on the efficiency of the steel connections and bolts.

Corrosion and pollution are interrelated processes as many particulates are released into the environment by power stations burning fossil fuels contributing to global warming. These pollutants produce corrosion products that in turn accelerate corrosion. Both processes are detrimental as they negatively impact the environment and the longevity of coastal structures and construction materials. These contaminants significantly increase the severity of corrosion in steel and reinforced concrete.

There is a real concern about the impact of global climate change on the corrosive and rapidly deteriorating effects of coastal infrastructure. It leads to higher temperatures that facilitate melting of glaciers and causing a rise in global sea level. This alters atmospheric moisture, depth of tidal and splash zones and rain precipitation patterns and increases the corrosion rate of reinforced concrete structures. Extreme weather conditions such as strong storms and winds and flood events erode the coastal areas and coastal structures are exposed for longer durations to severe environment and that adversely impact on the corrosive behavior of the environment and increase the likelihood of corrosion failures.

The salinity of water in ocean surface has increased drastically because of global warming as higher temperature lead to increased water loss by evaporation whereas the water gained by precipitation is low. However, the NaCl content of seawater varies from 2.0 to 3.5% depending on the location of the sea and addition of fresh river water. The salinity of sea tends to increase during high summer temperatures in tropical climates because of high rate of evaporation and the salt spray in the atmosphere will be more corrosive and affecting most coastal structures.

The sea is a natural system which is always experiencing movements in the form of currents and winds blowing over its surface generating ocean waves that reach the coast. These harsh and destructive waves break down in splash zones and generate a whitish, aerated foam causing local corrosion in reinforced concrete structures. These strong and high waves often slowly erode and are responsible for the severe damages caused to the coast. There is the problem of seawater intrusion due to overpumping of well for water consumption and foundation of structures is exposed to saline water which are more corrosive environments compared to fresh water.

The rapid development of industry, transport and the energy sector has dramatically increased the amount of carbon dioxide in air. This excess carbon dioxide

dissolves in the seawater and decreases the pH and thus creates a more corrosive environment. These carbon dioxide emissions ultimately lead to the production of acid rain, which is beneficial for steel reinforcement corrosion and detrimental to reinforced concrete structures.

Engineers from any disciplines are ethically responsible for the management of corrosion. Structural and civil engineers are completely responsible for taking into consideration the negative impacts of corrosion in building and infrastructure design because they have a direct relationship with social, economic and environmental factors. Understanding corrosion and its detrimental effects will enable engineers to design cost-effective, reliable and safer structures with minimal environmental impact.

Contractors engaged in piling works near the coastal areas should use steel formwork and check that the concrete spacer is positioned firmly in the correct place as it can be readily loosened or broken during the removal of steel formwork, and therefore, the thickness of concrete cover around steel reinforcement may be altered. The consultant should make the contractor aware of the importance of managing workmanship and materials during the construction of piles and it is the responsibility of the consulting engineer to emphasize the importance to the contracting engineer of using adequate thickness of concrete cover for the tidal zone.

Acknowledgements First and foremost, I would like to express my deepest appreciation to my project coordinator and supervisor Mr. Sailesh Kumar Singh Nunkoo for his valuable guidance and advice with regards to this degree project. He has shown the attitude and the substance of a genius and he always conveyed a spirit of adventure regarding the research project. Without his guidance and persistent help, this dissertation would not have been possible. It is my radiant sentiment to convey my deepest gratitude to the laboratory officers. They always gave prompt replied to my uncertainties during practical sessions. My deepest appreciation is expressed to my family and friends for their love, motivation, help and support during my four years of study.

References

1. Snow DA (2003) Plant engineer's reference book, 2nd edn. Butterworth-Heinemann, Oxford
2. Surnam BYR, Chocalingum A (2011) A survey on the inhibition of atmospheric corrosion in Mauritius. Univ Mauritius Res J 17(1):410
3. Surnam BYR (2013) Prevention and cost of atmospheric corrosion in Mauritius. Anti-Corrosion Methods Mater 60(2):73–83
4. Keulemans G (2016) The problem with reinforced concrete. University of New South Wales
5. Fernandez I, Herrador MF, Mari A, Bairán JM (2016) Structural effects of steel reinforcement corrosion on statically indeterminate reinforced concrete members. Mater Struct 49(12):4959–4973
6. BS 7545 (1991) Method for removal of corrosion products from corrosion test specimens of metals and alloys. British Standards Institution, UK
7. ASTM (2003) Standard practice for preparing, cleaning and evaluating corrosion tests specimens. American Society for Testing and Materials, USA

8. Alcántara J, De La Fuente D, Chico B, Simancas J, Díaz I, Morcillo M (2017) Marine atmospheric corrosion of carbon steel: a review. Materials 10(4):406
9. Surnam BYR, Chetty VO (2009) Investigations on atmospheric corrosion of low carbon steel in Mauritius through mass loss and 2D. Univ Mauritius Res J 15(1):157–168